



UNIVERSITEIT VAN PRETORIA
UNIVERSITY OF PRETORIA
YUNIBESITHI YA PRETORIA

SCHOOL OF ENGINEERING

ENHANCEMENT OF THE THERMAL PERFORMANCE OF SOLAR HEAT EXCHANGERS WITH POROUS INSERTS

By

Louis Cramer

Submitted in partial fulfilment of the requirements for the degree of

MASTER OF ENGINEERING

DEPARTMENT OF MECHANICAL AND AERONAUTICAL ENGINEERING

Mechanical Engineering in the Faculty of Engineering, Built Environment and Information
Technology

UNIVERSITY OF PRETORIA

December 2017

Supervisor: Dr. G.I. Mahmood

Co-supervisor: Prof J. P. Meyer

ABSTRACT

ENHANCEMENT OF THE THERMAL PERFORMANCE OF SOLAR HEAT EXCHANGERS WITH POROUS INSERTS.

Author: Louis Cramer
Supervisor: Dr G. I. Mahmood
Co-supervisor: Prof J. P. Meyer
Department: Mechanical and Aeronautical Engineering
Degree: Master of Engineering (Mechanical Engineering)

Keywords: Solar, porous, sinusoidal, screen insert, heat exchangers

For high thermal performance and effectiveness, the flat plate heat exchangers and cooling channels are designed based on the three basic criteria: (i) small heat transfer area or large surface area to volume ratio, (ii) high heat transfer rate, and (iii) small pumping power. Numerous amounts of research have been dedicated to the notion of enhancing the convective heat transfer inside the channels of a heat exchanger. Recently, the internal porous fins and porous foams of high thermal conductivity have gained considerable attentions in the research and development for their light weight, reduced fluid pumping power requirements, and high heat transfer characteristics. The results from the investigations show the enhancement of heat transfer coefficients and friction factors with the wavy screens relative to those in a smooth channel. This experimental research project aims to investigate the effects of the geometrical properties such the amplitude, period, and porosity of wavy porous mesh screen insert may have on the thermal performance of a heat exchanger and quantify the thermal performance of the channel employing the wavy porous screens for a wide range of applications at low to high Reynolds numbers. The friction factors, and heat transfer are measured in a rectangular channel when sinusoidal screen inserts are employed as turbulence promoters. The screen is made from porous mesh of flat metal screen available commercially. Two mesh screens are employed; one with a 68% porosity and one with a 48% porosity. Both mesh screens have a square shape pore and is delivered as a spool of material. The period of the screen is bent into the wavy mesh screen using a jig with two jaws. The screen wave vector is placed normal to the mean flow of the channel and allowed the peaks of the wave to make only line contact with the two larger side walls of the rectangular channel. The inlet Reynolds number for the experiments covered all three flow regimes: laminar, transition and turbulent. The measurements include the static pressure drop and wall temperature distributions along the channel. For the heat transfer experiments, the parallel walls of the channel touching the screen peaks are heated with a constant heat flux to simulate the channels in a flat plate heat exchanger. Heat transfer experiments are also

obtained with one heated wall with a constant heat flux to simulate the conditions of a single channel heat exchanger employed in solar heaters and electronic cooling. Baseline data in a smooth channel without the screen inserts are also measured for comparisons with the data obtained in the same channel with the screen insert. The results on friction factors and heat transfer coefficients are then presented as ratios of data from the screen channel to the smooth channel to provide the performance of the screen channel relative to the smooth channel. The data and ratios are also presented in such a manner that the effect of change in porosity, period and amplitude of the screen insert could be studied. The sinusoidal screen inserts in the channels of a flat plate heat exchanger can provide desirable effects on the heat transfer enhancements ($Nu/Nu_0 > 1.0$) only for the range of Reynolds number tested. The wire diameter of the mesh screen can significantly influence the thermal performance and pressure penalty provided by the wavy screen based on the present investigations and Mahmood et al. [18]. The present results are thus beneficial to the design of porous inserts for the heat exchangers operating over a wide range of flow rates. The effects of screen porosity and wave period are strong only on the efficiency index. The present results thus indicate the viability of the wavy porous inserts for the heat exchangers.

ACKNOWLEDGEMENTS

The authors would like to thank the following for their contribution and support during the process of completing this dissertation:

- my Lord and saviour Jesus Christ for giving me the talent and endurance to complete this task,
- my friends and family for supporting me and helping me in my endeavours,
- my supervisor Dr G.I. Mahmood for his supervision and guidance,
- the University of Pretoria and NRF for their financial support and facilities, and
- Chris Govender and Donald Keetse for their assistance and guidance in the laboratories.

CONTENTS

Abstract.....	i
Acknowledgements.....	iii
List of Figures	ix
List of Tables	xiii
Nomenclature	xv
Greek Letters	xv
Subscripts and Superscripts	xv
1 Introduction	1
1.1 Literature Studied	4
1.2 Conclusion.....	10
2 Literature study	12
2.1 Introduction.....	12
2.2 Non-dimensionless Numbers.....	12
2.2.1 <i>Reynolds Number</i>	12
2.2.2 <i>Nusselt Number</i>	12
2.2.3 <i>Friction Factor</i>	13
2.2.4 <i>Prandtl Number</i>	13
2.3 Thermal Entrance Length	14
2.4 Flow Regimes.....	14
2.4.1 <i>Laminar Flow</i>	14
2.4.2 <i>Turbulent Flow</i>	16
2.4.3 <i>Transitional Flow</i>	17
2.5 Numerical Simulations	18
2.5.1 <i>Data Block One – Geometry, PDE’s, Models, Units, and Fluid</i>	19
2.5.2 <i>Data Block Two – Boundary Conditions</i>	19
2.5.3 <i>Data Block Three – Integration and Print Control</i>	20
2.5.4 <i>Data Block Four – Initial Conditions – Internal Flow</i>	20
2.6 Conclusion.....	20
3 Experiment.....	22
3.1 Introduction.....	22
3.2 Experiment setup.....	22

3.2.1	<i>Test Channel and Instrumentation</i>	22
3.2.2	<i>Mesh-bender Geometry</i>	25
3.2.3	<i>Air-Screen Geometry</i>	27
3.3	<i>Instrumentation</i>	29
3.3.1	<i>Power Supplies</i>	29
3.3.2	<i>Pressure Transducers</i>	29
3.3.3	<i>Orifice Plates</i>	29
3.3.4	<i>Thermocouples</i>	30
3.3.5	<i>Data Logger</i>	30
3.3.6	<i>Multimeters</i>	30
3.4	<i>Data Reduction</i>	30
3.5	<i>Data Acquisition</i>	33
3.6	<i>Uncertainty</i>	34
3.7	<i>Conclusion</i>	37
4	<i>Results</i>	38
4.1	<i>Introduction</i>	38
4.2	<i>Validation</i>	38
4.2.1	<i>Pressure Drop</i>	38
4.2.2	<i>Two-Wall Heating</i>	41
4.2.3	<i>One-Wall Heating</i>	44
4.3	<i>Pressure Drop</i>	46
4.3.1	<i>14-mm Channel</i>	47
4.3.2	<i>5-mm Channel</i>	55
4.4	<i>Two Wall Heating</i>	61
4.4.1	<i>14-mm Channel</i>	62
4.4.2	<i>5-mm Channel</i>	71
4.5	<i>One Wall Heating</i>	77
4.5.1	<i>14-mm Channel</i>	77
4.5.2	<i>5-mm Channel</i>	85
4.6	<i>Thermal Performance Index</i>	91
4.6.1	<i>14-mm Channel</i>	91
4.6.2	<i>5-mm Channel</i>	99
4.7	<i>Summary</i>	108

5	Conclusion and Recommendations	110
5.1	Summary	110
5.2	Conclusion.....	111
5.3	Recommendations.....	114
Appendices		A-1
Appendix A: Numerical Simulation.....		A-1
	<i>Sample Code</i>	A-2
Appendix B: Calibration		B-5
	<i>B.1. Introduction</i>	B-5
	<i>B.2. Thermocouple calibration</i>	B-5
	<i>B.3. Pressure transducer calibration</i>	B-5
Appendix C: Uncertainty Analysis		C-8
	<i>Uncertainties: Sample Calculations</i>	C-13
	<i>Friction factor and pressure drop uncertainties for $Re = 400$</i>	C-13
	<i>Nu Sample Calculation for location 1</i>	C-14
Appendix D: Pressure Drop Data		D-16
	<i>5 mm Channel height - mesh 4.1</i>	D-16
	<i>5 mm Channel height – mesh 4.3</i>	D-22
	<i>5 mm Channel height – mesh 5.1</i>	D-28
	<i>5 mm Channel height – mesh 5.3</i>	D-34
	<i>14 mm Channel height – mesh 2.1</i>	D-40
	<i>14 mm Channel height – mesh 2.3</i>	D-44
Appendix E: Two Wall Heat Transfer Data		E-49
	<i>5 mm Channel height – mesh 4.1</i>	E-49
	<i>5 mm Channel height – mesh 4.3</i>	E-55
	<i>5 mm Channel height – mesh 5.1</i>	E-61
	<i>5 mm Channel height – mesh 5.3</i>	E-67
	<i>14 mm Channel height – mesh 2.1</i>	E-73
	<i>14 mm Channel height – mesh 2.3</i>	E-77
Appendix F: One Wall Heat Transfer Data		F-82
	<i>5 mm Channel height – mesh 4.1</i>	F-82
	<i>5 mm Channel height – mesh 4.3</i>	F-88
	<i>5 mm Channel height – mesh 5.1</i>	F-94

5 mm Channel height – mesh 5.3..... F-100
14 mm Channel height – mesh 2.1 F-106
14 mm Channel height – mesh 2.3..... F-110

LIST OF FIGURES

Figure 2.1: The four different flow regimes in terms of the Nusselt number against Reynolds number.....	17
Figure 3.1: (a) Schematic of experimental setup, elevation view, and (b) pressure tap location	23
Figure 3.2: (a) Plane view of thermocouple tip locations along test plate (dimensions in mm), (b) elevation view of thermocouples in test plate and (c) test section wall heater arrangement (not drawn to scale)	25
Figure 3.3: Mesh-bender geometry showing (a) the profile of the mesh bending jaw and (b) the mesh-bender assembled	27
Figure 3.4: Pore shape of mesh (a) 68% porosity mesh and (b) 48% porosity mesh	28
Figure 3.5: An Example of a mesh screen showing: (a) Image of the actual sinusoidal screen, and (b) schematic of the screen sinusoidal wave in YZ-plane, $\lambda = 12$ mm or 18 mm and $H = 5$ mm or 14 mm (X: mean flow direction).....	28
Figure 3.6: Uncertainty estimates as Re varies (a) ΔP^* , f , and Re uncertainties for pressure drop experiments, and (b) Nu (one wall heating and two wall heating) uncertainties and wall temperature uncertainties at a location $x/L < 0.4$ and a location $x/L > 0.6$ for one wall and two wall heating.	36
Figure 4.1: Baseline pressure drop distributions vs. X/L in smooth channel for (a) 14 mm channel height and (b) 5 mm channel height.	39
Figure 4.2: Baseline theoretical friction factor compared to experimental friction factor for experimental setup validation for 14 mm channel height	40
Figure 4.3: Baseline theoretical friction factor compared to experimental friction factor for experimental setup validation for 5 mm channel height	40
Figure 4.4: Baseline theoretical Nusselt numbers compared to experimental average Nusselt numbers (two-wall heating) for experimental setup validation for 14 mm channel height.....	42
Figure 4.5: Baseline theoretical Nusselt numbers compared to experimental average Nusselt numbers (two-wall heating) for experimental setup validation for 5 mm channel height.....	43
Figure 4.6: Baseline theoretical Nusselt numbers compared to experimental average Nusselt numbers (one-wall heating) for experimental setup validation for 14 mm channel height.....	44
Figure 4.7: Baseline theoretical Nusselt numbers compared to experimental average Nusselt numbers (one-wall heating) for experimental setup validation for 5 mm channel height.....	45

Figure 4.8: Normalised pressure drop data for Mesh 2.1 (irregular period - 68% porosity) and Mesh 3.1 (12 mm period - 68% porosity) versus X/L for (a) Laminar and early transitional regimes and (b) Turbulent regime	48
Figure 4.9: Normalised pressure drop data for Mesh 2.3 (irregular period - 48% porosity) and Mesh 3.3 (12 mm period - 48% porosity) versus X/L for (a) Laminar and early transitional regimes and (b) Turbulent regime	49
Figure 4.10: Friction factor (f) versus Reynolds number (Re) for Mesh 1.1 (22 mm period - 68% porosity), Mesh 2.1 (irregular period - 68% porosity) and Mesh 3.1 (12 mm period - 68% porosity).....	50
Figure 4.11: Friction factor (f) versus Reynolds number (Re) for Mesh 1.3 (22 mm period - 48% porosity), Mesh 2.3 (irregular period - 48% porosity) and Mesh 3.3 (12 mm period - 48% porosity).....	50
Figure 4.12: Friction factor ratio (f/f_0) versus Reynolds number (Re) for Mesh 1.1 (22 mm period - 68% porosity), Mesh 2.1 (irregular period - 68% porosity) and Mesh 3.1 (12 mm period - 68% porosity).....	52
Figure 4.13: Friction factor ratio (f/f_0) versus Reynolds number (Re) for Mesh 1.3 (22 mm period - 48% porosity), Mesh 2.3 (irregular period - 48% porosity) and Mesh 3.3 (12 mm period - 48% porosity).....	53
Figure 4.14: Normalised pressure drop data for 5 mm channel for Re = 1 000, 1 400, 3 000, 4 000, 11 000 for (a) Mesh 4.1 (68% porosity – 18 mm period), (b) Mesh 4.3 (48% porosity – 18 mm period), (c) Mesh 5.1 (68% porosity – 12 mm period), and (d) Mesh 5.3 (48% porosity – 12 mm period)*	58
Figure 4.15: Friction factor (f) versus Reynolds number (Re) for 5 mm channel height.....	59
Figure 4.16: f/f_0 ratio versus Reynolds number (Re) for 5 mm channel height.....	59
Figure 4.17: Local Nusselt number values along the X/L of the test section for (a) laminar and (b) turbulent region.....	63
Figure 4.18: Local Nusselt number values along the X/L of the test section for (a) laminar and (b) turbulent region.....	64
Figure 4.19: Average Nusselt number for Mesh 1.1 (22 mm period – 68% porosity), Mesh 2.1 (irregular period - 68% porosity) and Mesh 3.1 (12 mm period - 68% porosity) as Reynolds number varies	66
Figure 4.20: Average Nusselt number for Mesh 1.3 (22 mm period – 48% porosity), Mesh 2.3 (irregular period - 48% porosity) and Mesh 3.3 (12 mm period - 48% porosity) as Reynolds number varies	66
Figure 4.21: Average Nu/Nu_0 ratio for Mesh 1.1 (22 mm period – 68% porosity), Mesh 2.1 (irregular period - 68% porosity) and Mesh 3.1 (12 mm period - 68% porosity) as Reynolds number varies.....	67
Figure 4.22: Average Nu/Nu_0 ratio for Mesh 1.3 (22 mm period – 48% porosity), Mesh 2.3 (irregular period - 48% porosity) and Mesh 3.3 (12 mm period - 48% porosity) as Reynolds number varies.....	68

Figure 4.23: Local Nusselt numbers for various Reynolds numbers for two-wall heating boundary condition, 5-mm channel height: (a) Mesh 4.1 (18 mm period - 68% porosity), (b) Mesh 4.3 (18 mm period - 48% porosity), (c) Mesh 5.1 (12 mm period - 68% porosity), and (d) Mesh 5.3 (12 mm period - 48% porosity).....74

Figure 4.24: Average Nusselt number as Reynolds number varies for two-wall heating boundary condition comparing, 5-mm channel height75

Figure 4.25: Nu/Nu_0 ratio as Reynolds number varies for two-wall heating boundary condition comparing, 5-mm channel height: (a) Mesh 4.1 and Mesh 5.1, (b) Mesh 4.3 and Mesh 5.3, (c) Mesh 4.1 and Mesh 4.3, and (d) Mesh 5.1 and Mesh 5.3.....75

Figure 4.26: Local Nusselt number values along the X/L of the test section for 14 mm channel height and one-wall heating: (a) laminar and (b) turbulent region79

Figure 4.27: Local Nusselt number values along the X/L of the test section for 14 mm channel height and one-wall heating: (a) laminar and (b) turbulent region80

Figure 4.28: Average Nusselt number, Nu_{avg} for Mesh 1.1 (22 mm period – 68% porosity), Mesh 2.1 (irregular period - 68% porosity) and Mesh 3.1 (12 mm period - 68% porosity) as Reynolds number varies in 14 mm channel height and with one-wall heating.81

Figure 4.29: Average Nusselt number, Nu_{avg} for Mesh 1.3 (22 mm period – 48% porosity), Mesh 2.3 (irregular period - 48% porosity) and Mesh 3.3 (12 mm period - 48% porosity) as Reynolds number varies in 14 mm channel height and with one-wall heating81

Figure 4.30: Nu/Nu_0 ratio for Mesh 1.1 (22 mm period – 68% porosity), Mesh 2.1 (irregular period - 68% porosity) and Mesh 3.1 (12 mm period - 68% porosity) as Reynolds number varies82

Figure 4.31: Nu/Nu_0 ratio for Mesh 1.3 (22 mm period – 48% porosity), Mesh 2.3 (irregular period - 48% porosity) and Mesh 3.3 (12 mm period - 48% porosity) as Reynolds number varies82

Figure 4.32: Local Nusselt numbers for various Reynolds numbers for one-wall heating boundary condition: (a) Mesh 4.1 (18 mm period - 68% porosity), (b) Mesh 4.3 (18 mm period - 48% porosity), (c) Mesh 5.1 (12 mm period - 68% porosity), and (d) Mesh 5.3 (12 mm period - 48% porosity).....88

Figure 4.33: Average Nusselt number as Reynolds number varies for one-wall heating boundary condition88

Figure 4.34: Nu/Nu_0 ratio as Reynolds number varies for one-wall heating boundary89

Figure 4.35: Thermal performance index for one heated wall as Reynolds number varies in 14 mm channel height comparing: (a) Mesh 1.1, Mesh 2.1 and Mesh 3.1 (68% porosity screens- 22 mm, irregular, and 12 mm wave period, respectively), (b) Mesh 1.3, Mesh 2.3 and Mesh 3.3 (48% porosity screens- 22 mm, irregular, and 12 mm wave period, respectively), (c) Mesh 1.1 and Mesh 1.3 (22 mm period- 68% and 48% porosity, respective), and (d) Mesh 3.1 and Mesh 3.3 (12 mm period- 68% and 48% porosity, respective).95

Figure 4.36: Thermal efficiencies for two heated wall in 14 mm channel height as Reynolds number varies comparing: (a) Mesh 1.1, Mesh 2.1 and Mesh 3.1 (68% porosity screens-

22 mm, irregular, and 12 mm wave period, respectively), (b) Mesh 1.3, Mesh 2.3 and Mesh 3.3 (48% porosity screens- 22 mm, irregular, and 12 mm wave period, respectively), (c) Mesh 1.1 and Mesh 1.3 (22 mm period- 68% and 48% porosity, respective), and (d) Mesh 3.1 and Mesh 3.3 (12 mm period- 68% and 48% porosity, respective).....	98
Figure 4.37: Thermal performance index for one heated wall in 5 mm channel height as Reynolds number varies comparing: (a) Mesh 4.1 and Mesh 5.1 (68% porosity- 18 mm and 12 mm period, respectively), (b) Mesh 4.3 and Mesh 5.3 (48% porosity- 18 mm and 12 mm period, respectively), (c) Mesh 4.1 and Mesh 4.3 (18 mm period- 68% and 48% porosity, respectively), and (d) Mesh 5.1 and Mesh 5.3 (12 mm period- 68% and 48% porosity, respectively).....	101
Figure 4.38: Thermal performance index for two heated walls in 5mm channel height as Reynolds number varies comparing: (a) Mesh 4.1 and Mesh 5.1 (68% porosity- 18 mm and 12 mm period, respectively), (b) Mesh 4.3 and Mesh 5.3 (48% porosity- 18 mm and 12 mm period, respectively), (c) Mesh 4.1 and Mesh 4.3 (18 mm period- 68% and 48% porosity, respectively), and (d) Mesh 5.1 and Mesh 5.3 (12 mm period- 68% and 48% porosity, respectively).....	104
Figure 4.39: Thermal efficiencies for two heated walls as Reynolds number and channel height vary comparing: (a) Mesh 5.1 and Mesh 3.1 (68% porosity- 12 mm period- 5 mm and 14 mm channel height, respectively), and (b) Mesh 3.3 and Mesh 5.3 (48% porosity- 12 mm period- 5 mm and 14 mm channel height, respectively).....	105
Figure 4.40: Thermal efficiencies for one heated wall as Reynolds number and channel height vary comparing: (a) Mesh 5.1 and Mesh 3.1 (68% porosity- 12 mm period- 5 mm and 14 mm channel height, respectively), and (b) Mesh 3.3 and Mesh 5.3 (48% porosity- 12 mm period- 5 mm and 14 mm channel height, respectively).....	107
Figure B.1: Calibration curves for: (a) 10 inches of water differential pressure transducer, (b) 5 inches of water differential pressure transducer, (c) 2 inches of water differential pressure transducer and (d) 0.5 inches of water differential pressure transducer	B-6
Figure C.1: Uncertainty estimates as Re varies (a) ΔP^* , f, and Re uncertainties for pressure drop experiments, and (b) Nu and Re uncertainties for heat transfer experiments	C-12
Figure D.1: Channel Pressure for mesh 4.1 and Re = 400	D-16
Figure D.2: Channel Pressure for mesh 4.1 and Re = 600	D-16
Figure D.3: Channel Pressure for mesh 4.1 and Re = 1 000	D-17
Figure D.4: Channel Pressure for mesh 4.1 and Re = 1 400	D-17
Figure D.5: Channel Pressure for mesh 4.1 and Re = 3 000	D-18
Figure D.6: Channel Pressure for mesh 4.1 and Re = 4 000	D-18
Figure D.7: Channel Pressure for mesh 4.1 and Re = 5 000	D-19
Figure D.8: Channel Pressure for mesh 4.1 and Re = 6 000	D-19
Figure D.9: Channel Pressure for mesh 4.1 and Re = 7 000	D-20

Figure D.10: Channel Pressure for mesh 4.1 and $Re = 8\,000$	D-20
Figure D.11: Channel Pressure for mesh 4.1 and $Re = 9\,000$	D-21
Figure D.12: Channel Pressure for mesh 4.1 and $Re = 11\,000$	D-21
Figure D.13: Channel Pressure for mesh 4.3 and $Re = 400$	D-22
Figure D.14: Channel Pressure for mesh 4.3 and $Re = 600$	D-22
Figure D.15: Channel Pressure for mesh 4.3 and $Re = 1\,000$	D-23
Figure D.16: Channel Pressure for mesh 4.3 and $Re = 1\,400$	D-23
Figure D.17: Channel Pressure for mesh 4.3 and $Re = 3\,000$	D-24
Figure D.18: Channel Pressure for mesh 4.3 and $Re = 4\,000$	D-24
Figure D.19: Channel Pressure for mesh 4.3 and $Re = 5\,000$	D-25
Figure D.20: Channel Pressure for mesh 4.3 and $Re = 6\,000$	D-25
Figure D.21: Channel Pressure for mesh 4.3 and $Re = 7\,000$	D-26
Figure D.22: Channel Pressure for mesh 4.3 and $Re = 8\,000$	D-26
Figure D.23: Channel Pressure for mesh 4.3 and $Re = 9\,000$	D-27
Figure D.24: Channel Pressure for mesh 4.3 and $Re = 11\,000$	D-27
Figure D.25: Channel Pressure for mesh 5.1 and $Re = 400$	D-28
Figure D.26: Channel Pressure for mesh 5.1 and $Re = 600$	D-28
Figure D.27: Channel Pressure for mesh 5.1 and $Re = 1\,000$	D-29
Figure D.28: Channel Pressure for mesh 5.1 and $Re = 1\,400$	D-29
Figure D.29: Channel Pressure for mesh 5.1 and $Re = 3\,000$	D-30
Figure D.30: Channel Pressure for mesh 5.1 and $Re = 4\,000$	D-30
Figure D.31: Channel Pressure for mesh 5.1 and $Re = 5\,000$	D-31
Figure D.32: Channel Pressure for mesh 5.1 and $Re = 6\,000$	D-31
Figure D.33: Channel Pressure for mesh 5.1 and $Re = 7\,000$	D-32
Figure D.34: Channel Pressure for mesh 5.1 and $Re = 8\,000$	D-32
Figure D.35: Channel Pressure for mesh 5.1 and $Re = 9\,000$	D-33
Figure D.36: Channel Pressure for mesh 5.1 and $Re = 11\,000$	D-33
Figure D.37: Channel Pressure for mesh 5.3 and $Re = 400$	D-34
Figure D.38: Channel Pressure for mesh 5.3 and $Re = 600$	D-34
Figure D.39: Channel Pressure for mesh 5.3 and $Re = 1\,000$	D-35
Figure D.40: Channel Pressure for mesh 5.3 and $Re = 1\,400$	D-35
Figure D.41: Channel Pressure for mesh 5.3 and $Re = 3\,000$	D-36
Figure D.42: Channel Pressure for mesh 5.3 and $Re = 4\,000$	D-36

Figure D.43: Channel Pressure for mesh 5.3 and $Re = 5\,000$	D-37
Figure D.44: Channel Pressure for mesh 5.3 and $Re = 6\,000$	D-37
Figure D.45: Channel Pressure for mesh 5.3 and $Re = 7\,000$	D-38
Figure D.46: Channel Pressure for mesh 5.3 and $Re = 8\,000$	D-38
Figure D.47: Channel Pressure for mesh 5.3 and $Re = 9\,000$	D-39
Figure D.48: Channel Pressure for mesh 5.3 and $Re = 11\,000$	D-39
Figure D.49: Channel Pressure for mesh 2.1 and $Re = 400$	D-40
Figure D.50: Channel Pressure for mesh 2.1 and $Re = 1\,000$	D-40
Figure D.51: Channel Pressure for mesh 2.1 and $Re = 3\,000$	D-41
Figure D.52: Channel Pressure for mesh 2.1 and $Re = 5\,000$	D-41
Figure D.53: Channel Pressure for mesh 2.1 and $Re = 7\,000$	D-42
Figure D.54: Channel Pressure for mesh 2.1 and $Re = 10\,000$	D-42
Figure D.55: Channel Pressure for mesh 2.1 and $Re = 16\,000$	D-43
Figure D.56: Channel Pressure for mesh 2.1 and $Re = 24\,000$	D-43
Figure D.57: Channel Pressure for mesh 2.1 and $Re = 30\,000$	D-44
Figure D.58: Channel Pressure for mesh 2.3 and $Re = 400$	D-44
Figure D.59: Channel Pressure for mesh 2.3 and $Re = 1\,000$	D-45
Figure D.60: Channel Pressure for mesh 2.3 and $Re = 3\,000$	D-45
Figure D.61: Channel Pressure for mesh 2.3 and $Re = 5\,000$	D-46
Figure D.62: Channel Pressure for mesh 2.3 and $Re = 7\,000$	D-46
Figure D.63: Channel Pressure for mesh 2.3 and $Re = 10\,000$	D-47
Figure D.64: Channel Pressure for mesh 2.3 and $Re = 16\,000$	D-47
Figure D.65: Channel Pressure for mesh 2.3 and $Re = 24\,000$	D-48
Figure D.66: Channel Pressure for mesh 2.3 and $Re = 30\,000$	D-48
Figure E.1: Wall and mean air temperatures for mesh 4.1 under two-heated wall boundary condition at $Re = 400$	E-49
Figure E.2: Wall and mean air temperatures for mesh 4.1 under two-heated wall boundary condition at $Re = 600$	E-49
Figure E.3: Wall and mean air temperatures for mesh 4.1 under two-heated wall boundary condition at $Re = 1\,000$	E-50
Figure E.4: Wall and mean air temperatures for mesh 4.1 under two-heated wall boundary condition at $Re = 1\,400$	E-50
Figure E.5: Wall and mean air temperatures for mesh 4.1 under two-heated wall boundary condition at $Re = 3\,000$	E-51

Figure E.6: Wall and mean air temperatures for mesh 4.1 under two-heated wall boundary condition at $Re = 4\ 000$	E-51
Figure E.7: Wall and mean air temperatures for mesh 4.1 under two-heated wall boundary condition at $Re = 5\ 000$	E-52
Figure E.8: Wall and mean air temperatures for mesh 4.1 under two-heated wall boundary condition at $Re = 6\ 000$	E-52
Figure E.9: Wall and mean air temperatures for mesh 4.1 under two-heated wall boundary condition at $Re = 7\ 000$	E-53
Figure E.10: Wall and mean air temperatures for mesh 4.1 under two-heated wall boundary condition at $Re = 8\ 000$	E-53
Figure E.11: Wall and mean air temperatures for mesh 4.1 under two-heated wall boundary condition at $Re = 9\ 000$	E-54
Figure E.12: Wall and mean air temperatures for mesh 4.1 under two-heated wall boundary condition at $Re = 11\ 000$	E-54
Figure E.13: Wall and mean air temperatures for mesh 4.3 under two-heated wall boundary condition at $Re = 400$	E-55
Figure E.14: Wall and mean air temperatures for mesh 4.3 under two-heated wall boundary condition at $Re = 600$	E-55
Figure E.15: Wall and mean air temperatures for mesh 4.3 under two-heated wall boundary condition at $Re = 1\ 000$	E-56
Figure E.16: Wall and mean air temperatures for mesh 4.3 under two-heated wall boundary condition at $Re = 1\ 400$	E-56
Figure E.17: Wall and mean air temperatures for mesh 4.3 under two-heated wall boundary condition at $Re = 3\ 000$	E-57
Figure E.18: Wall and mean air temperatures for mesh 4.3 under two-heated wall boundary condition at $Re = 4\ 000$	E-57
Figure E.19: Wall and mean air temperatures for mesh 4.3 under two-heated wall boundary condition at $Re = 5\ 000$	E-58
Figure E.20: Wall and mean air temperatures for mesh 4.3 under two-heated wall boundary condition at $Re = 6\ 000$	E-58
Figure E.21: Wall and mean air temperatures for mesh 4.3 under two-heated wall boundary condition at $Re = 7\ 000$	E-59
Figure E.22: Wall and mean air temperatures for mesh 4.3 under two-heated wall boundary condition at $Re = 8\ 000$	E-59
Figure E.23: Wall and mean air temperatures for mesh 4.3 under two-heated wall boundary condition at $Re = 9\ 000$	E-60
Figure E.24: Wall and mean air temperatures for mesh 4.3 under two-heated wall boundary condition at $Re = 11\ 000$	E-60

Figure E.25: Wall and mean air temperatures for mesh 5.1 under two-heated wall boundary condition at $Re = 400$	E-61
Figure E.26: Wall and mean air temperatures for mesh 5.1 under two-heated wall boundary condition at $Re = 600$	E-61
Figure E.27: Wall and mean air temperatures for mesh 5.1 under two-heated wall boundary condition at $Re = 1\ 000$	E-62
Figure E.28: Wall and mean air temperatures for mesh 5.1 under two-heated wall boundary condition at $Re = 1\ 400$	E-62
Figure E.29: Wall and mean air temperatures for mesh 5.1 under two-heated wall boundary condition at $Re = 3\ 000$	E-63
Figure E.30: Wall and mean air temperatures for mesh 5.1 under two-heated wall boundary condition at $Re = 4\ 000$	E-63
Figure E.31: Wall and mean air temperatures for mesh 5.1 under two-heated wall boundary condition at $Re = 5\ 000$	E-64
Figure E.32: Wall and mean air temperatures for mesh 5.1 under two-heated wall boundary condition at $Re = 6\ 000$	E-64
Figure E.33: Wall and mean air temperatures for mesh 5.1 under two-heated wall boundary condition at $Re = 7\ 000$	E-65
Figure E.34: Wall and mean air temperatures for mesh 5.1 under two-heated wall boundary condition at $Re = 8\ 000$	E-65
Figure E.35: Wall and mean air temperatures for mesh 5.1 under two-heated wall boundary condition at $Re = 9\ 000$	E-66
Figure E.36: Wall and mean air temperatures for mesh 5.1 under two-heated wall boundary condition at $Re = 11\ 000$	E-66
Figure E.37: Wall and mean air temperatures for mesh 5.3 under two-heated wall boundary condition at $Re = 400$	E-67
Figure E.38: Wall and mean air temperatures for mesh 5.3 under two-heated wall boundary condition at $Re = 600$	E-67
Figure E.39: Wall and mean air temperatures for mesh 5.3 under two-heated wall boundary condition at $Re = 1\ 000$	E-68
Figure E.40: Wall and mean air temperatures for mesh 5.3 under two-heated wall boundary condition at $Re = 1\ 400$	E-68
Figure E.41: Wall and mean air temperatures for mesh 5.3 under two-heated wall boundary condition at $Re = 3\ 000$	E-69
Figure E.42: Wall and mean air temperatures for mesh 5.3 under two-heated wall boundary condition at $Re = 4\ 000$	E-69
Figure E.43: Wall and mean air temperatures for mesh 5.3 under two-heated wall boundary condition at $Re = 5\ 000$	E-70

Figure E.44: Wall and mean air temperatures for mesh 5.3 under two-heated wall boundary condition at $Re = 6\,000$	E-70
Figure E.45: Wall and mean air temperatures for mesh 5.3 under two-heated wall boundary condition at $Re = 7\,000$	E-71
Figure E.46: Wall and mean air temperatures for mesh 5.3 under two-heated wall boundary condition at $Re = 8\,000$	E-71
Figure E.47: Wall and mean air temperatures for mesh 5.3 under two-heated wall boundary condition at $Re = 9\,000$	E-72
Figure E.48: Wall and mean air temperatures for mesh 5.3 under two-heated wall boundary condition at $Re = 11\,000$	E-72
Figure E.49: Wall and mean air temperatures for mesh 2.1 under two-heated wall boundary condition at $Re = 400$	E-73
Figure E.50: Wall and mean air temperatures for mesh 2.1 under two-heated wall boundary condition at $Re = 1\,000$	E-73
Figure E.51: Wall and mean air temperatures for mesh 2.1 under two-heated wall boundary condition at $Re = 3\,000$	E-74
Figure E.52: Wall and mean air temperatures for mesh 2.1 under two-heated wall boundary condition at $Re = 4\,000$	E-74
Figure E.53: Wall and mean air temperatures for mesh 2.1 under two-heated wall boundary condition at $Re = 6\,000$	E-75
Figure E.54: Wall and mean air temperatures for mesh 2.1 under two-heated wall boundary condition at $Re = 10\,000$	E-75
Figure E.55: Wall and mean air temperatures for mesh 2.1 under two-heated wall boundary condition at $Re = 16\,000$	E-76
Figure E.56: Wall and mean air temperatures for mesh 2.1 under two-heated wall boundary condition at $Re = 24\,000$	E-76
Figure E.57: Wall and mean air temperatures for mesh 2.1 under two-heated wall boundary condition at $Re = 30\,000$	E-77
Figure E.58: Wall and mean air temperatures for mesh 2.3 under two-heated wall boundary condition at $Re = 400$	E-77
Figure E.59: Wall and mean air temperatures for mesh 2.3 under two-heated wall boundary condition at $Re = 1\,000$	E-78
Figure E.60: Wall and mean air temperatures for mesh 2.3 under two-heated wall boundary condition at $Re = 3\,000$	E-78
Figure E.61: Wall and mean air temperatures for mesh 2.3 under two-heated wall boundary condition at $Re = 4\,000$	E-79
Figure E.62: Wall and mean air temperatures for mesh 2.3 under two-heated wall boundary condition at $Re = 6\,000$	E-79

Figure E.63: Wall and mean air temperatures for mesh 2.3 under two-heated wall boundary condition at $Re = 10\,000$	E-80
Figure E.64: Wall and mean air temperatures for mesh 2.3 under two-heated wall boundary condition at $Re = 16\,000$	E-80
Figure E.65: Wall and mean air temperatures for mesh 2.3 under two-heated wall boundary condition at $Re = 24\,000$	E-81
Figure E.66: Wall and mean air temperatures for mesh 2.3 under two-heated wall boundary condition at $Re = 30\,000$	E-81
Figure F.1: Wall and mean air temperatures for mesh 4.1 under one-heated wall boundary condition at $Re = 400$	F-82
Figure F.2: Wall and mean air temperatures for mesh 4.1 under one-heated wall boundary condition at $Re = 600$	F-82
Figure F.3: Wall and mean air temperatures for mesh 4.1 under one-heated wall boundary condition at $Re = 1\,000$	F-83
Figure F.4: Wall and mean air temperatures for mesh 4.1 under one-heated wall boundary condition at $Re = 1\,400$	F-83
Figure F.5: Wall and mean air temperatures for mesh 4.1 under one-heated wall boundary condition at $Re = 3\,000$	F-84
Figure F.6: Wall and mean air temperatures for mesh 4.1 under one-heated wall boundary condition at $Re = 4\,000$	F-84
Figure F.7: Wall and mean air temperatures for mesh 4.1 under one-heated wall boundary condition at $Re = 5\,000$	F-85
Figure F.8: Wall and mean air temperatures for mesh 4.1 under one-heated wall boundary condition at $Re = 6\,000$	F-85
Figure F.9: Wall and mean air temperatures for mesh 4.1 under one-heated wall boundary condition at $Re = 7\,000$	F-86
Figure F.10: Wall and mean air temperatures for mesh 4.1 under one-heated wall boundary condition at $Re = 8\,000$	F-86
Figure F.11: Wall and mean air temperatures for mesh 4.1 under one-heated wall boundary condition at $Re = 9\,000$	F-87
Figure F.12: Wall and mean air temperatures for mesh 4.1 under one-heated wall boundary condition at $Re = 11\,000$	F-87
Figure F.13: Wall and mean air temperatures for mesh 4.3 under one-heated wall boundary condition at $Re = 400$	F-88
Figure F.14: Wall and mean air temperatures for mesh 4.3 under one-heated wall boundary condition at $Re = 600$	F-88
Figure F.15: Wall and mean air temperatures for mesh 4.3 under one-heated wall boundary condition at $Re = 1\,000$	F-89

Figure F.16: Wall and mean air temperatures for mesh 4.3 under one-heated wall boundary condition at $Re = 1\,400$	F-89
Figure F.17: Wall and mean air temperatures for mesh 4.3 under one-heated wall boundary condition at $Re = 3\,000$	F-90
Figure F.18: Wall and mean air temperatures for mesh 4.3 under one-heated wall boundary condition at $Re = 4\,000$	F-90
Figure F.19: Wall and mean air temperatures for mesh 4.3 under one-heated wall boundary condition at $Re = 5\,000$	F-91
Figure F.20: Wall and mean air temperatures for mesh 4.3 under one-heated wall boundary condition at $Re = 6\,000$	F-91
Figure F.21: Wall and mean air temperatures for mesh 4.3 under one-heated wall boundary condition at $Re = 7\,000$	F-92
Figure F.22: Wall and mean air temperatures for mesh 4.3 under one-heated wall boundary condition at $Re = 8\,000$	F-92
Figure F.23: Wall and mean air temperatures for mesh 4.3 under one-heated wall boundary condition at $Re = 9\,000$	F-93
Figure F.24: Wall and mean air temperatures for mesh 4.3 under one-heated wall boundary condition at $Re = 11\,000$	F-93
Figure F.25: Wall and mean air temperatures for mesh 5.1 under one-heated wall boundary condition at $Re = 400$	F-94
Figure F.26: Wall and mean air temperatures for mesh 5.1 under one-heated wall boundary condition at $Re = 600$	F-94
Figure F.27: Wall and mean air temperatures for mesh 5.1 under one-heated wall boundary condition at $Re = 1\,000$	F-95
Figure F.28: Wall and mean air temperatures for mesh 5.1 under one-heated wall boundary condition at $Re = 1\,400$	F-95
Figure F.29: Wall and mean air temperatures for mesh 5.1 under one-heated wall boundary condition at $Re = 3\,000$	F-96
Figure F.30: Wall and mean air temperatures for mesh 5.1 under one-heated wall boundary condition at $Re = 4\,000$	F-96
Figure F.31: Wall and mean air temperatures for mesh 5.1 under one-heated wall boundary condition at $Re = 5\,000$	F-97
Figure F.32: Wall and mean air temperatures for mesh 5.1 under one-heated wall boundary condition at $Re = 6\,000$	F-97
Figure F.33: Wall and mean air temperatures for mesh 5.1 under one-heated wall boundary condition at $Re = 7\,000$	F-98
Figure F.34: Wall and mean air temperatures for mesh 5.1 under one-heated wall boundary condition at $Re = 8\,000$	F-98

Figure F.35: Wall and mean air temperatures for mesh 5.1 under one-heated wall boundary condition at $Re = 9\ 000$	F-99
Figure F.36: Wall and mean air temperatures for mesh 5.1 under one-heated wall boundary condition at $Re = 11\ 000$	F-99
Figure F.37: Wall and mean air temperatures for mesh 5.3 under one-heated wall boundary condition at $Re = 400$	F-100
Figure F.38: Wall and mean air temperatures for mesh 5.3 under one-heated wall boundary condition at $Re = 600$	F-100
Figure F.39: Wall and mean air temperatures for mesh 5.3 under one-heated wall boundary condition at $Re = 1\ 000$	F-101
Figure F.40: Wall and mean air temperatures for mesh 5.3 under one-heated wall boundary condition at $Re = 1\ 400$	F-101
Figure F.41: Wall and mean air temperatures for mesh 5.3 under one-heated wall boundary condition at $Re = 3\ 000$	F-102
Figure F.42: Wall and mean air temperatures for mesh 5.3 under one-heated wall boundary condition at $Re = 4\ 000$	F-102
Figure F.43: Wall and mean air temperatures for mesh 5.3 under one-heated wall boundary condition at $Re = 5\ 000$	F-103
Figure F.44: Wall and mean air temperatures for mesh 5.3 under one-heated wall boundary condition at $Re = 6\ 000$	F-103
Figure F.45: Wall and mean air temperatures for mesh 5.3 under one-heated wall boundary condition at $Re = 7\ 000$	F-104
Figure F.46: Wall and mean air temperatures for mesh 5.3 under one-heated wall boundary condition at $Re = 8\ 000$	F-104
Figure F.47: Wall and mean air temperatures for mesh 5.3 under one-heated wall boundary condition at $Re = 9\ 000$	F-105
Figure F.48: Wall and mean air temperatures for mesh 5.3 under one-heated wall boundary condition at $Re = 11\ 000$	F-105
Figure F.49: Wall and mean air temperatures for mesh 2.1 under one-heated wall boundary condition at $Re = 400$	F-106
Figure F.50: Wall and mean air temperatures for mesh 2.1 under one-heated wall boundary condition at $Re = 1\ 000$	F-106
Figure F.51: Wall and mean air temperatures for mesh 2.1 under one-heated wall boundary condition at $Re = 3\ 000$	F-107
Figure F.52: Wall and mean air temperatures for mesh 2.1 under one-heated wall boundary condition at $Re = 4\ 000$	F-107
Figure F.53: Wall and mean air temperatures for mesh 2.1 under one-heated wall boundary condition at $Re = 10\ 000$	F-108

Figure F.54: Wall and mean air temperatures for mesh 2.1 under one-heated wall boundary condition at $Re = 16\ 000$	F-108
Figure F.55: Wall and mean air temperatures for mesh 2.1 under one-heated wall boundary condition at $Re = 24\ 000$	F-109
Figure F.56: Wall and mean air temperatures for mesh 2.1 under one-heated wall boundary condition at $Re = 30\ 000$	F-109
Figure F.57: Wall and mean air temperatures for mesh 2.3 under one-heated wall boundary condition at $Re = 400$	F-110
Figure F.58: Wall and mean air temperatures for mesh 2.3 under one-heated wall boundary condition at $Re = 1\ 000$	F-110
Figure F.59: Wall and mean air temperatures for mesh 2.3 under one-heated wall boundary condition at $Re = 3\ 000$	F-111
Figure F.60: Wall and mean air temperatures for mesh 2.3 under one-heated wall boundary condition at $Re = 4\ 000$	F-111
Figure F.61: Wall and mean air temperatures for mesh 2.3 under one-heated wall boundary condition at $Re = 6\ 000$	F-112
Figure F.62: Wall and mean air temperatures for mesh 2.3 under one-heated wall boundary condition at $Re = 10\ 000$	F-112
Figure F.63: Wall and mean air temperatures for mesh 2.3 under one-heated wall boundary condition at $Re = 16\ 000$	F-113
Figure F.64: Wall and mean air temperatures for mesh 2.3 under one-heated wall boundary condition at $Re = 24\ 000$	F-113
Figure F.65: Wall and mean air temperatures for mesh 2.3 under one-heated wall boundary condition at $Re = 30\ 000$	F-114

LIST OF TABLES

Table 2.1: Laminar Nusselt number correlations	15
Table 2.2: Laminar friction factor correlations	16
Table 2.3: Turbulent Nusselt number correlations	17
Table 2.4: Turbulent friction factor correlations	18
Table 3.1: Instrumentation uncertainties	34
Table 4.1: Percentage error of experimental friction factor data compared to theoretical correlations for 14 mm channel height	41
Table 4.2: Percentage error of experimental friction factor data compared to theoretical correlations for 5 mm channel height	41
Table 4.3: Percentage error of experimental Nusselt number data (two-wall heating, Baseline) compared to theoretical correlations for 14 mm channel height	43
Table 4.4: Percentage error of experimental Nusselt number data (two-wall heating, Baseline) compared to theoretical correlations for 5 mm channel height	44
Table 4.5: Percentage error of experimental Nusselt number data (one-wall heating, Baseline) compared to theoretical correlations for 14 mm channel height	46
Table 4.6: Percentage error of experimental Nusselt number data (one-wall heating, Baseline) compared to theoretical correlations for 5 mm channel height	46
Table 4.7: Pressure drop experimental test matrix	46
Table 4.8: Friction factor and f/f_0 ratio correlations for various screen inserts tests in 14 mm channel	54
Table 4.9: Friction factor and f/f_0 ratio correlations for various screen inserts tests in 5 mm channel	60
Table 4.10: Two-wall heat transfer experimental test matrix	62
Table 4.11: The increase and decrease in Nu/Nu_0 ratios from Reynolds number 400 to 30 000 for two-wall heating and 14 mm channel height	68
Table 4.12: Average Nusselt number and Nu/Nu_0 ratio correlations for various screen inserts in 14 mm channel	69
Table 4.13: Average Nusselt number and Nu/Nu_0 ratio correlations for 5 mm channel height - two-wall heating	76
Table 4.14: One-wall heat transfer experimental test matrix	77
Table 4.15: Average Nusselt number and Nu/Nu_0 ratio correlations for various screen inserts tests in 14 mm channel	83
Table 4.16: Average Nusselt number and Nu/Nu_0 ratio correlations for 5 mm channel height - one-wall heating	90

Table 4.17: Summary of the influence of geometrical properties of the sinusoidal screen insert on the thermal performance index as Reynolds number is constant..... 109

Table 4.18: Summary of the percentage change of friction factor and Nusselt number for the irregular screen (change in period of 55%) as Reynolds number is constant 109

Table A.1: TEXSTAN flags and variables A-1

Table B.1: Thermocouple calibration curves..... B-6

NOMENCLATURE

A_c = channel cross-sectional area
 A_s = surface area
 C = discharge coefficient of the orifice plate
 C_p = constant pressure specific heat of air
 d = inner diameter of the orifice plate
 D_h = hydraulic diameter
 f = Darcy friction factor
 H = height of test section
 k = thermal conductivity
 L_p = length of test section
 m_a = air-mass flow rate
 Nu = Nusselt number
 P = pressure
 Q = power from heated surface
 Re = Reynolds number
 T = temperature
 V_a = mean flow velocity
 W = width of test section
(X, Y, Z) = Cartesian coordinate system

GREEK LETTERS

β = beta value of the orifice plate
 Δ = difference between two quantities
 ϵ = expansion factor
 ρ_a = air density
 μ_a = Dynamic viscosity of air

SUBSCRIPTS AND SUPERSRIPTS

* = normalised value
a = air property
b = bulk property
C = convective
ex = exit location of test section
in = inlet location of test section
ins = insulation property
l = loss
m = local bulk-mean temperature of air
T = total
w = local wall temperature

x = local measurement location along the wall in X-direction
 0 = reference value or local total pressure

1 INTRODUCTION

Passages of the modern heat exchangers, cooling jackets of machine components, cooling base of fuel cells and electronic components, solar heater panels, and photovoltaic modules often employ special wall structures internal fins, porous metal foams, and mesh inserts to increase the heat transfer surface area and flow turbulence that aid in the convective heat transfer. For high thermal performance and effectiveness, the flat plate heat exchangers and cooling channels are designed based on the three basic criteria: (i) small heat transfer area or large surface area to volume ratio, (ii) high heat transfer rate, and (iii) small pumping power. Numerous amounts of research have been dedicated to the notion of enhancing the convective heat transfer inside the channels of a heat exchanger. The channels are often equipped with elements (like, surface roughness, porous metal foams, brushes, pin type geometries, and swirl generators) to enhance the convective heat transfer inside the channel at low Reynolds numbers [1]. Recently, the internal porous fins and porous foams of high thermal conductivity have gained considerable attentions in the research and development for their light weight, reduced fluid pumping power requirements, and high heat transfer characteristics. The porous materials in the channels are treated as the fins because of the significant surface contact the material makes with the channel walls. The purpose of such an element is to promote the formation of turbulent flow in each flow channel by causing flow instability near the channel wall. However, this enhancement of convective heat transfer comes at a penalty; the turbulence promoters cause high pressure drop because they provide large flow blockage across the heat exchanger channel than a channel without such turbulence promoters at the same Reynolds number. Hence, the enhancement of heat transfer relative to the pumping power known as the thermal performance suffers. As a result, the employment of porous fins and foams is sometimes unsuitable in the low Reynolds number applications. The present research investigates the wavy porous screens in a heat transfer channel as an alternative to the porous foams and fins. The wave vectors of the screen are arranged parallel to the channel mean flow and channel walls. The tips of the wave make only line contacts with the walls along the channel without any bond as such the screen does not contribute to the extended-surface heat transfer. This adds a structural addition inside the passage without changing the wall structural design of the existing heat exchangers and provide structural support to the channel walls. They can be easily modified and exchanged without altering the channel structure. The pores in the thin screen volume are perpendicular to the flow direction. The bulk of the fluid then flows between the screen walls of the wave. The pores serve as the turbulence promoters on the screen surface to increase the convection heat transfer in the channel. The wave structure of the screen at the contact locations with the channel also provide the structural support to the walls which can be beneficial for some flat-plate and annular channel heat exchanger applications.

The effects of different configurations of surface roughness and internal fins on the convective heat transfer, flow structure, and pressure drop in channels have been summarized by Webb and Kim [1]. The channel internal structures augment both the heat

transfer and pressure penalty as explained by [1] due to the formation of local flow unsteadiness and agitated boundary layer near the channel walls. Augmentations of the heat transfer at the channel wall and pressure drop along the channel filled with the porous foams are investigated by [2-9] in the recent years. The foam materials fill in the channel flow space either partially or completely as a single block or multiple sections in the investigations. The results in [2-7] are provided for low Reynolds numbers with varying porosities of the materials and show both the convection heat transfer coefficients and pressure drop increase along the channel significantly with the porous foams and reduced porosity. The researches of [8-10] report that the material and thickness of porous matrix embedded in channel influence the flow temperature uniformity and pressure penalty of the channel. The pore geometry of packed bed in a two-dimensional channel is optimized by [11] to affect the thermal boundary layer on the walls and maximize the heat transfer coefficient. The periodic arrangements of the porous fins and baffles between parallel walls of two-dimensional channels investigated by [12-14] report the enhancement of the heat transfer coefficients with some reduction in the friction factor relative to the solid fins and baffles. The thermal performance of the study [12-14] is dependent on the fin or baffle geometry and porosity. The investigations of [15, 16] employ the metal mesh screens in multiple layers as inserts perpendicular to the flow direction to augment the heat transfer coefficients with the minimal effects on the pressure drop in tubes. The mesh inserts of [15, 16] increase the heat transfer by undulating the flow velocity near the wall unlike the extended fin surfaces.

Kays and London [17] provide experimental friction factors and heat transfer coefficients in a narrow parallel channel with perforated wavy fins of porosity 16%. The tips of the fin-wave are soldered to the channel walls. The flow passes between the fin walls unlike the other porous fins and foams mentioned earlier. Mahmood et al. [18] report the thermal performance in a rectangular channel employing a sinusoidal screen of high porosity for low Reynolds number applications. The wave vector of the screen in [18] is parallel to the flow, but makes only line contacts with the channel walls. The investigations of [19] show the perforations in flat-plate parallel to the channel flow induce local turbulence. The heat transfer enhancements with the small increase in friction factors in [17, 18] can be explained by such local flow perturbations [19] formed by the small pores.

The present investigations employ various wavy porous screens of different porosities and different wave periods in a rectangular channel and measure the heat transfer coefficients and friction factors as the flow Reynolds number ranges from the laminar to turbulent, and as such are different from [18]. The results from the investigations show the enhancement of heat transfer coefficients and friction factors with the wavy screens relative to those in a smooth channel. The objectives are to quantify the thermal performance of the channel employing the wavy porous screens for a wide range of applications at low to high Reynolds numbers. Unlike the porous foams and fins, the results presented here are independent of the material of the wavy screen that does not serve as fins due to the line contacts with the channel walls as indicated earlier. Also, due to the arrangements of the screen-wave vectors parallel to flow, the pore structures contribute minimally to the bulk

flow resistance. Thus, the thermal performance of the channel with the screen insert will be measured. The thermal performance in a channel is an estimation of the increase of convection heat transfer with the increase of pumping power employing the turbulators, all relative to a smooth channel. The wavy porous mesh-insert will be placed inside the channel in such a way that the sinusoidal wave period is normal to the mean flow direction. The wave patterns follow the sinusoidal period and are formed from the commercial grade flat porous screen mesh. The peak-to-peak height of the wave is either 5 mm or 14 mm. The porosity and periodicity of the screen are also varied to form ten wave patterns:

- Mesh 1.1 – 22 mm period, 68% porosity and 14 mm height
- Mesh 2.1 – Irregular period (varying between 12 mm and 22 mm), 68% porosity and 14 mm height
- Mesh 3.1 – 12 mm period, 68% porosity and 14 mm height
- Mesh 1.3 – 22 mm period, 48% porosity and 14 mm height
- Mesh 2.3 – Irregular period (varying between 12 mm and 22 mm), 48% porosity and 14 mm height
- Mesh 3.3 – 12 mm period, 48% porosity and 14 mm height
- Mesh 4.1 – 18 mm period, 68% porosity and 5 mm height
- Mesh 5.1 – 12 mm period, 68% porosity and 5 mm height
- Mesh 4.3 – 18 mm period, 48% porosity and 5 mm height
- Mesh 5.3 – 12 mm period, 48% porosity and 5 mm height

The wave peaks of the screen only make line contacts with channel walls along the wave vector and are not soldered to the walls. The axes of the screen pores are then normal to the flow direction providing the minimum resistance to the bulk flow unlike porous metal foams. The screen insert acts as a means of a wall support in a flat plate heat exchanger where the wave peaks contact the walls. Because of the line contacts the wavy screen insert is not an extended surface for the convective heat transfer. The results measured in the present investigation are thus independent of the material of the screen employed. The objectives of the present research are to enhance the convective heat transfer in the channel with the minimal increase in the pressure drop, and thus, increase the thermal performance of the heat exchanger and cooling channels in the heat recovery unit of the HVAC system, solar panel, photovoltaic cells, fuel cells, electronic and machine components, and casing of the high speed motor. The thermal performance is a very significant design parameter for the heat transfer effectiveness, size, and pumping power requirements of the heat exchanger and cooling channels. The results are thus expected to contribute to the optimum thermal design and in the reduction of operating costs of the flat plate heat exchangers.

1.1 LITERATURE STUDIED

1.1.1 Chen, C-C., Huang, P-C., and Hwang, H-Y. [2]

These numerical investigations are conducted for enhancement of forced convection using metal-foam porous layers in a horizontal channel heated from multiple discrete sources on the bottom wall. The enhancement of heat transfer is characterised by the thermos-flow fields inside the porous regions and the models are based on local thermal non-equilibrium. The investigation parameters included the effect of Reynolds number, porosity, pore density, fibre diameter, and various metal foam materials with different effective thermal conductivity. The results of the study found that a lower porosity open-cell aluminium foam has a mean Nusselt number about two times larger than the higher porosity open-cell aluminium foam. However, the enhancement in heat transfer is always accompanied with increase in pressure drop; and this pressure drop is higher at the higher pore density, lower permeability, smaller porosity, or fibre diameter.

1.1.2 Lu, W., Zhang, T., and Yang, M. [4]

An analytical study is conducted to identify the forced convection flow and heat transfer characteristics of partially filled parallel-plate channels with metallic foams. The analytical simulation is configured in such a way as to derive solutions for fully developed flow and convection heat transfer in the entire plate channel including both the foam filled region and the non-foam region. The solution found the effect of porosity to be; a higher porosity has a lower heat transfer performance due to its higher thermal resistance of heat conduction through the metal foam and lower flow resistance. The optimum porosity, making the largest Nusselt number, is identified to be $H = 0,1$ or $H = 0,6$, where H is the height ratio of metal foam height to the channel height. The influence of Reynolds number on Nusselt number is shown to be proportionally dependent, meaning as the Reynolds number increases the Nusselt number increases as the convective heat transfer is enhanced. Finally, the effect of pore density on pressure drop is evaluated and the solution found the pressure drop increases with the increase of pore density, but the increase rate reduces with high pore density.

1.1.3 Park, S-H., Kim, T. H., and Jeong, J. H. [5]

The experimental investigations in this work are conducted to evaluate the heat transfer characteristics and convective heat transfer coefficient of open-cell porous metal fins in channels. The experiments are varied over a working fluid range of 0.007-0.17 m/s and a pore density of the porous metal fin of 20, 40 and 80 pores per inch. Through regression analysis of the Nusselt number data obtained the following empirical correlation is obtained:

$$Nu = 0.039Re^{0.8}Pr^{0.4} \quad (1.1)$$

This new correlation is adapted from the Dittus-Boelter equation and demonstrates the heat transfer characteristics of porous metal fins as a function of Reynolds number.

1.1.4 Wang, B., Hong, Y., Hou, X., Xu, Z., Wang, P., Fang, X., and Ruan, X. [6]

In this work, a novel gradient porous material (GPM)-filled pipe structure is proposed and numerically studied. Both the pore-size gradient and porosity gradient are investigated to correlate their relationship on the heat transfer and pressure drop of fluid flowing through gradient porous material filled pipe structures. The effects GPMs may have are compared with those under the conditions of non-porous materials and homogeneous porous materials (HPMs) as controls. Four GPM configurations are studied with a dimensionless radius of the porous material (R_p) being 0.6 and 1.0. The four GPM configuration considered are:

- (1) The GPM has a porosity gradient along the axial direction of the pipe.
- (2) The GPM has a porosity gradient along the radial direction of the pipe.
- (3) The GPM has a pore-size gradient along the axial direction of the pipe.
- (4) The GPM has a pore-size gradient along the radial direction of the pipe.

The numerical study revealed that there is an appropriate GPM configuration with a particular R_p to enhance the heat transfer with a reduced friction factor in comparison with conventional HPM configurations.

1.1.5 Kim, S.Y., Paek, J. W., and Kang, B. H. [7]

This experimental study investigated the effect of porous fins with different porosities and permeabilities on the pressure drop and heat transfer characteristics in plate-fin heat exchangers. The performance of porous fins is compared to those of conventional louvered fins. The experiments are conducted with 6 different porous fins of pore densities of 10, 20 and 40 and porosities of 0.89, 0.92, 0.94 and 0.96. Each porous fin and louvered fin is compared over a Reynolds number range of 100 to 10000. The results indicated that a porous fin has a lower friction factor to that of a louvered fin for low Reynolds numbers but higher friction factors for higher Reynolds numbers. The modified j-factors of porous fins decreased as the porosity of the fin decreased. It is therefore noted that the porous fins studied has similar thermal performance to those of conventional louvered fins. Finally, the results confirmed that low porosity fins are preferable for compactness of plate-porous fin heat exchangers.

1.1.6 Mohammadian, S. K., and Zhang, Y. [8]

Mohammadian et al. numerically investigated the effects of partially utilizing metal and non-metal materials on an air-cooled Lithium-ion battery module heatsink to improve temperature uniformity. A 2-dimensional transient numerical simulation is used to analyse aluminium and aluminium foam conductors and ceramic and ceramic foam insulators. The aluminium foam porosity is 0.85 and the ceramic foam porosity 0.90. The simulation results confirmed that a conducting porous material (aluminium foam) enhanced both the temperature reduction and temperature uniformity inside the airflow channel.

1.1.7 Mohammadian, S. K., Rassoulinejad-Mousavi, S. M., and Zhang, Y. [9]

This work is a continuation of the numerical study found in [8]. In this paper, a three-dimensional transient numerical simulation is used to evaluate the four cases of aluminium metal foam inserts inside the flow channels of an air-cooled Lithium-ion battery module. The effects of porosity and permeability of the porous material on the temperature uniformity and maximum temperature are investigated. The three porosities under investigation are 0.85, 0.90, and 0.95. The results found that decreasing the porosity of the metal foam increases the temperature uniformity and decreases the maximum temperature inside the battery module. The results also suggested that a porosity of 0.85 would be optimal for having a minimum ratio of the standard deviation of the temperature field over maximum temperature inside the battery.

1.1.8 Maerefat, M., Mahmoudi, S. Y., and Mazaheri, [10]

In this work, two porous material inserts are numerically studied to understand their effects on forced convection in a circular pipe. The two configurations considered are: A porous material is inserted at the core of the pipe, and an annulus porous material is attached to the inner wall. The following parameters are investigated to correlate their effect on the Nusselt number: porous thickness, Darcy number, and thermal conductivity. In the first configuration, the numerical study found the optimum porous thickness to maximise the Nusselt number to vary from 0.8 to 0.95 as the value of Darcy number decreased from 10^{-3} to 10^{-6} . The investigations into the second configuration showed the lowest Nusselt number lies at a porous thickness from 0.6 to 0.85 as the value of Darcy number decreases from 10^{-3} to 10^{-6} . The optimum porous thickness at the expense of reasonable pressure drop is found to be 0.6, which maximises the Nusselt number in the first configuration and minimises the Nusselt number in the second configuration.

1.1.9 Hobold, G. M., and da Silva, A. K. [11]

The enhancement of forced convection between uniformly heated parallel plates using saturated packed bed of spheres is investigated to augment heat exchanger performance. The analytical study is performed with three different porous media allocation methods, namely; uniform, 1-D (vertically layered) and 2-D variable porous matrices. The genetic algorithm used suggested that when only uniform or 1-D layered porous media are considered, the most effective way to minimize the maximum temperature is to either have the channel fully filled with high conductive material or leave it empty. Whereas, the 2-D shape function formulation uncovered optimised porous structures to minimise the maximum temperature.

1.1.10 Davari, A., and Maerefat, M. [13]

The following numerical study focused on the analysis of a channel with porous baffles and the effect the porous baffles would have on the fluid flow and heat transfer in the entrance and periodically fully developed regions. Only the laminar region is considered and a local thermal equilibrium model is adopted to evaluate the energy equation for the

solid and fluid temperatures. The porous material parameters considered are; baffle height, baffle spacing, Reynolds number, and thermal conductivity ratio between the porous baffles and the fluid flow field. The results showed that the porous baffles, when compared with a channel without baffles, lead to an increase in Nusselt number. They also revealed that there is an optimum height for reaching higher performance ratios when considering heat transfer and pressure drop.

1.1.11 Santos, N. B., and de Lemos, M. J. S. [14]

Numerical investigations into friction factor and Nusselt number of a channel containing baffles made with solid and porous materials are conducted in this paper. The numerical results are compared with available data and published results to verify the simulation results where within 5%. The simulations are conducted over Reynolds numbers range of 100 to 500 and a porosity of 0.4 and 0.9. The results indicated that for laminar flow and low porosities the porous material baffles has no advantage over solid baffles. However, the results are encouraging enough to motivate for further analyses in the turbulent regime.

1.1.12 Pavel B. I., and Mohamad A. A. [15]

The following experimental work investigated the effect metallic porous matrices, inserted in a pipe, would have on the rate of heat transfer. The experiments investigated the effects porosity and thickness of the porous matrix would have on the heat transfer rate, constant and uniform heat flux, and pressure drop. A Reynolds number range of 1000 – 4500, comprising both the laminar and turbulent regime, is used to compare the results of the porous matrices to the clear flow case where no porous material is inserted. 12 variations of the porous matrices, porosity variation of 96.6 – 99.3%, is investigated. The results showed that improved enhancement can be obtained by using a porous insert with a smaller porosity at a higher expense of pressure drop. The approximate highest increase in Nusselt number is 5.28 times for the fully filled pipe at an expense of a 64.8 Pa pressure drop.

1.1.13 Pavel B. I., and Mohamad A. A [16]

This experimental and numerical research investigated the enhancement of heat transfer in a pipe with a metallic porous material insert when compared to a clear flow case where no porous material is inserted. Twelve different metallic porous mediums are used with varying porosity, porous material diameter and thermal conductivity parameters. Each parameter is evaluated at different Reynolds numbers ($1000 < Re < 5000$) to determine its effect on heat transfer and pressure drop. The experimental investigations revealed that both the porosity and porous material diameter have a positive influence upon the heat transfer and a negative impact on pressure drop. The correlation between the heat transfer in the pipe and the three parameters investigated can be defined as follows: As the diameter of the porous insert approaches that of the diameter of the pipe, the porosity of the insert is decreased and the thermal conductivity if the insert is increased, the enhancement of heat transfer can be improved.

1.1.14 Mahmood, G. I., Simonson, C. J., and Besant, R. W. [18]

Mahmood et al. focused on the experimental investigations into enhancing turbulence and the heat transfer rate within a rectangular cross section air channel with a porous mesh-screen insert with a sinusoidal shape. The effects on heat transfer enhancement with the porous mesh-screen are compared to the same channel without the screen present over a Reynolds number range of 1360 to 3800. The heat transfer measurements are obtained with one or two parallel heated walls at several constant heat fluxes to simulate applications for air channels in flat plate heat exchangers. The results are evaluated using a screen channel heat convection performance index, $(Nu/Nu_0)/(f/f_0)^{1/3}$, where a value greater than 1.0 showed a greater positive enhancement in heat transfer over the penalty incurred in pressure drop. A screen channel heat convection performance index of greater than 1.0 is obtained for $Re > 2500$ and showed the screen insert promotes good mixing of fluid across the channel. This proved that the commercial sinusoidal porous screen insert in the channels of flat plate heat exchangers provides desirable effects on the heat transfer in the transition range.

1.1.15 Torii, S., and Yang, W-J. [19]

This numerical study investigated the unsteady, two-dimensional, incompressible laminar flow over both sides of a slot-perforated flat surface, which is placed in a narrow channel. The simulation studied the effects the ratio of plate thickness to channel width (blockage factor) would have on the heat transfer and the velocity and thermal fields. The simulations are run over a Reynolds number range of 100 to 1200 and three blockage factors of 0.1, 0.2 and 0.5. The simulation results found that an increase in blockage factor saw an increase in heat transfer enhancement whose trend becomes larger in the lower Reynolds number region.

1.1.16 Zimmerer, C., Gschwind, P., Gaiser, G., and Kottke, V. [25]

Zimmerer et al. reported on the effect of different geometrical parameters of corrugated structures on the local and integral heat and mass transfer of heat exchangers. Sinusoidal shaped walls generate the wall corrugation as well as crosswise corrugated cylinders of different cross-section on plane walls. The main geometrical parameters investigated are the inclination angle, the wavelength, the amplitude, and the shape of the corrugation. The experimentation is done over a Reynolds number range of 150 to 10,000, an inclination angle from 10° to 72° , and a wavelength over amplitude ratio of 7.45 or 14.25. For the Reynolds number considered, the smaller inclination angles result in higher mass transfer but a discernible higher pressure drop than the free-flow arrangement. Whereas, the higher inclination angle has a smaller mass transfer and pressure drop than the free-flow arrangement.

1.1.17 Huang, Z. F., Nakayama, A., Yang, K., Yang, C., and Liu, W. [26]

The flow resistance and heat transfer enhancement of porous media inserted in the core of a tube is studied in this paper. Any effect the porous medium may have is investigated at a

constant uniform heat flux over a Reynolds number range extending from the laminar region to the turbulent regime. Three different porosities are investigated in the experiments, namely; 0.951, 0.966, and 0.975. The results confirmed that the convective heat transfer is enhanced using porous inserts at a reasonable penalty of increase in pressure drop especially in the Laminar regime. This shows that enhancing heat transfer by turbulating the core of the flow is a viable enhancement method.

1.1.18 LePoudre, P. P., Simonson, C. J., and Besant, R. W. [27]

The previous work conducted is that of a direct numerical simulation of air flowing through a square channel at a low Reynolds number with a sinusoidal screen insert. The objective of the study is to determine if the sinusoidal screen insert would be an effective method for increasing the heat transfer rate in the channel. The channel, low Reynolds number air flow, and the sinusoidal screen insert are modelled and simulated using Computational Fluid Dynamics (CFD) software. The simulation is run for channel bulk flows of 2.1, 2.6, 3.4, and 4.2 m/s, which resulted in air flow Reynolds numbers – calculated using the hydraulic diameter of the channel – of 1370, 1700, 2220, and 2750 respectively. The results showed that the porous sinusoidal screen insert does, in fact, increase the heat transfer coefficient of the channel flow by destabilizing the flow through the creation of unstable shear layers in the flow. However, the enhancement in heat transfer performance does come at a pressure loss penalty, reducing the overall performance enhancement. Therefore, with modification, the porous sinusoidal screen inserts “can potentially be used as a performance enhancement device in a channel flow heat or mass exchanger”.

1.1.19 Varshney, L., and Saini, J. S. [28]

The goal of this experimental investigation is to develop an experimental correlation which would relate both the heat transfer between the wire mesh and the surrounding air flow as well as the pressure drop in a rectangular solar duct. The investigations covered a wide variety of parameters of the wire mesh screen matrix, namely; wire diameter, pitch, and number of layers. The investigations are carried over a Reynolds number range of 2000 to 10000, a wire diameter range of 0.36 to 0.795 mm, pitch range of 2.08 to 3.19 mm, and 5 to 14 number of layers. All the experimental heat transfer data points are represented by a single straight line represented by the following equation:

$$J_h = 0.647 \left[\frac{1}{nP} \left(\frac{\rho_t}{d_w} \right) \right]^{2.104} Re_p^{-0.55} \quad (1.2)$$

Furthermore, all the experimental friction factor data points are represented by a single straight line represented by the following equation:

$$f_p = 2.484 \left[\frac{1}{nP} \left(\frac{\rho_t}{d_w} \right) \right]^{0.699} Re_p^{-0.44} \quad (1.3)$$

1.2 CONCLUSION

For high thermal performance and effectiveness, the flat plate heat exchangers and cooling channels are designed based on the three basic criteria: (i) small heat transfer area or large surface area to volume ratio, (ii) high heat transfer rate, and (iii) small pumping power. Numerous amounts of research have been dedicated to the notion of enhancing the convective heat transfer inside the channels of a heat exchanger. The channels are often equipped with elements (like, surface roughness, porous metal foams, brushes, pin type geometries, and swirl generators) to enhance the convective heat transfer inside the channel at low Reynolds numbers [1].

Augmentations of the heat transfer at the channel wall and pressure drop along the channel filled with the porous foams are investigated by [2-9] in the recent years. The results in [2-7] are provided for low Reynolds numbers with varying porosities of the materials and show both the convection heat transfer coefficients and pressure drop increase along the channel significantly with the porous foams and reduced porosity. The researches of [8-10] report that the material and thickness of porous matrix embedded in channel influence the flow temperature uniformity and pressure penalty of the channel. The pore geometry of packed bed in a two-dimensional channel is optimized by [11] to affect the thermal boundary layer on the walls and maximize the heat transfer coefficient. The periodic arrangements of the porous fins and baffles between parallel walls of two-dimensional channels investigated by [12-14] report the enhancement of the heat transfer coefficients with some reduction in the friction factor relative to the solid fins and baffles. The thermal performance of the study [12-14] is dependent on the fin or baffle geometry and porosity. The investigations of [15, 16] employ the metal mesh screens in multiple layers as inserts perpendicular to the flow direction to augment the heat transfer coefficients with the minimal effects on the pressure drop in tubes. The mesh inserts of [15, 16] increase the heat transfer by undulating the flow velocity near the wall unlike the extended fin surfaces.

The heat transfer coefficient of flat plate exchangers can be increased using many techniques and methods such as the addition of porous metal foams, porous mesh inserts, perforated plate inserts, porous pin-fins, and porous ribs to name a few inside the exchanger channels. However, the increase in the pressure penalty by these techniques require higher pumping power and operating costs. The effects a wavy porous screen insert on these two factors (convective heat transfer coefficient and pressure penalty) are measured and compared with those in a smooth channel without any porous inserts and internal fins. The enhancement of thermal performance provided by the wavy porous screen in the channel is to be estimated to determine the viability of the screen for replacing the existing porous inserts and internal fins. Through independent tests with different wavy inserts, the effects of the geometrical properties such as the wave amplitude, periodicity of the screen, and porosity of the screen can be quantified. The optimal design of the screen can be obtained, by using the proper combination of the

geometrical properties to obtain the best thermal performance for applications in the flat plate heat exchangers.

This experimental research project aims to investigate the effects of the geometrical properties such the amplitude, period, and porosity of wavy porous mesh screen insert on the thermal performance of a heat exchanger channel. The effects of any changes in the above-mentioned properties on the heat transfer coefficient and the pressure drop will be measured and used to determine the changes in and optimize the thermal performance. This thermal performance can then be used to aid the design of the wavy porous inserts for their applications in the heat exchangers.

2 Literature study

2.1 INTRODUCTION

Heat exchangers employed in solar heaters rely heavily on convective heat transfer to heat or cool the fluid flowing through it. To increase the convective heat transfer to a fluid, the heat transfer coefficient of the fluid must be increased. This can be achieved by inserting a wavy porous meshscreen into the flow channel to ensure the fluid flow never develops; increasing the heat transfer coefficient. In this chapter, previous work and related knowledge required for this topic will be discussed.

2.2 NON-DIMENSIONLESS NUMBERS

2.2.1 REYNOLDS NUMBER

The early work of Osborne Reynolds (1842 – 1912) popularized the use of a dimensionless number that helped to predict similar flow patterns in different fluid flow situations. The concept of the dimensionless number was first introduced by George Gabriel Stokes in 1851 but was only popularized and named after Reynolds in 1883 [35].

The Reynolds number is, in essence, a ratio of the inertia ($\rho V^2/D$) to viscous ($\mu V/D^2$) forces and can be defined by the following equation [36]:

$$Re = \frac{\text{Inertia forces}}{\text{Viscous forces}} = \frac{\rho V D}{\mu} \quad (2.1)$$

When the Reynolds numbers are small, called the laminar flow regime, the viscous forces are large enough to be able to suppress the inertia forces and random fluctuations of the fluid. However, at larger Reynolds numbers the inertia forces are large compared to the viscous forces and are unable to suppress the random fluctuations in the fluid. This is called the turbulent flow regime.

2.2.2 NUSSELT NUMBER

The heat transfer through a fluid layer can either be defined by convective heat transfer or conductive heat transfer. Conductive heat transfer is primarily present in a fluid with no motion and convective heat transfer is present in a fluid layer that has motion. The Nusselt number is the ratio between the convective and conductive heat transfer modes and represents the enhancement of the heat transfer in the fluid layer due to the fluid motion. This dimensionless heat transfer coefficient was named after Wilhelm Nusselt, who made significant contributions to the field of convective heat transfer. The Nusselt number for a parallel plate configuration can be expressed as [30]:

$$Nu_L = \frac{\text{Total heat transfer}}{\text{Conductive heat transfer}} = \frac{hD_h}{k} \quad (2.2)$$

Where D_h represents the hydraulic diameter of the parallel plate system. The hydraulic diameter is defined as [30]:

$$D_h = \frac{4A_c}{P} \quad (2.3)$$

Where A_c is the cross-sectional area of the tube and P is its wetted perimeter. For a rectangular duct (parallel plate configuration) the hydraulic diameter reduces to:

$$D_h = \frac{4ab}{2(a+b)} = \frac{2ab}{a+b} \quad (2.4)$$

2.2.3 FRICTION FACTOR

A quantity just as important as heat transfer in fluid flow is the pressure drop, as it directly relates to the power requirements of a pump. The pressure drop due to viscous effects can be expressed as follows [30]:

$$\Delta P = f \frac{L}{D_h} \frac{\rho V^2}{2} \quad (2.5)$$

There are two methods of determining the friction factor, f , in the equation above, namely; the Darcy friction factor named after Henry Darcy, which is a dimensionless quantity used to describe the friction losses in pipe flow as well as open-channel flow, and the Fanning or skin friction factor. The Darcy friction factor can be defined as follows [30]:

$$f = \frac{8\tau_w}{\rho V^2} \quad (2.6)$$

Whereas the Fanning friction factor, which is four times smaller than the Darcy friction factor, can be expressed as follows [30]:

$$C_f = \frac{2\tau_w}{\rho V^2} = \frac{f}{4} \quad (2.7)$$

2.2.4 PRANDTL NUMBER

The Prandtl number, which is named after the German physicist Ludwig Prandtl, is defined as the ratio of momentum diffusivity to thermal diffusivity. It describes the relative growth of both the velocity boundary layer (δ) and the thermal boundary layer (δ_t). The boundary layer theory was first introduced by Ludwig Prandtl in 1904 and can be defined as:

$$Pr = \frac{\text{Molecular diffusivity of momentum}}{\text{Molecular diffusivity of heat}} = \frac{\nu}{\alpha} = \frac{\mu C_p}{k} \approx \left(\frac{1}{1.026} \frac{\delta}{\delta_t} \right)^3 \quad (2.8)$$

When the Prandtl number is unity, heat and momentum dissipate through a fluid at the same rate; this means that the thermal boundary layer and the velocity boundary layer are

the same thickness. If the Prandtl number is very small ($Pr \ll 1$) like with liquid metals the heat diffuses quickly and the thermal boundary layer is greater than the velocity boundary layer. Whereas with large Prandtl numbers ($Pr \gg 1$) like with oils heat dissipates slowly relative to momentum and the opposite trend in boundary layer thickness is present. The Prandtl number of air is close to that of unity (approximately 0.8 at 20°C) which means heat diffuses at the same rate momentum does through the boundary layer.

2.3 THERMAL ENTRANCE LENGTH

The thermal entrance length can be expressed as the tube length required for the thickness of thermal boundary layer to increase the size of the radius of the tube, also called thermally fully developed flow. The fluid downstream from this point will have a constant axial temperature distribution in a radial direction. This occurs when a fluid of uniform temperature enters onto a surface with a different surface temperature (for example a heated plate at a constant heat flux) the fluid particles in contact with the surface assume the same temperature as the surface through conduction heat transfer. The difference between this surface temperature and the temperature of the fluid at its centreline gives rise to a temperature differential. As the fluid has motion the heat is transferred radially through the fluid through convection. The thermal entrance length in the laminar (L_l) and turbulent (L_t) flow can be theoretically approximated using the following equations [30], [37]:

$$L_l^* = 0.0115439 = \frac{L_l}{ReD_h} \quad (2.9)$$

$$L_t = 10D_h \quad (2.10)$$

2.4 FLOW REGIMES

Fluid flow through channels can be subdivided into three traditional categories, namely; the laminar, transitional, and turbulent flow regimes. These three regimes are briefly discussed in Sections 2.4.1 to 2.4.3.

2.4.1 LAMINAR FLOW

The flow that occurs in the laminar regime is characterised by smooth and steady flow patterns, shown by Osborne Reynolds in his investigation in 1883. Reynolds determined that at sufficiently low velocities the dye streak injected into the flow formed a straight line [38]. A fluid in the laminar regime has the following physical fluid dynamics parameters:

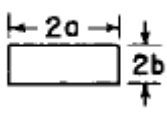
- high momentum diffusion
- low convection heat transfer
- velocity independent of time
- pressure independent of time

The laminar regime, however, can be susceptible to secondary flow and it can play a significant role in heat transfer. It is, therefore, important to distinguish between forced convection and mixed convection.

2.4.1.1 Heat Transfer Correlations

Existing correlations for heat transfer are required to validate the experimental set-up and the data obtained; this is done by direct comparison of the data and existing correlations and numerical data. This section is not a summary of all the laminar Nusselt number correlations, but rather to highlight the most important correlations used to validate the experimental set-up and the data reduction in Chapter 4. Table 2.1 contains the two possible Nusselt number correlations that can be used to validate the Nusselt numbers in the laminar flow regime. The next section (Section 2.5) deals with the numerical comparison and its creation.

Table 2.1: Laminar Nusselt number correlations

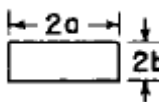
Shah and London [37]	
$Nu_{x,H} = \begin{cases} 1.490(x^*)^{-1/3} & \text{for } x^* \leq 0.0002 \\ 1.490(x^*)^{-1/3} - 0.4 & \text{for } 0.0002 < x^* \leq 0.001 \\ 8.235 + 8.68(10^3 x^*)^{-0.506} e^{-164x^*} & \text{for } x^* > 0.001 \end{cases}$	(2.11)
	(2.12)
	(2.13)
<p>where $x^* = x/D_h Re$</p> <p>For parallel plates, specified wall heat flux distribution, thermally developing flow and a fully developed velocity profile</p> <p>Percentage deviation: (2.11) -0.6% to +0.2%</p> <p>(2.12) ±0.8%</p> <p>(2.13) ±0.6%</p>	
Shah and London [37]	
$Nu_{H1} = 8.235[1 - 2.0421a^* + 3.0853a^{*2} - 2.4765a^{*3} + 1.0578a^{*4} - 0.1861a^{*5}]$	
<p>where $a^* = 2b/2a$</p> 	
<p>For rectangular ducts, specified axial wall heat flux distribution, fully developed thermally and a fully developed velocity profile</p> <p>Percentage deviation: ±0.03%</p>	
Cengel et al. [30]	
$Nu = 8.24$	
<p>For rectangular ducts with a spacing a/b ratio of ∞ and a fully developed laminar velocity profile</p> <p>Percentage deviation: uncertain</p>	

2.4.1.2 Pressure Drop Correlations

Table 2.2 provides the three friction factor correlations that can be used to predict and validate the friction factors in the laminar flow regime. Equations (2.20) and (2.21) were

developed from the basic parallel plate equation (2.18) and are just an adaption for rectangular duct applications.

Table 2.2: Laminar friction factor correlations

Rohsenow and Choi [39]	
$u = 0.5C_1(y^2 - b^2)$	(2.16)
$u_m = -1/3 C_1 b^2$	(2.17)
$fRe = 24$	(2.18)
For parallel plates with a spacing of 2b and a fully developed velocity profile Percentage deviation: uncertain	
Shah and London [37]	
$u_m = -\frac{c_1 a^2}{3} \left[1 - \frac{192}{\pi^5} \left(\frac{a}{b}\right) \sum_{n=1,3,\dots}^{\infty} \frac{1}{n^5} \tanh\left(\frac{n\pi b}{2a}\right) \right]$	(2.19)
$fRe = -\frac{8c_1 a^2}{u_m [1 + (a/b)]^2}$	(2.20)
For rectangular ducts with a spacing of 2b and a fully developed velocity profile Percentage deviation: uncertain	
Shah and London [37]	
$fRe = 24[1 - 1.3553a^* + 1.9467a^{*2} - 1.7012a^{*3} + 0.9564a^{*4} - 0.2537^{*5}]$	(2.21)
where $a^* = 2b/2a$	
	
For rectangular ducts with a spacing of 2b and a fully developed velocity profile Percentage deviation: + 0.05%	
Cengel et al. [30]	
$fRe = 24.00$	(2.22)
Fanning or skin friction factor for rectangular ducts with a spacing a/b ratio of ∞ and a fully developed laminar velocity profile Percentage deviation: uncertain	

2.4.2 TURBULENT FLOW

In his dye experiments, Osborne Reynolds discovered that at high flow rates of a fluid the dye made random and rapid zigzag formations [36]. This showed that at high velocities of the fluid, the fluid motion was highly disordered meaning the velocity of the fluid fluctuated inside the tube. In the turbulent flow regime, the heat transfer mechanism is dominated by forced convection since the fluid motion has enough energy to suppress any secondary flow effects inside the tube. The rapid mixing of particles causes the turbulent regime to have a high heat transfer coefficient.

2.4.2.1 Heat Transfer Correlations

As there are no secondary flow effects and the heat transfer coefficients are insensitive to different types of boundary conditions in the turbulent regime, unlike the laminar regime, it is not necessary to distinguish between the various types of convection and boundary conditions. Some of the correlations used to calculate the Nusselt number and validate the experimental setup and data reduction are given in

Table 2.3. The numerical data used for comparison is also given in Section 2.5.

2.4.2.2 Pressure Drop Correlations

Table 2.4 contains the correlations used to determine the friction factors and validate the experimental setup and data reduction in the turbulent regime.

2.4.3 TRANSITIONAL FLOW

The transition of flow from the laminar regime to the turbulent regime does not occur instantaneously, but over a region of Reynolds numbers called the transitional regime. In this regime, the flow goes from fully laminar (at the start) to fully turbulent (at the end) and alternates between the two in between. This region can be subdivided further into two regions, namely the transition region and the low-Reynolds-number-end region. In the low-Reynolds-number-end region, the flow approaches that of turbulent flow, but is not fully turbulent yet. The Figure 2.1 below summarises the different flow regimes in terms of the Nusselt numbers.

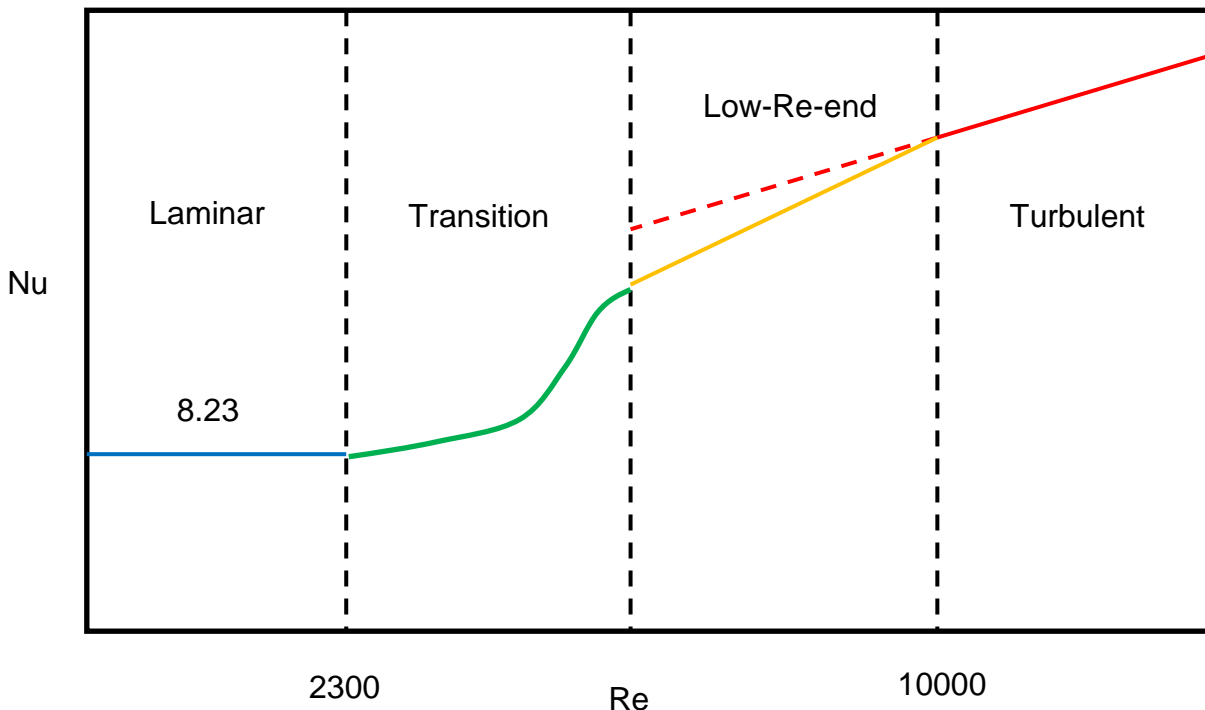


Figure 2.1: The four different flow regimes in terms of the Nusselt number against Reynolds number

Table 2.3: Turbulent Nusselt number correlations

Chilton and Colburn [31]

	$Nu = 0.125fRePr^{\frac{1}{3}}$ <p>where $f = (0.790 \ln Re - 1.64)^{-2}$</p> <p>For fully turbulent flow in smooth tubes and $3000 < Re < 5 \times 10^6$</p> <p>Percentage deviation: uncertain</p>	(2.23)
Colburn [32]	$Nu = 0.023Re^{0.8}Pr^{1/3} \begin{pmatrix} 0.7 \leq Pr \leq 160 \\ Re > 10000 \end{pmatrix}$ <p>For fully turbulent flow in smooth tubes</p> <p>Percentage deviation: uncertain</p>	(2.24)
Dittus and Boelter [33]	$Nu = 0.023Re^{0.8}Pr^n$ <p>where $n = 0.4$ for heating and 0.3 for cooling of the fluid</p> <p>For fully turbulent flow in smooth tubes</p> <p>Percentage deviation: uncertain</p>	(2.25)
Table 2.4: Turbulent friction factor correlations		
Blasius [29]	$f = \frac{0.079}{Re^{0.25}} \quad 3000 < Re < 5 \times 10^6$ <p>Fanning or skin friction factor for fully turbulent flow in smooth tubes</p> <p>Percentage deviation: uncertain</p>	(2.26)
Nikuradse [40]	$\frac{1}{\sqrt{f/2}} = 2.416 \ln(Re\sqrt{f/2}) + 0.3$ <p>Fanning or skin friction factor for fully turbulent flow in smooth tubes</p> <p>Percentage deviation: uncertain</p>	(2.27)
Chen [41]	$\frac{1}{\sqrt{4f}} = -2.0 \log \left\{ \frac{\varepsilon}{3.7065D} - \frac{5.0452}{Re} \log \left[\frac{1}{2.8257} \left(\frac{\varepsilon}{D} \right)^{1.1098} + \frac{5.8506}{Re^{0.8981}} \right] \right\}$ <p>$10^4 < Re < 4 \times 10^8$</p> <p>Fanning or skin friction factor for fully turbulent flow in both smooth and rough tubes</p> <p>Percentage deviation: uncertain</p>	(2.28)

2.5 NUMERICAL SIMULATIONS

The experimental data captured was verified by both the theoretical correlations and numerical simulations. The numerical simulation was performed on the TEXSTAN finite-difference computer code. This software was designed to solve the two-dimensional convective transport of heat, mass, and momentum transfer problems in numerous flow geometries.

To build a TEXSTAN dataset, the geometry and transfer problem needs to be translated into a convective heat, mass and/or momentum problem that TEXSTAN can understand.

The dataset is comprised of the description of the input variables, boundary conditions and flow conditions. The TEXSTAN code requires this information to be written into four data blocks of input variables. These data blocks and their description are given below. The various inputs used for each flow regime and heating case can be found in Appendix A.

2.5.1 DATA BLOCK ONE – GEOMETRY, PDE'S, MODELS, UNITS, AND FLUID

- *kgeom* - flow geometry
- *neq* - number of equations to be solved
- *kstart* - initial definition of initial conditions (TEXSTAN auto-generated profiles or user-supplied experimental profiles)
- *mode* - initial definition of the flow
- *ktmu* - momentum turbulence model (mixing length, one-eqn *k*, or two-eqn *k-ε*)
- *ktmtr* - transition model (abrupt, intermittency, two-eqn) (external flows only)
- *ktme* - energy equation turbulence model (turbulent Prandtl number)
- *kbfor* - source terms for the momentum: pressure gradient (and) body force if free convection
- *jsor(j)* - source terms for each diffusion equation
- *kunits* - units for the physical variables (US Customary Units or SI)
- *kfluid* - fluid physical model (constant properties or variable properties such as air or water or products of combustion, etc.)
- *po* - initial value of the fluid pressure - static for constant properties and stagnation for variable properties (initial temperature variable is read as a part of the input profile construction)
- *rhoc*, *viscoc*, *gam/cp* - if constant properties: density, dynamic viscosity, specific heat
- *prc(j)* - if constant properties: Prandtl or Schmidt number for each diffusion equation being solved

2.5.2 DATA BLOCK TWO – BOUNDARY CONDITIONS

- *nxbc(I)=nxbc(E)* - number of boundary condition (bc) points
- *jbc(I, j)* and *jbc(E, j)* - what type of boundary condition will each diffusion equation have at the I-surface and E-surface
- *x(m)* - *x*-location for each bc point
- *rw(m)=a* - half-height distance (centreline-wall) for parallel-planes channel
- *aux1(m)*, *aux2(m)*, and *aux3(m)* - an opportunity to provide up to three additional arrays of auxiliary information at each *x*-location (refined integration step size, etc.)
- *ubI(m)* - the I-surface momentum equation velocity (no-slip for external flows) at each *x*-location
- *am(I, m)* - the I-surface momentum equation mass flux (transpiration) at each *x*-location

- $fj(I, j, m)$ - the I-surface diffusion equation value at each x -location (for example surface temperature or surface heat flux, etc.)
- $ubE(m)$ - similar velocity for the momentum equation at the E-surface (free stream velocity for external flows and no-slip for internal flows)
- $fj(E, j, m)$ - the E-surface diffusion equation value at each x -location (for example surface temperature or surface heat flux, etc. if internal flows)

2.5.3 DATA BLOCK THREE – INTEGRATION AND PRINT CONTROL

- $xstart$ - the integration starting x location for the solution
- $xend$ - the integration ending x location for the solution
- $deltax$ - (recommended) integration step size
- $fra, enfra$ - (recommended) entrainment control variables (external flows only)
- $kout, kspace$ - which output routine to use and the flag to control print interval
- - flag to permit a more refined integration step size be used for certain x - kdx locations (mostly for internal flows)
- $kent$ - (recommended) additional entrainment control variable (only used for external flows)
- $k1, k2, k3, k4, k5, k6$ - flags $k1$ - $k6$ for special control - $k5$ is most important - causes `ftn.txt` data files to be printed for use with plot packages
- $k7, k8, k9, k10, k11, k12$ - flags $k7$ - $k12$ for special control - $k10$ is most important - controls how velocity and temperature profiles are printed for use with plot packages
- $axx, bxx, cxx, dxx, exx, fxx, gxx$ - special input variables generally linked to the k flags

2.5.4 DATA BLOCK FOUR – INITIAL CONDITIONS – INTERNAL FLOW

- $dyi, rate$ - (recommended) variables for generating the grid for the initial profiles
- $reyn$ - flow hydraulic diameter Reynolds number
- $tref$ - inflow value of the fluid mass-averaged temperature (static)
- $tuapp$ - inflow turbulence intensity
- $epsapp$ - inflow turbulence dissipation if a two-equation turbulence model is used
- $twa11$ - surface temperature to generate a flat initial temperature profile

2.6 CONCLUSION

In this chapter, a few fundamentals concepts, the different flow regimes as well as developing and fully developed flow were discussed. The theory revised covered the fundamental concepts of fluid flow in the different regimes as well as the heat transfer for

fluids in the different regimes. A numerical simulation was also revised and used in validating the smooth channel or baseline data.

3 EXPERIMENT

3.1 INTRODUCTION

The purpose of this chapter is to describe the experimental setup that is used to conduct the pressure drop and heat transfer measurements in a rectangular air channel with and without the porous screen inserts for various air mass flow rates or Reynolds number. The wavy screen is simply placed in the smooth test channel section without any soldering or adhesive when the measurements are obtained with the screen insert. The experimental setup gives an overview of the components materials, and instruments used in the experiments as well as how the test setup is instrumented for various measurements. This chapter also gives the experimental procedure followed to obtain the measurements and how the data is reduced into correct engineering units and normalised values. Finally, the chapter provides an uncertainty analysis of the data captured and data reduction process.

3.2 EXPERIMENT SETUP

3.2.1 TEST CHANNEL AND INSTRUMENTATION

The experimental measurements are obtained through a low-speed air channel test facility. The ambient laboratory air is drawn through the channel and test section using a centrifugal fan. [Figure 3.1 \(a\)](#) shows a schematic of the test setup and the four main sections it is subdivided into, which are; the two-dimensional (2D) contraction nozzle (length 500 mm), the flow development section (length 2000 mm), the test section (length 500 mm), and the extension section (length 500 mm). The experimental setup is already built by a previous student, Andrew Torr [42] on the University of Pretoria, Hatfield campus.

The contraction nozzle has a contraction ratio of 27:1 with an exit height that can be varied between 5 mm and 30 mm depending on the requirement of the experiment. The test facility sections have the flow area of rectangular cross-section with a width of 203 mm and a height that can adjusted between 5 mm and 30 mm. The channel walls are manufactured from commercial acrylic plastic (Plexiglas) plates with a thickness of 12 mm. The ambient air enters the nozzle, accelerates smoothly through the contraction, and enters the flow development section. The flow development section is designed with sufficient length to allow for smooth development of the air-flow boundary layer until it becomes fully developed as it enters the test section at the laminar flow regime.

Once the air-flow passes through the test section and the extension section it enters a large exit plenum box (203 mm x 500 mm x 500 mm). The air is sucked through either a metered 50 mm or 100 mm diameter (PVC) pipe; depending on the required Reynolds number. To alternate between the two different pipes, two ball valves are employed in the pipe lines. By closing one valve and opening the other, a different diameter pipe could be

selected as required. Each PVC pipe has an ISO standard orifice plate that determined the air mass flow rate. The pipe lengths, placement of pressure taps across the orifice plate and orifice plate placement are designed as per the minimum requirements in the ISO 5167-2002.

The centrifugal fan is connected to the other end of the pipe sections by a plenum box of dimensions 1 m x 0.5 m x 0.5 m. The fan is run by a 1.5 kW motor. The fan speed is controlled with a variable frequency drive to choose the required flow rate and Reynolds number in the test section. The seams between adjacent channel sections are sealed with weather caulks to prevent any air leaks into the channels.

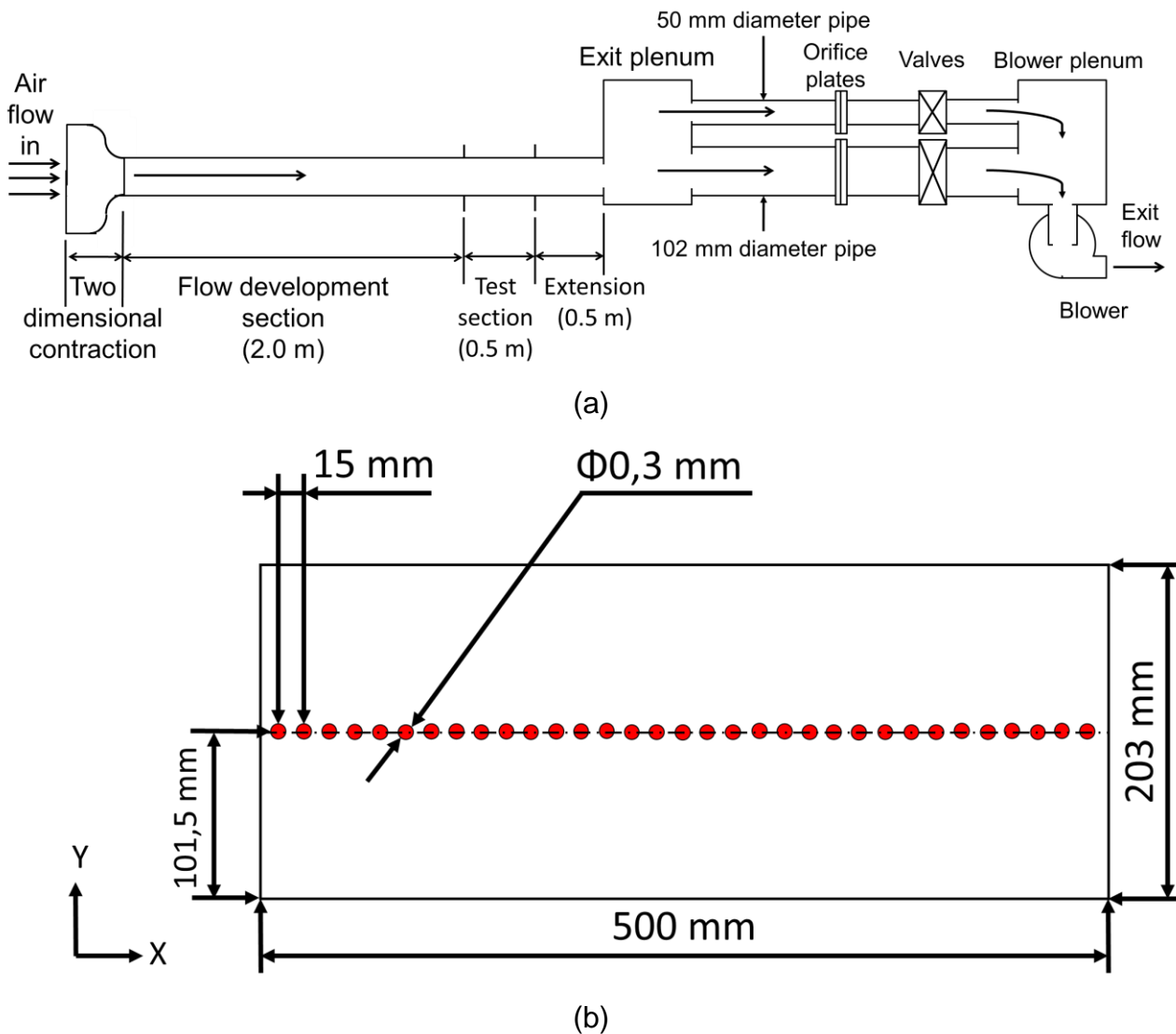
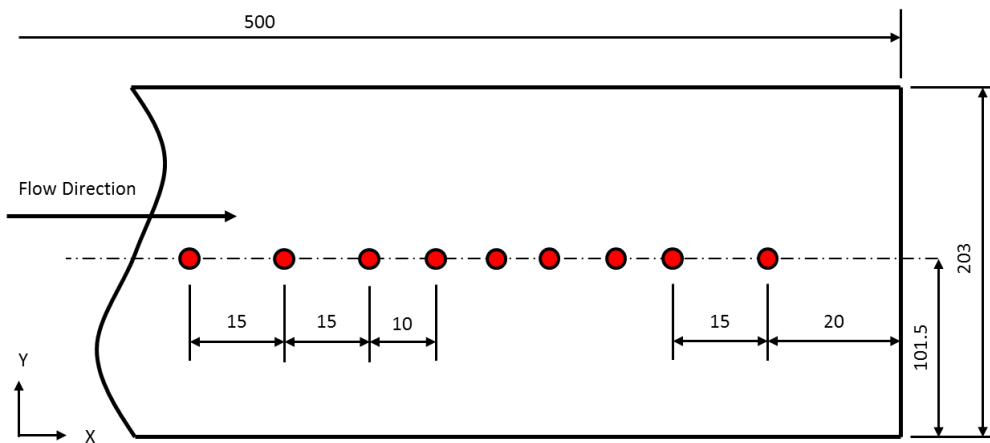


Figure 3.1: (a) Schematic of experimental setup, elevation view, and (b) pressure tap location

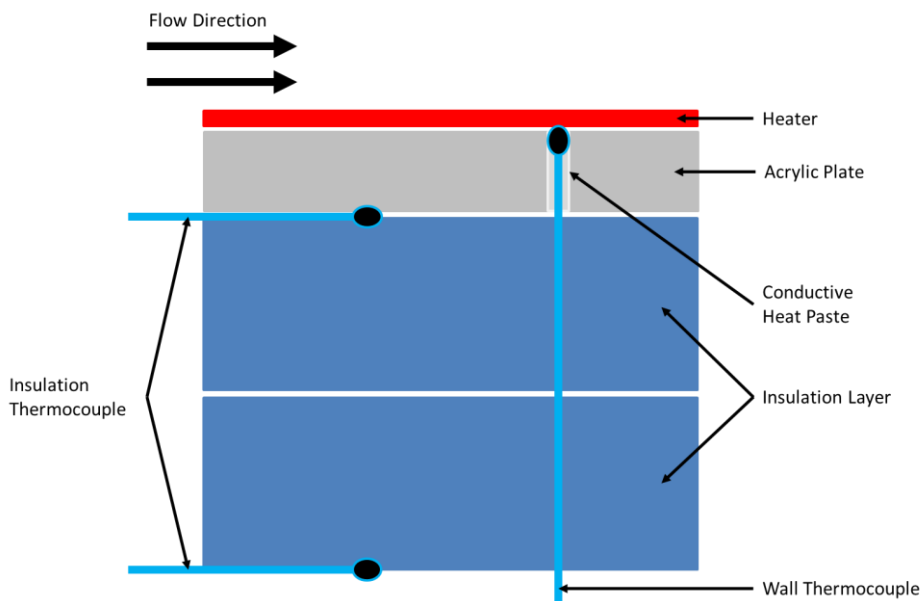
To capture the pressure drop data, one of the test section's 203 mm wide walls is drilled with 0.3 mm holes along the middle to form the static pressure taps, refer to Figure 3.1 (b). The thirty-three pressure taps are located 15 mm from one another along the streamwise direction and are connected to a manually rotating scanner (show a diagram of the scanner) through plastic tubing. The scanner in turn is connected to a differential pressure

transducer through plastic tubing. The scanner is manually rotated to select one pressure tap at a time without having to disconnect from the differential pressure transducer.

For heat transfer measurements, the 203 mm wide top and bottom walls are removed and replaced with 6 mm thick commercial acrylic plastic (Plexiglas) plates fitted with thin-film heaters and 30 T-type thermocouples as shown in Figure 3.2 (c). The commercial heaters from Omega™ are made of etched Inconel heating element encapsulated in Katon layers. The heaters have an adhesive back and are attached directly to the plates on the flow side of the wall. The heaters are covered with a commercial copper tape to provide a constant power flux along the test surface. The test section is insulated with two layers (each 23.5 mm thick) of Styrofoam™ insulation as shown in Figure 3.2 (c). Thermocouples are also located between the first insulation layer and the acrylic plate and the second insulation layer and the ambient to measure the conduction heat loss to the ambient. The details of heat loss estimations are discussed later in this chapter.



(a)



(b)

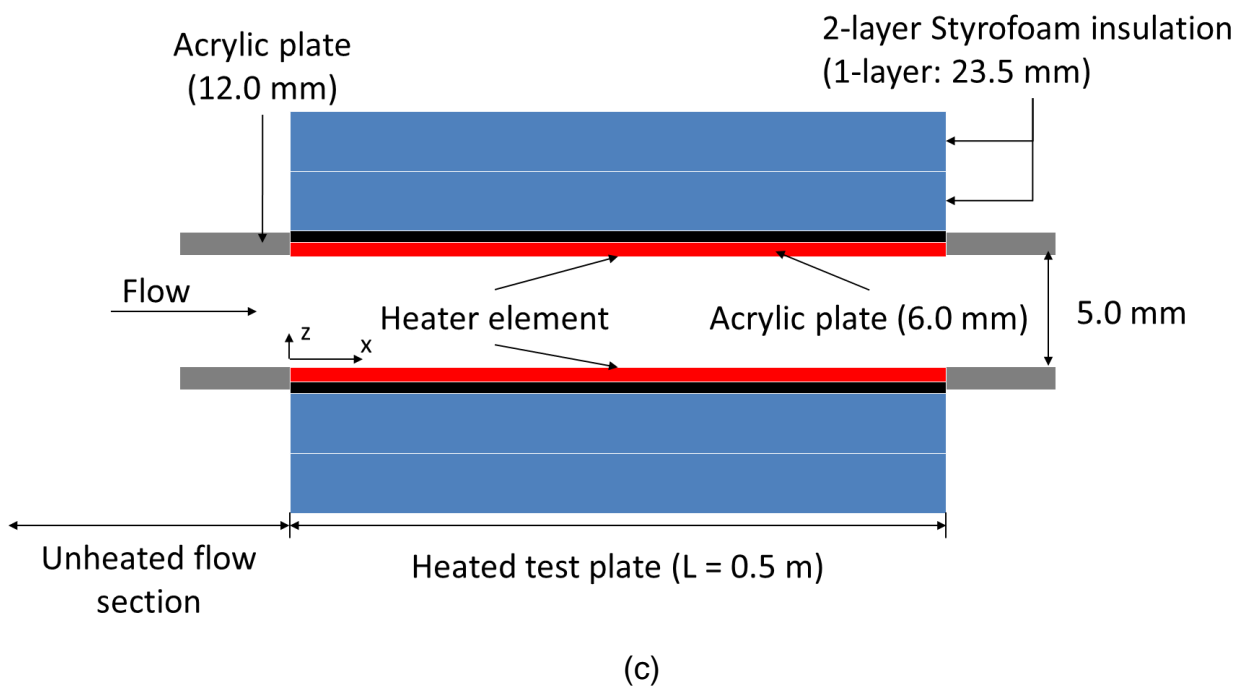


Figure 3.2: (a) Plane view of thermocouple tip locations along test plate (dimensions in mm), (b) elevation view of thermocouples in test plate and (c) test section wall heater arrangement (not drawn to scale)

The 30 T-type thermocouples are located along the x-axis centreline of the plate as shown in Figure 3.2 (a). The spacing between each thermocouple is either 15 mm or 10 mm depending on its location from the plate edge. The thermocouple tips are inserted into the test plate and placed just in contact with the heater surface through drill holes in the plate [refer to Figure 3.2 (b)]. The drill holes are filled with thermally conductive heat paste and partially with adhesive paste to fix the thermocouples inside the holes.

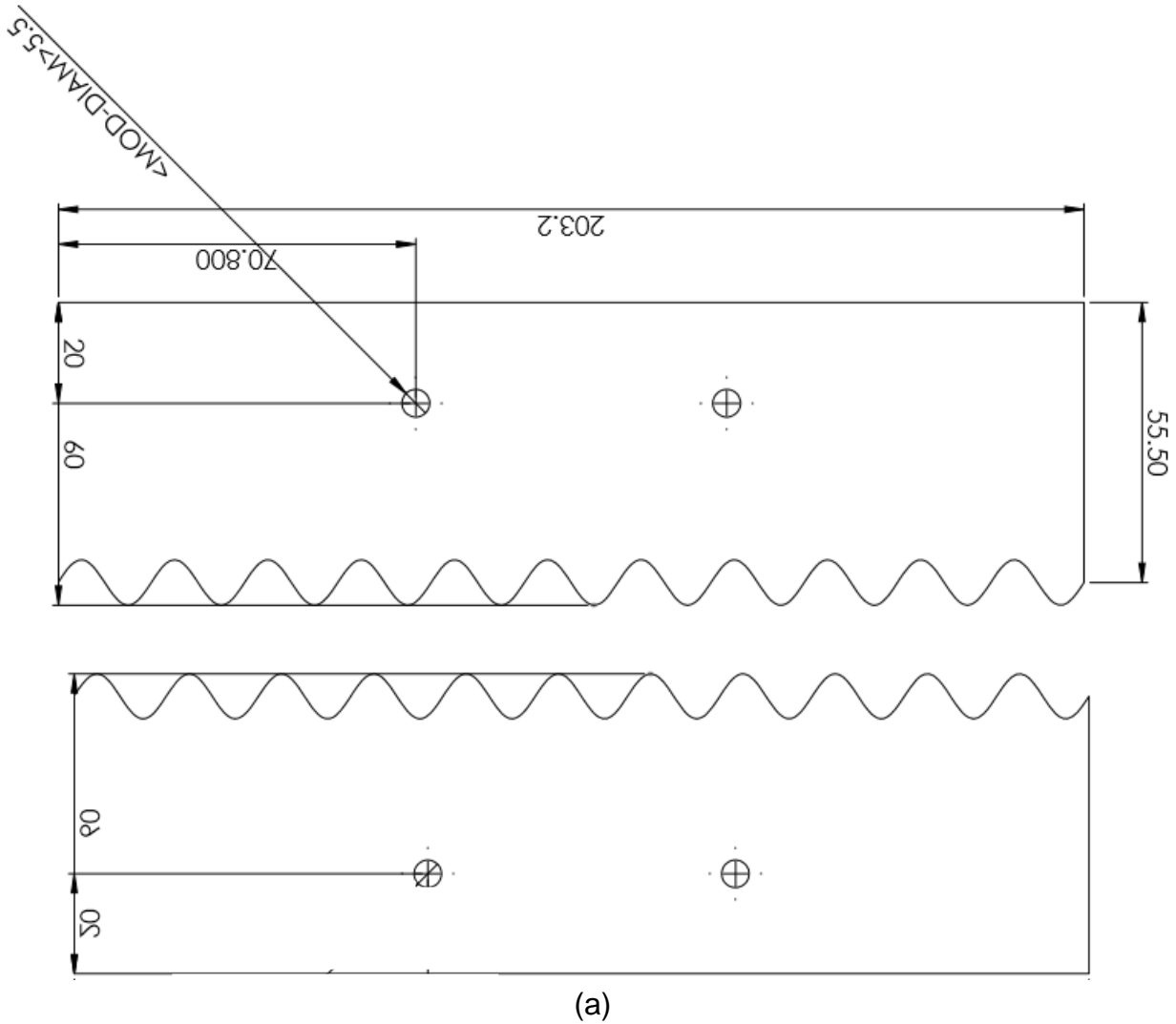
3.2.2 MESH-BENDER GEOMETRY

The porous screen inserts tested are formed in-house at the University of Pretoria. To produce the sinusoidal shape of the porous screen inserts a mesh bending jig is designed and manufactured. The sinusoidal curve is laser cut into steel plates (200 mm by 60 mm by 10 mm) and then bolted together in two separate jaws. Ten plates are laser cut and bolted to the bottom jaw and 10 inverted plates are laser cut and bolted to the top jaw. The two jaws would fit together like the teeth on gears. The plates are cut with the following configurations for various porous screen geometries;

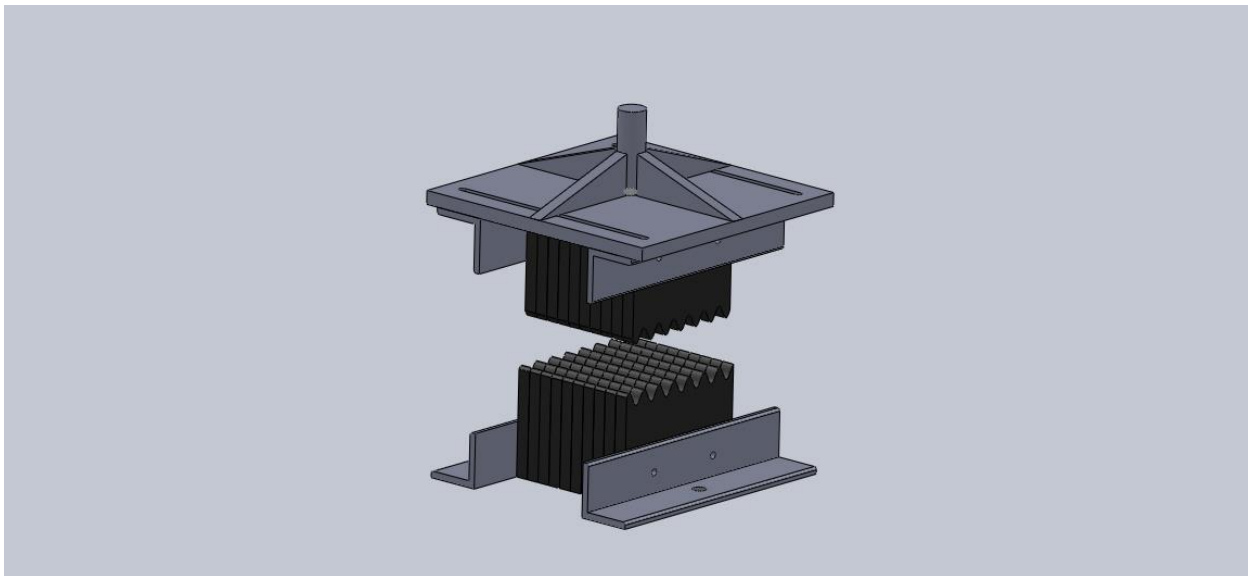
- 12 mm period and 14 mm peak-to-peak height,
- Irregular period (varying between 12 mm and 22 mm) and 14 mm peak-to-peak height,
- 22 mm period and 14 mm peak-to-peak height,
- 12 mm period and 5 mm peak-to-peak height,
- 18 mm period and 5 mm peak-to-peak height,
- 12 mm period and 8 mm peak-to-peak height,

- 18 mm period and 8 mm peak-to-peak height.

Once the bending jig is manufactured the mesh screen could be cut to size and laid on the bottom jaw. A butterfly press is used to press the top jaw down on the bottom one to form the mesh into its final wave form. Sufficient tolerance is given in the design to allow for spring back of the steel mesh. The final step is to cut the mesh insert into the required size of 203 mm by 500 mm to fit within the channel space of the test section.



(a)



(b)

Figure 3.3: Mesh-bender geometry showing (a) the profile of the mesh bending jaw and (b) the mesh-bender assembled

3.2.3 AIR-SCREEN GEOMETRY

The mesh screens are the commercial air filter screens purchased from Merco Industries (Pty) Ltd., South Africa. The mesh screens come in spooled lengths of 2 m by 1.3 m. Two different porosity meshes are purchased; one of approximately 48% porosity and one of approximately 68% porosity. The mesh screens are made from Type 304 stainless steel with a 0.28 mm wire diameter, and have a square like pore shape as shown in [Figure 3.4](#). The 48% porosity mesh have a square pore aperture of 0.567 mm and the 68% porosity mesh have a square pore aperture of 1.308 mm. The number of pores is about 12/cm for the 48% porosity mesh and 6/cm for the 68% porosity mesh.

Ten different wavy mesh screens with varying porosity, period and height/amplitude are tested. Each of the screens is identified as “Mesh (identity number)” as in the following. The height of the mesh refers to the peak-to-peak height of the sinusoidal wave form of the screen geometry.

- Mesh 1.1 – 22 mm period, 68% porosity and 14 mm height
- Mesh 2.1 – Irregular period (varying between 12 mm and 22 mm), 68% porosity and 14 mm height
- Mesh 3.1 – 12 mm period, 68% porosity and 14 mm height
- Mesh 1.3 – 22 mm period, 48% porosity and 14 mm height
- Mesh 2.3 – Irregular period (varying between 12 mm and 22 mm), 48% porosity and 14 mm height
- Mesh 3.3 – 12 mm period, 48% porosity and 14 mm height
- Mesh 4.1 – 18 mm period, 68% porosity and 5 mm height
- Mesh 5.1 – 12 mm period, 68% porosity and 5 mm height

- Mesh 4.3 – 18 mm period, 48% porosity and 5 mm height
- Mesh 5.3 – 12 mm period, 48% porosity and 5 mm height

The irregular screen inserts (Mesh 2.1 and 2.3) are formed by hand pressing the flat screens on the bending jig. The irregular wave periods of the screens indicate the sensitivity of the measured data on the manufacturing inaccuracy of the wave form. The channel height along the entire length from the 2-dimensional contraction to exit plenum (refer to Figure 3.1(a)) is adjusted according to the screen wave-height employed. The peaks of the screen wave are then in line contact with the 203 mm wide walls along the wave vector. As indicated earlier, the contact locations are not soldered or glued to the walls. Only visual inspection is carried out to ensure the proper contact between the wave peaks and walls. Because of the spring back property of the wire mesh during the bending process, some locations along the wave vector may not make any contact with the walls. However, the contact locations do not contribute to the heat transfer in the tests for the present wavy screen and are thus, not important for the measurements.

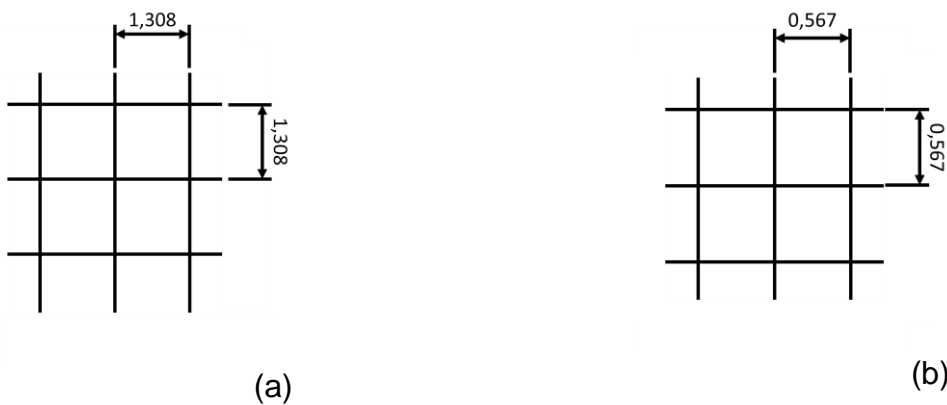


Figure 3.4: Pore shape of mesh (a) 68% porosity mesh and (b) 48% porosity mesh

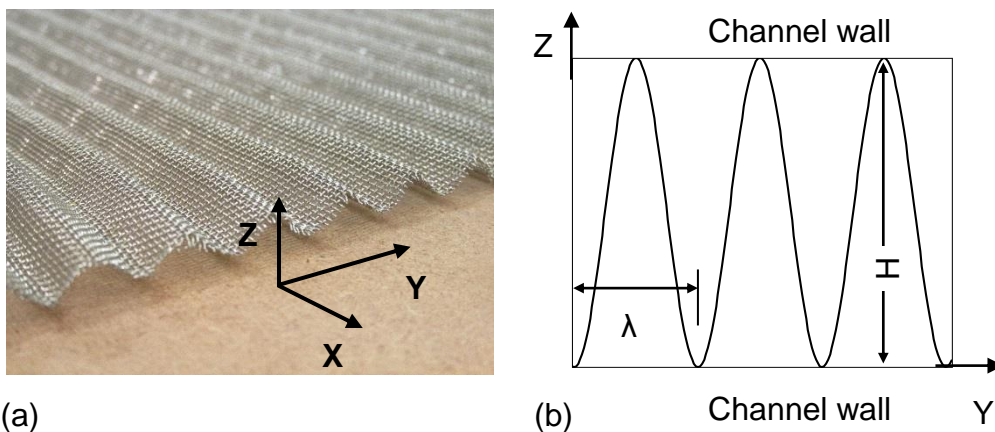


Figure 3.5: An Example of a mesh screen showing: (a) Image of the actual sinusoidal screen, and (b) schematic of the screen sinusoidal wave in YZ-plane, $\lambda = 12 \text{ mm}$ or 18 mm and $H = 5 \text{ mm}$ or 14 mm (X: mean flow direction).

3.3 INSTRUMENTATION

3.3.1 POWER SUPPLIES

Two direct current (DC) power supplies and one variable alternating current (AC) power supply are used in this experimental setup. QJE DC power supply has a maximum voltage output of 30 VDC and a maximum current output of 20 A. The Green Energy DC power supply has a maximum voltage output of 30 VDC and a maximum current output of 10 A. The variable AC power supply (Variac) has a maximum voltage output of 230 VAC and a maximum current output of 3 A. The accuracy of each power supply is given in Section 3.6 under [Table 3.1](#).

The Green Energy DC power supply is used to supply 10 VDC to the pressure transducers. The GJE DC power supply is used to supply 8 VDC to the pressure transducers in the pressure drop experiments and used to heat the downstream sections in the heat transfer experiments. The variac is used to supply AC to the heating pads to heat up the test section walls in the heat transfer experiments.

3.3.2 PRESSURE TRANSDUCERS

Differential pressure transducers are used to measure the pressure drop across the test section. To minimize the uncertainties of the pressure drop measurements, four different pressure transducers from the Omega EngineeringTM with different pressure ranges are used [refer to [Table 3.1](#)]. For laminar and early transitional Reynolds numbers (400 – 3 000) a PX 2650-0.5D5V differential pressure transducer is used with a full-scale range of 0 - 125 Pa. A PX 2650-2D5V differential pressure transducer is used for transitional Reynolds numbers up to the turbulent regime (3 000 – 7 000), and has a full-scale range of 0 - 250 Pa. The PX 164-005D5V and PX 164-010D5V differential pressure transducers are used for the turbulent regime of Reynolds number 7 000 – 20 000 and 20 000 – 35 000, respectively. The two latter pressure transducers have a full-scale range of 0 – 1 245 Pa and 0 - 2 490 Pa, respectively. The accuracy of each pressure transducer is also given in Section 3.6 under [Table 3.1](#).

Each pressure transducer is calibrated using a Betz manometer with an accuracy of 2.5 Pa. The details of the pressure transducer calibration are given in Appendix B.

3.3.3 ORIFICE PLATES

Each downstream PVC pipe (50 mm pipe and 100 mm pipe, refer to [Figure 3.1 \(a\)](#)) is metered with its own orifice plate. The orifice plates are used to determine the mass flow rate of air and the Reynolds number of the flow in the test section. The 50 mm pipe is used for Reynolds numbers between 400 – 3 000 and the 100 mm pipe is used for Reynolds numbers of greater than 3 000. The orifice plates are designed in accordance with standard 5167-2002 (1980). The 50 mm pipe has an orifice plate with a beta ratio of 0.21

and the 100 mm pipe has an orifice plate with a beta ratio of 0.5. The accuracy of the orifice plates is shown in Section 3.6 under [Table 3.1](#).

The differential pressure across the orifice plates is measured using a PX 164-010D5V differential pressure transducer. The accuracy of which is also shown in Section 3.6 under [Table 3.1](#).

3.3.4 THERMOCOUPLES

The thermocouples employed in the heat transfer experiments are commercial Teflon PTFE coated T-type copper-constantan thermocouples. The wire diameter of the thermocouples is 1 mm with an average tip diameter of 3 mm after preparation. The tip of the thermocouple is prepared by stripping the PTFE coating off the copper end and constantan end and soldering them together.

3.3.5 DATA LOGGER

A National Instrument data acquisition system (NiDaq mainframe and modules) is used to acquire the voltages from the thermocouple and pressure transducers. The thermocouples are connected to the mainframe via four NI 9213 data-card modules and the pressure transducers are connected to the mainframe via a single NI 9201 data-card module. The module NI 9213 card has its own internal cold junction for the thermocouple measurements. The accuracy of the data logging system is given in Section 3.6 under [Table 3.1](#).

The NiDaq mainframe is connected to a computer for recording the data using the National Instruments Labview programmes built in-house. The voltages are acquired from each pressure transducer at 200 Hz for 10 sec and from each thermocouples at 2 kHz for 2 sec, and are then time-averaged. An Excel spreadsheet is used to convert the voltage data into the pressure units and temperatures by applying the appropriate calibration curves.

3.3.6 MULTIMETERS

Two multimeters are used to capture the current and voltage supplied by the variac to the wall heaters. A UNI-T UT33A multimeter is used to measure the voltage supplied to the heaters, and has a voltage capacity of 500 VAC. A UNI-T UT60A multimeter is used to measure the current supplied to the heaters, and has a current capacity of 10 A. The accuracy of the respective multimeters is given in Section 3.6 under [Table 3.1](#).

3.4 DATA REDUCTION

The Reynolds number in the test section is calculated from the mass flow rate obtained from the measurement of pressure difference across the orifice plate. Equation. (3.1) in the following from [20] provides the mass flow rate:

$$\dot{m}_a = C\varepsilon \frac{\pi}{4} d^2 (1 - \beta^4)^{-0.5} \sqrt{2\Delta P \rho} \quad (3.1)$$

where C is the discharge coefficient of the orifice plate, ε is the expansion factor, d is the diameter of the orifice hole, β is the diameter ratio of the orifice hole to pipe, ΔP is the pressure differential across the orifice plate and ρ is the density of air. The value of the expansion factor, ε is essentially 1 because of the incompressible nature of flow over the entire range of Reynolds number employed for the tests.

The mass-averaged velocity of the air-flow in the channel is calculated using the cross-sectional area, A_c of the test section and the density of the air from Eq. (3.2). The maximum pressure drop along the channel is (use the value here for screen channel, 5 mm height, $Re = 11\,000$, ΔP between inlet and outlet of test section) and the flow can be considered incompressible. The flow density, ρ in Eq. (3.2) is then estimated based on the ideal gas law.

$$V_a = \frac{\dot{m}_a}{\rho A_c} \quad (3.2)$$

The cross-sectional area of the test section is calculated as follows:

$$A_c = H \times W \quad (3.3)$$

Finally, the Reynolds number inside the test section could be calculated as follows:

$$Re = \frac{V D_H \rho}{\mu} \quad (3.4)$$

where ρ is the density of the air, μ is the dynamic viscosity of air and D_H is the hydraulic diameter of the test section calculated as:

$$D_H = \frac{4A_c}{P} \quad (3.5)$$

where P is the perimeter of the test section calculated as:

$$P = 2(H + W) \quad (3.6)$$

The dynamic viscosity of air, μ is determined using the thermophysical properties of air at room temperature. For the heat transfer experiments, the thermal conductivity of air (k_a) is calculated at the bulk fluid temperature by interpolating between values given in Cengel et al. [30]. The bulk fluid temperature is determined using the average of the inlet temperature (obtained using a thermocouple measuring the ambient air) and the outlet temperature (obtained using the mean air temperature inside the test section):

$$T_b = \frac{T_i + T_o}{2} \quad (3.7)$$

The static wall pressure difference, $(P_x - P_0)$ is normalised relative to the dynamic pressure of flow at the average velocity in the channel. The reference static pressure P_0 is

measured at the inlet of the test section. The normalized static wall-pressure, ΔP^* is determined from Eq. (3.8) as follows:

$$\Delta P^* = \frac{P_x - P_0}{0.5\rho_a V_a^2} \quad (3.8)$$

The friction factor, f of Eq. (3.9) is then determined from the static wall pressure difference and average velocity of the air:

$$f = \frac{2\left(\frac{\Delta P}{\Delta X}\right)D_H}{\rho V_a^2} \quad (3.9)$$

Where $(\Delta P/\Delta X)$ is the slope of the distribution of wall-static pressure difference along the test section length.

In the heat transfer experiments, only either of the two 203 mm walls (top or bottom wall) is heated in the test section. Therefore, the thermal boundary layer only starts to develop when the ambient air enters the test section and encounters the heated plates. As the surface heaters are connected to the plates on the air stream side (meaning they are in direct contact with the air inside the channel) and the opposing side of the plates are insulated, it can be assumed that most of the heat is transferred to the air flow through convection and only a small amount is lost through conduction of the walls. Using thermocouples placed on the heated plate and embedded inside the insulation layers the conduction losses are determined. The two side walls of the test section are also insulated and assumed to be adiabatic. A one-dimensional conduction analysis is used, along with a trapezoidal rule integration scheme to determine the conduction loss through the insulation. The conduction analysis consisted of the following Fourier conduction law equation (Eq. (3.10)):

$$Q_l = k_{ins}A_s \frac{\Delta T}{\Delta x} \quad (3.10)$$

where k_{ins} is the thermal conductivity of the insulation material, A_s is the surface area of the plate, ΔT is the measured temperature difference across the insulation layer and Δx is the thickness of the insulation layer.

According to Maranzana et al. [44] the conductive heat transfer in walls in a channel with large gap is largely perpendicular to the direction of flow. According to the results of their analytical models it can be assumed that the axial conduction through the present heated walls is negligible. As the present test set up replicates that in Mahmood et al. [18], the conduction flow in the heated walls along the y-direction is also negligible. The one-dimensional conduction through the heated wall and insulation layer is estimated to be less than 3% of the total power input to each heater. The heat transferred to the air via convection could then be expressed as:

$$Q_c = Q_T - Q_l \quad (3.11)$$

where Q_c is the convective power, Q_T is the total power supplied to each heater and Q_l is the heat loss through conduction to the surroundings. The total power supplied to each heater equals the electric power (voltage multiplied by current) measured with the multimeter. The lengths of electric cables connecting the AC power supply and heater are kept at the minimum to reduce the voltage drop and power loss in the cables.

The heat loss to the surrounding due to the radiation is neglected as the maximum temperature difference between the heater surface and surroundings is only 33 °C. The convective heat flux boundary condition for the heat transfer in the test section can thus be reasonably assumed to be constant along the heated walls and same as the average convective heat flux of $Q_c/(L_p \cdot W)$.

The local mean-bulk temperature of the air in the test section is calculated using the steady-state energy balance between the test section inlet and the streamwise position x in the test section. The average convective heat flux from a heater surface, $Q_c/(L_p \cdot W)$ is employed in the energy balance. The local mean-bulk temperature is then calculated from Eq. (3.12) as in the following. The total convective power in the equation, $\Sigma Q_{c,x}$ either from two or one surface is obtained from the average convective flux multiplied by the surface area in Δx ($x = 0$ to x).

$$T_{m,x} = T_{a,in} + \frac{\Sigma Q_{c,x}}{\dot{m}_a C_p} \quad (3.12)$$

The local Nusselt number can now be calculated using the local bulk-mean temperature of air and local wall temperature as in Eq. (3.13). The convective heat flux level is adjusted depending on the Reynolds number to provide a temperature difference, $(T_{w,x} - T_{m,x}) \geq 10$ °C in the equation. The average heat flux level is thus not the same between the comparative cases of the baseline smooth channel and with the wavy screen insert for a given Reynolds number.

$$Nu_x = \frac{Q_c D_H}{[L_p \cdot W (T_{w,x} - T_{m,x}) k_a]} \quad (3.13)$$

3.5 DATA ACQUISITION

Before any measurement of data is recorded, the flow and temperature in the test section is ensured to be at the quasi steady-state condition. This condition is obtained when the pressure and temperature change by less than 2.0 Pa and 0.1 °C, respectively, over a period of 10 minutes. The time it took for each experiment to reach steady state depended on the mass flow rate inside the test section and the heat flux applied to the heaters. Once the data capturing process is completed for a Reynolds number, the mass flow rate is changed, and the process is repeated for the new Reynolds number.

3.6 UNCERTAINTY

The uncertainties in the measured data are estimated based on the 95% confidence interval and the errors in the computed values are determined based on the propagation of uncertainty as in [23], [34] and [43]. Table 3.1 provides a summary of the instruments used with their operating ranges and accuracy. The range and accuracy are obtained from the respective manufacturer’s specifications. The zero-offset voltage of an instrument is the voltage before any measurement is accounted in the measured data. The bias error thus includes the accuracy of the instrument or measuring device and the respective calibrator. The precision error is estimated by multiplying the standard deviation in the measured data with the Student’s t-variable [34]. The accuracy is the total uncertainty in a measured value and is estimated using the root square sum of bias error, precision error, and calibration error. Appendix C provides the details of error estimations in the measured data. The total uncertainties in the calculated quantities based on the propagation of errors are then estimated using equations in Sec. 3.4. Appendix C provides the details of the expressions used for the total uncertainties in the calculated quantities.

Table 3.1: Instrumentation uncertainties

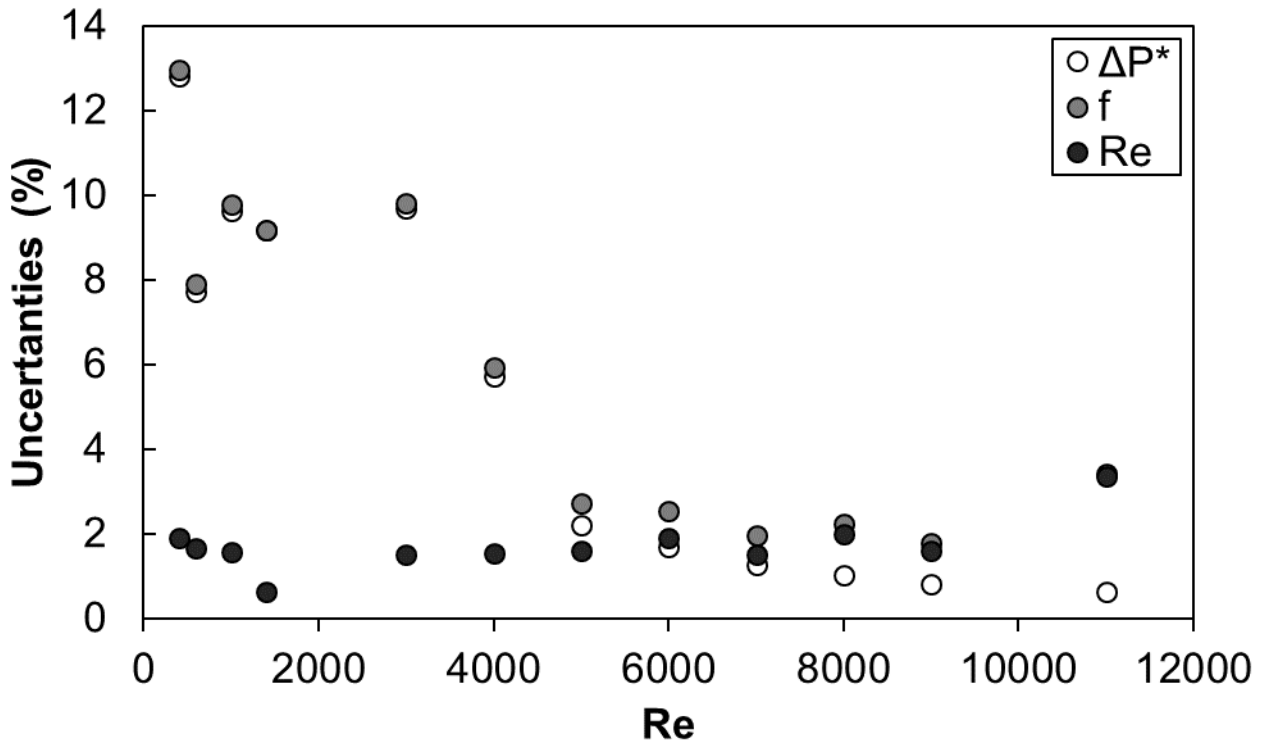
Instrument	Range	Accuracy
Thermocouple	<150 °C	0.1 °C
NI 9213	-40 - 70 °C	0.02 °C
Pressure Transducers		
PX 2650-0.5D5V	0 - 125 Pa	± 0.8721 Pa
PX 2650-2D5V	0 - 500 Pa	± 2.213 Pa
PX 164-005D5V	0 - 1 245 Pa	± 3.491 Pa
PX 164-010D5V	0 - 2 490 Pa	± 1.872 Pa
NI 9201	10.53 VDC	± 0.25%
QJE Power Supply		
Voltage	0 - 30 VDC	± 0.2% reading + 3 digits
Current	0 - 20 A	± 0.2% reading + 3 digits
Green Energy Power Supply		
Voltage	0 - 30 VDC	± 0.5% reading + 1 digit
Current	0 - 10 A	± 0.5% reading + 1 digit
Variac		
Voltage	0 - 230 VAC	N/A
Current	0 - 3 A	N/A
UNI-T UT33A	0 – 200 V	± 0.8% + 1
UNI-T UT33A	200 – 500 V	± 1% + 3
UNI-T UT60A	0 - 10 A	± 2% + 5
ISO 5167 Orifice Plate		
2 inch - $\beta = 0.2$	$2.772 \leq Re_D$	C - 0.6%

4 inch - $\beta = 0.5$	$34.65 \leq Re_D$	C - 0.6%
Orifice Pipe Diameter	2 - 4 inch	$\pm 0.4\%$
Orifice Diameter	0.012 - 0.051 m	$\pm 0.1\%$

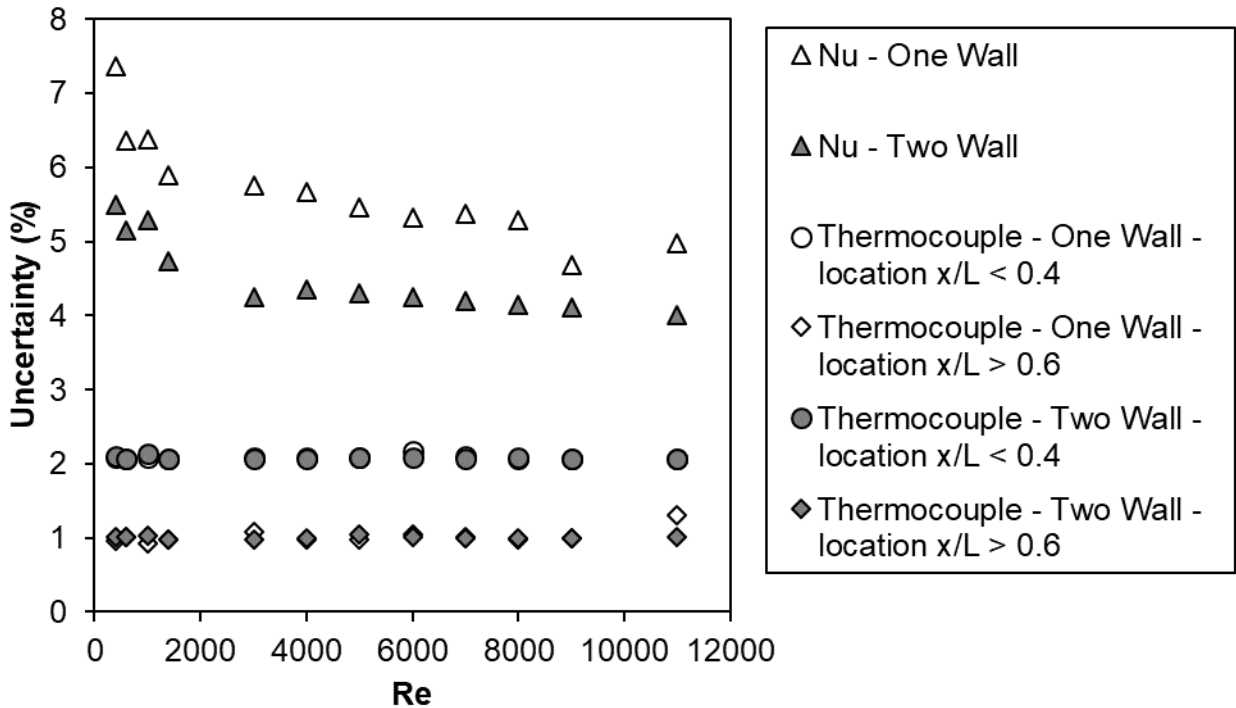
Figure 3.6 (a) shows the distribution of the calculated precision uncertainties for each significant variable used in the pressure measurements as Reynolds number varies. At low Reynolds numbers $400 \leq Re \leq 1\,000$ the test setup has the highest precision uncertainty. This is due to the small differential pressure across the orifice plate and in the wall pressure measurements. For the pressure measurements, there is a spike in precision uncertainty for normalised pressure drop (ΔP^*) at $Re = 4\,000$ as this is when the differential pressure transducers were swapped. Two different differential pressure transducers were used in the experiments to minimise the uncertainty in the wall pressure measurements. The first transducer was a PX 2650-2D5V with a full-scale range of $0 \leq Pa \leq 480$ used for $400 \leq Re \leq 3\,000$. The second was a PX 164-010D5V with a full-scale range of $0 \leq Pa \leq 2\,490$ used for $4\,000 \leq Re \leq 11\,000$. For Reynolds numbers greater than 600 the normalised pressure drop uncertainty is less than 10%.

Figure 3.6 (a) also shows that the calculated friction factor (f) uncertainty is less for all Reynolds number greater than 400. Like with the normalised pressure drop the friction factor uncertainty is the highest in the laminar region. This is again due to the small pressure differential across the orifice plate and the wall pressure measurements. However, the influence of changing the pressure transducers is not evident like in the normalised pressure drop data. Except for at Reynolds number 400 the friction factor uncertainty is less than 10%.

Figure 3.6 (b) shows the distribution of the calculated precision uncertainties for each significant variable used in the heat transfer measurements as Reynolds number varies. At low Reynolds numbers $400 \leq Re \leq 1\,000$ the test setup has the highest precision uncertainty. This is due to the small differential pressure across the orifice plate and the low $T_{w,x} - T_{m,x}$ values for low Reynolds number tests. As the Reynolds number increases the difference between the measured wall temperature and the mixed mean air temperature increases. Thus, reducing the precision uncertainty in the determined Nu_x . For both one-wall heating and two-wall heating the Nusselt number uncertainty was less than 6%.



(a)



(b)

Figure 3.6: Uncertainty estimates as Re varies (a) ΔP^* , f, and Re uncertainties for pressure drop experiments, and (b) Nu (one wall heating and two wall heating) uncertainties and wall temperature uncertainties at a location $x/L < 0.4$ and a location $x/L > 0.6$ for one wall and two wall heating.

3.7 CONCLUSION

The experimental setup, data reduction and experimental procedure are described in this chapter. The experimental setup consisted of a rectangular air channel connected to the suction side of a centrifugal fan. The test section consisted of a 500 mm long rectangular Perspex section located 2 m from the inlet. The width of the channel and test section is constant at 203 mm throughout with the height could be varied from 5 mm to 30 mm. Through increasing or decreasing the speed of the centrifugal fan, the Reynolds number could be varied between 400 and 30 000. For pressure drop measurements, two differential pressure transducers are used to capture the wall static-pressure data from 50 pressure taps located along the test section. One transducer is used for Reynolds number between 400 and 3 000 and the other for Reynolds numbers greater than 4 000. A constant heat flux boundary condition is applied to the test section for the heat transfer measurements. The test section is adequately insulated to ensure the heat lost to the surroundings is less than 5%. The wall temperature is measured with 30 thermocouples located along the test section heated wall. The inlet air temperature to the test section is measured using a thermocouple placed at the inlet of the air channel. Thin foil heaters are attached on the flow side of the 203 mm walls of the test section to provide the constant convective heat flux.

Sufficient time is given for both the heat transfer measurements and the pressure measurements to reach the steady state. The pressure drop measurements and heat transfer measurements are taken once the pressure changes by less than 2.0 Pa and the wall temperature changes by less than 0.1°C in 10 minutes. The pressure measurements are taken at adiabatic wall conditions to prevent a change in fluid properties influencing the pressure drop data.

An uncertainty analysis is done to predict the accuracy of the results obtained through the measurements and subsequent data reduction. The analyses found that the Reynolds number uncertainty remained less than 5% for all Reynolds numbers. The highest uncertainty for any measured data or reduced data is in the laminar region or Reynolds number lower than 400. For Reynolds numbers greater than 1000 the normalised pressure drop, friction factor and Nusselt number (both two wall heated and one wall heated) uncertainties are less than 10%, 10% and 6%, respectively. The wall temperature uncertainties are 2% at a location $x/L < 0.4$ and 1% at a location $x/L > 0.6$ for one wall and two wall heating.

4 RESULTS

4.1 INTRODUCTION

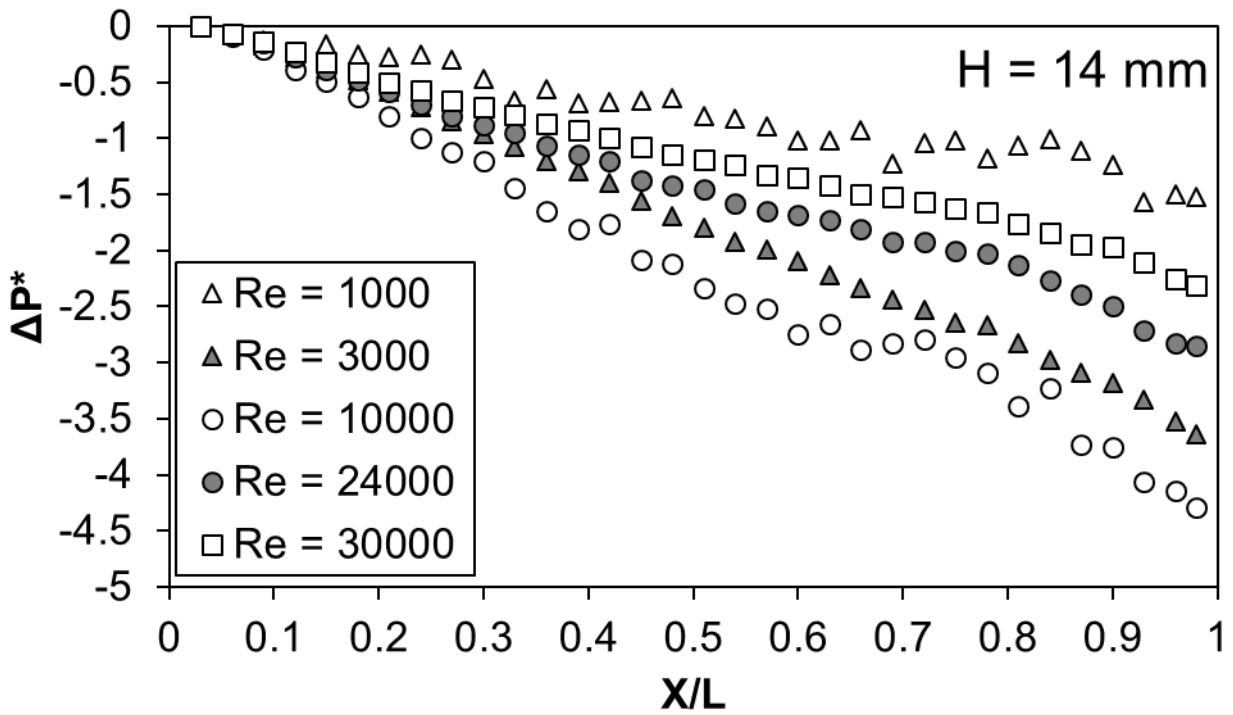
This chapter begins with a validation of the experimental set-up and data reduction by comparing the heat transfer and pressure drop data in the smooth channel without any inserts with the existing correlations for the smooth channel in the laminar and turbulent flow regimes. The smooth channel experimental data are also compared with the numerical data from the Texstan™ simulations. The validations will ensure that the results presented later in this chapter can be used and discussed with confidence. For the pressure drop, the experimental Darcy friction factors are compared with the friction factors of the existing correlations. For the heat transfer, the average Nusselt numbers are compared with the existing correlations and Texstan™ simulations for both two wall and one wall heating at the constant heat flux boundary conditions. All experimental data in the smooth channel are obtained at a channel height of 14 mm and 5 mm, the same as the screen insert channel height.

Following the validations, are the presentations of the local pressure drop and Nusselt number data, and the average friction factor and Nusselt number data for the various heat flux conditions and Reynolds numbers for the different porous screen inserts. From the Chapter 2, it is concluded that a porous screen insert is a viable option for increasing the thermal performance of the flat plate heat exchangers. The main purpose of this section is to compare the effects the porosity and period of the screen have on the thermal performance of the channel. Finally, the thermal performance of the porous screen insert are compared with each other.

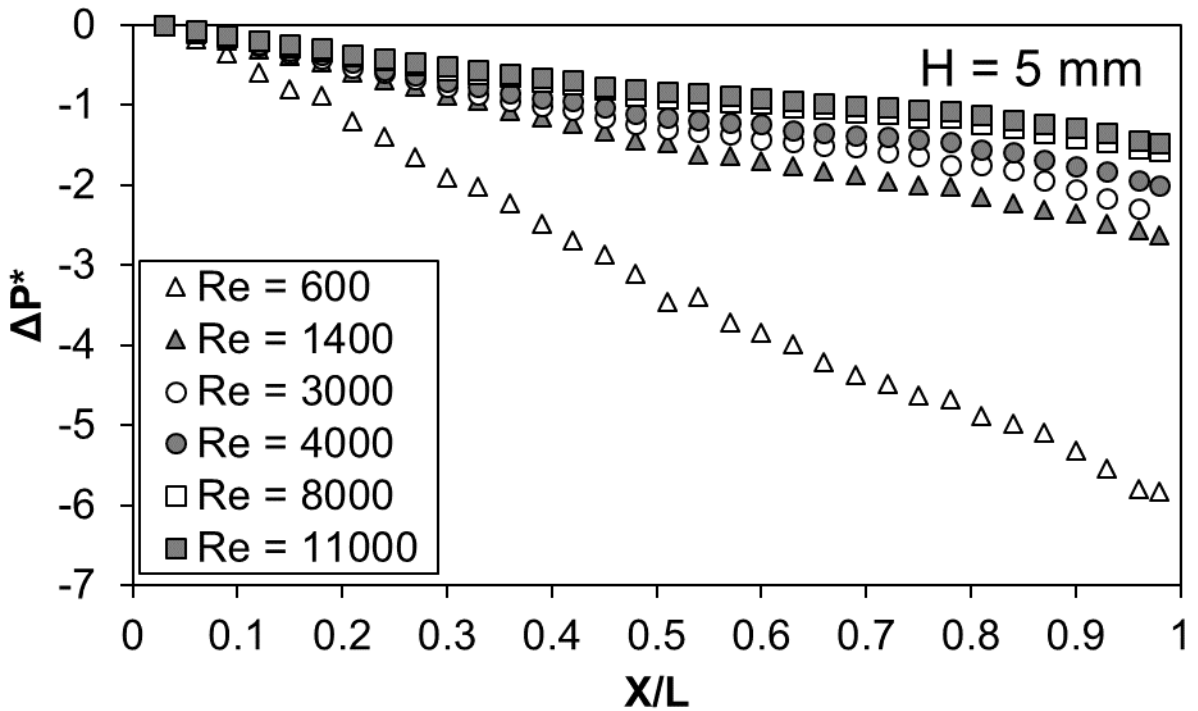
4.2 VALIDATION

4.2.1 PRESSURE DROP

The friction factors from the measured pressure drop along the channel are obtained in the isothermal conditions employing the adiabatic walls. The Reynolds numbers for the experimental friction factors cover the laminar transition, and turbulent flow regimes. The measured pressure drop distributions along the channel are used in Eq. (3.8) compute the Darcy friction factors. The $\Delta p/\Delta x$ in Eq. (3.8) is obtained from the slope of the straight line fitted with the regression linear-regression analysis between $0.58 < X/L < 1.0$, see [Figure 4.1](#). The results of the baseline friction factors, f_0 versus Re are summarised in [Figure 4.2](#) and [Figure 4.3](#). In both figures the experimental (present study) baseline f_0 decreases as Re increases.



(a)



(b)

Figure 4.1: Baseline pressure drop distributions vs. X/L in smooth channel for (a) 14 mm channel height and (b) 5 mm channel height.

Figure 4.2 and Figure 4.3 also include the theoretical friction factors from Shah and London [37] and Nikuradse correlation [40]. For the laminar regime ($Re = 400$ to $2\,000$) in Figure 4.2, the theoretical friction factor is calculated using the correlation specified in

Shah and London [37], see Equation (2.14), for the rectangular ducts. The experimental data correlated well with the correlation given by Shah and London [37] with an average deviation of approximately 5%. The deviations are well within the uncertainties of the experimental data.

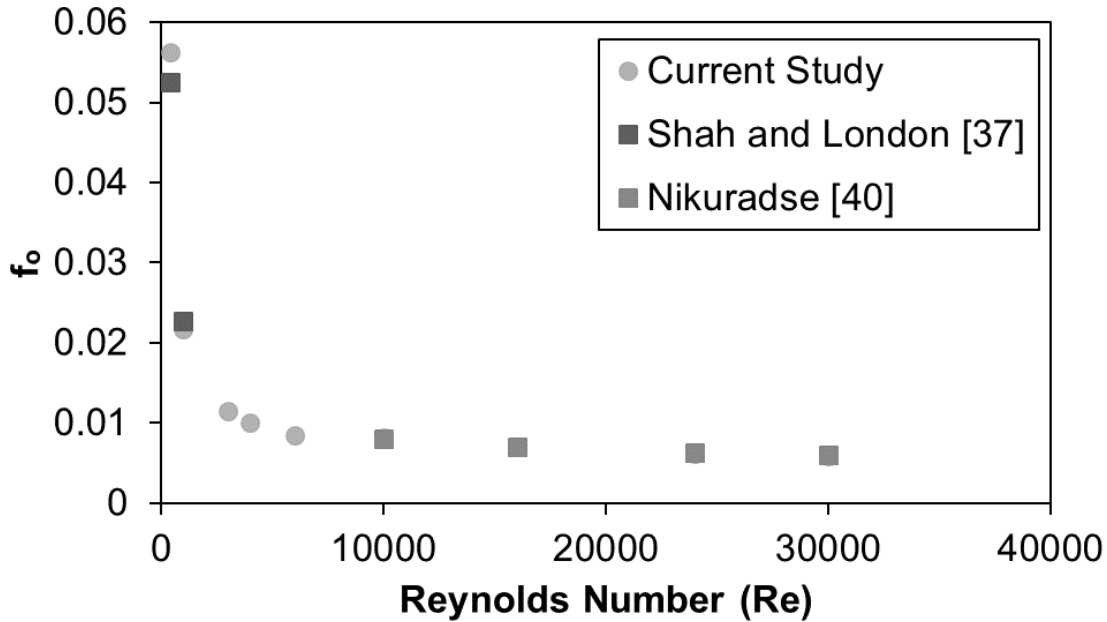


Figure 4.2: Baseline theoretical friction factor compared to experimental friction factor for experimental setup validation for 14 mm channel height

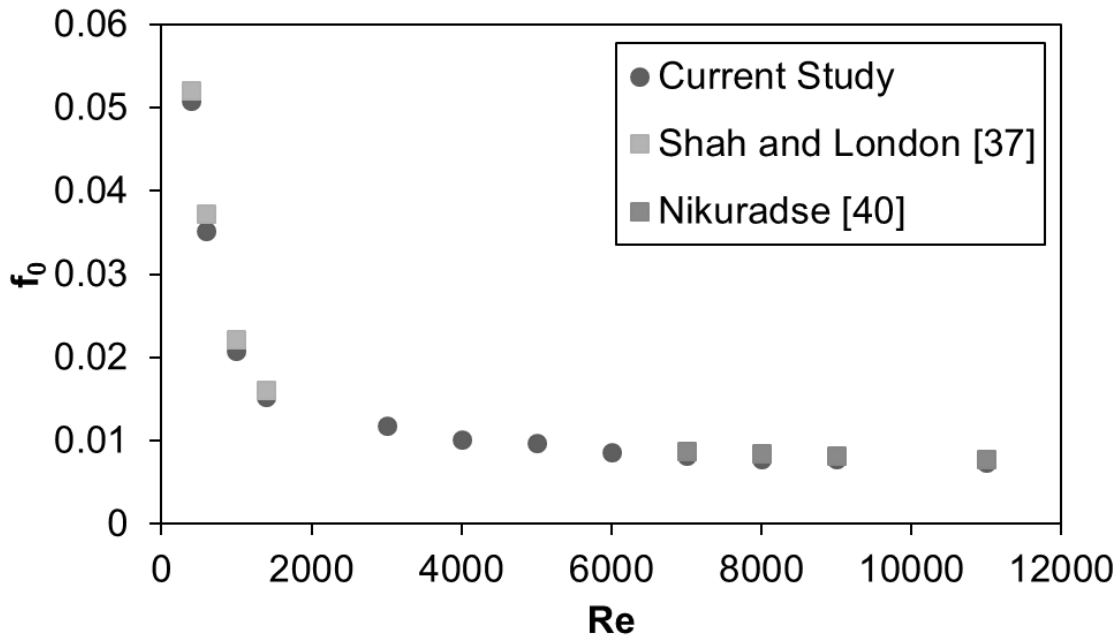


Figure 4.3: Baseline theoretical friction factor compared to experimental friction factor for experimental setup validation for 5 mm channel height

In the turbulent regime ($Re > 7\,000$), the theoretical friction factor is found using the correlation developed by Nikuradse [40] see Equation (2.27). The experimental data correlated extremely well with the correlation found for the turbulent flow with an average deviation of 2%.

Table 4.1 and Table 4.2 shows the percentage error that the experimental friction factors had when compared to the theoretical correlations. The percentage error values show that the experimental baseline values agree reasonably within the experimental uncertainties with those determined by the known correlations. This confirmed that the flow is hydrodynamically fully developed before the test section.

Table 4.1: Percentage error of experimental friction factor data compared to theoretical correlations for 14 mm channel height

Reynolds number (Re)	Theoretical friction factor (f_{theo})	Experimental friction factor (f_{exp})	Percentage error (%)
400	0.05255 ⁽¹⁾	0.05625	6.58
1 000	0.02274 ⁽¹⁾	0.02169	4.60
10 000	0.007998 ⁽²⁾	0.008130	1.62
16 000	0.007027 ⁽²⁾	0.007046	0.26
24 000	0.006378 ⁽²⁾	0.006149	3.72
30 000	0.006048 ⁽²⁾	0.005885	2.77

⁽¹⁾ Shah and London [37]

⁽²⁾ Nikuradse [40]

Table 4.2: Percentage error of experimental friction factor data compared to theoretical correlations for 5 mm channel height

Reynolds number (Re)	Theoretical friction factor (f_{theo})	Experimental friction factor (f_{exp})	Percentage error (%)
400	0.05203 ⁽¹⁾	0.05079	2.40
600	0.03721 ⁽¹⁾	0.03516	5.50
1 000	0.02218 ⁽¹⁾	0.02074	6.48
1 400	0.01606 ⁽¹⁾	0.01523	5.17
9 000	0.008156 ⁽²⁾	0.007850	3.89
11 000	0.007730 ⁽²⁾	0.007394	4.54

⁽¹⁾ Shah and London [37]

⁽²⁾ Nikuradse [40]

4.2.2 TWO-WALL HEATING

The heat transfer data is varied for both two wall and one wall heating. The average Nusselt numbers are estimated based on the local Nu at the wall thermocouple locations in the downstream half of the test section. The local Nu are computed from the measured

local wall temperature and bulk mean fluid temperature from the Eqn. (3.13). The results are compared with known correlations for thermodynamically fully developed flow in the literature [18], [37] and [40]. The average Nusselt numbers in the baseline channel contained the laminar flow regime, the transitional flow regime, and the turbulent flow regime. The results of the baseline average Nusselt numbers for the range of $400 < Re < 33\ 000$ are summarised in Figure 4.4 and Figure 4.5.

For the laminar regime ($400 Re - 2\ 000 Re$), the fully developed theoretical Nusselt number for a rectangular duct of aspect ratio 0.069 and a two-wall constant heat flux boundary condition is 7.55 as determined by Shah and London [37]. For a parallel plate configuration with the wall separation of 5 mm and a two-wall constant heat flux boundary condition the fully developed theoretical Nusselt number is 8.235 in the laminar regime by Shah and London [37]. The experimental data correlated well with the value determined by Shah and London [37] with an average deviation of less than or equal to 7% as shown in Table 4.3 and Table 4.4.

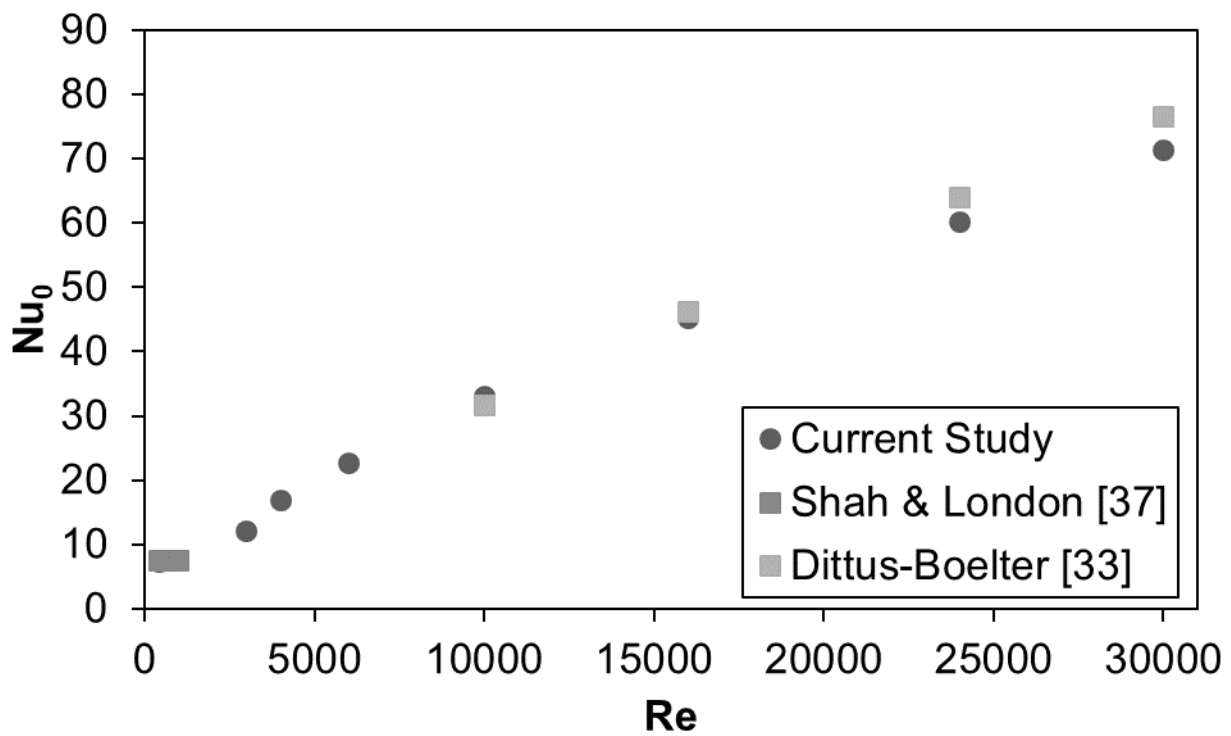


Figure 4.4: Baseline theoretical Nusselt numbers compared to experimental average Nusselt numbers (two-wall heating) for experimental setup validation for 14 mm channel height

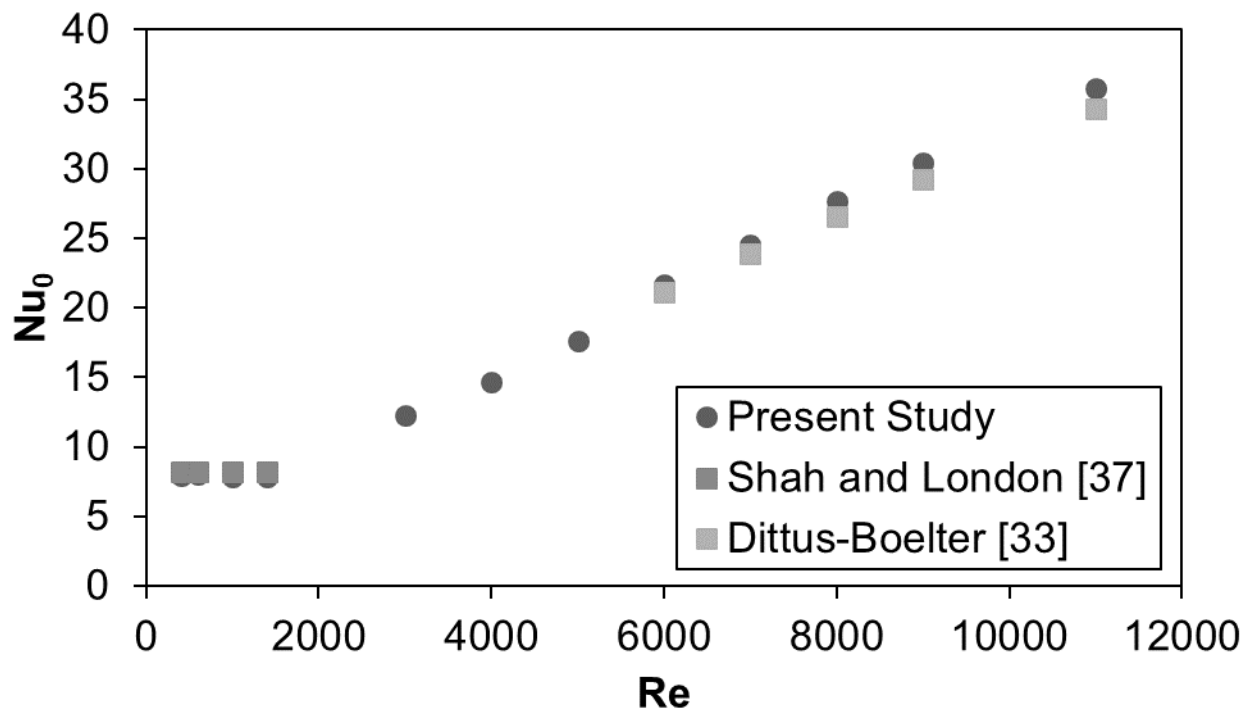


Figure 4.5: Baseline theoretical Nusselt numbers compared to experimental average Nusselt numbers (two-wall heating) for experimental setup validation for 5 mm channel height

In the turbulent regime ($Re > 10\,000$), the theoretical Nusselt number is calculated using the correlation determined by Dittus and Boelter [33]. The experimental data are expected to deviate slightly from the values determined from this correlation as it is determined for heat transfer in circular ducts with a constant heat flux around the circumference of the duct.

Baseline experiments are conducted at all the required Reynolds numbers that are used for testing in the same channel with the screen inserts. The percentage error between experimental and theoretical values in Tables 4.3 and 4.4 shows that the experimental baseline values are thermodynamically fully developed in the downstream half of the test section..

Table 4.3: Percentage error of experimental Nusselt number data (two-wall heating, Baseline) compared to theoretical correlations for 14 mm channel height

Reynolds number (Re)	Theoretical Nusselt number (Nu_{theo})	Experimental Nusselt number (Nu_{exp})	Percentage error (%)
400	7.55 ⁽¹⁾	7.88	4.33
1 000	7.55 ⁽¹⁾	7.95	5.31
10 000	32.13 ⁽²⁾	33.52	4.30
16 000	46.80 ⁽²⁾	45.41	2.96
24 000	64.73 ⁽²⁾	60.85	6.00
30 000	77.39 ⁽²⁾	71.80	7.21

⁽¹⁾ Shah and London [37]

(2) Dittus and Boelter [33]

Table 4.4: Percentage error of experimental Nusselt number data (two-wall heating, Baseline) compared to theoretical correlations for 5 mm channel height

Reynolds number (Re)	Theoretical Nusselt number (NU_{theo})	Experimental Nusselt number (NU_{exp})	Percentage error (%)
400	8.235 ⁽¹⁾	7.97	3.25
600	8.235 ⁽¹⁾	8.00	2.93
1 000	8.235 ⁽¹⁾	7.86	4.60
1 400	8.235 ⁽¹⁾	7.86	4.54
9 000	29.23 ⁽²⁾	30.46	4.21
11 000	34.32 ⁽²⁾	35.83	4.39

(1) Shah and London [37]

(2) Dittus and Boelter [33]

4.2.3 ONE-WALL HEATING

The average Nusselt numbers are found from the local Nu in the downstream half of the test section with one wall heating and other walls insulated (adiabatic). Equations (3.13) are used to estimate the local Nu at the wall-thermocouple locations. The results are compared with known Correlations in thermodynamically fully developed flow [33], [37]. The Nusselt numbers contained the laminar flow regime, the transitional flow regime, and the turbulent flow regime. The results of the baseline average Nusselt numbers are summarised in Figure 4.6 and Figure 4.7.

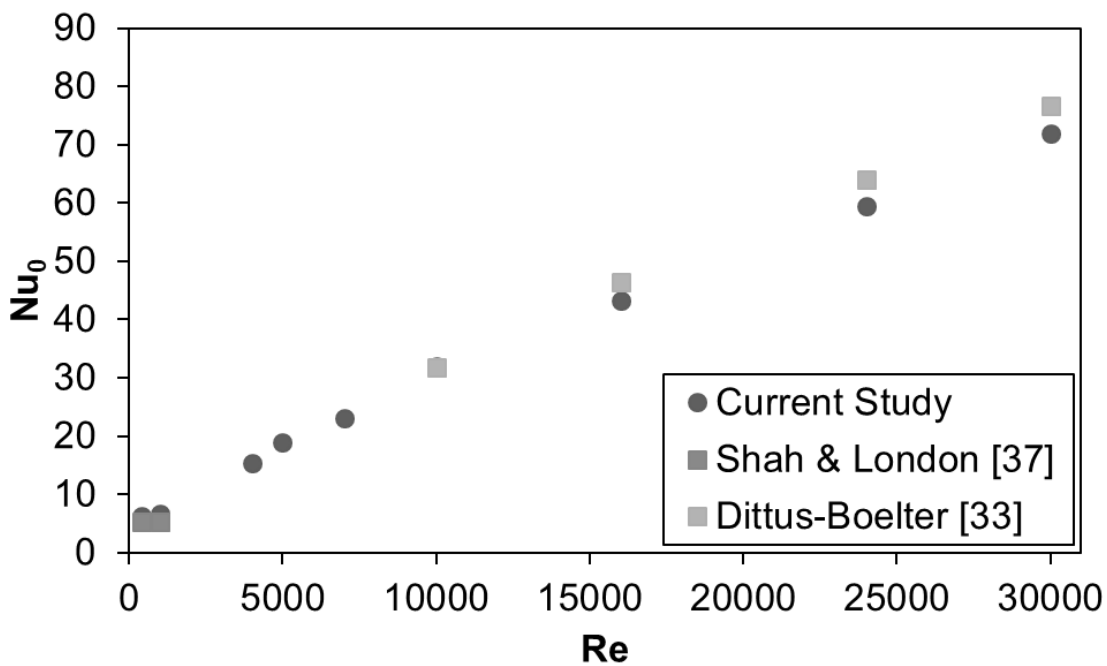


Figure 4.6: Baseline theoretical Nusselt numbers compared to experimental average Nusselt numbers (one-wall heating) for experimental setup validation for 14 mm channel height

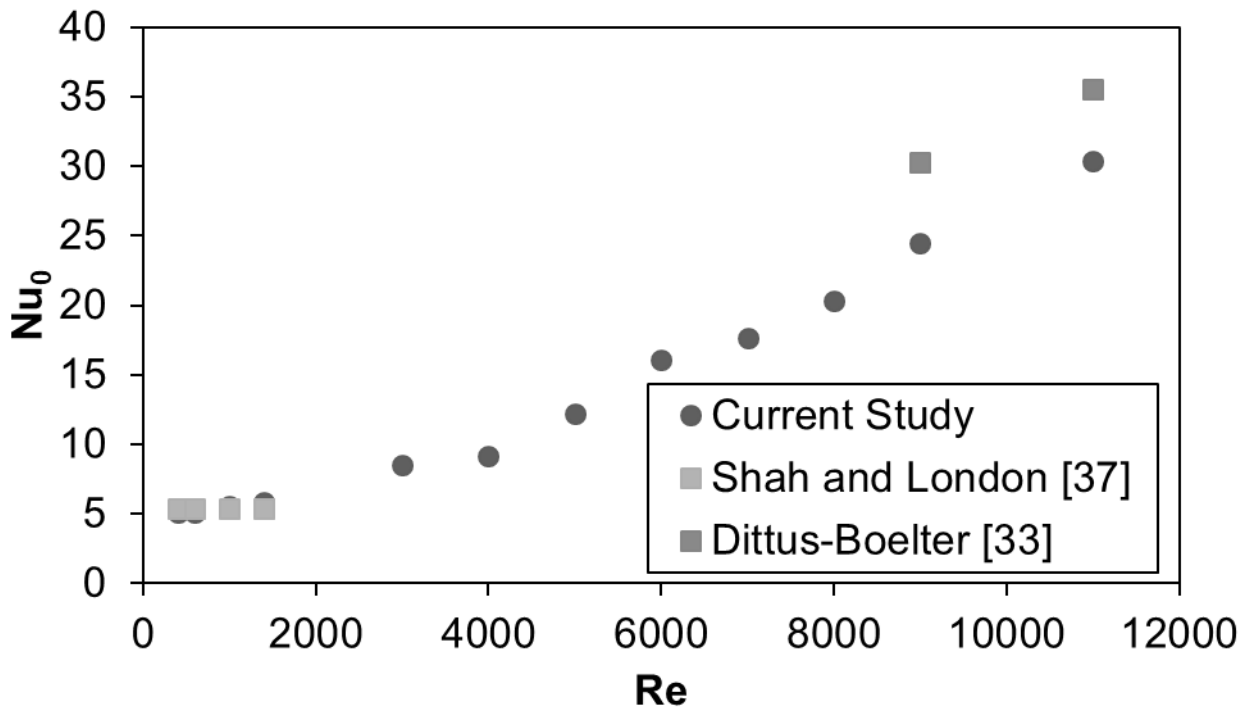


Figure 4.7: Baseline theoretical Nusselt numbers compared to experimental average Nusselt numbers (one-wall heating) for experimental setup validation for 5 mm channel height

For the laminar regime ($400 \text{ Re} - 2\,000 \text{ Re}$), the fully developed theoretical Nusselt number for a rectangular duct of aspect ratio 0.069 and a one-wall constant heat flux boundary condition is 5.23 as determined by Shah and London [37]. The hydraulic diameter for the 5 mm height of the test section is about same as the hydraulic diameter of a parallel channel with 5 mm wall-separation ($2H$). A one-wall constant heat flux boundary condition provides the fully developed theoretical Nusselt number as 5.385. The experimental data for the 14 mm channel height did not correlate well with the value determined by Shah and London [37] as indicated in Table 4.5. The large discrepancies between the experiments and theoretical data at $\text{Re} \leq 1\,000$ indicate the flow is still thermally developing along the downstream half of the test channel. Whereas, the experimental data in Table 4.6 for the 5 mm channel height did correlate well with theoretical data in the laminar Re range of 1400 and below with an average error of 5%.

In the turbulent regime ($\text{Re} > 9\,000$), the theoretical Nusselt number is calculated using the correlation determined by Dittus and Boelter [33]. The experimental data are expected to deviate slightly from the values determined from this correlation as it estimates the heat transfer in circular ducts with a constant heat flux around the circumference and along the length of the duct.

Baseline experiments are conducted at all the required Reynolds numbers that are used for testing in the same channel with the screen inserts. Table 4.5 and Table 4.6 show the percentage difference between the experimental and theoretical data. The differences then indicate the flow is thermally fully developed for $\text{Re} \geq 10\,000$ in the 14 mm channel and for

all Re in the 5 mm channel. The percentage error values show that the experimental baseline values are thermodynamically fully developed.

Table 4.5: Percentage error of experimental Nusselt number data (one-wall heating, Baseline) compared to theoretical correlations for 14 mm channel height

Reynolds number (Re)	Theoretical Nusselt number (Nu_{theo})	Experimental Nusselt number (Nu_{exp})	Percentage error (%)
400	5.23 ⁽¹⁾	6.51	24.42
1 000	5.23 ⁽¹⁾	7.06	34.94
10 000	32.13 ⁽²⁾	32.20	1.25
16 000	46.80 ⁽²⁾	43.76	5.52
24 000	64.73 ⁽²⁾	60.08	6.22
30 000	77.39 ⁽²⁾	72.17	5.77

(1) Shah and London [37]

(2) Dittus and Boelter [33]

Table 4.6: Percentage error of experimental Nusselt number data (one-wall heating, Baseline) compared to theoretical correlations for 5 mm channel height

Reynolds number (Re)	Theoretical Nusselt number (Nu_{theo})	Experimental Nusselt number (Nu_{exp})	Percentage error (%)
400	5.385 ⁽¹⁾	6,51	5.02
600	5.385 ⁽¹⁾	7,06	5.82
1 000	5.385 ⁽¹⁾	32,20	3.32
1 400	5.385 ⁽¹⁾	43,76	7.47
9 000	29.23 ⁽²⁾	24.44	23.78
11 000	34.32 ⁽²⁾	30.40	16.83

(1) Shah and London [37]

(2) Dittus and Boelter [33]

4.3 PRESSURE DROP

The pressure drop measurements along the channel with the screen inserts experiments are conducted under isothermal and adiabatic conditions. A total of 102 pressure drop experiments are conducted, which consisted of 9 Reynolds numbers for the 14 mm channel height and 12 Reynolds numbers for the 5 mm channel height for 10 different porous screen inserts. The measurement matrix is summarised in [Table 4.7](#).

Table 4.7: Pressure drop experimental test matrix

Porous screen insert	Reynolds number range	Mass flow rate measurements	Channel Heights
Mesh 1.1 ⁽¹⁾	400 ≤ Re ≤ 30 000	9	14
Mesh 2.1	400 ≤ Re ≤ 30 000	9	14

Mesh 3.1 ⁽¹⁾	$400 \leq Re \leq 30\,000$	9	14
Mesh 1.3 ⁽¹⁾	$400 \leq Re \leq 30\,000$	9	14
Mesh 2.3	$400 \leq Re \leq 30\,000$	9	14
Mesh 3.3 ⁽¹⁾	$400 \leq Re \leq 30\,000$	9	14
Mesh 4.1	$400 \leq Re \leq 11\,000$	12	5
Mesh 5.1	$400 \leq Re \leq 11\,000$	12	5
Mesh 4.3	$400 \leq Re \leq 11\,000$	12	5
Mesh 5.3	$400 \leq Re \leq 11\,000$	12	5

⁽¹⁾ Pressure drop data obtained by Andrew Torr [42] in the present test section. The data are presented in this thesis for comparison purposes only.

4.3.1 14-MM CHANNEL

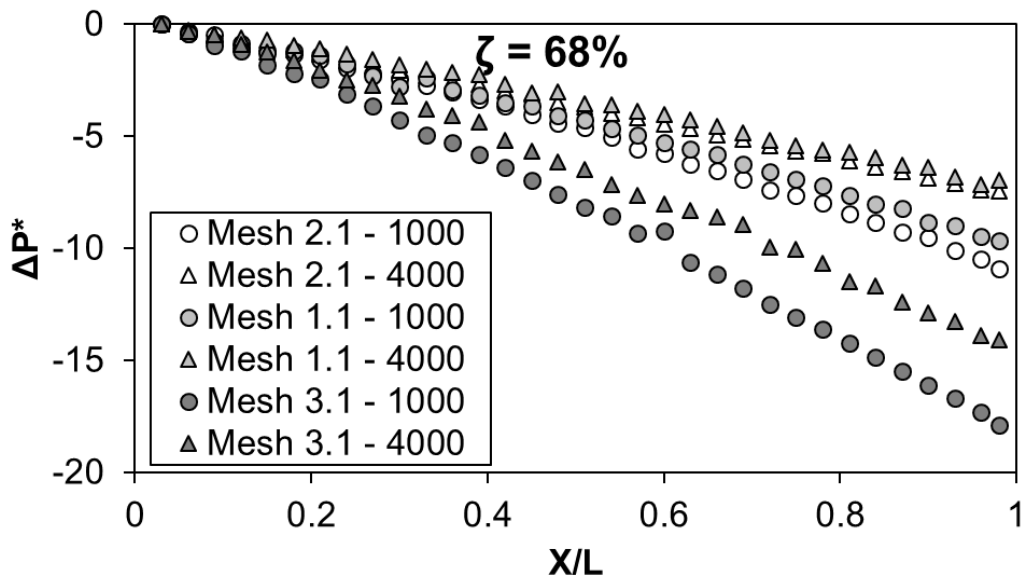
Figure 4.8 and Figure 4.9 shows the normalised pressure drop data (ΔP^*) in the X/L direction of the test section for four porous screen inserts, namely: mesh 2.1, mesh 3.1, mesh 2.3 and mesh 3.3. Meshes 2.1 and 2.3 had an irregular period (a period alternating between a 12 mm wavelength and a 22 mm wavelength) to determine the effects of irregularity in wave period on the pressure drop along the test section. To show the differences between the pressure drop distributions clearly, the data for the air mass flow rates corresponding to Reynolds numbers 1 000, 3 000, 4 000, 10 000, 16 000 and 30 000 are included in Figure 4.8 (a) and (b) and Figure 4.9 (a) and (b). The ΔP^* data in the figure is calculated from Equation (3.8). Note that the higher the negative value for ΔP^* the higher the pressure drop along the channel. Only the last 40% of the pressure drop data is shown as the ΔP^* drop is linear along X/L for this region and indicated a fully developed hydrodynamic flow.

As shown by LePoudre et al. [27] and Mahmood et al. [18], the smooth inlet flow into the screen test section undergoes transition between $0 < X/L < 0.6$ and becomes fully turbulent only after $X/L = 0.6$. The developing length, X/L, for a turbulent velocity profile increased with Reynolds number and varied for porous screen type. At a Reynolds number of 30 000 and mesh 3.3 the developing length is $X/L=0.6$.

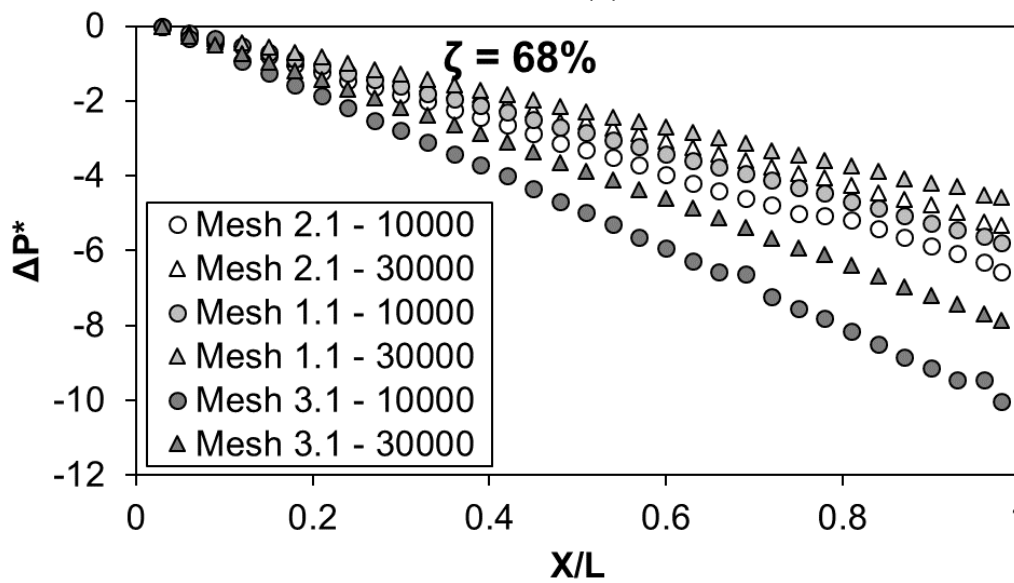
The friction factor (f) in the test section is determined by fitting a linear regression line on the pressure drop data such as those of Figs. 4.7 and 4.8 in the fully developed flow region. The slope of the fitted line is used as dp/dx in Eq. (3.9) where the correlation coefficient for the fitted line is always more than or equal to 0.98 in Equation (3.9). Figure 4.10 and Figure 4.11 show the determined friction factors for the various porous screen inserts tested at varying Reynolds number. It is evident from these two figures that the period and porosity of the screen insert influences the friction factor. At a given Re, the fluid pumping power in the screen channel increases for one screen from the other if the friction factor increases.

For the 68% porosity screen inserts (Mesh 1.1, Mesh 2.1, and Mesh 3.1), Figure 4.10, the friction factor is a maximum at Reynolds number 400 and decreases to a minimum at 30 000. The friction factor, f for Mesh 1.1 decrease by 69%, mesh 2.1 decreases by 67%

and mesh 3.1 decreases by 74% over the Reynolds number range from 400 to 30 000. The average difference of f in Figure 4.10 between mesh 1.1 and mesh 3.1 is 40% in the laminar region ($400 \leq Re \leq 1\,000$) and 35% in the transition and turbulent regimes ($3\,000 \leq Re \leq 30\,000$), with mesh 3.1 having slightly higher friction factors than that of mesh 1.1 for corresponding Reynolds numbers. The data in Figure 4.10 clearly demonstrate that the friction factor for given porosity screen and Re is reduced significantly as the periodicity of the screen wave is increased. The irregularity of the wave period has small effects on the friction factor. As indicated previously, the smaller wave period provides more flow blockage in the channel to increase the pressure drop and friction factor at a given Re .

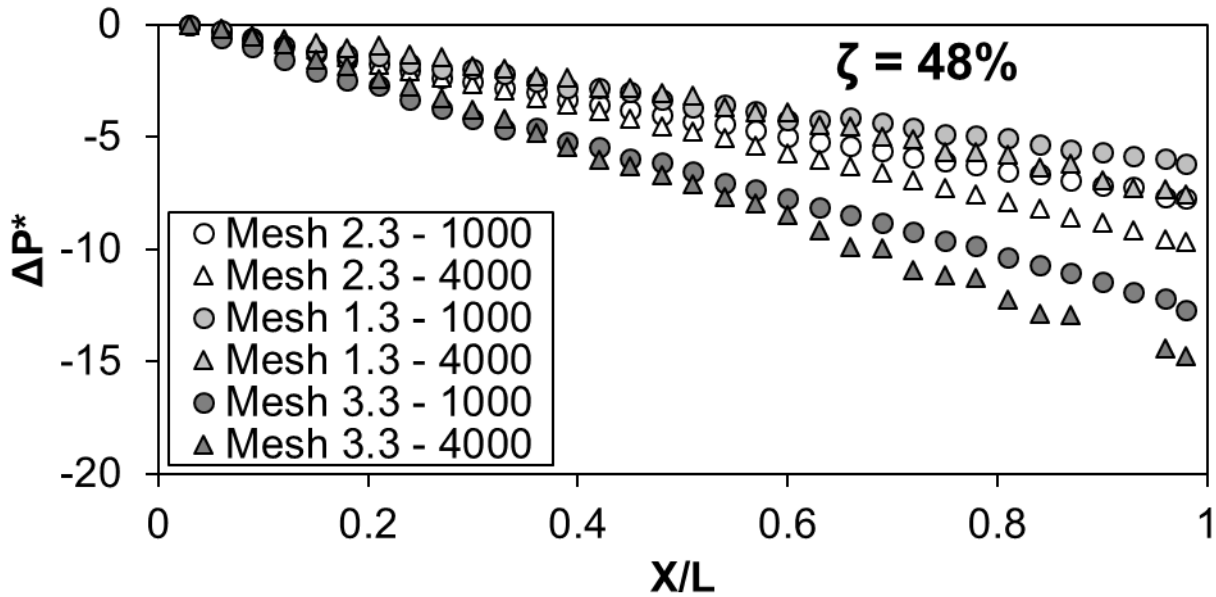


(a)

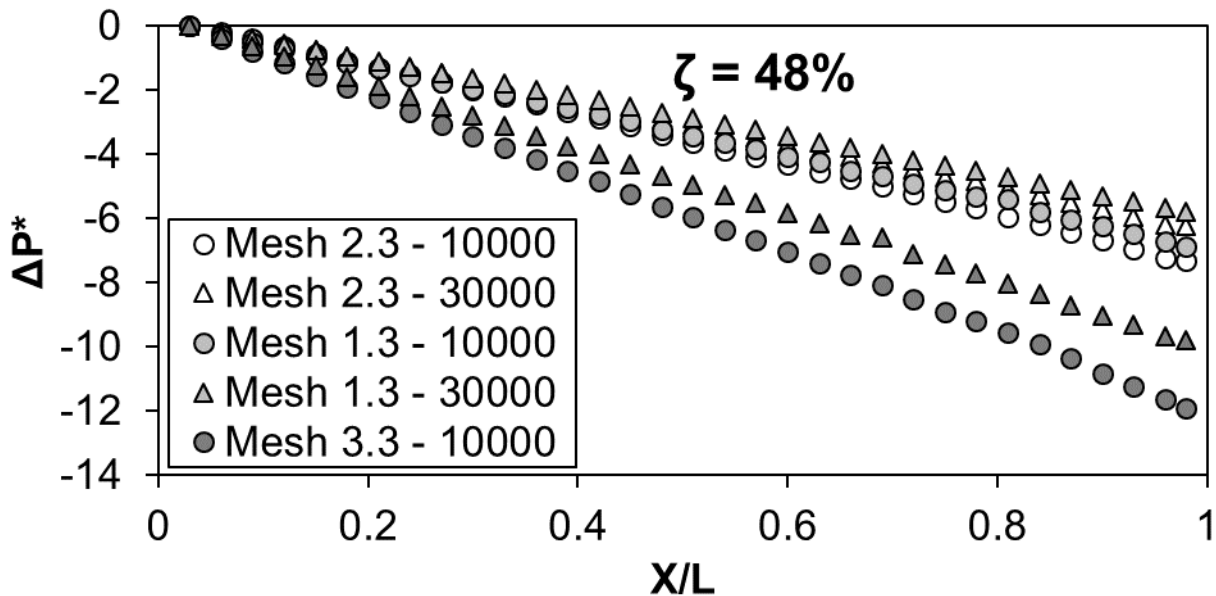


(b)

Figure 4.8: Normalised pressure drop data for Mesh 2.1 (irregular period - 68% porosity) and Mesh 3.1 (12 mm period - 68% porosity) versus X/L for (a) Laminar and early transitional regimes and (b) Turbulent regime



(a)



(b)

Figure 4.9: Normalised pressure drop data for Mesh 2.3 (irregular period - 48% porosity) and Mesh 3.3 (12 mm period - 48% porosity) versus X/L for (a) Laminar and early transitional regimes and (b) Turbulent regime

For all the 48% porosity screen inserts (Mesh 1.3, Mesh 2.3, and Mesh 3.3), [Figure 4.11](#), the friction factor plot looks slightly different to that of the 68% porosity screen inserts. The friction factor decreases by 60% for all three meshes in the Reynolds number range between 400 and 1 000, then it increases by 42% for mesh 1.3, 65% for mesh 2.3 and 46% for mesh 3.3 between $1\ 000 \leq Re \leq 3\ 000$, and finally decreases by 32% for mesh 1.3, and 46% for both meshes 2.3 and 3.3 for $Re > 3\ 000$. The average difference of f in [Figure 4.11](#) between mesh 1.3 and mesh 3.3 is 43% in the laminar region and 37% in the

transition and turbulent regimes, with mesh 2.3 and mesh 3.3 having slightly higher friction factors than that of mesh 1.3 for corresponding Reynolds numbers.

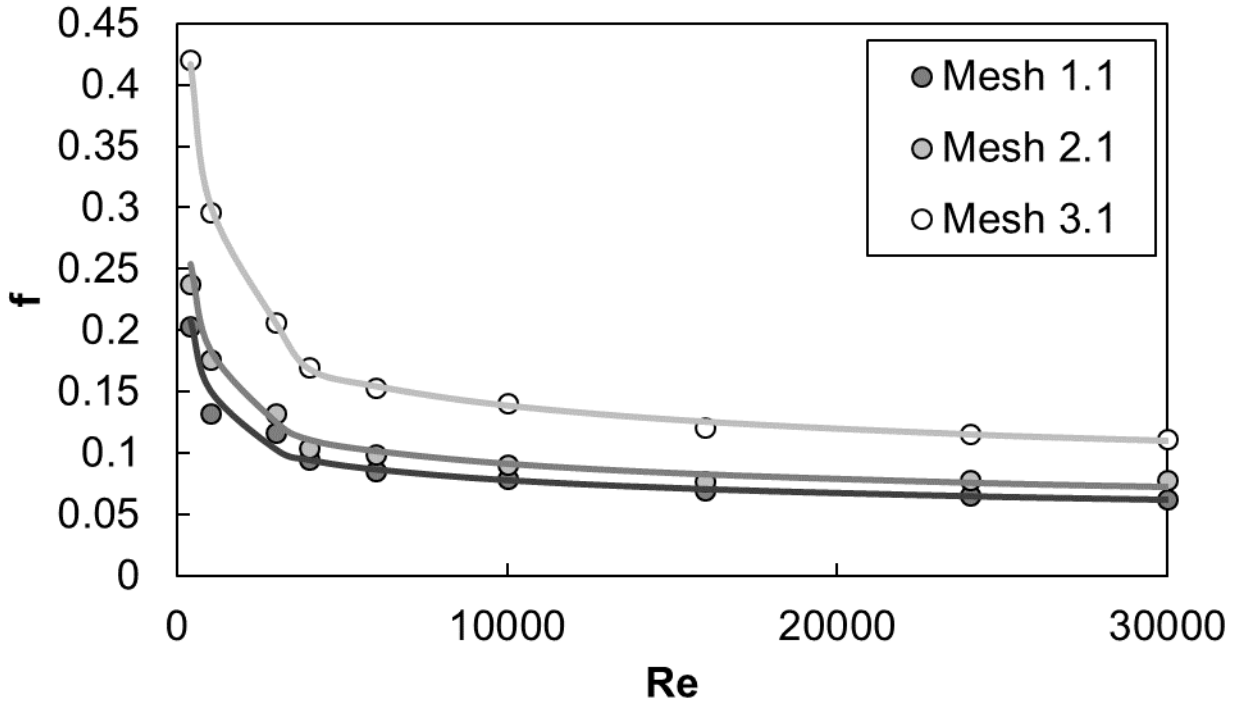


Figure 4.10: Friction factor (f) versus Reynolds number (Re) for Mesh 1.1 (22 mm period - 68% porosity), Mesh 2.1 (irregular period - 68% porosity) and Mesh 3.1 (12 mm period - 68% porosity)

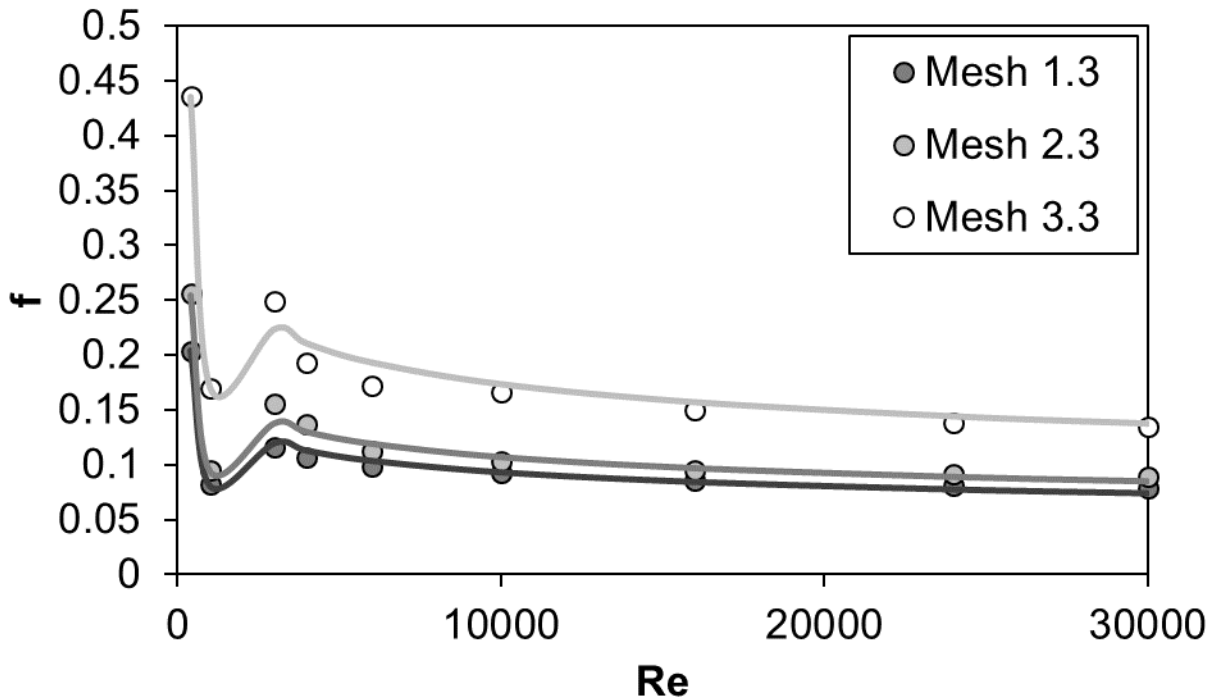


Figure 4.11: Friction factor (f) versus Reynolds number (Re) for Mesh 1.3 (22 mm period - 48% porosity), Mesh 2.3 (irregular period - 48% porosity) and Mesh 3.3 (12 mm period - 48% porosity)

If we compare the friction factors between mesh 1.1 and mesh 1.3 or mesh 3.1 and mesh 3.3 to show the effects of porosity for a given wave period of the screen, we can see that the friction factor decreases with the mesh porosity over the Reynolds number range between 400 and 3 000 but increases as the mesh porosity decreases from 68% to 48% for turbulent Reynolds numbers. The average difference of f between mesh 1.1 and mesh 1.3 is significant between $400 < Re < 3\ 000$ where the f of mesh 1.3 is 60% smaller than of mesh 1.1 and 16% greater in the transition and turbulent regimes. The average difference of f between mesh 3.1 and mesh 3.3 is significant between $400 < Re < 3\ 000$ where the f of mesh 3.3 is 74% smaller than of mesh 3.1 and 17% greater in the transition and turbulent regimes. The comparisons data between [Figure 4.10](#) and [Figure 4.11](#) thus indicate that the friction factor is influenced significantly in the range of $400 < Re < 3\ 000$ as the porosity changes. However, in the range of $4\ 000 < Re < 30\ 000$, the influences of porosity on the f are not as significant as those of the wave period of screen on the f . In turbulent regime of Re , the bulk of the flow passes in between the wave walls rather than flowing through the pores of the walls from one side to the other. The flow through the pores affect the near wall turbulence and profile losses or drag over the screen walls as indicated by LePoudre et al. [27]. Less flow through the pores then reduces the profile drag reducing the effects of porosity on the overall flow blockages and pressure drop in the screen channel. The mesh porosity thus does not influence much in the flow blockage in the screen channel at the higher Re .

The effects of wave period and mesh porosity of the screen with irregular wave patterns on the friction factor data in [Figure 4.10](#) and [Figure 4.11](#) are also evident. Mesh 2.1 friction factor is 18% higher than that of mesh 1.1 for Reynolds number up to and including 3 000 and 15% higher for Reynolds numbers greater than 3 000. Mesh 2.3 friction factor is 20% higher than mesh 1.3 for Reynolds number equal to 400, 15% higher for Reynolds number equal to 1 000 and then 13% higher for Reynolds number equal to and greater than 3 000. However, when compared mesh 2.1 is compared to mesh 3.1 and mesh 2.3 to mesh 3.3 the differences become significantly higher. Mesh 2.1 friction factor is 50% lower than that of mesh 3.1 for Reynolds number up to and including 3 000 and 44% lower for Reynolds numbers greater than 3 000. Mesh 2.3 friction factor is 53% lower than mesh 3.3 for Reynolds number up to 3 000 and 46% lower for Reynolds number equal to and greater than 3 000.

For the 68% porosity screen inserts (Mesh 1.1, Mesh 2.1, and Mesh 3.1), [Figure 4.10](#), the friction factor is a maximum at Reynolds number 400 and decreases to a minimum at 30 000. The friction factor, f for Mesh 1.1 decrease by 69%, mesh 2.1 decreases by 67% and mesh 3.1 decreases by 74% over the Reynolds number range from 400 to 30 000. The average difference of f in [Figure 4.10](#) between mesh 1.1 and mesh 3.1 is 40% in the laminar region ($400 \leq Re \leq 1\ 000$) and 35% in the transition and turbulent regimes ($3\ 000 \leq Re \leq 30\ 000$), with mesh 3.1 having slightly higher friction factors than that of mesh 1.1 for corresponding Reynolds numbers. The data in [Figure 4.10](#) clearly demonstrate that the friction factor for given porosity screen and Re is reduced significantly as the periodicity of the screen wave is increased. The irregularity of the wave period has small effects on the

friction factor. As indicated previously, the smaller wave period provides more flow blockage in the channel to increase the pressure drop and friction factor at a given Re.

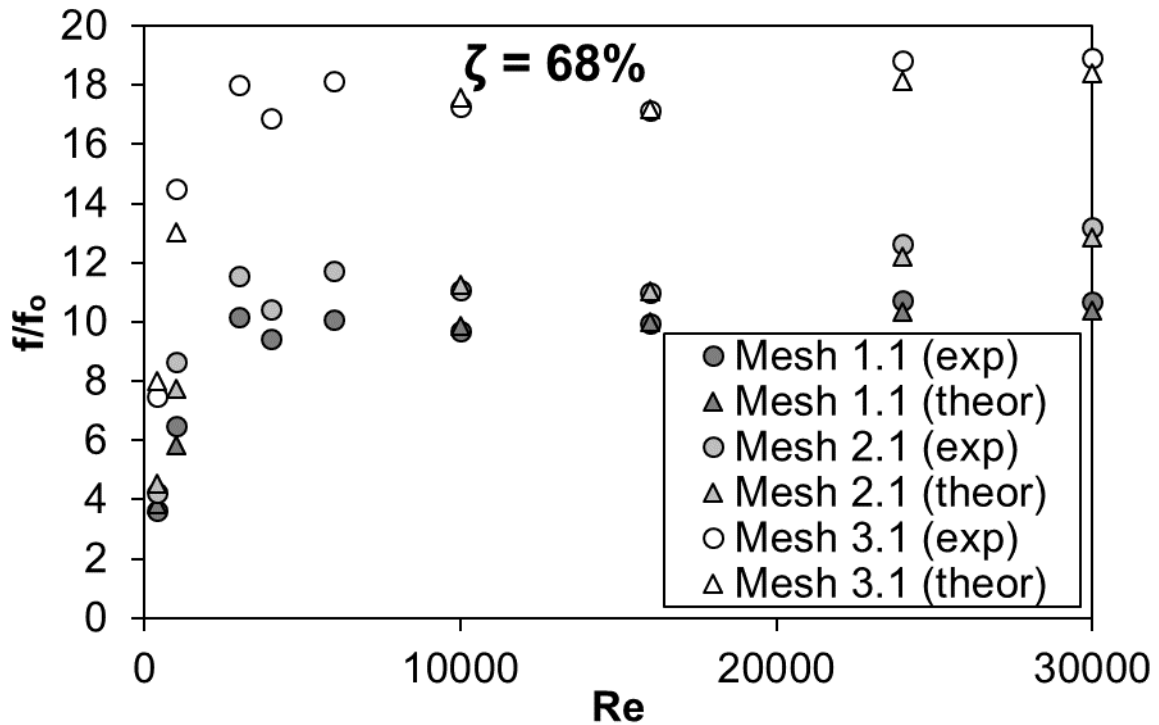


Figure 4.12: Friction factor ratio (f/f_0) versus Reynolds number (Re) for Mesh 1.1 (22 mm period - 68% porosity), Mesh 2.1 (irregular period - 68% porosity) and Mesh 3.1 (12 mm period - 68% porosity)

If we compare the f/f_0 data between mesh 1.1 and mesh 1.3 or mesh 3.1 and mesh 3.3 to show the effects of porosity for a given wave period of the screen, we can see that the f/f_0 data is similar for $400 \leq Re \leq 3\,000$ and increases with the mesh porosity over the Reynolds greater than 3 000. The average difference of f/f_0 between mesh 1.1 and mesh 1.3 is significant between $400 < Re < 3\,000$ where the f of mesh 1.3 is 60% smaller than of mesh 1.1 and 16% greater in the transition and turbulent regimes. The average difference of f/f_0 between mesh 3.1 and mesh 3.3 is significant between $400 < Re < 3\,000$ where the f/f_0 of mesh 3.3 is 74% smaller than of mesh 3.1 and 17% greater in the transition and turbulent regimes. The comparisons data between Figure 4.12 and Figure 4.13 thus indicate that the friction factor is influenced significantly in the range of $400 < Re < 3\,000$ as the porosity changes. However, in the range of $4\,000 < Re < 30\,000$, the influences of porosity on the f/f_0 are not as significant as those of the wave period of screen on the f/f_0 . In turbulent regime of Re, the bulk of the flow passes in between the wave walls rather than flowing through the pores of the walls from one side to the other. The flow through the pores affect the near wall turbulence and profile losses or drag over the screen walls as indicated by LePoudre et al. [27]. Less flow through the pores then reduces the profile drag reducing the effects of porosity on the overall flow blockages and pressure drop in the screen channel. The mesh porosity thus does not influence much in the flow blockage in the screen channel at the higher Re.

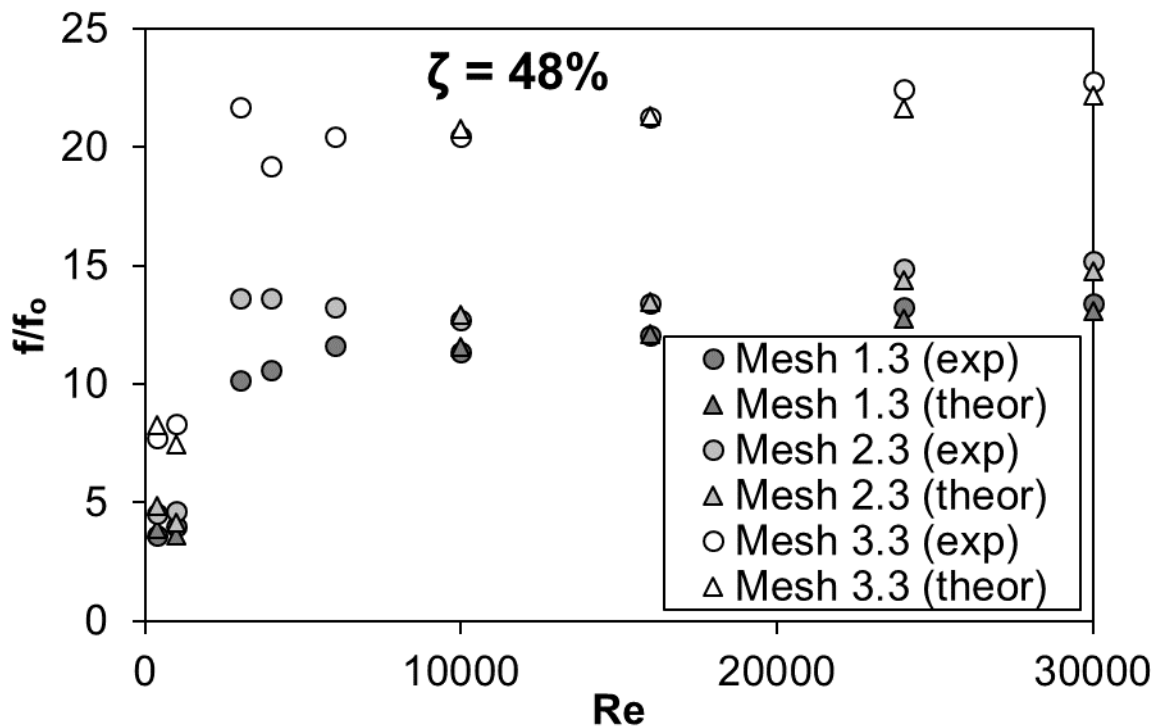


Figure 4.13: Friction factor ratio (f/f_0) versus Reynolds number (Re) for Mesh 1.3 (22 mm period - 48% porosity), Mesh 2.3 (irregular period - 48% porosity) and Mesh 3.3 (12 mm period - 48% porosity)

The values of f_0 in Figure 4.12 and Figure 4.13 are obtained from the results in Section 4.2 for the baseline smooth channel measurements at the corresponding channel height. The effects of wave period and mesh porosity of the screen with irregular wave patterns on the f/f_0 data in Figure 4.12 and Figure 4.13 are also evident. Mesh 2.1 f/f_0 is 18% higher than that of mesh 1.1 for Reynolds number up to and including 3 000 and 15% higher for Reynolds numbers greater than 3 000. Mesh 2.3 f/f_0 is 20% higher than mesh 1.3 for Reynolds number equal to 400, 15% higher for Reynolds number equal to 1 000 and then 13% higher for Reynolds number equal to and greater than 3 000. However, when compared mesh 2.1 is compared to mesh 3.1 and mesh 2.3 to mesh 3.3 the differences become significantly higher. Mesh 2.1 friction factor is 50% lower than that of mesh 3.1 for Reynolds number up to and including 3 000 and 44% lower for Reynolds numbers greater than 3 000. Mesh 2.3 f/f_0 is 53% lower than mesh 3.3 for Reynolds number up to 3 000 and 46% lower for Reynolds number equal to and greater than 3 000.

The influences of the two geometrical properties; period and porosity, are once again visible in these figures. A more porous screen with a larger period will require less pumping power, except for in the range of $400 < Re < 3\,000$ where the higher porosity screen insert requires less pumping power (lower f/f_0 ratio) than that of a lower porosity screen insert of the same period.

Table 4.8 shows determined correlations for the friction factor and f/f_0 ratios as functions of Reynolds number for the various screen inserts tested at a 14 mm channel height. Each correlation is determined using a linear regression curve fit for the natural logarithm plots of the data points. The accuracy of the correlation is calculated using Eq. (4.1) is also

given for each data set. The subscripts in f and (f/f_0) in Eqs. (4.2) - (4.13) indicate the mesh number for the correlations. Finally, a factor is calculated to obtain the friction factor, f or f/f_0 ratio of a screen insert from the other screen insert of the same porosity. This also indicates the effect porosity has on both the friction factor in the screen channel as well as the pumping power required for the screen inserts.

$$Accuracy = \frac{|f_{exp} - f_{corr}|}{f_{exp}} \quad (4.1)$$

Table 4.8: Friction factor and f/f_0 ratio correlations for various screen inserts tests in 14 mm channel

Friction factor – 68% porosity screen insert

Mesh 1.1:

$$f_{1.1} = \begin{cases} 1.721Re^{-0.352}, & Re \leq 3\,000 \\ 0.546Re^{-0.212}, & Re \geq 4\,000 \end{cases} \quad (4.2)$$

Accuracy: $\pm 3\%$

Mesh 2.1:

$$f_{2.1} = \begin{cases} 2.099Re^{-0.352}, & Re \leq 3\,000 \\ 0.644Re^{-0.212}, & Re \geq 4\,000 \end{cases} \quad (4.3)$$

Accuracy: $\pm 7\%$

Mesh 3.1:

$$f_{3.1} = \begin{cases} 3.441Re^{-0.352}, & Re \leq 3\,000 \\ 0.975Re^{-0.212}, & Re \geq 4\,000 \end{cases} \quad (4.4)$$

Accuracy: $\pm 4\%$

Factor:

$$f_{1.1} = \begin{cases} 0.50f_{3.1}, & Re \leq 3\,000 \\ 0.56f_{3.1}, & Re \geq 4\,000 \end{cases}$$

$$f_{2.1} = \begin{cases} 0.61f_{3.1}, & Re \leq 3\,000 \\ 0.66f_{3.1}, & Re \geq 4\,000 \end{cases}$$

Friction factor – 48% porosity screen insert

Mesh 1.3:

$$f_{1.3} = \begin{cases} 95.61Re^{-1.026}, & Re \leq 1\,000 \\ 0.653Re^{-0.230}, & Re \geq 3\,000 \end{cases} \quad (4.5)$$

Accuracy: $\pm 6\%$

Mesh 2.3:

$$f_{2.3} = \begin{cases} 115.953Re^{-1.026}, & Re \leq 1\,000 \\ 0.898Re^{-0.230}, & Re \geq 3\,000 \end{cases} \quad (4.6)$$

Accuracy: $\pm 6\%$

Mesh 3.3:

$$f_{3.3} = \begin{cases} 203.426Re^{-1.026}, & Re \leq 1\,000 \\ 1.372Re^{-0.230}, & Re \geq 3\,000 \end{cases} \quad (4.7)$$

Accuracy: $\pm 5\%$

Factor:

$$f_{1.3} = \begin{cases} 0.47f_{3.3}, & Re \leq 1\,000 \\ 0.67f_{3.3}, & Re \geq 3\,000 \end{cases}$$

$$f_{2.3} = \begin{cases} 0.57f_{3.3}, & Re \leq 1\,000 \\ 0.77f_{3.3}, & Re \geq 3\,000 \end{cases}$$

f/f_0 ratio – 68% porosity screen insert

Mesh 1.1:

$$f/f_{0.1.1} = \begin{cases} 0.0450Re^{0.724}, & Re \leq 1\,000 \\ 8.091Re^{0.0221}, & Re \geq 3\,000 \end{cases} \quad (4.8)$$

Accuracy: $\pm 5\%$

Mesh 2.1:

$$f/f_{0.2.1} = \begin{cases} 0.0567Re^{0.724}, & Re \leq 1\,000 \\ 9.536Re^{0.0221}, & Re \geq 3\,000 \end{cases} \quad (4.9)$$

Accuracy: $\pm 10\%$

Mesh 3.1:

$$f/f_{0.3.1} = \begin{cases} 0.0978Re^{0.724}, & Re \leq 1\,000 \\ 14.448Re^{0.0221}, & Re \geq 3\,000 \end{cases} \quad (4.10)$$

Accuracy: $\pm 5\%$

Factor:

$$f/f_{0.1.1} = \begin{cases} 0.46f/f_{0.3.1}, & Re \leq 1\,000 \\ 0.56f/f_{0.3.1}, & Re \geq 3\,000 \end{cases}$$

$$f/f_{0.2.1} = \begin{cases} 0.58f/f_{0.3.1}, & Re \leq 1\,000 \\ 0.66f/f_{0.3.1}, & Re \geq 3\,000 \end{cases}$$

f/f_0 ratio – 48% porosity screen insert

Mesh 1.3:

$$f/f_{0.1.3} = \begin{cases} 2.218Re^{0.0827}, & Re \leq 1\,000 \\ 5.600Re^{0.0797}, & Re \geq 3\,000 \end{cases} \quad (4.11)$$

Accuracy: $\pm 5\%$

Mesh 2.3:

$$f/f_{0.2.3} = \begin{cases} 2.690Re^{0.0827}, & Re \leq 1\,000 \\ 6.605Re^{0.0797}, & Re \geq 3\,000 \end{cases} \quad (4.12)$$

Accuracy: $\pm 8\%$

Mesh 3.3:

$$f/f_{0.3.3} = \begin{cases} 4.719Re^{0.0827}, & Re \leq 1\,000 \\ 10.567Re^{0.0797}, & Re \geq 3\,000 \end{cases} \quad (4.13)$$

Accuracy: $\pm 8\%$

Factor:

$$f/f_{0.1.3} = \begin{cases} 0.47f/f_{0.3.3}, & Re \leq 1\,000 \\ 0.53f/f_{0.3.3}, & Re \geq 3\,000 \end{cases}$$

$$f/f_{0.2.3} = \begin{cases} 0.57f/f_{0.3.3}, & Re \leq 1\,000 \\ 0.63f/f_{0.3.3}, & Re \geq 3\,000 \end{cases}$$

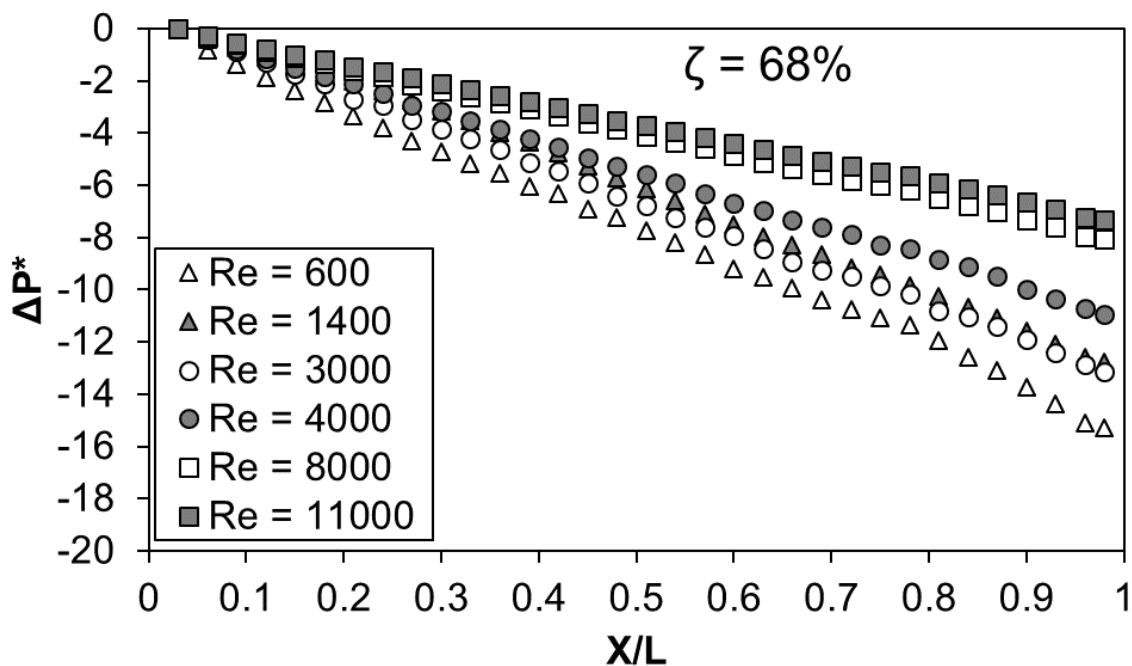
4.3.2 5-MM CHANNEL

Figure 4.14 shows the normalised pressure drop data (ΔP^*) in the X/L direction of the test section for four porous screen inserts, namely: (a) mesh 4.1, (b) mesh 4.3, (c) mesh 5.1 and (d) mesh 5.3. To condense the amount of data shown, only the air mass flow rates

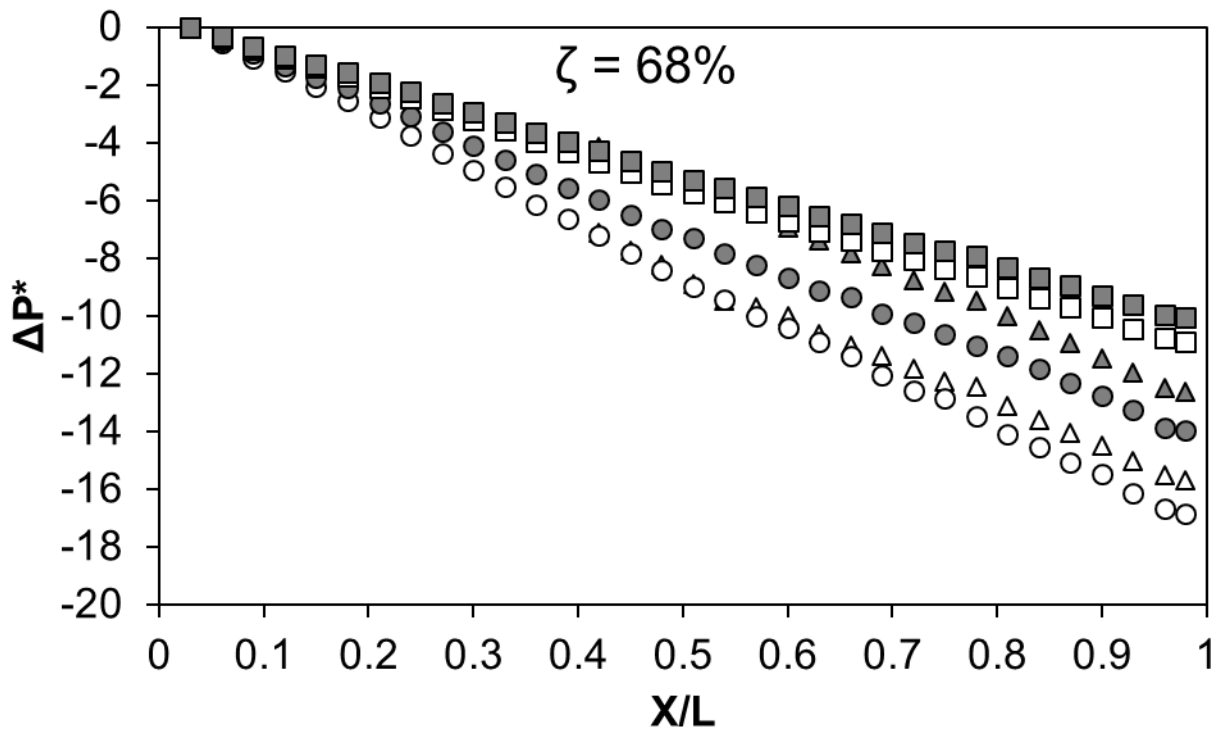
corresponding to Reynolds numbers 1 000, 1 400, 3 000, 4 000, and 11 000 are included in Figure 4.14. The ΔP^* data in the figure is calculated from Equation (3.8). The ΔP^* drops along the length of the test section (X/L) for both porous screens as proven by Mahmood et al. (2015). Note that the higher the negative value for ΔP^* the higher the pressure drop is along the channel. Only the last 40% of the pressure drop data is shown as the ΔP^* drop is linear along X/L for this region and indicated a fully developed hydrodynamic flow.

The friction factor (f) in the test section is determined by fitting a linear regression line on the pressure drop data in the fully developed flow region and using the slope of the fitted line in Equation (3.9). Figure 4.15 shows the determined friction factors for the various porous screen inserts for all Reynolds number tested. For all four screen inserts the friction factor is a maximum at Reynolds number 400 and decreases to a minimum at 30 000. The friction factor for mesh 4.1 and mesh 5.1 decreases by 62% and 64%, respectively, for $400 \leq Re \leq 11\ 000$ and decreases by 38% and 25% for meshes 4.3 and 5.3, respectively, for $400 \leq Re \leq 1\ 000$. The friction factor then increases by 28% and 11% for meshes 4.3 and 5.3, respectively, for $1\ 000 \leq Re \leq 3\ 000$ and decreases a further 41% and 39% for meshes 4.3 and 5.3, respectively, for $Re \geq 3\ 000$. This shows that the 48% porosity screen inserts shift the start of the transition regime to $Re = 1\ 000$, whereas, it remains the same (between $1\ 400 \leq Re \leq 3\ 000$) for the 68% porosity screen inserts.

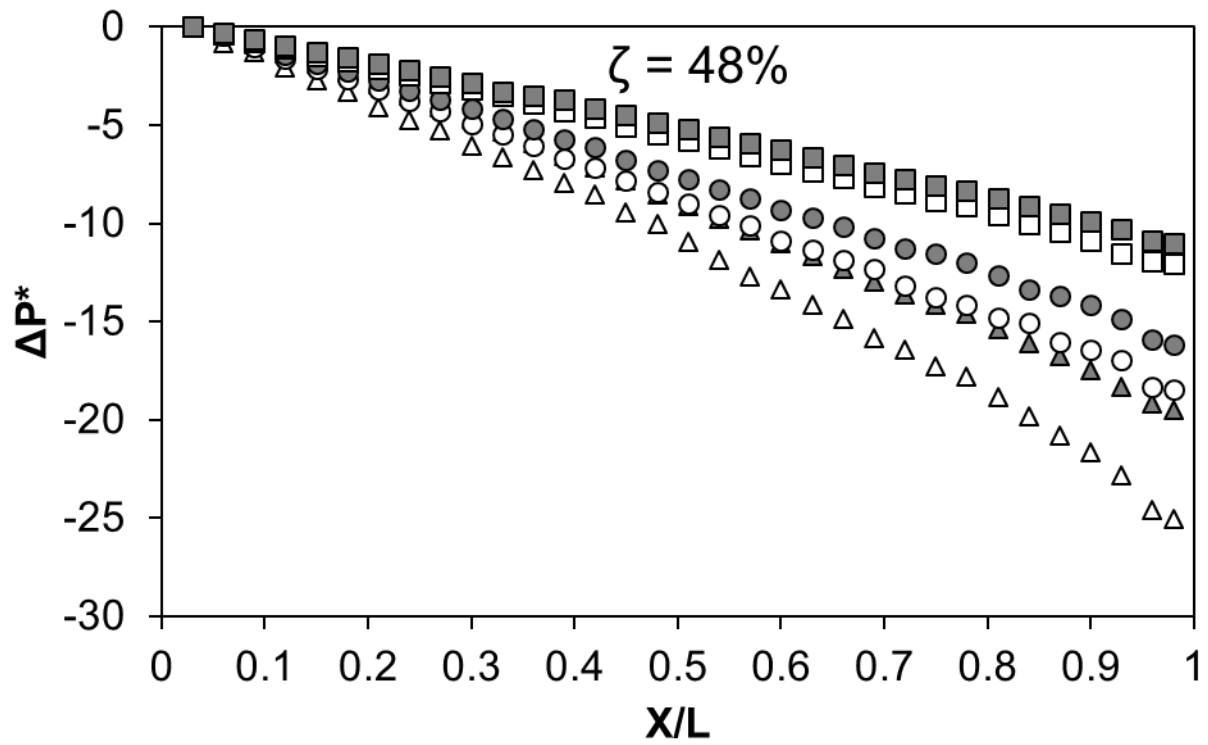
From Figure 4.15 it is evident that the period of the screen insert influences the friction factor. For both the 68% porosity screen inserts, Figure 4.15, and the 48% porosity screen inserts, Figure 4.15, the 12 mm period screen inserts' friction factors are higher than that of the 18 mm period screen inserts for all Reynolds numbers. An increase of 33% in period gives a 43% and 23% increase in friction factors for the 68% porosity screen inserts and 48% porosity screen inserts, respectively, for corresponding Reynolds numbers.



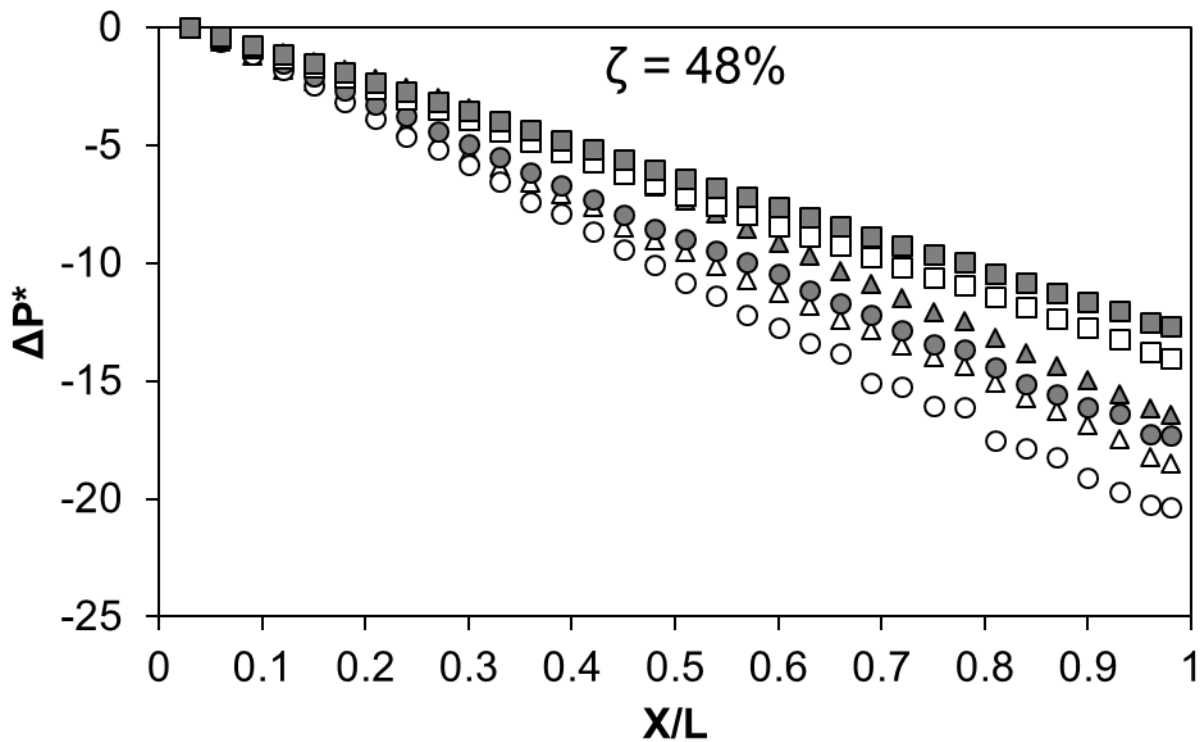
(a)



(b)



(c)



(d)

Figure 4.14: Normalised pressure drop data for 5 mm channel for $Re = 1\ 000, 1\ 400, 3\ 000, 4\ 000, 11\ 000$ for (a) Mesh 4.1 (68% porosity – 18 mm period), (b) Mesh 4.3 (48% porosity – 18 mm period), (c) Mesh 5.1 (68% porosity – 12 mm period), and (d) Mesh 5.3 (48% porosity – 12 mm period)*

* legends for the symbols are provided in Fig. 4.13(a)

Figure 4.15 presents the friction factor, f for the entire range of Re tested with both the 68% and 48% porosity screens with the wave periods of 12 mm and 18 mm. The f in the figure incorporates pressure drop caused by both the shear stress and form drag on the screen. As shown in Figure 4.15, the value of f decreases, in general, as the Re increases for all four screens. The exception occurs for the 12 mm period screens when f increases with Re in the transition flow regime of $1\ 000 \leq Re \leq 2\ 700$. For the 12 mm wave period in Fig. 5(a), the effects of porosity are evidenced at $Re > 400$ where f is about 30% greater for the 48% porosity than for the 68% porosity screen. However, for the 18 mm wave period, the f values are about 25% smaller, in general, for the 68% porosity than for the 48% porosity screen at $Re \geq 2\ 700$. The effects of wave period on the f data are also evident in Fig. 5(a). The 18 mm wave period provides about 10% less f at $1\ 000 \leq Re \leq 2\ 700$ and about 40% greater f at $Re > 2\ 700$ than the 12 mm wave period for the 68% porosity screen. For the 48% porosity screen, the f data are about 25% less f at $Re \leq 2\ 700$ and about 10% greater f at $Re > 2\ 700$ with the 12 mm wave period compared to the 18 mm wave period as the flow blockage is less in the larger period of the wavy screen. Also, note that f is much more sensitive to Re change at $Re < 2\ 000$ than at $Re \geq 2\ 700$ for the screens. The value of f drops about by 30% between $400 \leq Re < 2\ 000$ and by 60% between $2\ 700 \leq Re \leq 11\ 000$ for the screens.

Figure 4.15 also includes the best-fit $f-Re$ correlations determined from the experimental data. The solid and dotted lines in the plot represent the simple correlations in Table 4.9. Only two $f-Re$ correlation equations are fitted for the entire range of $Re \leq 11\,000$ at a given screen porosity and wave period. Note that the $f-Re$ correlations for 68% and 48% porosity at a given Re range and wave period are related by a simple multiplying factor.

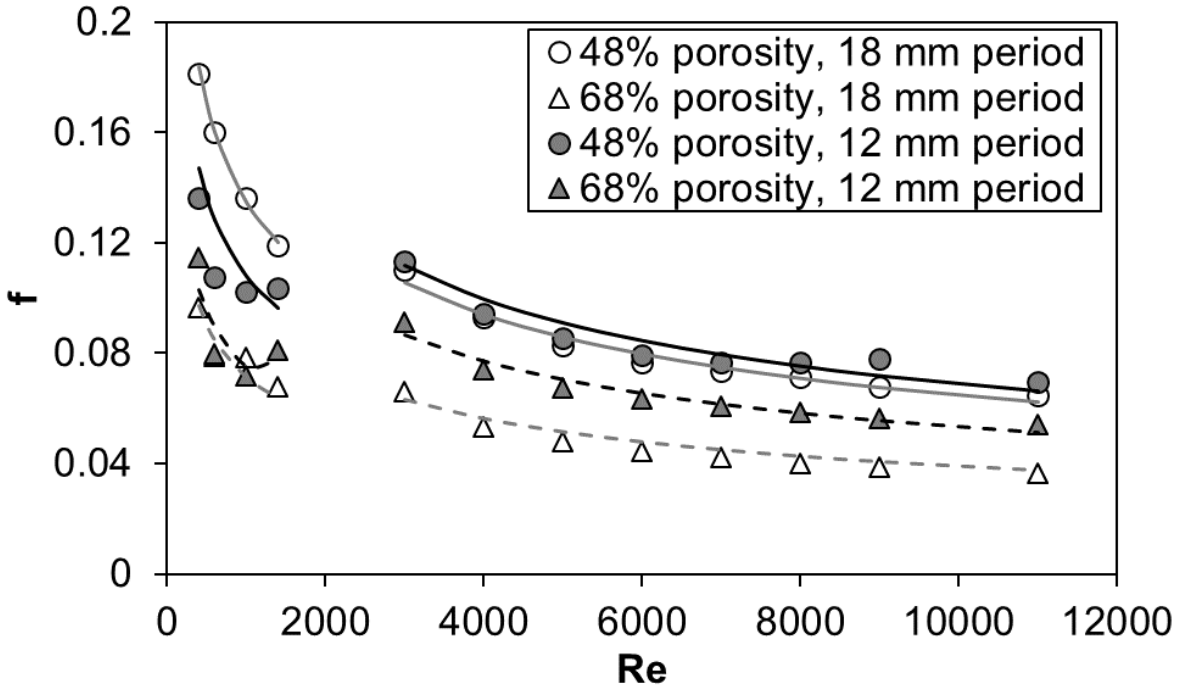


Figure 4.15: Friction factor (f) versus Reynolds number (Re) for 5 mm channel height

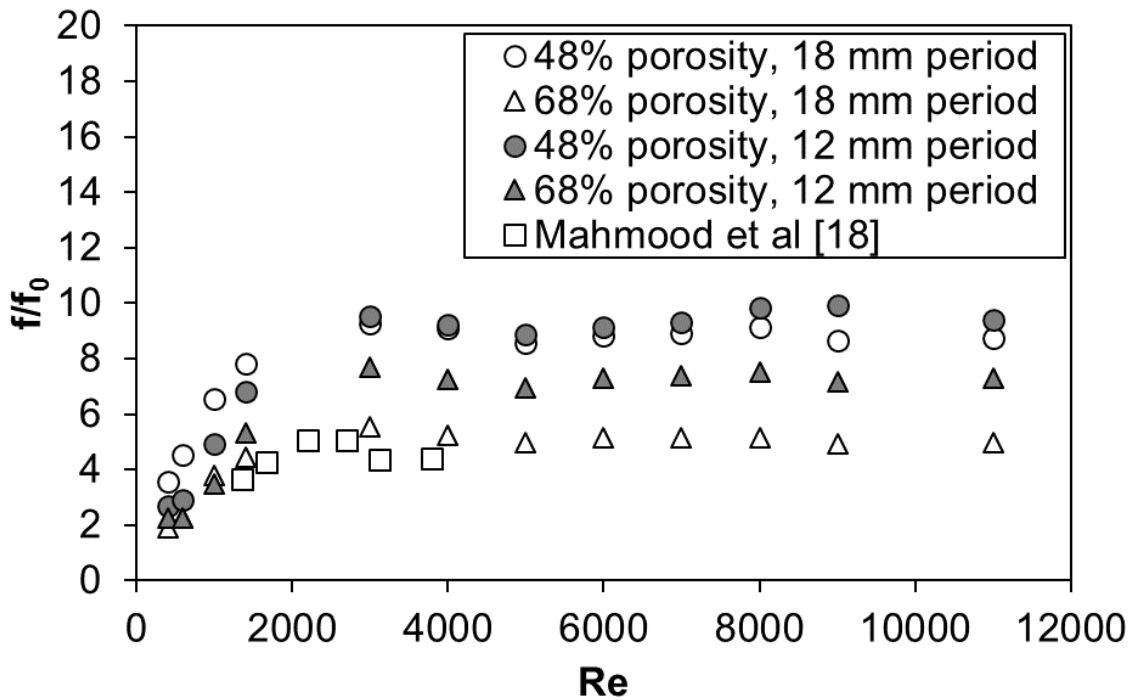


Figure 4.16: f/f_0 ratio versus Reynolds number (Re) for 5 mm channel height

The friction factors of Figure 4.15 are normalized with the measured baseline friction factor, f_0 in the smooth channel and presented in Figure 4.16. The ratio $f/f_0 > 1.0$ indicates the pumping power enhancement in the channel with the screen compared to the smooth channel at the same Re . As shown in Figure 4.16 for the screen inserts, the ratio f/f_0 generally increases with the $Re \leq 2\,700$, but then changes little as the Re increases further. For the 12 mm period, the f/f_0 values change little between the 48% and 68% porosity screens at all Re . For the 18 mm period, the f/f_0 are generally smaller for the 68% porosity compared to the 48% porosity screen at all Re . To compare the effects of the wave period in Figure 4.16, the f/f_0 are always smaller for the 18 mm period than for the 12 mm period irrespective of the screen porosity. Table 4.9 provides the simple equations of the (f/f_0) - Re correlations and the maximum difference, $\Delta(f/f_0)$ between the correlations and experimental f/f_0 . Here also, only two correlations of (f/f_0) - Re are developed to fit the experimental data for all the $Re \leq 11\,000$ at a given porosity and wave period. Figure 4.16 also compares the present data with those in Mahmood et al. [18] at $Re < 4\,000$. The present f/f_0 are much higher, except for the 68% porosity screen with 18 mm wave period, as the wavy screen in [18] employs a much higher porosity of 80% and lower wire diameter of 0.13 mm providing smaller flow blockage.

Table 4.9 shows the friction factor correlations and the f/f_0 ratio correlations as functions of Reynolds number for all four screen inserts tested at a 5 mm channel height. The factor for getting a screen inserts' correlation from that of another is also given in the table. These simple factors also show the effect that the period and the porosity of the screen insert has on the friction factor and required pumping power factor (f/f_0 ratio).

Table 4.9: Friction factor and f/f_0 ratio correlations for various screen inserts tests in 5 mm channel

Friction factor – 68% porosity screen inserts

Mesh 4.1:

$$f_{4.1} = \begin{cases} 0.743Re^{-0.339}, & Re \leq 1\,400 \\ 1.617Re^{-0.405}, & Re \geq 3\,000 \end{cases} \quad (4.14)$$

Accuracy: $\pm 7\%$

Mesh 5.1:

$$f_{5.1} = \begin{cases} 1.401Re^{-0.339}, & Re \leq 1\,400 \\ 2.694Re^{-0.405}, & Re \geq 3\,000 \end{cases} \quad (4.15)$$

Accuracy: $\pm 4\%$

Factor:

$$f_{4.1} = \begin{cases} 0.53f_{5.1}, & Re \leq 1\,400 \\ 0.60f_{5.1}, & Re \geq 3\,000 \end{cases}$$

Friction factor – 48% porosity screen inserts

Mesh 4.3:

$$f_{4.3} = \begin{cases} 0.841Re^{-0.339}, & Re \leq 1\,000 \\ 2.209Re^{-0.405}, & Re \geq 3\,000 \end{cases} \quad (4.16)$$

Accuracy: $\pm 9\%$

Mesh 5.3:

$$f_{5.3} = \begin{cases} 1.121Re^{-0.339}, & Re \leq 1\,000 \\ 2.856Re^{-0.405}, & Re \geq 3\,000 \end{cases} \quad (4.17)$$

Accuracy: $\pm 8\%$

Factor:

$$f_{4.3} = \begin{cases} 0.80f_{5.1}, & Re \leq 1\,000 \\ 1.06f_{5.1}, & Re \geq 3\,000 \end{cases}$$

$$f_{5.3} = \begin{cases} 0.60f_{5.1}, & Re \leq 1\,000 \\ 0.82f_{5.1}, & Re \geq 3\,000 \end{cases}$$

f/f_0 ratio – 68% porosity screen inserts

Mesh 4.1:

$$f/f_{0.4.1} = \begin{cases} 0.0369Re^{0.654}, & Re \leq 1\,400 \\ 7.897Re^{-0.0504}, & Re \geq 3\,000 \end{cases} \quad (4.18)$$

Accuracy: $\pm 5\%$

Mesh 5.1:

$$f/f_{0.5.1} = \begin{cases} 0.0697Re^{0.654}, & Re \leq 1\,400 \\ 13.854Re^{-0.0504}, & Re \geq 3\,000 \end{cases} \quad (4.19)$$

Accuracy: $\pm 3\%$

Factor:

$$f/f_{0.4.1} = \begin{cases} 0.53f/f_{0.5.1}, & Re \leq 1\,400 \\ 0.56f/f_{0.5.1}, & Re \geq 3\,000 \end{cases}$$

f/f_0 ratio – 48% porosity screen inserts

Mesh 4.3:

$$f/f_{0.4.3} = \begin{cases} 0.0439Re^{0.654}, & Re \leq 1\,400 \\ 11.222Re^{-0.0504}, & Re \geq 3\,000 \end{cases} \quad (4.20)$$

Accuracy: $\pm 5\%$

Mesh 5.3:

$$f/f_{0.5.3} = \begin{cases} 0.0558Re^{0.654}, & Re \leq 1\,400 \\ 14.686Re^{-0.0504}, & Re \geq 3\,000 \end{cases} \quad (4.21)$$

Accuracy: $\pm 7\%$

Factor:

$$f/f_{0.4.3} = \begin{cases} 0.63f/f_{0.5.1}, & Re \leq 1\,400 \\ 0.81f/f_{0.5.1}, & Re \geq 3\,000 \end{cases}$$

$$f/f_{0.5.3} = \begin{cases} 0.80f/f_{0.5.1}, & Re \leq 1\,400 \\ 1.06f/f_{0.5.1}, & Re \geq 3\,000 \end{cases}$$

4.4 TWO WALL HEATING

A total of 102 sets of heat transfer measurements with two-wall heating are obtained, which consisted of 9 mass Reynolds numbers for the 14 mm channel and 12 Reynolds numbers for the 5 mm channel for 10 different porous screen inserts. The two-wall heat transfer experiments are summarised in [Table 4.10](#).

Table 4.10: Two-wall heat transfer experimental test matrix

Porous screen insert	Reynolds number range	Re numbers measurements	Porosity	Period	Channel Height
Mesh 1.1	$400 \leq Re \leq 30\,000$	9	68%	22	14
Mesh 2.1	$400 \leq Re \leq 30\,000$	9	68%	Irregular	14
Mesh 3.1	$400 \leq Re \leq 30\,000$	9	68%	12	14
Mesh 1.3	$400 \leq Re \leq 30\,000$	9	48%	22	14
Mesh 2.3	$400 \leq Re \leq 30\,000$	9	48%	Irregular	14
Mesh 3.3	$400 \leq Re \leq 30\,000$	9	48%	12	14
Mesh 4.1	$400 \leq Re \leq 11\,000$	12	68%	18	5
Mesh 5.1	$400 \leq Re \leq 11\,000$	12	68%	12	5
Mesh 4.3	$400 \leq Re \leq 11\,000$	12	48%	18	5
Mesh 5.3	$400 \leq Re \leq 11\,000$	12	48%	12	5

4.4.1 14-MM CHANNEL

Figure 4.17 provides the local Nusselt number (Nu_x) along the normalized length of the channel (X/L) at the centreline for the 68% porosity screen inserts and Figure 4.18 provides the local Nu_x along the X/L at the centreline for the 48% porosity screen inserts for the heated walls as the Reynolds number varies. The data are measured with both the bottom and the top walls (203 mm walls) heated when the channel height is 14 mm. The magnitude of the heat flux is varied as far as possible with each Reynolds number to maintain a sufficient temperature difference between the wall and bulk air flow to reduce uncertainty in the measurements. The differences ($T_{w,x} - T_{m,x}$) in Equation (3.13) for the 68% and 48% porosity screen inserts are between 5°C and 8°C depending on the Reynolds number. The first location of the data in Figure 4.17 and Figure 4.18 is $X/L = 0.04$ and ends at $X/L = 0.96$. In the screen channel the slope of Nu_x decreases along X/L decreases at a Re in the range of $0.0 \leq X/L \leq 0.6$ and then becomes constant for $X/L > 0.6$. The smooth inlet flow into the screen test section undergoes development in $0.0 \leq X/L \leq 0.6$ before it becomes thermally fully turbulent near $X/L > 0.6$ resulting in a constant Nu_x along X/L at a Re in the screen channel. It is worthy to note that the value of Nu_x along X/L in Figure 4.17 and Figure 4.18 are always higher for the screen channel than for the 14 mm baseline channel at the corresponding locations and Reynolds number. The distributions of Nu_x in Figs. 4.16 and 4.17 also decreases with the Re because the mass flow rate reduces. For a given mesh porosity and a Re either in Fig. 4.16 or Fig. 4.17, the Nu_x distributions are higher as the wave period is reduced. However, the influences of mesh porosity on the Nu_x distributions are small as the Nu_x values at a corresponding Re and a wave period change little with the porosity between Fig. 4.16 and Fig. 4.17.

An average Nusselt number, shown in Figure 4.19 and Figure 4.20, is determined using the average of the local Nusselt numbers in $0.6 < X/L < 0.96$ at a specific Reynolds number. Figure 4.19 and Figure 4.20 show the effects a change in period have on the average Nu when the porosity remains the same. Figure 4.19 compares three screen inserts of different periods made with a 68% porosity wire mesh and Figure 4.20 compares three

screen inserts of different periods made with a 48% porosity wire mesh. Mesh 2.1 and 2.3 are used to identify the effects of the irregular period might have on the Nusselt number results due to the manufacturing inaccuracies.

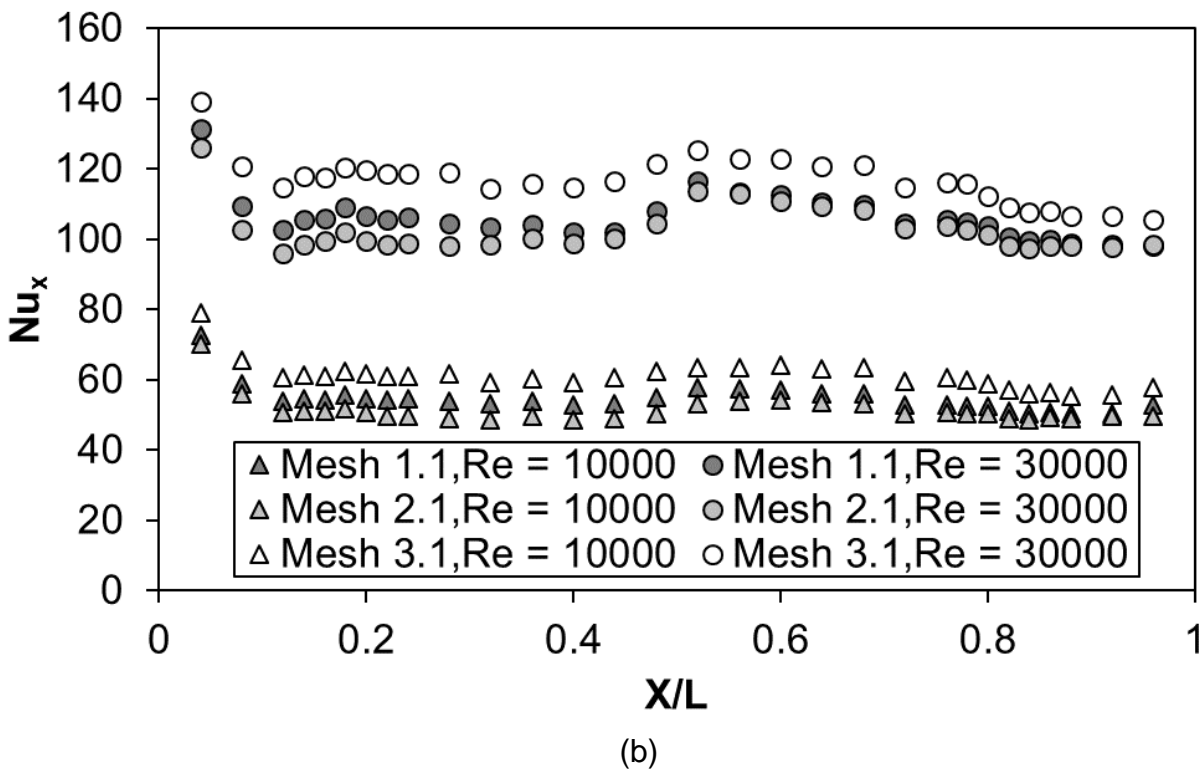
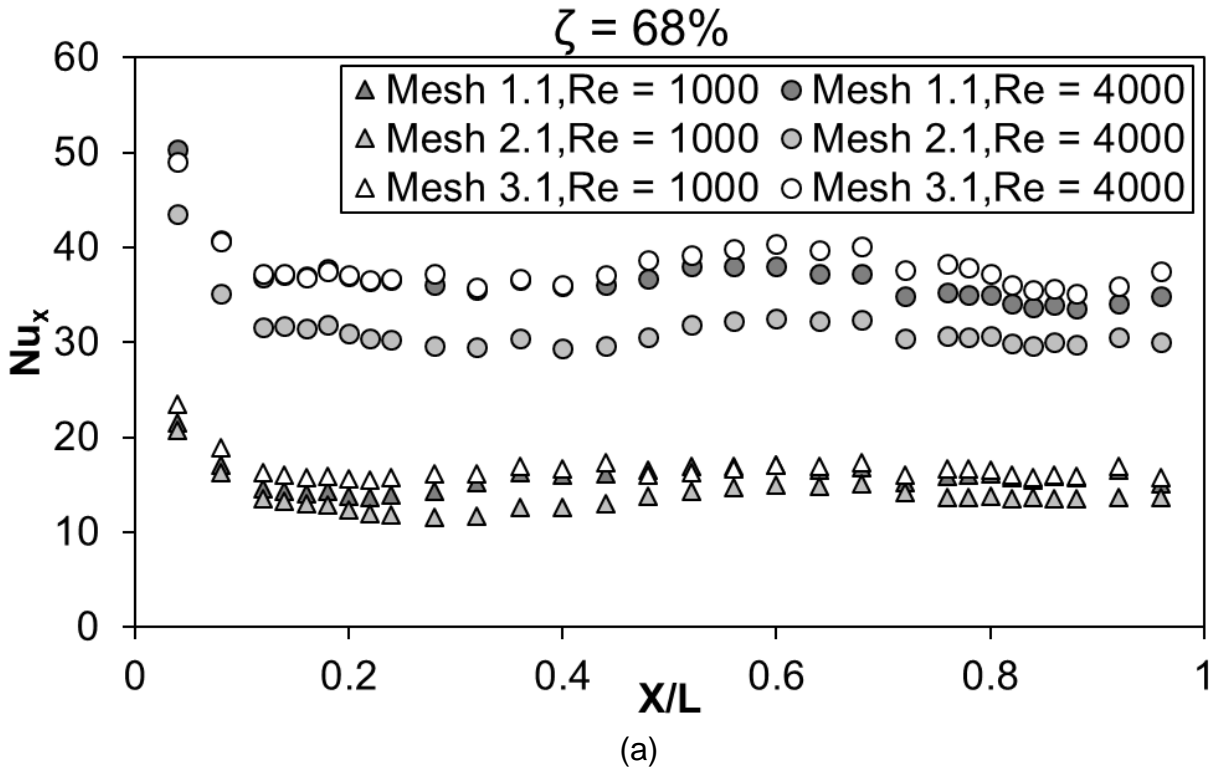
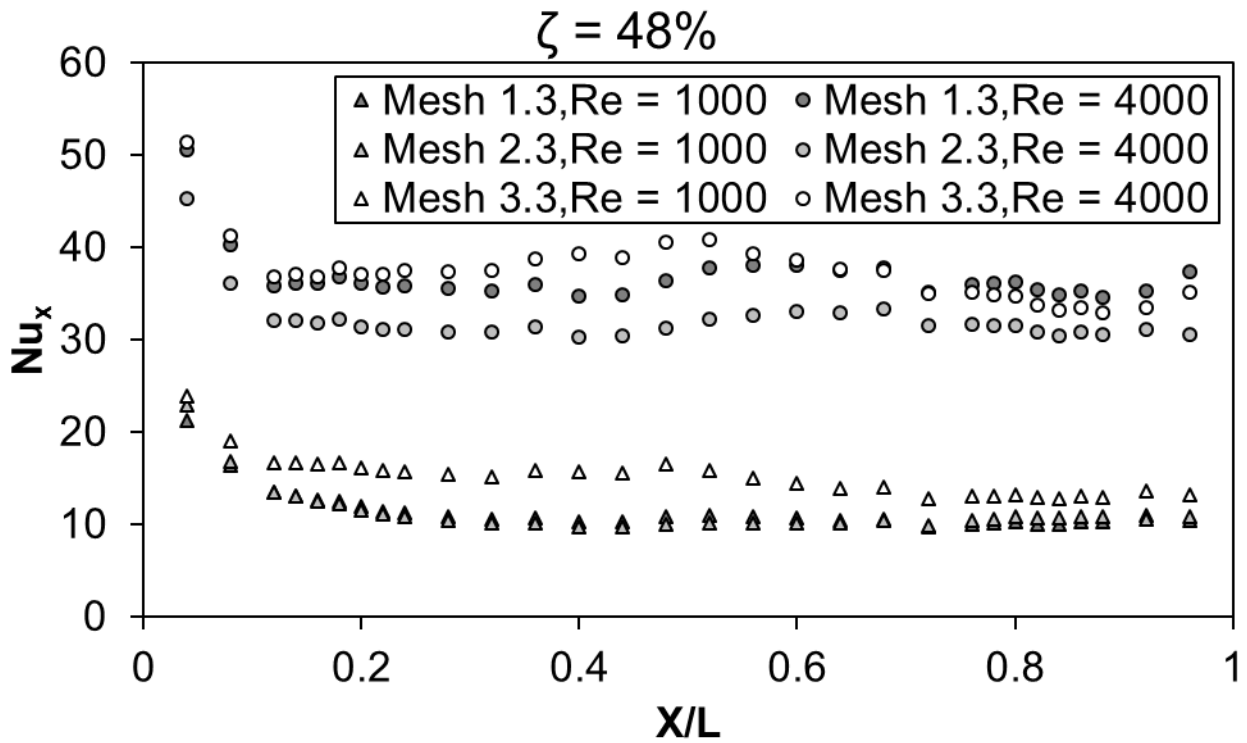
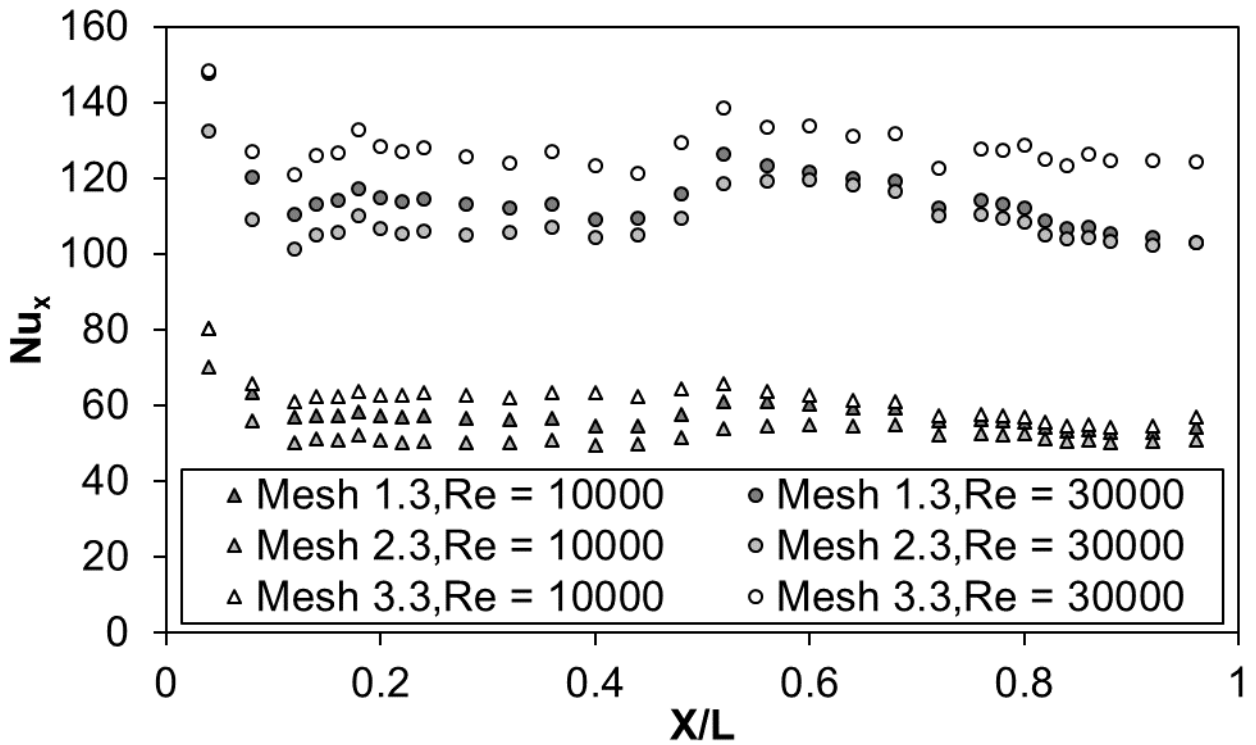


Figure 4.17: Local Nusselt number values along the X/L of the test section for (a) laminar and (b) turbulent region



(a)



(b)

Figure 4.18: Local Nusselt number values along the X/L of the test section for (a) laminar and (b) turbulent region

For the 68% porosity screen inserts, [Figure 4.19](#), the average Nusselt number is a minimum at Reynolds number 400 and increases to a maximum at 30 000. Mesh 1.1 increased by 838%, mesh 2.1 increased by 1 151% and mesh 3.1 increased by 789% over the Reynolds number range from 400 to 30 000. The increase in Nusselt number from Reynolds number 1 000 to 3 000 (transition regime) for mesh 1.1 is by 76%, mesh 2.1 is by 108% and mesh 3.1 is by 96%. The average difference of Nu_{avg} in [Figure 4.19](#) between mesh 1.1 and mesh 3.1 is 5% in the laminar region ($Re = 400$ to $3\,000$) and 10% in the transition ($Re = 3\,000$ to $10\,000$) and turbulent regimes ($Re = 10\,000$ to $30\,000$), with mesh 3.1 having higher Nusselt numbers than those for mesh 1.1 for corresponding Reynolds numbers.

For all the 48% porosity screen inserts, [Figure 4.20](#), the average Nusselt number is a minimum at Reynolds number 400 and increases to a maximum at 30 000, just like the 68% porosity screen inserts. Mesh 1.3 increased by 1 060%, mesh 2.3 increased by 1 117% and mesh 3.3 increased by 880% over the Reynolds number range from 400 to 30 000. The increase in Nusselt number from Reynolds number 1 000 to 3 000 (transition regime) for mesh 1.3 is by 180%, mesh 2.3 is by 194% and mesh 3.3 is by 137%. The average difference of Nu_{avg} in [Figure 4.20](#) between mesh 1.3 and mesh 3.3 is 35% in the laminar region ($Re = 400$ to $3\,000$) and 7% in the transition ($Re = 3\,000$ to $10\,000$) and turbulent regimes ($Re = 10\,000$ to $30\,000$), with mesh 3.3 having higher Nusselt numbers than those for mesh 1.3 for corresponding Reynolds numbers.

Both of [Figure 4.19](#) and [Figure 4.20](#) indicate that the Nu_{avg} increases as the wave period decreases for a given mesh porosity and flow Re . The flow velocity and turbulence increase between the wave walls as the wave period decreases at a given mass flow rate, thus increasing the Nusselt number. If we compare between mesh 1.1 and mesh 1.3 or mesh 3.1 and mesh 3.3 in Figs. 4.18 and 4.19 to see the effects of porosity at a wave period, the Nu_{avg} , in general, increases slightly (13% or less) as the porosity decreases over the entire range of $400 \leq Re \leq 30,000$. Note that at the lower mesh porosity the pore size decreases but the wave walls then contain more number of pores. As indicated previously, the effects of mesh porosity on the local flow are only important at the low Reynolds number of 1,000 or less. At a higher Re , most of the mass flow is channelled in between the wave walls and the local secondary flows caused by the pores in the wave walls become less dominant. Thus, the Nu_{avg} values increase slightly as the mesh porosity decrease at a Re and a wave period when $Re > 1,000$.

For mesh 2.1 of 68% porosity screen, [Figure 4.19](#), and mesh 2.3 of 48% porosity screen, [Figure 4.20](#), the average Nusselt numbers followed closely to that of mesh 1.1 and mesh 1.3, respectively. Mesh 2.1 Nusselt number is 15% lower for $Re \leq 3,000$ and 4% higher for $Re > 3,000$ than those for mesh 1.1. Mesh 2.3 average Nusselt number is 6% lower for $Re \leq 3,000$ and 5% lower $Re > 3,000$ than those for mesh 1.3. However, when compared, the Nu_{avg} for mesh 2.1 and mesh 2.3 the differ significantly from Nu_{avg} for mesh 3.1 and mesh 3.3 in Figs. 4.18 and 4.19, respectively. Mesh 2.1 average Nusselt number is 30% lower in $Re \leq 3,000$ and 16% lower in $Re > 3,000$ than Nu_{avg} of mesh 3.1. The Nu_{avg} for mesh 2.3 is

30% lower in $Re \leq 3,000$ and 10% lower in $Re > 3,000$ than the Nu_{avg} for mesh 3.3. The effects of irregular wave patterns on the Nu_{avg} are thus dominant in the high Reynolds number range of $Re > 3,000$ where the Nu_{avg} values for the mesh 2.1 and 2.3 are lower by 16% or less than the Nu_{avg} for the mesh 3.1 and 3.3.

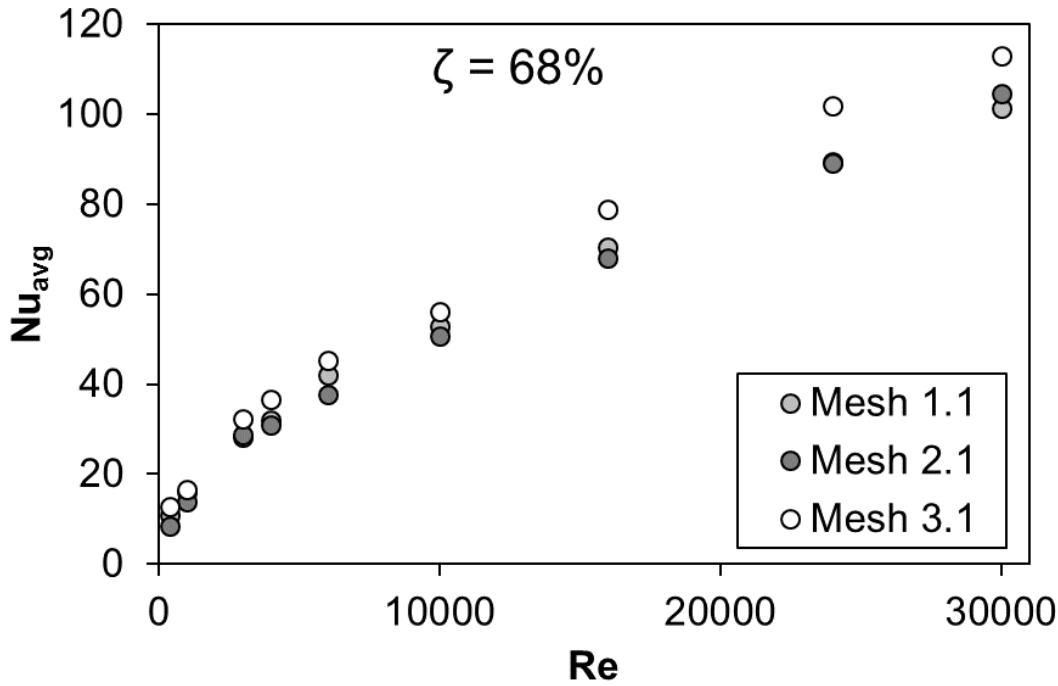


Figure 4.19: Average Nusselt number for Mesh 1.1 (22 mm period – 68% porosity), Mesh 2.1 (irregular period - 68% porosity) and Mesh 3.1 (12 mm period - 68% porosity) as Reynolds number varies

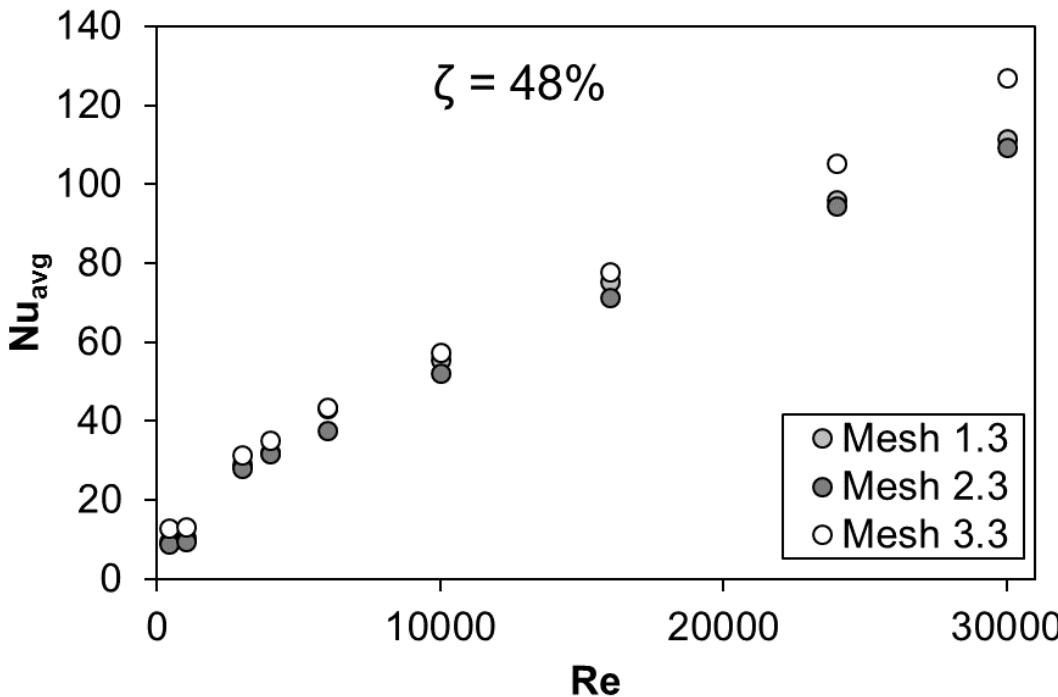


Figure 4.20: Average Nusselt number for Mesh 1.3 (22 mm period – 48% porosity), Mesh 2.3 (irregular period - 48% porosity) and Mesh 3.3 (12 mm period - 48% porosity) as Reynolds number varies

Figure 4.21 and Figure 4.22 show the ratio of the porous screen channel Nusselt number to the experimental baseline Nusselt number, Nu/Nu_0 as the Reynolds number varies. The ratios are computed using the average Nu_{avg} values of Figure 4.19 and Figure 4.20 and the baseline average Nu_0 at the corresponding Re in the channel of height 14 mm. The ratio then indicates the increase in convective heat transfer in the channel when the screen insert is employed as the difference between the wall temperature and mean air temperature remain the same as in the baseline channel. The influences of the two geometrical properties such as the period and porosity are once again visible in Figure 4.21 and Figure 4.22.

For the 68% porosity screen inserts in Figure 4.21, and the 48% porosity screen inserts in Figure 4.22, the distributions of Nu/Nu_0 ratio as the Re changes are similar. They begin with an increase of Nu/Nu_0 ratio from Reynolds number 400 to 3 000 and then decrease from 3 000 to 30 000. As expected, the average Nu/Nu_0 distributions are always higher for mesh 3.1 and mesh 3.3 in Figure 4.21 and Figure 4.22, respectively, compared to the other mesh screens as the wave period decreases. The influences of the mesh porosity to increase the Nu/Nu_0 as the porosity decreases at a Re and wave period are small. The increase and decrease in Nu/Nu_0 ratios from Reynolds number 400 to 30 000 are tabulated in the Table 4.11. The column of $400 \leq Re \leq 3,000$ indicates the overall increase of Nu/Nu_0 between $Re = 400$ and 3,000 for a screen insert. For the same insert in Table 4.11: The increase and decrease in Nu/Nu_0 ratios from Reynolds number 400 to 30 000 for two-wall heating and 14 mm channel height the column of $3,000 \leq Re \leq 30,000$ indicates the overall decrease of Nu/Nu_0 between $Re = 3,000$ and 30,000.

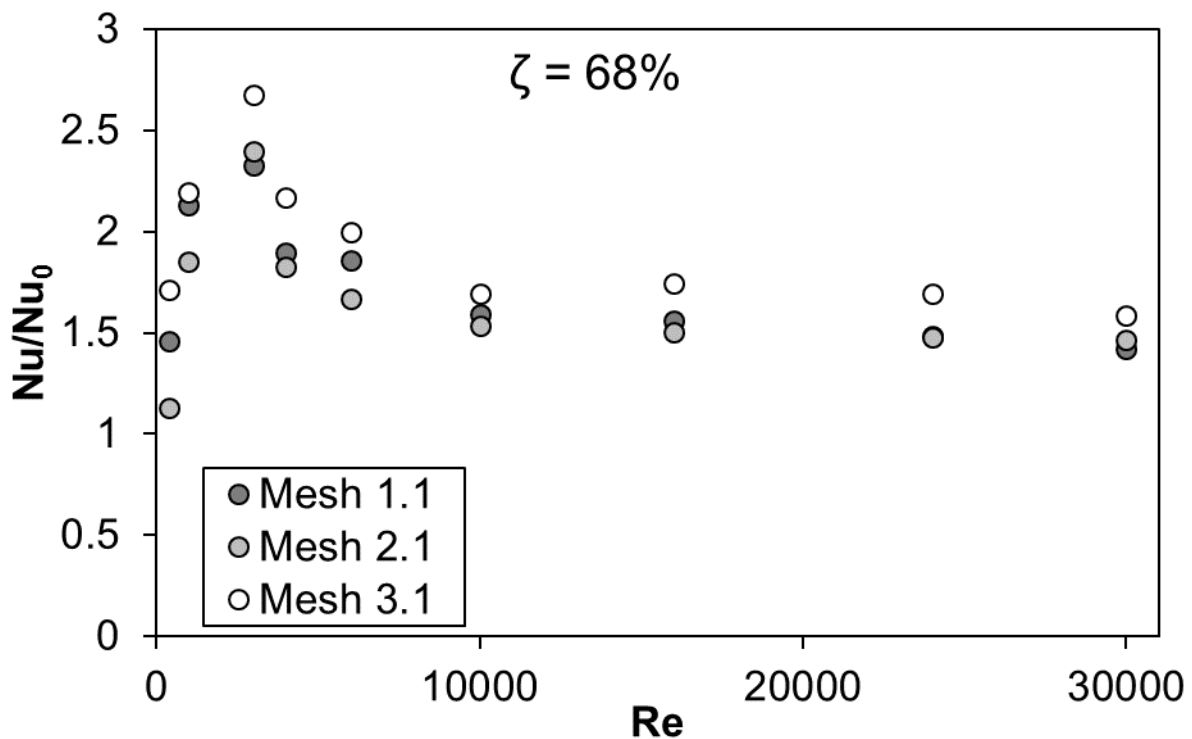


Figure 4.21: Average Nu/Nu_0 ratio for Mesh 1.1 (22 mm period – 68% porosity), Mesh 2.1 (irregular period - 68% porosity) and Mesh 3.1 (12 mm period - 68% porosity) as Reynolds number varies.

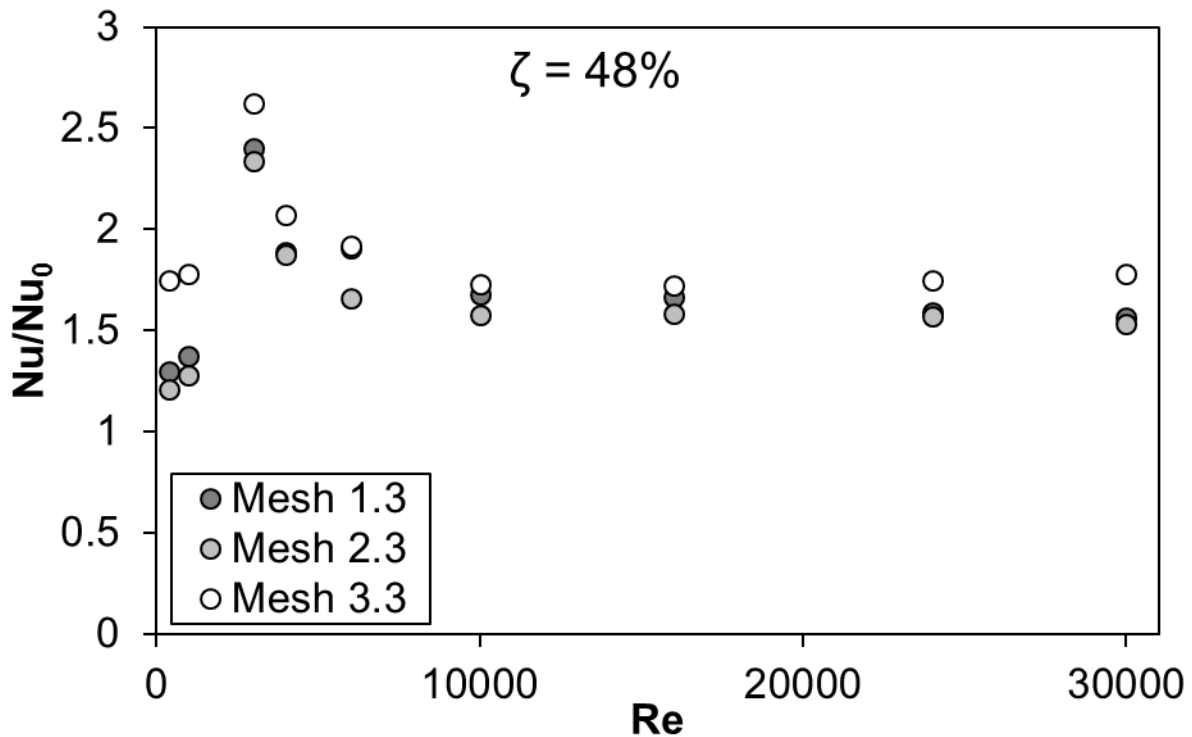


Figure 4.22: Average Nu/Nu_0 ratio for Mesh 1.3 (22 mm period – 48% porosity), Mesh 2.3 (irregular period - 48% porosity) and Mesh 3.3 (12 mm period - 48% porosity) as Reynolds number varies.

Table 4.11: The increase and decrease in Nu/Nu_0 ratios from Reynolds number 400 to 30 000 for two-wall heating and 14 mm channel height

Screen insert	% Increase of Nu/Nu_0 $400 \leq Re \leq 3\ 000$	% Decrease of Nu/Nu_0 $3\ 000 \leq Re \leq 30\ 000$
Mesh 1.1	60	39
Mesh 1.3	85	35
Mesh 2.1	112	39
Mesh 2.3	93	35
Mesh 3.1	56	41
Mesh 3.3	50	32

Table 4.12 shows determined correlations for the average Nusselt numbers and Nu/Nu_0 ratios as functions of Reynolds number for the various screen inserts in the 14 mm channel height. Each correlation is determined using a linear regression curve fit through the data points in the natural logarithm plot. The accuracy of the correlation is also given for each data set. Finally, a factor is calculated to obtain either the Nusselt number or Nu/Nu_0 ratio of a screen insert from another screen insert of the same porosity. This also indicates the effect porosity has on the Nusselt number and Nu/Nu_0 in the screen channel.

Table 4.12: Average Nusselt number and Nu/Nu_0 ratio correlations for various screen inserts in 14 mm channel

Average Nusselt number – 68% porosity screen insert

Mesh 1.1:

$$Nu_{1.1} = \begin{cases} 2.070Re^{0.293}, & Re \leq 1\,000 \\ 0.259Re^{0.579}, & Re \geq 3\,000 \end{cases} \quad (4.22)$$

Accuracy: $\pm 5\%$

Mesh 2.1:

$$Nu_{2.1} = \begin{cases} 1.853Re^{0.293}, & Re \leq 1\,000 \\ 0.265Re^{0.579}, & Re \geq 3\,000 \end{cases} \quad (4.23)$$

Accuracy: $\pm 7\%$

Mesh 3.1:

$$Nu_{3.1} = \begin{cases} 2.180Re^{0.293}, & Re \leq 1\,000 \\ 0.288Re^{0.579}, & Re \geq 3\,000 \end{cases} \quad (4.24)$$

Accuracy: $\pm 4\%$

Factor:

$$Nu_{1.1} = \begin{cases} 0.95Nu_{3.1}, & Re \leq 1\,000 \\ 0.90Nu_{3.1}, & Re \geq 3\,000 \end{cases}$$

$$Nu_{2.1} = \begin{cases} 0.85Nu_{3.1}, & Re \leq 1\,000 \\ 0.92Nu_{3.1}, & Re \geq 3\,000 \end{cases}$$

Average Nusselt number – 48% porosity screen insert

Mesh 1.3:

$$Nu_{1.3} = \begin{cases} 8.038Re^{0.0317}, & Re \leq 1\,000 \\ 0.162Re^{0.634}, & Re \geq 3\,000 \end{cases} \quad (4.25)$$

Accuracy: $\pm 5\%$

Mesh 2.3:

$$Nu_{2.3} = \begin{cases} 7.502Re^{0.0317}, & Re \leq 1\,000 \\ 0.158Re^{0.634}, & Re \geq 3\,000 \end{cases} \quad (4.26)$$

Accuracy: $\pm 6\%$

Mesh 3.3:

$$Nu_{3.3} = \begin{cases} 10.718Re^{0.0317}, & Re \leq 1\,000 \\ 0.174Re^{0.634}, & Re \geq 3\,000 \end{cases} \quad (4.27)$$

Accuracy: $\pm 5\%$

Factor:

$$Nu_{1.3} = \begin{cases} 0.75Nu_{3.3}, & Re \leq 1\,000 \\ 0.93Nu_{3.3}, & Re \geq 3\,000 \end{cases}$$

$$Nu_{2.3} = \begin{cases} 0.70Nu_{3.3}, & Re \leq 1\,000 \\ 0.91Nu_{3.3}, & Re \geq 3\,000 \end{cases}$$

Nu/Nu_0 ratio – 68% porosity screen insert

Mesh 1.1:

$$Nu/Nu_{0.1.1} = \begin{cases} 0.434Re^{0.214}, & Re \leq 1\,000 \\ 10.706Re^{-0.199}, & 3\,000 \leq Re < 10\,000 \\ 6.421Re^{-0.145}, & Re \geq 10\,000 \end{cases} \quad (4.28)$$

Accuracy: $\pm 6\%$

Mesh 2.1:

$$Nu/Nu_{02.1} = \begin{cases} 0.425Re^{0.214}, & Re \leq 1\,000 \\ 10.231Re^{-0.199}, & 3\,000 \leq Re < 10\,000 \\ 6.421Re^{-0.145}, & Re \geq 10\,000 \end{cases} \quad (4.29)$$

Accuracy: $\pm 7\%$

Mesh 3.1:

$$Nu/Nu_{03.1} = \begin{cases} 0.483Re^{0.214}, & Re \leq 1\,000 \\ 11.896Re^{-0.199}, & 3\,000 \leq Re < 10\,000 \\ 7.135Re^{-0.145}, & Re \geq 10\,000 \end{cases} \quad (4.30)$$

Accuracy: $\pm 5\%$

Factor:

$$Nu/Nu_{01.1} = \begin{cases} 0.9Nu/Nu_{03.1}, & Re \leq 1\,000 \\ 0.9Nu/Nu_{03.1}, & 3\,000 \leq Re < 10\,000 \\ 0.9Nu/Nu_{03.1}, & Re \geq 10\,000 \end{cases}$$

$$Nu/Nu_{02.1} = \begin{cases} 0.88Nu/Nu_{03.1}, & Re \leq 1\,000 \\ 0.86Nu/Nu_{03.1}, & 3\,000 \leq Re < 10\,000 \\ 0.9Nu/Nu_{03.1}, & Re \geq 10\,000 \end{cases}$$

Nu/Nu₀ – 48% porosity screen insert

Mesh 1.3:

$$Nu/Nu_{01.3} = \begin{cases} 1.175Re^{0.0182}, & Re \leq 1\,000 \\ 37.100Re^{-0.344}, & 3\,000 \leq Re < 10\,000 \\ 0.948Re^{0.0527}, & Re \geq 10\,000 \end{cases} \quad (4.31)$$

Accuracy: $\pm 5\%$

Mesh 2.3:

$$Nu/Nu_{02.3} = \begin{cases} 1.113Re^{0.0182}, & Re \leq 1\,000 \\ 35.106Re^{-0.344}, & 3\,000 \leq Re < 10\,000 \\ 0.917Re^{0.0527}, & Re \geq 10\,000 \end{cases} \quad (4.32)$$

Accuracy: $\pm 6\%$

Mesh 3.3:

$$Nu/Nu_0(Re)_{3.3} = \begin{cases} 1.567Re^{0.0182}, & Re \leq 1\,000 \\ 39.893Re^{-0.344}, & 3\,000 \leq Re < 10\,000 \\ 1.031Re^{0.0527}, & Re \geq 10\,000 \end{cases} \quad (4.33)$$

Accuracy: $\pm 4\%$

Factor:

$$Nu/Nu_{01.3} = \begin{cases} 0.75Nu/Nu_{03.3}, & Re \leq 1\,000 \\ 0.93Nu/Nu_{03.3}, & 3\,000 \leq Re < 10\,000 \\ 0.92Nu/Nu_{03.3}, & Re \geq 10\,000 \end{cases}$$

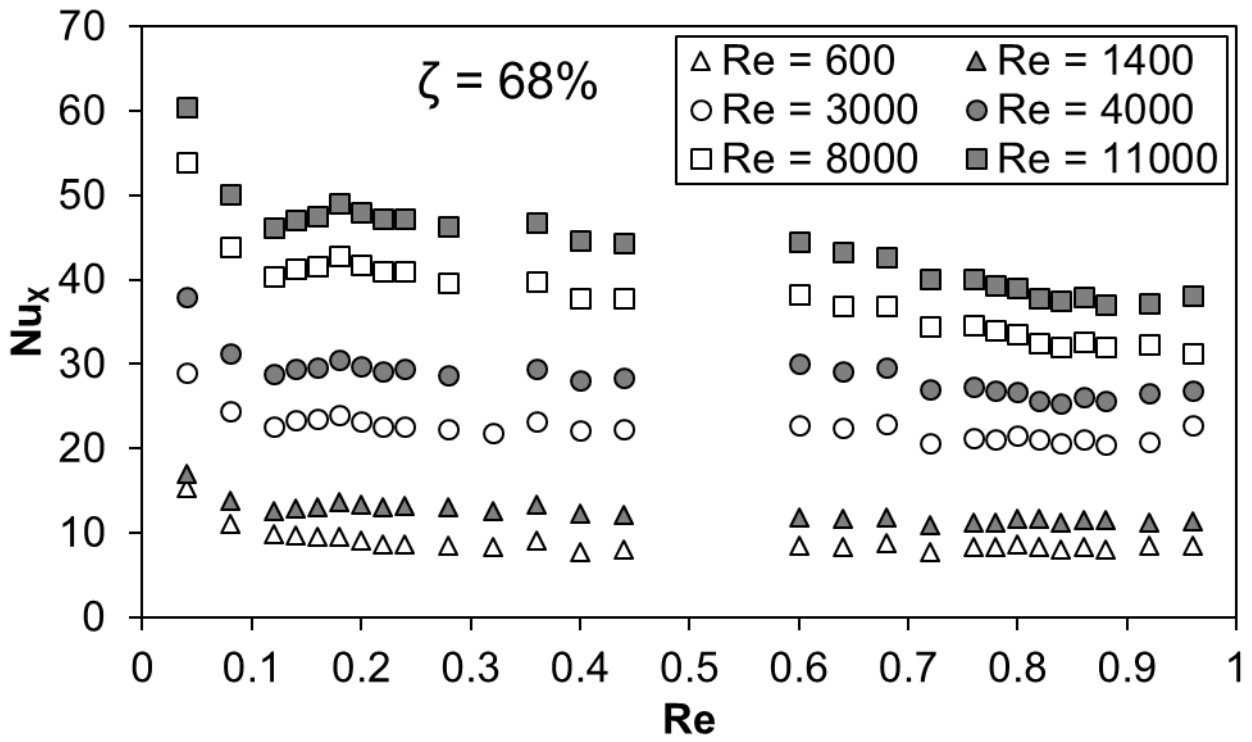
$$Nu/Nu_{02.3} = \begin{cases} 0.71Nu/Nu_{03.3}, & Re \leq 1\,000 \\ 0.88Nu/Nu_{03.3}, & 3\,000 \leq Re < 10\,000 \\ 0.89Nu/Nu_{03.3}, & Re \geq 10\,000 \end{cases}$$

4.4.2 5-MM CHANNEL

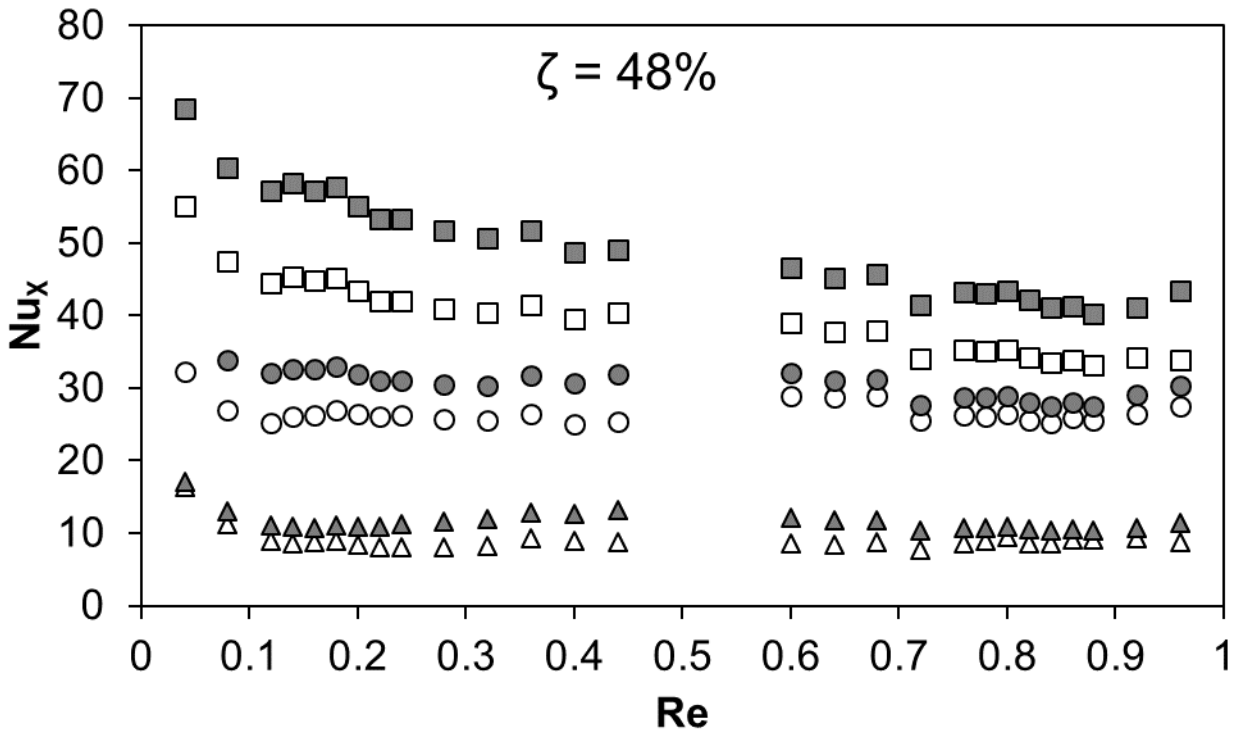
Figure 4.23 provides the local Nusselt number (Nu) along the normalized length of the channel (X/L) at the centreline of the 203 mm wall with a 5 mm channel height. The data are presented for four porous screen inserts: 18 mm wave period 68% and 48% porosity, and 12 mm wave period 68% and 48% porosity. The Reynolds number for the data varies from 1,000 to 11,000. The data are measured with both 203 mm walls heated. The magnitude of the heat flux is varied as far as possible with each Reynolds number to maintain a sufficient temperature difference between the wall ($T_{w,x}$) and bulk air flow ($T_{m,x}$) to reduce uncertainty in the measurements. The differences ($T_{w,x} - T_{m,x}$) in Equation (3.13) for the 68% and 48% porosity screen inserts are between 5 °C and 8 °C depending on the Reynolds number. The Nu_x with X/L decreases for any given screen at a Re in Figure 4.23 in the range of $0.0 \leq X/L \leq 0.6$ as the flow develops thermally and then becomes constant for $X/L > 0.6$ as the flow is thermally developed. It is worthy to note that the values of local Nu_x along X/L in Figure 4.23 are always higher for the screen channel than for the baseline channel at the corresponding Reynolds number and location.

The average Nusselt numbers, shown in are determined using the average of the local Nusselt numbers in $0.6 < X/L < 0.96$ Figure 4.24 shows the effects a change in mesh porosity with the wave period being constant have on the Nu_{avg} and the effects a change in wave period with the mesh porosity being constant have on the Nu_{avg} . Figure 4.24 shows a smaller period means a higher Nusselt number for the same Reynolds number. For the 68% porosity screen inserts, the 12 mm period mesh has 12% higher average Nusselt number than 18 mm period mesh for the laminar region ($Re = 400 - 3\,000$), a 30% higher Nusselt number for $Re = 3\,000$, and a 12% higher Nusselt number for Reynolds numbers greater than 3 000. For the 48% porosity screen inserts, the 12 mm period mesh has approximately a 7% higher average Nusselt number than 18 mm period mesh for all Reynolds numbers.

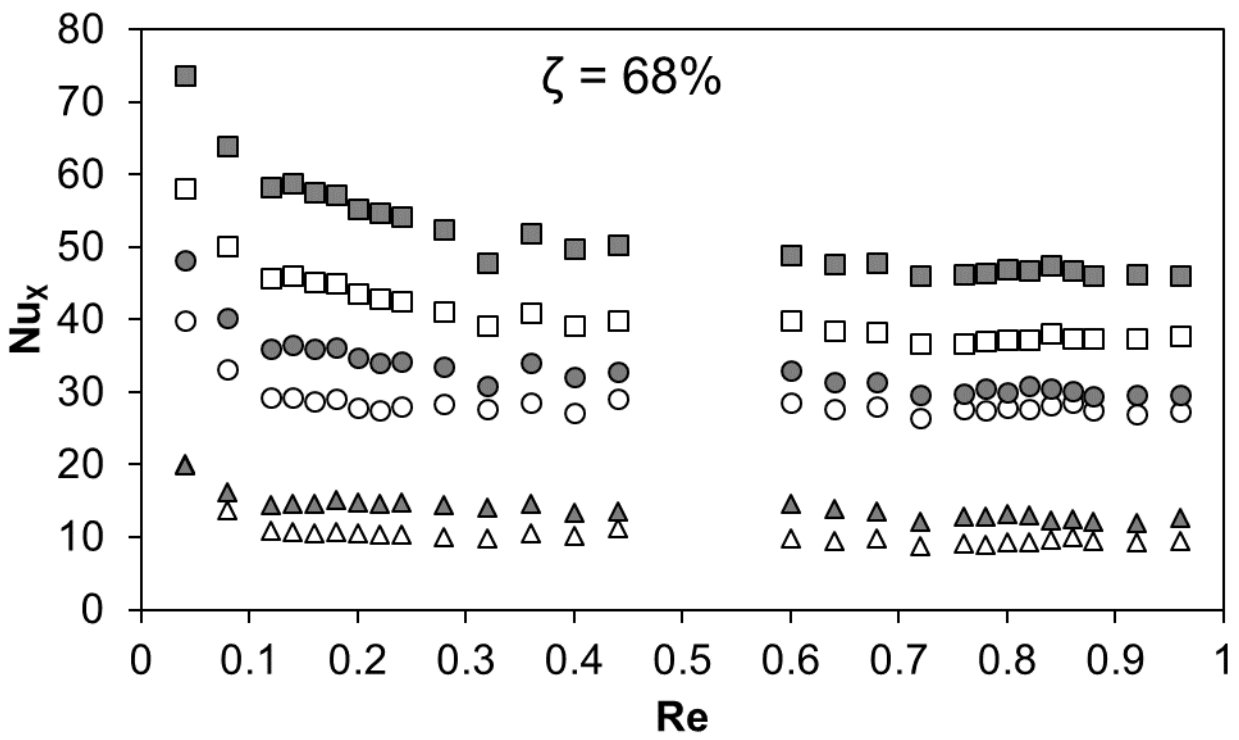
Figure 4.24 shows the effect of porosity of the screen insert on the Nusselt number. The effect is more visible for the 18 mm period screen insert where a smaller porosity means a higher Nusselt number for the same Reynolds number; however it is not as visible for the 12 mm period screen insert. For the 18 mm period screen inserts, mesh 4.3 (48 % porosity) has no significant increase in Nu_{avg} compared to those for mesh 4.1 (68% porosity) for the laminar region ($Re = 400 - 3\,000$), a 23% higher Nusselt number for $Re = 3\,000$, and an 8% higher Nusselt number for Reynolds numbers greater than 3 000. For the 48% porosity screen inserts, mesh 5.3 (48% porosity) has approximately equal Nu_{avg} to those for mesh 4.3 (68% porosity) for all Reynolds numbers.



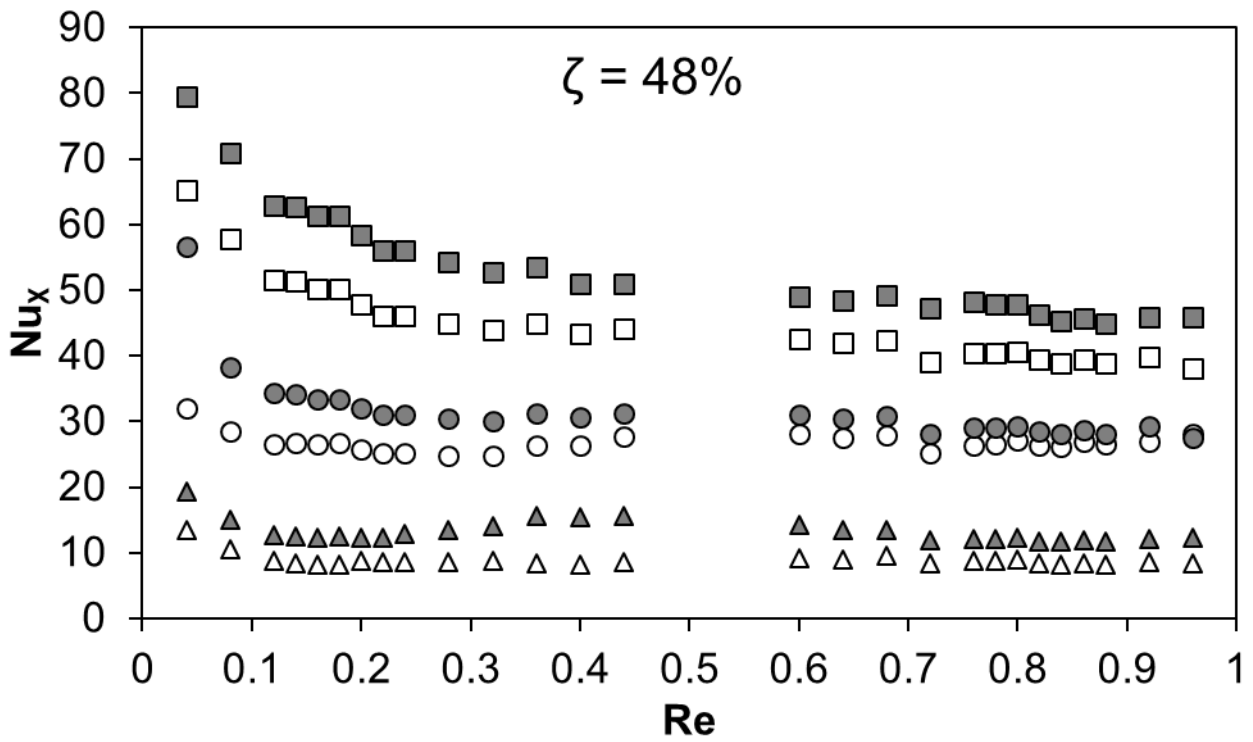
(a)



(b)



(c)



(d)

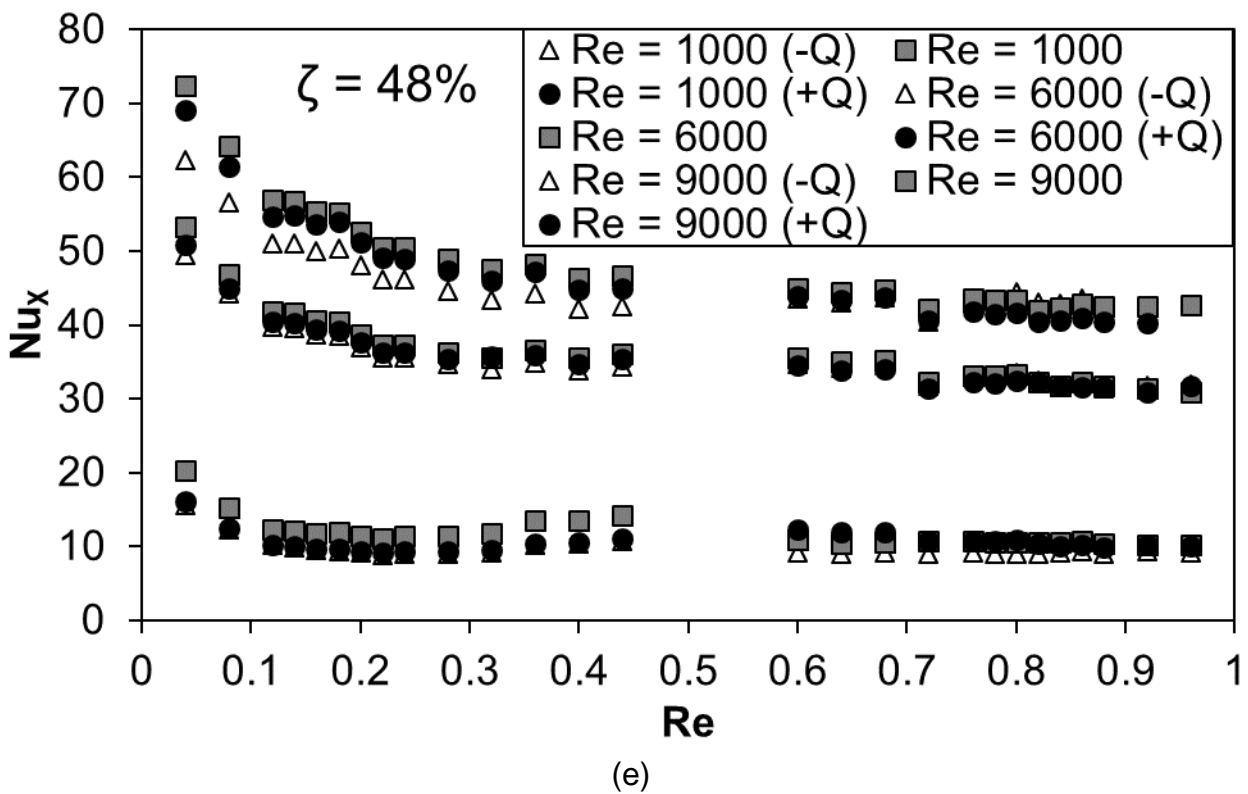


Figure 4.23: Local Nusselt numbers for various Reynolds numbers for two-wall heating boundary condition, 5-mm channel height: (a) Mesh 4.1 (18 mm period - 68% porosity), (b) Mesh 4.3 (18 mm period - 48% porosity), (c) Mesh 5.1 (12 mm period - 68% porosity), and (d) Mesh 5.3 (12 mm period - 48% porosity)

Table 4.13 shows the screen insert correlations for average Nusselt number and average Nu/Nu_0 ratio as functions of Reynolds number for the 5 mm channel height and two-wall heating boundary condition. Each correlation is determined using a linear regression curve fit through the data points in the natural logarithm plots. The accuracy of the correlation is also given for each data set. Finally, a factor is calculated to obtain either the Nu_{avg} or Nu/Nu_0 ratio of a screen insert from the other screen insert of the same porosity.

The Nu/Nu_0 ratios, shown in Figure 4.25, are determined using the average Nusselt numbers divided by the experimental baseline Nusselt numbers captured in Section 4.2.2. Figure 4.25 show the effect a change in period (in other words the porosity of the screen insert remains the same) of the screen insert has on the Nu/Nu_0 ratio, and Figure 4.25 show the effect a change in porosity (in other words the period of the screen insert remains the same) of the screen insert has on the Nu/Nu_0 ratio. Figure 4.25, shows the same trends in the effects of period and porosity of the screen insert on the Nu/Nu_0 ratio as discussed above for the Nu_{avg} in Figure 4.23. The period of the screen affects the Nu/Nu_0 ratio for both porosities (Figure 4.25) where the porosity of the screen insert only effects the 18 mm period screen insert Nu/Nu_0 ratio results (Figure 4.25).

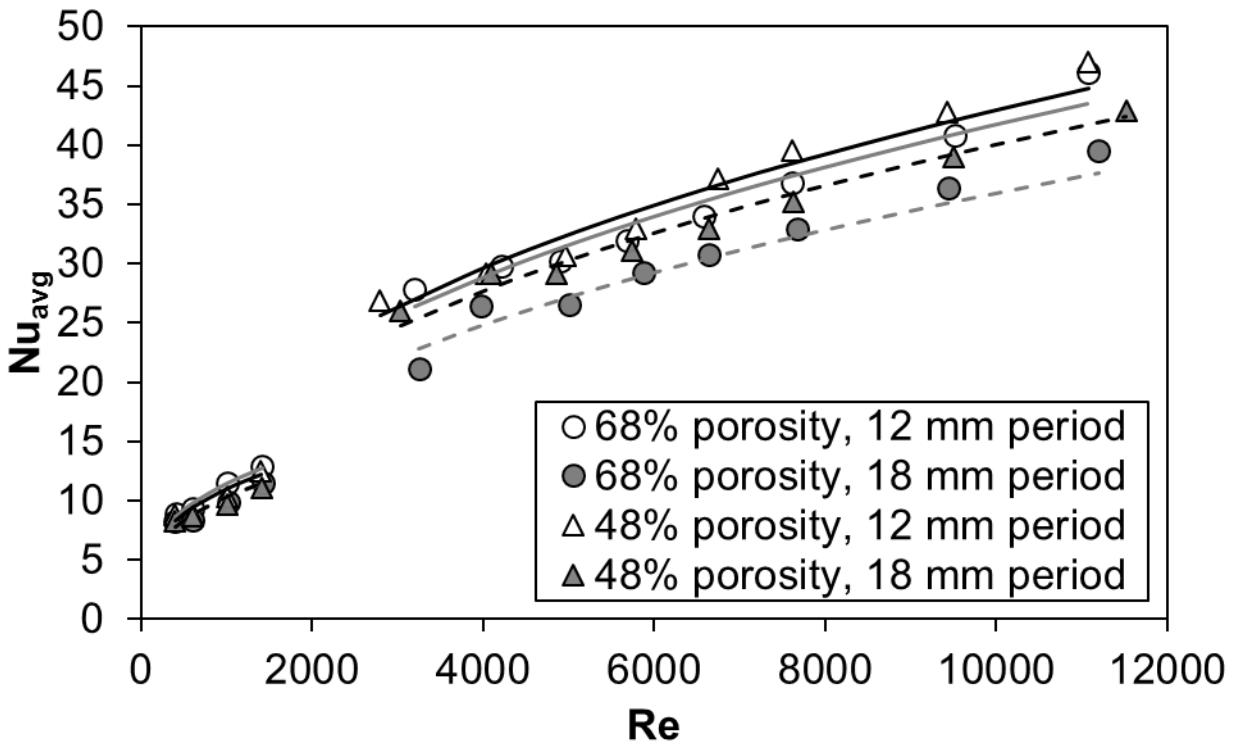


Figure 4.24: Average Nusselt number as Reynolds number varies for two-wall heating boundary condition comparing, 5-mm channel height

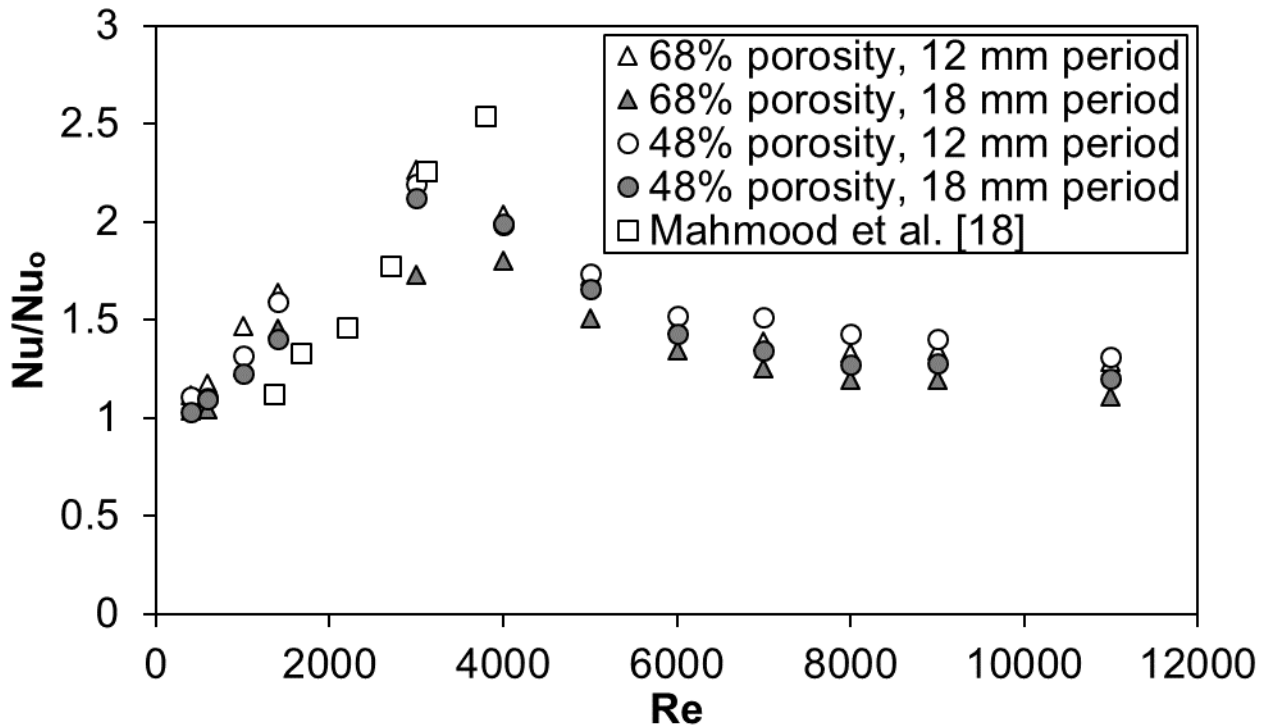


Figure 4.25: Nu/Nu_0 ratio as Reynolds number varies for two-wall heating boundary condition comparing, 5-mm channel height: (a) Mesh 4.1 and Mesh 5.1, (b) Mesh 4.3 and Mesh 5.3, (c) Mesh 4.1 and Mesh 4.3, and (d) Mesh 5.1 and Mesh 5.3

Table 4.13: Average Nusselt number and Nu/Nu0 ratio correlations for 5 mm channel height - two-wall heating

Average Nusselt number – 68% porosity screen inserts

Mesh 4.1:

$$Nu_{4.1} = \begin{cases} 1.203Re^{0.311}, & Re \leq 1\,400 \\ 0.865Re^{0.405}, & Re \geq 3\,000 \end{cases} \quad (4.34)$$

Accuracy: $\pm 6\%$

Mesh 5.1:

$$Nu_{5.1} = \begin{cases} 1.336Re^{0.311}, & Re \leq 1\,400 \\ 1.006Re^{0.405}, & Re \geq 3\,000 \end{cases} \quad (4.35)$$

Accuracy: $\pm 4\%$

Factor:

$$Nu_{4.1} = \begin{cases} 0.90Nu_{5.1}, & Re \leq 1\,400 \\ 0.86Nu_{5.1}, & Re \geq 3\,000 \end{cases}$$

Average Nusselt number – 48% porosity screen inserts

Mesh 4.3:

$$Nu_{4.3} = \begin{cases} 1.203Re^{0.311}, & Re \leq 1\,400 \\ 0.965Re^{0.405}, & Re \geq 3\,000 \end{cases} \quad (4.36)$$

Accuracy: $\pm 4\%$

Mesh 5.3:

$$Nu_{5.3} = \begin{cases} 1.283Re^{0.311}, & Re \leq 1\,400 \\ 1.036Re^{0.405}, & Re \geq 3\,000 \end{cases} \quad (4.37)$$

Accuracy: $\pm 6\%$

Factor:

$$Nu_{4.3} = \begin{cases} 0.90Nu_{5.1}, & Re \leq 1\,400 \\ 0.96Nu_{5.1}, & Re \geq 3\,000 \end{cases}$$

$$Nu_{5.3} = \begin{cases} 0.96Nu_{5.1}, & Re \leq 1\,400 \\ 1.03Nu_{5.1}, & Re \geq 3\,000 \end{cases}$$

Nu/Nu0 ratio – 68% porosity screen inserts

Mesh 4.1:

$$Nu/Nu_{0.4.1} = \begin{cases} 0.114Re^{0.355}, & Re \leq 1\,400 \\ 92.753Re^{-0.482}, & Re \geq 3\,000 \end{cases} \quad (4.38)$$

Accuracy: $\pm 6\%$

Mesh 5.1:

$$Nu/Nu_{0.5.1} = \begin{cases} 0.127Re^{0.355}, & Re \leq 1\,400 \\ 103.059Re^{-0.482}, & Re \geq 3\,000 \end{cases} \quad (4.39)$$

Accuracy: $\pm 7\%$

Factor:

$$Nu/Nu_{0.4.1} = \begin{cases} 0.9Nu/Nu_{0.5.1}, & Re \leq 1\,400 \\ 0.9Nu/Nu_{0.5.1}, & Re \geq 3\,000 \end{cases}$$

f/f0 ratio – 48% porosity screen inserts

Mesh 4.3:

$$Nu/Nu_{0.4.3} = \begin{cases} 0.114Re^{0.355}, & Re \leq 1\,400 \\ 100.998Re^{-0.482}, & Re \geq 3\,000 \end{cases} \quad (4.40)$$

Accuracy: $\pm 8\%$

Mesh 5.3:

$$Nu/Nu_{0.5.3} = \begin{cases} 0.122Re^{0.355}, & Re \leq 1\,400 \\ 107.181Re^{-0.482}, & Re \geq 3\,000 \end{cases} \quad (4.41)$$

 Accuracy: $\pm 8\%$

Factor:

$$Nu/Nu_{0.4.3} = \begin{cases} 0.90Nu/Nu_{0.5.1}, & Re \leq 1\,400 \\ 0.98Nu/Nu_{0.5.1}, & Re \geq 3\,000 \end{cases}$$

$$Nu/Nu_{0.5.3} = \begin{cases} 0.96Nu/Nu_{0.5.1}, & Re \leq 1\,400 \\ 1.04Nu/Nu_{0.5.1}, & Re \geq 3\,000 \end{cases}$$

4.5 ONE WALL HEATING

A total of 102 one-wall heat transfer experiments are conducted, which consisted of 9 mass flow rate measurements for the 14 mm channel and 12 mass flow rate measurements for the 5 mm channel for 10 different porous screen inserts. The one-wall heat transfer experiments are summarised in [Table 4.14](#). The heat transfer in flat channels with one-wall heating is found in applications such as the solar panels, base cooling of electronic chips, and side panels of flat plate heat exchangers.

Table 4.14: One-wall heat transfer experimental test matrix

Porous screen insert	Reynolds number range	Re numbers measurements	Porosity	Period	Channel Height
Mesh 1.1	$400 \leq Re \leq 30\,000$	9	68%	22	14
Mesh 2.1	$400 \leq Re \leq 30\,000$	9	68%	Irregular	14
Mesh 3.1	$400 \leq Re \leq 30\,000$	9	68%	12	14
Mesh 1.3	$400 \leq Re \leq 30\,000$	9	48%	22	14
Mesh 2.3	$400 \leq Re \leq 30\,000$	9	48%	Irregular	14
Mesh 3.3	$400 \leq Re \leq 30\,000$	9	48%	12	14
Mesh 4.1	$400 \leq Re \leq 11\,000$	12	68%	18	5
Mesh 5.1	$400 \leq Re \leq 11\,000$	12	68%	12	5
Mesh 4.3	$400 \leq Re \leq 11\,000$	12	48%	18	5
Mesh 5.3	$400 \leq Re \leq 11\,000$	12	48%	12	5

4.5.1 14-MM CHANNEL

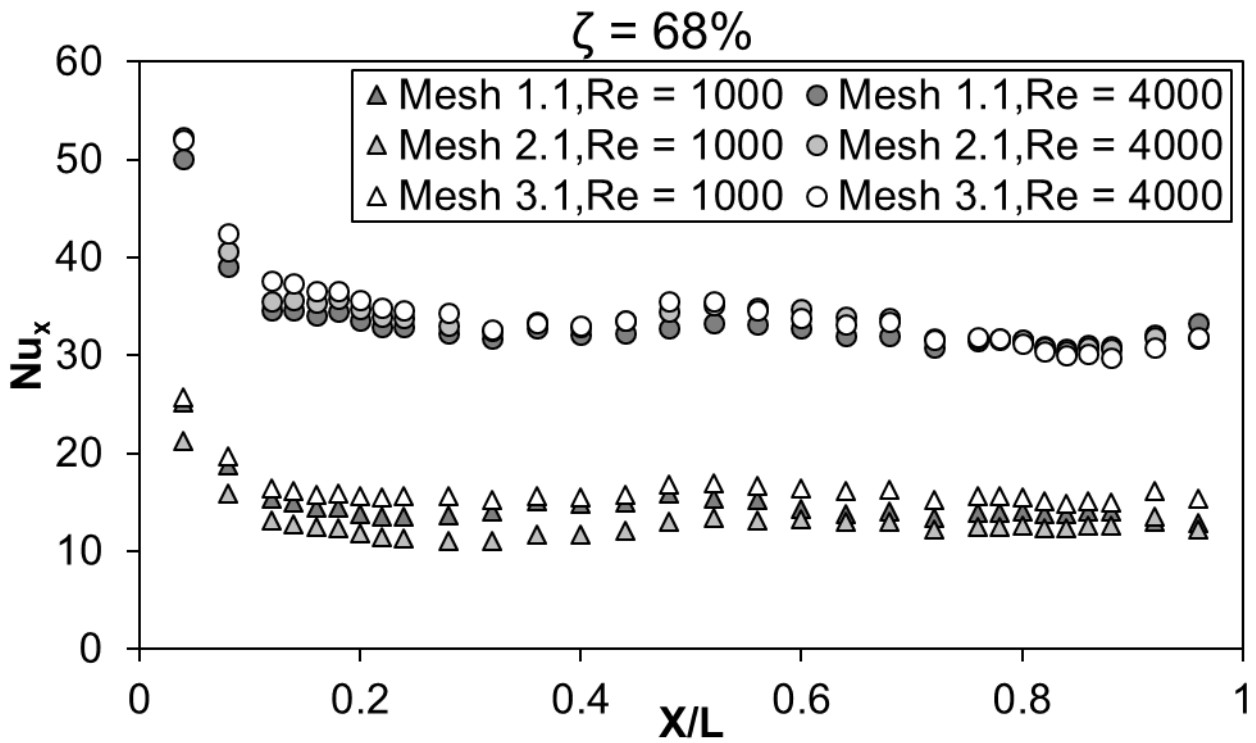
[Figure 4.26](#) provides the local Nusselt number (Nu_x) along the normalized length of the channel (X/L) at the centreline of 203 mm plate for the 68% porosity screen inserts. [Figure 4.27](#) provides the local Nu_x along the X/L at the centreline of 203 mm plate for the 48% porosity screen inserts. The data in [Figure 4.26](#) and [Figure 4.27](#) are obtained for the one-wall heating in the 14 mm channel height as the Reynolds number varies. The magnitude of the heat flux was varied as far as possible with each Reynolds number to maintain a sufficient temperature difference between the wall and bulk air flow to reduce uncertainty

in the Nusselt number estimates. The differences ($T_{w,x} - T_{m,x}$) in Equation (3.13) for the 68% and 48% porosity screen inserts were between 5°C and 8°C depending on the Reynolds number. The first location of the data in [Figure 4.26](#) and [Figure 4.27](#) is $X/L = 0.04$ and ends at $X/L = 0.96$. In the screen channel the values of Nu_x with X/L decreases in the range of $0.0 \leq X/L \leq 0.6$ and then becomes constant for $X/L > 0.6$ at a Reynolds number. The smooth inlet flow into the screen test section undergoes transition in $0.0 \leq X/L \leq 0.6$ before it becomes thermally fully turbulent near $X/L > 0.6$ where Nu_x change little with X/L . It is worthy to note that the value of Nu_x along X/L in [Figure 4.26](#) and [Figure 4.27](#) are always higher for the screen channel than for the baseline channel (one-wall heating) at the corresponding Reynolds number and location.

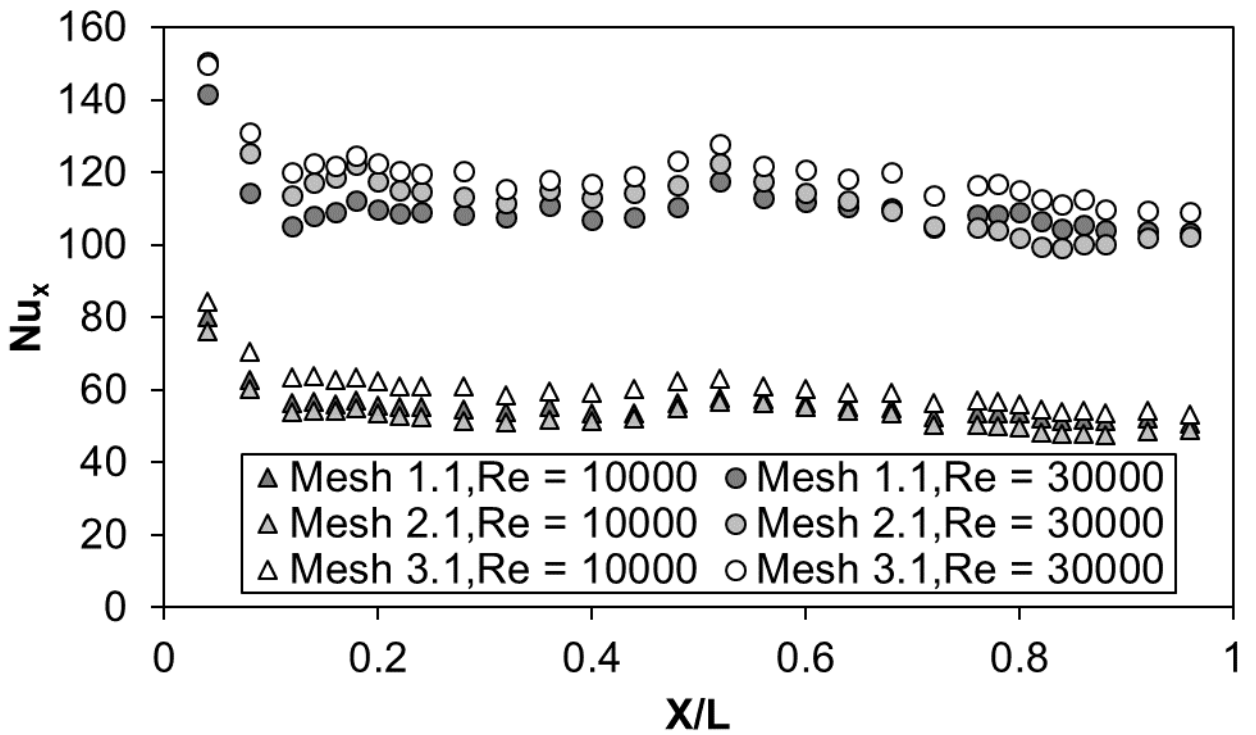
The average Nusselt number, Nu_{avg} at a Re shown in [Figure 4.28](#) and [Figure 4.29](#) was determined using the average of the local Nusselt numbers in $0.6 < X/L < 0.96$ at that specific Reynolds number. [Figure 4.28](#) and [Figure 4.29](#) show the effects a change in the wave period have on the Nu_{avg} vs. Re distributions when the mesh porosity remains the constant. [Figure 4.28](#) compares the three screen inserts of different periods made with a 68% porosity wire mesh. [Figure 4.29](#) compares the three screen inserts of different periods made with a 48% porosity wire mesh. Mesh 2.1 and 2.3 are used to identify the effects of wave pattern irregularity due to the manufacturing constraints on the Nusselt number results.

For the 68% porosity screen inserts, [Figure 4.28](#), the average Nusselt number is a minimum at Reynolds number 400 and increases to a maximum at 30 000. Mesh 1.1 increased by 915%, mesh 2.1 increased by 942% and mesh 3.1 increased by 883% over the Reynolds number range from 400 to 30 000. The biggest increase in Nusselt number is from Reynolds number 1 000 to 4 000 (transition regime) where mesh 1.1 increased by 127%, mesh 2.1 increased by 152% and mesh 3.1 increased by 103%. The Nu_{avg} data for mesh 3.1 is higher than those for mesh 1.1 by 10% in the laminar region ($Re = 400 - 3 000$) and by less than 8% in the transition ($Re = 3 000 - 7 000$) and turbulent regimes ($Re = 7 000 - 11 000$).

For the 48% porosity screen inserts, [Figure 4.29](#), the average Nusselt number is a minimum at Reynolds number 400 and increases to a maximum at 30 000, just like the 68% porosity screen inserts. Mesh 1.3 increased by 952%, mesh 2.3 increased by 1 033% and mesh 3.3 increased by 816% over the Reynolds number range from 400 to 30 000. The biggest increase in Nusselt number is from Reynolds number 1 000 to 4 000 (transition regime) where mesh 1.3 increased by 200%, mesh 2.3 increased by 198% and mesh 3.3 increased by 174%. The Nu_{avg} for mesh 3.1 is higher than those for mesh 1.1 by 15% in the laminar region ($Re = 400 - 3 000$) and by about 8% in the transition ($Re = 3 000 - 7 000$) and turbulent regimes ($Re = 7 000 - 11 000$).

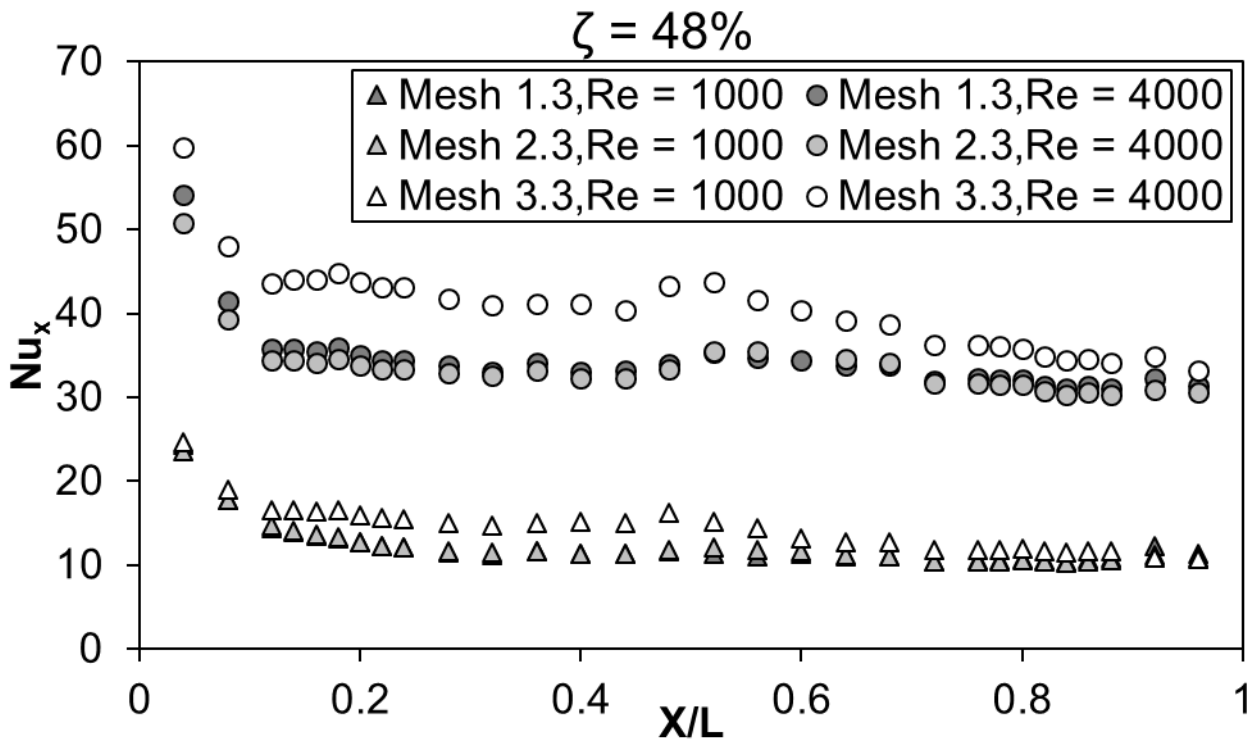


(a)

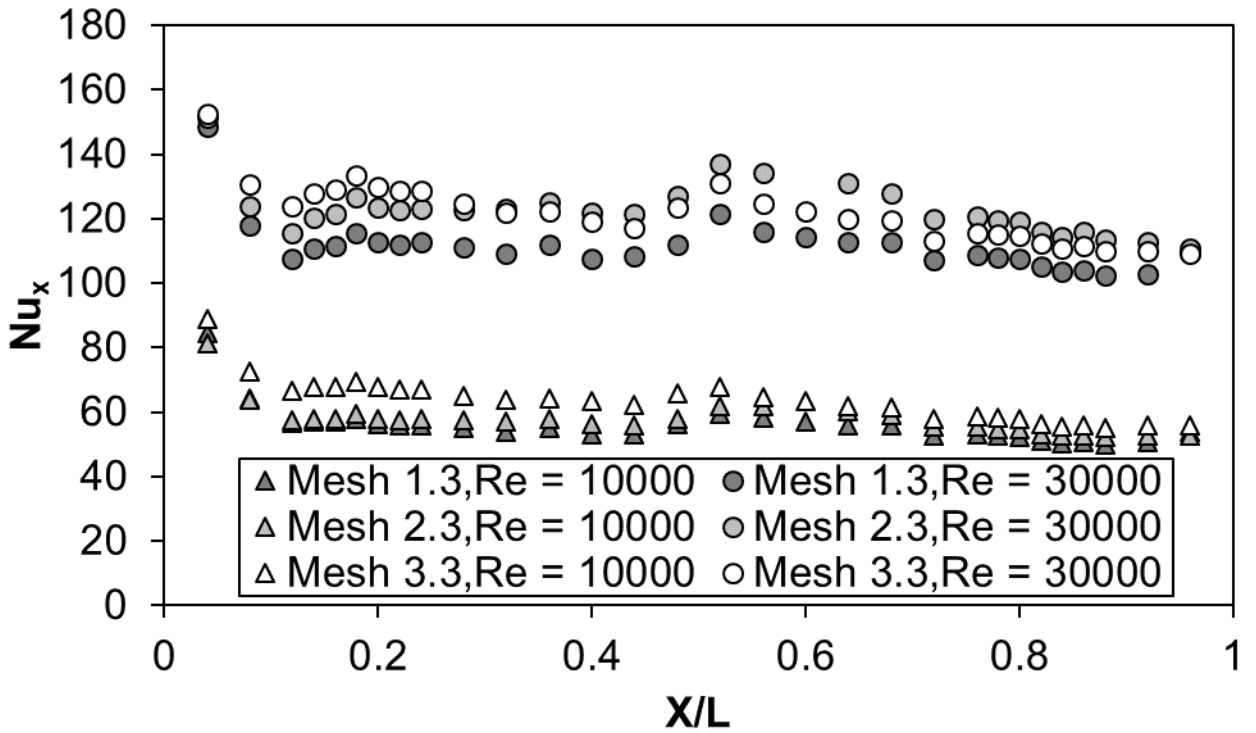


(b)

Figure 4.26: Local Nusselt number values along the X/L of the test section for 14 mm channel height and one-wall heating: (a) laminar and (b) turbulent region



(a)



(b)

Figure 4.27: Local Nusselt number values along the X/L of the test section for 14 mm channel height and one-wall heating: (a) laminar and (b) turbulent region

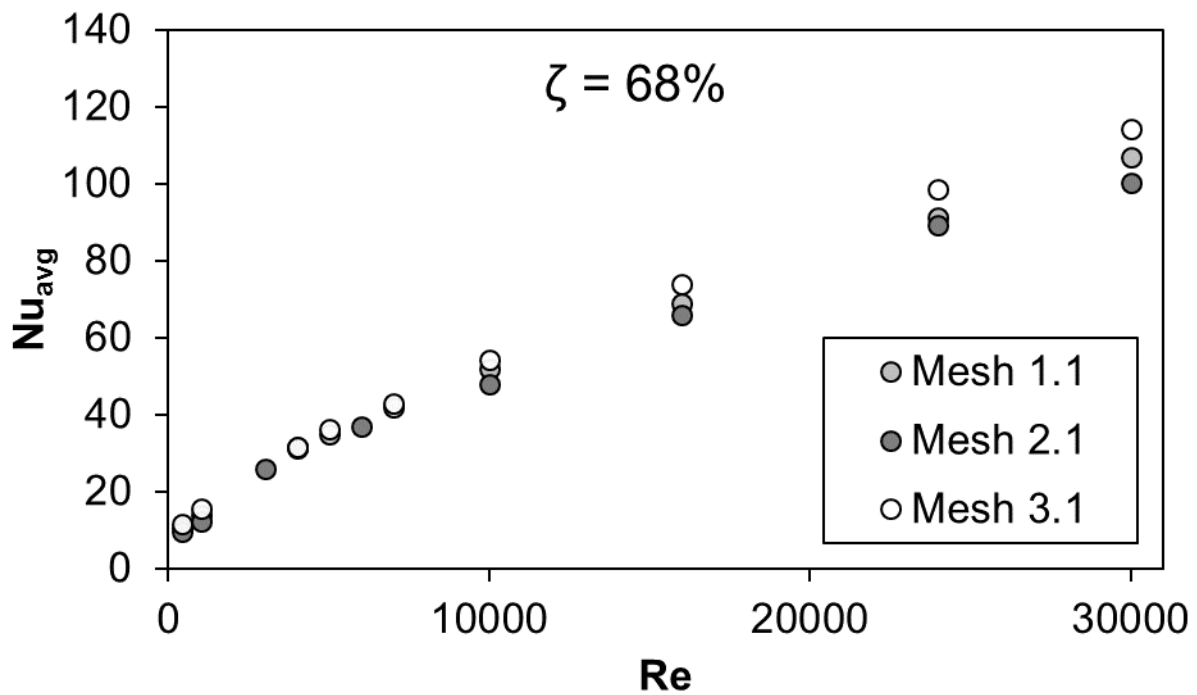


Figure 4.28: Average Nusselt number, Nu_{avg} for Mesh 1.1 (22 mm period – 68% porosity), Mesh 2.1 (irregular period - 68% porosity) and Mesh 3.1 (12 mm period - 68% porosity) as Reynolds number varies in 14 mm channel height and with one-wall heating.

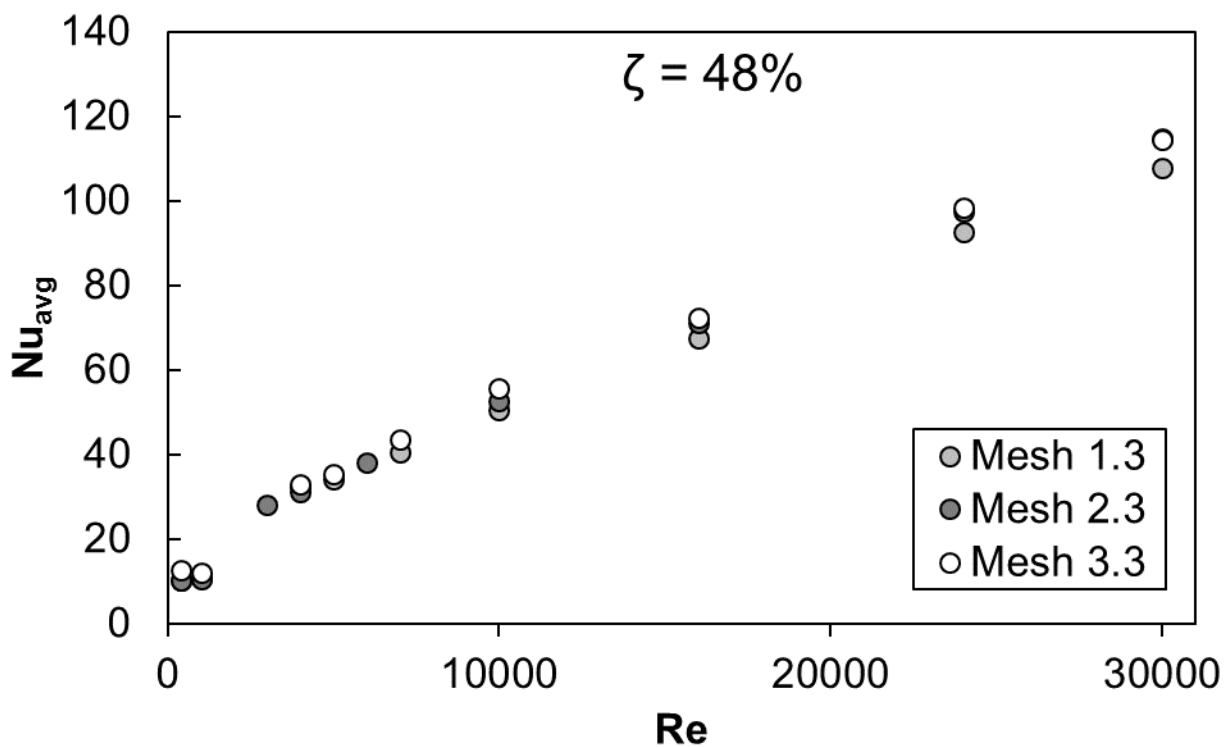


Figure 4.29: Average Nusselt number, Nu_{avg} for Mesh 1.3 (22 mm period – 48% porosity), Mesh 2.3 (irregular period - 48% porosity) and Mesh 3.3 (12 mm period - 48% porosity) as Reynolds number varies in 14 mm channel height and with one-wall heating

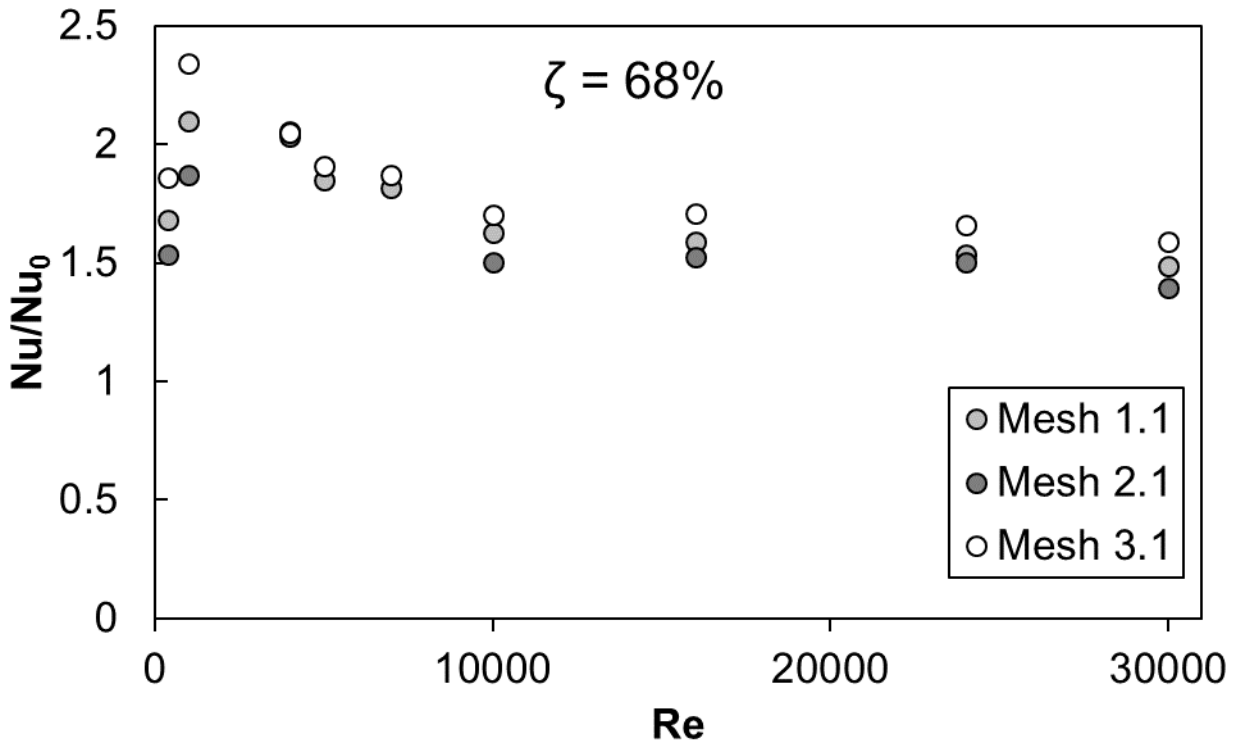


Figure 4.30: Nu/Nu_0 ratio for Mesh 1.1 (22 mm period – 68% porosity), Mesh 2.1 (irregular period - 68% porosity) and Mesh 3.1 (12 mm period - 68% porosity) as Reynolds number varies

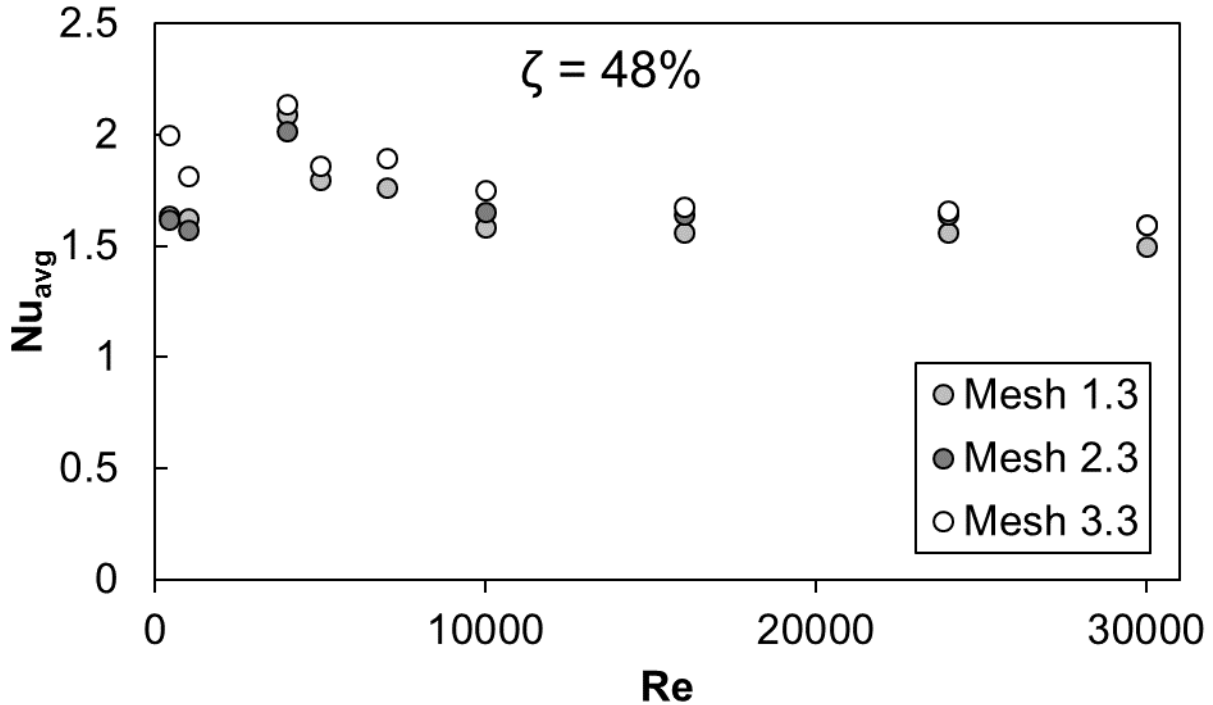


Figure 4.31: Nu/Nu_0 ratio for Mesh 1.3 (22 mm period – 48% porosity), Mesh 2.3 (irregular period - 48% porosity) and Mesh 3.3 (12 mm period - 48% porosity) as Reynolds number varies

If we compare the data of mesh 1.1 with mesh 1.3 or mesh 3.1 with mesh 3.3 in Figure 4.28 and Figure 4.29, we can see that the Nusselt number increases over the Reynolds

number range between 400 to 30 000 as the mesh porosity increases. The difference of Nu_{avg} between mesh 1.1 and mesh 1.3 is significant when the Reynolds number is equal to 1 000 where mesh 1.3 data is 23% smaller than of mesh 1.1 data, whereas every other Reynolds number it is within less than 3% of mesh 1.1 data. The difference between mesh 3.1 data and mesh 3.3 data is also only significant at Reynolds number equal to 1 000 where the Nu_{avg} for mesh 3.3 is 23% smaller than that for mesh 3.1.

For both the 68% porosity screen inserts, [Figure 4.28](#), and the 48% porosity screen inserts, [Figure 4.29](#), the average Nusselt numbers of the mesh 2.1 and mesh 2.3 follow closely to those of the mesh 1.1 and mesh 1.3, respectively. Mesh 2.1 Nusselt numbers are 10% lower than those of mesh 1.1 for Reynolds numbers up to 3 000 and 5% lower for Reynolds numbers greater than 3 000. Mesh 2.3 Nusselt numbers are less than 3% lower than those for mesh 1.3 for Reynolds numbers up to 3 000 and 5% higher for Reynolds number greater than 3 000. However, when Nu_{avg} for mesh 2.1 are compared to those for mesh 3.1 and for mesh 2.3 are compared to those for mesh 3.3, the differences become significantly higher. Mesh 2.1 Nusselt numbers are 23% lower than those of mesh 3.1 for Reynolds number up to 3 000 and 12% lower for Reynolds numbers greater than 3 000. Mesh 2.3 average Nusselt numbers are 19% lower than those for mesh 3.3 for Reynolds number up to 3 000 and less than 5% lower for Reynolds number greater than 3 000. This means that the irregularities in the wave period for the 22 mm period screen inserts result in a low change in the average Nusselt numbers; whereas, the irregularities in period for the 12 mm period screen have a higher change in the average Nusselt numbers.

Table 4.15: Average Nusselt number and Nu/Nu_0 ratio correlations for various screen inserts tests in 14 mm channel

Average Nusselt number – 68% porosity screen insert

Mesh 1.1:

$$Nu_{1.1} = \begin{cases} 0.672Re^{0.445}, & Re \leq 1\,000 \\ 0.123Re^{0.658}, & Re \geq 3\,000 \end{cases} \quad (4.42)$$

Accuracy: $\pm 6\%$

Mesh 2.1:

$$Nu_{2.1} = \begin{cases} 0.620Re^{0.445}, & Re \leq 1\,000 \\ 0.118Re^{0.658}, & Re \geq 3\,000 \end{cases} \quad (4.43)$$

Accuracy: $\pm 8\%$

Mesh 3.1:

$$Nu_{3.1} = \begin{cases} 0.747Re^{0.445}, & Re \leq 1\,000 \\ 0.127Re^{0.658}, & Re \geq 3\,000 \end{cases} \quad (4.44)$$

Accuracy: $\pm 3\%$

Factor:

$$Nu_{1.1} = \begin{cases} 0.90Nu_{3.1}, & Re \leq 1\,000 \\ 0.97Nu_{3.1}, & Re \geq 3\,000 \end{cases}$$

$$Nu_{2.1} = \begin{cases} 0.83Nu_{3.1}, & Re \leq 1\,000 \\ 0.93Nu_{3.1}, & Re \geq 3\,000 \end{cases}$$

Average Nusselt number – 48% porosity screen insert

Mesh 1.3:

$$Nu_{1.3} = \begin{cases} 14.219Re^{-0.0476}, & Re \leq 1\,000 \\ 0.133Re^{0.649}, & Re \geq 3\,000 \end{cases} \quad (4.45)$$

Accuracy: $\pm 7\%$

Mesh 2.3:

$$Nu_{2.3} = \begin{cases} 140.52Re^{-0.0476}, & Re \leq 1\,000 \\ 0.132Re^{0.649}, & Re \geq 3\,000 \end{cases} \quad (4.46)$$

Accuracy: $\pm 8\%$

Mesh 3.3:

$$Nu_{3.3} = \begin{cases} 16.728Re^{-0.0476}, & Re \leq 1\,000 \\ 0.139Re^{0.649}, & Re \geq 3\,000 \end{cases} \quad (4.47)$$

Accuracy: $\pm 3\%$

Factor:

$$Nu_{1.3} = \begin{cases} 0.85Nu_{3.3}, & Re \leq 1\,000 \\ 0.96Nu_{3.3}, & Re \geq 3\,000 \end{cases}$$

$$Nu_{2.3} = \begin{cases} 0.84Nu_{3.3}, & Re \leq 1\,000 \\ 0.95Nu_{3.3}, & Re \geq 3\,000 \end{cases}$$

Nu/Nu₀ ratio – 68% porosity screen insert

Mesh 1.1:

$$Nu/Nu_{0.1.1} = \begin{cases} 0.296Re^{0.284}, & Re \leq 1\,000 \\ 5.000Re^{-0.114}, & Re \geq 3\,000 \end{cases} \quad (4.48)$$

Accuracy: $\pm 5\%$

Mesh 2.1:

$$Nu/Nu_{0.2.1} = \begin{cases} 0.270Re^{0.284}, & Re \leq 1\,000 \\ 4.742Re^{-0.114}, & Re \geq 3\,000 \end{cases} \quad (4.49)$$

Accuracy: $\pm 8\%$

Mesh 3.1:

$$Nu/Nu_{0.3.1} = \begin{cases} 0.329Re^{0.284}, & Re \leq 1\,000 \\ 5.154Re^{-0.114}, & Re \geq 3\,000 \end{cases} \quad (4.50)$$

Accuracy: $\pm 3\%$

Factor:

$$Nu/Nu_{0.1.1} = \begin{cases} 0.90Nu/Nu_{0.3.1}, & Re \leq 1\,000 \\ 0.97Nu/Nu_{0.3.1}, & Re \geq 3\,000 \end{cases}$$

$$Nu/Nu_{0.2.1} = \begin{cases} 0.82Nu/Nu_{0.3.1}, & Re \leq 1\,000 \\ 0.92Nu/Nu_{0.3.1}, & Re \geq 3\,000 \end{cases}$$

Nu/Nu₀ – 48% porosity screen insert

Mesh 1.3:

$$Nu/Nu_{0.1.3} = \begin{cases} 3.487Re^{-0.118}, & Re \leq 1\,000 \\ 5.448Re^{-0.124}, & Re \geq 3\,000 \end{cases} \quad (4.51)$$

Accuracy: $\pm 5\%$

Mesh 2.3:

$$Nu/Nu_{0.2.3} = \begin{cases} 3.405Re^{-0.118}, & Re \leq 1\,000 \\ 5.618Re^{-0.124}, & Re \geq 3\,000 \end{cases} \quad (4.52)$$

Accuracy: $\pm 4\%$

Mesh 3.3:

$$Nu/Nu_{0.3.3} = \begin{cases} 4.103Re^{-0.118}, & Re \leq 1\,000 \\ 5.675Re^{-0.124}, & Re \geq 3\,000 \end{cases} \quad (4.53)$$

Accuracy: $\pm 3\%$

Factor:

$$Nu/Nu_{0.1.3} = \begin{cases} 0.85Nu/Nu_{0.3.3}, & Re \leq 1\,000 \\ 0.96Nu/Nu_{0.3.3}, & Re \geq 3\,000 \end{cases}$$

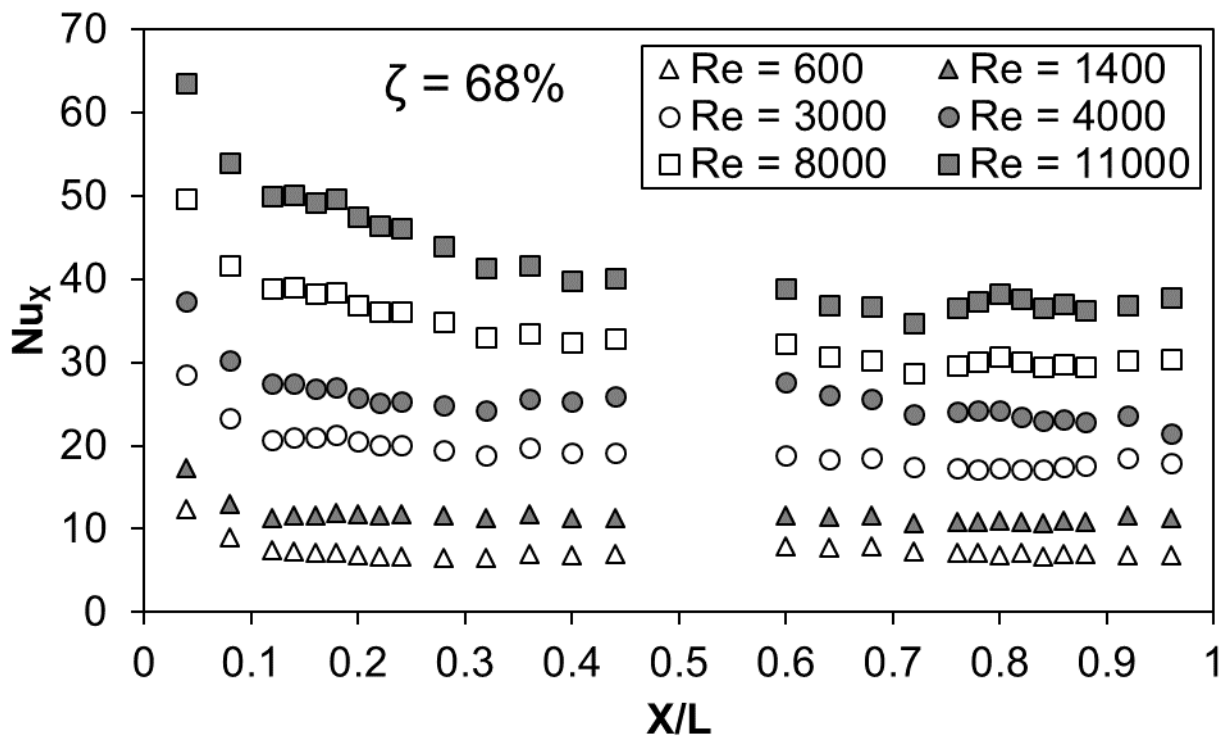
$$Nu/Nu_{0.2.3} = \begin{cases} 0.83Nu/Nu_{0.3.3}, & Re \leq 1\,000 \\ 0.99Nu/Nu_{0.3.3}, & Re \geq 3\,000 \end{cases}$$

4.5.2 5-MM CHANNEL

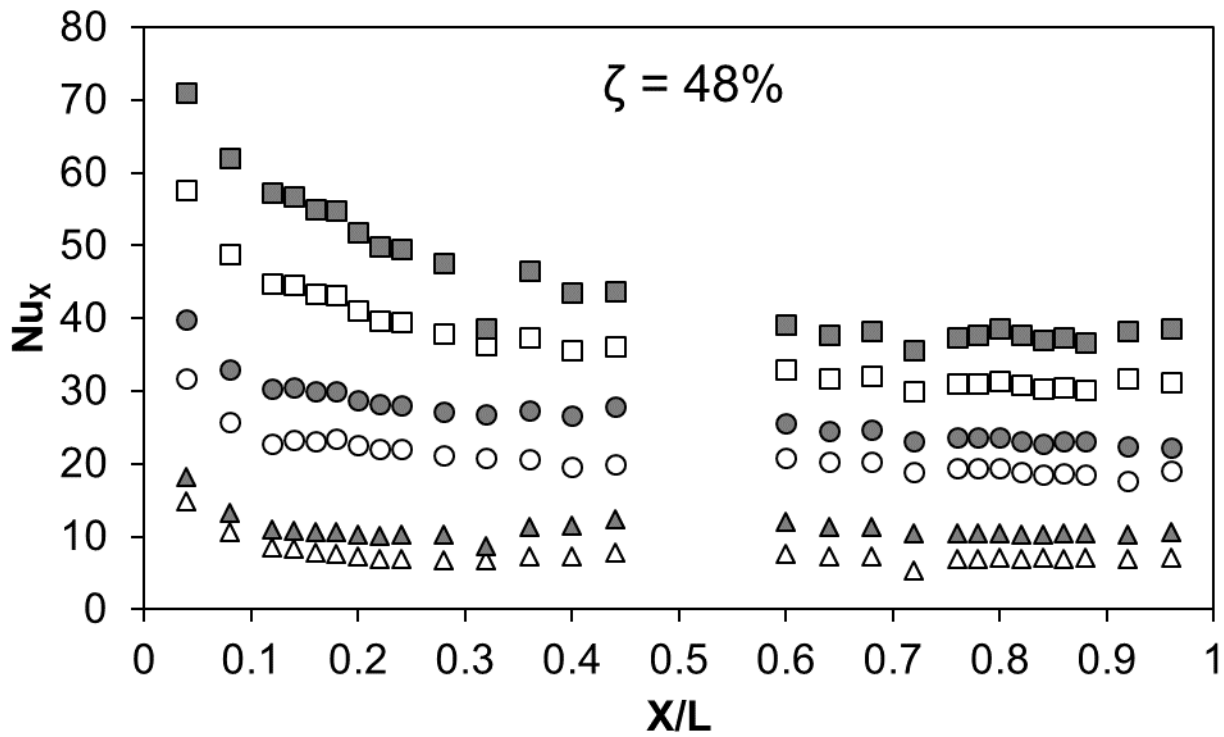
Figure 4.32 provides the local Nusselt number (Nu) along the normalized length of the channel (X/L) at $y = 101.5$ mm locations for the heated wall in the screen channel as Reynolds number varies. The data are measured with only the top wall (203 mm wall) heated. The magnitude of the heat flux was varied as far as possible with each Reynolds number to maintain a sufficient temperature difference between the wall and bulk air flow to reduce uncertainty in the measurements. The differences of $(T_{w,x} - T_{m,x})$ in Equation (3.13) for the 68% and 48% porosity screen inserts were between 5°C and 8°C depending on the Reynolds number. The first location of the data in Figure 4.32 is $X/L = 0.04$ and ends at $X/L = 0.96$. In the screen channel the slope of Nu_x with X/L decreases in the range of $0.0 \leq X/L \leq 0.6$ and then becomes constant for $X/L > 0.6$. The smooth inlet flow into the screen test section undergoes transition in $0.0 \leq X/L \leq 0.6$ before it becomes thermally fully developed near $X/L \approx 0.6$ to result in a constant Nu_x along X/L in the screen channel at $X/L > 0.6$. It is worthy to note that the value of local Nu_x along X/L in Figure 4.32 are always higher for the screen channel than for the baseline channel data at the corresponding locations for the similar Reynolds number. The data in Figure 4.32 compare the effects of screen wave period and porosity on the local Nusselt number distributions.

The average Nusselt numbers, shown in Figure 4.33, were determined using the average of the local Nusselt numbers in $0.6 \leq X/L \leq 0.96$. Figure 4.33 shows the effects a change in porosity (the wave period remains the same) of the screen insert have on the Nusselt number. Figure 4.33 shows the effects a change in wave period (the mesh porosity remains the same) of the screen insert have on the Nusselt number.

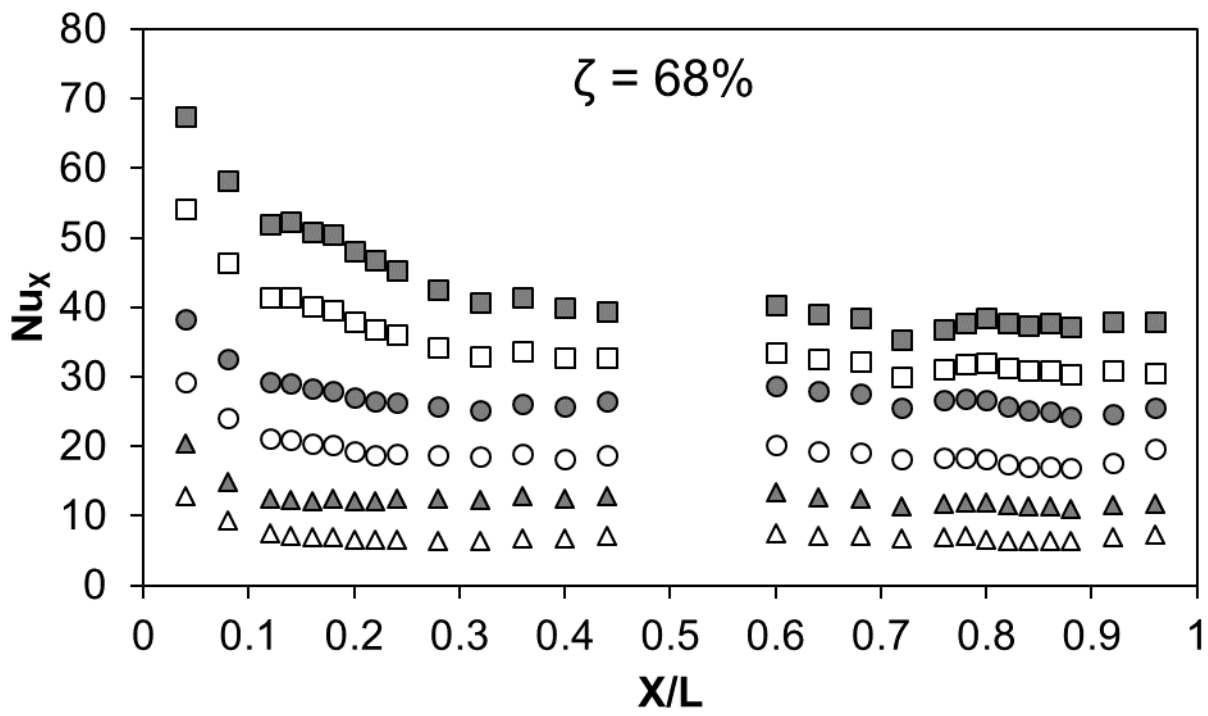
For the 68% and 48% porosity screen inserts with the 18 mm wave period, Figure 4.33, mesh 5.1 (48% porosity) has a 5% lower average Nusselt number than mesh 4.1 (68% porosity) for the Reynolds numbers between 400 and 600, a 10% higher Nusselt number for Reynolds numbers greater than 600 up to 6 000, and a 5% higher Nusselt number for Reynolds numbers greater than 6 000. For the 68% and 48% porosity screen inserts with the 12 mm wave period, Figure 4.33, mesh 5.3 has approximately 7% higher average Nusselt number than mesh 4.3 for all the Reynolds numbers.



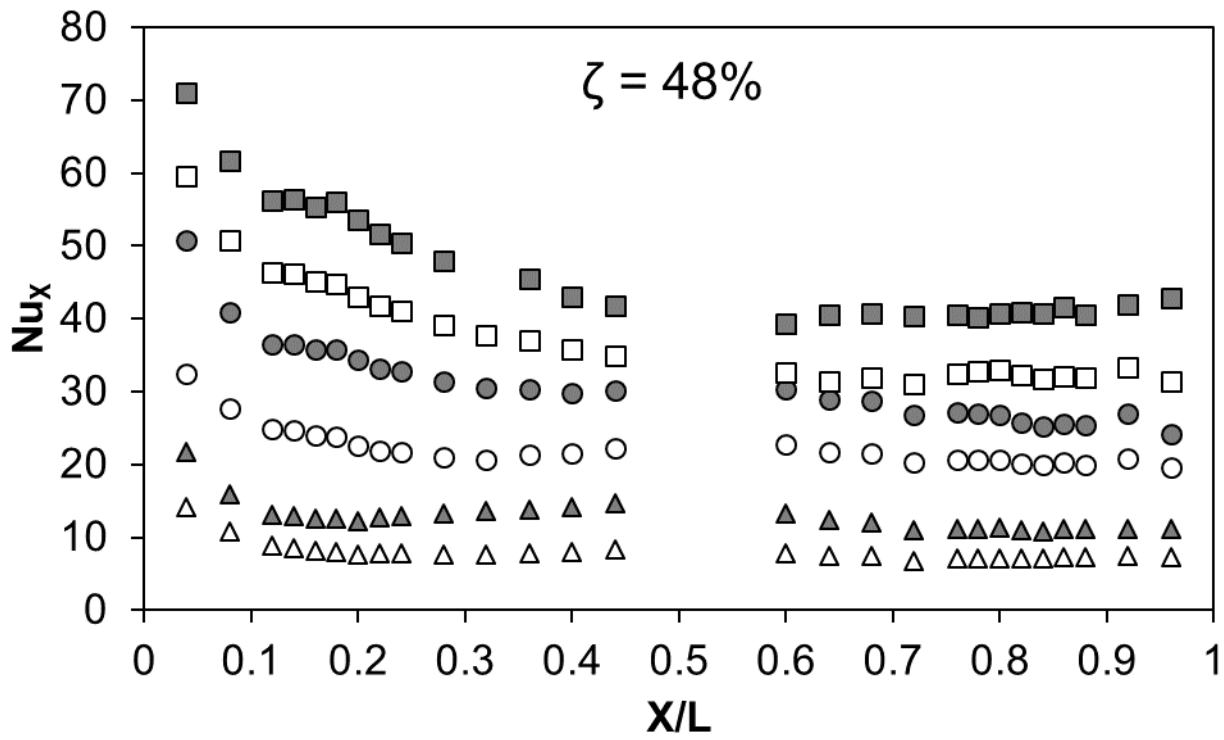
(a)



(b)



(c)



(d)

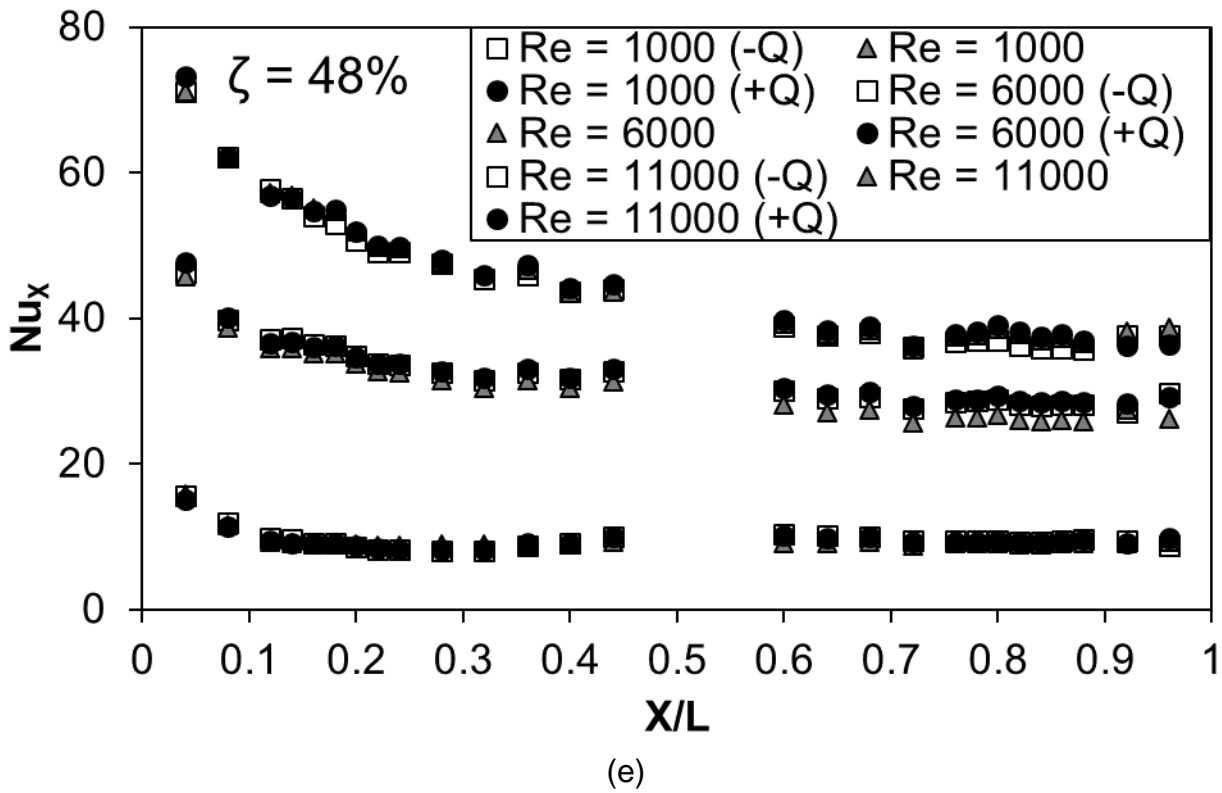


Figure 4.32: Local Nusselt numbers for various Reynolds numbers for one-wall heating boundary condition: (a) Mesh 4.1 (18 mm period - 68% porosity), (b) Mesh 4.3 (18 mm period - 48% porosity), (c) Mesh 5.1 (12 mm period - 68% porosity), and (d) Mesh 5.3 (12 mm period - 48% porosity)

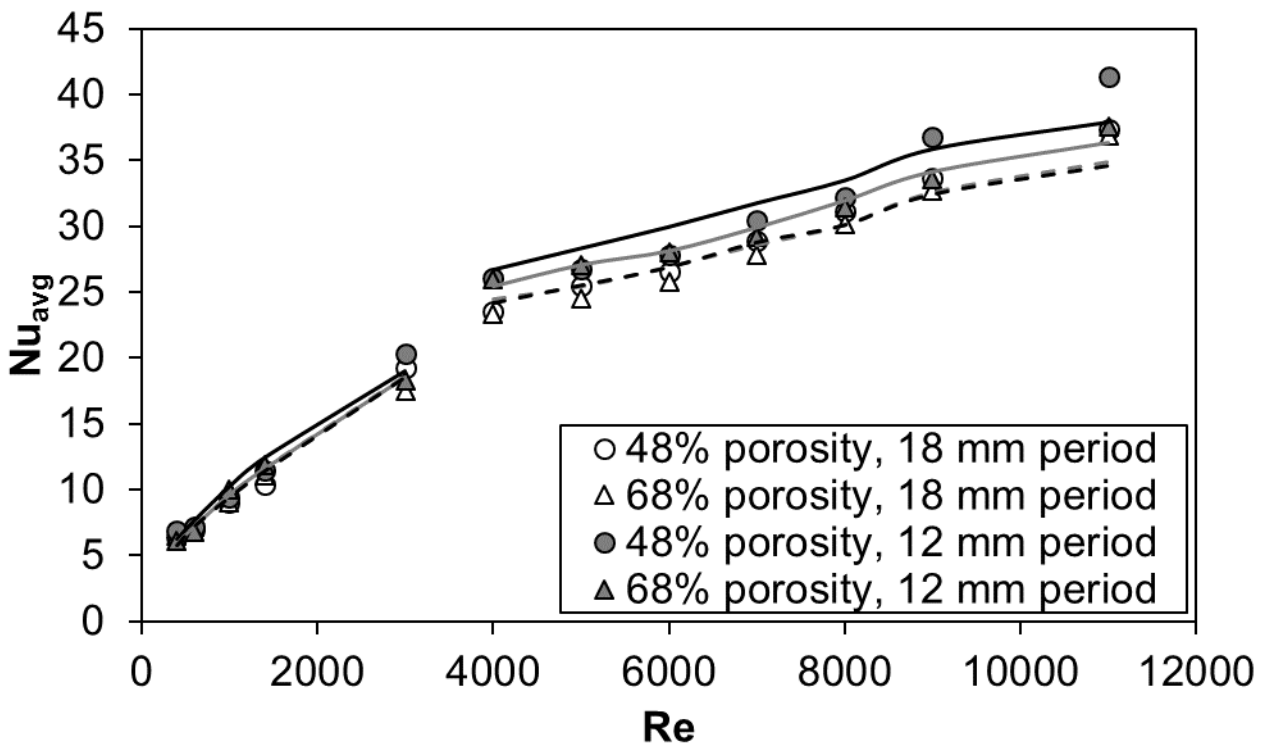


Figure 4.33: Average Nusselt number as Reynolds number varies for one-wall heating boundary condition

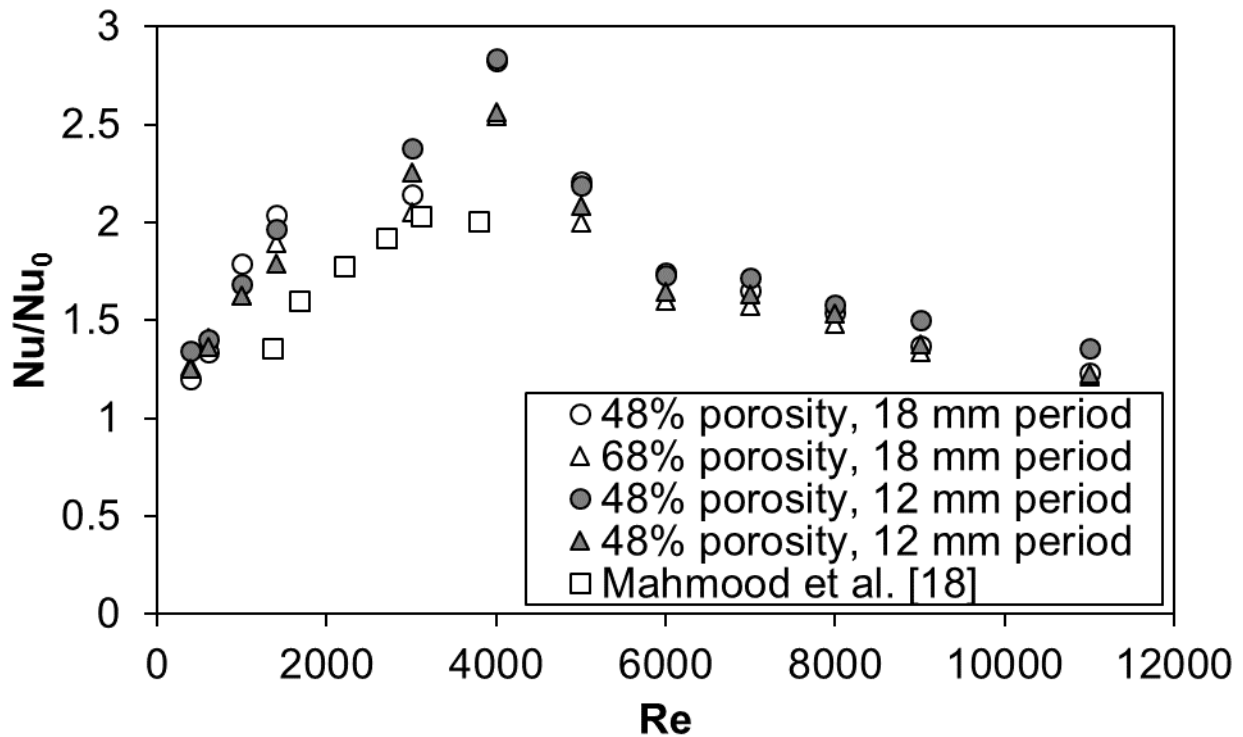


Figure 4.34: Nu/Nu_0 ratio as Reynolds number varies for one-wall heating boundary

For the 68% porosity screen inserts mesh 5.1 (12 mm period) has no significant increase in the average Nusselt number than mesh 4.1 (18 mm period) except for Reynolds number equal to 3 000 where mesh 5.1 Nusselt number is 10 % higher than mesh 4.1. For the 48% porosity screen inserts mesh 5.3 (12 mm period) has also approximately equal Nusselt numbers to those of mesh 4.3 (18 mm period) except for the Reynolds number equal to 3 000 where mesh 5.3 Nusselt number is 11% greater than mesh 4.3 and for the Reynolds numbers greater than 9 000 where mesh 5.3 Nusselt numbers are 10% greater than mesh 5.1 Nusselt numbers. The Nu/Nu_0 ratios, shown in Figure 4.34, were determined dividing the average Nusselt numbers of Figure 4.33 by the experimental baseline Nusselt numbers captured in Section 4.2.3. Figure 4.34 shows the effects a change in porosity (the wave period remains the same) of the screen insert have on the Nu/Nu_0 ratio. Figure 4.34 shows the effects a change in wave period (the mesh porosity remains the same) of the screen insert have on the Nu/Nu_0 ratio. The data in Figure 4.34 show similar distribution patterns in the effects of period and porosity of the screen insert on the average Nu/Nu_0 ratio to those in the average Nusselt numbers of Figure 4.33. The changes in period or the porosity of the screen inserts make no significant differences in the average Nu/Nu_0 ratios in Figure 4.34 for the one-wall heating boundary condition.

Table 4.16 shows the screen insert correlations for the average Nusselt number and Nu/Nu_0 ratio with the Reynolds number for the 5 mm channel height and one-wall heating boundary condition. Each correlation was determined using a linear regression curve fit through the natural logarithm plots of the data points. The accuracy of the correlation is also given for each data set. Finally, a factor was calculated to obtain either the average

Nusselt number or average Nu/Nu_0 ratio of a screen insert from the correlation of another screen insert of the same porosity.

Table 4.16: Average Nusselt number and Nu/Nu_0 ratio correlations for 5 mm channel height - one-wall heating

Average Nusselt number – 68% porosity screen inserts

Mesh 4.1:

$$Nu_{4.1} = \begin{cases} 0.178Re^{0.576}, & Re \leq 1\,400 \\ 1.242Re^{0.357}, & Re \geq 3\,000 \end{cases} \quad (4.54)$$

Accuracy: $\pm 6\%$

Mesh 5.1:

$$Nu_{5.1} = \begin{cases} 0.178Re^{0.576}, & Re \leq 1\,400 \\ 1.307Re^{0.357}, & Re \geq 3\,000 \end{cases} \quad (4.55)$$

Accuracy: $\pm 4\%$

Factor:

$$Nu_{4.1} = \begin{cases} 1.00Nu_{5.1}, & Re \leq 1\,400 \\ 0.95Nu_{5.1}, & Re \geq 3\,000 \end{cases}$$

Average Nusselt number – 48% porosity screen inserts

Mesh 4.3:

$$Nu_{4.3} = \begin{cases} 0.175Re^{0.576}, & Re \leq 1\,400 \\ 1.242Re^{0.357}, & Re \geq 3\,000 \end{cases} \quad (4.56)$$

Accuracy: $\pm 7\%$

Mesh 5.3:

$$Nu_{5.3} = \begin{cases} 0.191Re^{0.576}, & Re \leq 1\,400 \\ 1.373Re^{0.357}, & Re \geq 3\,000 \end{cases} \quad (4.57)$$

Accuracy: $\pm 9\%$

Factor:

$$Nu_{4.3} = \begin{cases} 0.98Nu_{5.1}, & Re \leq 1\,400 \\ 0.95Nu_{5.1}, & Re \geq 3\,000 \end{cases}$$

$$Nu_{5.3} = \begin{cases} 1.07Nu_{5.1}, & Re \leq 1\,400 \\ 1.05Nu_{5.1}, & Re \geq 3\,000 \end{cases}$$

Nu/Nu_0 ratio – 68% porosity screen inserts

Mesh 4.1:

$$Nu/Nu_{0.4.1} = \begin{cases} 0.0971Re^{0.395}, & Re \leq 1\,400 \\ 344.537Re^{-0.605}, & Re \geq 3\,000 \end{cases} \quad (4.58)$$

Accuracy: $\pm 10\%$

Mesh 5.1:

$$Nu/Nu_{0.5.1} = \begin{cases} 0.110Re^{0.395}, & Re \leq 1\,400 \\ 344.537Re^{-0.605}, & Re \geq 3\,000 \end{cases} \quad (4.59)$$

Accuracy: $\pm 7\%$

Factor:

$$Nu/Nu_{0.4.1} = \begin{cases} 0.88Nu/Nu_{0.5.1}, & Re \leq 1\,400 \\ 1.00Nu/Nu_{0.5.1}, & Re \geq 3\,000 \end{cases}$$

f/f_0 ratio – 48% porosity screen inserts

Mesh 4.3:

$$Nu/Nu_{0.4.3} = \begin{cases} 0.0971Re^{0.395}, & Re \leq 1\,400 \\ 344.537Re^{-0.605}, & Re \geq 3\,000 \end{cases} \quad (4.60)$$

Accuracy: $\pm 8\%$

Mesh 5.3:

$$Nu/Nu_{0.5.3} = \begin{cases} 0.111Re^{0.395}, & Re \leq 1\,400 \\ 351.427Re^{-0.605}, & Re \geq 3\,000 \end{cases} \quad (4.61)$$

Accuracy: $\pm 8\%$

Factor:

$$Nu/Nu_{0.4.3} = \begin{cases} 0.88Nu/Nu_{0.5.1}, & Re \leq 1\,400 \\ 1.00Nu/Nu_{0.5.1}, & Re \geq 3\,000 \end{cases}$$

$$Nu/Nu_{0.5.3} = \begin{cases} 1.01Nu/Nu_{0.5.1}, & Re \leq 1\,400 \\ 1.02Nu/Nu_{0.5.1}, & Re \geq 3\,000 \end{cases}$$

4.6 THERMAL PERFORMANCE INDEX

The following sections contains the comparison of the various screen inserts by a performance parameter known as the thermal performance index. This parameter is defined as the ratio of enhanced convective heat transfer (Nu/Nu_0) to enhanced pumping power required (f/f_0) at a given mass flow rate (Re) for a screen insert relative to the smooth channel without any screen [1,18, 24]. For a screen insert to have a possible benefit in increasing the effectiveness of solar or regular flat plate heat exchangers with the pumping power, its thermal performance index should be equal to or greater than one at a specific Reynolds number. Using the thermal performance index property of each screen insert it is possible to compare the influences of the geometrical properties of the screen insert, namely; channel or screen height, period of the screen insert, and porosity of the screen insert. The thermal performance index provided in this section are estimated based on the average Nu/Nu_0 and f/f_0 data at the corresponding Re , wave period, porosity, and channel height presented in the previous sections.

4.6.1 14-MM CHANNEL

The thermal performance index, $(Nu/Nu_0)/(f/f_0)^{(1/3)}$ defined by [1, 24] for the screen channel is computed from the f/f_0 and average Nu/Nu_0 data presented earlier. The definition of the performance index is based on the three basic design objectives of the heat exchanger: (i) reduced heat transfer area, (ii) enhanced heat transfer rate, and (iii) reduced pumping power, all relative to the smooth channel. Figure 4.35 shows the thermal performance index of the various screen inserts at a channel height of 14 mm and a one-heated wall boundary condition as the Re changes. Figure 4.35 (a) and (b) compare the data for the screen inserts with varying periods and Figure 4.35 (c) and (d) compare the data for the screen inserts with varying porosity. Figure 4.35 (a) compares the thermal performance index of the three 68% porosity screen inserts, Figure 4.35 (b) compares the thermal performance index of the three 48% porosity screen inserts, Figure 4.35 (c) compares the

thermal performance index of the two 22 mm period screen inserts, and [Figure 4.35 \(d\)](#) compares the thermal performance index of the two 12 mm period screen inserts. For good thermal performance, the $(Nu/Nu_0)/(f/f_0)^{1/3} \geq 1.0$ are expected [18, 24].

For the case of the 68% porosity screen inserts, [Figure 4.35 \(a\)](#) shows that the useful range of Reynolds number is between 400 and 3 000 for mesh 1.1 and 2.1, but only up to a Reynolds number of 1 000 for mesh 3.1; this is when the thermal performance index is equal to or above unity. The maximum thermal performance index for the screen inserts of [Figure 4.35 \(a\)](#) is at Reynolds numbers between 400 and 1 000 and then the performance index decreases with Re to a minimum at $Re = 30\,000$. The thermal performance index decreases by approximately 60% over the entire Reynolds number range.

[Figure 4.35 \(a\)](#) shows that a decrease in the period of the screen insert for the 68% porosity mesh causes a decrease in the thermal performance index at a Re . Mesh 3.1 thermal performance index is 10% lower than those for the mesh 1.1 for Reynolds numbers in the region of $Re < 4000$, 20% lower for Reynolds number equal to 4 000 and 12% lower for Reynolds number greater than 5 000.

When comparing the data of irregular period screen insert (Mesh 2.1) for the 68% porosity with the data of other screens in [Figure 4.35 \(a\)](#), it reveals a strange trend. Mesh 2.1 data only are only smaller by less than 5% from mesh 1.1 data in the laminar and transition region ($Re < 10\,000$) and higher by less than 12% from mesh 3.1 in the same region of Reynolds number ($Re < 10\,000$). For the turbulent regime ($10\,000 < Re < 30\,000$), the differences in the thermal performance index between the screens are much smaller in [Figure 4.35 \(a\)](#). This means that for the range of $Re \leq 30\,000$ the thermal performance for a sinusoidal screen with a period between 22 mm and 12 mm, and 68% porosity is expected to be in between the thermal performance provided by Mesh 1.1 and Mesh 3.1.

For the case of the 48% porosity screen inserts, [Figure 4.35 \(b\)](#) shows that the useful range Reynolds number is between 400 and 1 000 for mesh 1.3 and 2.3, but only at the Reynolds number of 400 for mesh 3.3; this is when the thermal performance index is equal to or above unity. The maximum thermal performance index for these screen inserts is at the Reynolds numbers of 400 and then the performance index decreases with Re to a minimum at $Re = 30\,000$ in [Figure 4.35 \(b\)](#). The thermal performance index decrease of the performance index is by approximately 70% over the entire Reynolds number range for all the screens of [Figure 4.35 \(b\)](#).

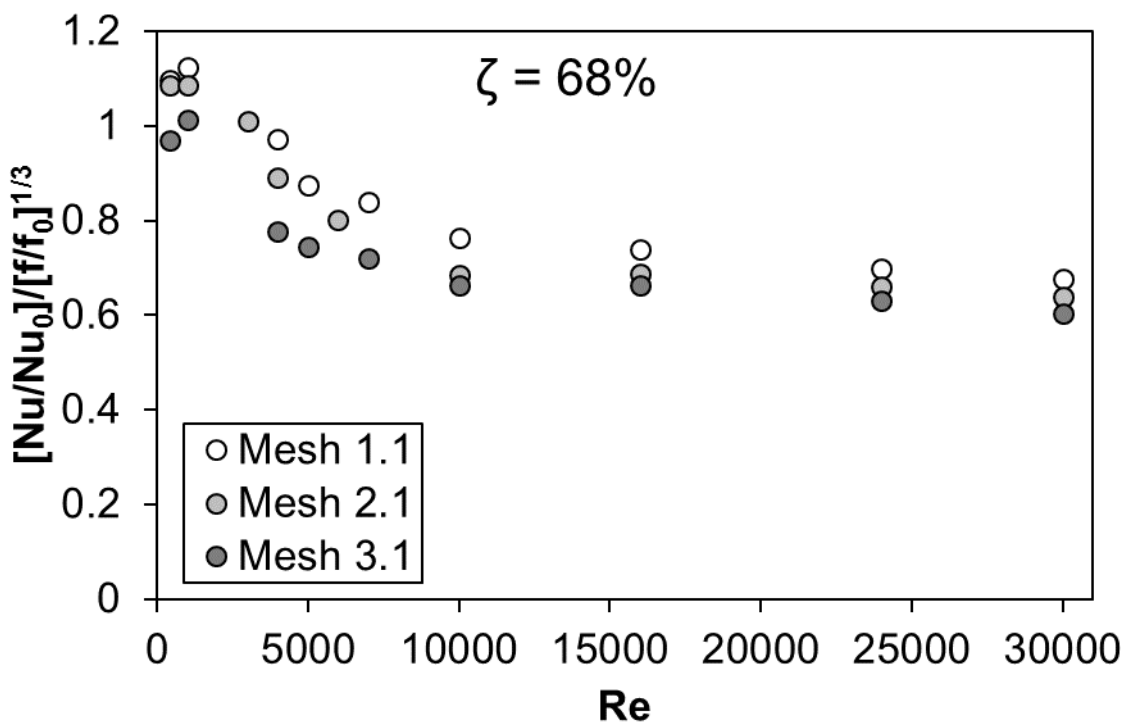
[Figure 4.35 \(b\)](#) shows that a decrease in the period of the screen insert for the 48% porosity mesh causes a decrease in the value of the thermal performance index at the corresponding Reynolds number. Mesh 3.3 thermal performance index is 10% lower than that for mesh 1.3 for Reynolds numbers in the laminar region ($Re < 3\,000$), 17% lower for Reynolds number equal to 4 000 and 10% lower than that for mesh 1.3 for Reynolds number greater than 5 000.

When comparing the irregular screen insert (Mesh 2.3) data for the 48% porosity screen insert in [Figure 4.35 \(b\)](#) with those for mesh 1.3 and mesh 3.3, it reveals that the thermal

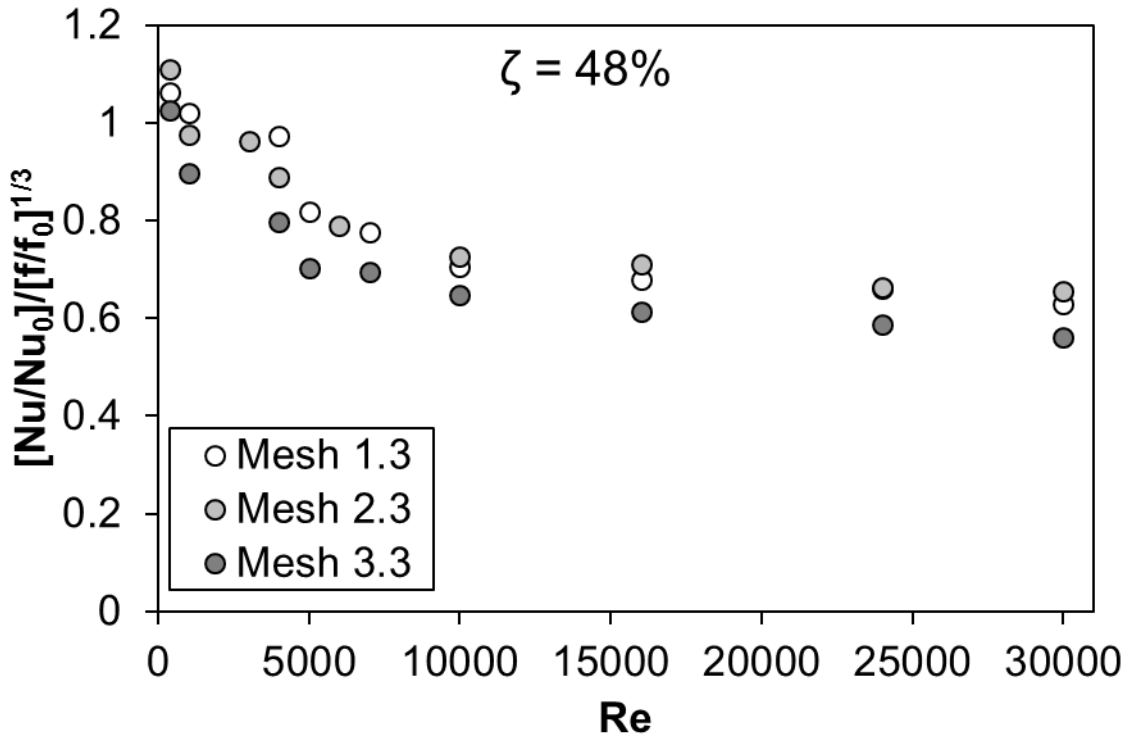
performance index distribution of mesh 2.3 is almost identical to that of mesh 1.3. Mesh 2.3 data only differ by less than 5% from mesh 1.3 in the laminar and transition region and are 10% higher than mesh 3.3 data in the same region of $Re < 10\,000$. For the turbulent Reynolds numbers ($10\,000 < Re < 30\,000$), mesh 1.3 data again only differ by 4% from mesh 2.3 data and mesh 3.3 data are 12% lower than mesh 2.3 data in [Figure 4.35 \(b\)](#). This means that the irregularity in the 22 mm or 12 mm wave period for the 48% porosity screen will influence the thermal performance index according to the occurrences of the larger periods.

For the case of the 22 mm period screen inserts, [Figure 4.35 \(c\)](#) shows that a decrease in the porosity of the screen insert causes a decrease in the value of the thermal performance index at the corresponding Reynolds number. Mesh 1.3 thermal performance index are 6% lower for Reynolds numbers $< 4\,000$, and 7% lower for Reynolds numbers $> 4\,000$ than those for Mesh 1.1.

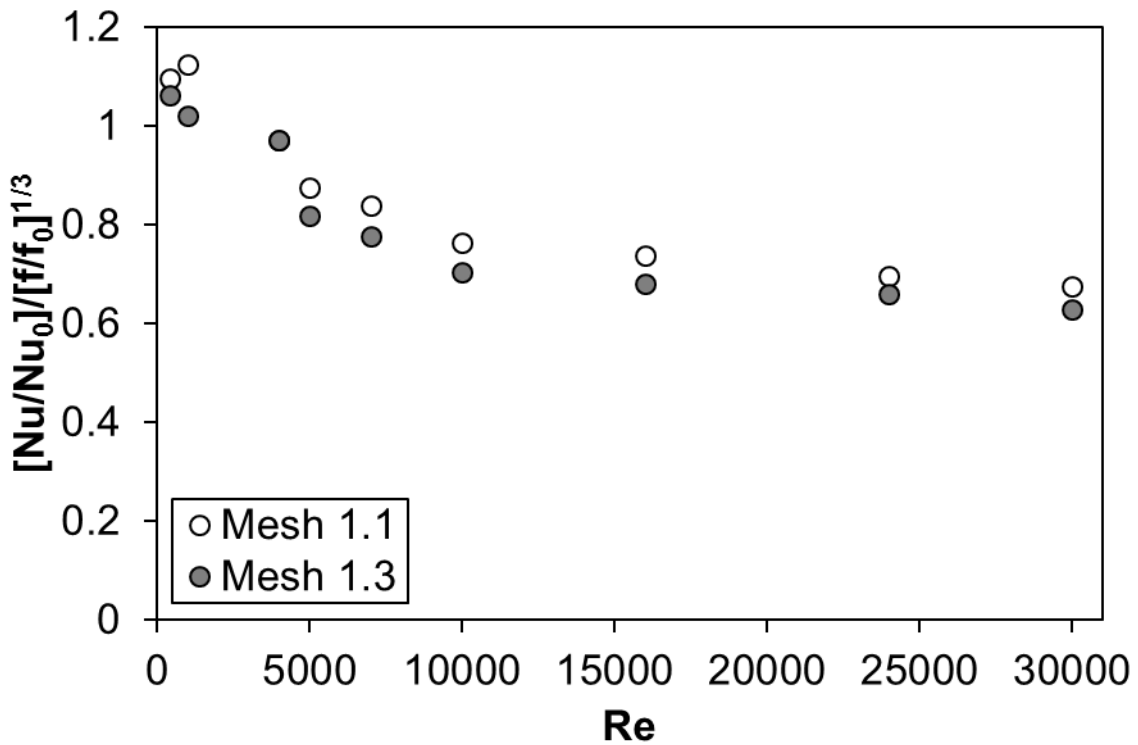
For the case of the 12 mm period screen inserts, [Figure 4.35 \(d\)](#) shows that a decrease in porosity of the screen insert also decreases the value of the thermal performance index at the corresponding Reynolds number. Mesh 3.3 thermal performance index are 8% lower for Reynolds numbers $< 4\,000$, and 6% lower for Reynolds number $> 4\,000$ than those for mesh 3.1.



(a)



(b)



(c)

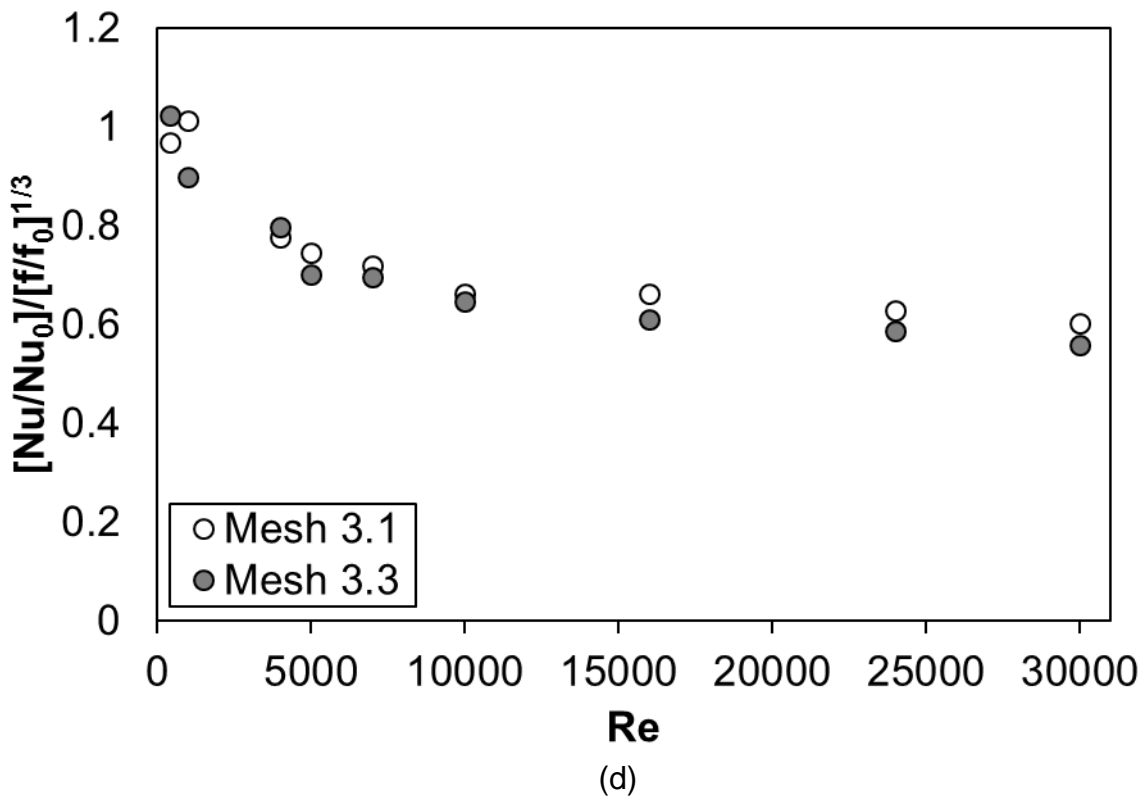


Figure 4.35: Thermal performance index for one heated wall as Reynolds number varies in 14 mm channel height comparing: (a) Mesh 1.1, Mesh 2.1 and Mesh 3.1 (68% porosity screens- 22 mm, irregular, and 12 mm wave period, respectively), (b) Mesh 1.3, Mesh 2.3 and Mesh 3.3 (48% porosity screens- 22 mm, irregular, and 12 mm wave period, respectively), (c) Mesh 1.1 and Mesh 1.3 (22 mm period- 68% and 48% porosity, respective), and (d) Mesh 3.1 and Mesh 3.3 (12 mm period- 68% and 48% porosity, respective).

Figure 4.36 shows the thermal performance index of the various screen inserts at a channel height of 14 mm and a two-heated wall boundary condition. Figure 4.36 (a) and (b) compare the screen inserts with varying periods and Figure 4.36 (c) and (d) compare the screen inserts with varying porosity. Figure 4.36 (a) compares the thermal performance index of the three 68% porosity screen inserts, Figure 4.36 (b) compares the thermal performance index of the three 48% porosity screen inserts, Figure 4.36 (c) compares the thermal performance index of the two 22 mm period screen inserts, and Figure 4.35 (d) compares the thermal performance index of the two 12 mm period screen inserts. For good thermal performance, the $(Nu/Nu_0)/(f/f_0)^{1/3} \geq 1.0$ are expected [18, 24].

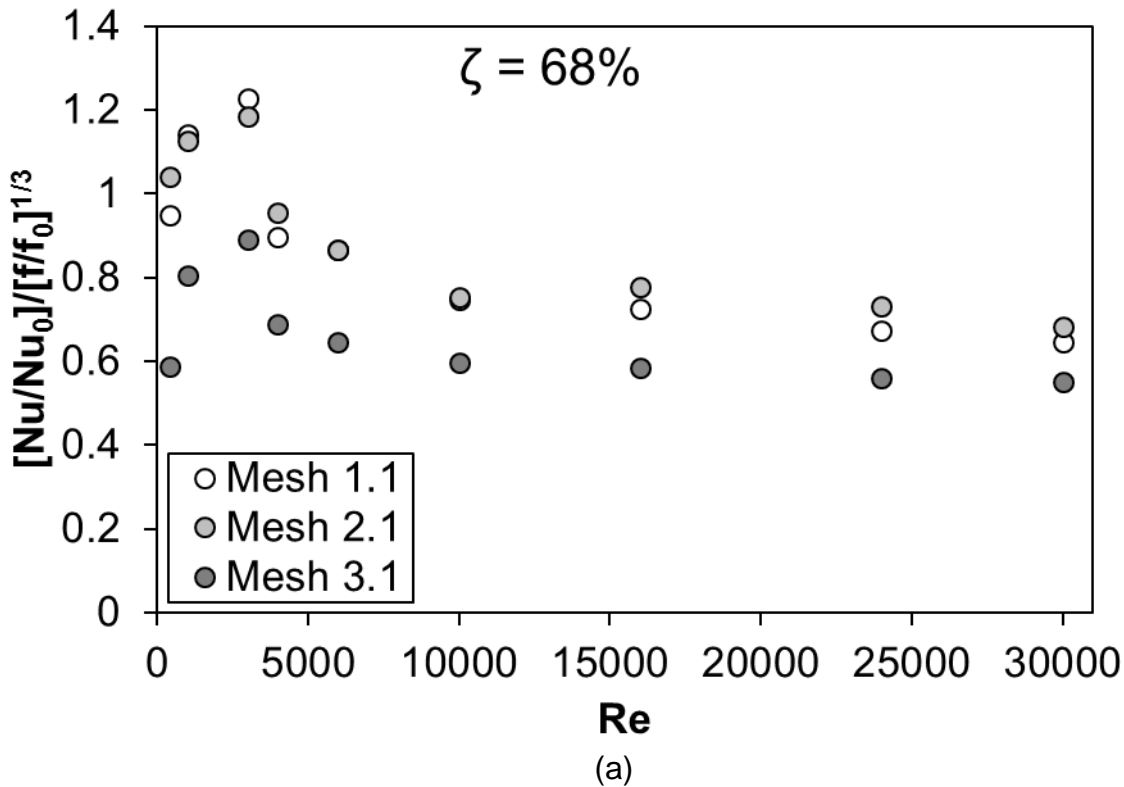
For the case of the 68% porosity screen inserts, Figure 4.36 (a) shows that the effective range of Reynolds number is between 400 and 3 000 for mesh 1.1 and 2.1 and no effective range for mesh 3.1; this is when the thermal performance index is equal to or above unity. The maximum thermal performance index for the screen inserts of Figure 4.36 (a) is at Reynolds numbers between 400 and 3 000 and then the performance index decreases with Re to a minimum at Re = 30 000. The thermal performance index decreases by approximately 40% over the entire Reynolds number range.

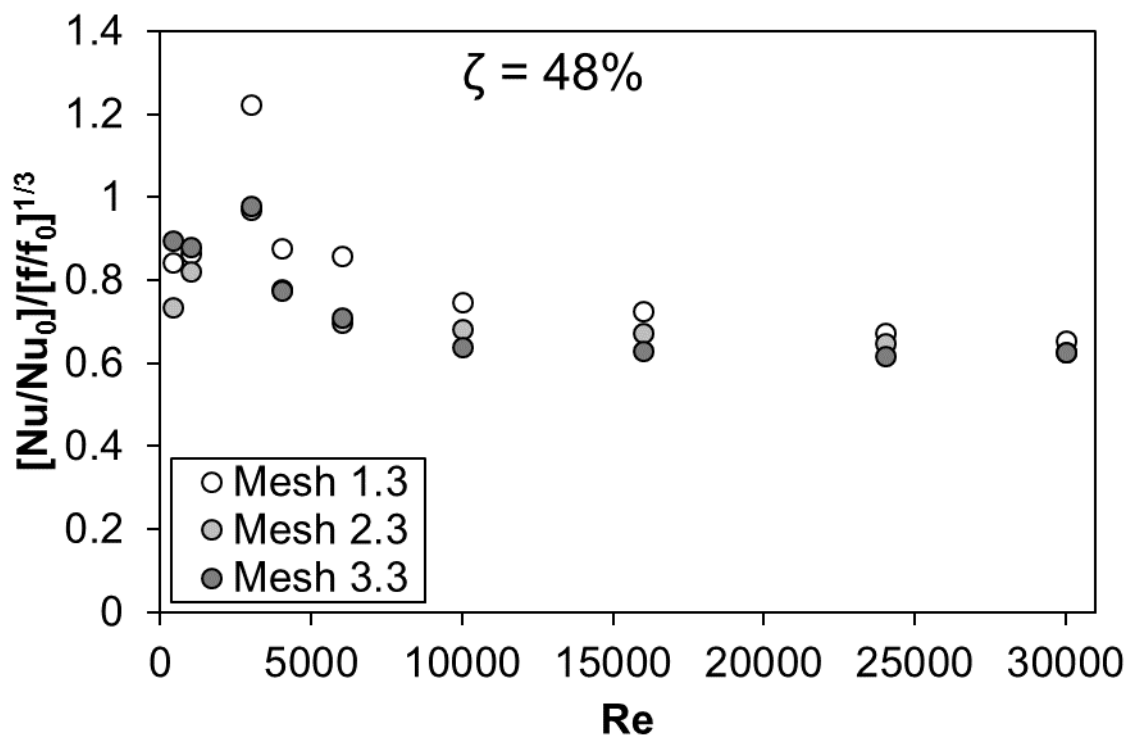
Figure 4.36 (a) shows that a decrease in the period of the screen insert for the 68% porosity mesh causes a decrease in the thermal performance index at a Re. Mesh 3.1

thermal performance index is 30% lower than those for the mesh 1.1 for Reynolds numbers in the region of $Re < 4000$, 25% lower for Reynolds number between 4 000 and 10 000 and 20% lower for Reynolds number greater than 10 000.

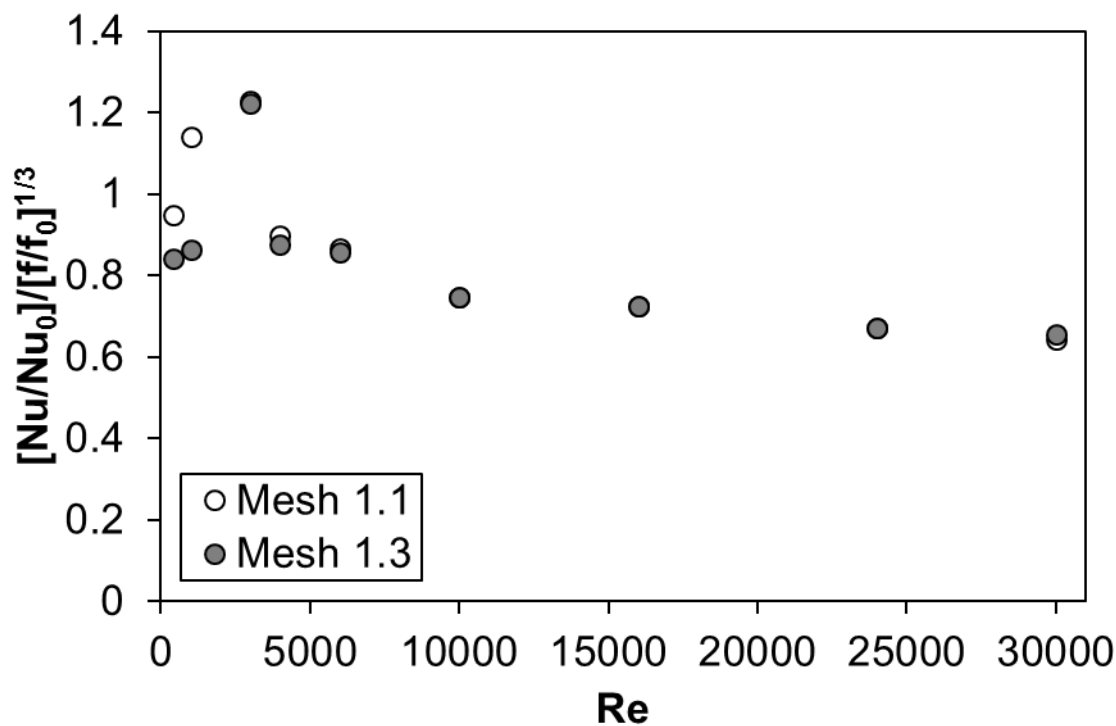
When comparing the data of irregular period screen insert (Mesh 2.1) for the 68% porosity with the data of other screens in Figure 4.36 (a), it reveals a strange trend. Mesh 2.1 data only are only smaller by less than 5% from mesh 1.1 data in $Re < 30\,000$ and higher by less than 27% from mesh 3.1 in the same region of Reynolds number ($Re < 30\,000$). This means that for the range of $Re \leq 30\,000$ the thermal performance for a sinusoidal screen with a period between 22 mm and 12 mm, and 68% porosity is expected to be in between the thermal performance provided by Mesh 1.1 and Mesh 3.1.

For the case of the 48% porosity screen inserts, Figure 4.36 (b) shows that the effective range Reynolds number is between 400 and 3 000 for mesh 1.3, 2.3 and 3.3; this is when the thermal performance index is equal to or above unity. The maximum thermal performance index for these screen inserts is at the Reynolds numbers of 3 000 and then the performance index decreases with Re to a minimum at $Re = 30\,000$ in Figure 4.36 (b). The thermal performance index decrease of the performance index is by approximately 30% over the entire Reynolds number range for all the screens of Figure 4.36 (b).

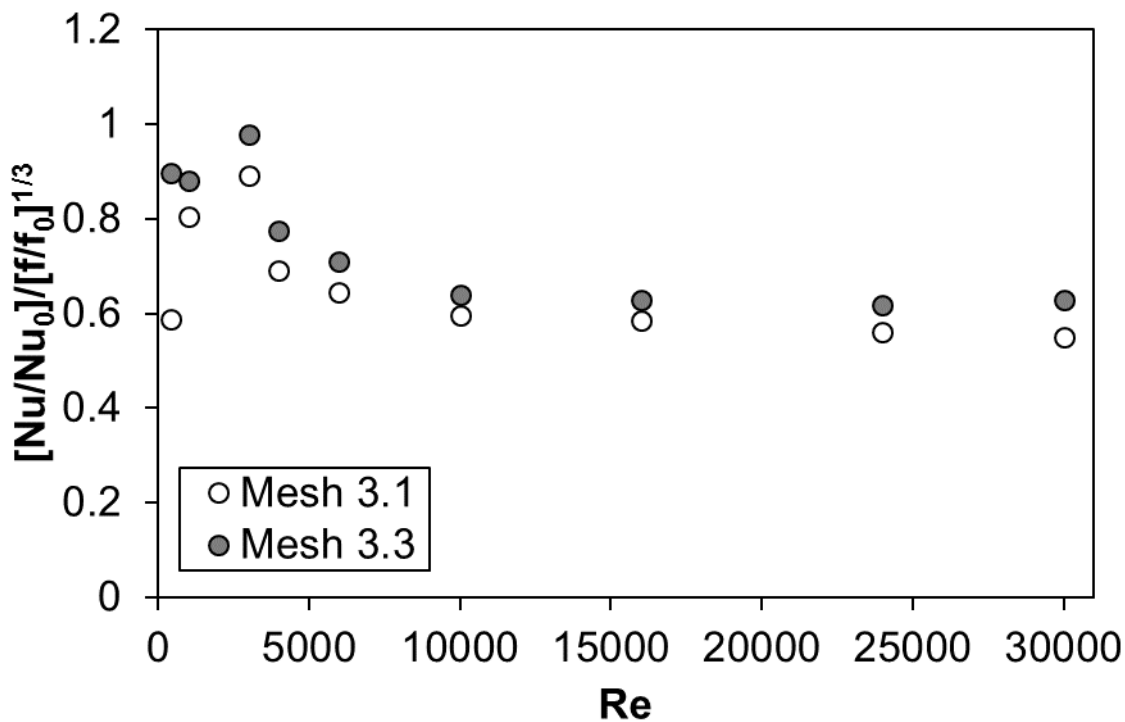




(b)



(c)



(d)

Figure 4.36: Thermal efficiencies for two heated wall in 14 mm channel height as Reynolds number varies comparing: (a) Mesh 1.1, Mesh 2.1 and Mesh 3.1 (68% porosity screens- 22 mm, irregular, and 12 mm wave period, respectively), (b) Mesh 1.3, Mesh 2.3 and Mesh 3.3 (48% porosity screens- 22 mm, irregular, and 12 mm wave period, respectively), (c) Mesh 1.1 and Mesh 1.3 (22 mm period- 68% and 48% porosity, respective), and (d) Mesh 3.1 and Mesh 3.3 (12 mm period- 68% and 48% porosity, respective).

Figure 4.36 (b) shows that a decrease in the period of the screen insert for the 48% porosity mesh causes a decrease in the value of the thermal performance index at the corresponding Reynolds number. Mesh 3.3 thermal performance index is 4% lower than that for mesh 1.3 for Reynolds numbers in the laminar region ($Re < 3\,000$), 15% lower for Reynolds number in the transition region ($3\,000 < Re < 10\,000$) and 8% lower than that for mesh 1.3 for Reynolds number greater than 10 000.

When comparing the irregular screen insert (Mesh 2.3) data for the 48% porosity screen insert in Figure 4.36 (b) with those for mesh 1.3 and mesh 3.3, it reveals that the thermal performance index distribution of mesh 2.3 is almost identical to that of mesh 3.3. Mesh 2.3 data only differ by less than 15% from mesh 3.3 in the laminar, less than 2% in the transition region and are less than 5% higher in the turbulent region. For the turbulent Reynolds numbers ($10\,000 < Re < 30\,000$), mesh 1.3 data again only differ by 10% from mesh 2.3 data and mesh 3.3 data are 5% lower than mesh 2.3 data in Figure 4.36 (b). This means that the irregularity in the 22 mm or 12 mm wave period for the 48% porosity screen will influence the thermal performance index according to the occurrences of the larger periods.

For the case of the 22 mm period screen inserts, Figure 4.36 (c) shows that a decrease in the porosity of the screen insert causes a decrease in the value of the thermal

performance index at the corresponding Reynolds number. Mesh 1.3 thermal performance index are 17% lower for Reynolds numbers $< 4\,000$, and 3% lower for Reynolds numbers $> 4\,000$ than those for Mesh 1.1.

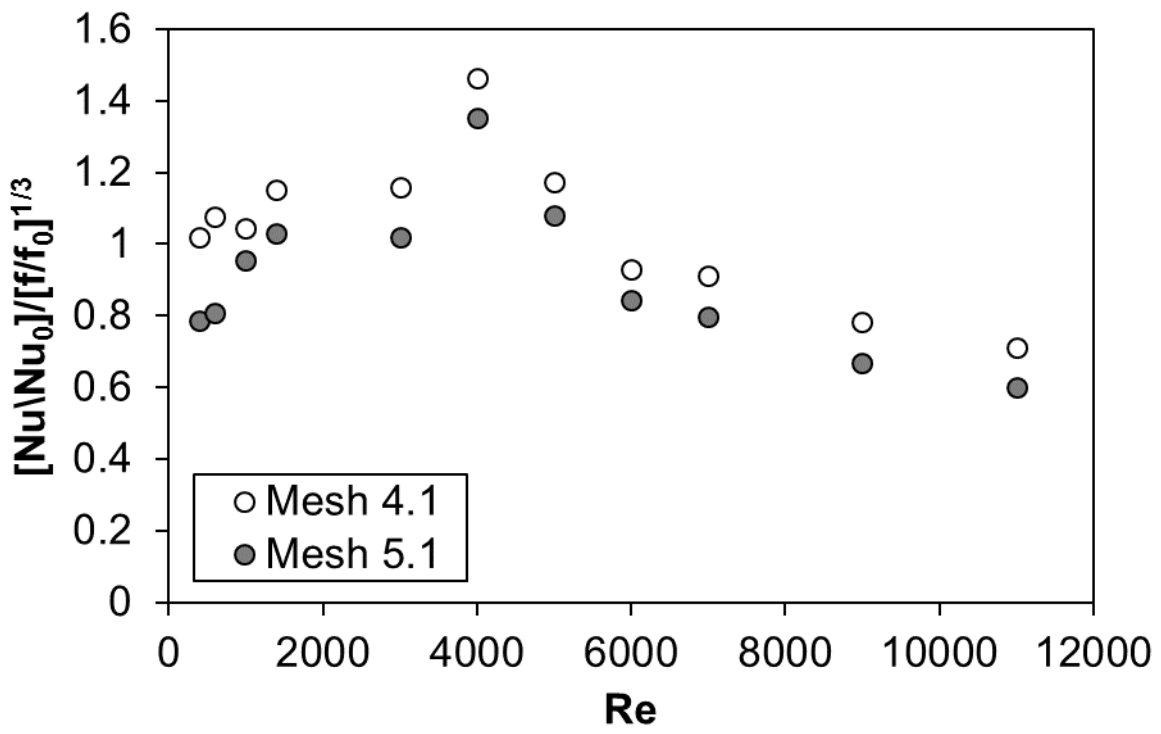
For the case of the 12 mm period screen inserts, [Figure 4.36 \(d\)](#) shows that a decrease in porosity of the screen insert increases the value of the thermal performance index at the corresponding Reynolds number. Mesh 3.3 thermal performance index are 10% higher than that for the mesh 3.1 for all Reynolds numbers.

4.6.2 5-MM CHANNEL

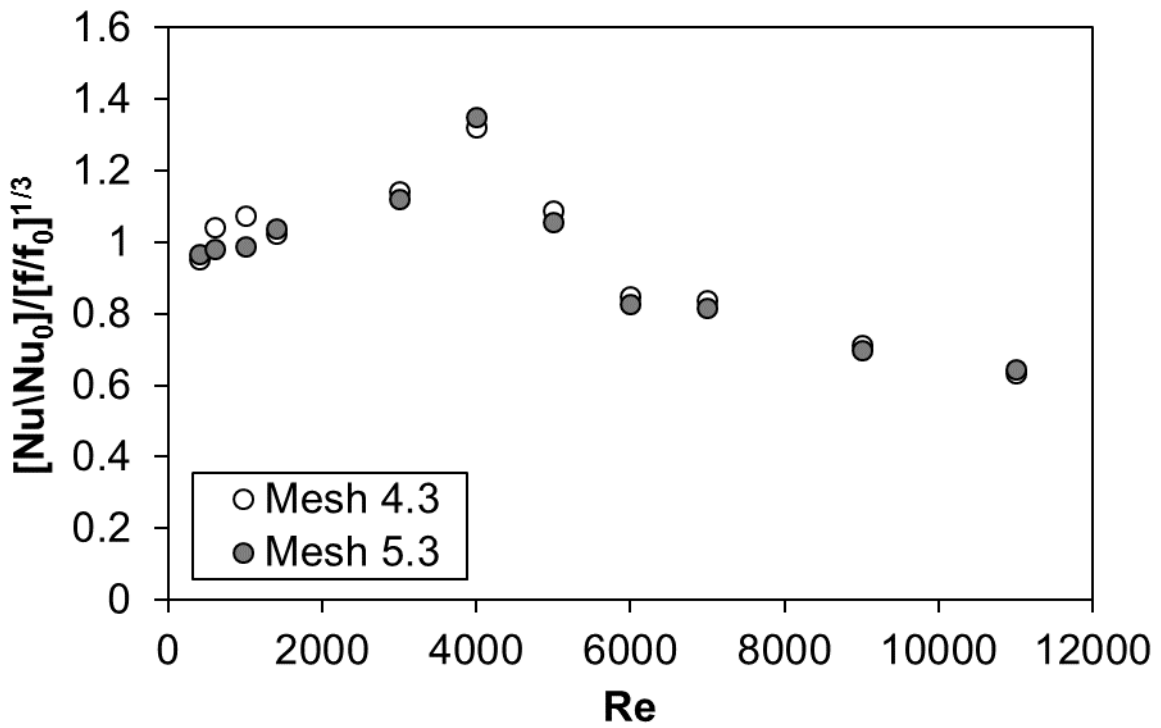
[Figure 4.37](#) shows the thermal performance index of the various screen inserts at a channel height of 5 mm and one-heated wall boundary condition as the Re varies. [Figure 4.37 \(a\)](#) and [\(b\)](#) compare the screen inserts with varying periods and [Figure 4.37 \(c\)](#) and [\(d\)](#) compare the screen inserts with varying porosity. [Figure 4.37 \(a\)](#) compares the thermal performance index of the two 68% porosity screen inserts, [Figure 4.37 \(b\)](#) compares the thermal performance index of the two 48% porosity screen inserts, [Figure 4.37 \(c\)](#) compares the thermal performance index of the two 18 mm period screen inserts, and [Figure 4.37 \(d\)](#) compares the thermal performance index of the two 12 mm period screen inserts.

For the case of the 68% porosity screen inserts, [Figure 4.37 \(a\)](#) shows that the effective range of Reynolds number is between 400 and 6 000 for mesh 4.1; however, the effective range of Reynolds number is between 1 400 and 6 000 for mesh 5.1; the Re effective range provides the thermal performance index of about or above one. The thermal performance index increases with the Reynolds number in $Re = 400$ to $Re = 4\,000$ and then decreases to a minimum as the Reynolds number increases further to $Re = 11\,000$. The thermal performance index increases by 43% for mesh 4.1 and 72% for mesh 5.1 over the Reynolds number range from 400 to 4 000; and decrease by 106% for mesh 4.1 and 125% for mesh 5.1 from a Reynolds number of 4 000 to 11 000.

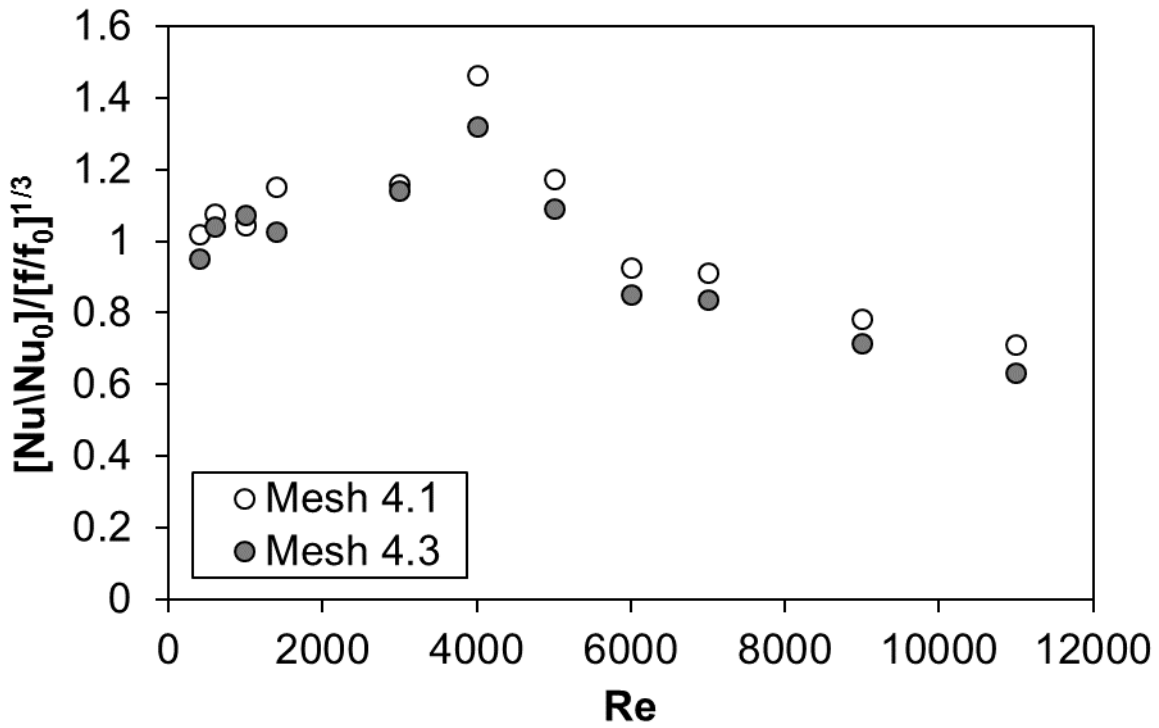
[Figure 4.37 \(a\)](#) also shows that a decrease in the period of the screen insert for the 68% porosity mesh causes a decrease in the thermal performance index at the corresponding Reynolds number. Mesh 5.1 thermal performance index is 30% lower for $400 \leq Re \leq 600$ and approximately 13% lower for Reynolds number $> 1\,000$ than those for mesh 4.1.



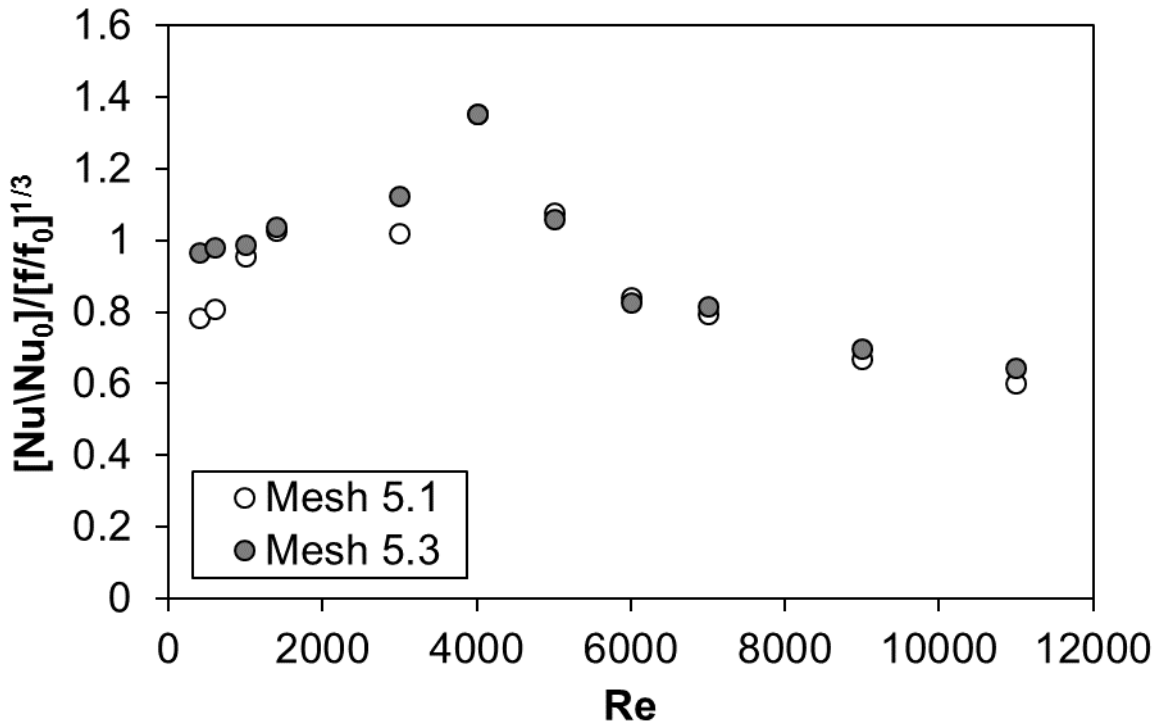
(a)



(b)



(c)



(d)

Figure 4.37: Thermal performance index for one heated wall in 5 mm channel height as Reynolds number varies comparing: (a) Mesh 4.1 and Mesh 5.1 (68% porosity- 18 mm and 12 mm period, respectively), (b) Mesh 4.3 and Mesh 5.3 (48% porosity- 18 mm and 12 mm period, respectively), (c) Mesh 4.1 and Mesh 4.3 (18 mm period- 68% and 48% porosity, respectively), and (d) Mesh 5.1 and Mesh 5.3 (12 mm period- 68% and 48% porosity, respectively).

For the case of the 48% porosity screen inserts, [Figure 4.37 \(b\)](#) shows that the effective range of Reynolds number is between 600 and 6 000 for mesh 4.3 and between 1 400 and 6 000 for mesh 5.3; the effective range of Re here also provides the thermal performance index of one and higher. The thermal performance index increases with the Reynolds number from $Re = 400$ to 4 000 and then decreases as the Re increases further to $Re = 11\ 000$. The thermal performance index increases by 39% for mesh 4.3 and 40% for mesh 5.3 over the Reynolds number range from 400 to 4 000; and decrease by 109% for mesh 4.3 and 110% for mesh 5.3 from the Reynolds number of 4 000 to 11 000.

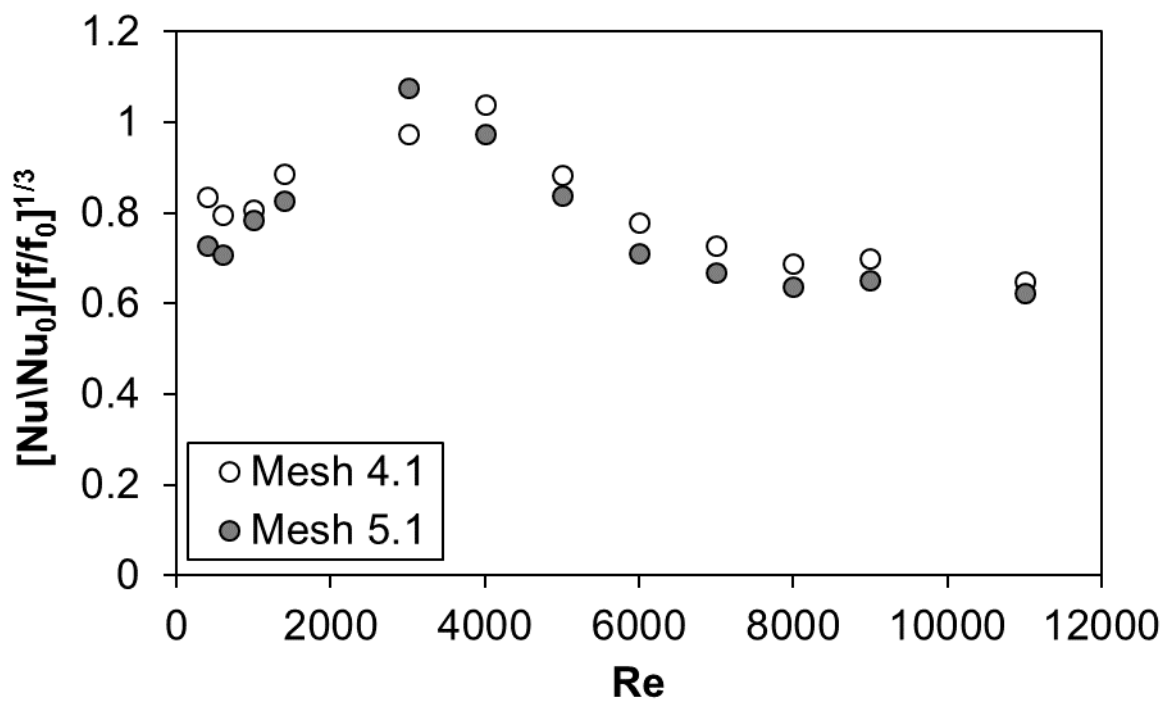
[Figure 4.37 \(b\)](#) also shows that a decrease in the period of the screen insert for the 48% porosity mesh does not affect the distribution of the thermal performance index as the Reynolds number changes. Mesh 5.3 thermal performance index is only 8% lower for $Re < 1\ 400$ and less than 4% lower for all other $Re > 1\ 400$ than those for mesh 4.3.

For the case of the 18 mm period screen comparing the porosity effects, [Figure 4.37 \(c\)](#) shows that a decrease in the porosity of the screen mesh causes a slight decrease in the value of the thermal performance at the corresponding Reynolds number. Mesh 4.3 thermal performance index is 4% lower for Reynolds number $< 4\ 000$ in the laminar region and 10% lower for Reynolds number $> 4\ 000$ than mesh 4.1 thermal performance index.

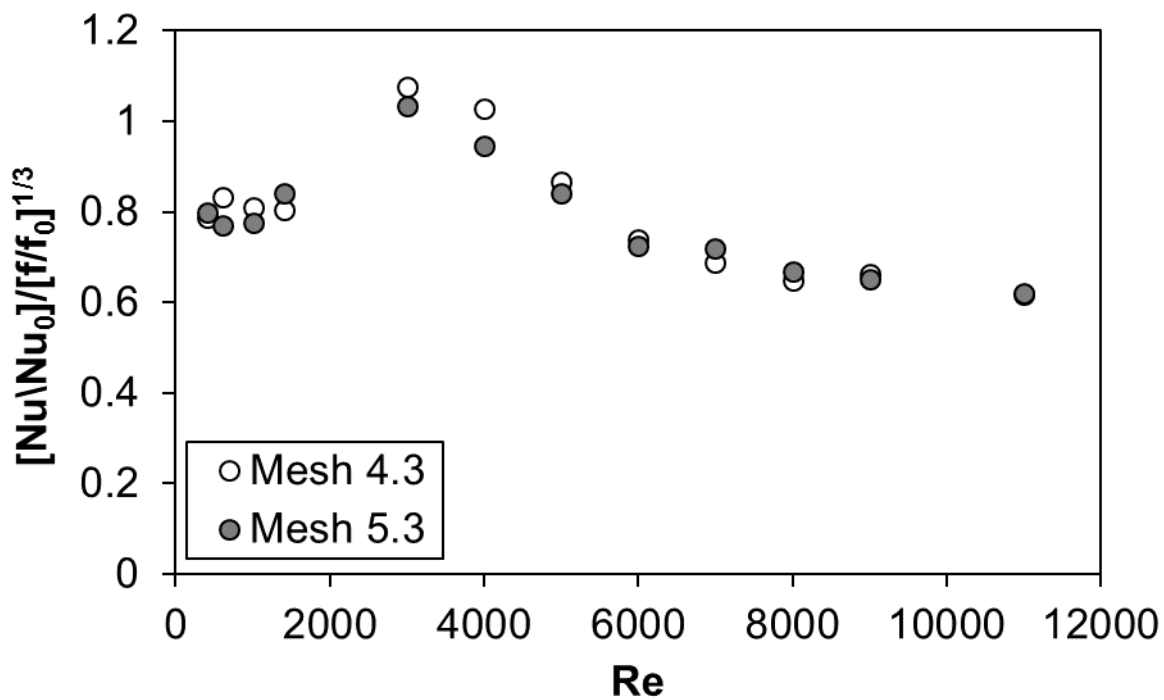
For the case of the 12 mm period screen comparing the porosity effects, [Figure 4.37 \(d\)](#) shows that A decrease in porosity of the screen mesh has only significant effects on the thermal performance for Reynolds numbers smaller than 1 400. Mesh 5.3 thermal performance index is 17% lower for Reynolds number $< 1\ 400$, and less than 6% lower for Reynold number $> 1\ 400$ than mesh 5.1 thermal performance.

[Figure 4.38](#) shows the thermal performance index of the various screen inserts at a channel height of 5 mm with the two-heated walls boundary condition. [Figure 4.38 \(a\)](#) and [\(b\)](#) compare the screen inserts with varying periods and [Figure 4.38 \(c\)](#) and [\(d\)](#) compare the screen inserts with varying porosity. [Figure 4.38 \(a\)](#) compares the thermal performance index of the two 68% porosity screen inserts, [Figure 4.38 \(b\)](#) compares the thermal performance index of the two 48% porosity screen inserts, [Figure 4.38 \(c\)](#) compares the thermal performance index of the two 18 mm period screen inserts, and [Figure 4.38 \(d\)](#) compares the thermal performance index of the two 12 mm period screen inserts.

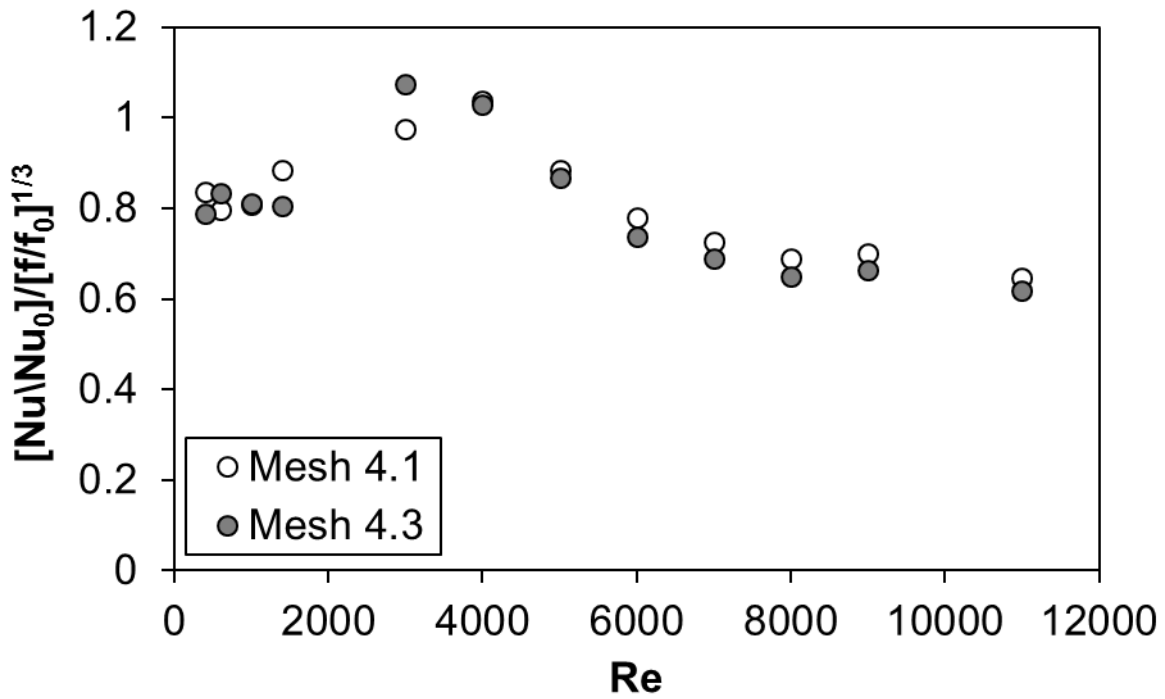
For the 68% porosity screen inserts, [Figure 4.38 \(a\)](#) shows that the Reynolds numbers between 3 000 and 4 000 provide the thermal performance of 1 or higher for both screens. The thermal performance index increases from $Re = 400$ to a maximum at $Re = 4\ 000$ for the mesh 4.1 and at $Re = 3\ 000$ for mesh 5.1. The thermal performance then decreases to a minimum in Fig. 4.37(a) as the Re increases to 11 000. The thermal performance index increases by 24% for mesh 4.1 and 48% for mesh 5.1 over the Reynolds number range from 400 to 4 000; and decrease by 38% for mesh 4.1 and 36% for mesh 5.1 for the Reynolds numbers from 4 000 to 11 000.



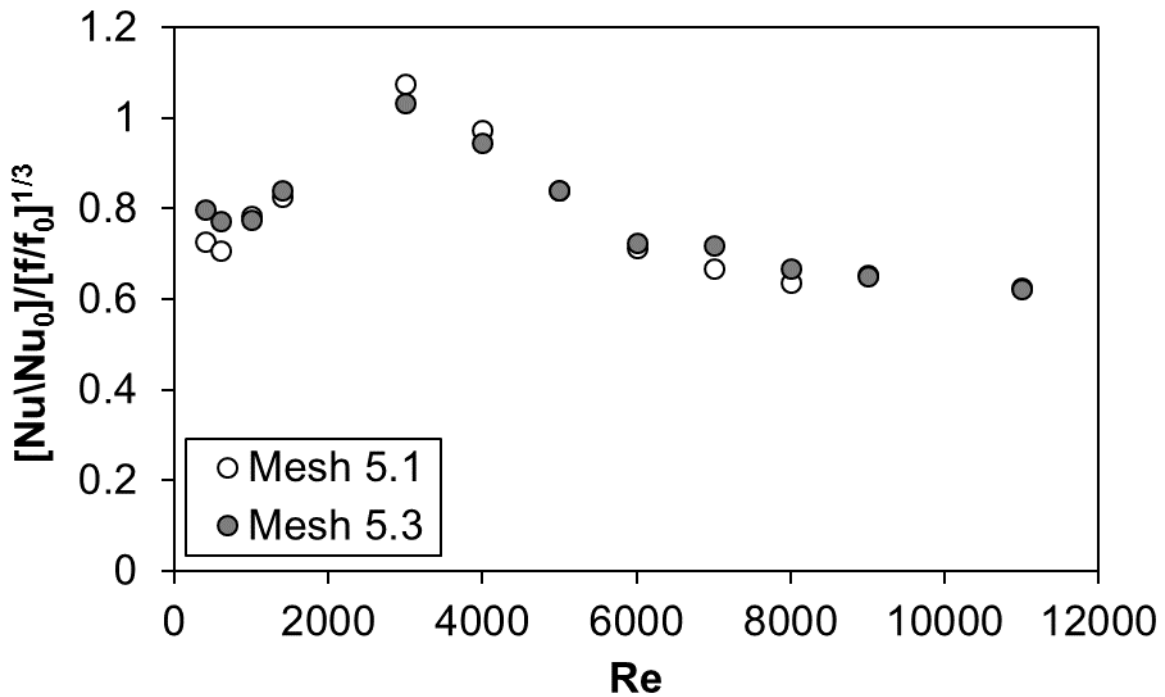
(a)



(b)

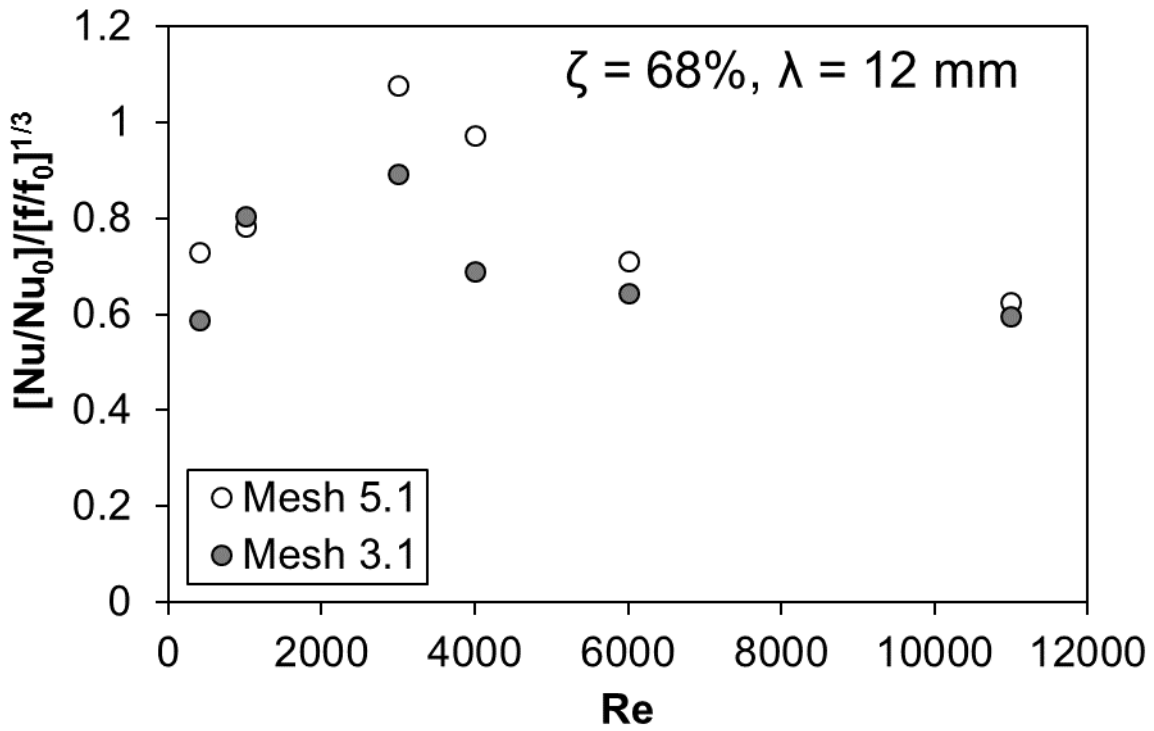


(c)

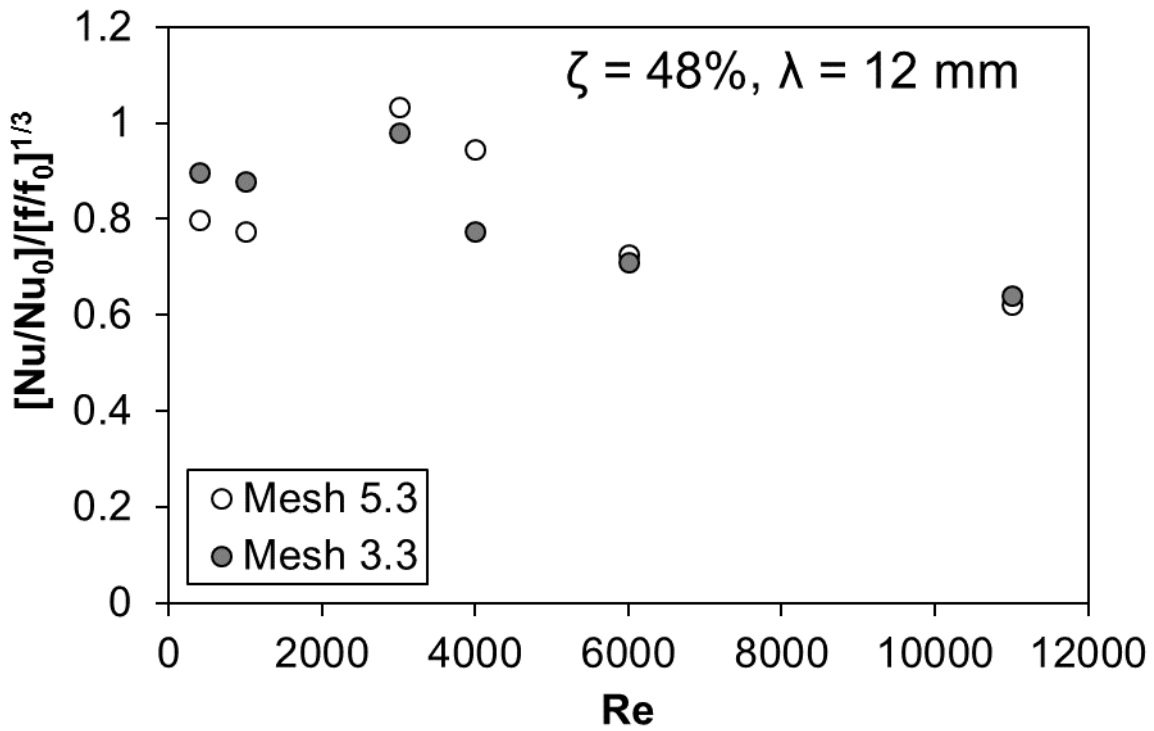


(d)

Figure 4.38: Thermal performance index for two heated walls in 5mm channel height as Reynolds number varies comparing: (a) Mesh 4.1 and Mesh 5.1 (68% porosity- 18 mm and 12 mm period, respectively), (b) Mesh 4.3 and Mesh 5.3 (48% porosity- 18 mm and 12 mm period, respectively), (c) Mesh 4.1 and Mesh 4.3 (18 mm period- 68% and 48% porosity, respectively), and (d) Mesh 5.1 and Mesh 5.3 (12 mm period- 68% and 48% porosity, respectively).



(a)



(b)

Figure 4.39: Thermal efficiencies for two heated walls as Reynolds number and channel height vary comparing: (a) Mesh 5.1 and Mesh 3.1 (68% porosity- 12 mm period- 5 mm and 14 mm channel height, respectively), and (b) Mesh 3.3 and Mesh 5.3 (48% porosity- 12 mm period- 5 mm and 14 mm channel height, respectively)

Figure 4.38 (a) shows that a decrease in the period of the 68% porosity mesh causes the thermal performance to decrease at the corresponding Reynolds number. Mesh 5.1 thermal performance is 13% lower in the early laminar region ($400 \leq Re \leq 600$) and approximately 8% lower for Reynolds number $> 1\,000$ than mesh 4.1 thermal performance.

For the case of the 48% porosity comparing the effects of screen period, Figure 4.38 (b) shows that the thermal performance is 1 or higher in $3000 \leq Re \leq 4000$ for mesh 4.3 and at $Re = 3\,000$ for mesh 5.3. The thermal performance increases from $Re = 400$ to a maximum $Re = 3\,000$ for the screens. As the Re increases further i.e. $Re > 3000$ in Fig. 4.37(b) the performance decreases to a minimum at $Re = 11\,000$. The thermal performance increases by 37% for mesh 4.3 and 30% for mesh 5.3 over $Re = 400$ to $3\,000$; the performance decreases by 40% for mesh 4.3 and 34% for mesh 5.3 $Re = 3\,000$ to $11\,000$.

Figure 4.38 (b) also shows that a decrease in the period of the screen for the 48% porosity mesh causes a decrease in the thermal performance in the early laminar region ($Re < 1\,000$). At $Re > 1000$, the change in the period of the screen affects the value of the thermal performance little. Mesh 5.3 thermal performance is 6% lower for $Re < 1\,400$ and less than 4% lower for all other Reynolds numbers than mesh 4.3 thermal performance.

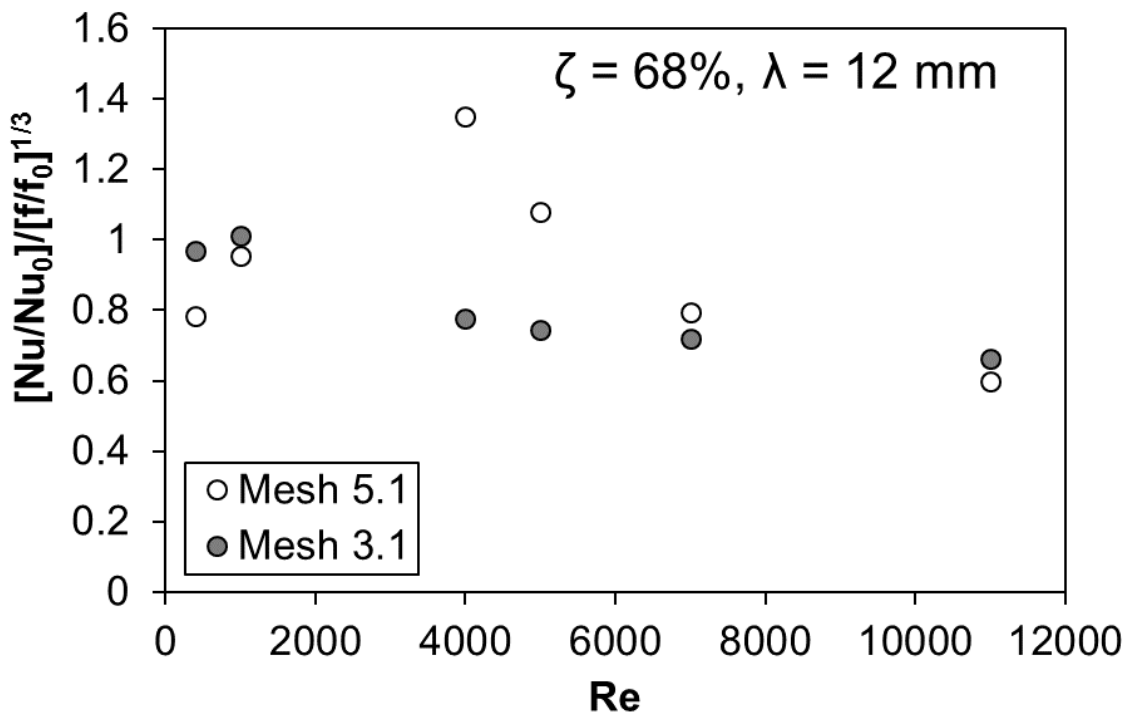
For the 18 mm period screen comparing the effects of mesh porosity, Figure 4.38 (c) shows that a decrease in the porosity has no significant effect on the value of the thermal performance for the corresponding Reynolds numbers. Mesh 4.3 thermal performance is less than 5% lower than mesh 4.1 for most of the Reynolds numbers, except at $Re = 3\,000$ when it is 9% higher for mesh 4.3 than that for mesh 4.1.

For the 12 mm period screen, Figure 4.38 (d) also shows that has no significant effect on the value of the thermal performance at $Re > 1000$. Mesh 5.3 thermal performance is 8% lower $Re < 1\,000$, and less than 4% lower for $Re > 1\,400$ than mesh 5.1 thermal performance.

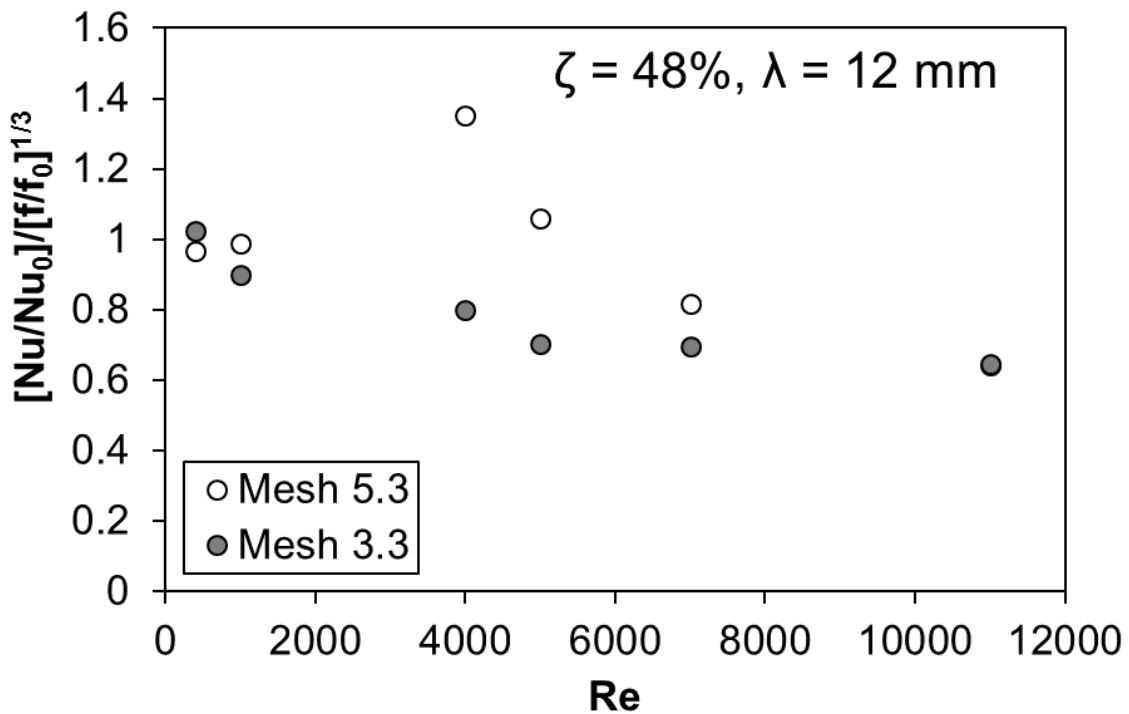
Figure 4.39 shows the thermal performance of the various screen inserts as the channel height varies between 5 mm and 14 mm for a two-heated walls boundary condition. Figure 4.39 (a) compares the thermal performance of the two 68% porosity screen inserts with a 12 mm period, and Figure 4.39 (b) compares the thermal performance index of the two 48% porosity screen inserts with a 12 mm period.

Figure 4.39 (a) shows that the thermal performance is 1 or higher for Re between $3\,000$ and $4\,000$ for mesh 5.1 and $Re = 3\,000$ for mesh 3.1. Figure 4.39 (a) shows that a decrease in the channel height for the 68% porosity and 12 mm period screen causes also decreases the value of the thermal performance at the corresponding Reynolds number. Mesh 5.1 thermal performance is 10% higher in the early laminar region ($400 \leq Re < 1\,000$) and approximately 3% lower for $Re = 1\,000$ compared to the mesh 3.1 thermal performance. At $Re > 3\,000$, thermal performance for mesh 5.1 is 15% higher than for mesh 3.1. At the higher channel height of 14 mm in Figure 4.39 (a), thermal performance

for the mesh 3.1 is usually lower as the Nusselt number ratio (Nu/Nu_0) is lower at a given Re .



(a)



(b)

Figure 4.40: Thermal efficiencies for one heated wall as Reynolds number and channel height vary comparing: (a) Mesh 5.1 and Mesh 3.1 (68% porosity- 12 mm period- 5 mm and 14 mm channel height, respectively), and (b) Mesh 3.3 and Mesh 5.3 (48% porosity- 12 mm period- 5 mm and 14 mm channel height, respectively)

For the 48% porosity screens, [Figure 4.39 \(b\)](#) shows that thermal performance is about 1 only at $Re = 3\ 000$ for mesh 5.3 when $H = 5\text{ mm}$ and for mesh 3.3 when $H = 14\text{ mm}$. Except for the early laminar region $Re < 1\ 000$ and at $Re = 4000$ the change in the channel height affects the value of the thermal performance insignificantly for the corresponding Reynolds numbers. Mesh 5.3 thermal performance is 13% lower for $Re < 3000$ and 22% higher at $Re = 4000$ than mesh 3.3 thermal performance.

[Figure 4.40](#) shows the thermal performance of the various screen inserts as the channel height changes from 5 mm to 14 mm for the one-heated wall boundary condition. [Figure 4.40 \(a\)](#) compares the thermal performance of the two 68% porosity screen inserts with the 12 mm period, and [Figure 4.40 \(b\)](#) compares the thermal performance of the two 48% porosity screen inserts with the 12 mm period.

For the 68% porosity screens with 12 mm period, [Figure 4.40 \(a\)](#) shows that the thermal performance is 1 or higher for $1\ 000 \leq Re \leq 5\ 000$ for mesh 5.1 and for $Re \leq 1000$ for mesh 3.1. [Figure 4.40 \(a\)](#) also shows that a decrease in the channel height from 14 mm to 5 mm increases the value of the thermal performance for most of the Reynolds numbers as the Nu/Nu_0 ratio increases. Mesh 5.1 thermal performance is 35% higher in $3\ 000 \leq Re \leq 4\ 000$ than mesh 3.1 thermal performance. The differences in thermal performance between the two meshes at $Re = 400$ and 11000 in [Figure 4.40 \(a\)](#) are caused by the lower Nu/Nu_0 ratios of mesh 3.1 as the channel height increases. The Nu/Nu_0 ratio of mesh 5.1 at $Re = 6000$ is much higher than that of mesh 3.1.

For the 48% porosity screens with 12 mm period, [Figure 4.40 \(b\)](#) shows the distribution patterns almost like those in [Figure 4.40 \(a\)](#) as the channel height decreases from 14 mm to 5 mm.

4.7 SUMMARY

The purpose of this chapter is to investigate the influences the following geometric properties had on the thermal performance index of a sinusoidal porous screen insert: (i) porosity, (ii) period, and (iii) channel height. The chapter also investigated the irregularities of the period of the screen insert to influence the friction factor (f), Nusselt number (Nu), and thermal performance. The experiments included all three flow regimes: laminar, transition and turbulent. The data are presented for a wide range of Reynolds numbers. The solar panels, solar heat exchangers, and flat plate heat exchangers typically operate in the laminar and transition regimes of the Reynolds number. The thermal performance indexes in many cases of the screen channel are estimated between 0.9 and 1.4 which are encouraging for the smaller Reynolds number applications. The data in the turbulent Reynolds number are applicable in the electronic and machine component cooling. The thermal performance indexes are between 0.6 and 0.8 for the screen channels. However, for many of the high Reynolds number applications, the enhancement of heat transfer are more important irrespective of the increase in the pumping power. The baseline measurements (f_0 , Nu_0) are obtained for comparisons. The pressure drop experiments are

presented to estimate the friction factor (f) and required increase in the pumping power (f/f_0 ratio). The heat transfer experiments are presented to estimate the Nusselt number (Nu) and increased convective heat transfer (Nu/Nu_0 ratio). The thermal performance index, $[(Nu/Nu_0)/(f/f_0)^{1/3}]$ is then presented to indicate the increased convective heat transfer as the required pumping power is increased for different Reynolds numbers. There is no change in physical geometry of the porous screen insert after the heat transfer and pressure drop experiments. Both the pressure drop and heat transfer baseline (smooth channel) data correlated well with existing correlations, except for the transient flow conditions where no correlations exist.

Table 4.17 summarises the effects each geometrical property has on the performance index.

Table 4.17: Summary of the influence of geometrical properties of the sinusoidal screen insert on the thermal performance index as Reynolds number is constant

		Effects on thermal performance when geometrical property is decreased		
Channel Height	Heating condition	Period change effects	Porosity change effects	Channel Height change effects
14 mm	One-Wall	Decrease	Decrease	Increase
	Two-Wall	Decrease	Decrease	Increase
5 mm	One-Wall	Decrease	Increase	N/A
	Two-Wall	Decrease	No change	N/A

Table 4.18 shows a summarized version of the change in friction factor and Nusselt number when an irregular screen insert (period alternating between 12 mm and 22 mm) is employed. The table indicates the sensitivity of the data as the manufacturing inaccuracies can cause irregular wave patterns.

Table 4.18: Summary of the percentage change of friction factor and Nusselt number for the irregular screen (change in period of 55%) as Reynolds number is constant

		Percentage change		
Screen Insert		Laminar	Transition	Turbulent
Mesh 1.1	Friction factor	25%	14%	17%
	Nu – One-Wall	10%	2%	4%
	Nu – Two-Wall	22%	6%	3%
Mesh 1.3	Friction factor	20%	26%	12%
	Nu – One-Wall	2%	4%	5%
	Nu – Two-Wall	7%	5%	4%
Mesh 3.1	Friction factor	115%	79%	76%
	Nu – One-Wall	23%	1%	12%
	Nu – Two-Wall	35%	17%	12%
Mesh 3.3	Friction factor	111%	90%	74%
	Nu – One-Wall	15%	5%	2%
	Nu – Two-Wall	29%	11%	10%

5 CONCLUSION AND RECOMMENDATIONS

5.1 SUMMARY

To gain a better understanding of how the geometrical properties of a sinusoidal porous screen insert effect the thermal performance index of the channels in the flat-plate heat exchangers, experiments are conducted to obtain the pressure drop and heat transfer data for various screen inserts with varying geometrical properties. The geometrical properties of the sinusoidal porous screen insert investigated in this study are; (i) porosity, (ii) period, and (iii) amplitude. Measurements are obtained in a low speed atmospheric wind tunnel having rectangular flow cross-section. The tunnel height is adjustable to the desired flow cross-section. The long developing section of the tunnel provides a fully developed flow as it enters the test channel. The measurements in the test channel are obtained with and without (smooth channel case) the screen. The smooth channel data referred to as the baseline data (f_0 , Nu_0) are used to qualify the channel flow and measurement techniques as well as for comparisons with the data for the screen insert. The heat transfer data are measured with constant wall heat flux boundary conditions for all the cases. The heat flux level varies between the cases to provide a temperature difference of about 10 °C between the wall and mean flow temperature. The measured pressure drop data are presented as the Darcy friction factor (f and f_0) and screen insert to baseline friction factor ratio f/f_0 . The measured heat transfer data are presented as the Nusselt number (Nu and Nu_0) and screen insert to baseline Nusselt number ratio Nu/Nu_0 . The ratio f/f_0 then indicates the increase in the pumping power requirements in the channel when the screen insert is employed for a given Reynolds number or mass flow rate. Similarly, the ratio Nu/Nu_0 then indicates the increase in the heat transfer in the channel when the screen insert is employed for a given Reynolds number and heat duty or wall to mean-flow temperature difference. The performance index is then estimated as $(Nu/Nu_0)/(f/f_0)^{1/3}$.

The pressure drop, friction factors, and heat transfer coefficients are measured in the same test channel as the baseline when the wavy porous screens are employed as inserts. The sinusoidal wave of the screen is formed in-house from the porous metal mesh-screen available commercially. The pores are square in shape. The wire diameter of the mesh is 0.28 mm. Two porosities of the mesh are tested: porosity of 68% (square pore aperture of 1.308 mm and approximately 6 pores per cm) and porosity of 48% (square pore aperture of 0.567 mm and approximately 12 pores per cm). In total, ten wavy screens of different porosities and wave periods are tested:

1. Mesh 1.1 – 22 mm period, 68% porosity and 14 mm height,
2. Mesh 2.1 – Irregular period (varying between 12 mm and 22 mm), 68% porosity and 14 mm height,
3. Mesh 3.1 – 12 mm period, 68% porosity and 14 mm height,
4. Mesh 1.3 – 22 mm period, 48% porosity and 14 mm height,

5. Mesh 2.3 – Irregular period (varying between 12 mm and 22 mm), 48% porosity and 14 mm height,
6. Mesh 3.3 – 12 mm period, 48% porosity and 14 mm height,
7. Mesh 4.1 – 18 mm period, 68% porosity and 5 mm height,
8. Mesh 5.1 – 12 mm period, 68% porosity and 5 mm height,
9. Mesh 4.3 – 18 mm period, 48% porosity and 5 mm height,
10. Mesh 5.3 – 12 mm period, 48% porosity and 5 mm height.

The peaks of the screen wave make only line contacts with the channel walls as the wave vectors are placed parallel to the channel mean flow. The pore-axis lies perpendicular to the mean flow. The wave-peaks are not soldered to the channel walls and as such, a screen insert can be easily removed to be replaced by another screen insert in the same test channel. The screen inserts thus do not act as fins for the heated walls during the heat transfer measurements. The inlet Reynolds number, Re based on the channel mass flow for the experiments varies from 400 to 11 000 for the 5 mm channel height experiments and from 400 to 30 000 for the 14 mm channel height experiments. The Re thus covers all the three flow regimes of laminar, transition and turbulent flows. For the heat transfer experiments, the parallel walls of the channel touching the screen peaks are heated to simulate the channel of a flat plate heat exchanger. The measurements with one heated wall simulate the conditions of heat exchanger channels for the solar panels and electronic cooling. The main conclusions from the results are indicated in the following section.

5.2 CONCLUSION

The effects of porosity, period and amplitude of the sinusoidal screen inserts on f/f_0 and Nu/Nu_0 can be summarized as follows:

1. For the laminar regime ($Re = 400$ to $2\,000$) the theoretical friction factor, f_0 for the baseline smooth channel is calculated using the correlation in Eq. (2.14) as specified in Shah and London [37], for the rectangular ducts. The experimental data differ within approximately $\pm 5\%$ from the correlation given by Shah and London [37]. In the turbulent regime ($Re > 7\,000$), the theoretical friction factor for the baseline is found using the correlation in Eq. (2.27) as developed by Nikuradse [40]. The experimental data fall with $\pm 2\%$ of the correlation found for the turbulent flow. For the laminar regime ($400 Re - 2\,000 Re$), the fully developed theoretical Nusselt number, Nu_0 is 7.55 for a rectangular smooth duct of aspect ratio 0.069 and a two-wall constant heat flux boundary condition in Shah and London [37]. For a parallel plate configuration with the wall separation of 5 mm and a two-wall constant heat flux boundary condition the fully developed theoretical Nusselt number is 8.235 in the laminar regime by Shah and London [37]. The experimental data for the baseline fall within $\pm 7\%$ of the value determined by Shah and London [37]. In the turbulent regime ($Re > 10\,000$), the theoretical Nusselt number, Nu_0 for the baseline channel is calculated using the correlation determined by Dittus and Boelter [33]. For the laminar regime ($400 Re - 2\,000 Re$), the fully developed theoretical Nusselt

- number for a rectangular duct of aspect ratio 0.069 and a one-wall constant heat flux boundary condition is 5.23 in Shah and London [37]. A one-wall constant heat flux boundary condition in the laminar regime provides the fully developed theoretical Nusselt number, Nu_0 as 5.385 for the baseline parallel channel in [37]. The experimental baseline Nu_0 data in the laminar regime for the 14 mm channel height and one wall heating differ significantly from the theoretical values of [37]. The large discrepancies between the experiments and theoretical data at $Re \leq 1\,000$ indicate the flow is still thermally developing along the entire length of the test channel. However, the experimental baseline data for the 5 mm channel height with one-wall heating differ by only $\pm 5\%$ from the theoretical data in the laminar $Re \leq 1\,400$. In the turbulent regime ($Re > 9\,000$), the theoretical Nusselt number, Nu_0 for baseline is calculated from the Dittus and Boelter correlation [33]. The difference is primarily due the circumferential heating of the duct in the Dittus-Boelter correlation.
2. At low Reynolds numbers $400 \leq Re \leq 1\,000$ the test setup has the highest precision uncertainty. This is due to the small differential pressure across the orifice plate and in the wall pressure measurements. For Reynolds numbers greater than 600 the normalised pressure drop uncertainty is less than 10%. Like with the normalised pressure drop the friction factor uncertainty is the highest in the laminar region. Except for at Reynolds number 400 the friction factor uncertainty is less than 5%. As the Reynolds number increases the difference between the measured wall temperature and the mixed mean air temperature increases. Thus, reducing the precision uncertainty in the determined Nu_x . For both one-wall heating and two-wall heating the Nusselt number uncertainty was less than 6%.
 3. The friction factor, f in the screen channel depends strongly on the Reynolds number, Re and wave period of the screen and decreases as Re or wave period increases at a given screen porosity. The screen porosity affects f strongly at the higher wave period (22 mm period for 14 mm channel height and 18 mm period for 5 mm channel height) when $Re \geq 2\,700$. When the porosity is changed from 68% to 48% for any period, the f in the screen channel increases for all Re .
 4. The ratio of screen to smooth channel friction factor, f/f_0 increases with the $Re \leq 2\,700$. The f/f_0 ratios are always higher for the screens with the 12 mm wave period than the other screens with the 18 mm period (5 mm channel height) or 22 mm period (14 mm channel height). The screen with the 48% porosity also provides higher f/f_0 than the 68% porosity at all the Reynolds numbers and periods.
 5. To compare the effects of the wave period, the f/f_0 are always smaller for the 18 mm (5 mm channel height) and 22 mm (14 mm channel height) period screen inserts than for the 12 mm (both 5 mm and 14 mm channel height) period screen inserts irrespective of the screen porosity. For two wall heating the effects of the wave period on the Nu/Nu_0 ratio are always smaller for the 18 mm (5 mm channel height) and 22 mm (14 mm channel height) period screen inserts than for the 12 mm (both 5 mm and 14 mm channel height) period screen inserts irrespective of the screen porosity. For one wall heating the 18 mm (5 mm channel height) and 22 mm (14 mm channel height) screen inserts, the 48% porosity screen insert has a 5% lower

Nu/Nu_0 ratio for the Reynolds numbers between 400 and 600, a 10% higher Nu/Nu_0 ratio for Reynolds numbers greater than 600 up to 6 000, and a 5% higher Nu/Nu_0 ratio for Reynolds numbers greater than 6 000, all compared to the 68% porosity screen insert. The changes in period of the screen inserts make no significant differences in the average Nu/Nu_0 ratios for the one-wall heating boundary condition.

6. For the 12 mm (both 5 mm and 14 mm channel height) period screen inserts, the f/f_0 values change little between the 48% and 68% porosity screens at all Re . For the 18 mm (5 mm channel height) and 22 mm (14 mm channel height) period screen inserts, the f/f_0 are generally smaller for the 68% porosity compared to the 48% porosity screen at all Re . The effects of porosity in two wall heating are more visible for the 18 mm (5 mm channel height) and 22 mm (14 mm channel height) screen inserts where a 48% porosity means a higher Nusselt number than a 68% porosity screen insert for the same Reynolds number; however, the effect of porosity is not as visible for the 12 mm period screen inserts (both 5 mm and 14 mm channel height).
7. For two heated walls or one heated wall, the fully-developed average Nusselt numbers, Nu_{avg} and ratio of screen to smooth channel Nusselt numbers, Nu/Nu_0 are generally slightly higher for the screens with the 12 mm wave period than the screens with the larger 18 mm wave period (5 mm channel height) or 22 mm wave period (14 mm channel height) at all the Re . The screen porosity influences the average Nu_{avg} and Nu/Nu_0 marginally. The effects of Reynolds number indicate while the Nu_{avg} values increase with the $Re \leq 30\,000$ for all screens, the average Nu/Nu_0 increases with Re only in the range of $Re \leq 2\,700$ for two heated walls and $Re \leq 4\,000$ for one heated wall, beyond which the Nu/Nu_0 ratio decreases as the Re increases for all the cases. Also, the Nu_{avg} values are more sensitive to the Re change at $Re < 2\,000$ for all the cases. In general, the f , f/f_0 , Nu , Nu/Nu_0 values are more sensitive to the change in the wave period than the porosity for the present screens. For all screens, the Nu/Nu_0 ratios vary between 1.0 and 3.0 as the Re changes for two and one heated wall. Simple correlations are developed to predict the experimental friction factors and Nusselt numbers in the screen channel for low range of $Re \leq 1\,400$ and high range of $Re \geq 2\,700$ within an accuracy of $\pm 10\%$.
8. The thermal performance index, $(Nu/Nu_0)/(f/f_0)^{1/3}$ relates to the design objectives of reducing the heat transfer area or pumping power and enhancing the heat transfer rate in the screen channel relative to the smooth channel. The performance index with the screen insert is sensitive to the Reynolds number for all screens and increases with the $Re \leq 4\,000$ and decreases as the Re increases in the range of $5\,000 \leq Re \leq 30\,000$. The maximum of $(Nu/Nu_0)/(f/f_0)^{1/3}$ is achieved when $3\,000 \leq Re \leq 4\,000$ for the two and one heated walls for all four screens and a channel height of 5 mm. The maximum of $(Nu/Nu_0)/(f/f_0)^{1/3}$ is achieved when $400 \leq Re \leq 1\,000$ for the one heated wall and when $400 \leq Re \leq 3\,000$ for the two heated wall for a channel height of 14 mm. The influences of the wave period and porosity on the $(Nu/Nu_0)/(f/f_0)^{1/3}$ seem to be insignificant for the present screens.

The sinusoidal screen inserts in the channels of a flat-plate heat exchanger can provide desirable effects on the heat transfer enhancements only for an operating range of the Reynolds number between 400 and 3 000. The wire diameter of the mesh screen can significantly influence the thermal performance and pressure penalty provided by the wavy screen based on the present investigations and Mahmood et al. [18]. The present results are thus beneficial to the design of porous inserts and flat-plate heat exchangers.

5.3 RECOMMENDATIONS

The following work is recommended:

- an experimental setup where two continuous heaters are used for two wall heating (one on each side of the test section) and one continuous heater is used for one wall heating,
- purchasing mesh material with different pore geometries to identify the effects of pore geometry on the thermal performance index of the screen insert,
- purchasing mesh material with varying porosities (higher than 68%) to identify the effects of higher porosities on the thermal performance index of the screen insert,
- testing more periods by increasing and decreasing the maximum and minimum periods of the screen inserts,
- testing more amplitudes or channels heights to determine the effects amplitude on the thermal performance index,
- the porous screen inserts showed a very low yield - $(Nu/Nu_0)/(f/f_0)^{1/3}$ values greater than 1 – for a small band of Reynolds numbers. Other forms of porous inserts arrangements like baffle type porous inserts arranged in a staggered manner could be investigated for better thermo-hydraulic performance.

Comprehensive study is needed to determine the effects of pore geometry, porosity, wire diameter, wave height, and wave period of the mesh screen on heat transfer and pressure drop in the channel so that correlations can be created to aid the design process of screen inserts for flat-plate heat exchangers.

References

- [1] Webb, R. L., and Kim, N-H, 2005, Principles of Enhanced Heat Transfer, second ed., Taylor and Francis, New York, USA, pp.57-60, 210-227, 246-269.
- [2] Chen, C-C., Huang, P-C., and Hwang, H-Y., 2013, "Enhanced forced convective cooling of heat sources by metal-foam porous layers,". International Journal of Heat and Mass Transfer, 58, pp. 356- 373.
- [3] Alhusseny, A., Turan, A., and Nasser, A., 2015, "Developing convective flow in a square channel partially filled with a high porosity metal foam and rotating in a parallel-mode," International Journal of Heat and Mass Transfer, 90, pp. 578-590.
- [4] Lu, W., Zhang, T., and Yang, M., 2016, "Analytical solution of forced convective heat transfer in parallel-plate channel partially filled with metallic foams," International Journal of Heat and Mass Transfer, 100, pp. 718-727.
- [5] Park, S-H., Kim, T. H., and Jeong, J. H., 2016, "Experimental investigation of the convective heat transfer coefficient for open-cell porous metal fins at low Reynolds numbers," International Journal of Heat and Mass Transfer, 100, pp. 608-614.
- [6] Wang, B., Hong, Y., Hou, X., Xu, Z., Wang, P., Fang, X., and Ruan, X., 2015, "Numerical configuration design and investigation of heat transfer enhancement in pipes filled with gradient porous materials," Energy Conversion and Management, pp. 206-215.
- [7] Kim, S.Y., Paek, J. W., and Kang, B. H., 2000, "Flow and heat transfer correlations for porous fin in a plate-fin heat exchanger," ASME J Heat Trans., 122, pp. 572-578.
- [8] Mohammadian, S. K., and Zhang, Y., 2016, "Temperature uniformity improvement of an aircooled high-power Lithium-ion battery using metal and non-metal foams," ASME J Heat Trans., 138, pp. 1145021-1145024.
- [9] Mohammadian, S. K., Rassoulinejad-Mousavi, S. M., and Zhang, Y., 2015, "Thermal management improvement of an air-cooled high-power Lithium-ion battery by embedding metal foam," Journal of Power Sources, 296, pp. 305-313.
- [10] Maerefat, M., Mahmoudi, S. Y., and Mazaheri, K, 2011, "Numerical simulation of forced convection enhancement in a pipe by porous inserts," Heat Transfer Engineering, 32(1), pp. 45-56.
- [11] Hobold, G. M., and da Silva, A. K., 2017, "Two-dimensional porosity optimization of saturated porous media for maximal thermal performance under forced convection," International Journal of Heat and Mass Transfer, 108, pp. 1689-1701.
- [12] Hamdan, M., and Al-Nimr, M. A., 2010, "The use of porous fins for heat transfer augmentation in parallel-plate channels," Transport in Porous Media, 84(2), pp. 409-420.

- [13] Davari, A., and Maerefat, M., 2016, "Numerical analysis of fluid flow and heat transfer in entrance and fully developed regions of a channel with porous baffles," *ASME J Heat Trans.*, 138, pp. 0626011-06260110.
- [14] Santos, N. B., and de Lemos, M. J. S., 2006, "Flow and heat transfer in a parallel-plate channel with porous and solid baffles," *Numerical Heat Transfer, Part A*, 49, pp. 471-494.
- [15] Pavel B. I., and Mohamad A. A., 2004, "Experimental investigation of the potential of metallic porous inserts in enhancing forced convective heat transfer," *ASME J Heat Trans.*, 126, pp. 540-545.
- [16] Pavel B. I., and Mohamad A. A., 2004, "An experimental and numerical study on heat transfer enhancement for gas heat exchangers fitted with porous media," *International Journal of Heat and Mass Transfer*, 47, pp. 4939-4952.
- [17] Kays, W. M., and London, A. L., 1964, *Compact Heat Exchangers*, second ed., McGraw-Hill, USA, pp. 155, 219.
- [18] Mahmood, G. I., Simonson, C. J., and Besant, R. W., 2015, "Experimental pressure drop and heat transfer in a rectangular channel with a sinusoidal porous screen," *ASME J Heat Trans.*, 137(4), pp. 0426011-04260111.
- [19] Torii, S., and Yang, W-J., 2007, "Thermal-fluid flow transport phenomenon over slot-perforated flat plates placed in narrow channel," *Journal of Thermophysics and Heat Transfer*, 21(2), pp. 346- 351.
- [20] International Standard, ISO 5167-1980(E), *Measurement of Fluid Flow by Means of Orifice Plates, Nozzles and Venture Tubes Inserted in Circular Cross-Section Conduits Running Full*, 1980- 07-15.
- [21] Kays, W. M., and Crawford, M. E., 1993, *Convective Heat and Mass Transfer*, third ed., McGraw-Hill Inc., USA, pp. 79, 125, 249, 332.
- [22] Beckwith, T. G., Marangoni, R. D., and Lienhard, J. H., 2007, *Mechanical Measurements*, sixth ed., Pearson Prentice Hall, New Jersey, pp. 42-45, 54-59.
- [23] Moffat, R. J., 1988, "Describing the Uncertainties in Experimental Results," *Experimental Thermal and Fluid Science*, 1(1), pp. 3-17.
- [24] Gee, D. L., and Webb, R. L., 1980, "Forced Convection Heat Transfer in Helically Rib Roughened Tubes," *International Journal of Heat Mass Transfer*, 23, pp. 1127-1136.
- [25] Zimmerer, C., Gschwind, P., Gaiser, G., and Kottke, V., 2001, "Comparison of Heat and Mass Transfer in Different Heat Exchanger Geometries with Corrugated Walls," *Experimental Thermal and Fluid Science*, 26, pp. 269-273.

- [26] Huang, Z. F., Nakayama, A., Yang, K., Yang, C., and Liu, W., 2009, "Enhancing Heat Transfer in the Core Flow by Using Porous Medium Insert in a Tube," *International Journal of Heat and Mass Transfer*, 53, pp. 1164-1174.
- [27] LePoudre, P.P., Simonson, C.J. and Besant, R.W., 2011, "Channel flow with sinusoidal screen insert," In *Proceedings of the 19th Annual Conference of the CFD Society of Canada*, pp. 27-29.
- [28] Varshney, L., and Saini, J. S., 1998, "Heat Transfer and Friction Factor Correlations for Rectangular Solar Air Heater Duct Packed with Wire Mesh Screen Matrices," *Solar Energy*, 62, pp. 255-262.
- [29] Blasius, H. 1913. "Das Ähnlichkeitsgesetz bei Reibungsvorgängen in Flüssigkeiten," Springer.
- [30] Cengel, Y. A., Ghajar, A. J. & MA, H. 2011. "Heat and Mass Transfer: Fundamentals & Applications," 4e, McGraw-Hill
- [31] Chilton, T. H. & Colburn, A. P. 1934. Mass transfer (absorption) coefficients prediction from data on heat transfer and fluid friction. *Industrial & engineering chemistry*, 26, 1183-1187.
- [32] Colburn, A. P. 1964. A method of correlating forced convection heat-transfer data and a comparison with fluid friction. *International Journal of Heat and Mass Transfer*, 7, 1359-1384.
- [33] Dittus, F. & Boelter, L. 1930. University of California publications on engineering. *University of California publications in Engineering*, 2, 371.
- [34] Figliola, R. S. & Beasley, D. E. 2006. *Theory and design for mechanical measurements*, Hoboken, N.J. :, John Wiley.
- [35] Meyer, J. P. Heat transfer in tubes in the transitional flow regime. *Proceedings of the 15th International Heat Transfer Conference*, Kyoto, paper KN03, 2014. 11-15.
- [36] White, F. 2015. *Fluid Mechanics*, McGraw-Hill Education
- [37] Shah, R. & London, A. 1978. *Laminar flow forced convection in ducts: a source book for compact heat exchanger analytical data*, Supl. 1. *Adv. Heat Transfer*, 179 - 182, 305 - 308.
- [38] Reynolds, O. 1883. *An Experimental Investigation of the Circumstances which Determine Whether the Motion of Water Shall be Direct Or Sinuous: And of the Law of Resistance in Parallel Channels*, Royal Society of London.
- [39] Rohsenow, W. M. & Choi, H. Y. 1961. *Heat, Mass and Momentum Transfer*, Englewood Cliffs, New Jersey, Prentice-Hall.
- [40] Nikuradse, J. 1933. *Strömungsgestze in rauhen Rohren*.
- [41] Chen, N. H. 1979. An explicit equation for friction factor in pipe. *Industrial & Engineering Chemistry Fundamentals*, 18, 296-297.
- [42] Torr, A., 2017, *Masters Thesis*, University of Pretoria.

[43] Kline, S.J. and McClintock, F.A., 1953. Analysis of Uncertainty in Single-Sample Experiments. *Mechanical Engineering*, 75.

[44] Maranzana, G., Perry, I. and Maillet, D., 2004. Mini-and micro-channels: influence of axial conduction in the walls. *International Journal of Heat and Mass Transfer*, 47(17), pp.3993-4004.

APPENDICES

Appendix A: NUMERICAL SIMULATION

TEXSTAN is a teaching tool for solving convective transport of heat, mass, and momentum transfer problems in numerous flow geometries. It is designed to meet three major objectives:

- to assist the student or researcher in understanding the behaviour of external and internal boundary layer flows
- to enhance analysis and understanding of the flow fields that accompany surface friction and heat and mass transfer
- to solve boundary layer flows with convective boundary conditions that do not permit analytical or approximate solutions

The Texstan® software is used to run numerical simulations for the smooth channel at all Reynolds numbers under investigation. This data is used to verify the baseline or smooth channel experimental data for the assumption of parallel plates. Both the two-heated wall boundary condition and the one-heated wall boundary condition are simulated.

Table A.1 shows the flags and variables that appear in an input dataset for TEXSTAN. The section glossary on the TEXSTAN website contains definitions and explanations of terms that are often used in convective heat, mass, and momentum transfer. Definitions of the variables that appear in the output files are found in external flows: output files and internal flows: output files sections of this website.

Table A.1: TEXSTAN flags and variables

1	title						
2	kgeom	neq	kstart	mode	ktmu	ktmtr	ktme
3	kbfor	jsor(1)	jsor(2)	jsor(3)	jsor(4)	jsor(5)	
4	kfluid	kunits					
5	po	rhoc	viscoc	amolwt	gam/cp		
6	prc(1)	prc(2)	prc(3)	prc(4)	prc(5)		
7	nxbc(l)	jbc(l,1)	jbc(l,2)	jbc(l,3)	jbc(l,4)	jbc(l,5)	

8	nxbc(E)	jbc(E,1)	jbc(E,2)	jbc(E,3)	jbc(E,4)	jbc(E,5)	
9	x(m)	rw(m)	aux1(m)	aux2(m)	aux3(m)		
9	ubl(m)	am(l,m)	fj(l,1,m)	fj(l,2,m))	fj(l,3,m)	fj(l,4,m)	fj(l,5,m)
10	ubE(m)	am(E,m)	fj(E,1,m)	fj(E,2,m))	fj(E,3,m)	fj(E,4,m)	fj(E,5,m)
11	xstart	xend	deltax	fra	enfra		
12	kout	kspace	kdx	kent			
13	k1	k2	k3	k4	k5	k6	
14	k7	k8	k9	k10	k11	k12	
15	axx	bxx	cxx	dxx	exx	fxx	gxx
16-ext	dyl	rate	tstag	vapp	tuapp	epsapp	
16-int	dyl	rate	reyn	tref	tuapp	epsapp	twall

SAMPLE CODE

```

### 'title of data set'
400.dat lam entry flow, parallel planes channel, q(E)=c
###   kgeom   neq   kstart mode ktmu  ktmtr  ktme
      5       2    2     1    0    0    0
###   kbfor  jsor(1) jsor(2) jsor(3) jsor(4) jsor(5)
      1     1
###   kfluid  kunits
      1     1
###   po   rhoc       viscoc       amolwt       gam/cp
      87600.0 1.17660    1.853E-05    00.00       1005.00
###   prc(1) prc(2) prc(3) prc(4) prc(5)

```

0.711

nxbc(l) jbc(l,1) jbc(l,2) jbc(l,3) jbc(l,4) jbc(l,5)

5 0

nxbc(E) jbc(E,1) jbc(E,2) jbc(E,3) jbc(E,4) jbc(E,5)

5 2

x(m) rw(m) aux1(m) aux2(m) aux3(m)

0.0000000 0.0025 0.0100 0.0000 0.0000

0.1250000 0.0025 0.0100 0.0000 0.0000

0.2500000 0.0025 0.0100 0.0000 0.0000

0.3250000 0.0025 0.0100 0.0000 0.0000

0.5000000 0.0025 0.0100 0.0000 0.0000

ubl(m) am(l,m) fj(l,1,m) fj(l,2,m) fj(l,3,m) fj(l,4,m) fj(l,5,m)

ubE(m) am(E,m) fj(E,1,m) fj(E,2,m) fj(E,3,m) fj(E,4,m) fj(E,5,m)

0.00 0.0 0.000

0.00 0.000 400.0

0.00 0.0 0.000

0.00 0.000 400.0

0.00 0.0 0.000

0.00 0.000 400.0

0.00 0.0 0.000

0.00 0.000 400.0

0.00 0.0 0.000

0.00 0.000 400.0

xstart xend deltax fra enfra

0.0000000 0.500000 0.000 0.000 0.000E+00

kout kspace kdx kent

4 100 1 0

k1 k2 k3 k4 k5 k6

0 0 0 0 40 0

k7 k8 k9 k10 k11 k12

0 0 0 0 0 0

axx bxx cxx dxx exx fxx gxx

0.000E+00 0.000E+00 0.000E+00 0.000E+00 0.000E+00 0.000E+00 0.000E+00

dyi rate reyn tref tuapp epsapp twall

5.000E-04 0.0900 400.00 300.0 0.0 0.00 300.0

Appendix B: CALIBRATION

B.1. INTRODUCTION

This appendix describes the calibration process of the thermocouples and differential pressure transducers. The calibration curves of the thermocouples and differential pressure transducers are also given.

B.2. THERMOCOUPLE CALIBRATION

The thermocouples were soldered and connected to the NiDAQ module before being calibrated using a thermostat bath. This was done to limit the likeliness of a change in the properties of the thermocouple during the attachment process. Once the calibration was complete the thermocouples were located in the heated wall and kept in place using thermal paste.

The thermocouples were calibrated using a LAUDA ECO RE 1225 thermostat bath with an accuracy of 0.03°C and one PT-100 probes, each having a calibrated accuracy of 0.1°C. The PT-100 probe along with the thermocouples were placed in the thermostat bath to record the water temperature. The thermocouples were calibrated between 20°C and 50°C at 5°C intervals. Once the thermostat bath reached the required temperature and the PT-100 probe measure the same temperature (change 0.1°C in 10 minutes), a measurement of at minimum 10 data points for each thermocouple was taken. The process was also repeated for decreasing the temperatures (from 50°C to 20°C) to ensure accurate and reliable data was obtained.

The measured points of each thermocouple for each measured temperature were averaged and plotted against the average PT-100 temperature. A linear curve fit was done through the data points to obtain the calibration curves of each thermocouple, the results are summarised in Table B.1.

The calibrated temperatures were obtained using the following equation:

$$T_{cal} = mT_{uncal} + c \quad (B.1)$$

B.3. PRESSURE TRANSDUCER CALIBRATION

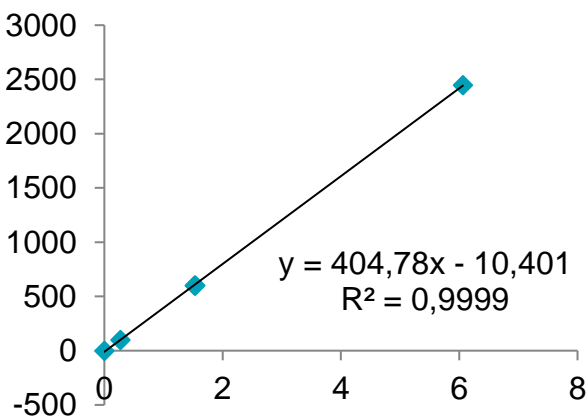
Various differential pressure transducers with varying differential pressure ranges were used to measure the pressure drop across the test section and pressure differential across the orifice plate. The pressure transducers used can be found in Table 3.1. The differential pressure transducers were calibrated using a digital pressure calibrator with a range of 3 000 kPa.

Each transducer was calibrated with a minimum of 5 increments in pressure. The digital pressure calibrator was set to the required pressure value and the voltage signal obtained from the Labview program was recorded. The relationship between the pressure recorded

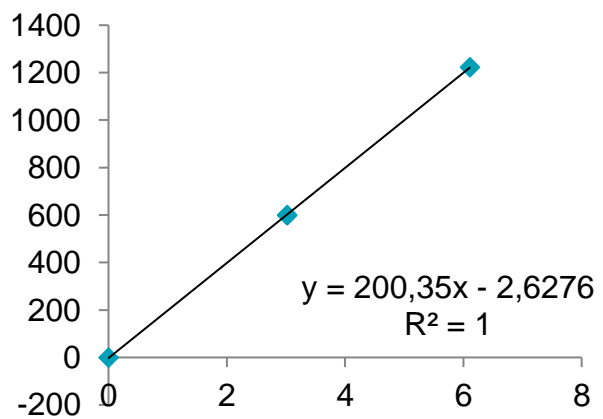
from the digital pressure calibrator and the voltage readings of each transducer was then plotted in Excel and a linear regression curve fit was added. The calibration curves are shown in Figure B.1.

Table B.1: Thermocouple calibration curves

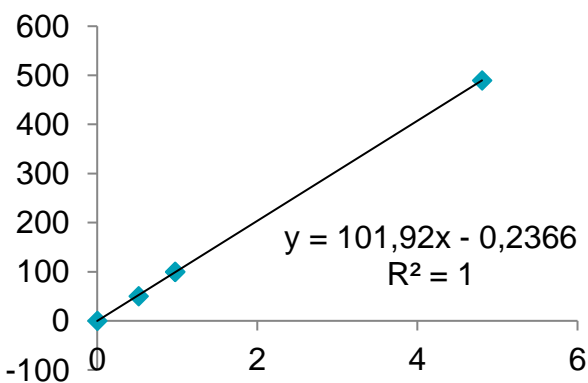
	m	c		m	c		m	c
T1	0.9946	0.6704	T11	0.9988	0.3289	T21	0.9895	0.8363
T2	0.9959	0.8360	T12	0.9995	0.4558	T22	0.9877	0.3592
T3	0.9957	0.9101	T13	0.9946	0.2286	T23	0.9854	0.4289
T4	0.9980	1.0302	T14	0.9940	0.1087	T24	0.9849	0.6664
T5	1.0006	0.4533	T15	0.9907	0.1206	T25	0.9986	0.5372
T6	0.9993	0.4314	T16	0.9906	0.2475	T26	0.9984	0.3772
T7	0.9998	0.0725	T17	0.9980	0.6739	T27	0.9963	0.2638
T8	1.0003	0.0491	T18	0.9985	0.3323	T28	0.9952	0.3194
T9	0.9962	0.0321	T19	0.9995	0.2548	T29	0.9941	0.8013
T10	0.9974	0.1542	T20	0.9980	0.5452	T30	0.9959	0.6601



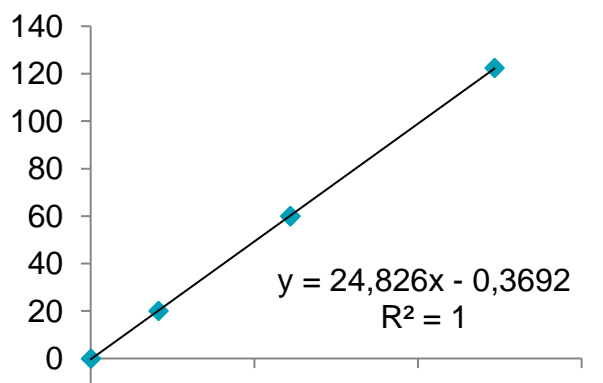
(a)



(b)



(c)



(d)

Figure B.1: Calibration curves for: (a) 10 inches of water differential pressure transducer, (b) 5 inches of water differential pressure transducer, (c) 2 inches of water differential pressure transducer and (d) 0.5 inches of water differential pressure transducer

B.4. CONCLUSION

This appendix contained the calibration procedure and results of the thermocouple and differential pressure transducers. The thermocouples were calibrated using a thermostat bath with an accuracy of 0.03°C and a PT-100 probe with an accuracy of 0.1°. The differential pressure transducers were calibrated using a digital pressure calibrator with a pressure range of 3 000 kPa. A linear regression curve fit through both the thermocouple calibration data and the pressure transducer data gave the calibration curves used.

Appendix C: UNCERTAINTY ANALYSIS

The uncertainties in the measured data were estimated based on the 95% confidence interval and the errors in the computed values were determined based on the propagation of uncertainty (Figliola and Beasley, 2006, Kline and McClintock, 1953, Moffat, 1988). Table 3.1 provides a summary of the instruments used with their range, bias, precision, and accuracy. The range and bias was obtained from the manufacturer's specifications while the precision was obtained by multiplying the standard deviation with the Student's t-variable (Figliola and Beasley, 2006). The accuracy was obtained from the bias and precision (Kline and McClintock, 1953). The total uncertainty for a single measurement or calculated value was determined using the propagation of error method derived by Moffat (1988).

The precision uncertainty for air mass flow rate, \dot{m} , determined from the orifice plate is given in Equation (C.2) (International Organization for, 1980):

$$\frac{\delta \dot{m}}{\dot{m}} = \left[\left(\frac{\delta C}{C} \right)^2 + \left(\frac{\delta \varepsilon_1}{\varepsilon} \right)^2 + \left(\frac{2\beta^4}{1-\beta^4} \right)^2 \left(\frac{\delta D}{D} \right)^2 + \left(\frac{2}{1-\beta^4} \right)^2 \left(\frac{\delta d}{d} \right)^2 + \frac{1}{4} \left(\frac{\delta \Delta p}{\Delta p} \right)^2 + \frac{1}{4} \left(\frac{\delta \rho_a}{\rho_a} \right)^2 \right]^{0.5} \quad (\text{C.2})$$

The precision uncertainty in the pressure differential across the orifice plate, Δp , was calculated using the precision uncertainty for pressure (P) from the transducer calibration based on the standard deviation of the data set. The following equation was used in determining the precision uncertainty in Δp :

$$\delta \Delta p = \left[(U_{cal,eqn})^2 + (a_1 U_{x,i})^2 \right]^{0.5} \quad (\text{C.3})$$

where $U_{cal,eqn}$ refers to the precision uncertainty of the pressure from the differential pressure transducer calibration, a_1 refers to the gradient of the linear fit used in the calibration equation and $U_{x,i}$ refers to the precision uncertainty from the measured average voltage from the differential pressure transducer.

$$U_{cal,eqn} = \left[(t_{v,95} S_{yx})^2 + (A_{cal})^2 + (a_1 U_x)^2 \right]^{0.5} \quad (\text{C.4})$$

where $t_{v,95}$ refers to the probability value from the Student's t-distribution table for v degrees of freedom, determined using Equation (C.5), and the 95% confidence interval, S_{yx} is the standard deviation based on the deviation of each data point and the linear fit – Equation (C.6), A_{cal} is the calibration accuracy.

$$v = N - (m + 1) \quad (\text{C.5})$$

where N is the number of data points used in the calibration process and $m = 1$ for a linear fit.

$$S_{yx} = \left[\frac{\sum_{i=1}^N (y_i - y_{c,i})^2}{v} \right]^{0.5} \quad (\text{C.6})$$

where y_i is the calibration pressure at a voltage x_i and $y_{c,i}$ is the pressure value at the same voltage x_i determined from the linear fit.

$$U_x = \left[(t_{v,95} S_x)^2 + (A_{trans})^2 \right]^{0.5} \quad (\text{C.7})$$

where S_x is the standard deviation based on the deviation of each voltage reading and A_{trans} is the accuracy of the differential pressure transducer in volts.

$$S_x = \left[\frac{1}{n-1} \sum_{i=1}^n (X_i - \bar{X})^2 \right]^{0.5} \quad (\text{C.8})$$

where n is the number of samples (voltage readings) taken during the calibration or the sampling rate of the transducer during experimentation, X_i is the sample voltage and \bar{X} is the average voltage of n -samples.

$$\bar{X} = \frac{1}{n} \sum_{i=1}^n X_i \quad (\text{C.9})$$

The precision uncertainty for Reynolds number can be calculated as follows:

$$\frac{\delta Re}{Re} = \left[\left(2 \frac{\delta \dot{m}}{\dot{m}} \right)^2 + \left(\frac{\delta \rho_a}{\rho_a} \right)^2 \right]^{0.5} \quad (\text{C.10})$$

The precision uncertainty for friction factor can be calculated as follows:

$$\frac{\delta f}{f} = \left[\left(2 \frac{\delta \dot{m}}{\dot{m}} \right)^2 + \left(\frac{\delta \left(\frac{\Delta p}{\Delta x} \right)}{\frac{\Delta p}{\Delta x}} \right)^2 \right]^{0.5} \quad (\text{C.11})$$

where the uncertainty in the slope or linear fit ($\Delta p/\Delta x$) can be calculated as:

$$\delta \left(\frac{\Delta p}{\Delta x} \right) = S_{yx} \left[\frac{N}{N \sum_{i=1}^N X_i^2 - (\sum_{i=1}^N X_i)^2} \right]^{0.5} \quad (\text{C.12})$$

where S_{yx} is calculated using Equation (C.6), and X_i refers to distance along the centreline of the test section.

The precision uncertainty in the power lost to the atmosphere (Q_l) was calculated as follows:

$$\frac{\delta Q_l}{Q_l} = \left[\left(\frac{\delta \Delta T}{\Delta T} \right)^2 \right]^{0.5} \quad (\text{C.13})$$

The precision uncertainty in the temperature difference, ΔT , was calculated using the precision uncertainty for temperature (T) from the water-bath calibration based on the

standard deviation of the data set. The following equation was used in determining the precision uncertainty in T:

$$\delta T = \left[(U_{cal,eqn})^2 + (a_1 U_{x,i})^2 \right]^{0.5} \quad (C.14)$$

where $U_{cal,eqn}$ refers to the precision uncertainty of the temperature from the water-bath calibration, a_1 refers to the gradient of the linear fit used in the calibration equation and $U_{x,i}$ refers to the precision uncertainty from the measured average temperature from the thermocouples.

The precision uncertainty in the total power delivered to the heated plate(s) (Q_T) was calculated as follows:

$$\frac{\delta Q_T}{Q_T} = \left[\left(\frac{\delta VDC}{VDC} \right)^2 + \left(\frac{\delta Amp}{Amp} \right)^2 \right]^{0.5} \quad (C.15)$$

The precision uncertainty in the total convective power delivered to the air by the heated plate(s) (Q_c) was calculated as follows:

$$\frac{\delta Q_c}{Q_c} = \left[\left(\frac{\delta Q_T}{Q_T} \right)^2 + \left(\frac{\delta Q_l}{Q_l} \right)^2 \right]^{0.5} \quad (C.16)$$

The precision uncertainty in the mixed-mean air temperature ($T_{m,x}$) was calculated as follows:

$$\frac{\delta T_{m,x}}{T_{m,x}} = \left[\left(\frac{\delta T_{air,in}}{T_{air,in}} \right)^2 + \left(\frac{\delta Q_{c,x}}{Q_{c,x}} \right)^2 + \left(\frac{\delta \dot{m}}{\dot{m}} \right)^2 \right]^{0.5} \quad (C.17)$$

The precision uncertainty in the temperature difference, $T_{air,in}$, was calculated using the precision uncertainty for temperature (T) from the water-bath calibration based on the standard deviation of the data set. The following equation was used in determining the precision uncertainty in $T_{air,in}$:

$$\frac{\delta T_{air,in}}{T_{air,in}} = \left[(U_{cal,eqn})^2 + (a_1 U_{x,i})^2 \right]^{0.5} \quad (C.18)$$

The precision uncertainty in the Nusselt number (Nu_x) was calculated as follows:

$$\frac{\delta Nu_x}{Nu_x} = \left[\left(\frac{\delta Q_c}{Q_c} \right)^2 + \left(\frac{\delta T_{w,x}}{T_{w,x}} \right)^2 + \left(\frac{\delta T_{m,x}}{T_{m,x}} \right)^2 \right]^{0.5} \quad (C.19)$$

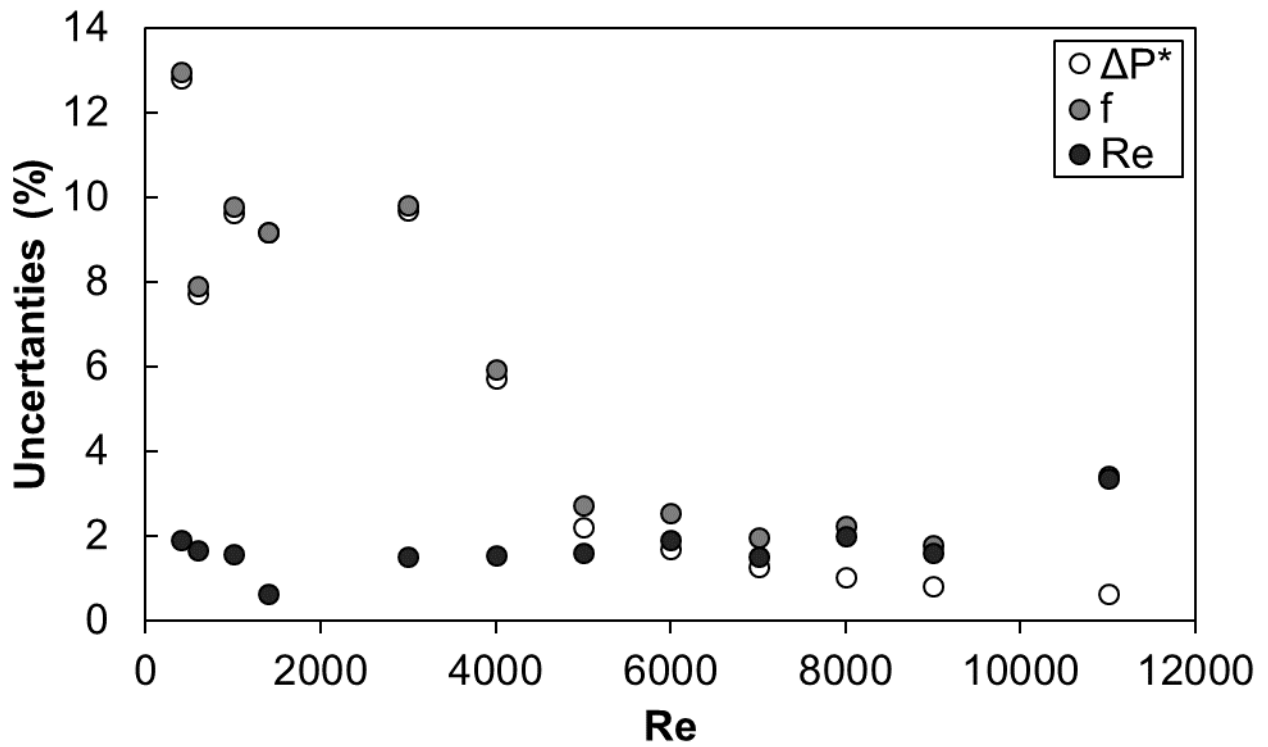
The precision uncertainty in the temperature difference, $T_{w,x}$, was calculated using the precision uncertainty for temperature (T) from the water-bath calibration based on the standard deviation of the data set. The following equation was used in determining the precision uncertainty in $T_{w,x}$:

$$\frac{\delta T_{w,x}}{T_{w,x}} = \left[(U_{cal,eqn})^2 + (a_1 U_{x,i})^2 \right]^{0.5} \quad (C.20)$$

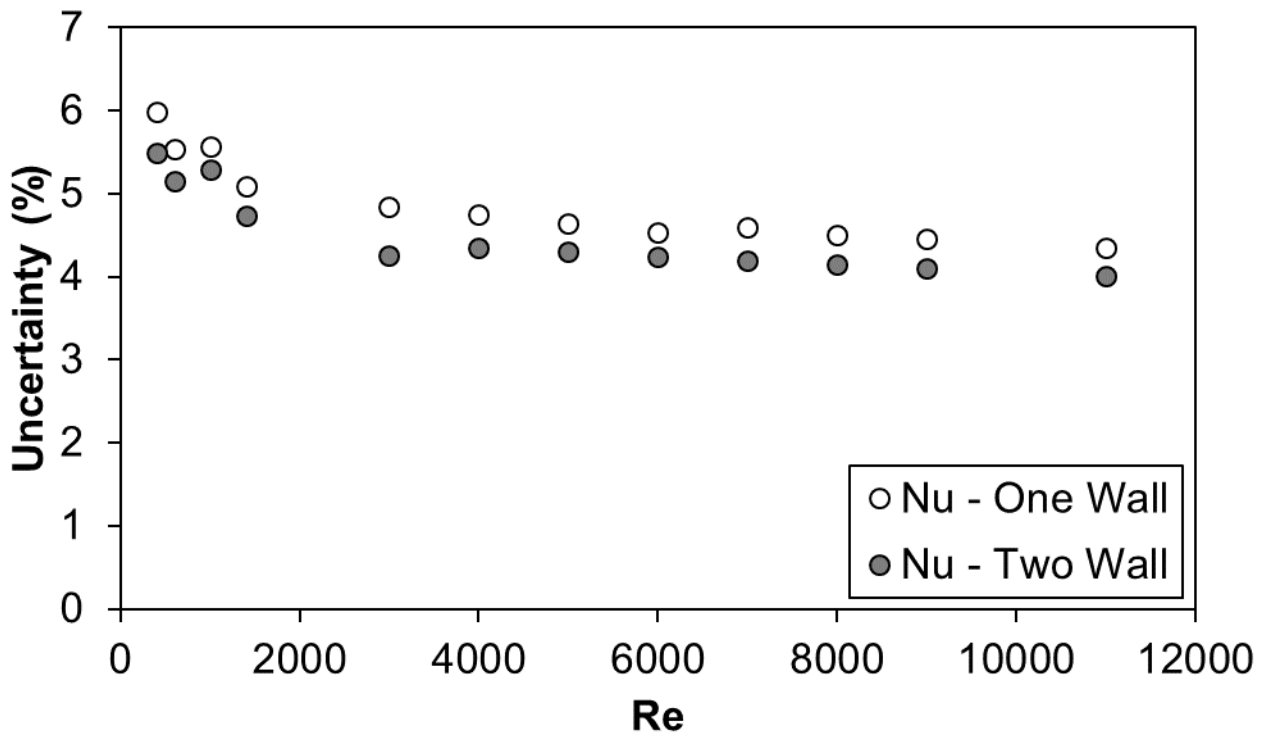
Figure 3.6 (a) shows the distribution of the calculated precision uncertainties for each significant variable used in the pressure measurements as Reynolds number varies. At low Reynolds numbers $400 \leq Re \leq 1\,000$ the test setup has the highest precision uncertainty. This is due to the small differential pressure across the orifice plate and in the wall pressure measurements. For the pressure measurements, there is a spike in precision uncertainty for normalised pressure drop (ΔP^*) at $Re = 4\,000$ as this is when the differential pressure transducers were swapped. Two different differential pressure transducers were used in the experiments to minimise the uncertainty in the wall pressure measurements. The first transducer was a PX 2650-2D5V with a full-scale range of $0 \leq Pa \leq 480$ used for $400 \leq Re \leq 3\,000$. The second was a PX 164-010D5V with a full-scale range of $0 \leq Pa \leq 2\,490$ used for $4\,000 \leq Re \leq 11\,000$. For Reynolds numbers greater than 600 the normalised pressure drop uncertainty is less than 10%.

Figure 3.6 (a) also shows that the calculated friction factor (f) uncertainty is less for all Reynolds number greater than 400. Like with the normalised pressure drop the friction factor uncertainty is the highest in the laminar region. This is again due to the small pressure differential across the orifice plate and the wall pressure measurements. However, the influence of changing the pressure transducers is not evident like in the normalised pressure drop data. Except for at Reynolds number 400 the friction factor uncertainty is less than 5%.

Figure 3.6 (b) shows the distribution of the calculated precision uncertainties for each significant variable used in the heat transfer measurements as Reynolds number varies. At low Reynolds numbers $400 \leq Re \leq 1\,000$ the test setup has the highest precision uncertainty. This is due to the small differential pressure across the orifice plate and the low $T_{w,x} - T_{m,x}$ values for low Reynolds number tests. As the Reynolds number increases the difference between the measured wall temperature and the mixed mean air temperature increases. Thus, reducing the precision uncertainty in the determined Nu_x . For both one-wall heating and two-wall heating the Nusselt number uncertainty was less than 6%.



(a)



(b)

Figure C.1: Uncertainty estimates as Re varies (a) ΔP^* , f , and Re uncertainties for pressure drop experiments, and (b) Nu and Re uncertainties for heat transfer experiments

UNCERTAINTIES: SAMPLE CALCULATIONS

FRICITION FACTOR AND PRESSURE DROP UNCERTAINTIES FOR RE = 400

$$\delta\Delta p = \left[(U_{cal,eqn})^2 + (a_1 U_{x,i})^2 \right]^{0.5}$$

$$U_{cal,eqn} = \left[(t_{v,95} S_{yx})^2 + (A_{cal})^2 + (a_1 U_x)^2 \right]^{0.5}$$

A _{cal}	0.8721Pa
v	4
t _{v,95}	2.776
a ₁	24.917 Pa/V
U ₁	0.05 V
S _{y1}	1.2394 Pa

$$U_{cal,eqn} = [(2.776 * 1.2394)^2 + (0.8721)^2 + (24.917 * 0.05)^2]^{0.5}$$

$$U_{cal,eqn} = 2.1079Pa$$

$$\delta\Delta p = \left[(2.1079)^2 + (24.917 * U_{x,i})^2 \right]^{0.5}$$

$$U_x = \left[(t_{v,95} S_x)^2 + (A_{trans})^2 \right]^{0.5}$$

A _{trans}	0.05V
v	2000
t _{v,95}	1.960
S ₁	0.00118V

$$U_1 = [(1.96 * 0.00118)^2 + (0.05)^2]^{0.5}$$

$$U_1 = 0.050048V$$

$$\delta\Delta p = [(2.1079)^2 + (24.917 * 0.050048)^2]^{0.5}$$

$$\delta\Delta p = 2.449Pa$$

The precision uncertainty for friction factor can be calculated as follows:

$$\frac{\delta f}{f} = \left[\left(\frac{\delta \dot{m}}{\dot{m}} \right)^2 + \left(\frac{\delta \left(\frac{\Delta p}{\Delta x} \right)}{\frac{\Delta p}{\Delta x}} \right)^2 \right]^{0.5}$$

$$\frac{\delta f}{f} = [(0.01897)^2 + (0.071332)^2]^{0.5}$$

$$\frac{\delta f}{f} = 0.073811$$

where the uncertainty in the slope or linear fit ($\Delta p/\Delta x$) can be calculated as:

$$\delta \left(\frac{\Delta p}{\Delta x} \right) = S_{yx} \left[\frac{N}{N \sum_{i=1}^N X_i^2 - (\sum_{i=1}^N X_i)^2} \right]^{0.5}$$

$$\delta \left(\frac{\Delta p}{\Delta x} \right) = S_{yx} \left[\frac{13}{13(0.3383) - 4.0733} \right]^{0.5}$$

$$\delta \left(\frac{\Delta p}{\Delta x} \right) = (0.14329)(6.3226)$$

$$\delta \left(\frac{\Delta p}{\Delta x} \right) = 0.9059$$

NU SAMPLE CALCULATION FOR LOCATION 1

$$\frac{\delta Nu_1}{Nu_1} = \left[\left(\frac{\delta Q_c}{Q_c} \right)^2 + \left(\frac{\delta T_{w,1}}{T_{w,1}} \right)^2 + \left(\frac{\delta T_{m,1}}{T_{m,1}} \right)^2 \right]^{0.5}$$

Uncertainties for thermocouples were calculated as follows:

$$\delta T_{w,1} = \left[(U_{cal,eqn})^2 + (a_1 U_{1,i})^2 \right]^{0.5}$$

$$U_{cal,eqn} = \left[(t_{v,95} S_{y1})^2 + (A_{cal})^2 + (a_1 U_1)^2 \right]^{0.5}$$

A _{cal}	0.12°C
v	15
t _{v,95}	2.132
a ₁	0.994646992°C/°C
U ₁	0.004203574°C
S _{y1}	0.003252724°C

$$U_{cal,eqn} = [(2.132 * 0.00325)^2 + (0.12)^2 + (0.995 * 0.0042)^2]^{0.5}$$

$$U_{cal,eqn} = 0.12068^\circ C$$

$$\delta T_{w,1} = \left[(U_{cal,eqn})^2 + (a_1 U_{1,i})^2 \right]^{0.5}$$

$$\delta T_{w,1} = \left[(0.12068)^2 + (0.995 * U_{1,i})^2 \right]^{0.5}$$

$$U_1 = \left[(t_{v,95} S_1)^2 + (A_{trans})^2 \right]^{0.5}$$

A _{trans}	0.2°C
v	10
t _{v,95}	2.228
S ₁	0.0068599°C

$$U_1 = [(2.228 * 0.0068599)^2 + (0.2)^2]^{0.5}$$

$$U_1 = 0.20058^\circ C$$

$$\delta T_{w,1} = [(0.12068)^2 + (0.995 * 0.20058)^2]^{0.5}$$

$$\delta T_{w,1} = 0.23323^\circ C$$

In the same manner:

$$\delta T_{air} = 0.24608^{\circ}C$$

$$\delta T_{ins,1} = 0.23956^{\circ}C$$

Heat lost to atmosphere uncertainty was calculated as follows:

$$\begin{aligned} \frac{\delta Q_l}{Q_l} &= \left[\left(\frac{\delta \Delta T}{\Delta T} \right)^2 \right]^{0.5} = \left[\left(\frac{\delta T_{ins,1}}{T_{ins,1}} \right)^2 + \left(\frac{\delta T_{air}}{T_{air}} \right)^2 \right]^{0.5} \\ \frac{\delta Q_l}{Q_l} &= \left[\left(\frac{\delta \Delta T}{\Delta T} \right)^2 \right]^{0.5} = [(0.016332)^2 + (0.018252)^2]^{0.5} \\ \frac{\delta Q_l}{Q_l} &= \left[\left(\frac{\delta \Delta T}{\Delta T} \right)^2 \right]^{0.5} = 0.02475 \end{aligned}$$

Total power into heater uncertainty was calculated as follows:

$$\begin{aligned} \frac{\delta Q_T}{Q_T} &= \left[\left(\frac{\delta VDC}{VDC} \right)^2 + \left(\frac{\delta Amp}{Amp} \right)^2 \right]^{0.5} \\ \frac{\delta Q_T}{Q_T} &= [(0.010335)^2 + (0.03506)^2]^{0.5} \\ \frac{\delta Q_T}{Q_T} &= 0.03655 \end{aligned}$$

Heat transferred to air in channel uncertainty was calculated as follows:

$$\begin{aligned} \frac{\delta Q_c}{Q_c} &= [(0.03655)^2 + (0.02475)^2]^{0.5} \\ \frac{\delta Q_c}{Q_c} &= 0.044147 \end{aligned}$$

Mean air temperature in channel uncertainty was calculated as follows:

$$\begin{aligned} \frac{\delta T_{m,1}}{T_{m,1}} &= \left[\left(\frac{\delta \dot{m}}{\dot{m}} \right)^2 + \left(\frac{\delta T_{air}}{T_{air}} \right)^2 + \left(\frac{\delta Q_{c,1}}{Q_{c,1}} \right)^2 \right]^{0.5} \\ \frac{\delta T_{m,1}}{T_{m,1}} &= [(0.02279)^2 + (0.018252)^2 + (0.044147)^2]^{0.5} \\ \frac{\delta T_{m,1}}{T_{m,1}} &= 0.05293 \end{aligned}$$

Local Nusselt number uncertainty was calculated as follows:

$$\begin{aligned} \frac{\delta Nu_1}{Nu_1} &= \left[\left(\frac{\delta Q_c}{Q_c} \right)^2 + \left(\frac{\delta T_{w,1}}{T_{w,1}} \right)^2 + \left(\frac{\delta T_{m,1}}{T_{m,1}} \right)^2 \right]^{0.5} \\ \frac{\delta Nu_1}{Nu_1} &= [(0.044147)^2 + (0.017657)^2 + (0.05293)^2]^{0.5} = 0.0667 \end{aligned}$$

Appendix D: PRESSURE DROP DATA

5 MM CHANNEL HEIGHT - MESH 4.1

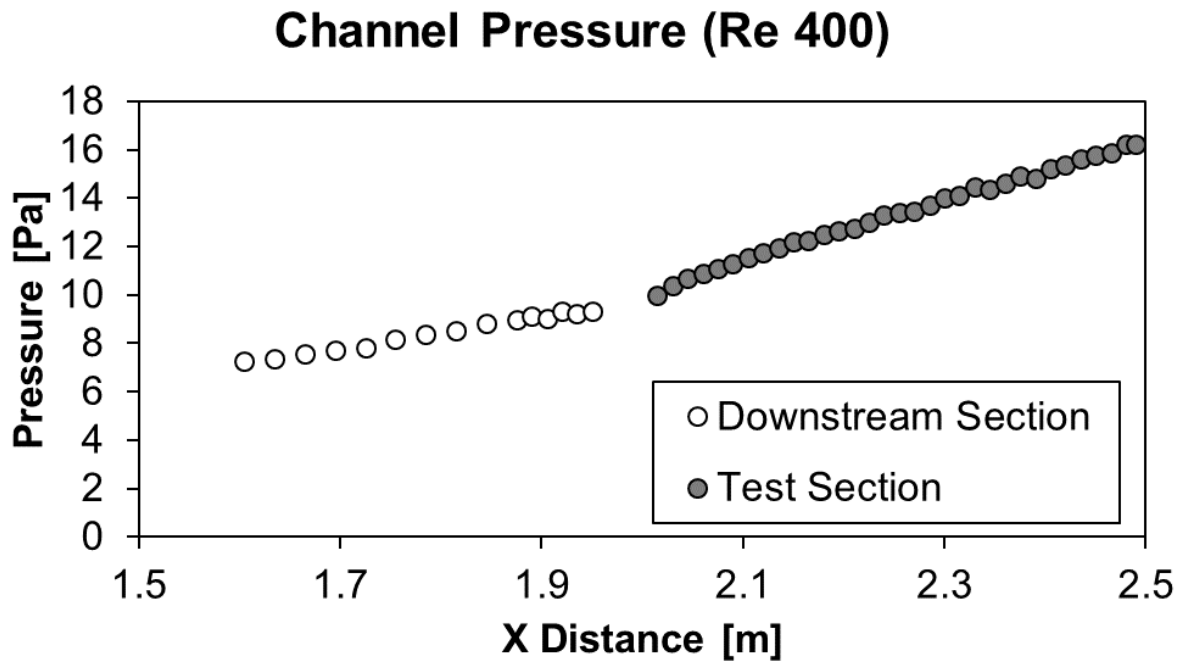


Figure D.1: Channel Pressure for mesh 4.1 and Re = 400

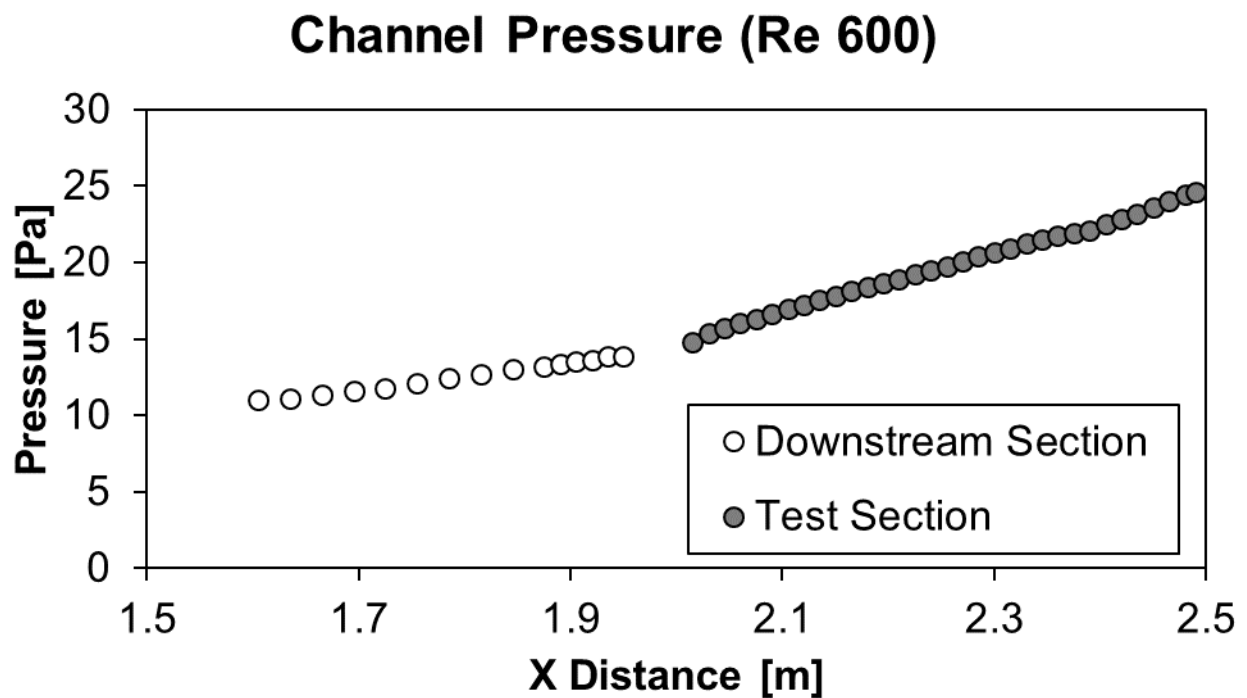


Figure D.2: Channel Pressure for mesh 4.1 and Re = 600

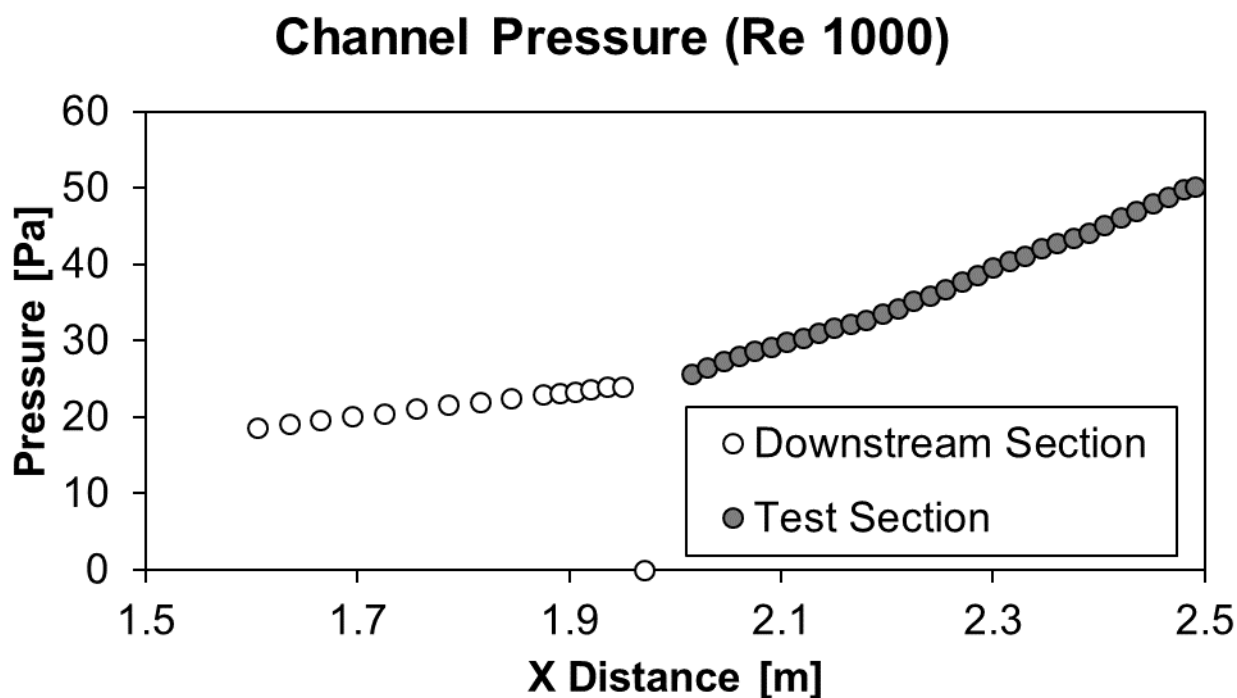


Figure D.3: Channel Pressure for mesh 4.1 and Re = 1 000

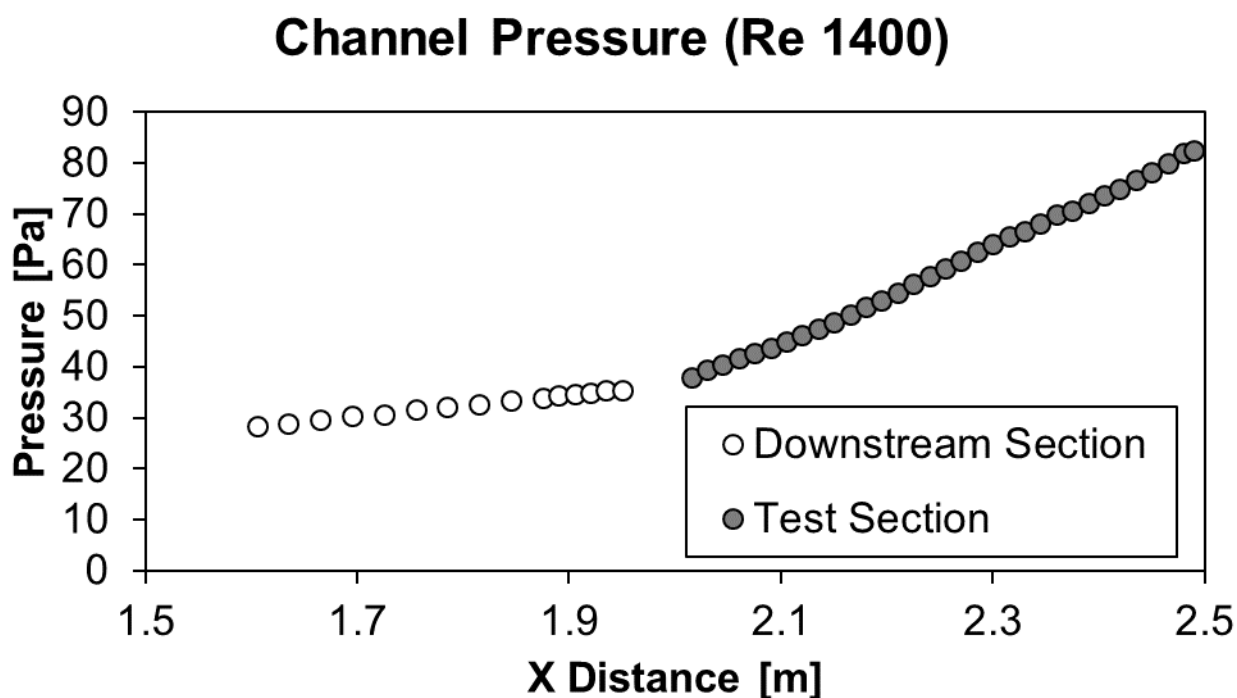


Figure D.4: Channel Pressure for mesh 4.1 and Re = 1 400

Channel Pressure (Re 3000)

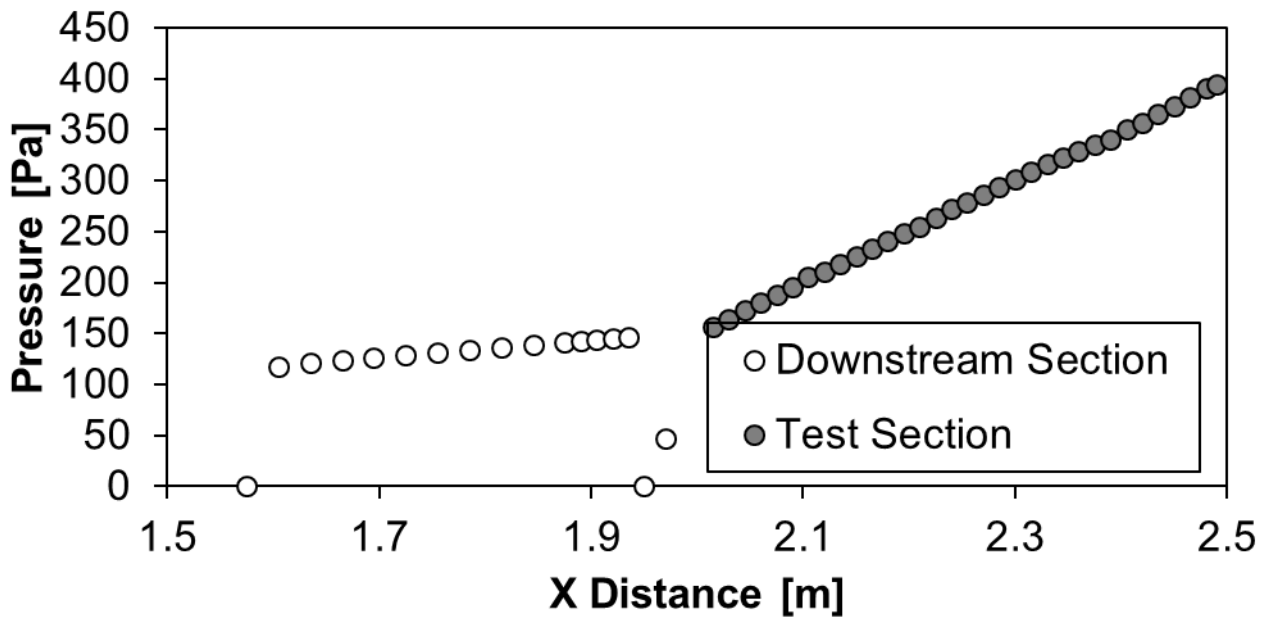


Figure D.5: Channel Pressure for mesh 4.1 and Re = 3 000

Channel Pressure (Re 4000)

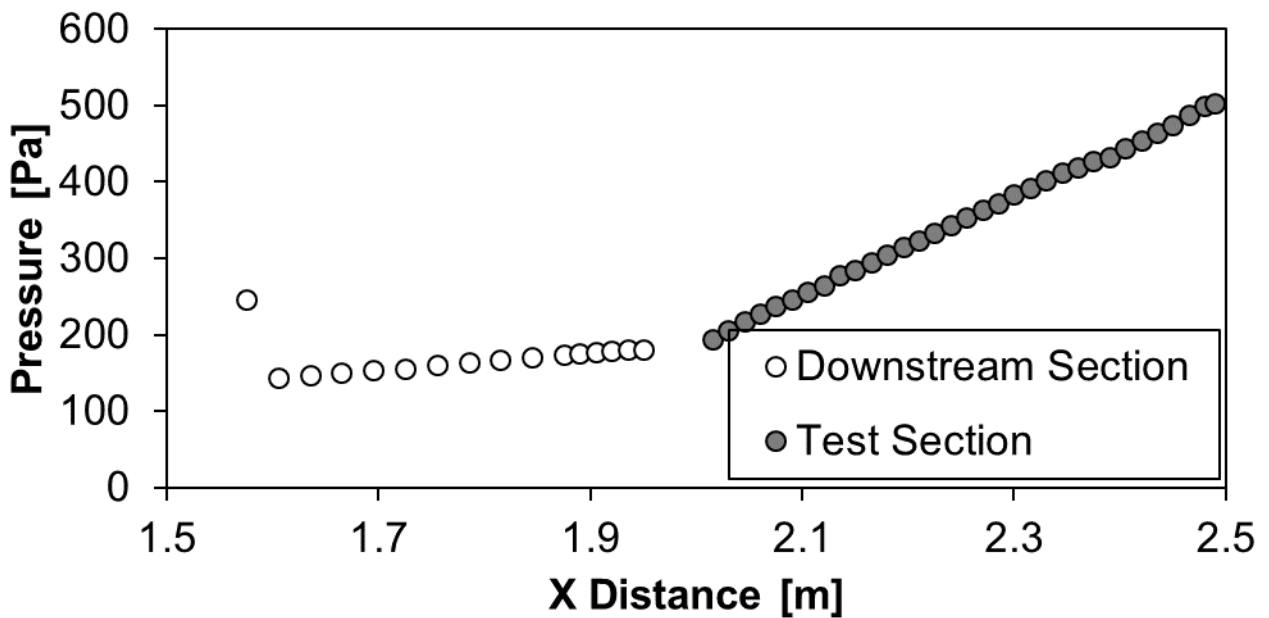


Figure D.6: Channel Pressure for mesh 4.1 and Re = 4 000

Channel Pressure (Re 5000)

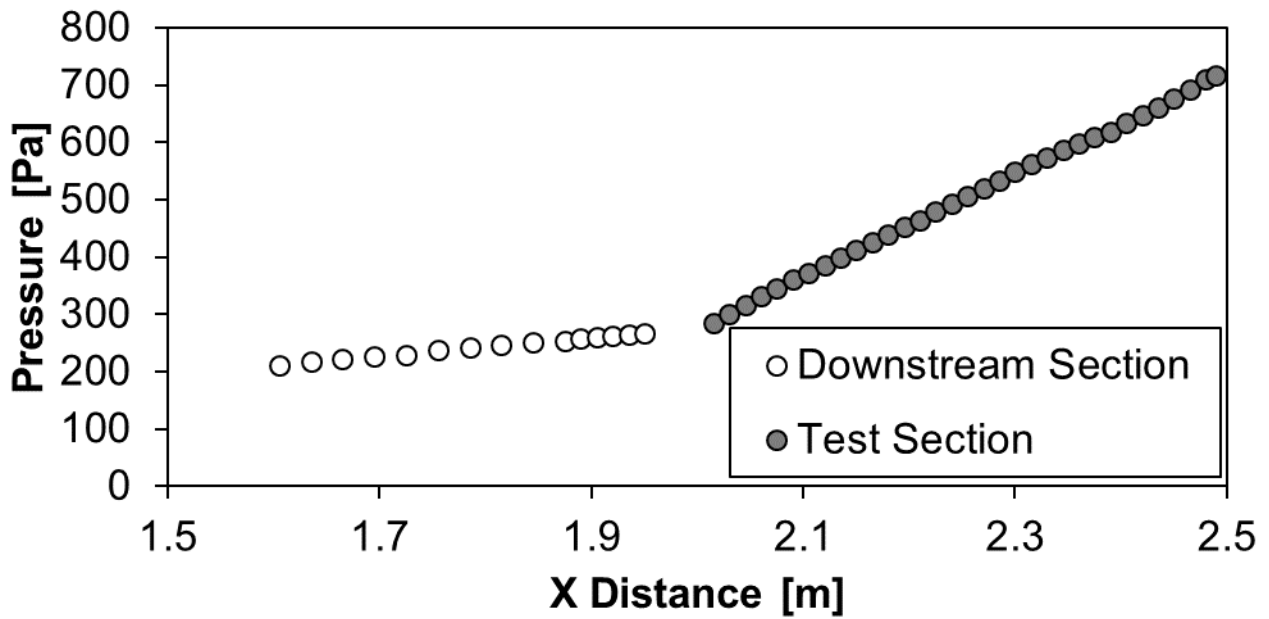


Figure D.7: Channel Pressure for mesh 4.1 and Re = 5 000

Channel Pressure (Re 6000)

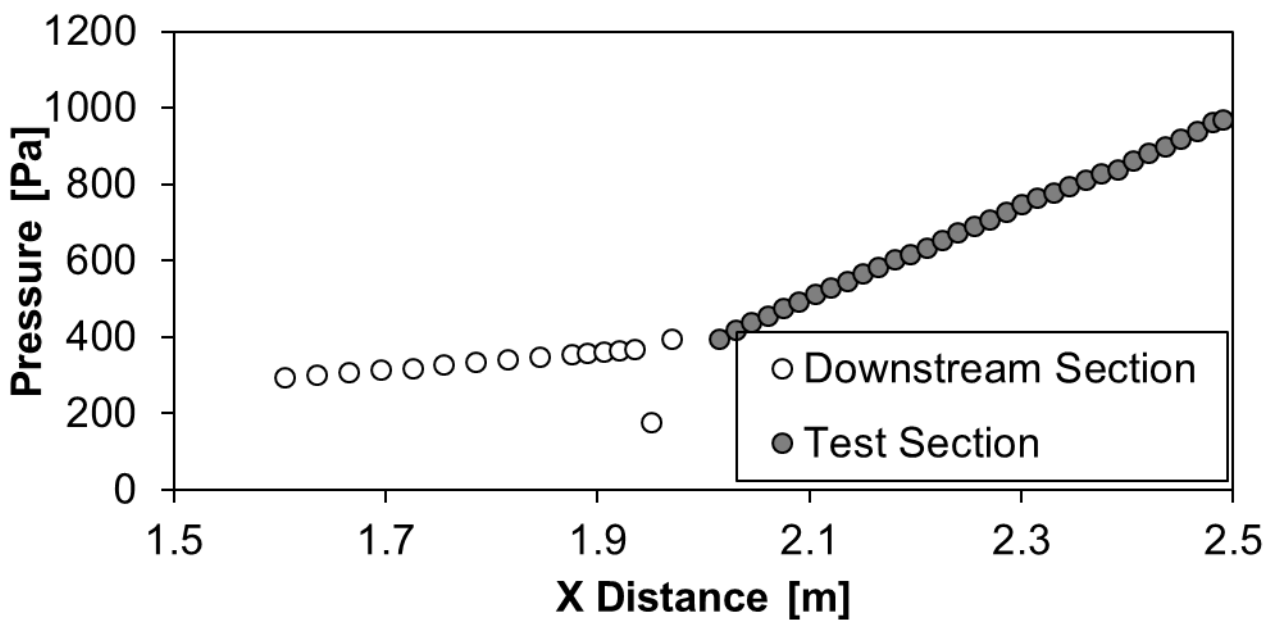


Figure D.8: Channel Pressure for mesh 4.1 and Re = 6 000

Channel Pressure (Re 7000)

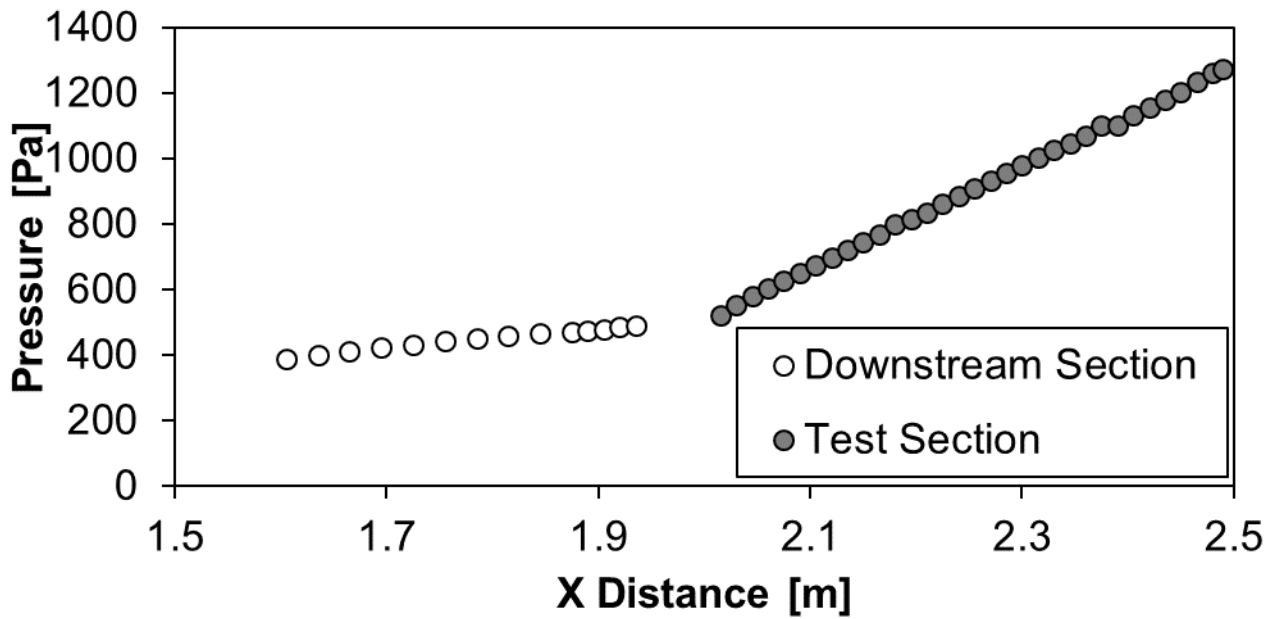


Figure D.9: Channel Pressure for mesh 4.1 and Re = 7 000

Channel Pressure (Re 8000)

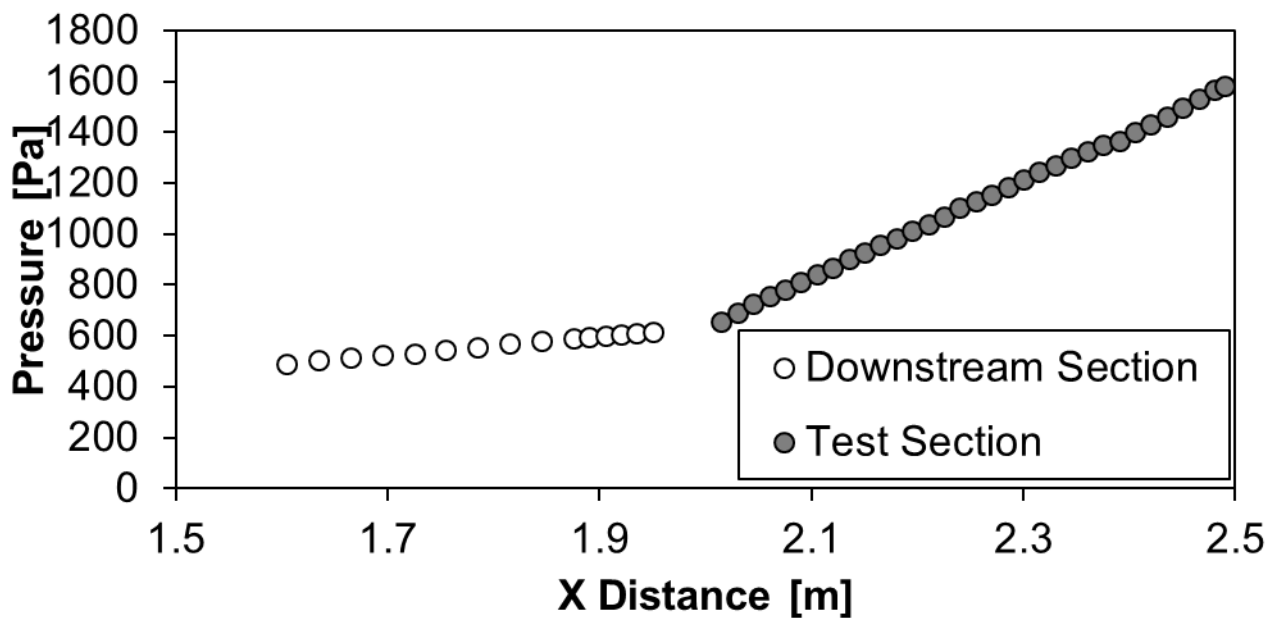


Figure D.10: Channel Pressure for mesh 4.1 and Re = 8 000

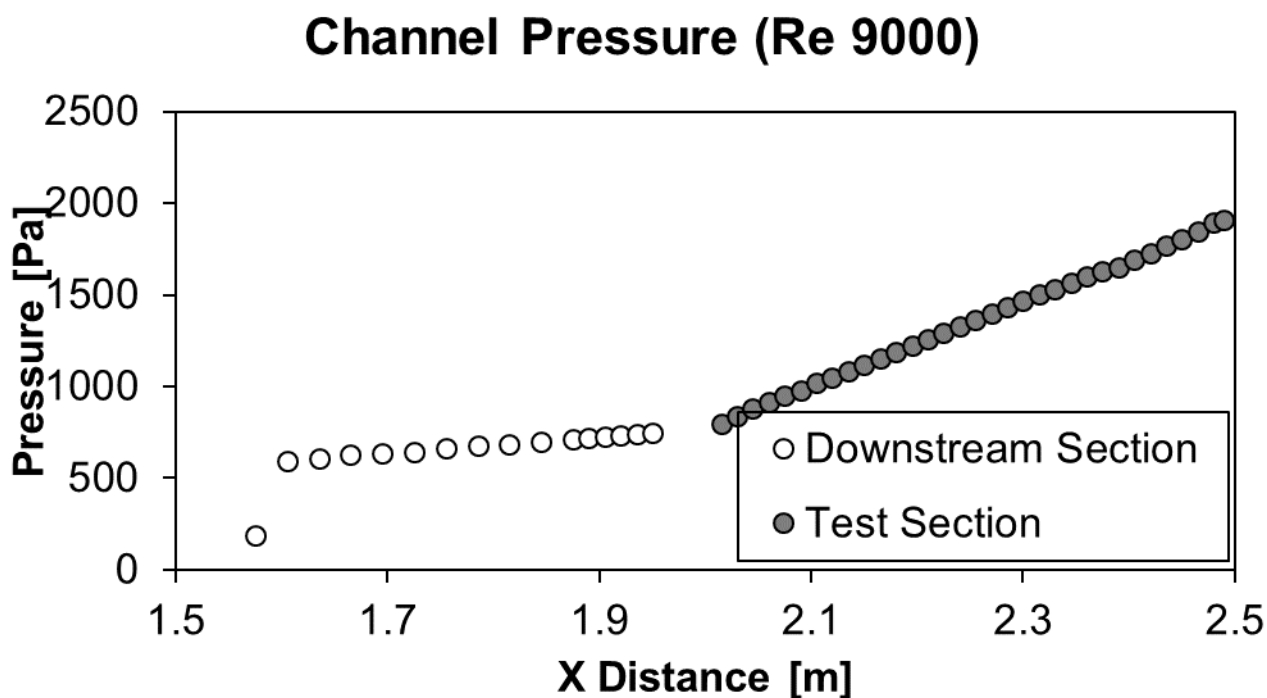


Figure D.11: Channel Pressure for mesh 4.1 and Re = 9 000

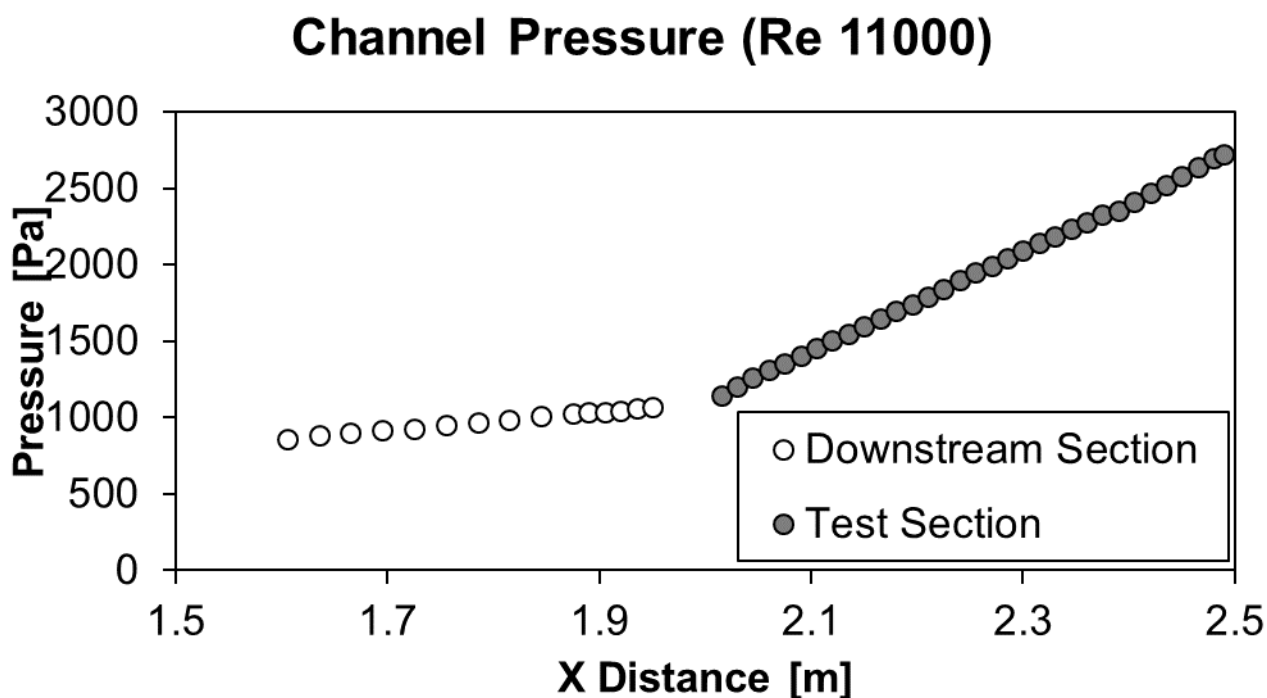


Figure D.12: Channel Pressure for mesh 4.1 and Re = 11 000

5 MM CHANNEL HEIGHT – MESH 4.3

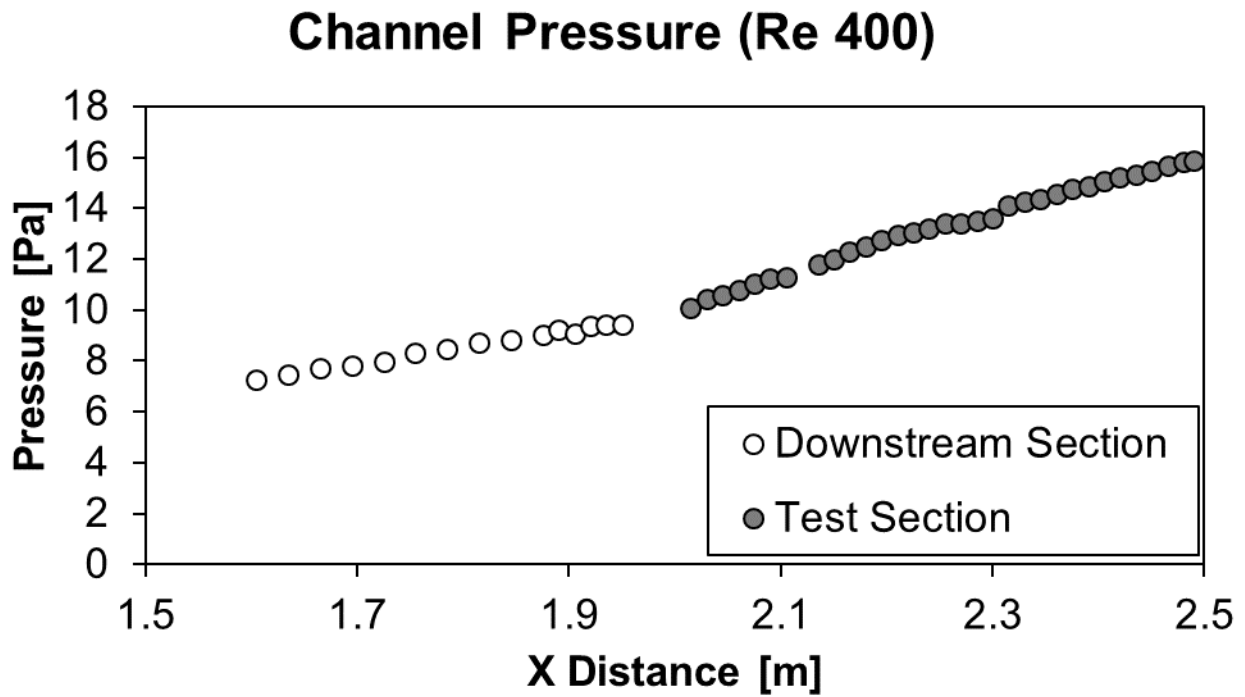


Figure D.13: Channel Pressure for mesh 4.3 and Re = 400

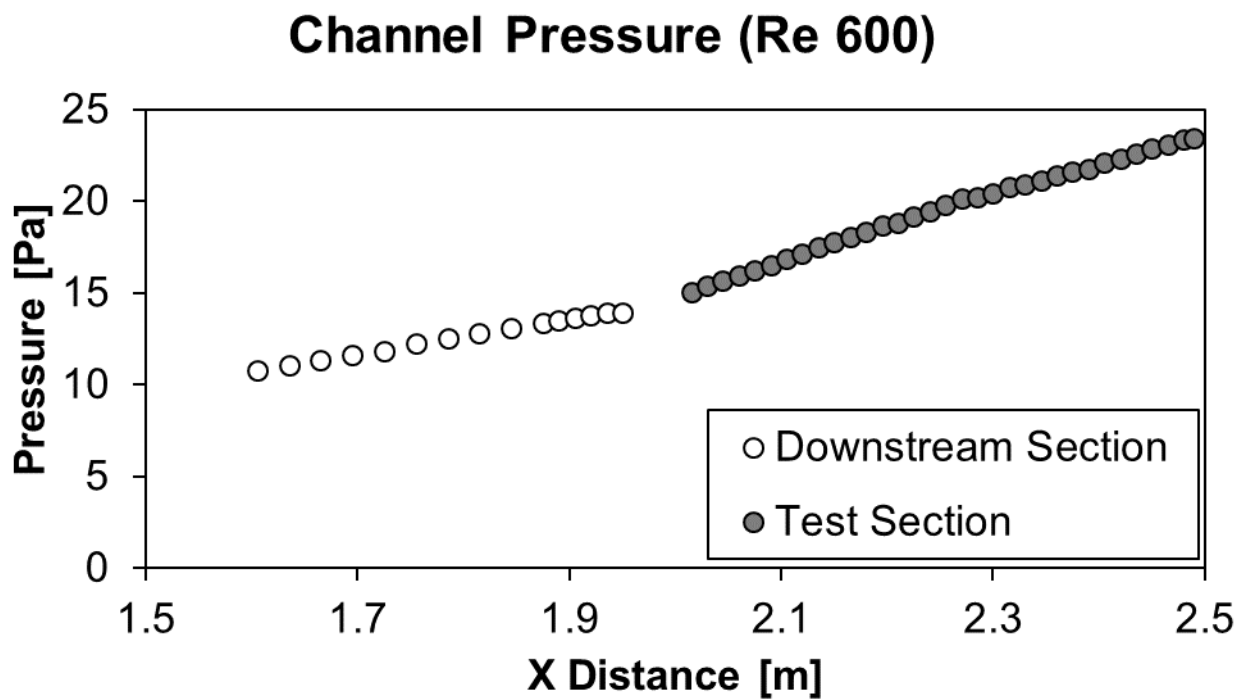


Figure D.14: Channel Pressure for mesh 4.3 and Re = 600

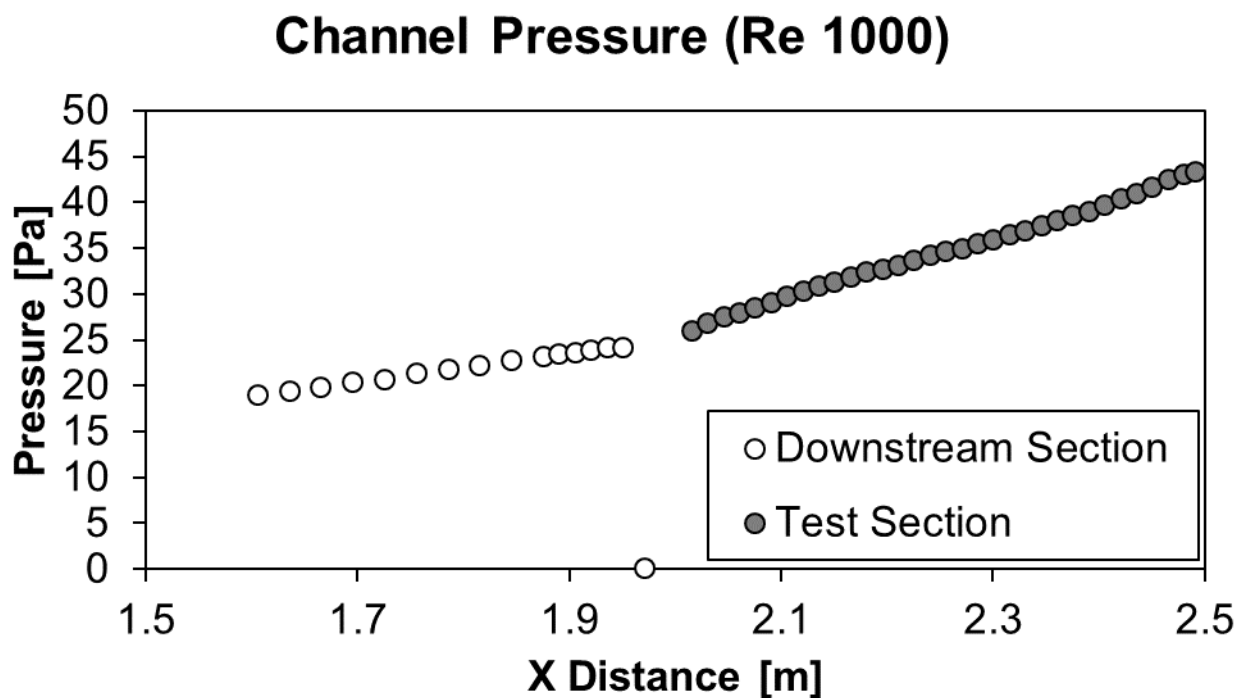


Figure D.15: Channel Pressure for mesh 4.3 and Re = 1 000

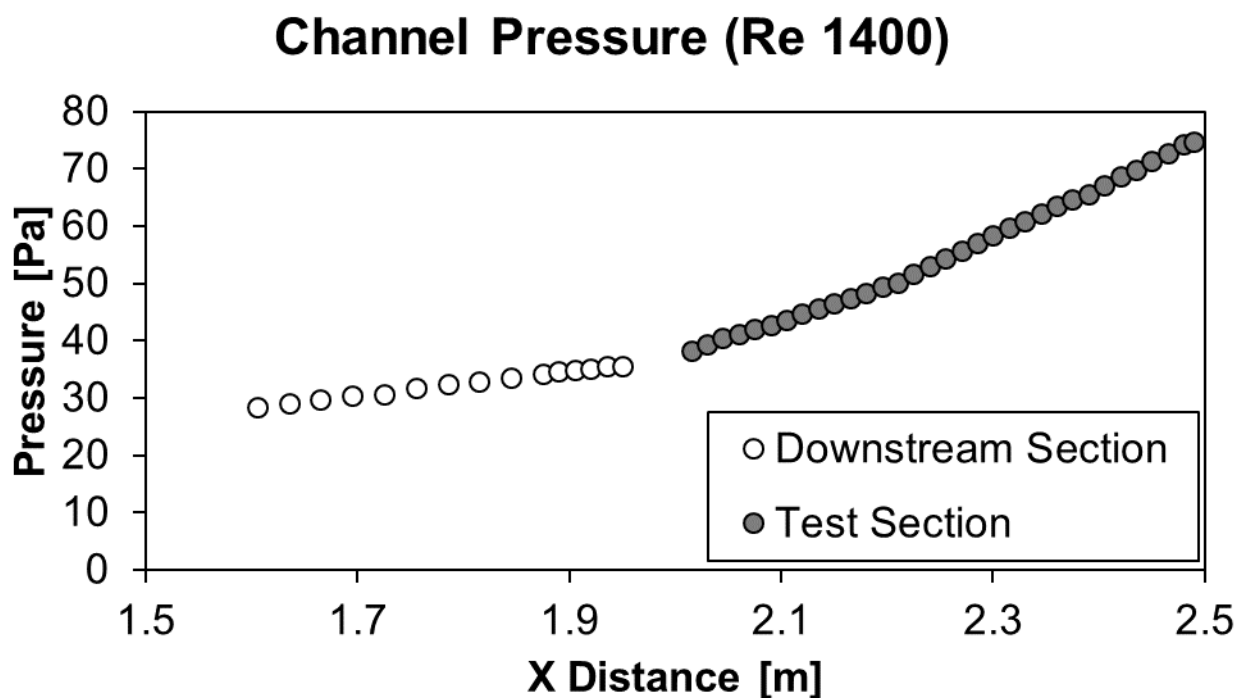


Figure D.16: Channel Pressure for mesh 4.3 and Re = 1 400

Channel Pressure (Re 3000)

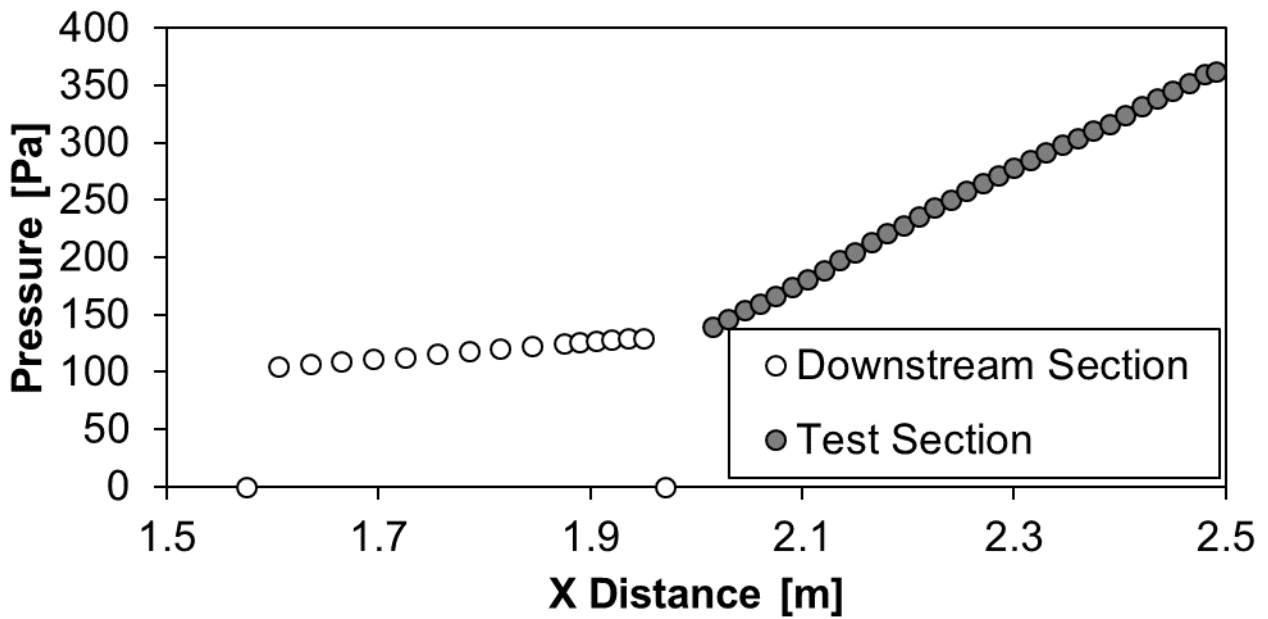


Figure D.17: Channel Pressure for mesh 4.3 and Re = 3 000

Channel Pressure (Re 4000)

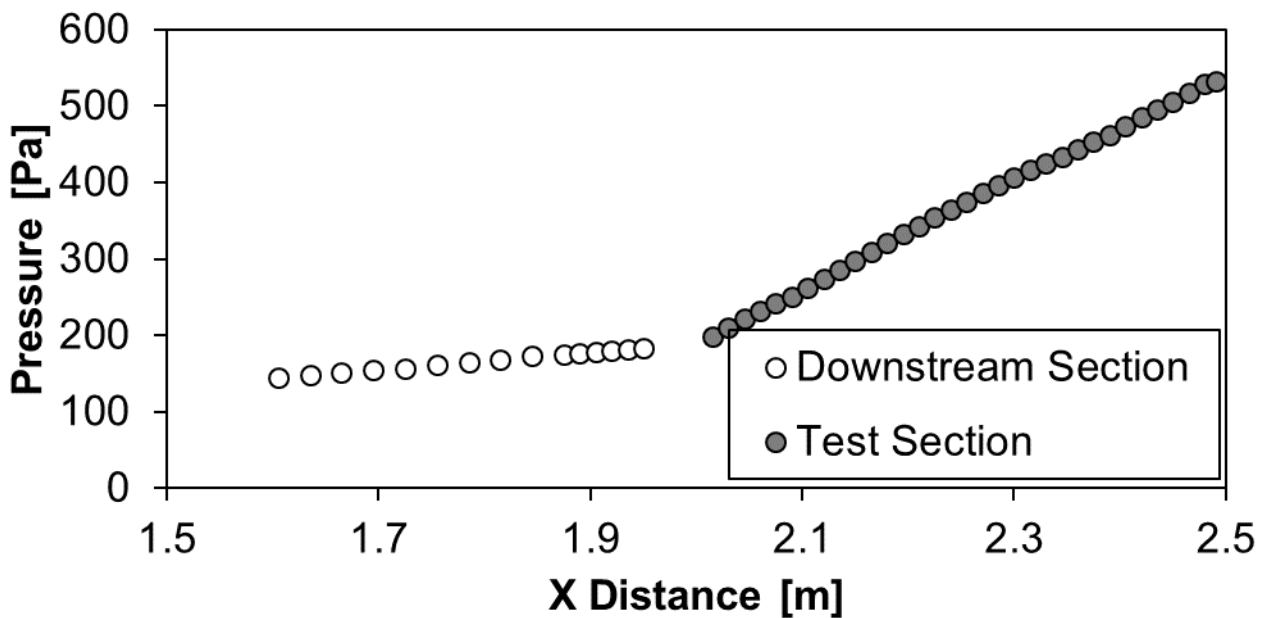


Figure D.18: Channel Pressure for mesh 4.3 and Re = 4 000

Channel Pressure (Re 5000)

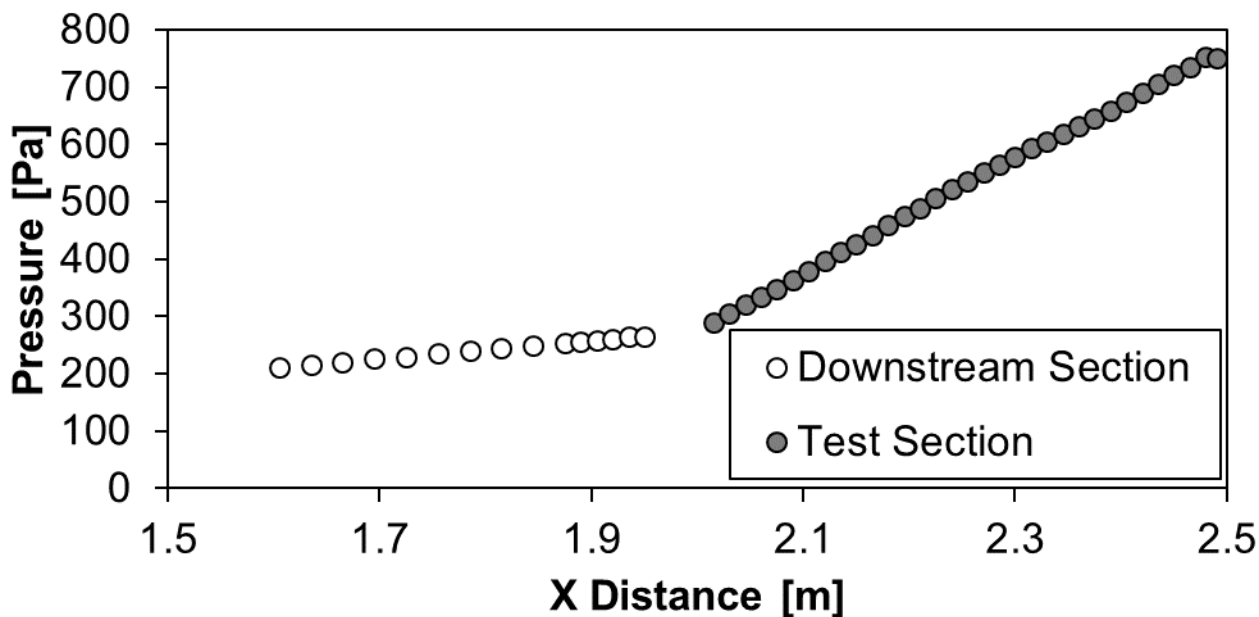


Figure D.19: Channel Pressure for mesh 4.3 and Re = 5 000

Channel Pressure (Re 6000)

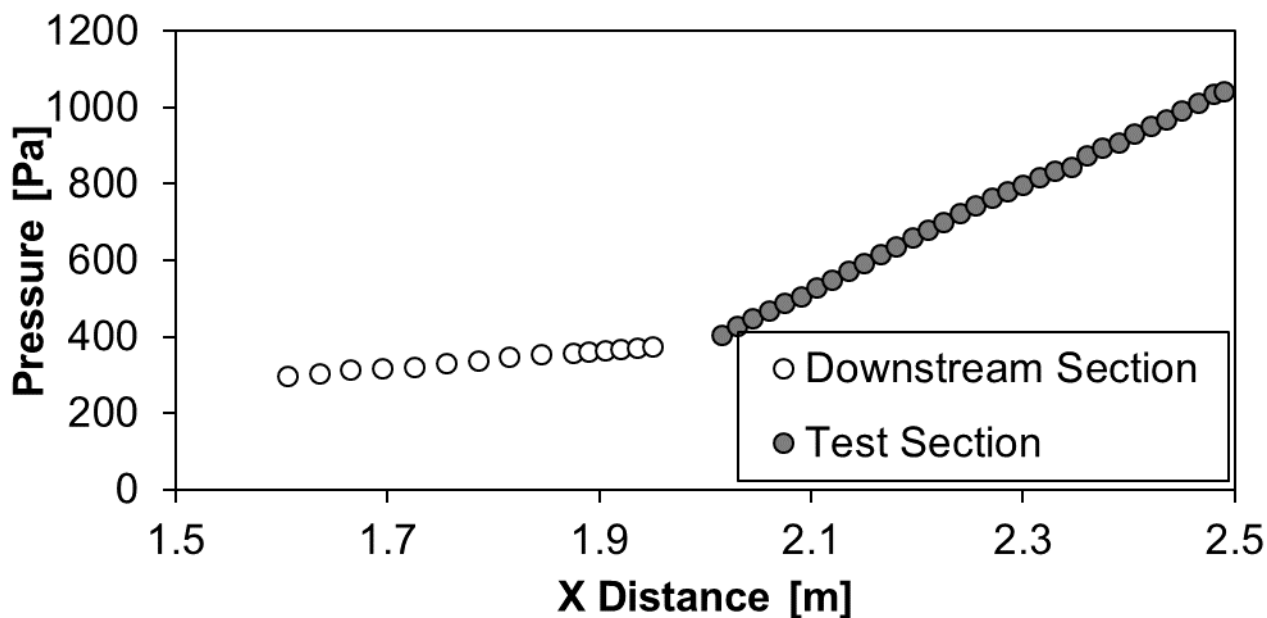


Figure D.20: Channel Pressure for mesh 4.3 and Re = 6 000

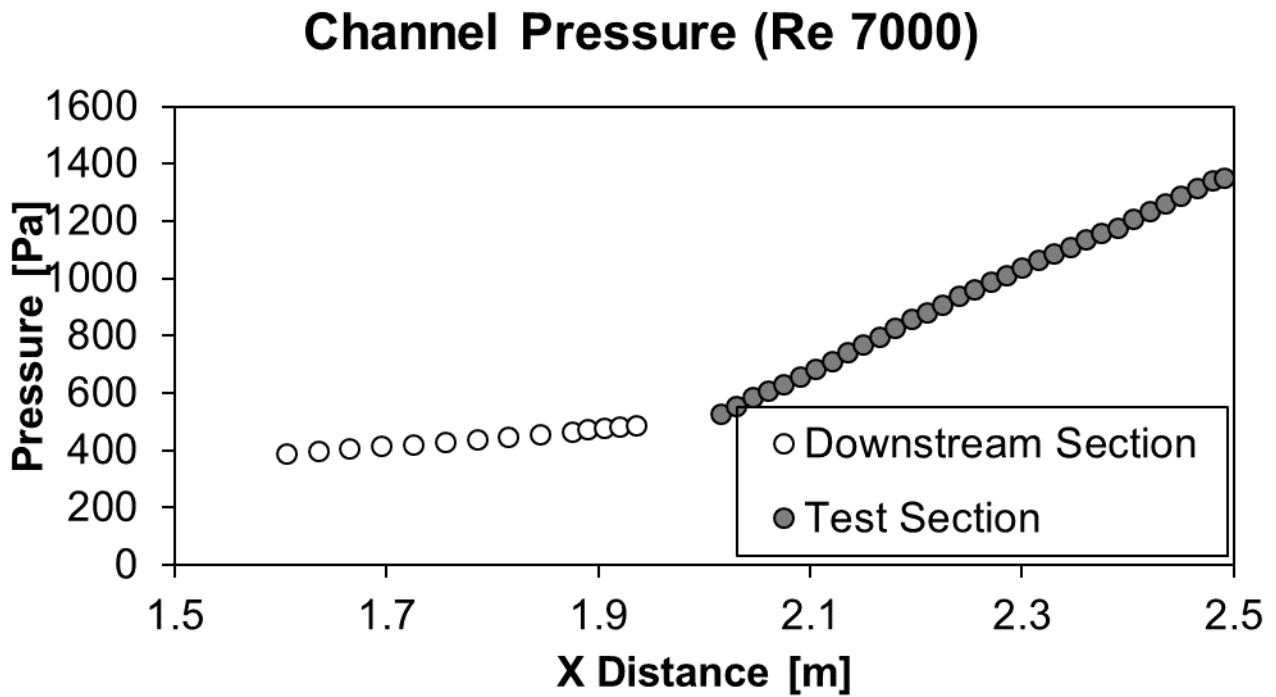


Figure D.21: Channel Pressure for mesh 4.3 and Re = 7 000

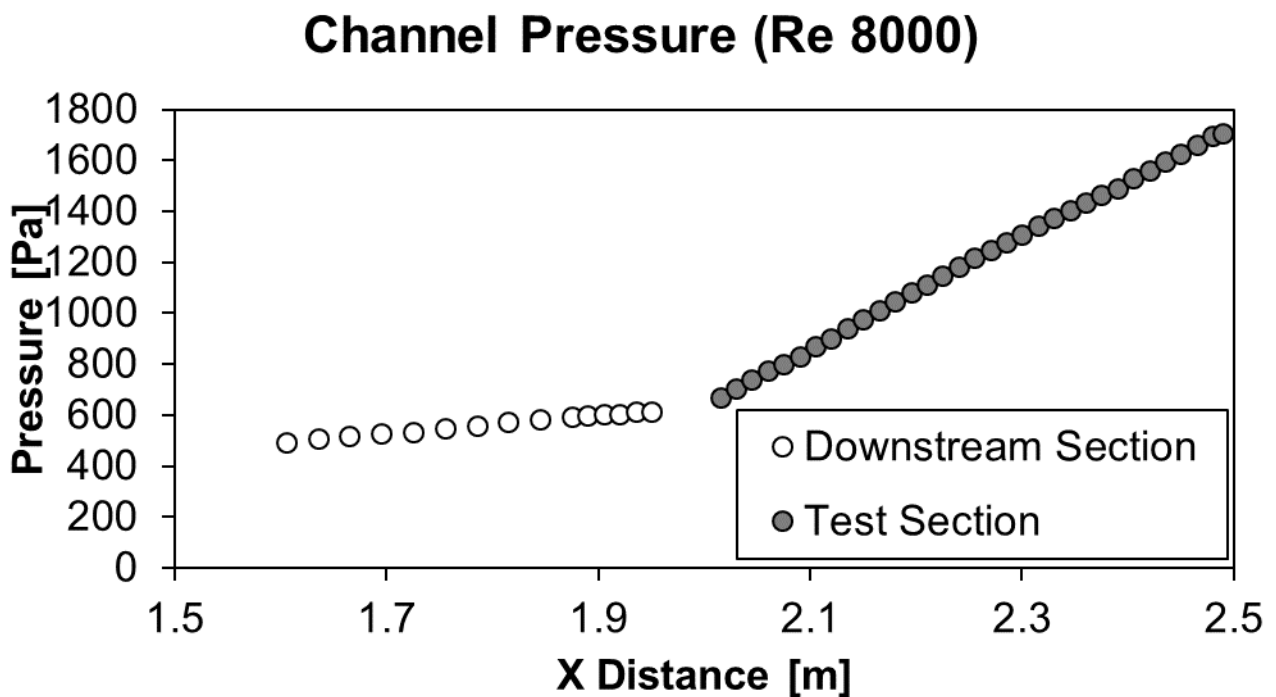


Figure D.22: Channel Pressure for mesh 4.3 and Re = 8 000

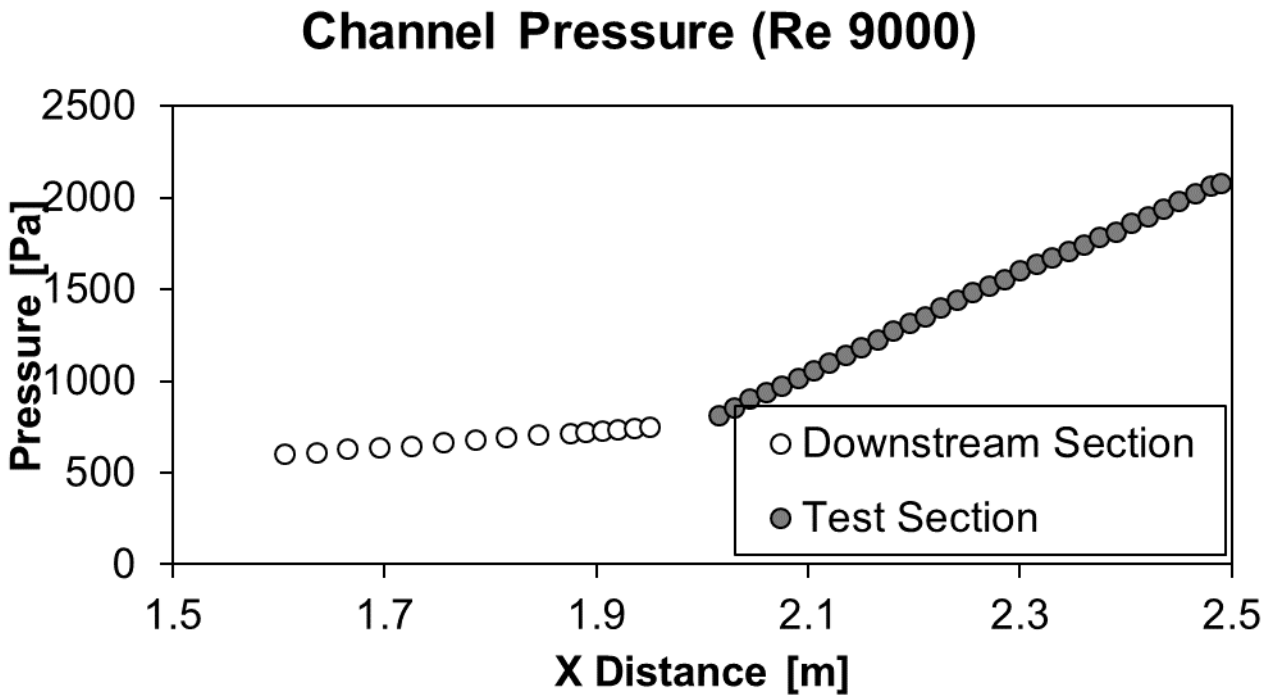


Figure D.23: Channel Pressure for mesh 4.3 and Re = 9 000

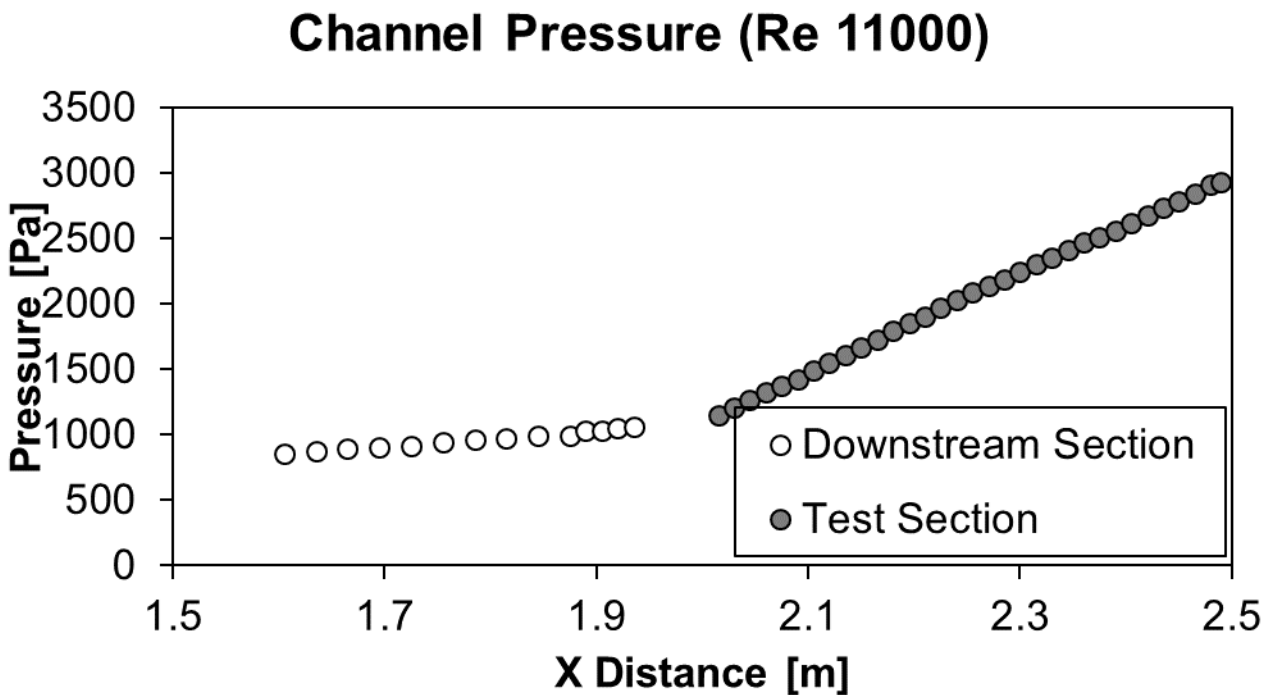


Figure D.24: Channel Pressure for mesh 4.3 and Re = 11 000

5 MM CHANNEL HEIGHT – MESH 5.1

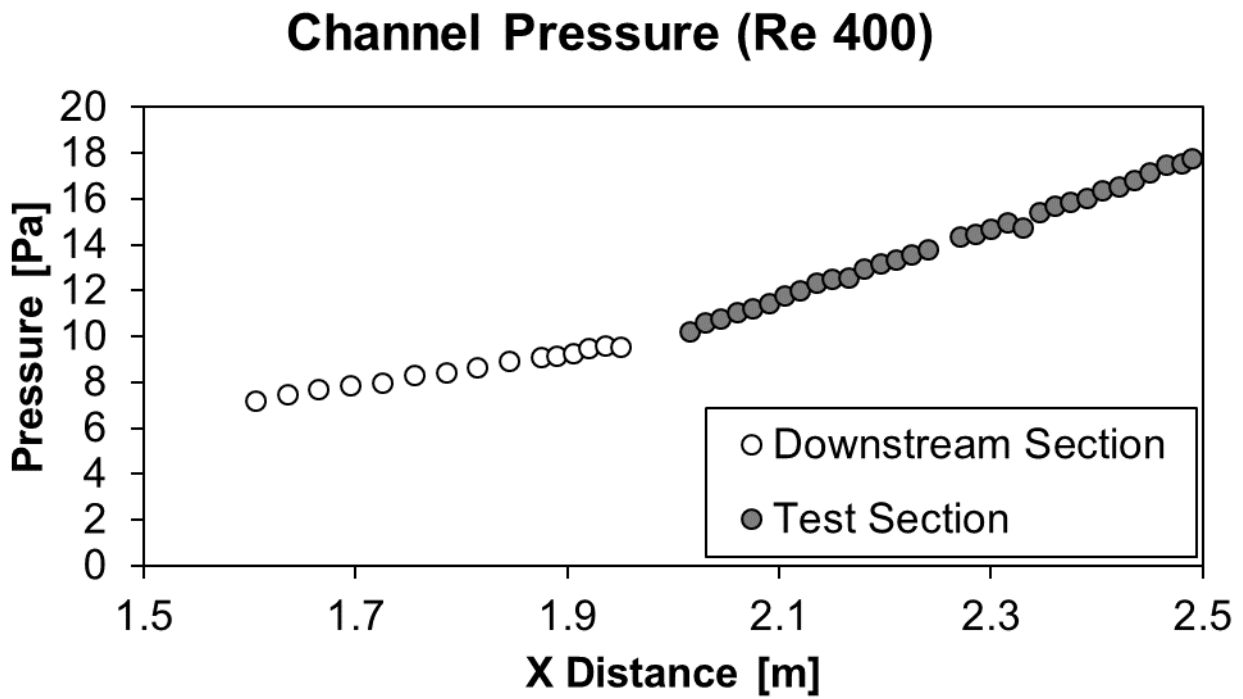


Figure D.25: Channel Pressure for mesh 5.1 and Re = 400

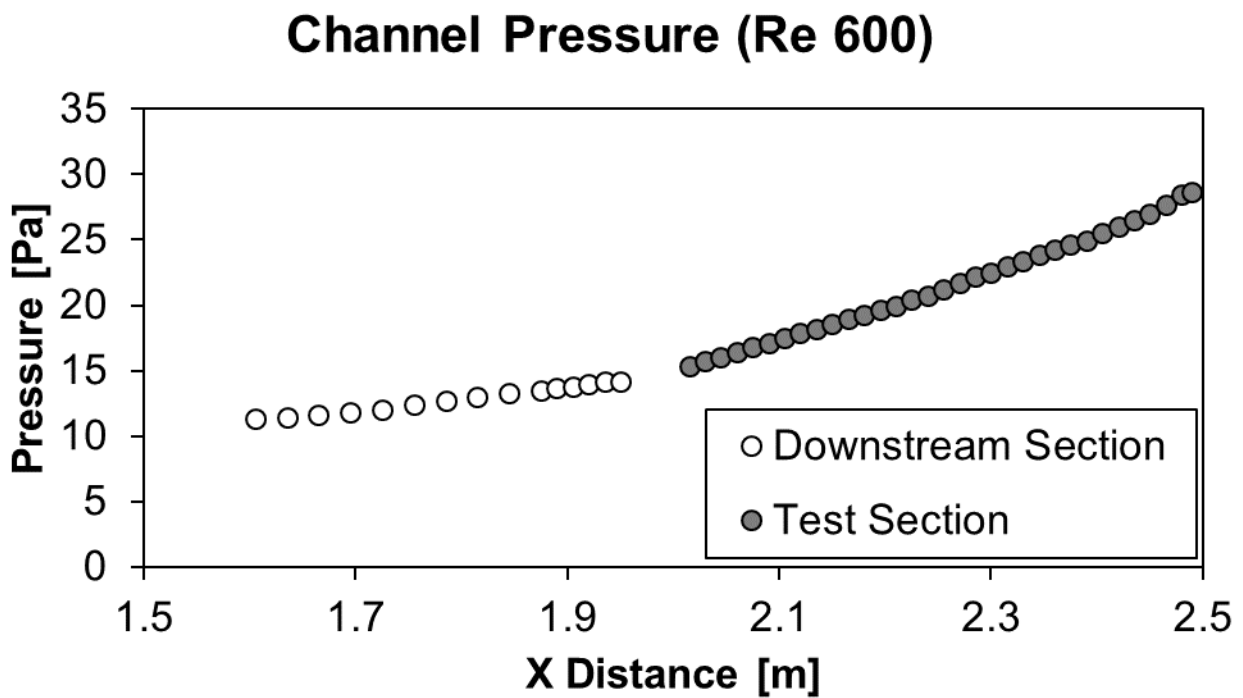


Figure D.26: Channel Pressure for mesh 5.1 and Re = 600

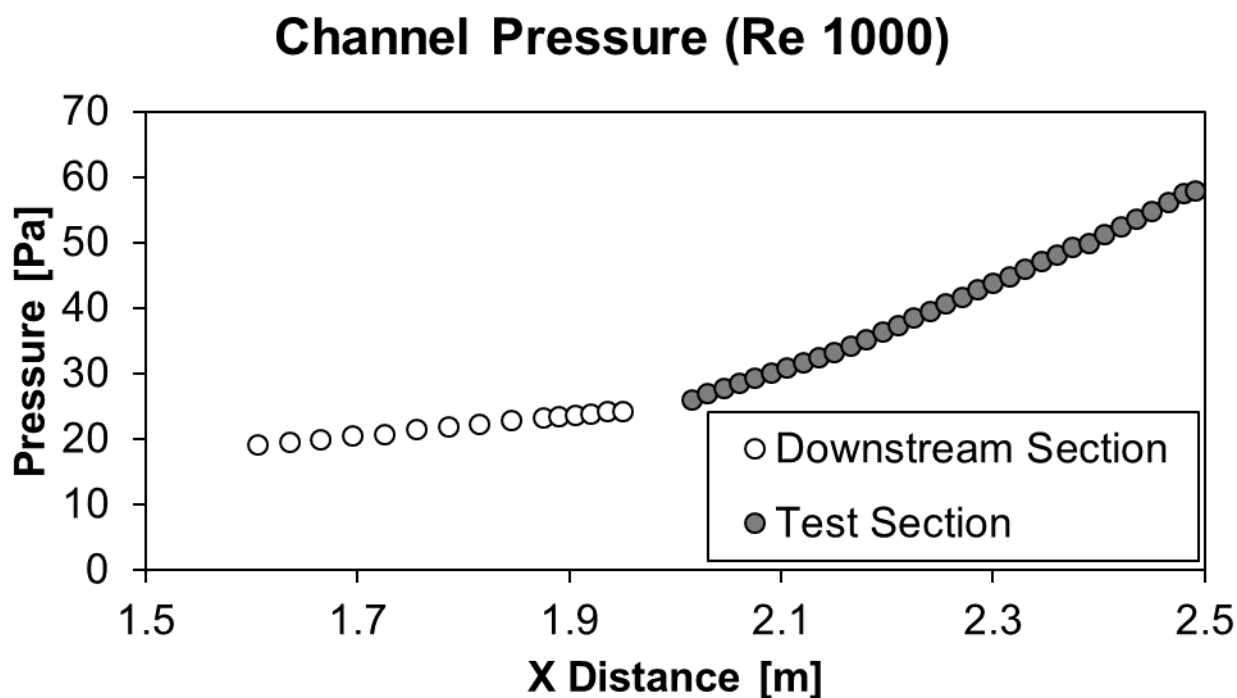


Figure D.27: Channel Pressure for mesh 5.1 and Re = 1 000

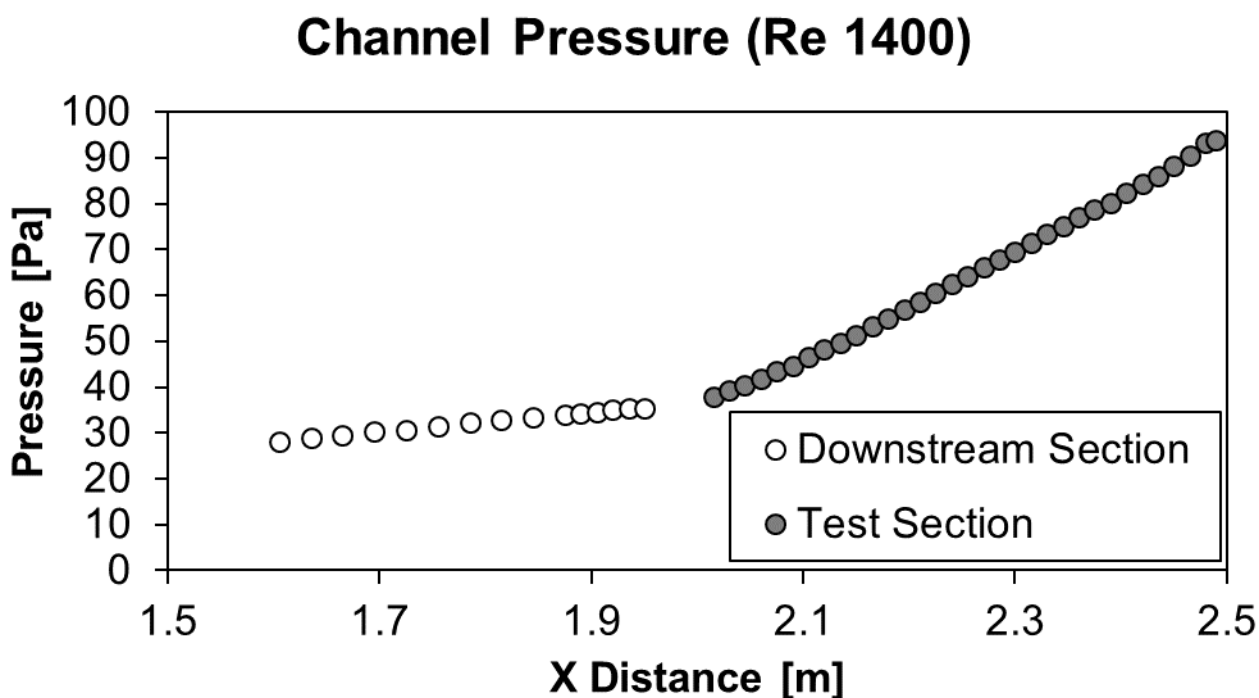


Figure D.28: Channel Pressure for mesh 5.1 and Re = 1 400

Channel Pressure (Re 3000)

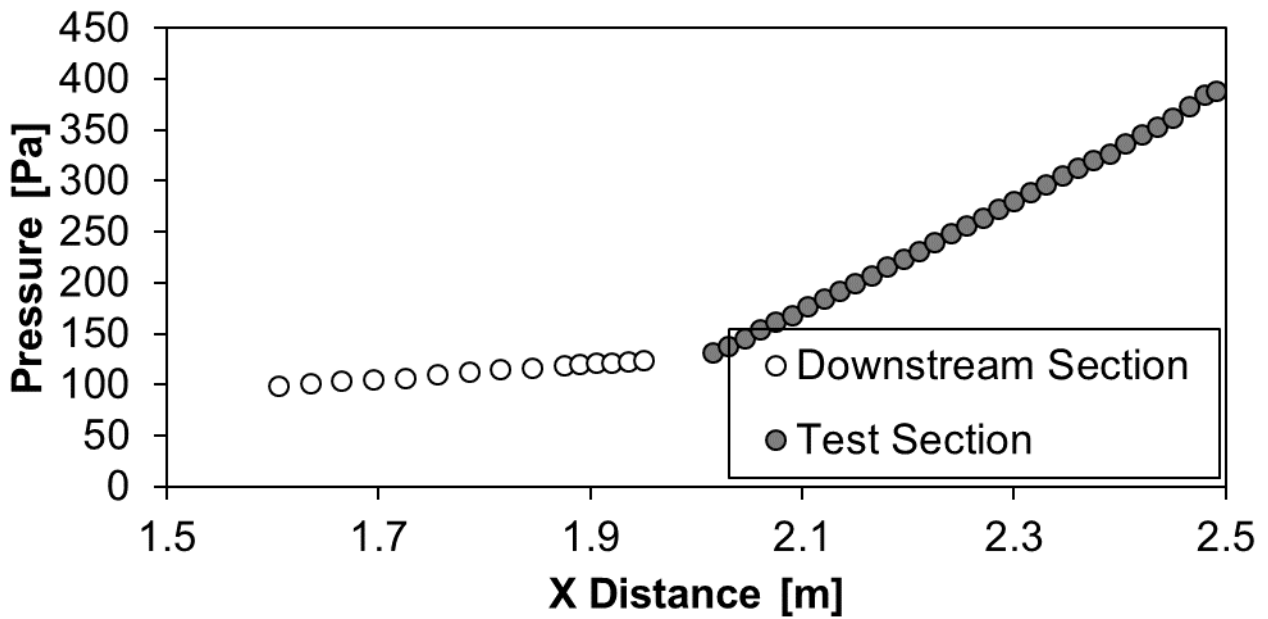


Figure D.29: Channel Pressure for mesh 5.1 and Re = 3 000

Channel Pressure (Re 4000)

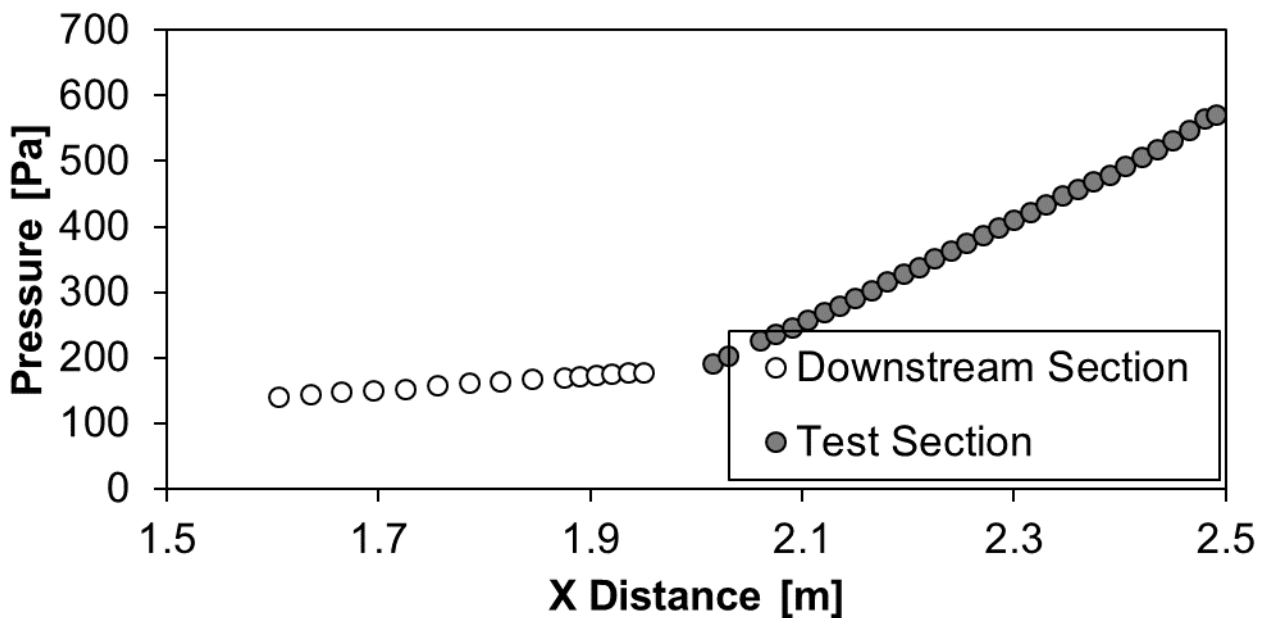


Figure D.30: Channel Pressure for mesh 5.1 and Re = 4 000

Channel Pressure (Re 5000)

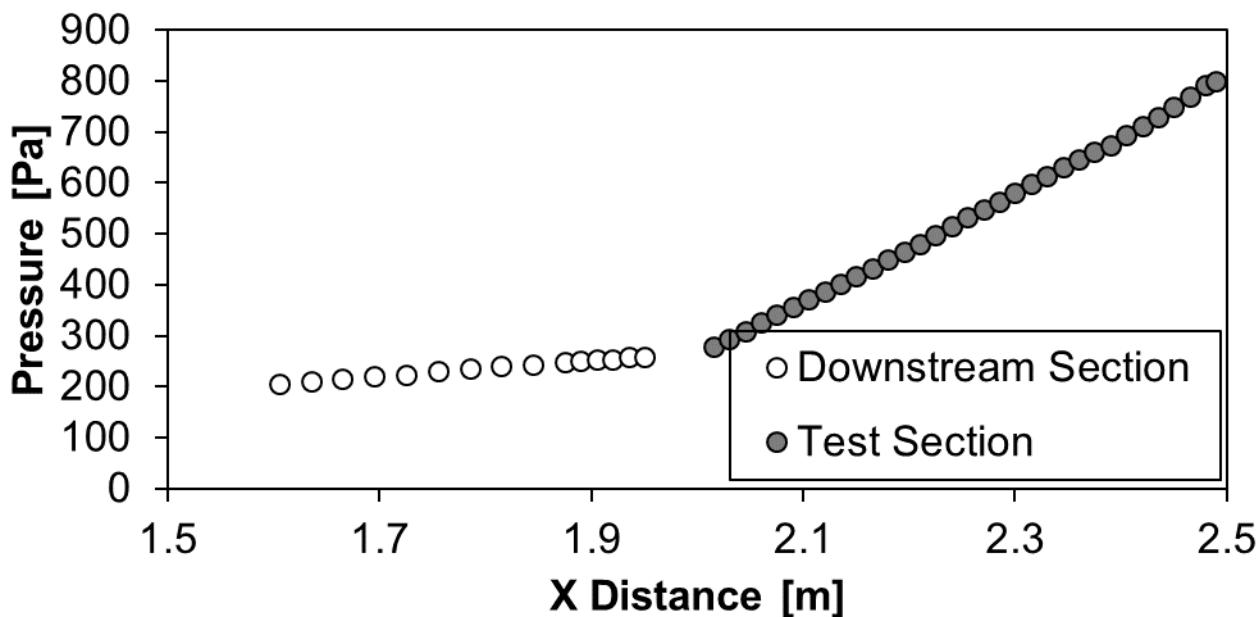


Figure D.31: Channel Pressure for mesh 5.1 and Re = 5 000

Channel Pressure (Re 6000)

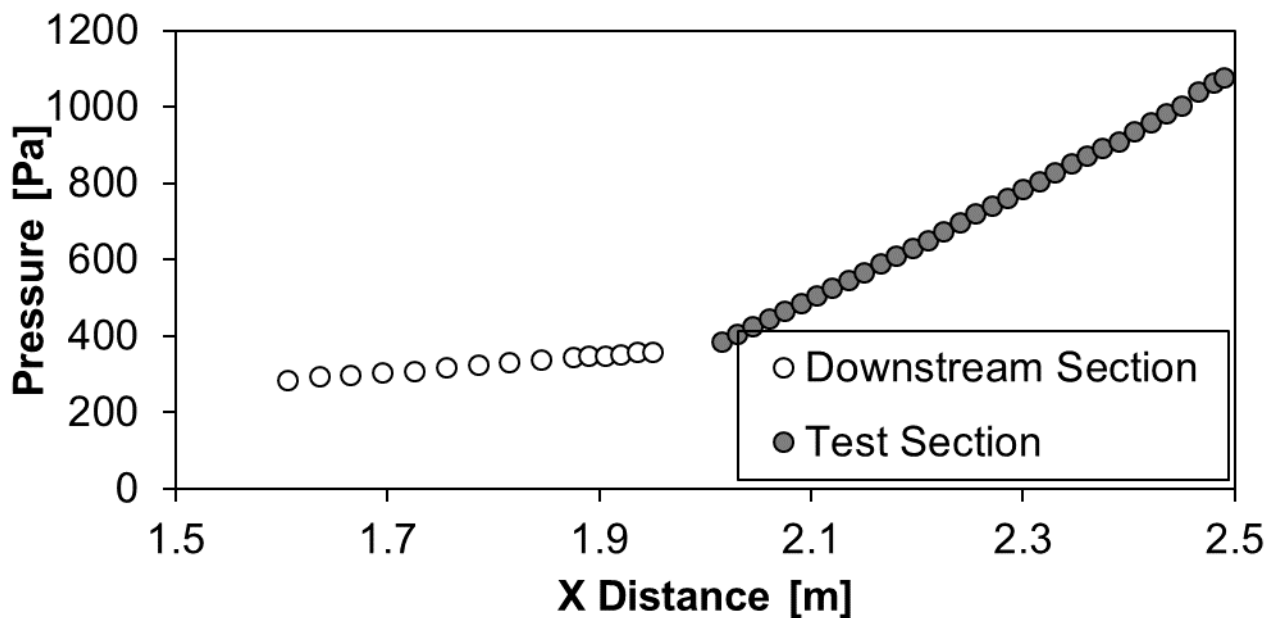


Figure D.32: Channel Pressure for mesh 5.1 and Re = 6 000

Channel Pressure (Re 7000)

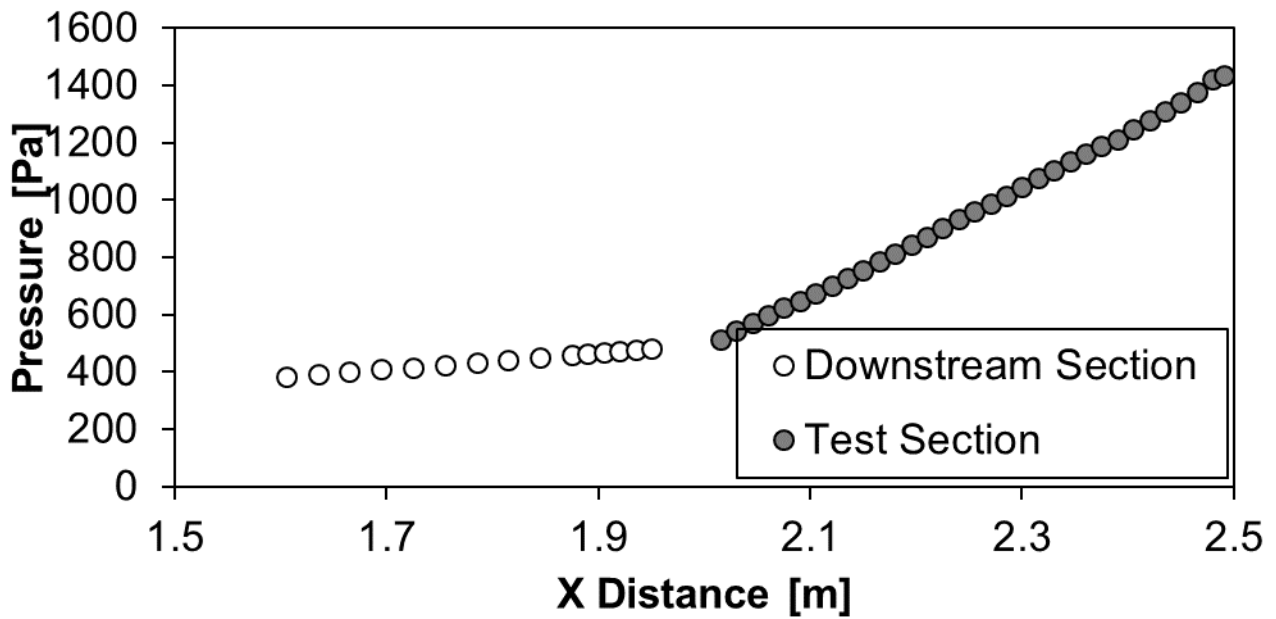


Figure D.33: Channel Pressure for mesh 5.1 and Re = 7 000

Channel Pressure (Re 8000)

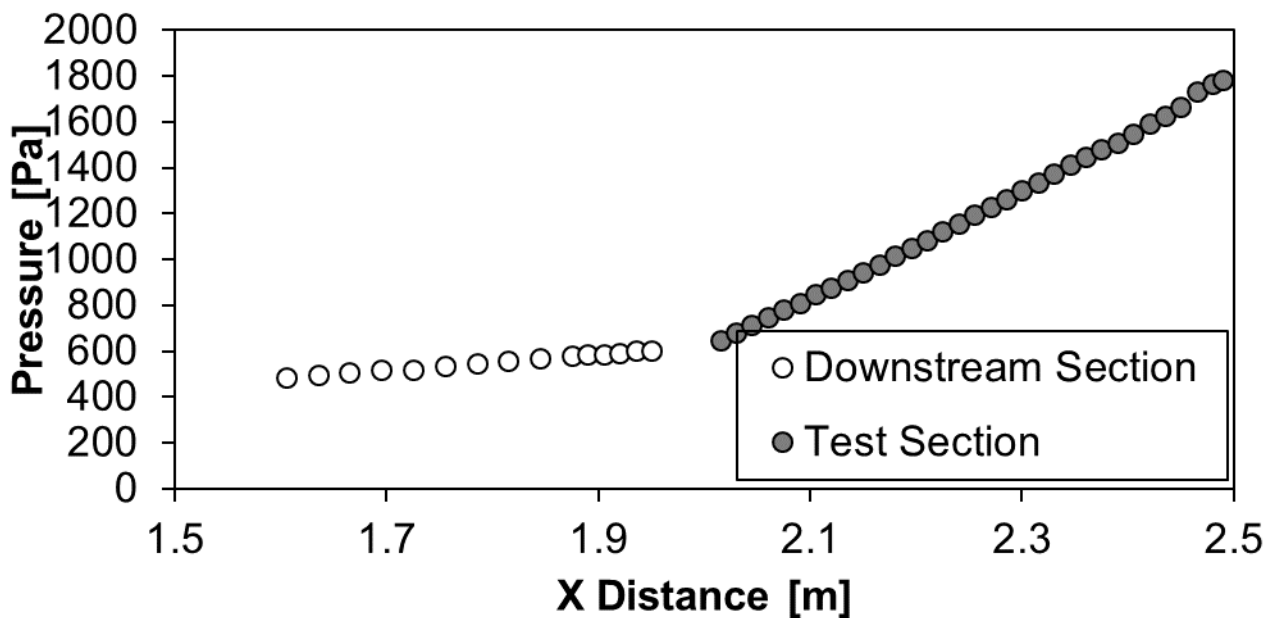


Figure D.34: Channel Pressure for mesh 5.1 and Re = 8 000

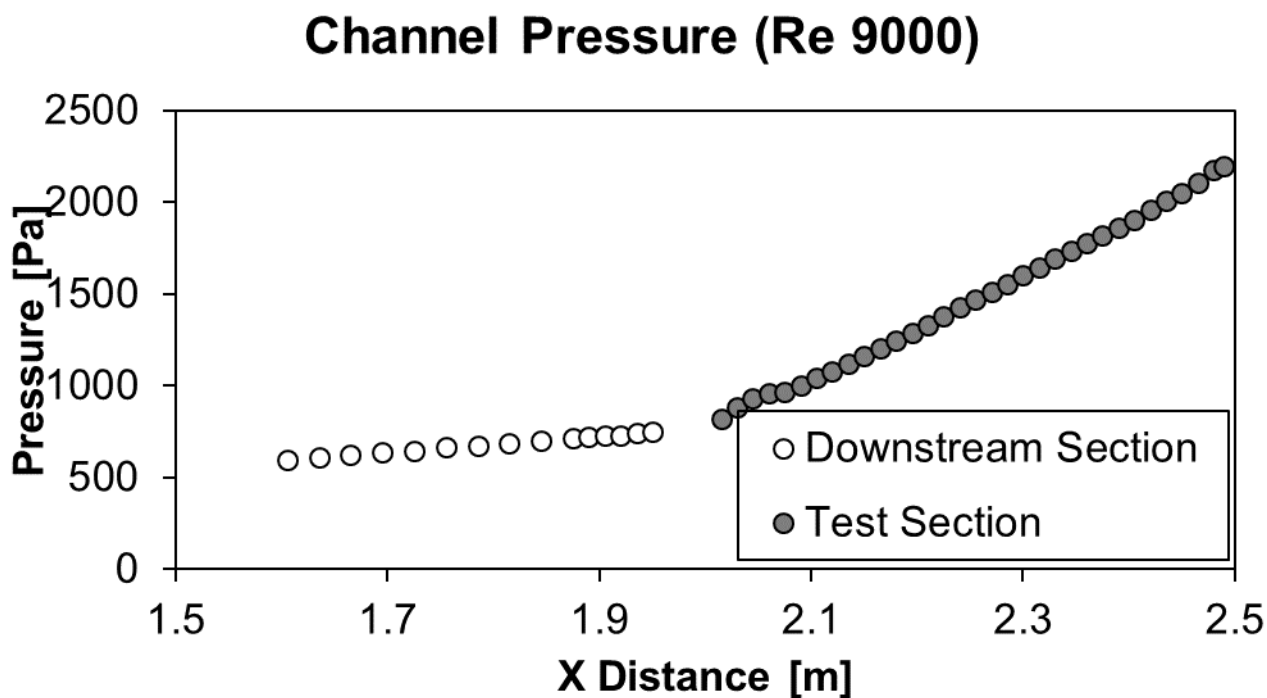


Figure D.35: Channel Pressure for mesh 5.1 and Re = 9 000

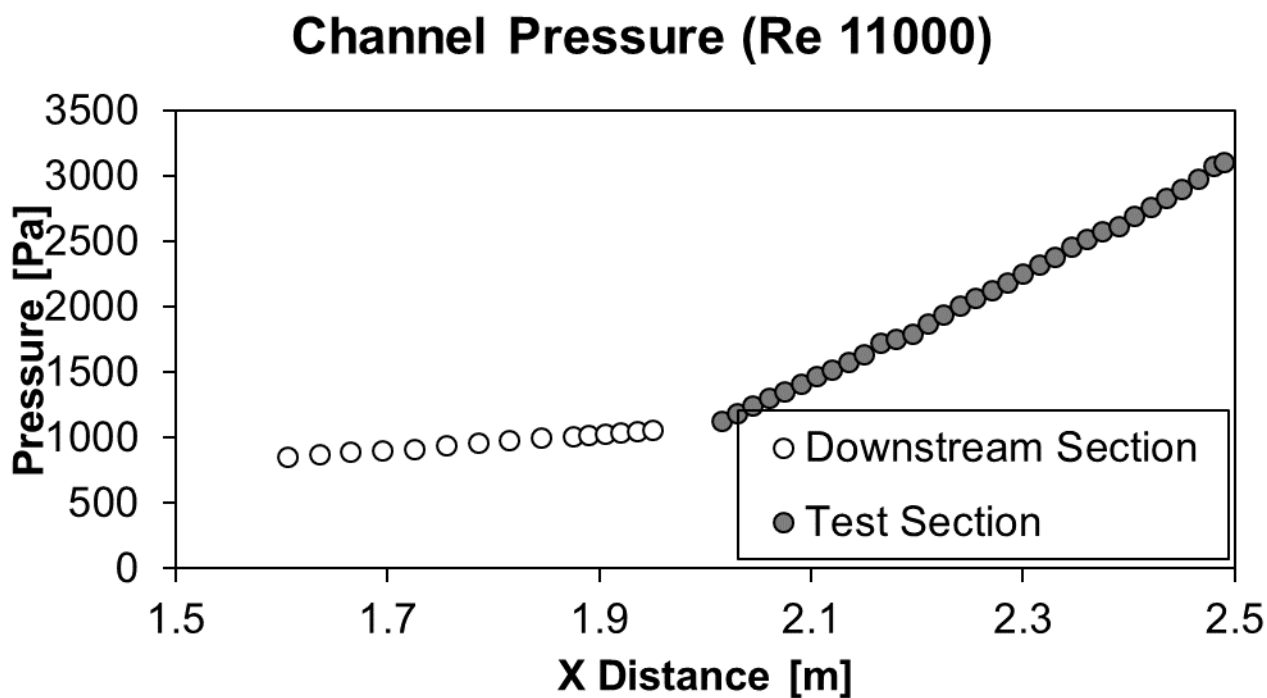


Figure D.36: Channel Pressure for mesh 5.1 and Re = 11 000

5 MM CHANNEL HEIGHT – MESH 5.3

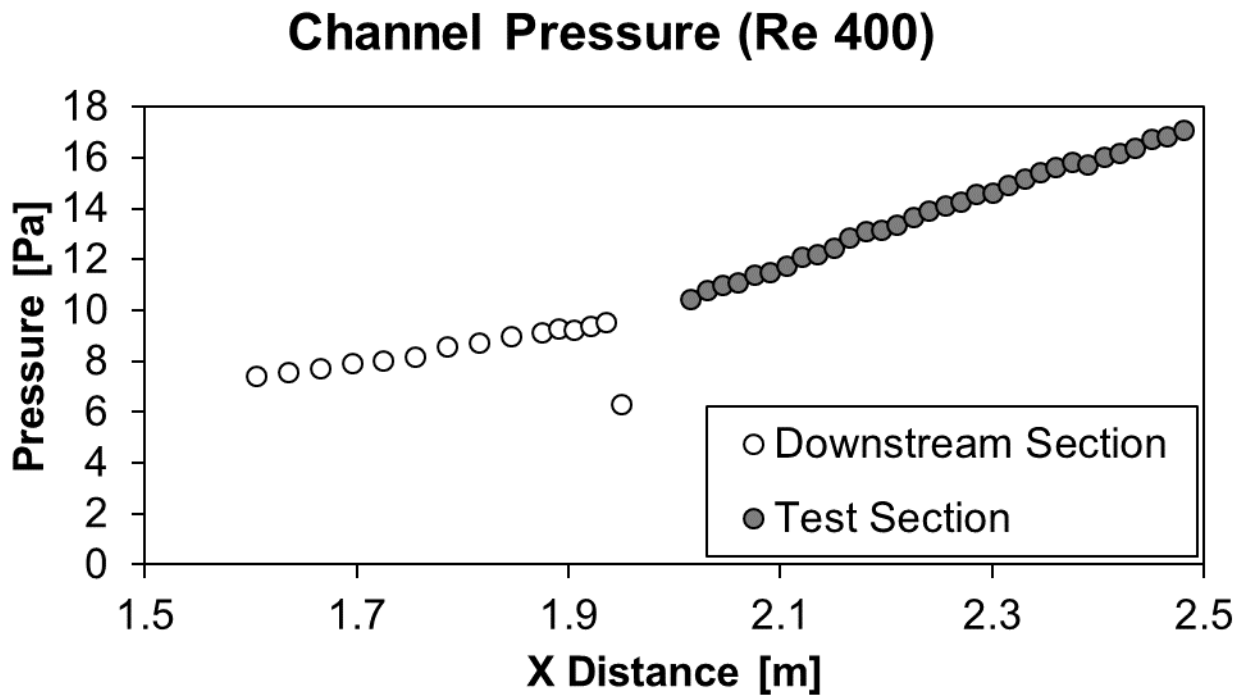


Figure D.37: Channel Pressure for mesh 5.3 and Re = 400

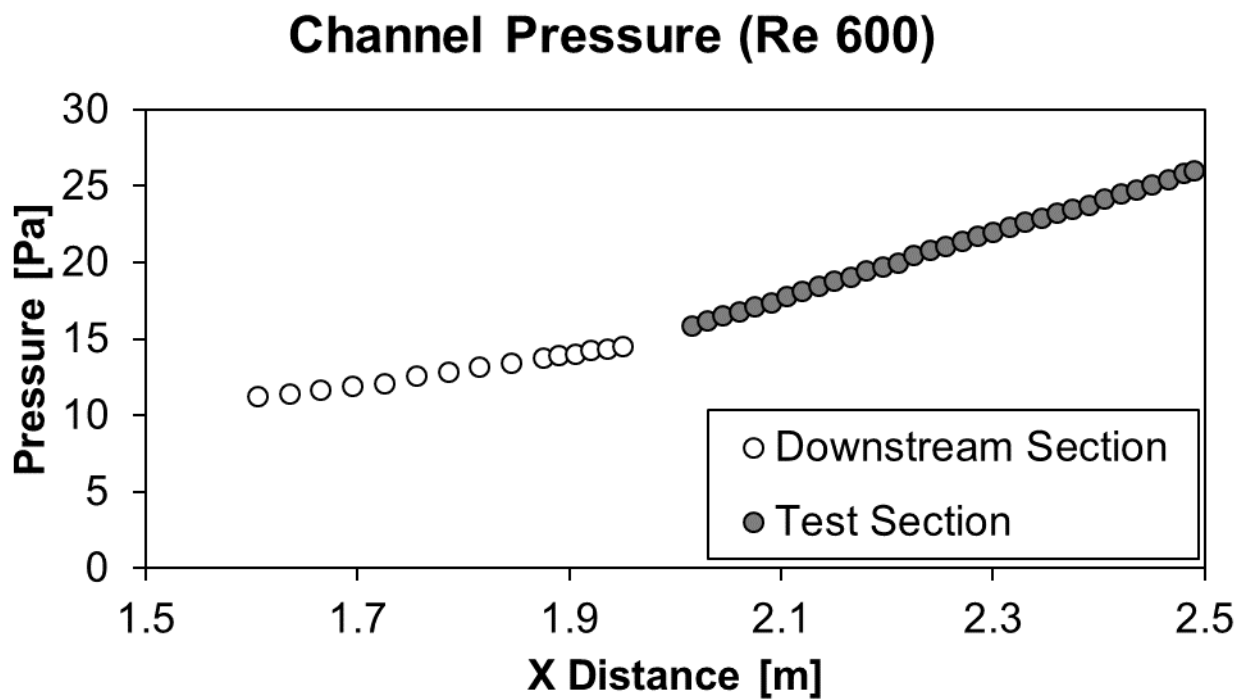


Figure D.38: Channel Pressure for mesh 5.3 and Re = 600

Channel Pressure (Re 1000)

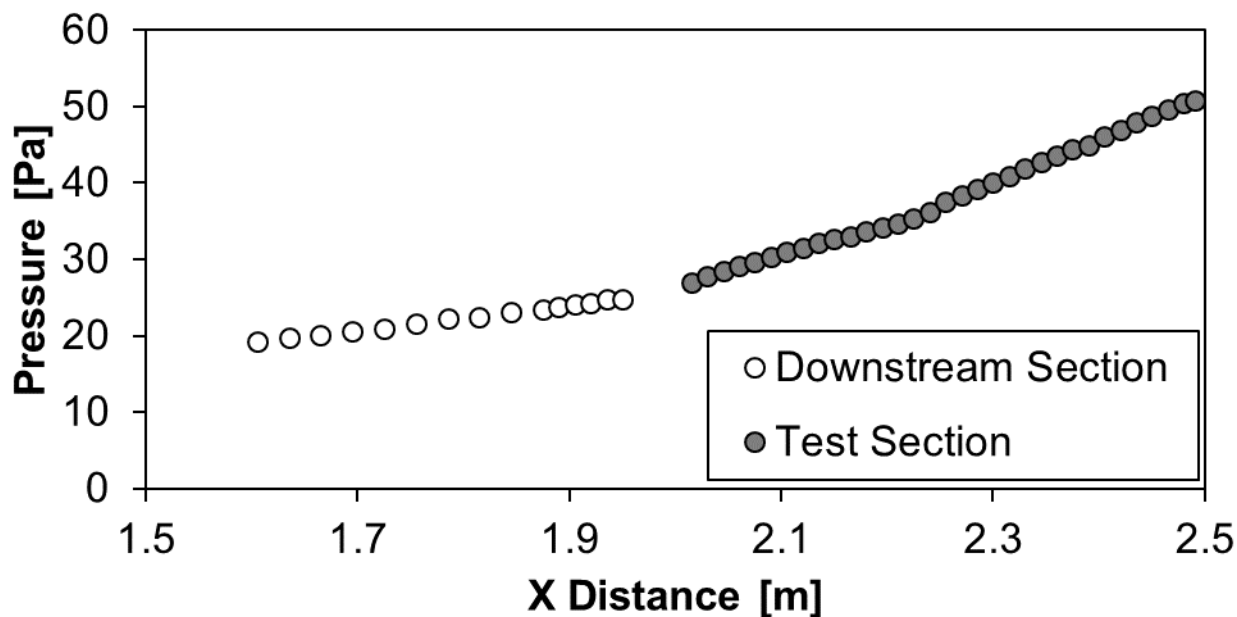


Figure D.39: Channel Pressure for mesh 5.3 and Re = 1 000

Channel Pressure (Re 1400)

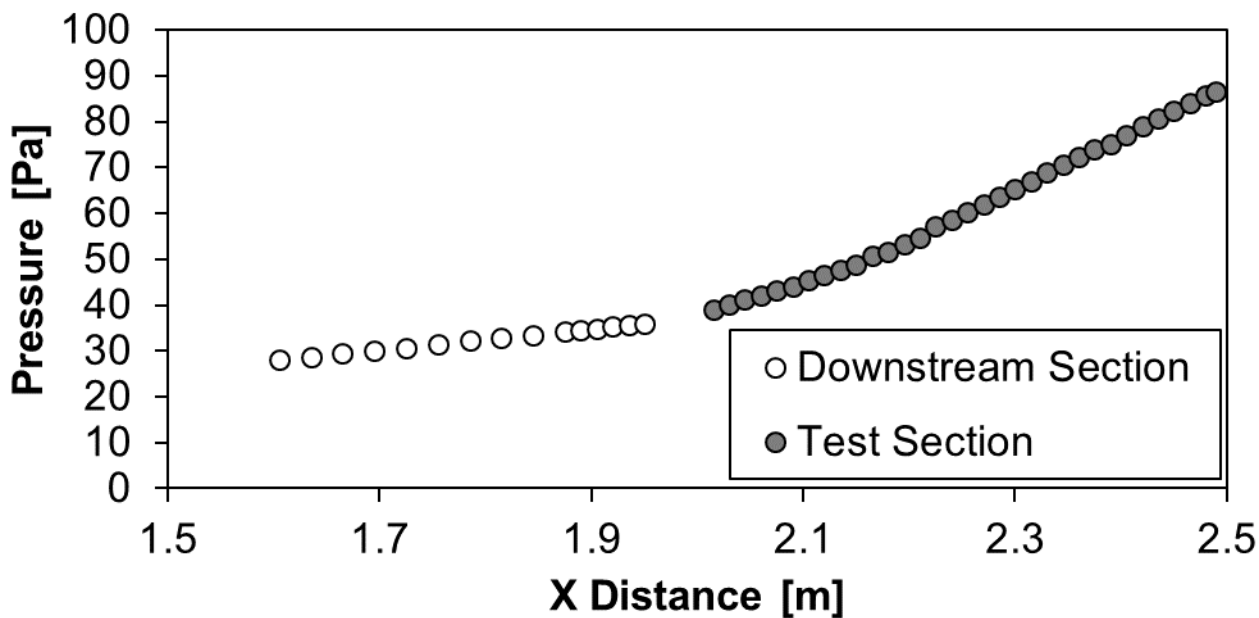


Figure D.40: Channel Pressure for mesh 5.3 and Re = 1 400

Channel Pressure (Re 3000)

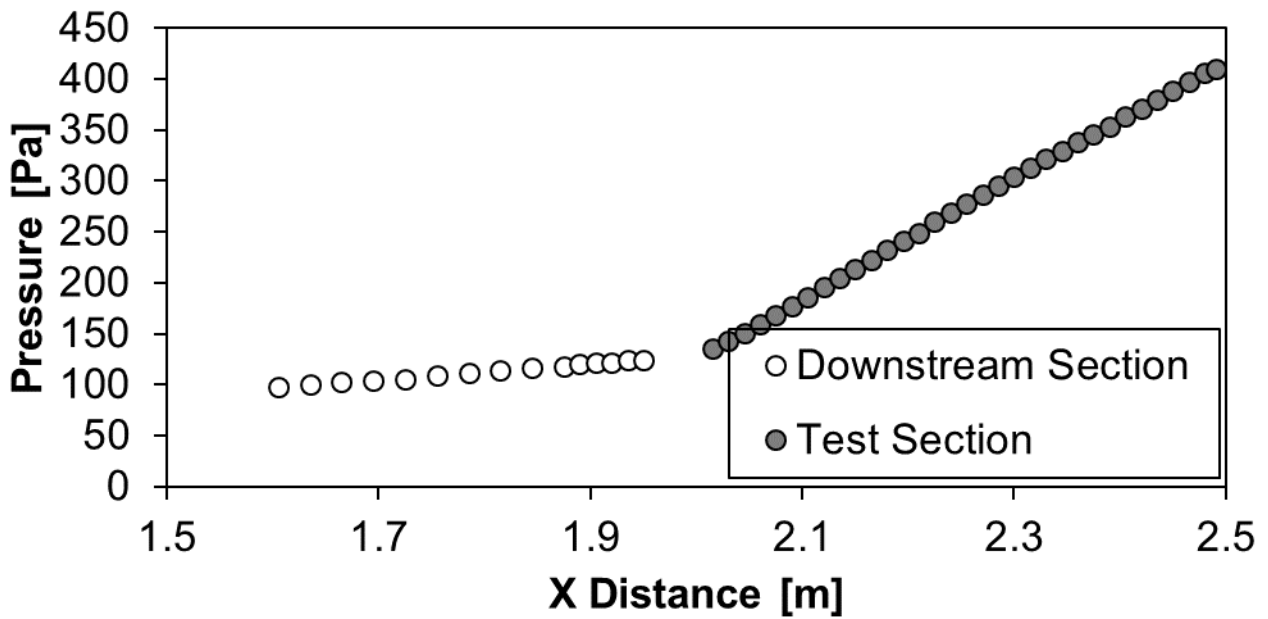


Figure D.41: Channel Pressure for mesh 5.3 and Re = 3 000

Channel Pressure (Re 4000)

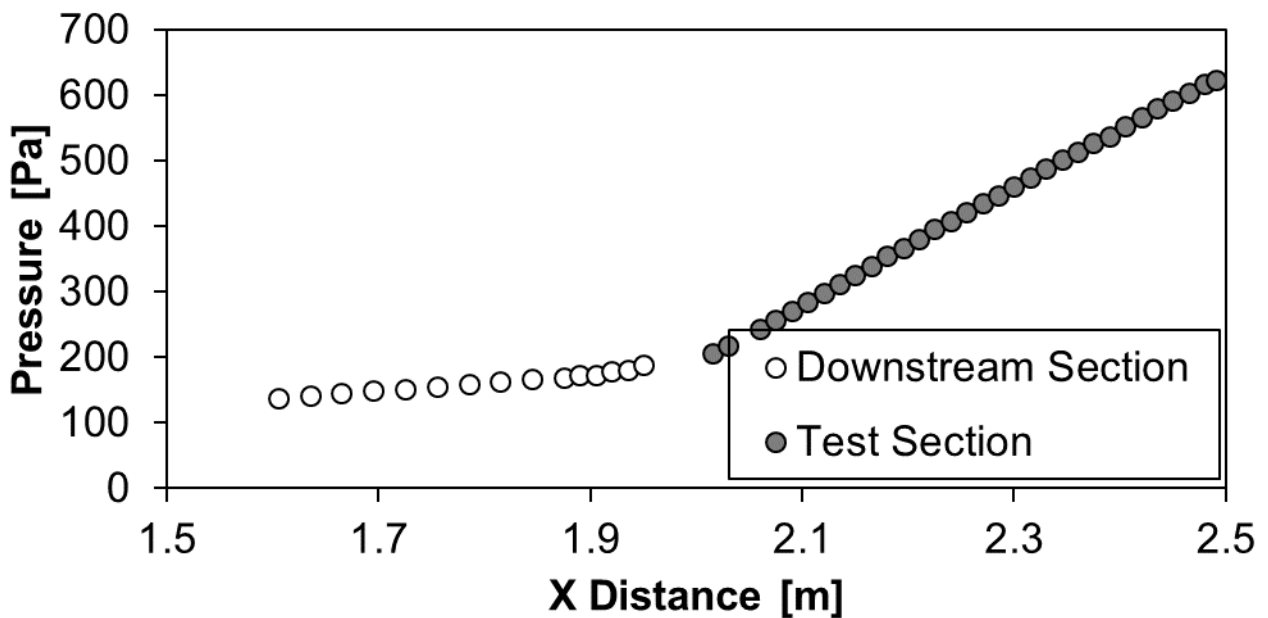


Figure D.42: Channel Pressure for mesh 5.3 and Re = 4 000

Channel Pressure (Re 5000)

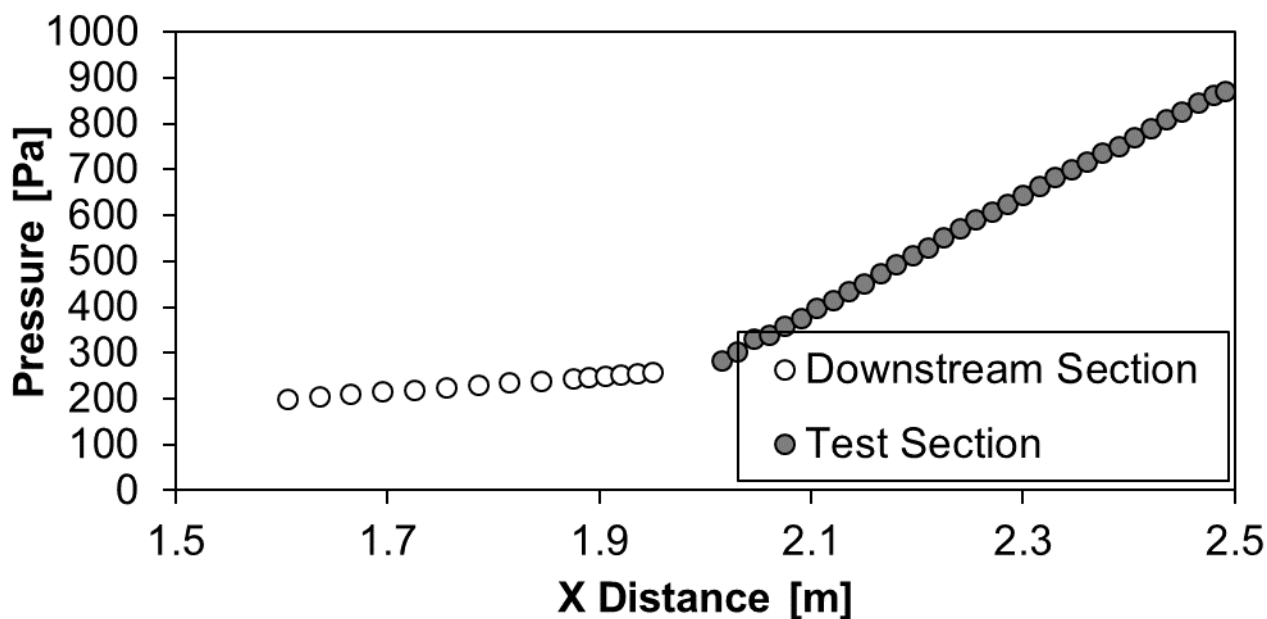


Figure D.43: Channel Pressure for mesh 5.3 and Re = 5 000

Channel Pressure (Re 6000)

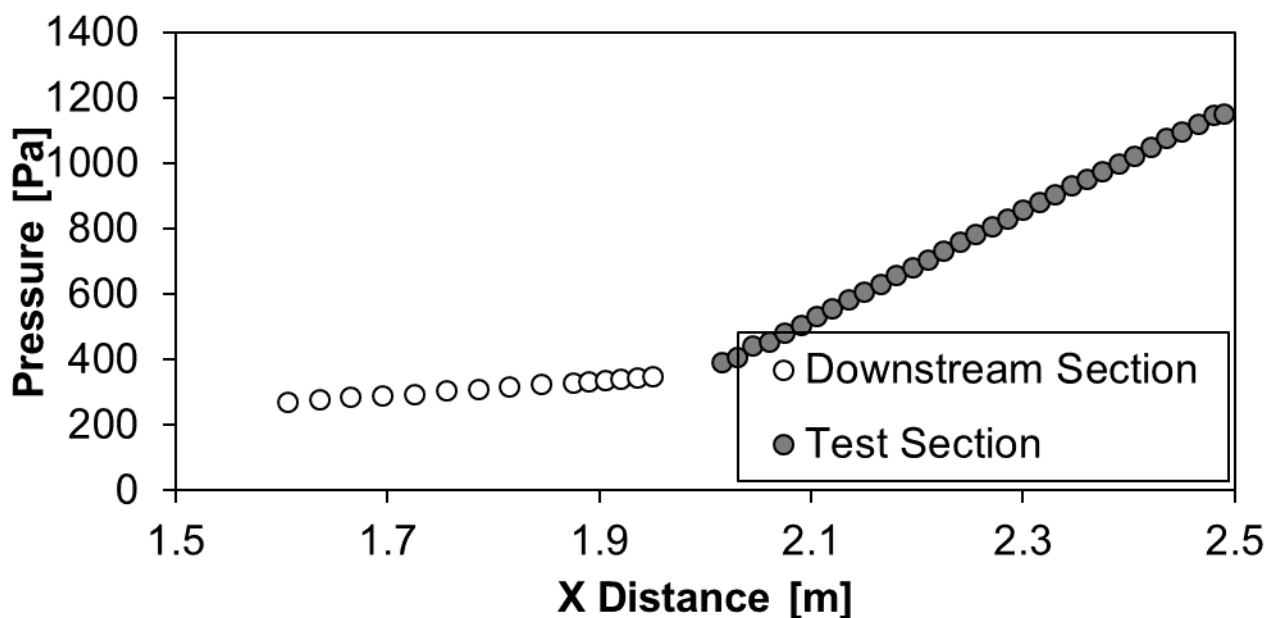


Figure D.44: Channel Pressure for mesh 5.3 and Re = 6 000

Channel Pressure (Re 7000)

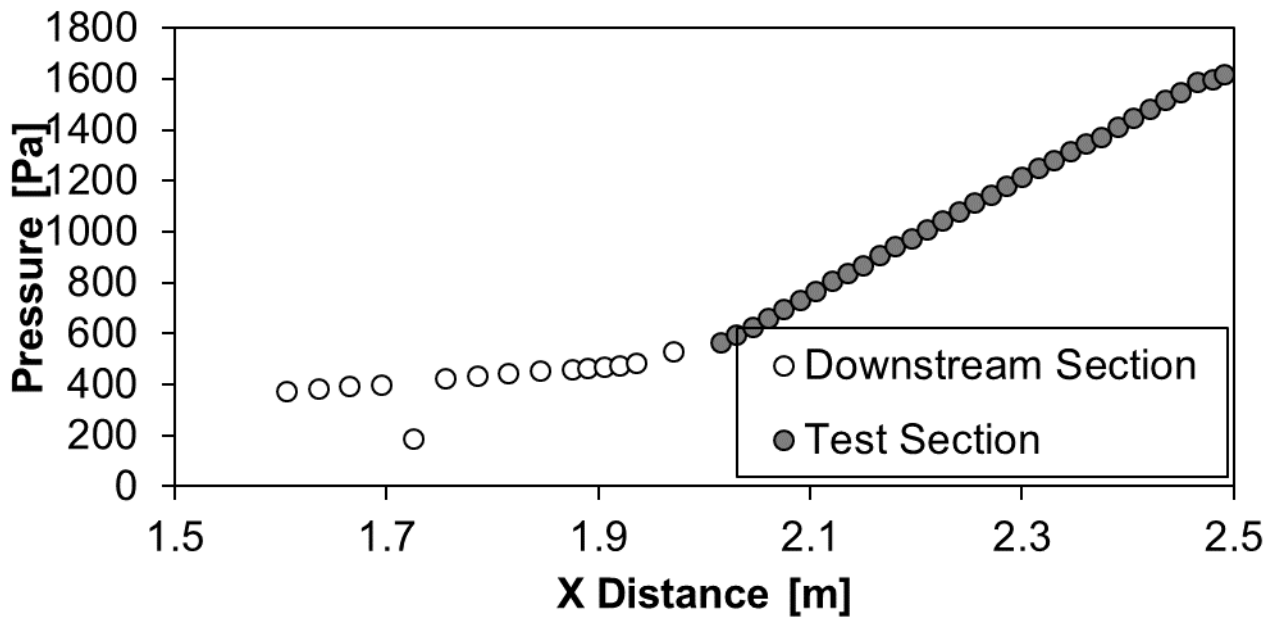


Figure D.45: Channel Pressure for mesh 5.3 and Re = 7 000

Channel Pressure (Re 8000)

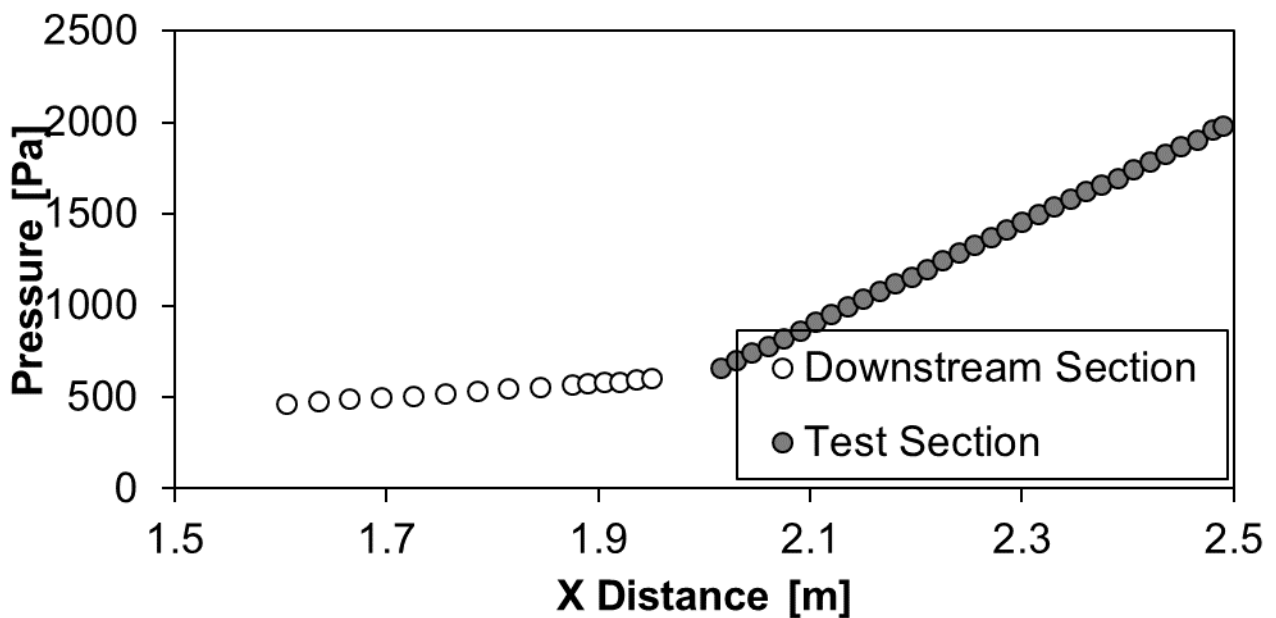


Figure D.46: Channel Pressure for mesh 5.3 and Re = 8 000

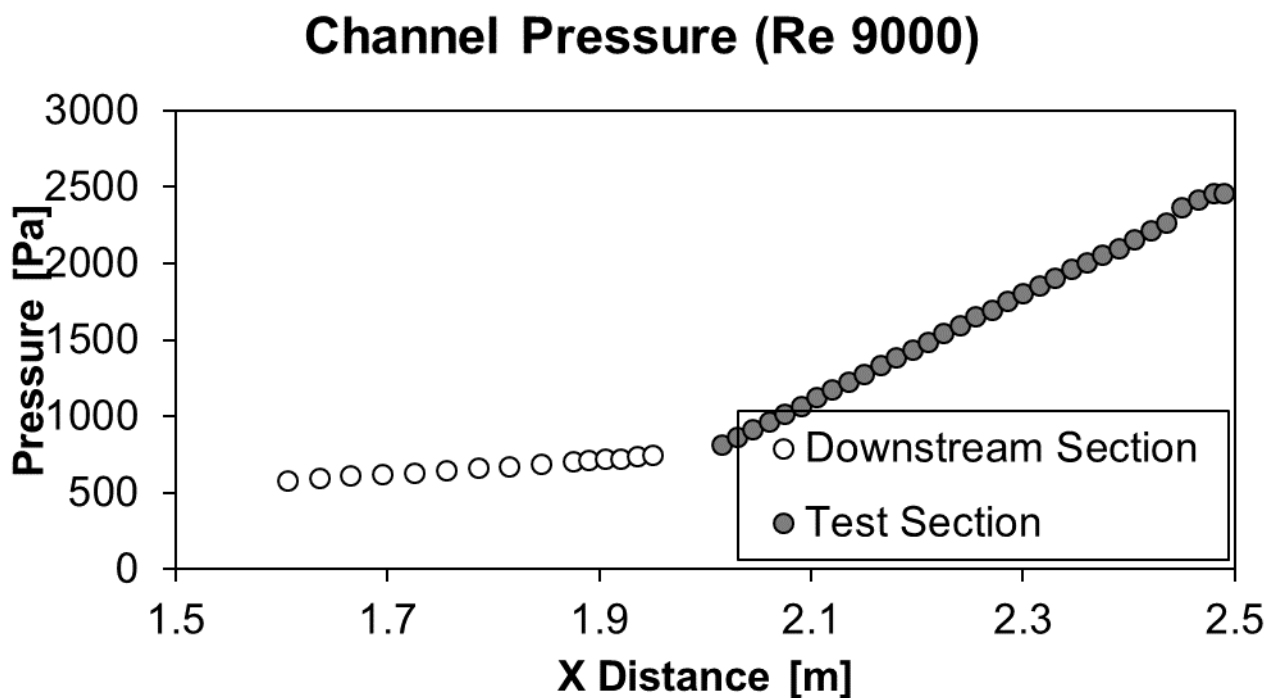


Figure D.47: Channel Pressure for mesh 5.3 and Re = 9 000

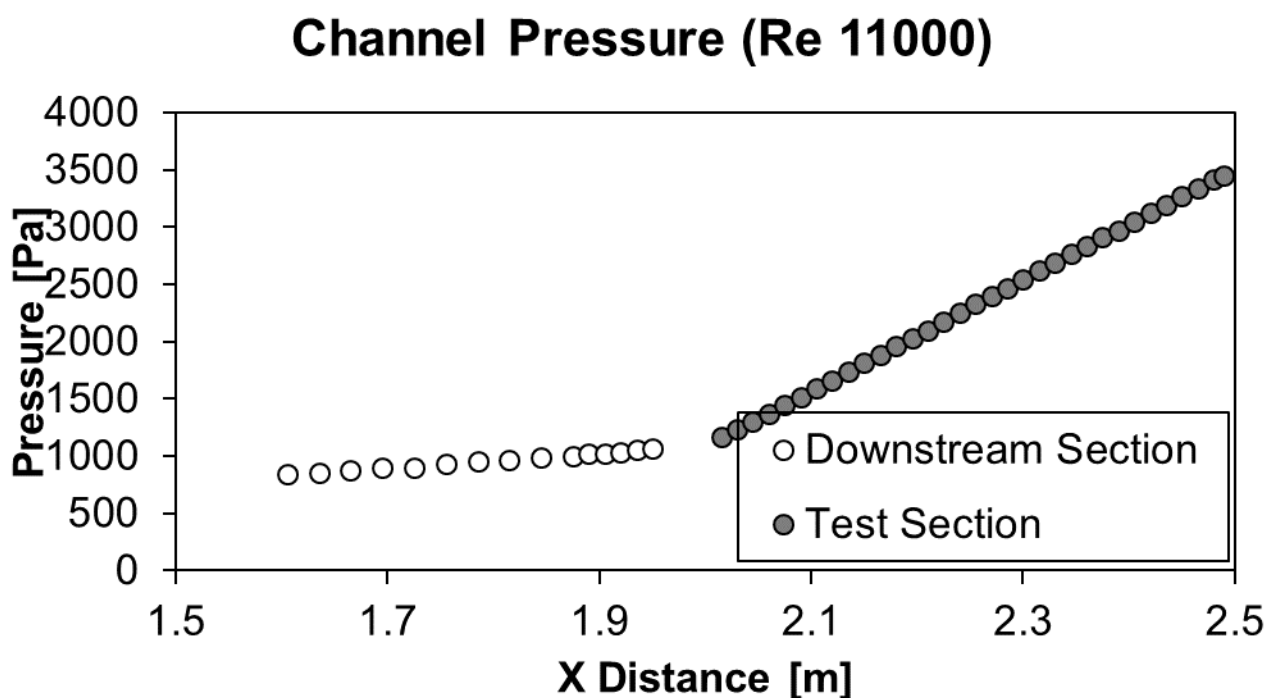


Figure D.48: Channel Pressure for mesh 5.3 and Re = 11 000

14 MM CHANNEL HEIGHT – MESH 2.1

Channel Pressure (Re 400)

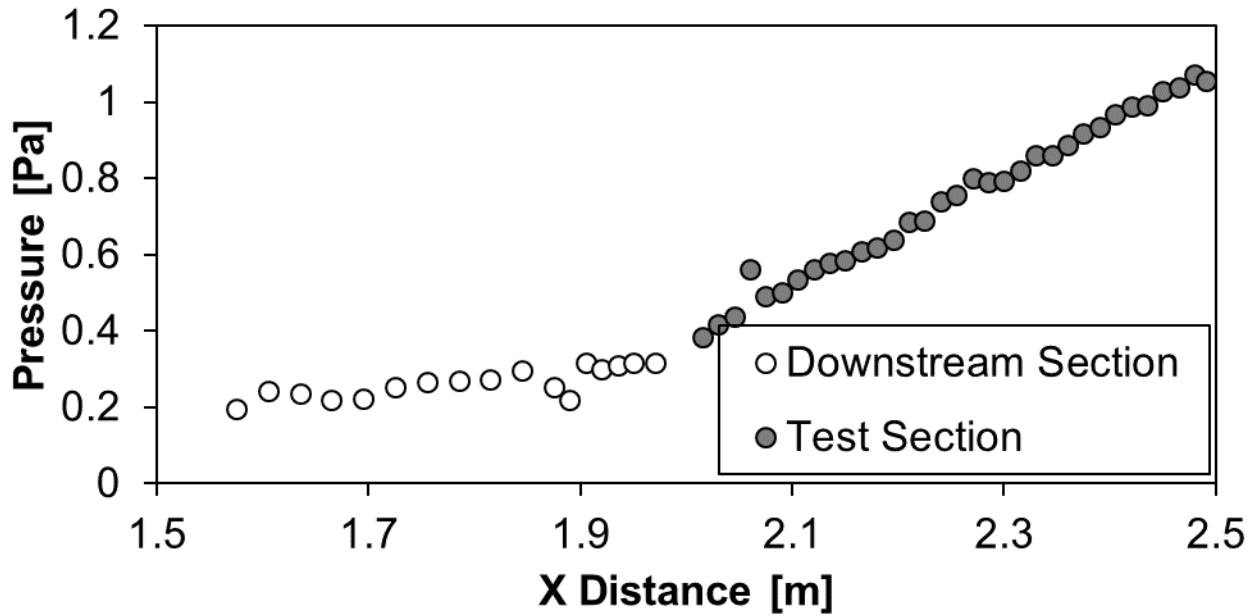


Figure D.49: Channel Pressure for mesh 2.1 and Re = 400

Channel Pressure (Re 1000)

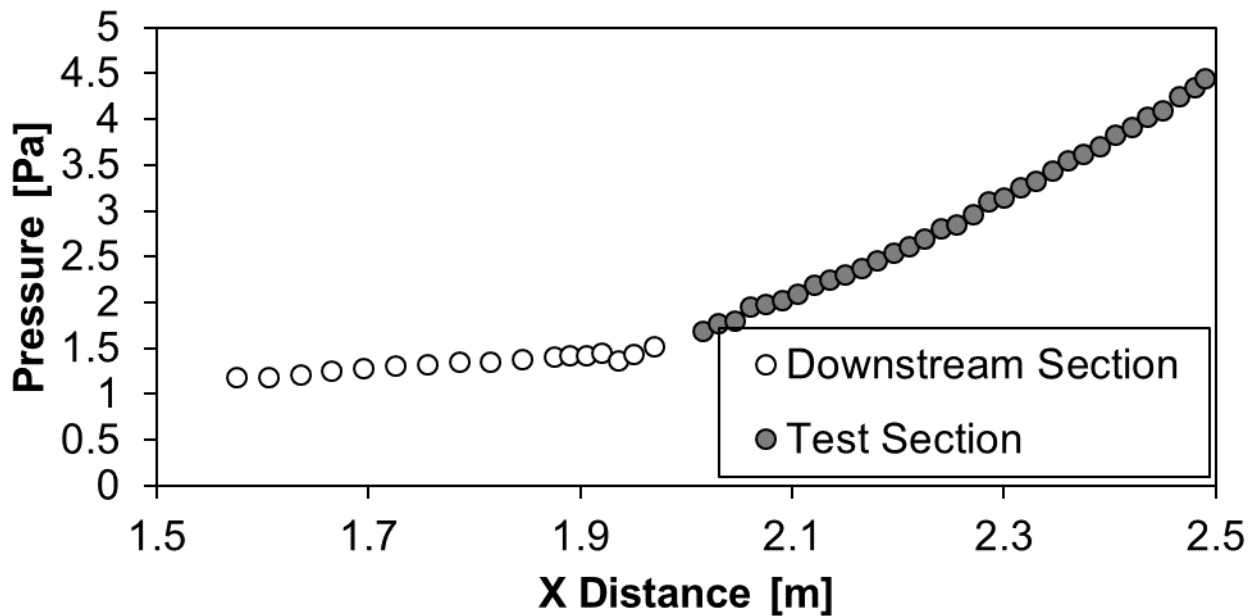


Figure D.50: Channel Pressure for mesh 2.1 and Re = 1 000

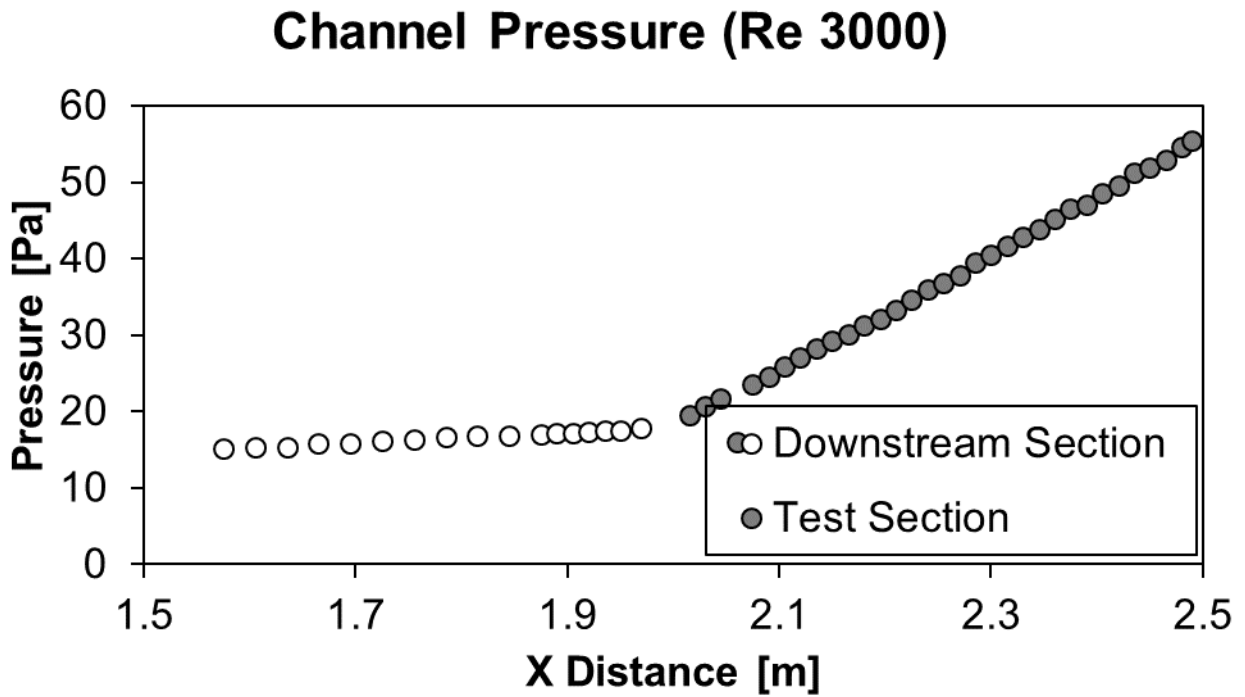


Figure D.51: Channel Pressure for mesh 2.1 and Re = 3 000

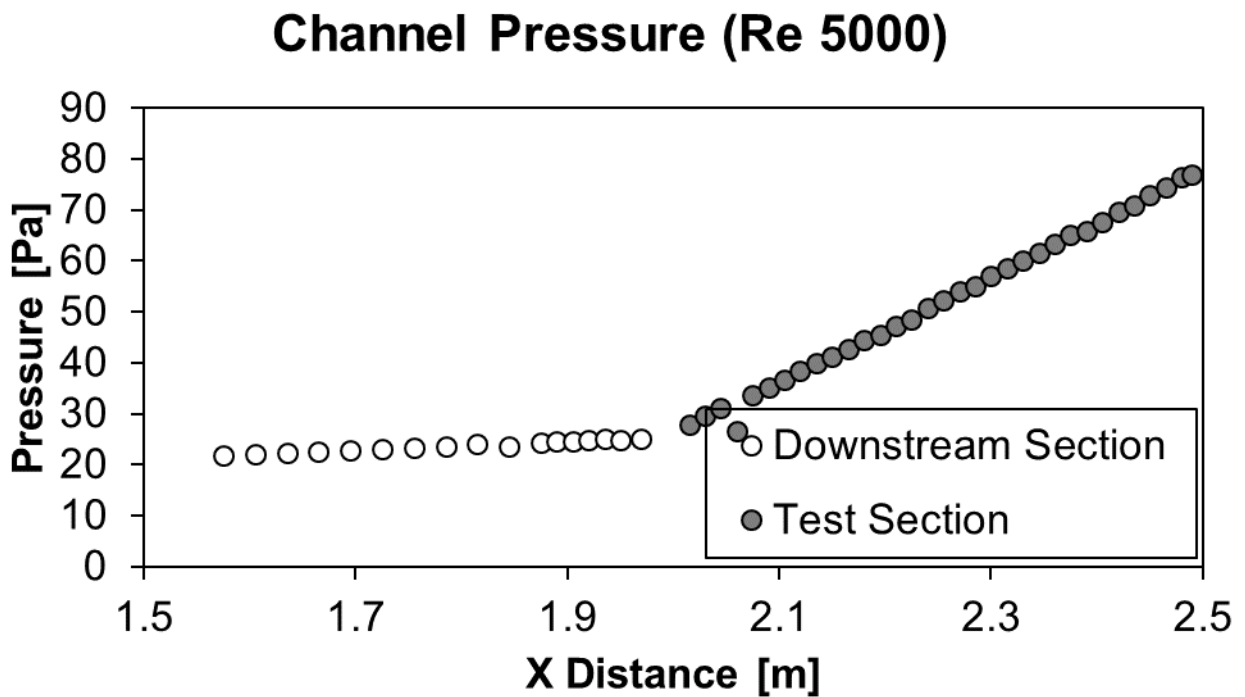


Figure D.52: Channel Pressure for mesh 2.1 and Re = 5 000

Channel Pressure (Re 7000)

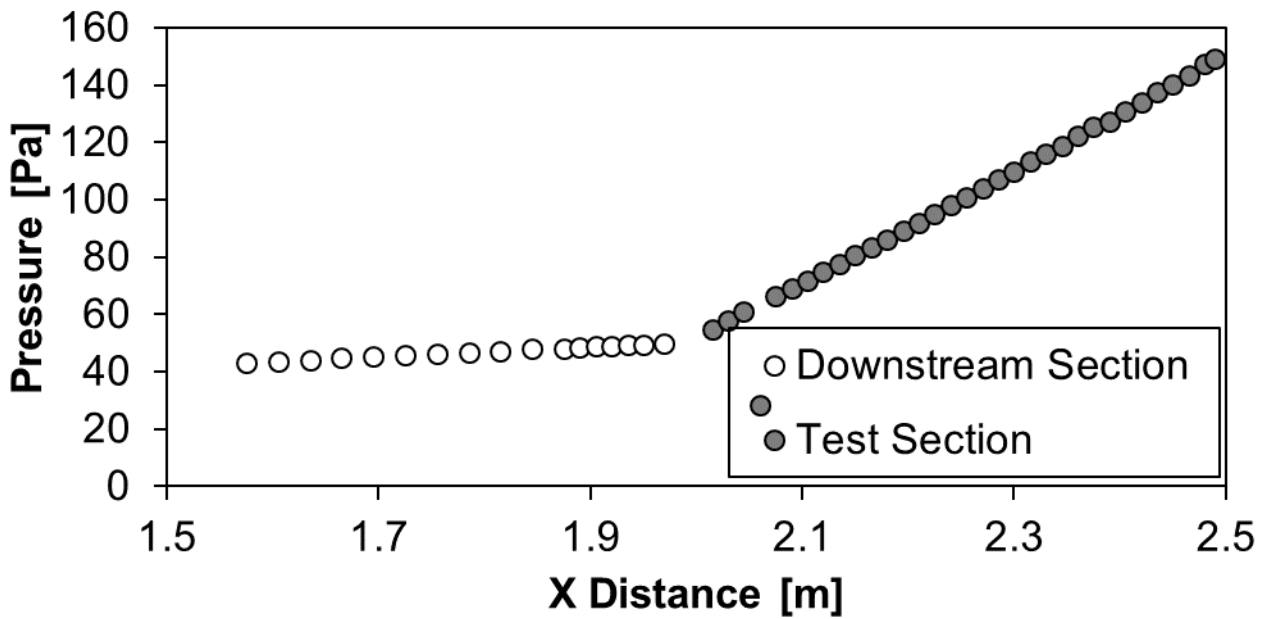


Figure D.53: Channel Pressure for mesh 2.1 and Re = 7 000

Channel Pressure (Re 10000)

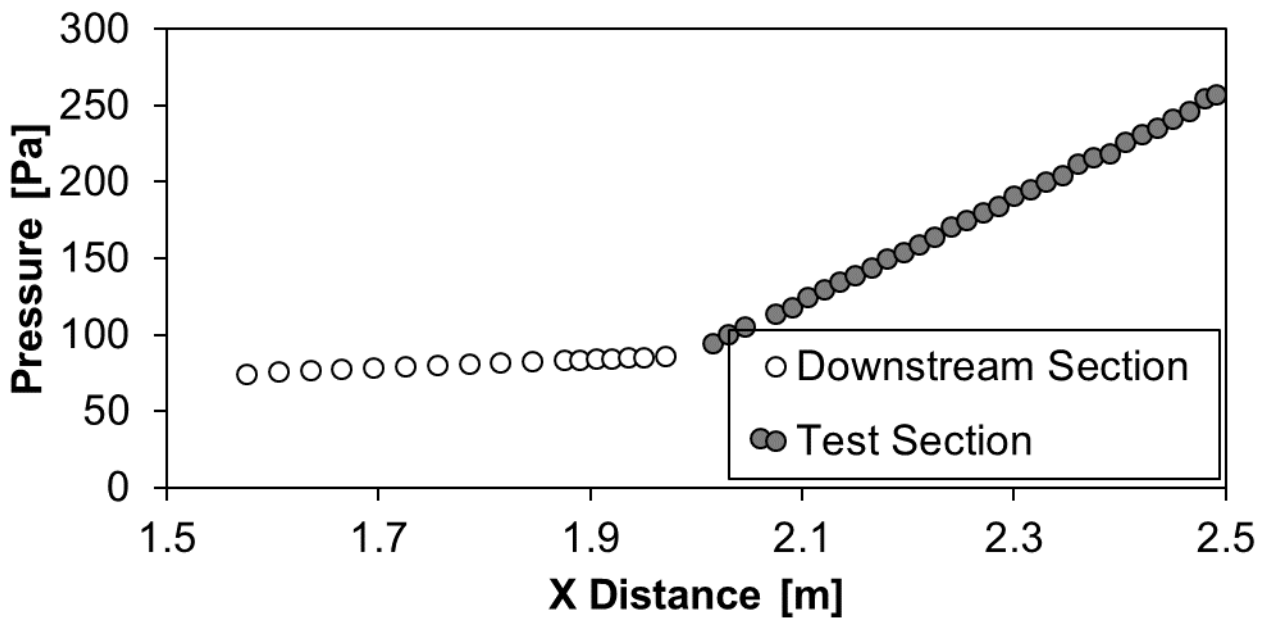


Figure D.54: Channel Pressure for mesh 2.1 and Re = 10 000

Channel Pressure (Re 16000)

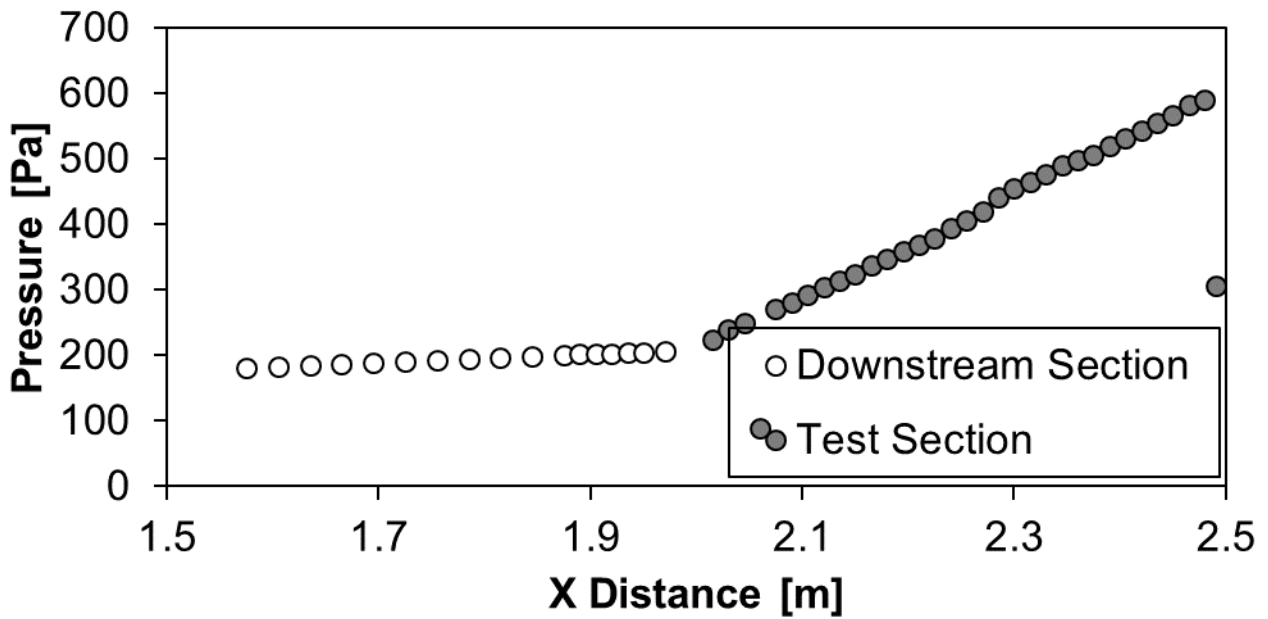


Figure D.55: Channel Pressure for mesh 2.1 and Re = 16 000

Channel Pressure (Re 24000)

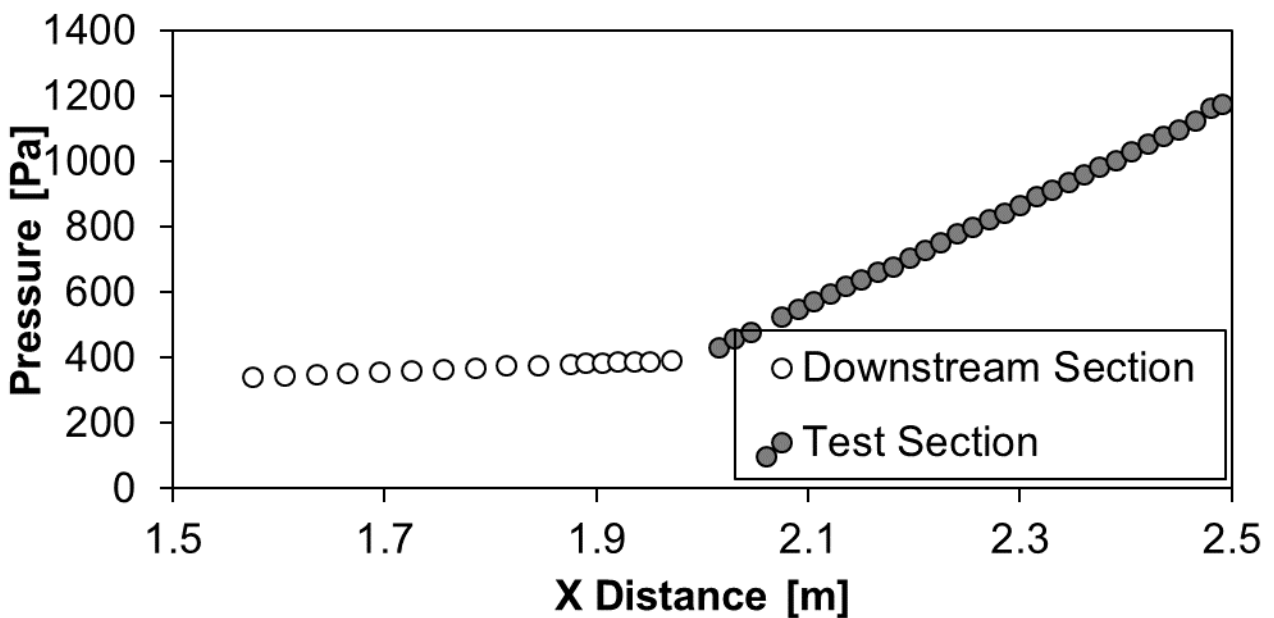


Figure D.56: Channel Pressure for mesh 2.1 and Re = 24 000

Channel Pressure (Re 30000)

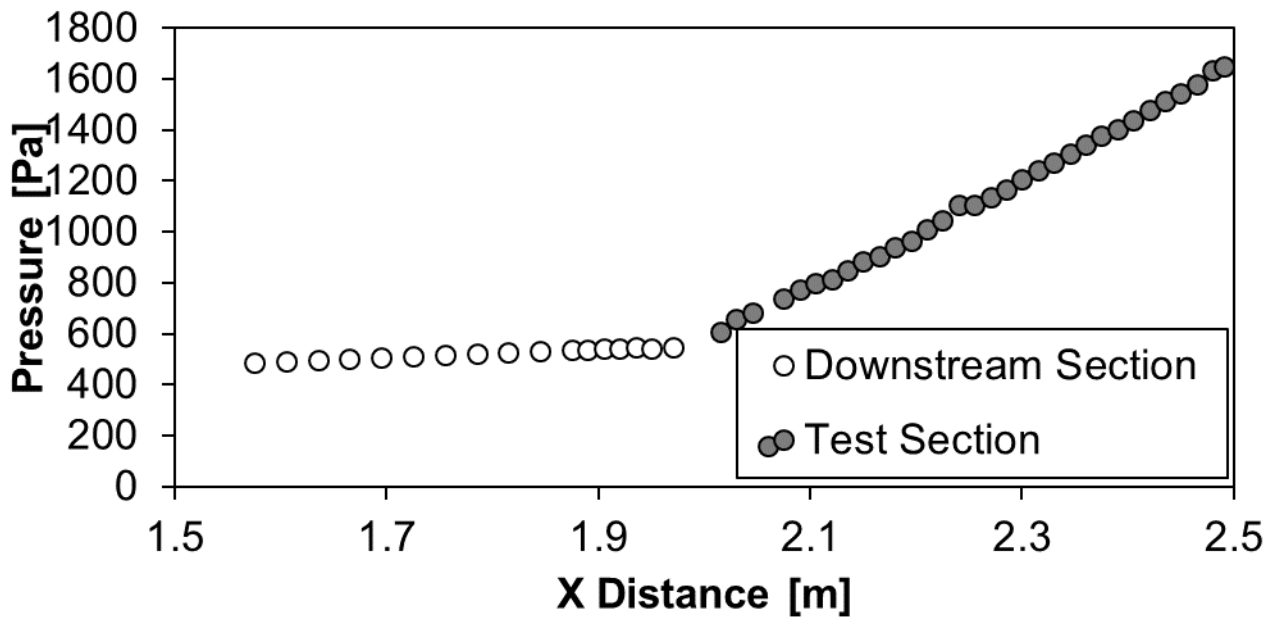


Figure D.57: Channel Pressure for mesh 2.1 and Re = 30 000

14 MM CHANNEL HEIGHT – MESH 2.3

Channel Pressure (Re 400)

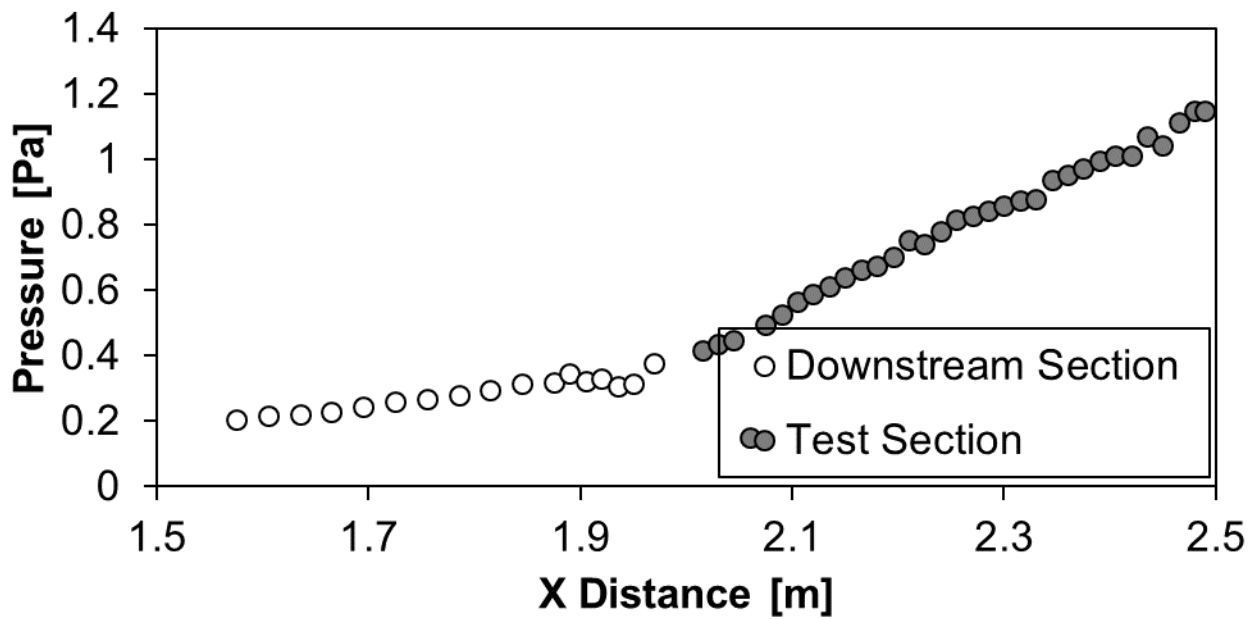


Figure D.58: Channel Pressure for mesh 2.3 and Re = 400

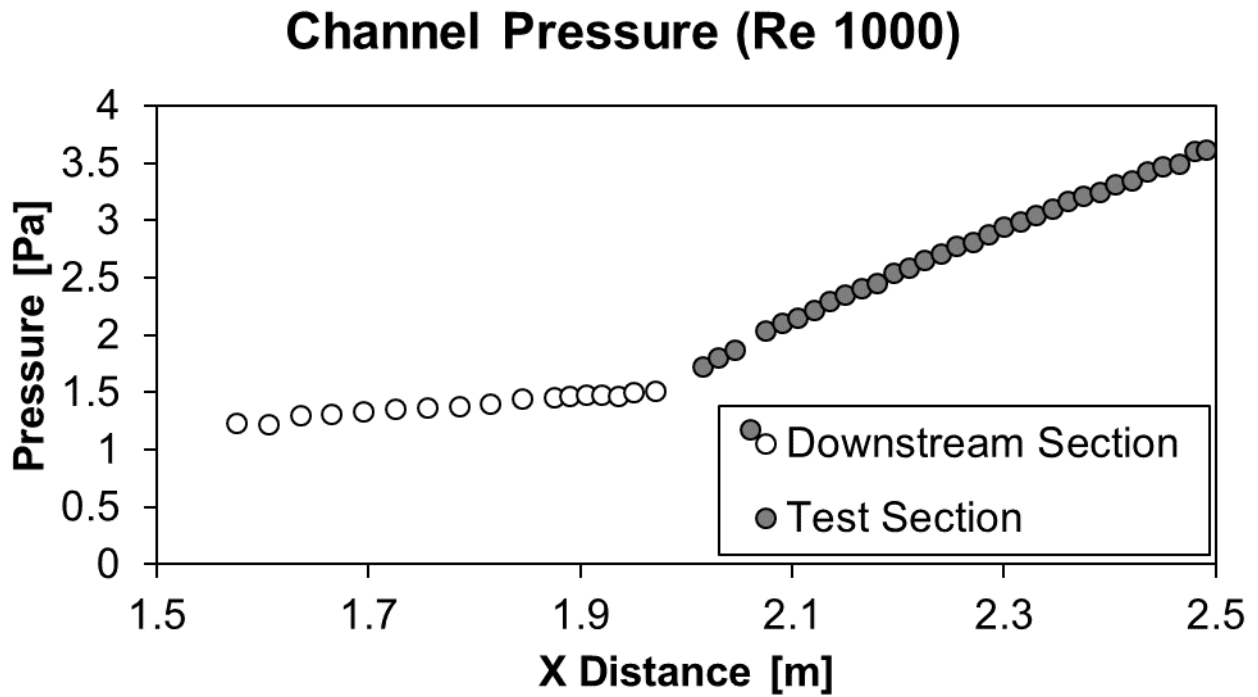


Figure D.59: Channel Pressure for mesh 2.3 and Re = 1 000

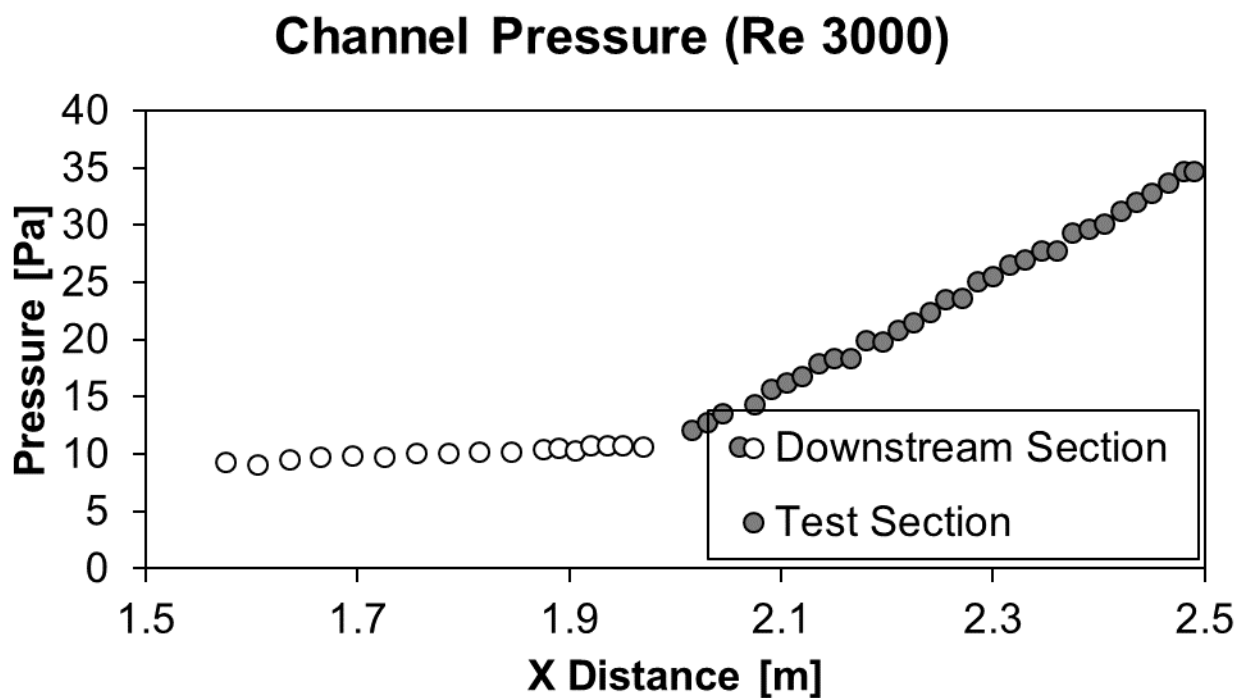


Figure D.60: Channel Pressure for mesh 2.3 and Re = 3 000

Channel Pressure (Re 5000)

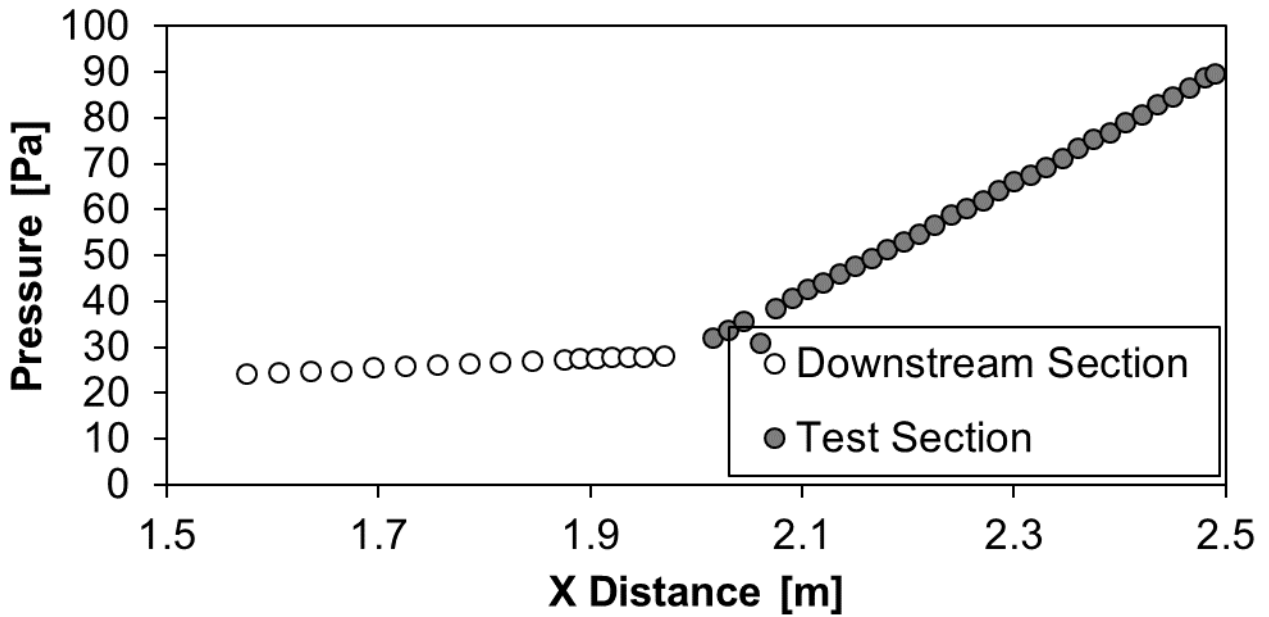


Figure D.61: Channel Pressure for mesh 2.3 and Re = 5 000

Channel Pressure (Re 7000)

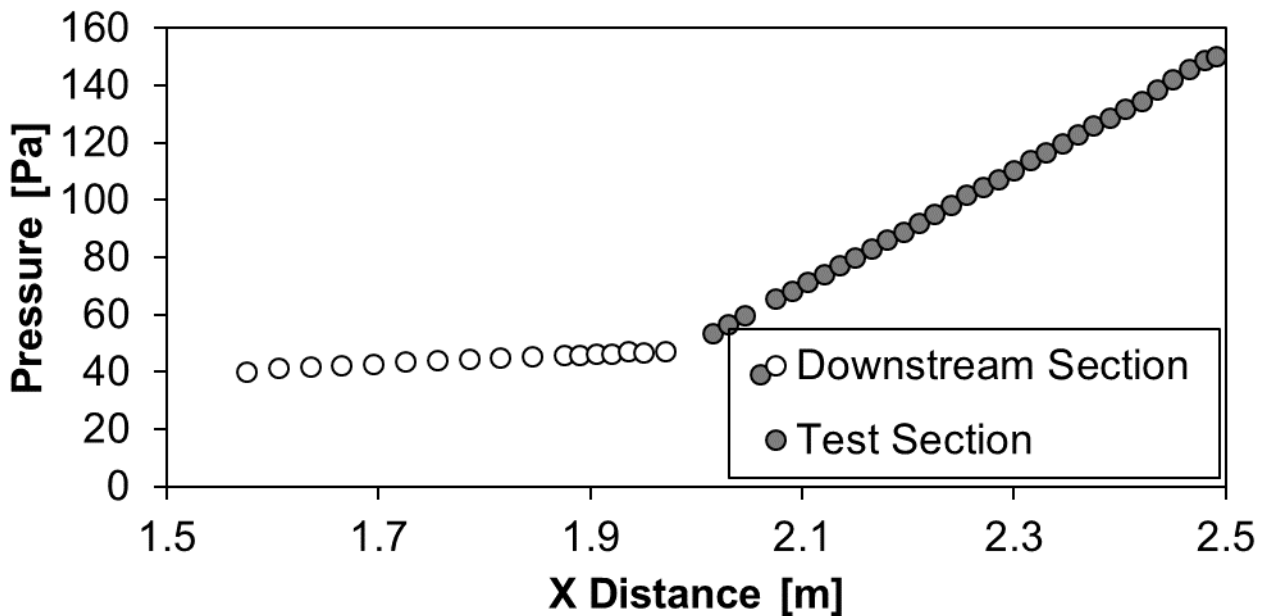


Figure D.62: Channel Pressure for mesh 2.3 and Re = 7 000

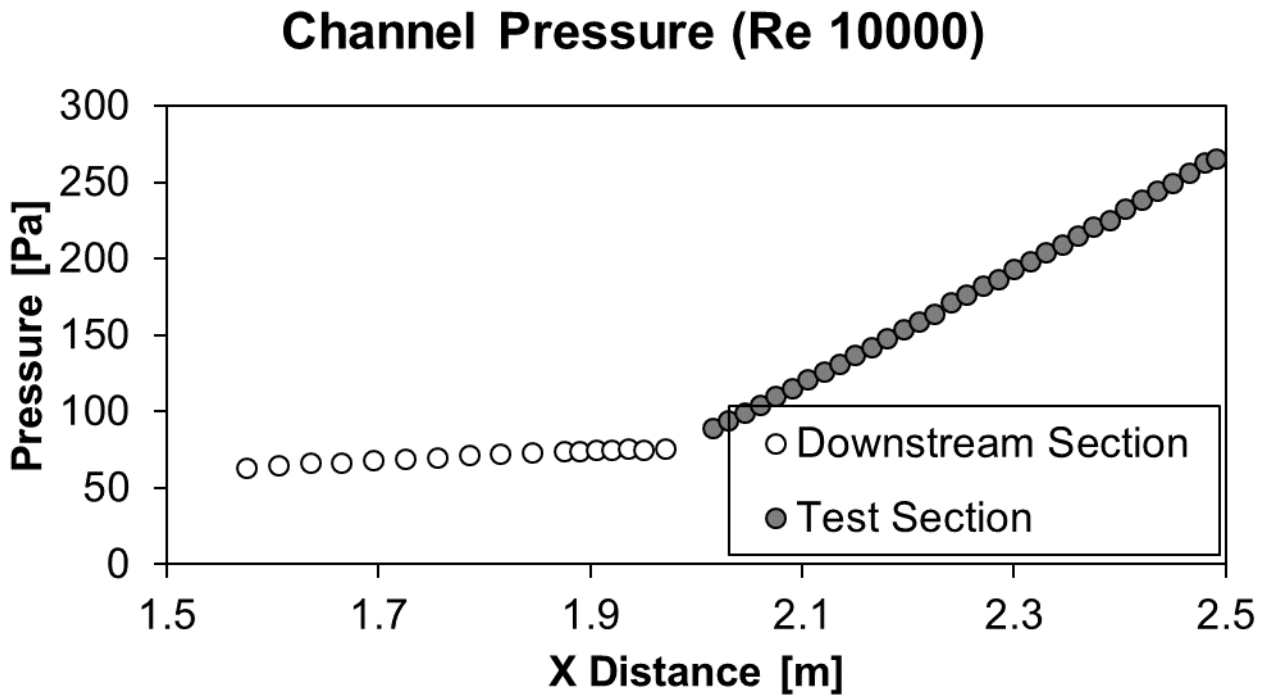


Figure D.63: Channel Pressure for mesh 2.3 and Re = 10 000

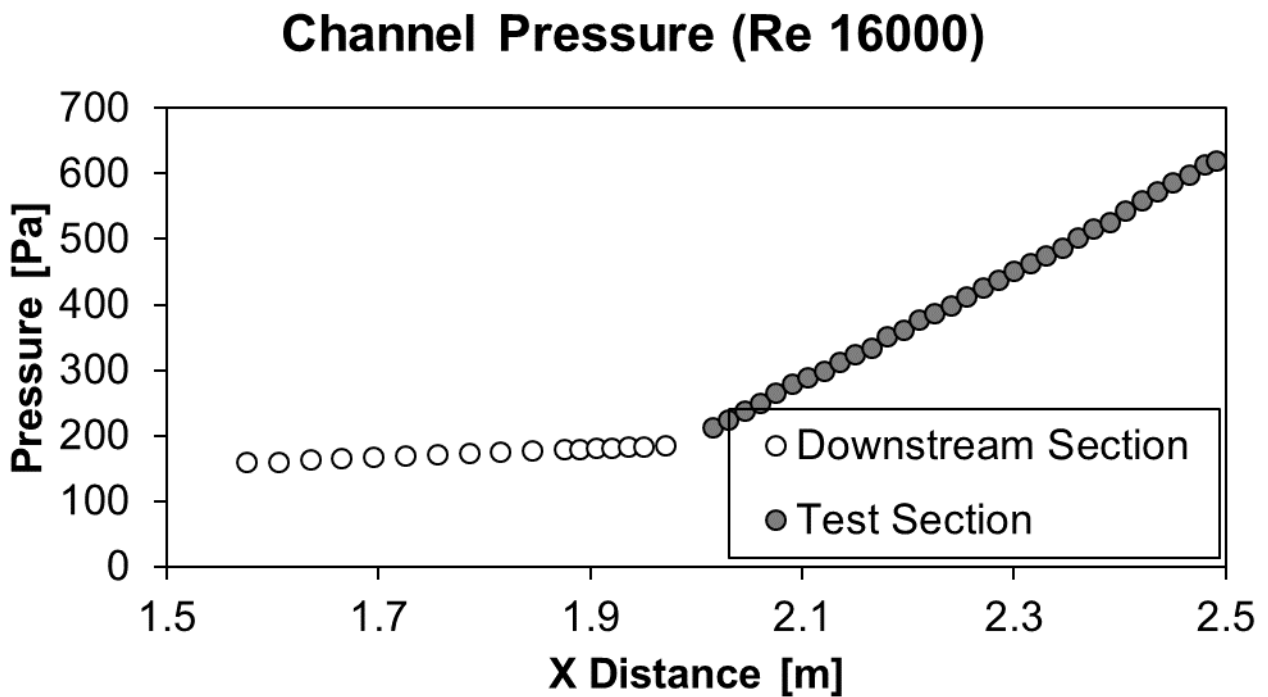


Figure D.64: Channel Pressure for mesh 2.3 and Re = 16 000

Channel Pressure (Re 24000)

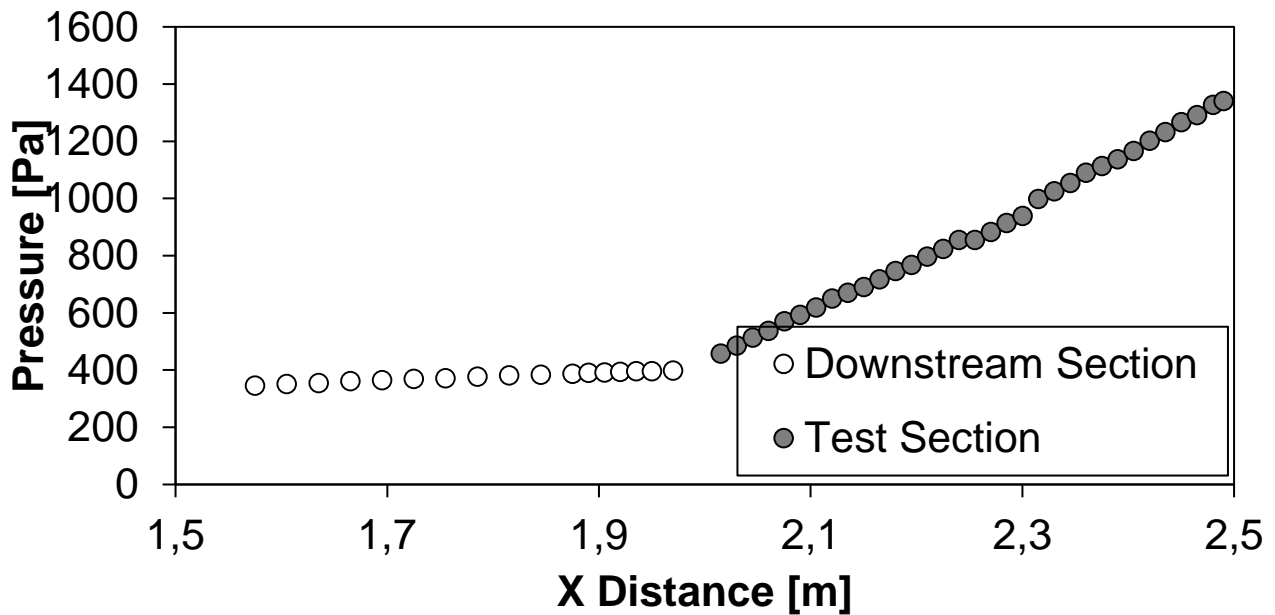


Figure D.65: Channel Pressure for mesh 2.3 and Re = 24 000

Channel Pressure (Re 30000)

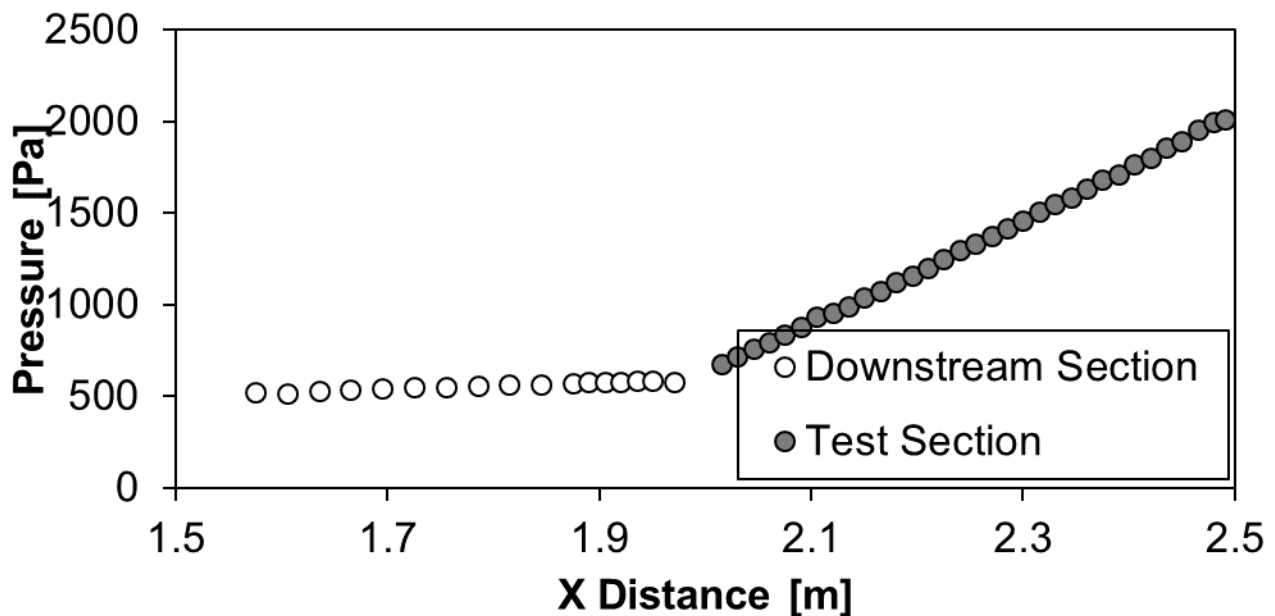


Figure D.66: Channel Pressure for mesh 2.3 and Re = 30 000

Appendix E: TWO WALL HEAT TRANSFER DATA

5 MM CHANNEL HEIGHT – MESH 4.1

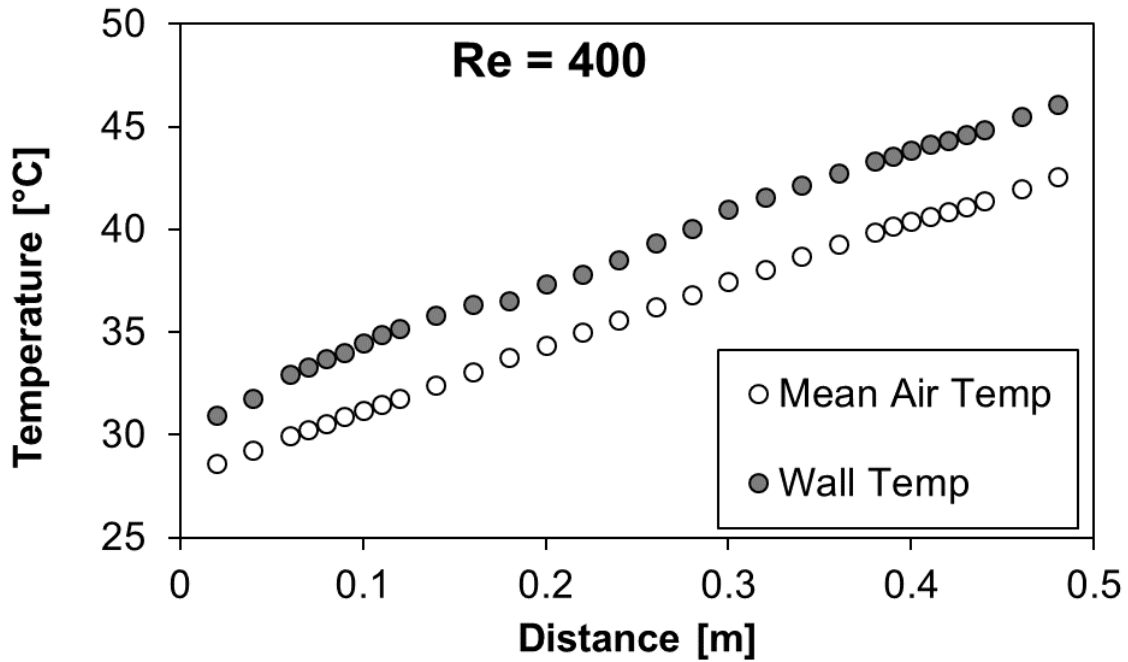


Figure E.1: Wall and mean air temperatures for mesh 4.1 under two-heated wall boundary condition at Re = 400

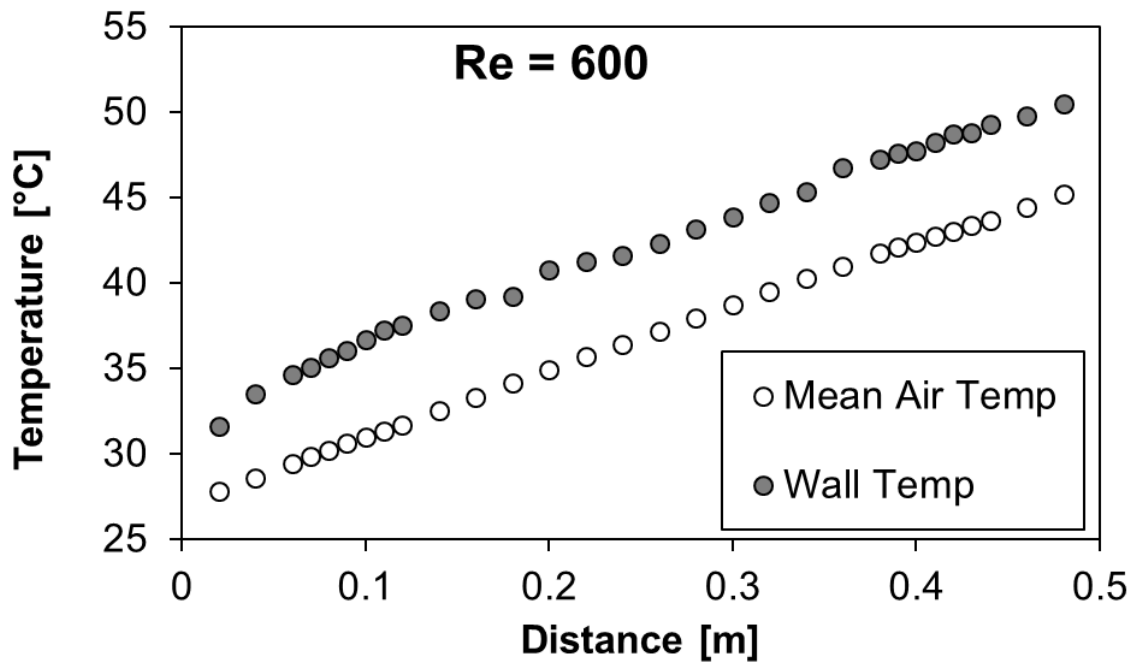


Figure E.2: Wall and mean air temperatures for mesh 4.1 under two-heated wall boundary condition at Re = 600

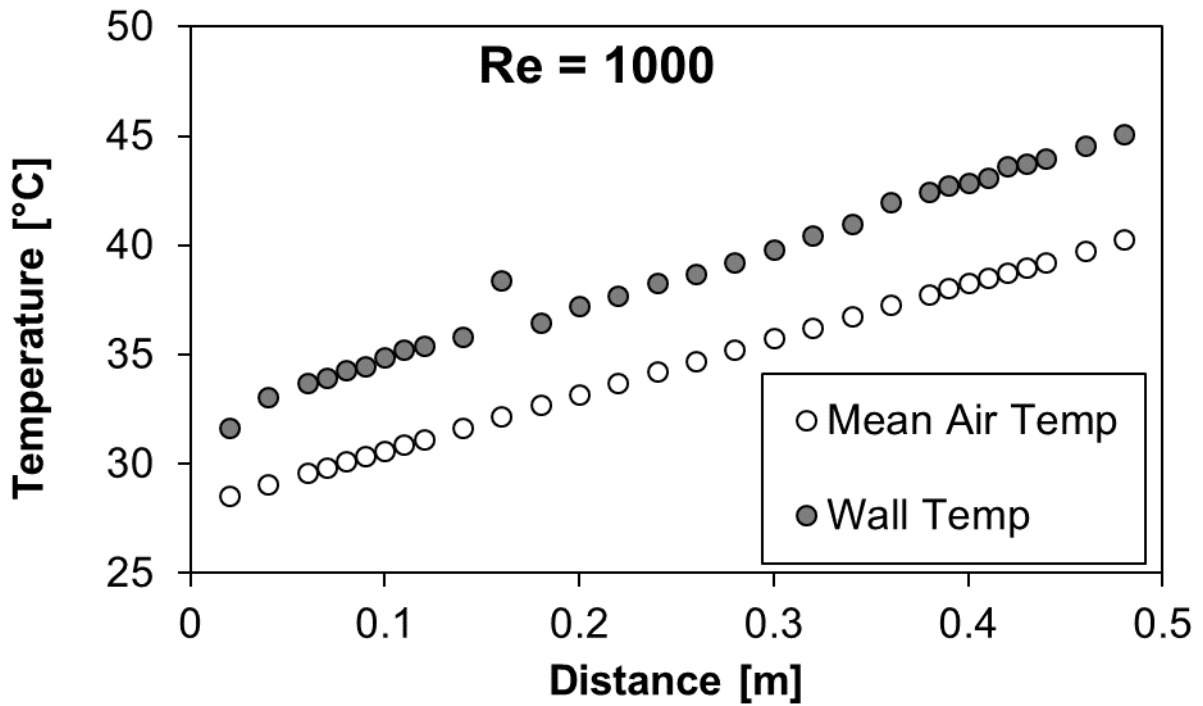


Figure E.3: Wall and mean air temperatures for mesh 4.1 under two-heated wall boundary condition at Re = 1 000

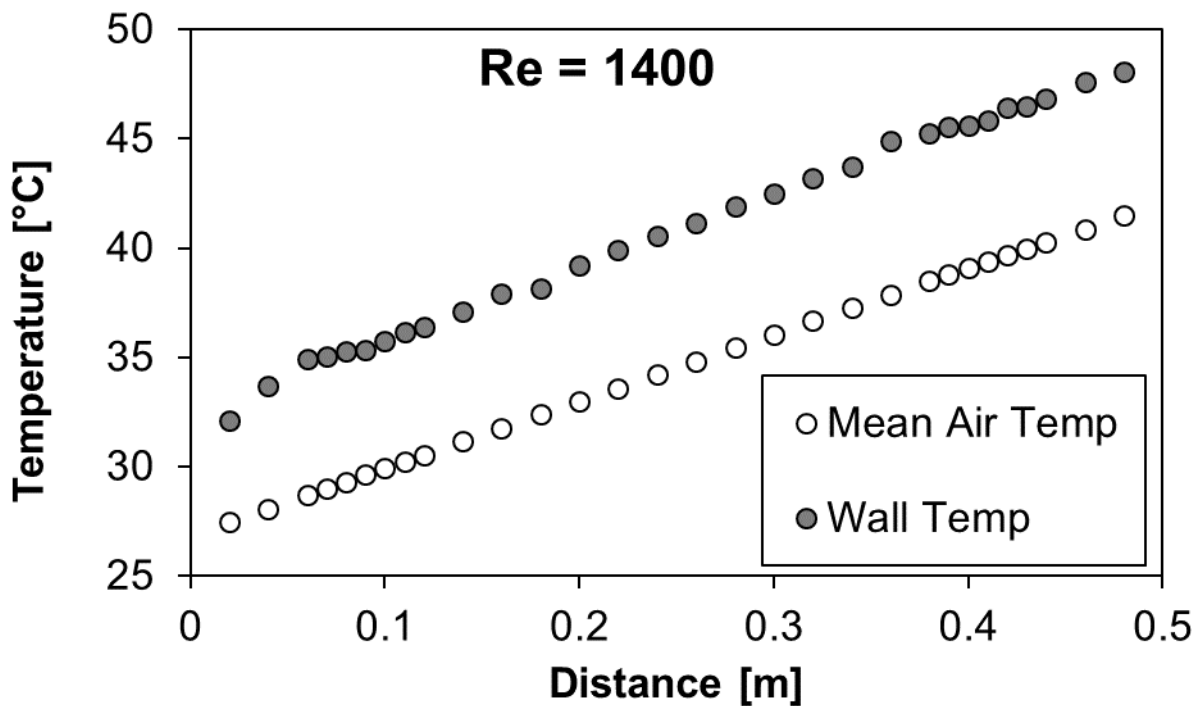


Figure E.4: Wall and mean air temperatures for mesh 4.1 under two-heated wall boundary condition at Re = 1 400

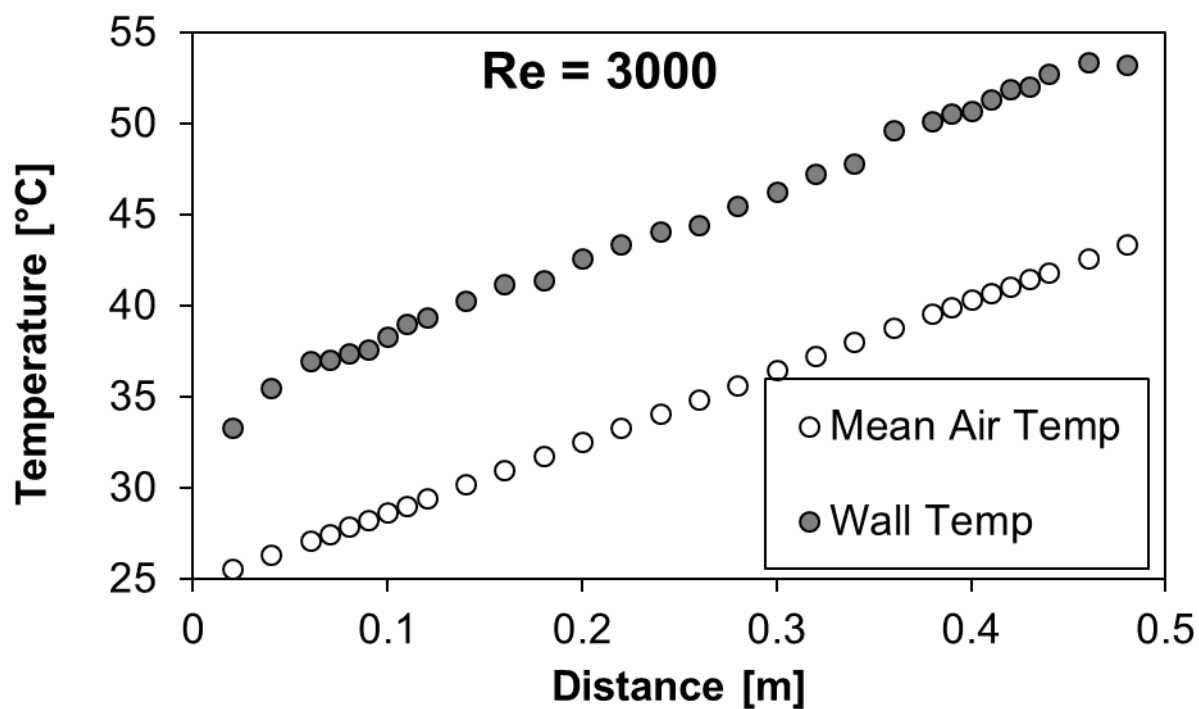


Figure E.5: Wall and mean air temperatures for mesh 4.1 under two-heated wall boundary condition at Re = 3 000

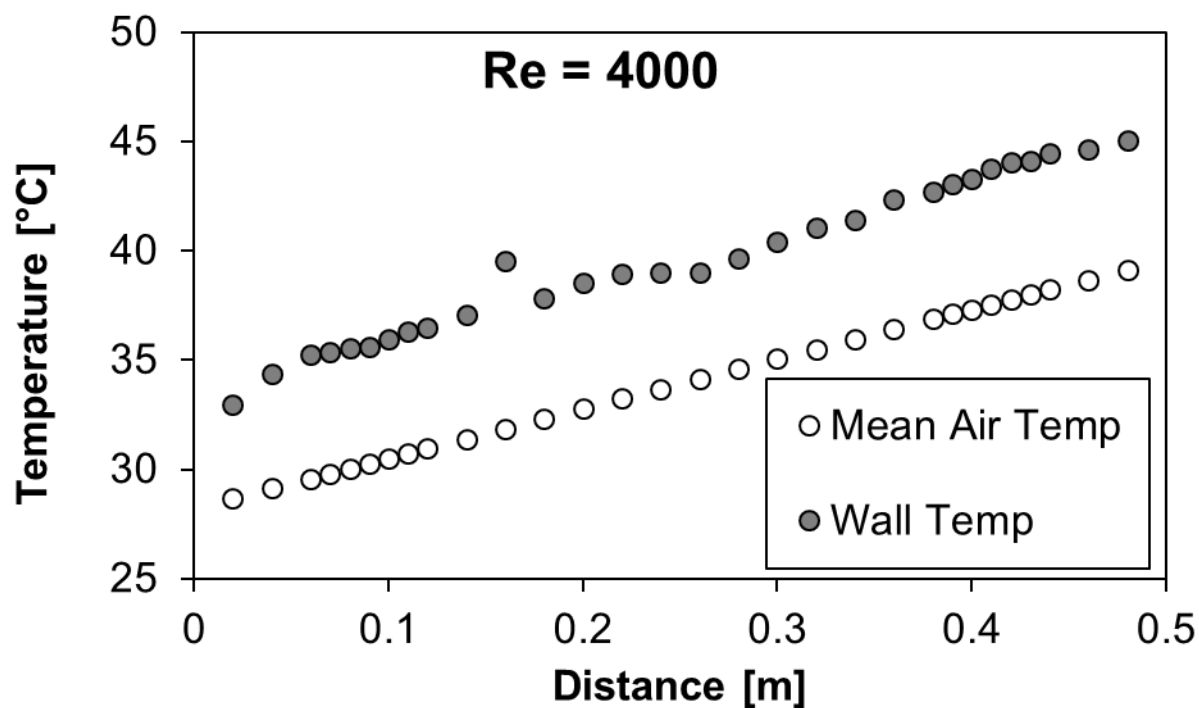


Figure E.6: Wall and mean air temperatures for mesh 4.1 under two-heated wall boundary condition at Re = 4 000

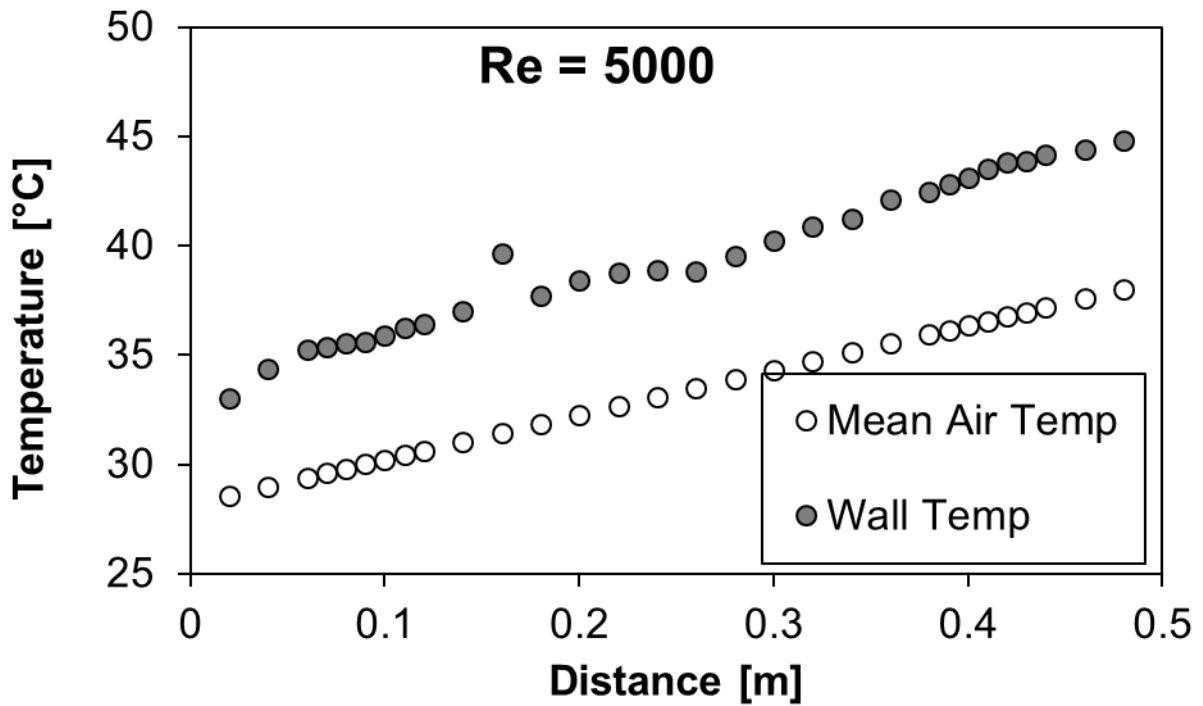


Figure E.7: Wall and mean air temperatures for mesh 4.1 under two-heated wall boundary condition at Re = 5 000

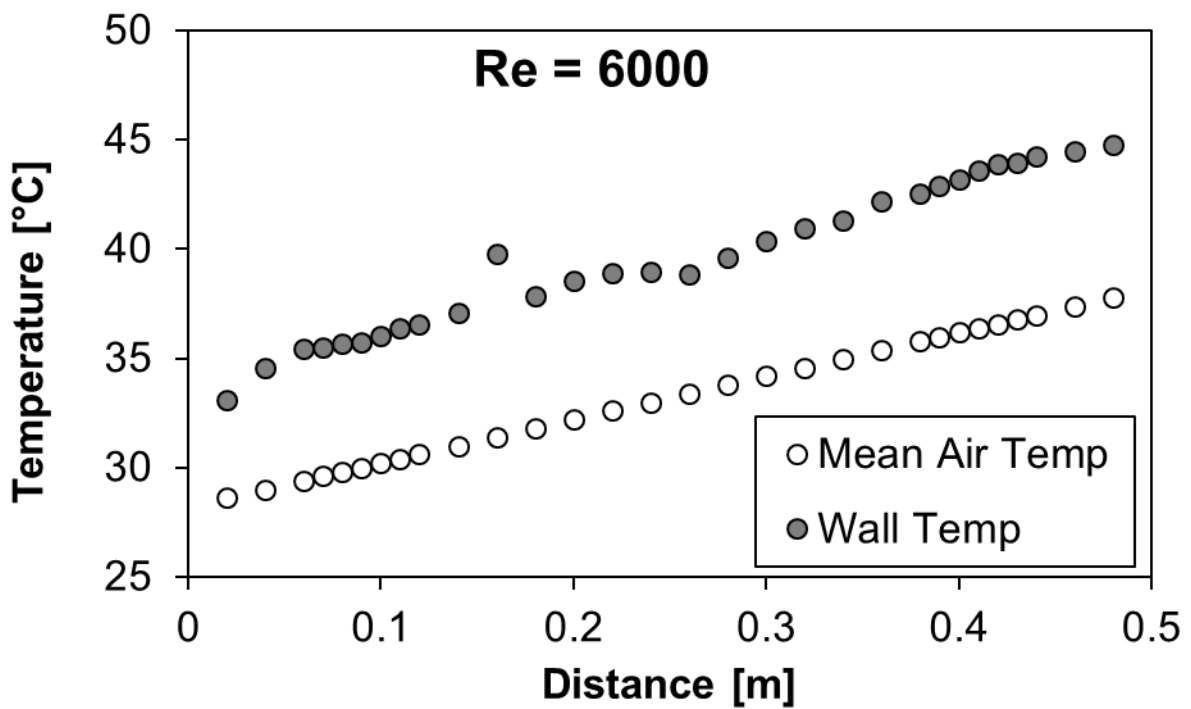


Figure E.8: Wall and mean air temperatures for mesh 4.1 under two-heated wall boundary condition at Re = 6 000

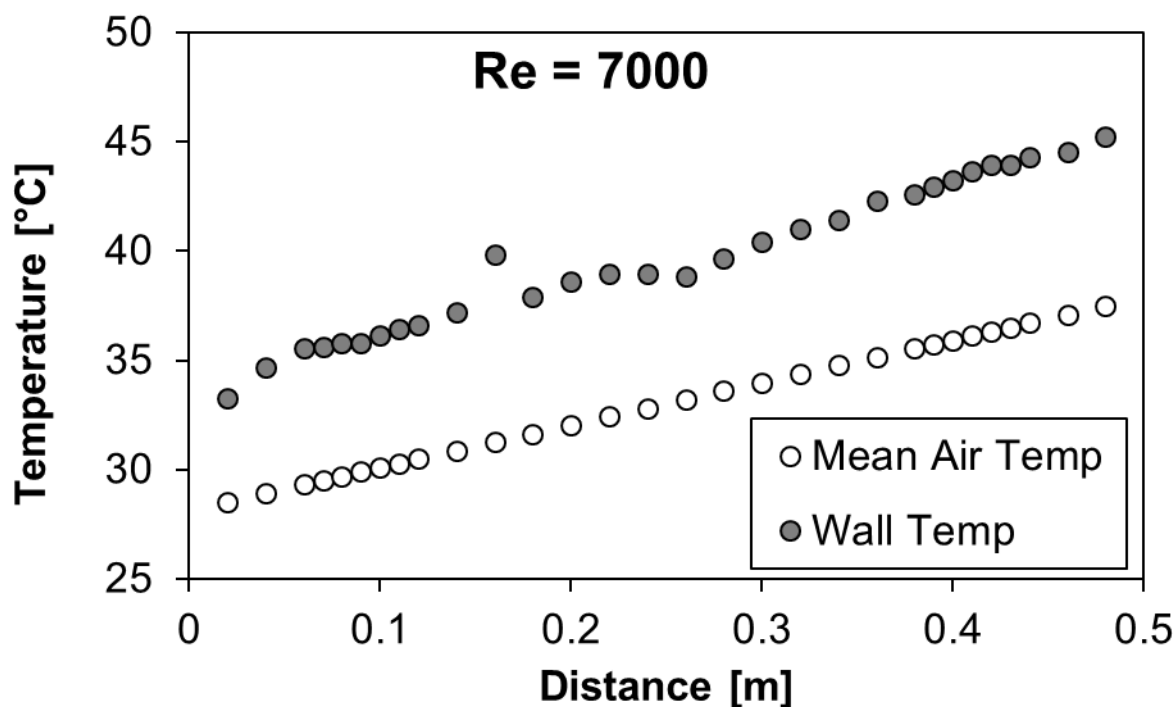


Figure E.9: Wall and mean air temperatures for mesh 4.1 under two-heated wall boundary condition at Re = 7 000

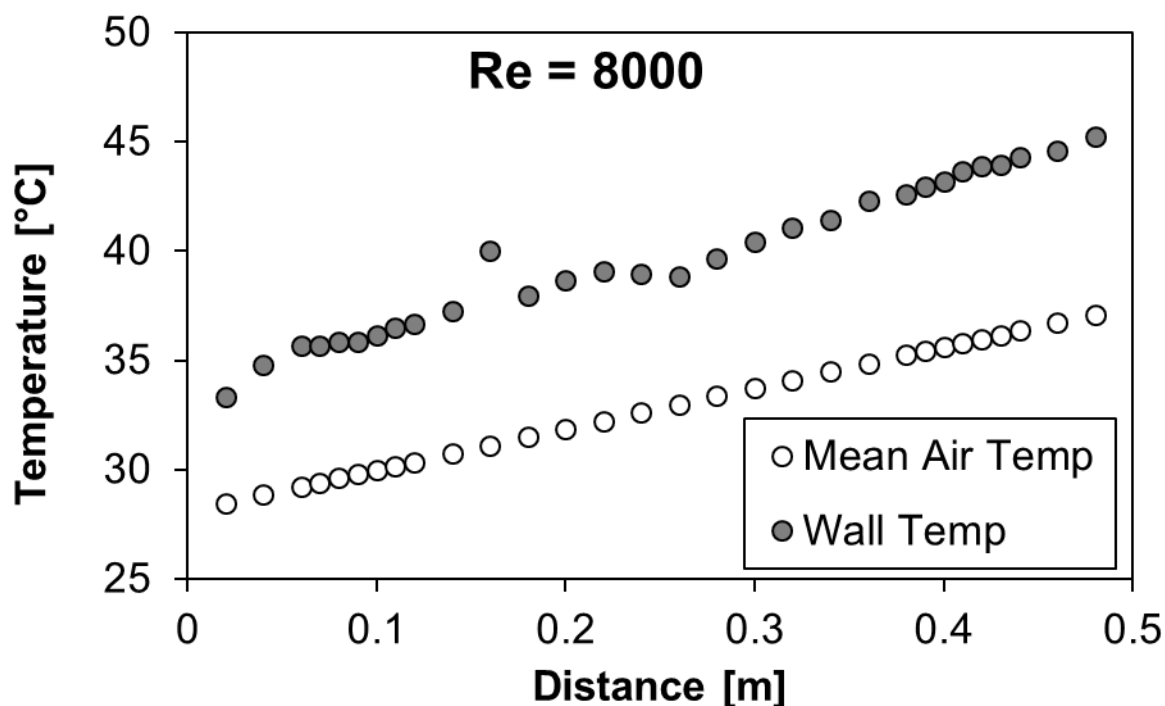


Figure E.10: Wall and mean air temperatures for mesh 4.1 under two-heated wall boundary condition at Re = 8 000

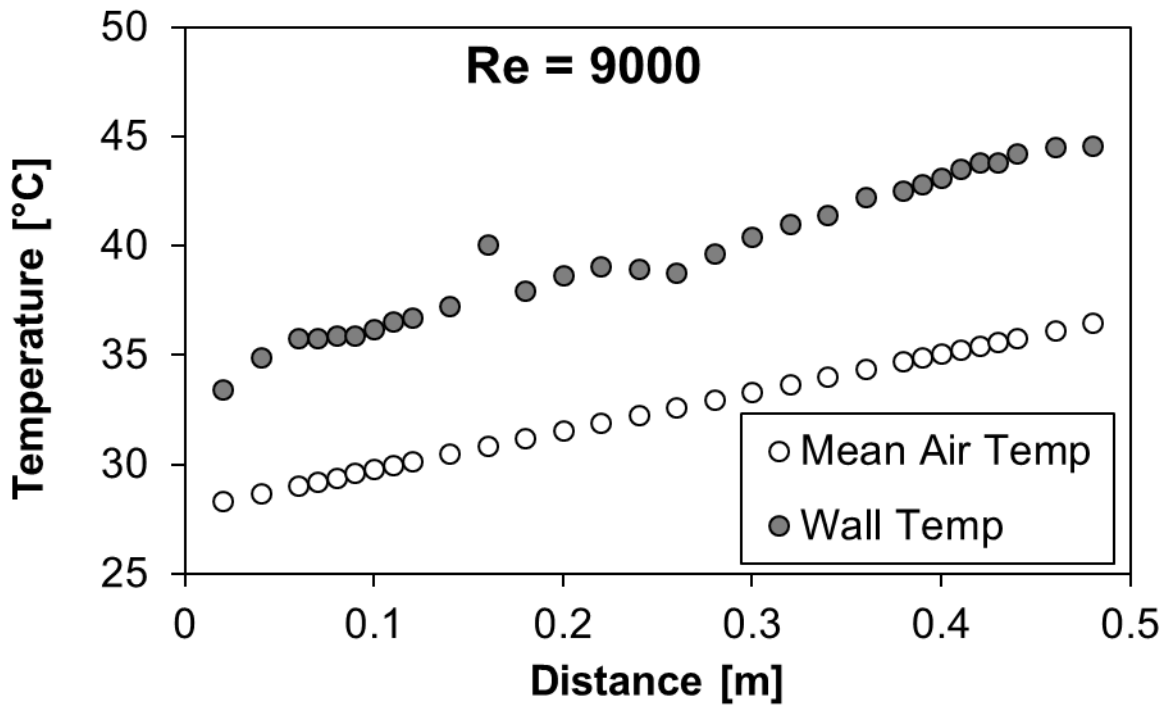


Figure E.11: Wall and mean air temperatures for mesh 4.1 under two-heated wall boundary condition at Re = 9 000

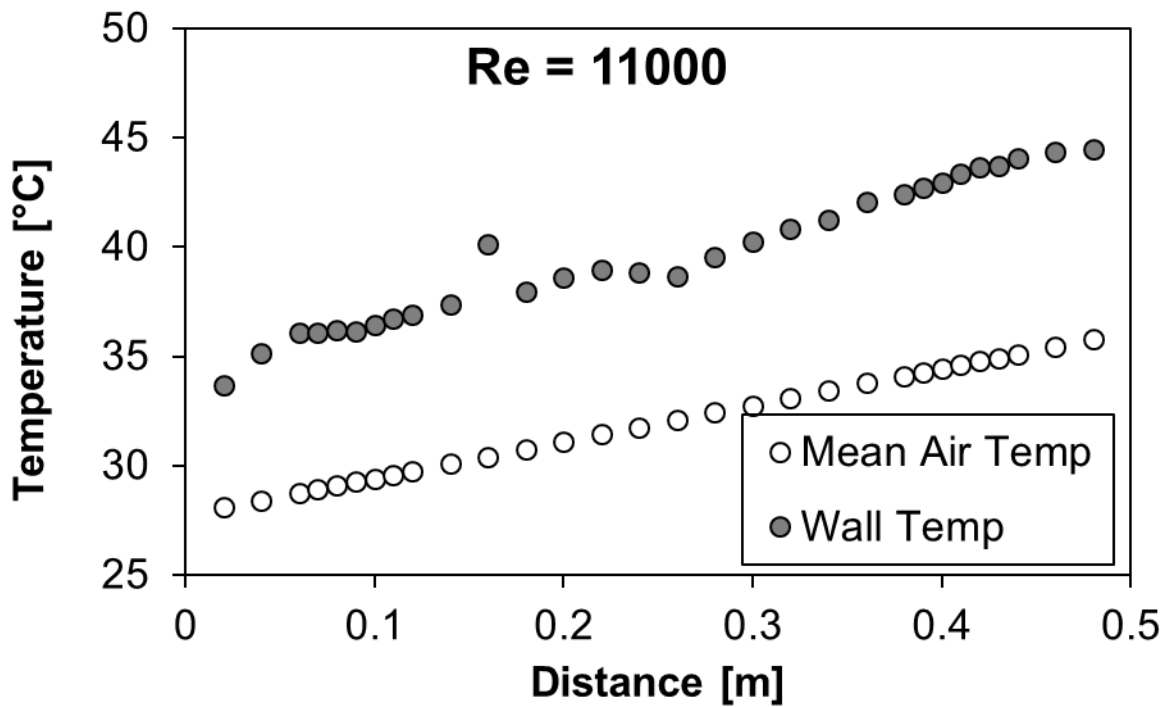


Figure E.12: Wall and mean air temperatures for mesh 4.1 under two-heated wall boundary condition at Re = 11 000

5 MM CHANNEL HEIGHT – MESH 4.3

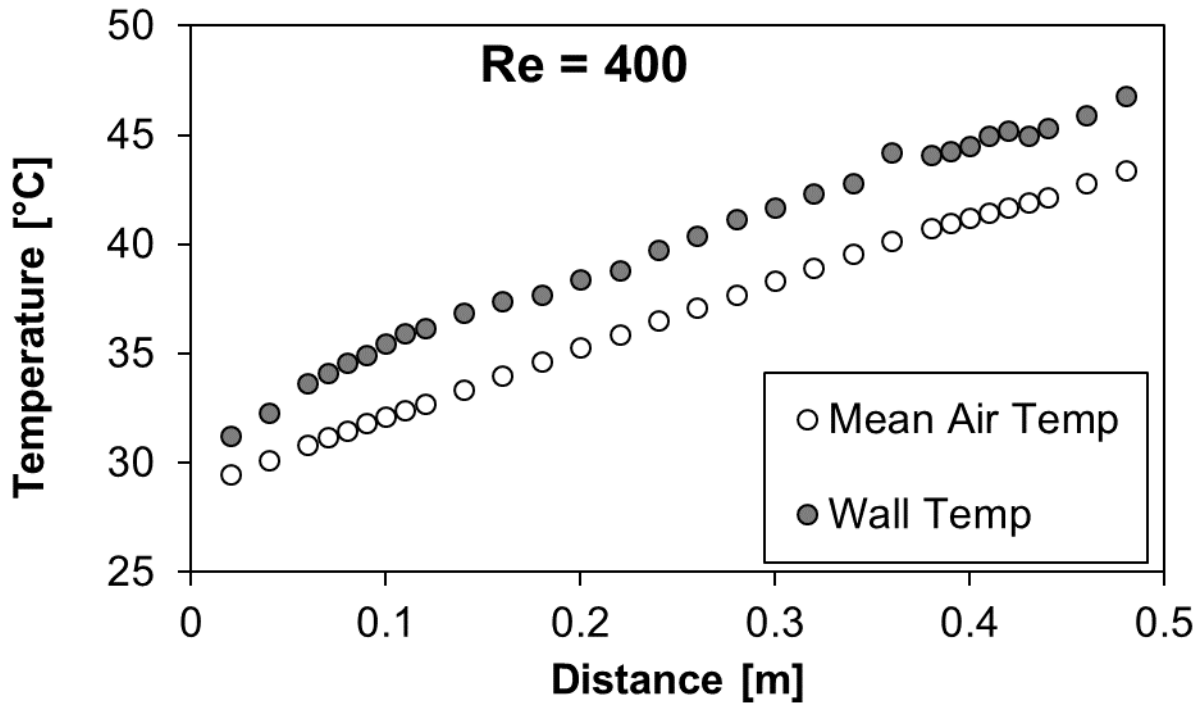


Figure E.13: Wall and mean air temperatures for mesh 4.3 under two-heated wall boundary condition at Re = 400

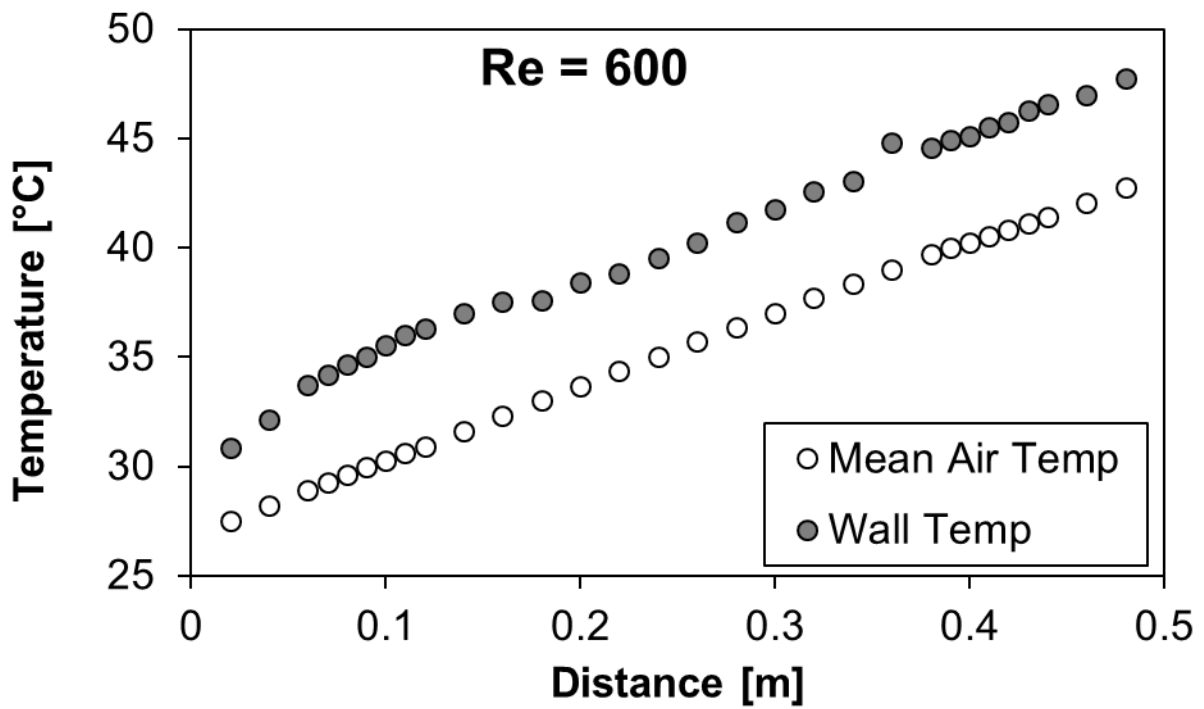


Figure E.14: Wall and mean air temperatures for mesh 4.3 under two-heated wall boundary condition at Re = 600

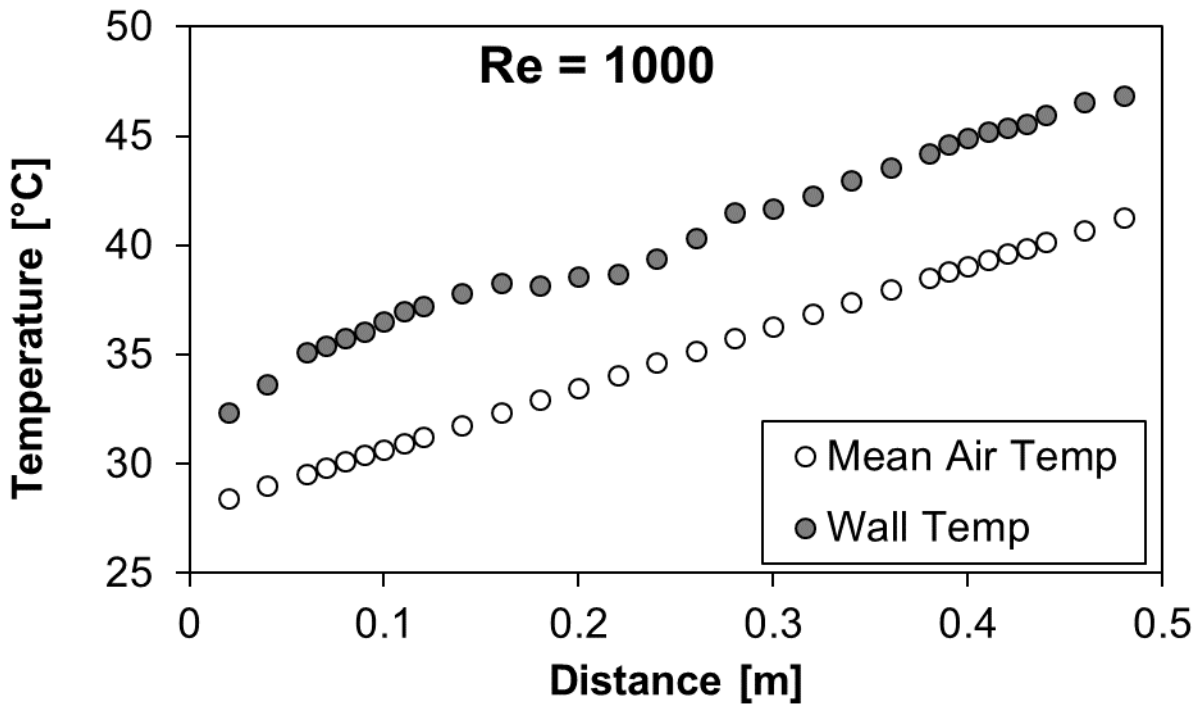


Figure E.15: Wall and mean air temperatures for mesh 4.3 under two-heated wall boundary condition at Re = 1 000

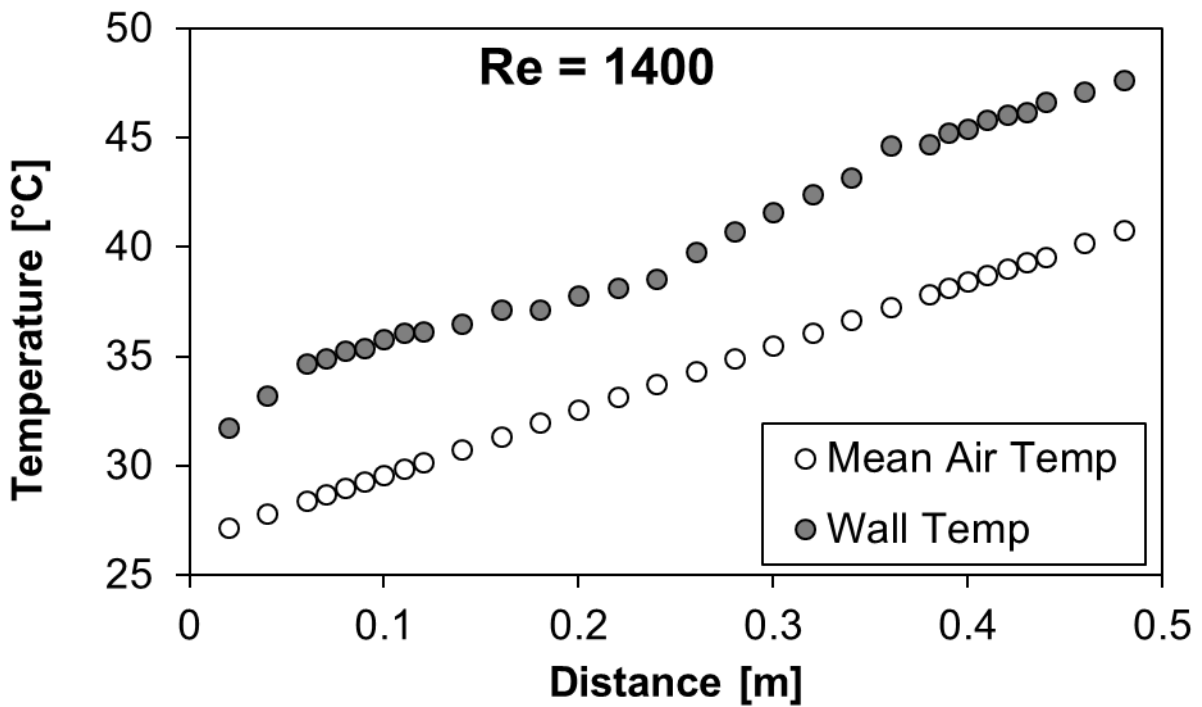


Figure E.16: Wall and mean air temperatures for mesh 4.3 under two-heated wall boundary condition at Re = 1 400

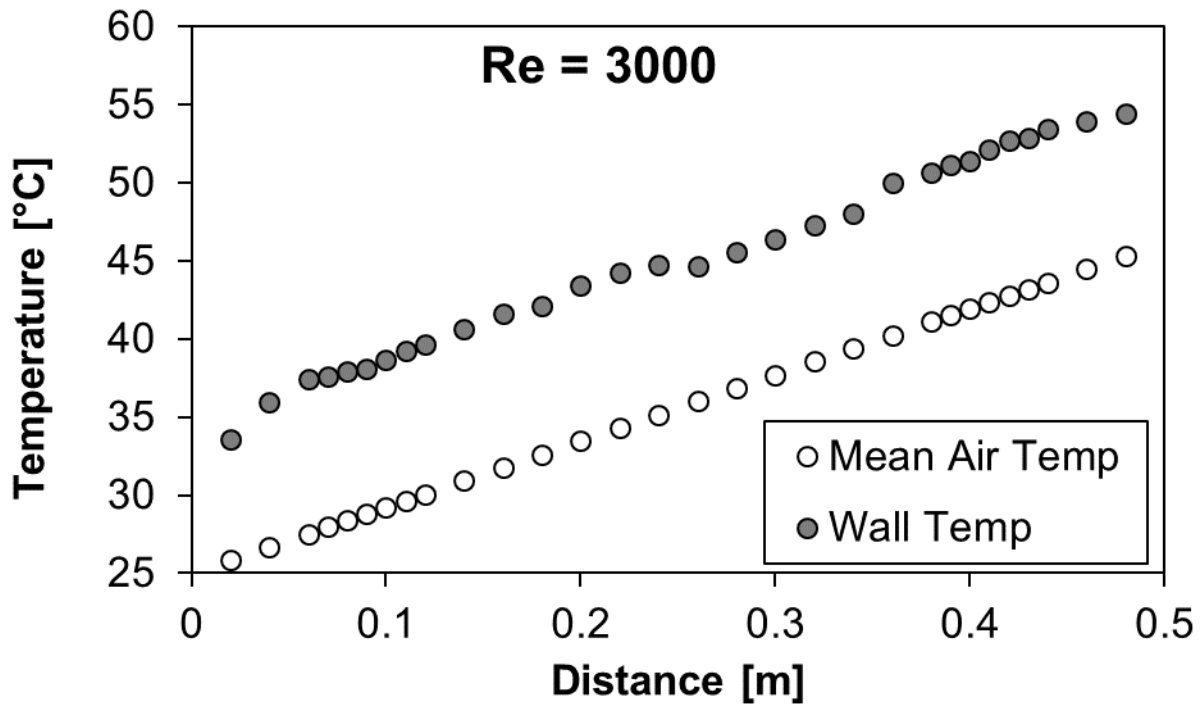


Figure E.17: Wall and mean air temperatures for mesh 4.3 under two-heated wall boundary condition at Re = 3 000

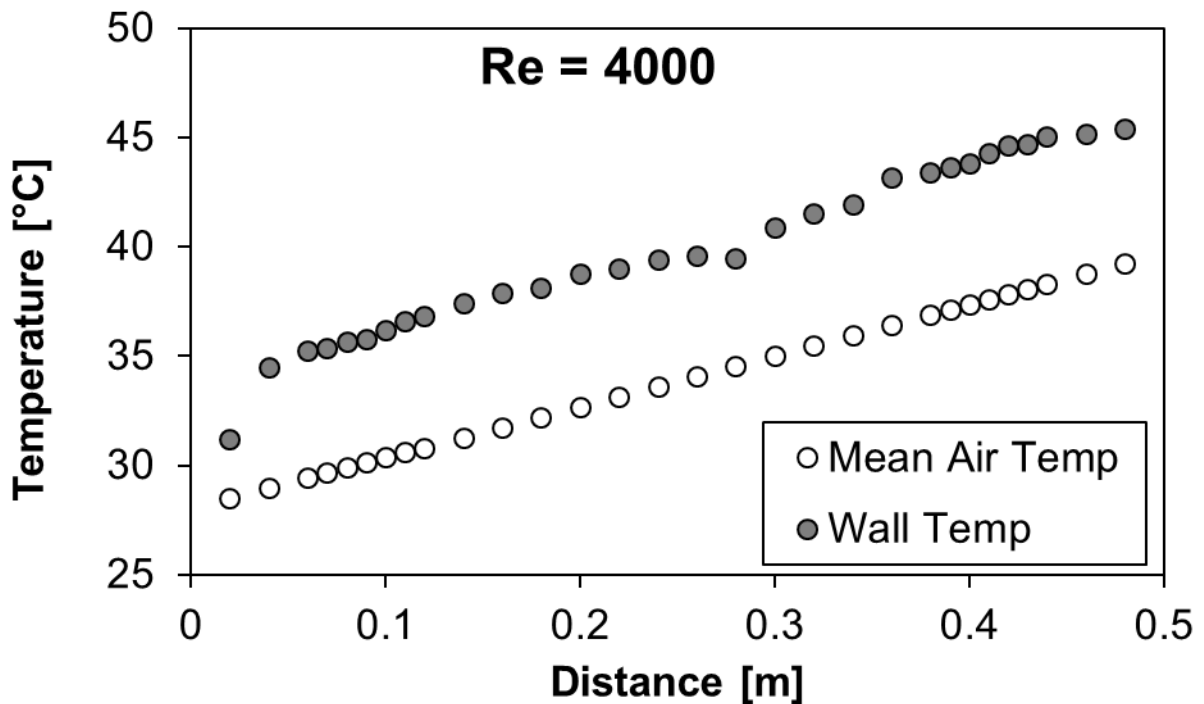


Figure E.18: Wall and mean air temperatures for mesh 4.3 under two-heated wall boundary condition at Re = 4 000

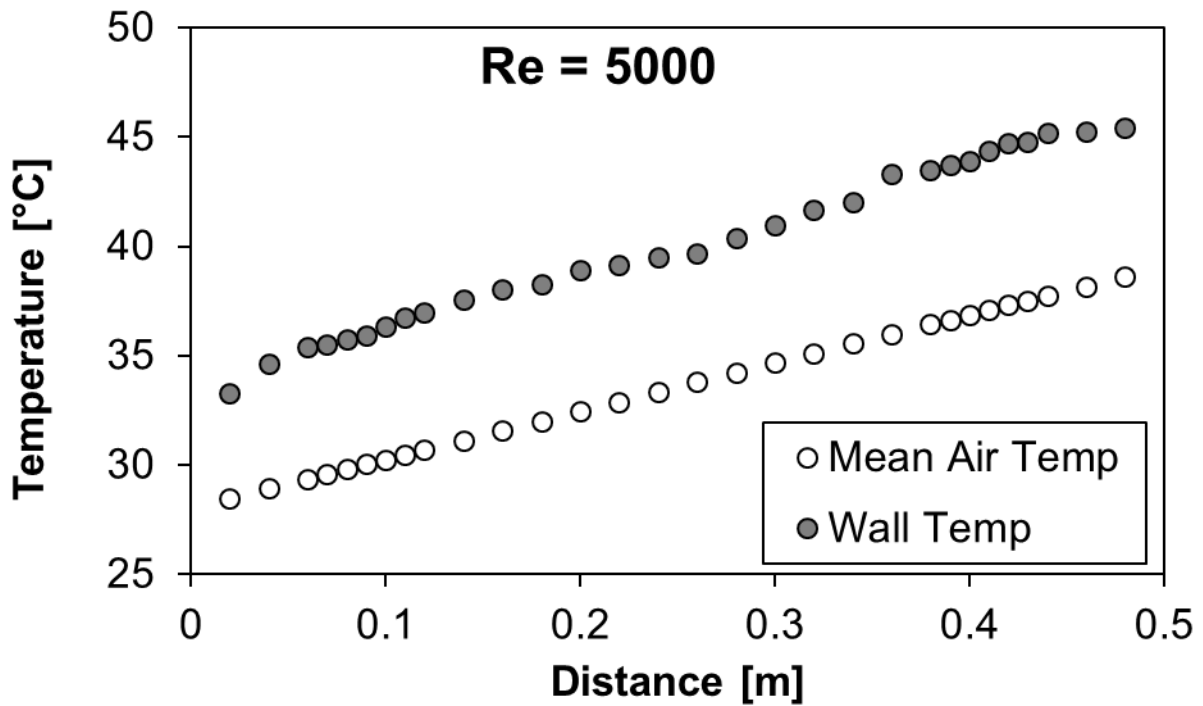


Figure E.19: Wall and mean air temperatures for mesh 4.3 under two-heated wall boundary condition at Re = 5 000

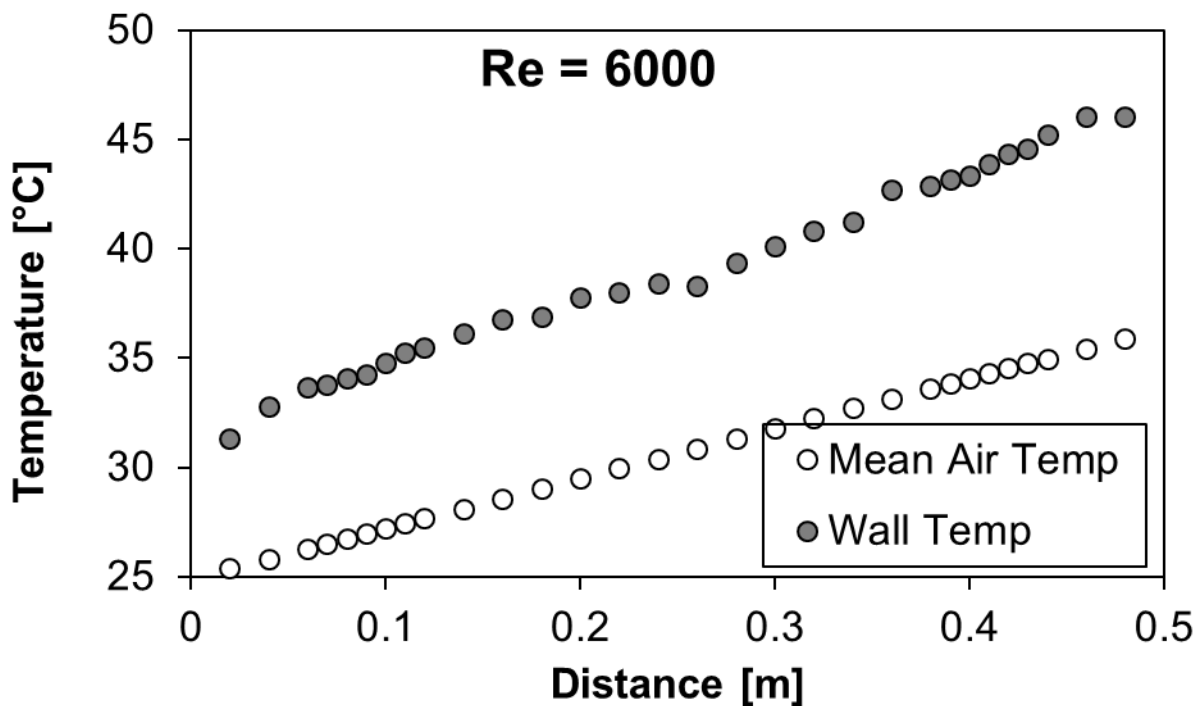


Figure E.20: Wall and mean air temperatures for mesh 4.3 under two-heated wall boundary condition at Re = 6 000

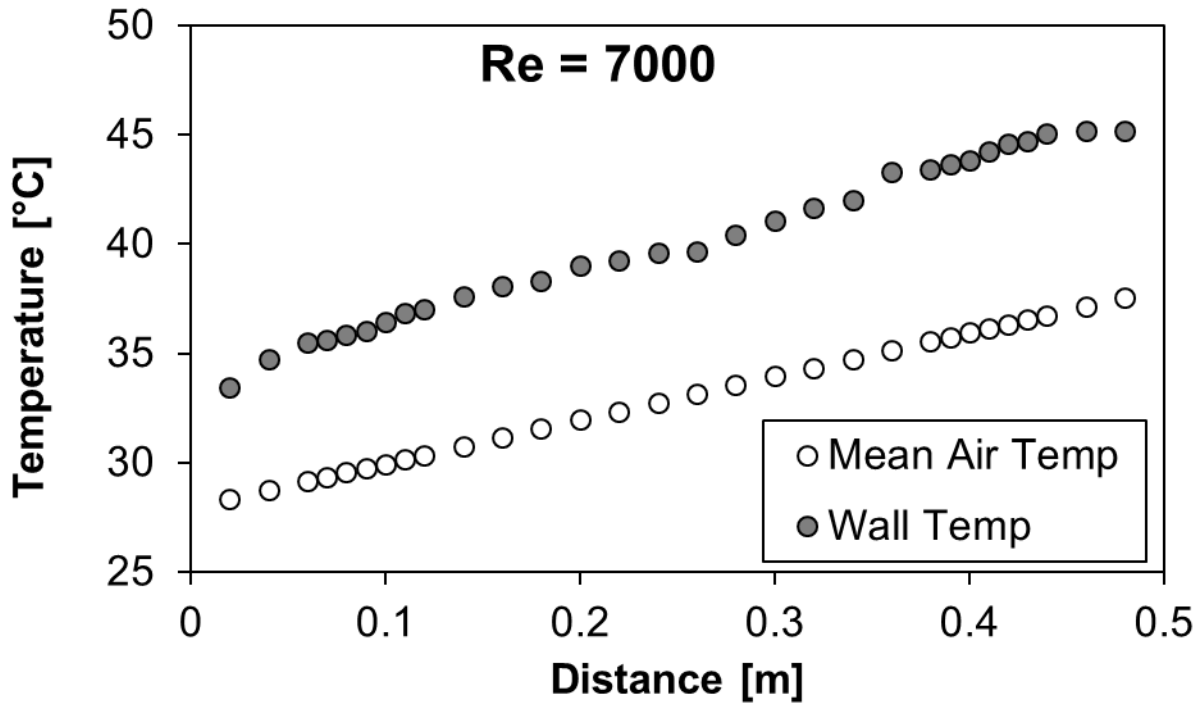


Figure E.21: Wall and mean air temperatures for mesh 4.3 under two-heated wall boundary condition at Re = 7 000

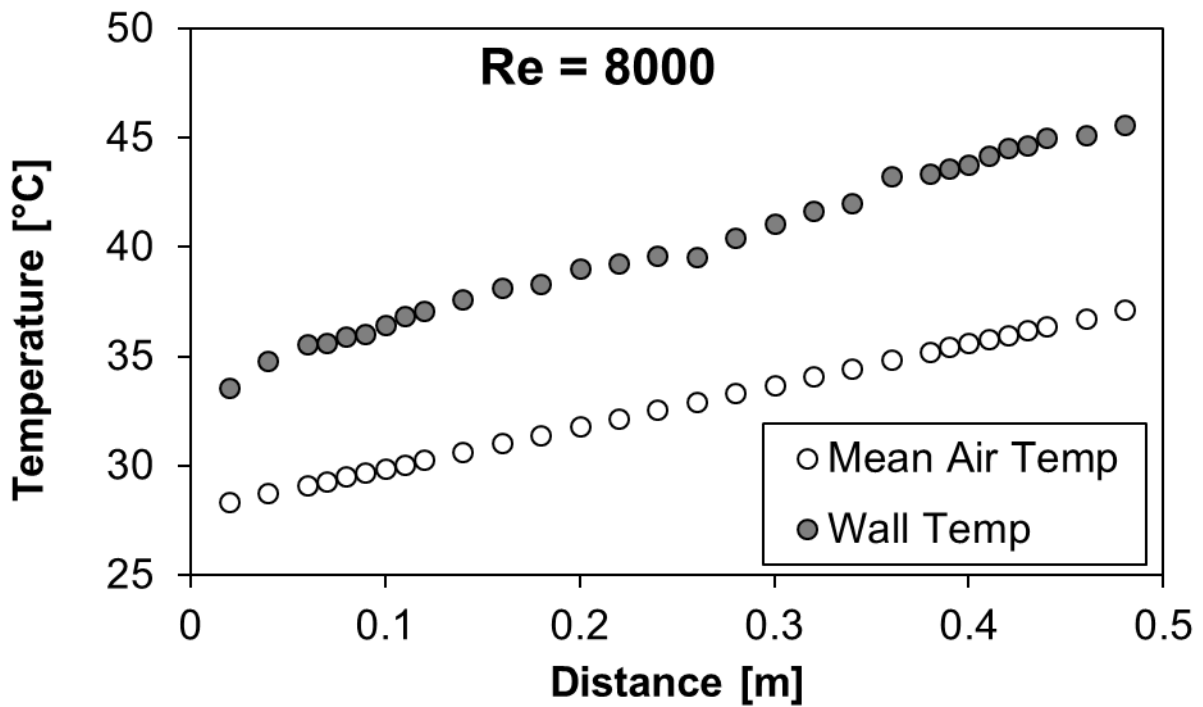


Figure E.22: Wall and mean air temperatures for mesh 4.3 under two-heated wall boundary condition at Re = 8 000

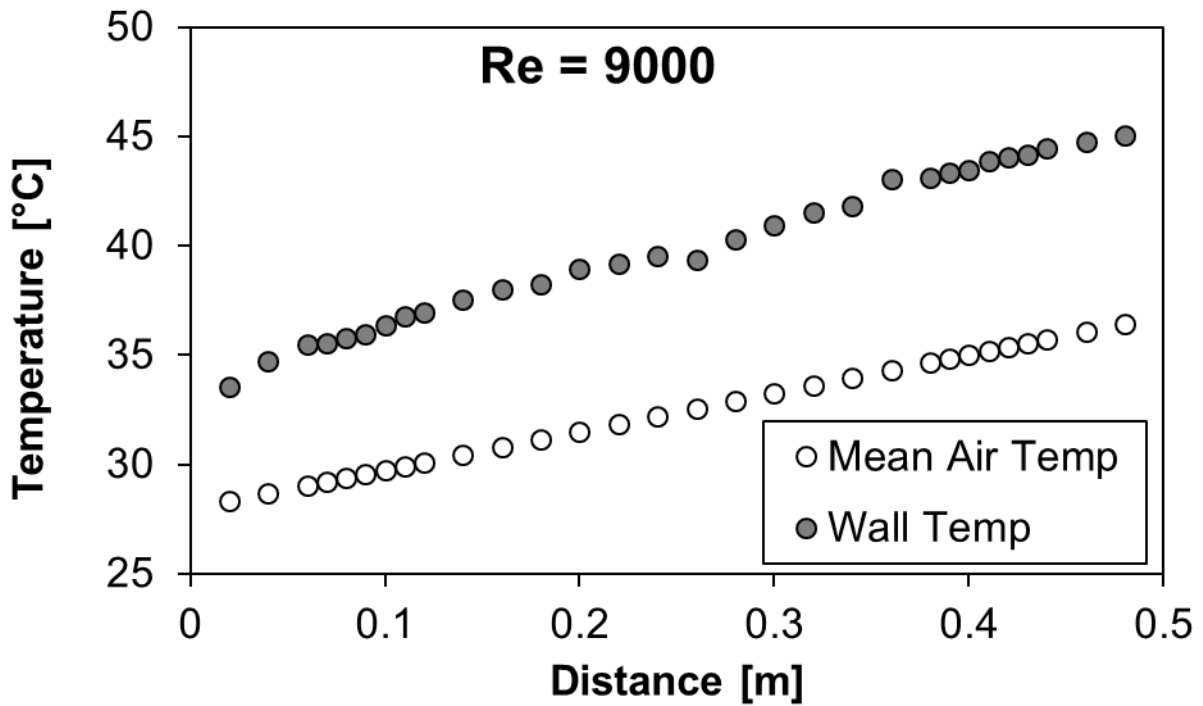


Figure E.23: Wall and mean air temperatures for mesh 4.3 under two-heated wall boundary condition at Re = 9 000

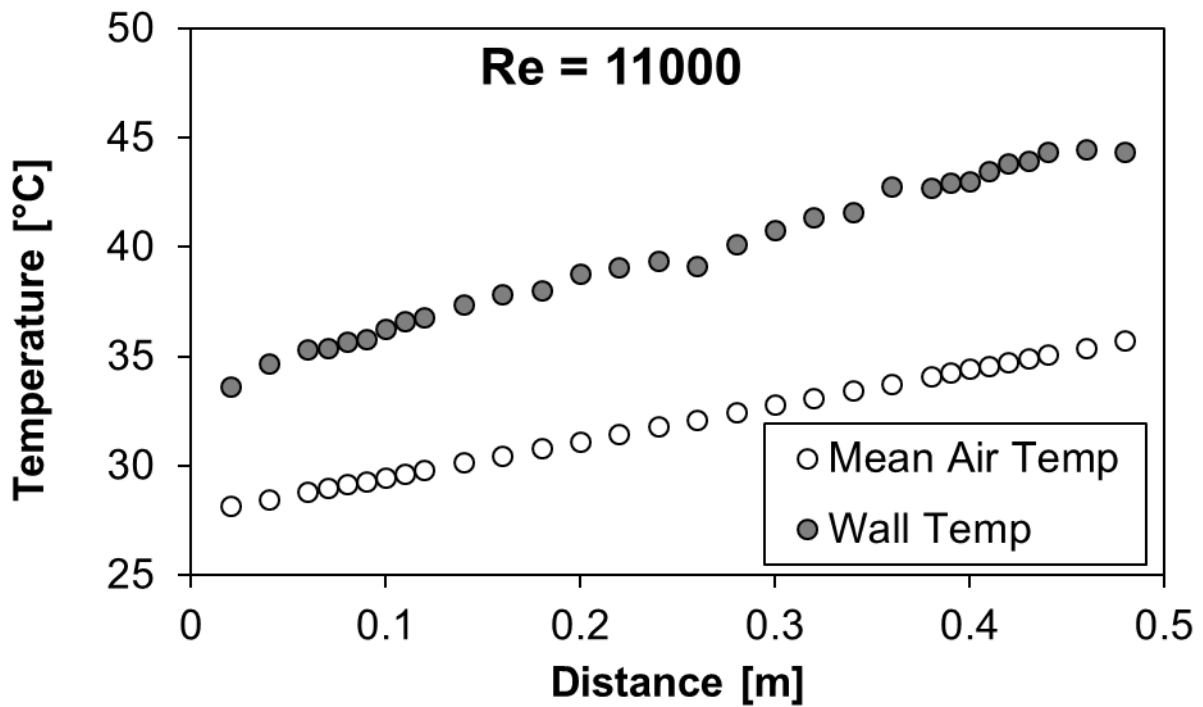


Figure E.24: Wall and mean air temperatures for mesh 4.3 under two-heated wall boundary condition at Re = 11 000

5 MM CHANNEL HEIGHT – MESH 5.1

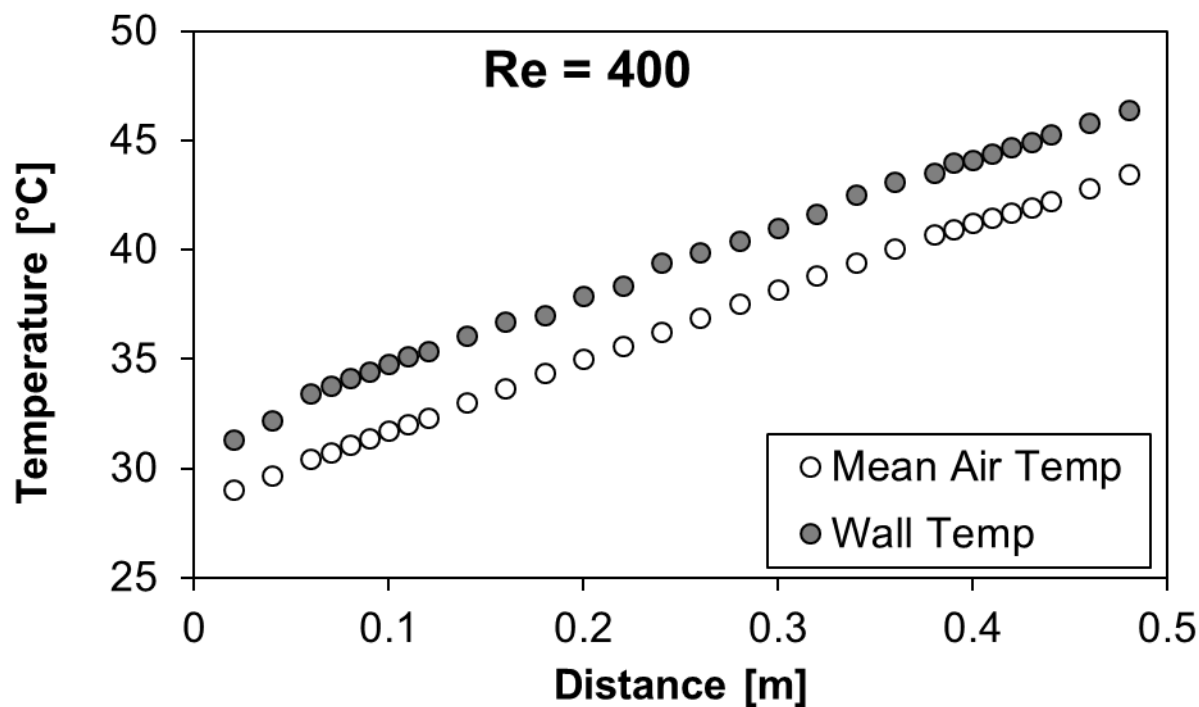


Figure E.25: Wall and mean air temperatures for mesh 5.1 under two-heated wall boundary condition at Re = 400

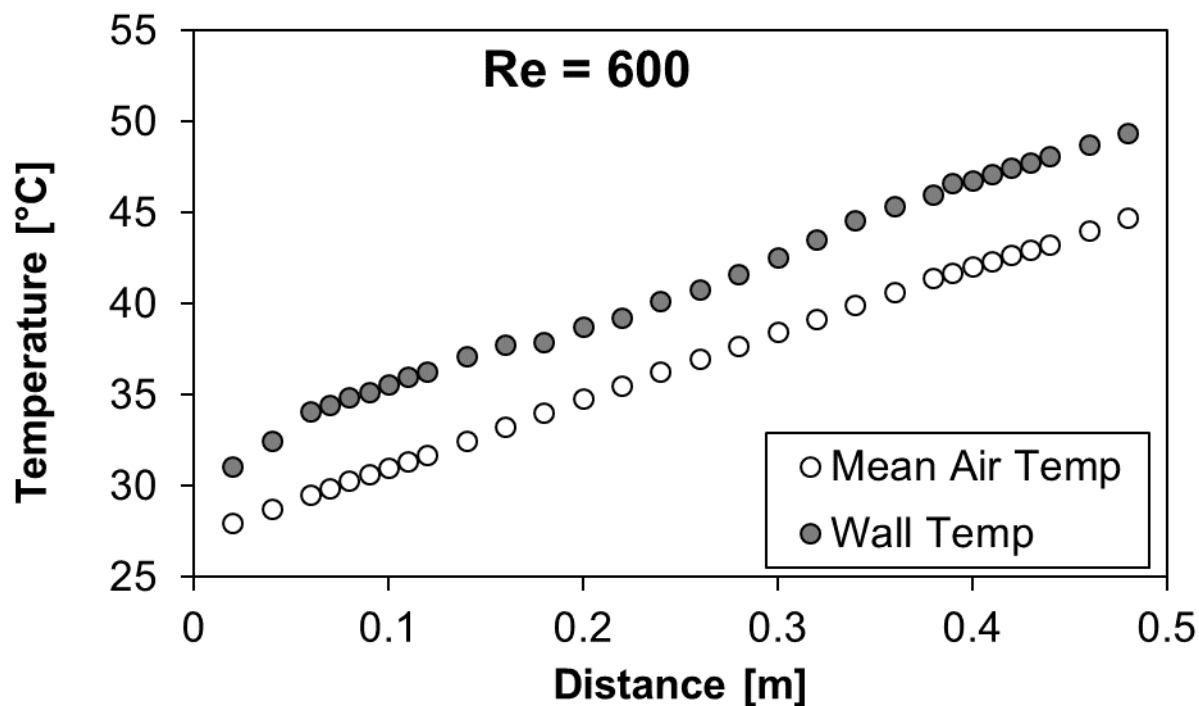


Figure E.26: Wall and mean air temperatures for mesh 5.1 under two-heated wall boundary condition at Re = 600

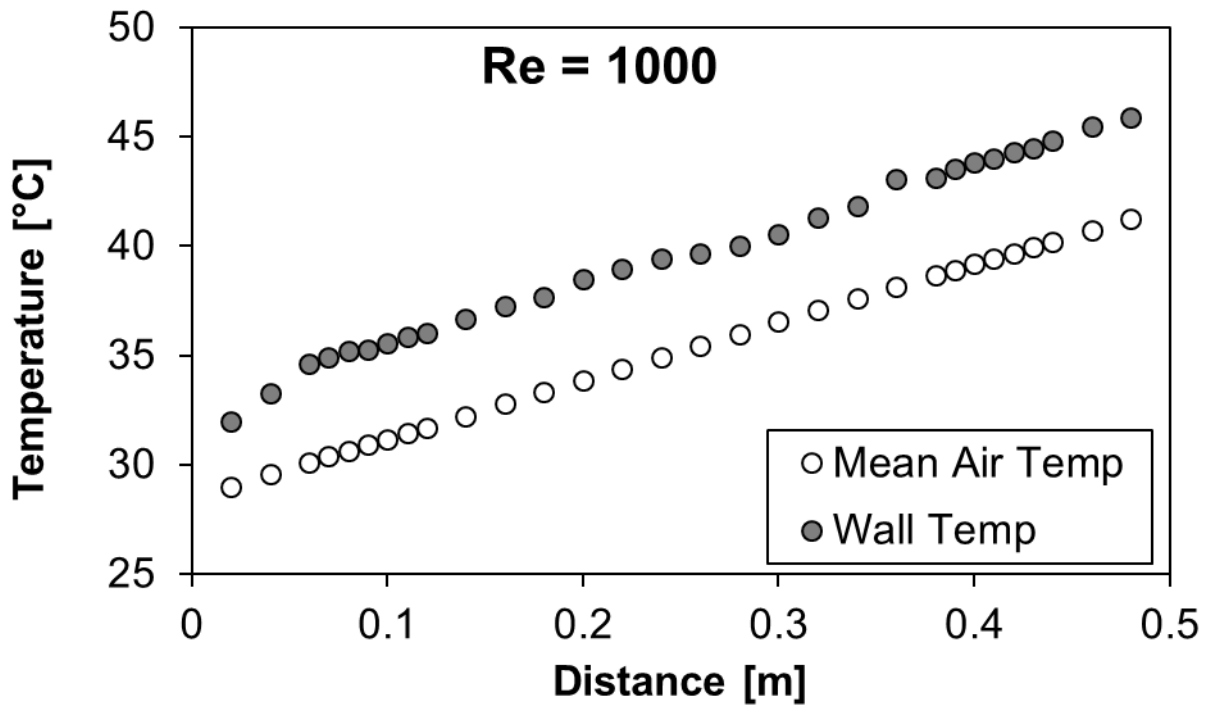


Figure E.27: Wall and mean air temperatures for mesh 5.1 under two-heated wall boundary condition at Re = 1 000

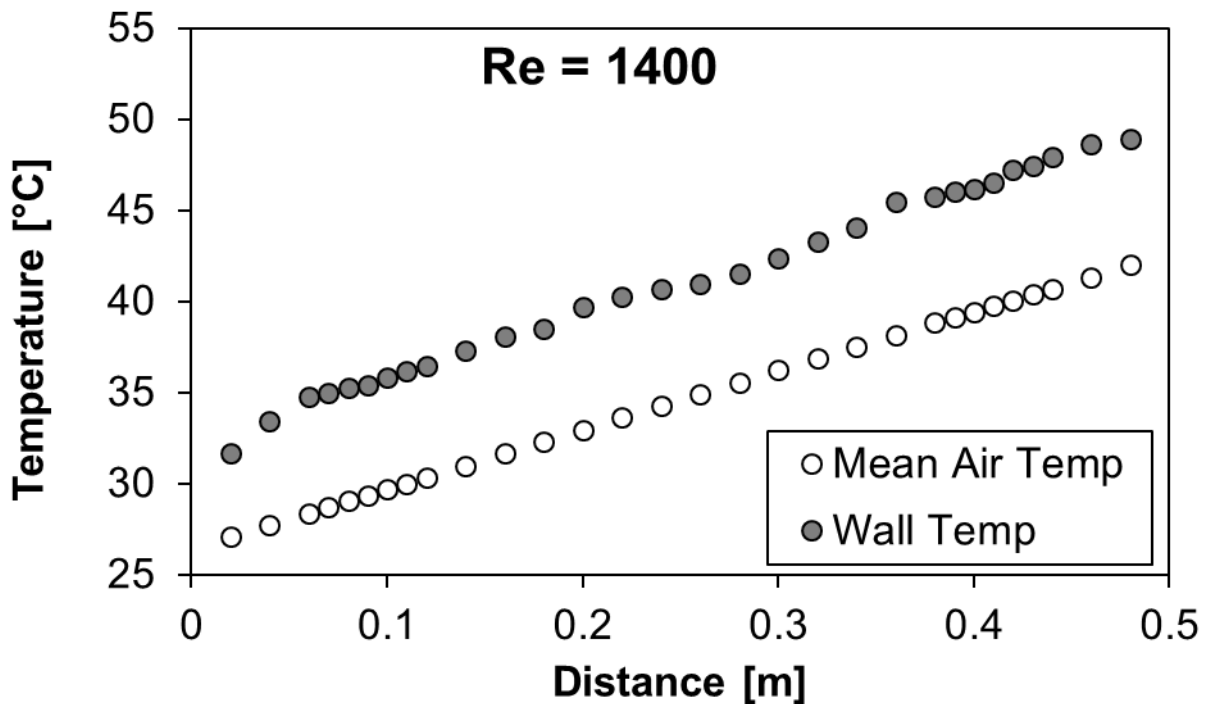


Figure E.28: Wall and mean air temperatures for mesh 5.1 under two-heated wall boundary condition at Re = 1 400

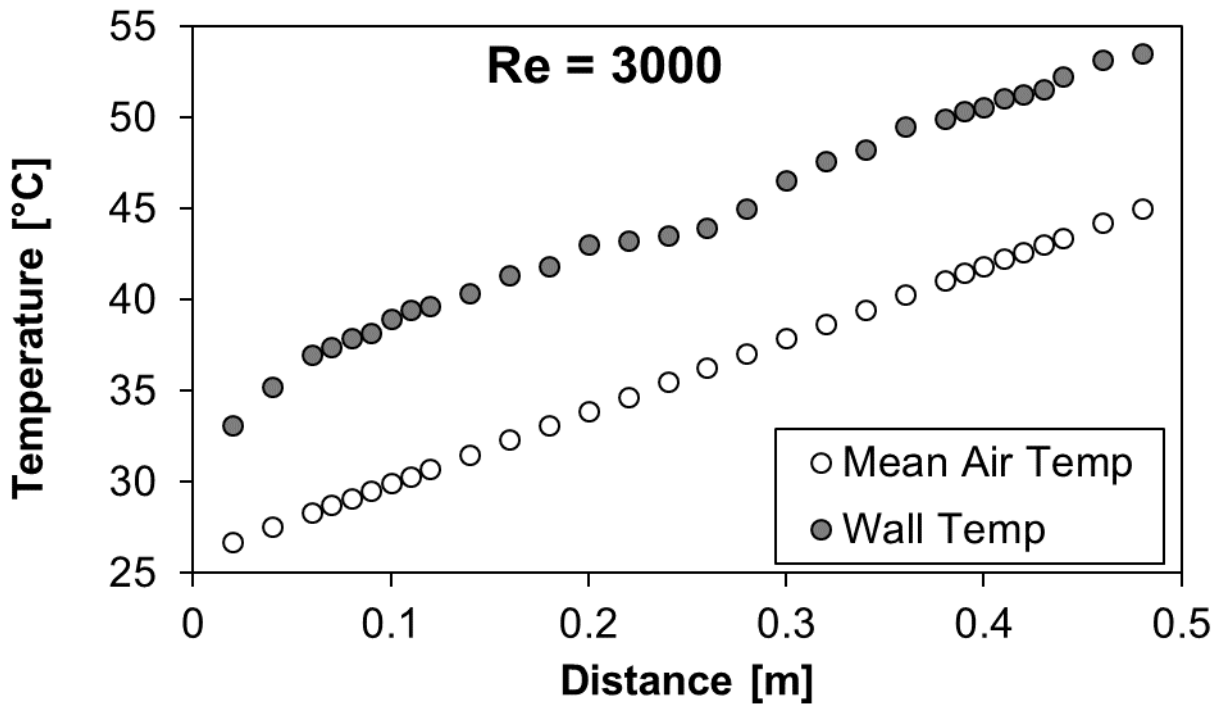


Figure E.29: Wall and mean air temperatures for mesh 5.1 under two-heated wall boundary condition at Re = 3 000

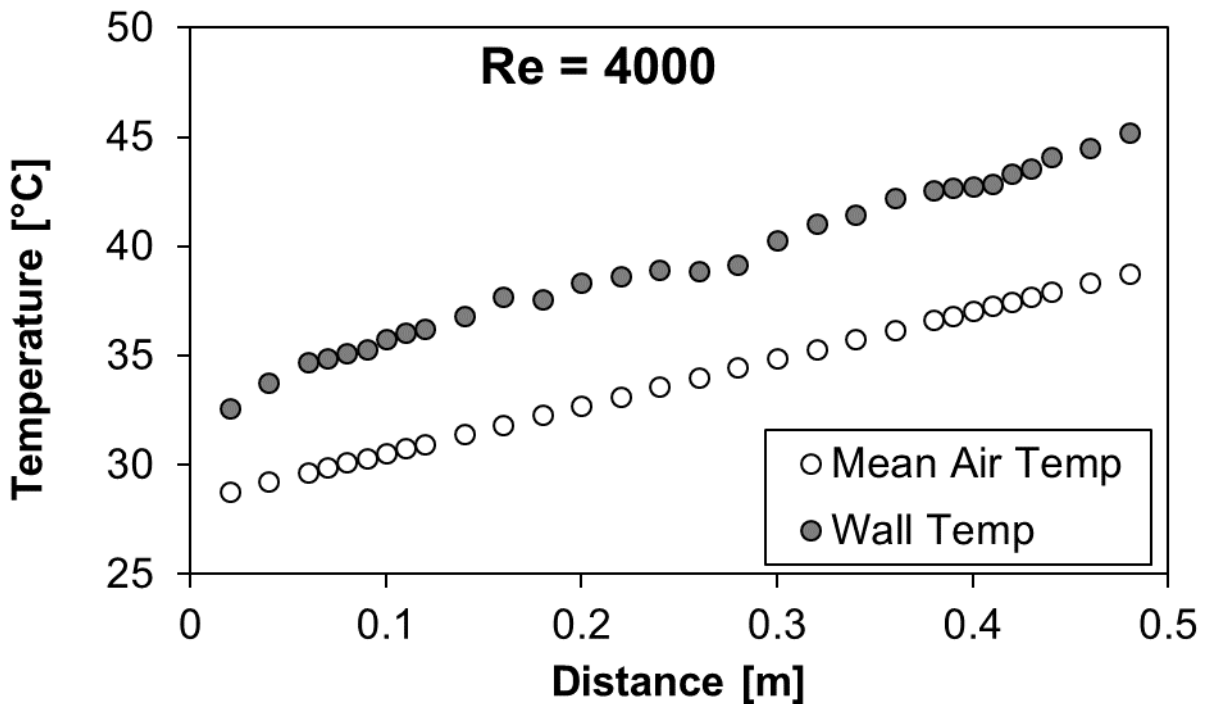


Figure E.30: Wall and mean air temperatures for mesh 5.1 under two-heated wall boundary condition at Re = 4 000

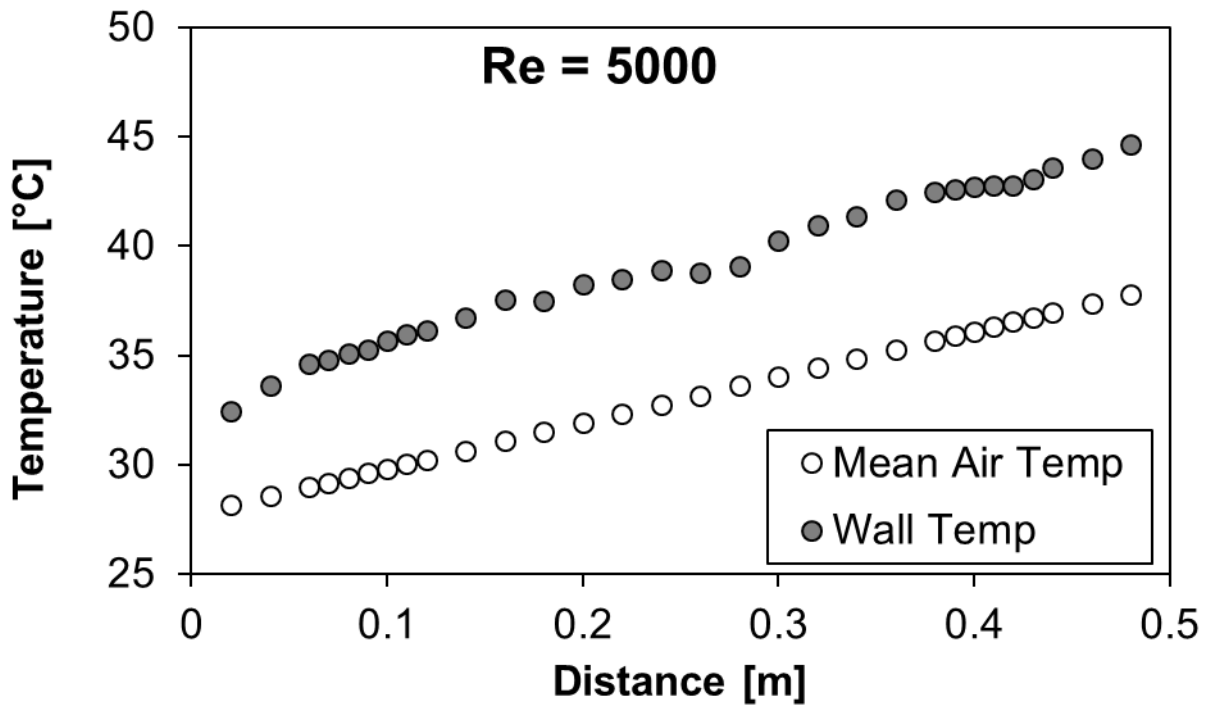


Figure E.31: Wall and mean air temperatures for mesh 5.1 under two-heated wall boundary condition at Re = 5 000

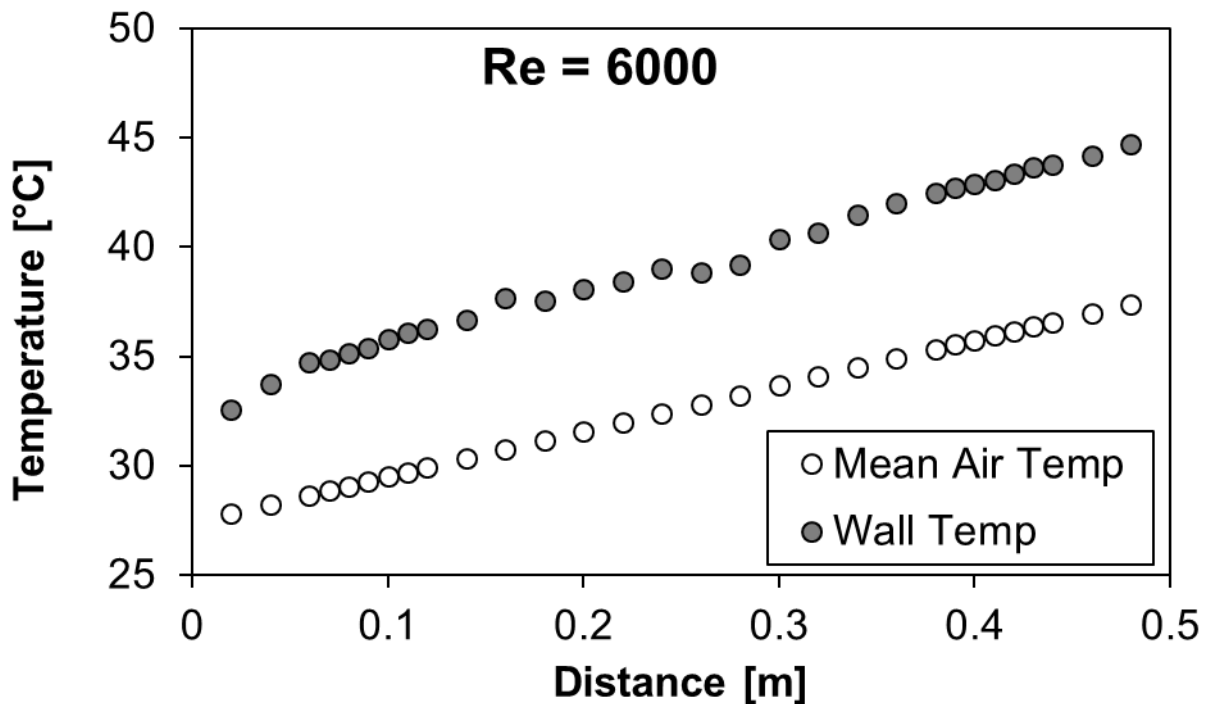


Figure E.32: Wall and mean air temperatures for mesh 5.1 under two-heated wall boundary condition at Re = 6 000

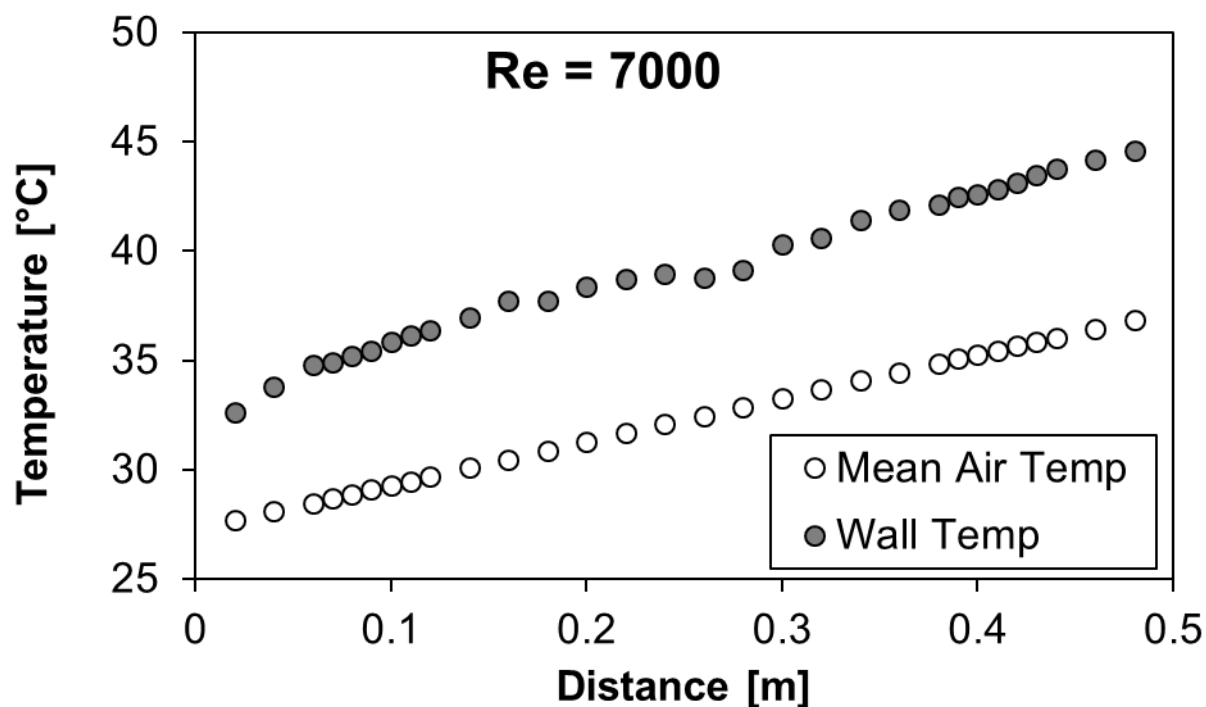


Figure E.33: Wall and mean air temperatures for mesh 5.1 under two-heated wall boundary condition at Re = 7 000

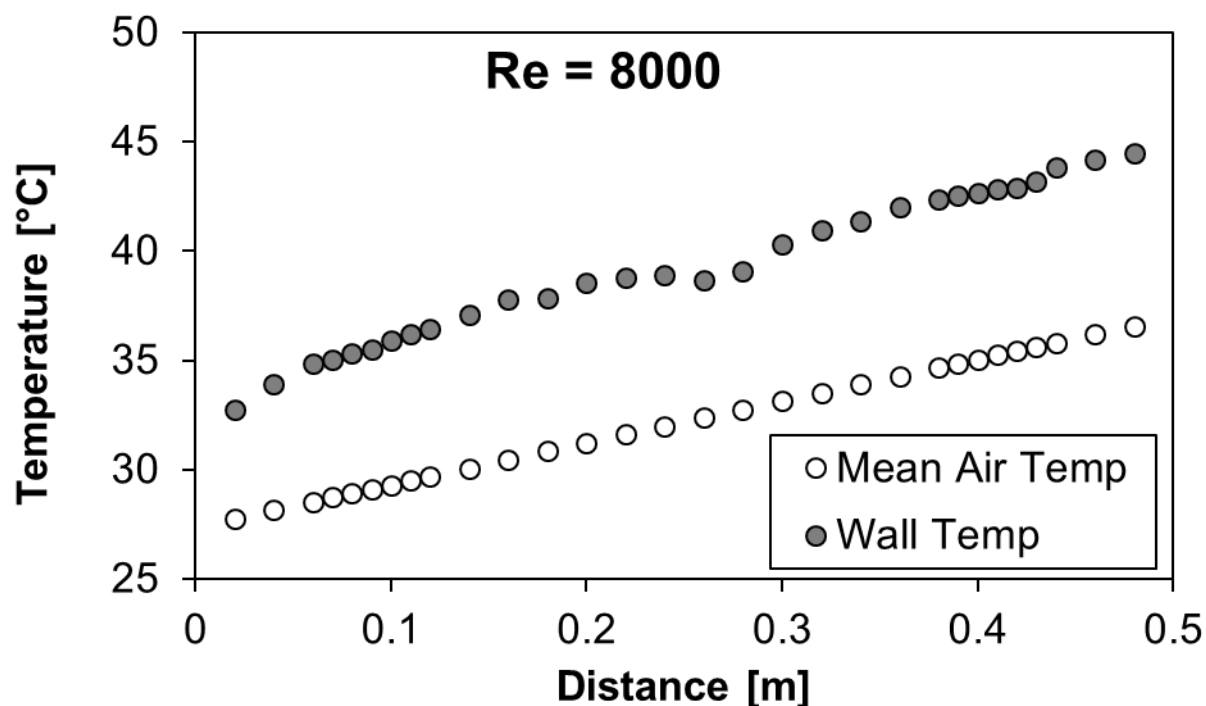


Figure E.34: Wall and mean air temperatures for mesh 5.1 under two-heated wall boundary condition at Re = 8 000

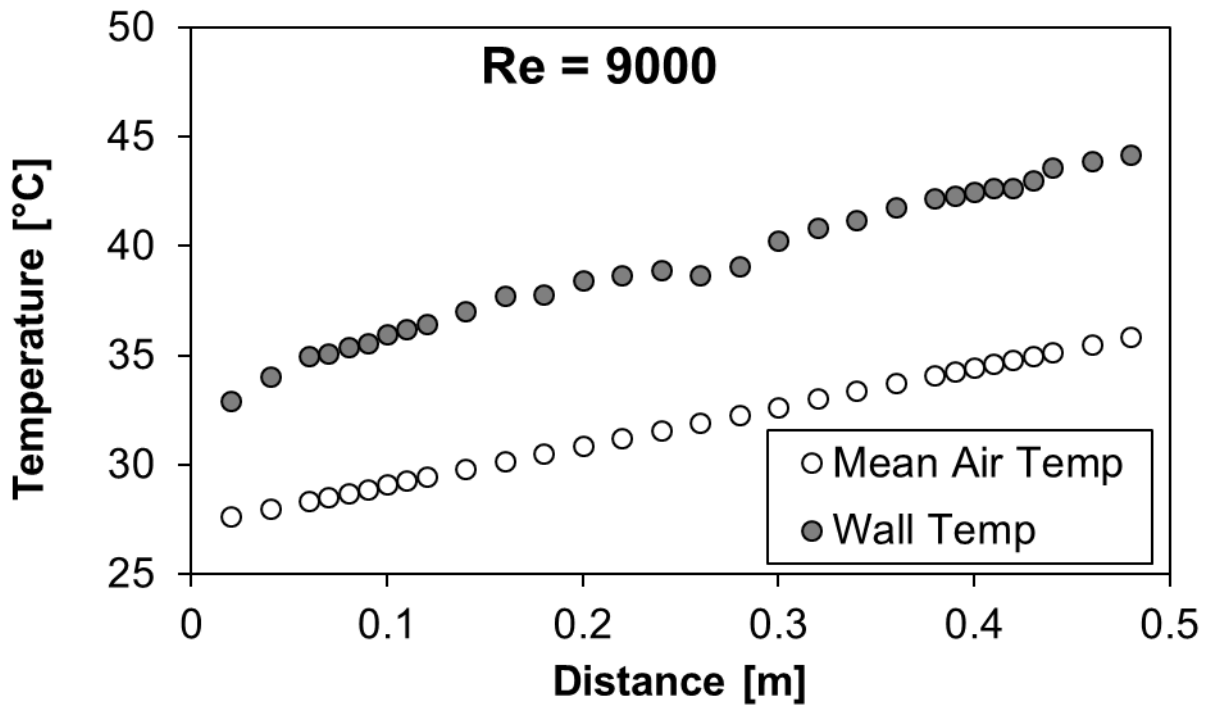


Figure E.35: Wall and mean air temperatures for mesh 5.1 under two-heated wall boundary condition at Re = 9 000

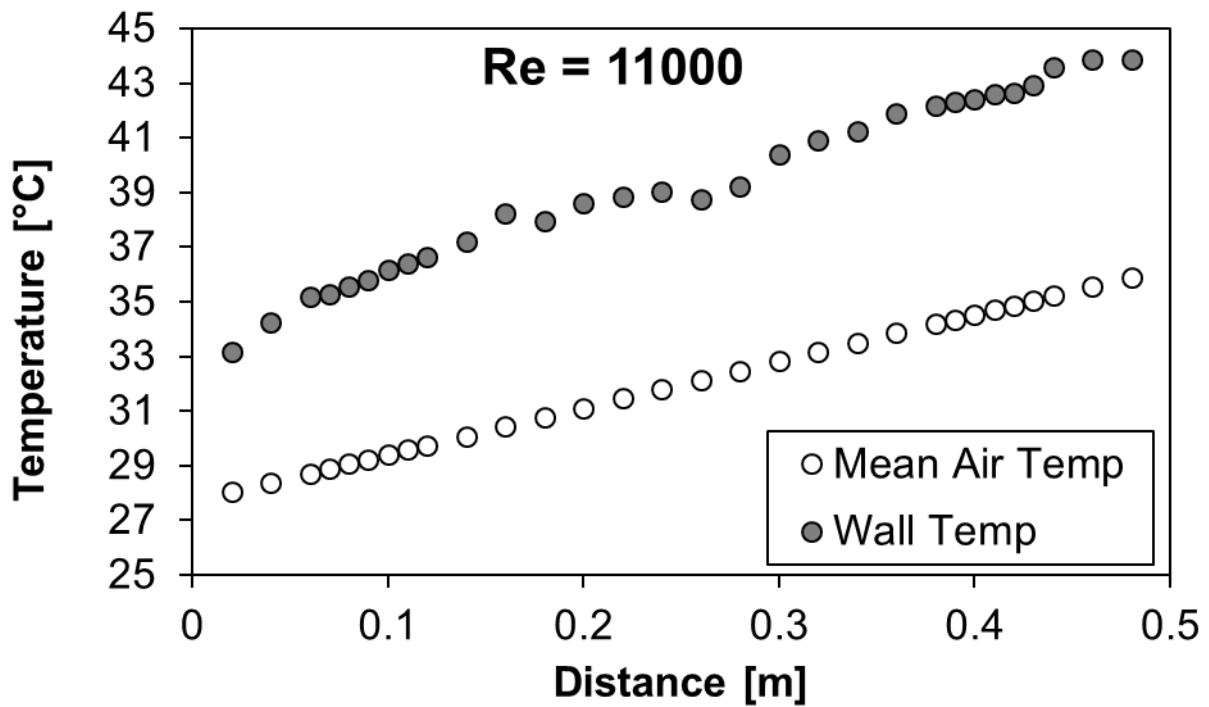


Figure E.36: Wall and mean air temperatures for mesh 5.1 under two-heated wall boundary condition at Re = 11 000

5 MM CHANNEL HEIGHT – MESH 5.3

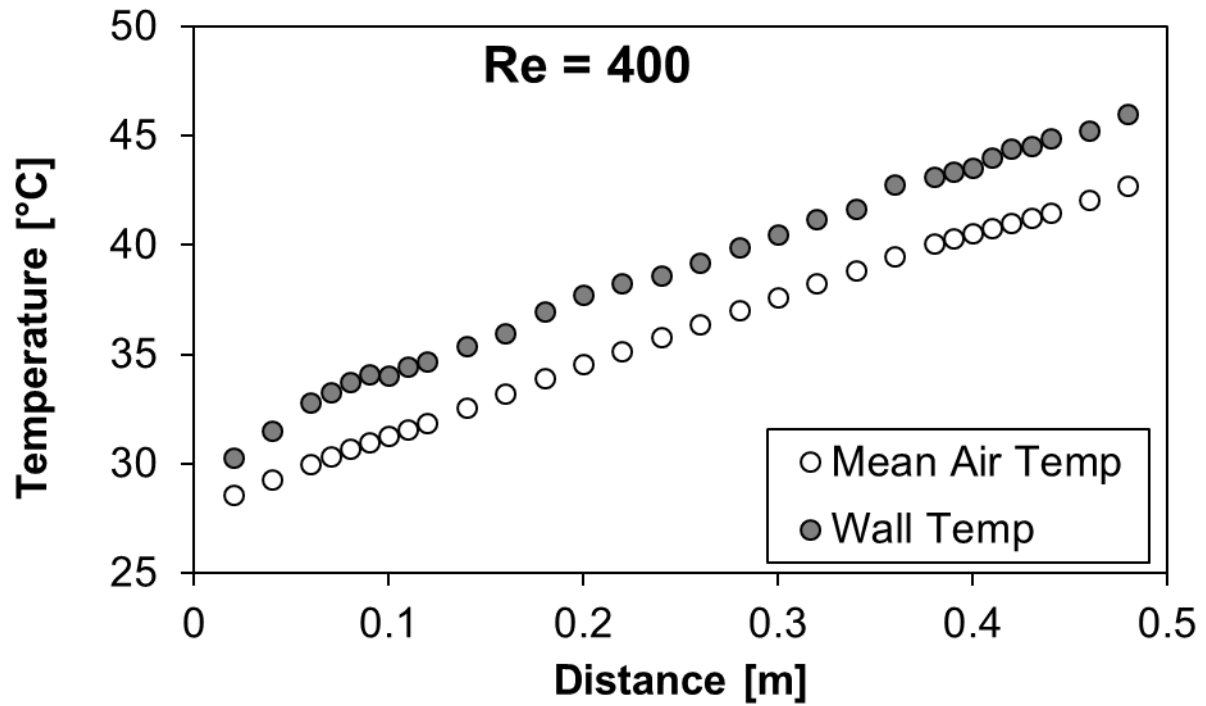


Figure E.37: Wall and mean air temperatures for mesh 5.3 under two-heated wall boundary condition at Re = 400

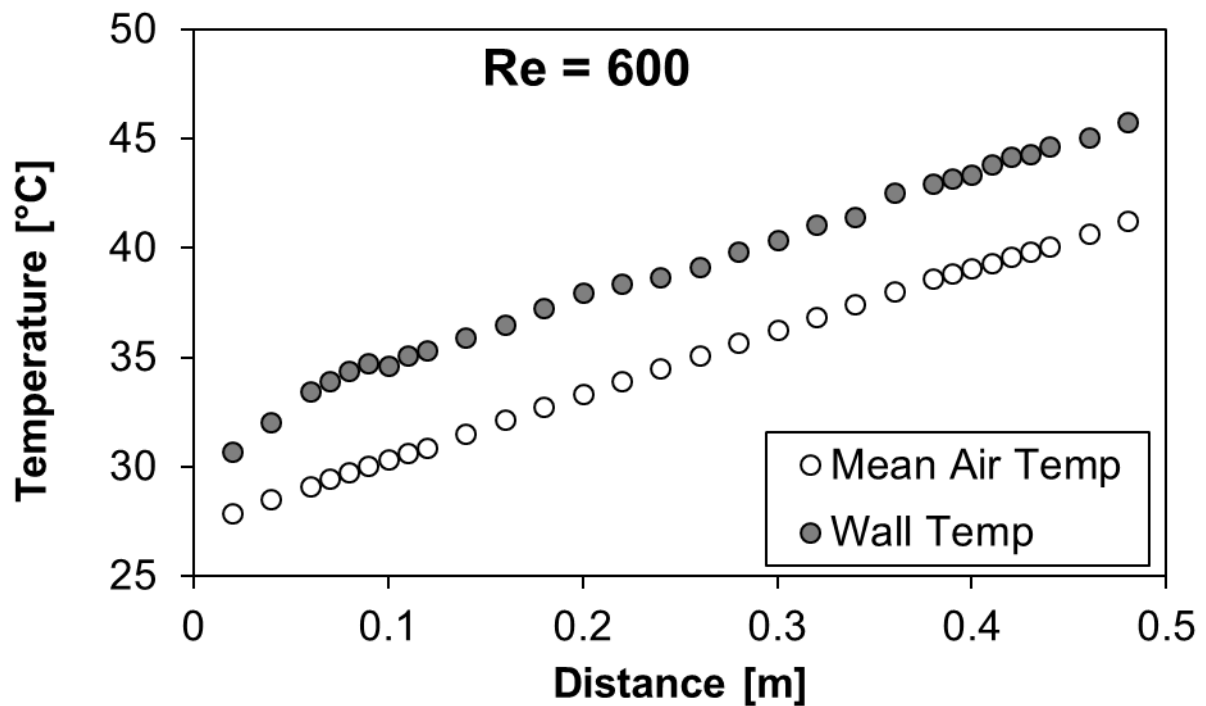


Figure E.38: Wall and mean air temperatures for mesh 5.3 under two-heated wall boundary condition at Re = 600

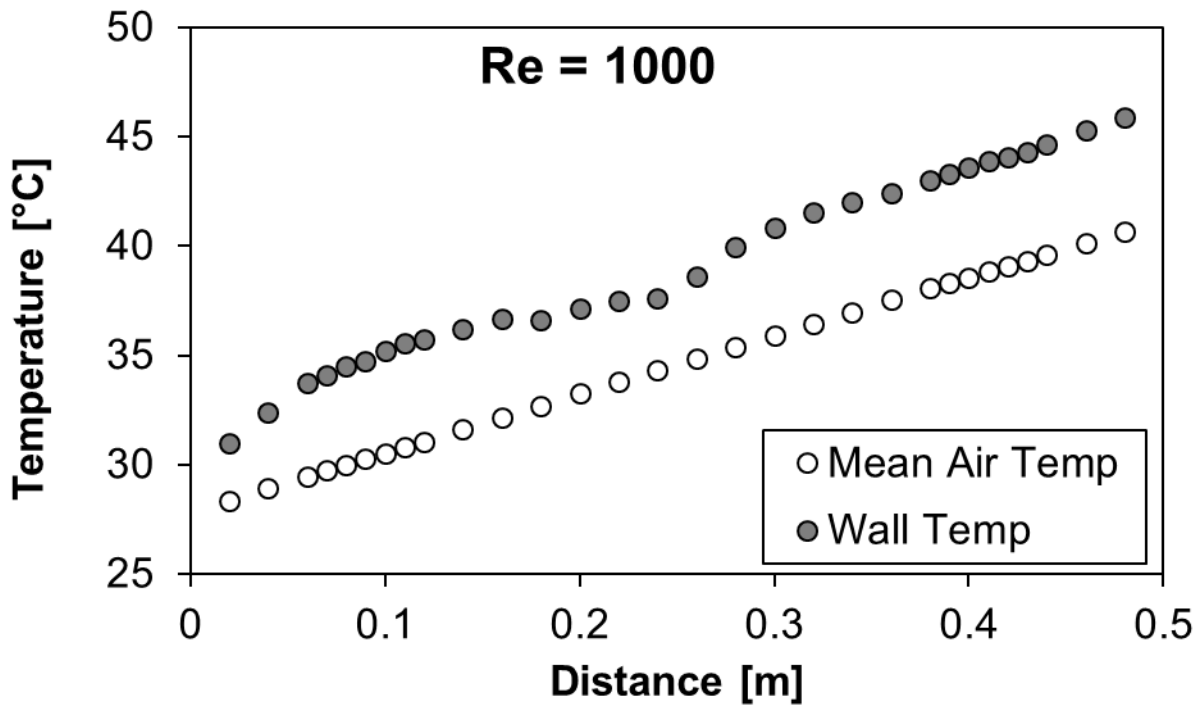


Figure E.39: Wall and mean air temperatures for mesh 5.3 under two-heated wall boundary condition at Re = 1 000

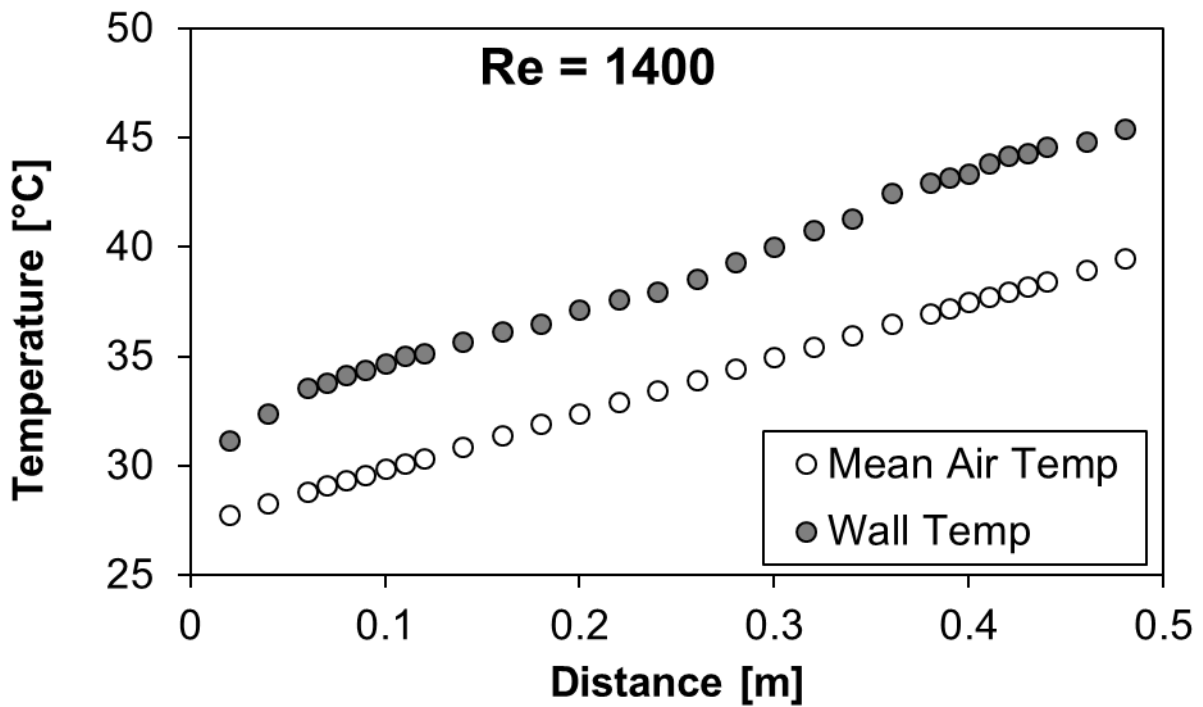


Figure E.40: Wall and mean air temperatures for mesh 5.3 under two-heated wall boundary condition at Re = 1 400

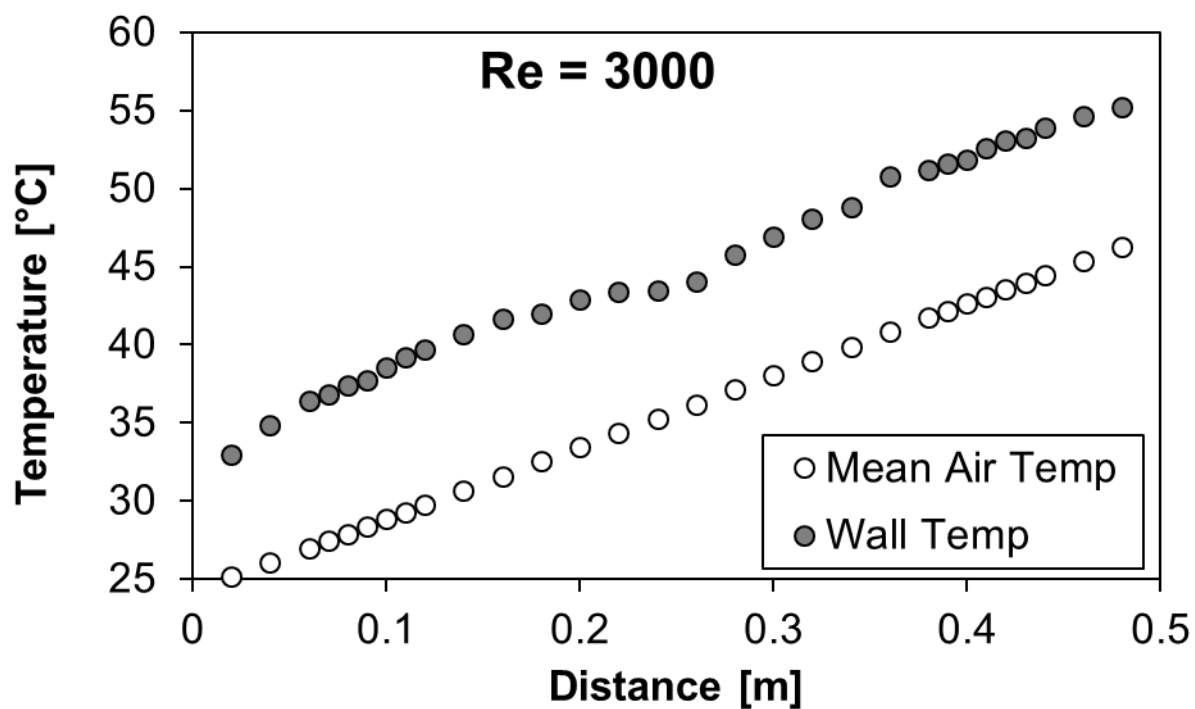


Figure E.41: Wall and mean air temperatures for mesh 5.3 under two-heated wall boundary condition at Re = 3 000

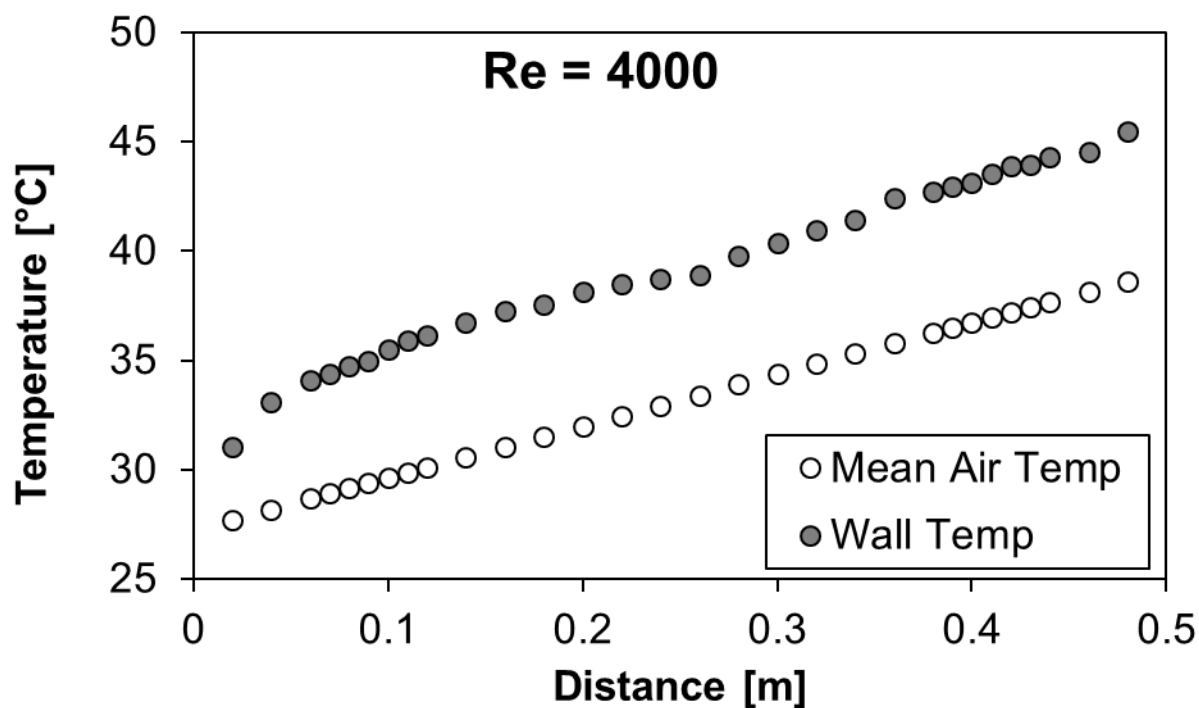


Figure E.42: Wall and mean air temperatures for mesh 5.3 under two-heated wall boundary condition at Re = 4 000

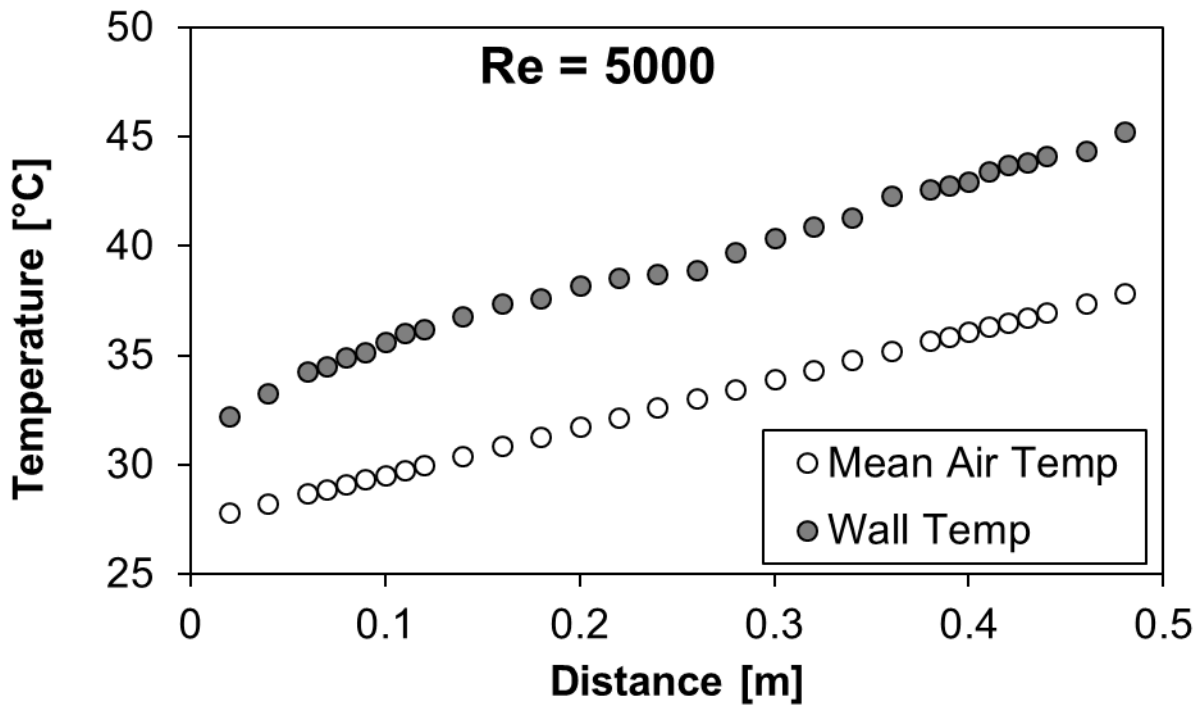


Figure E.43: Wall and mean air temperatures for mesh 5.3 under two-heated wall boundary condition at Re = 5 000

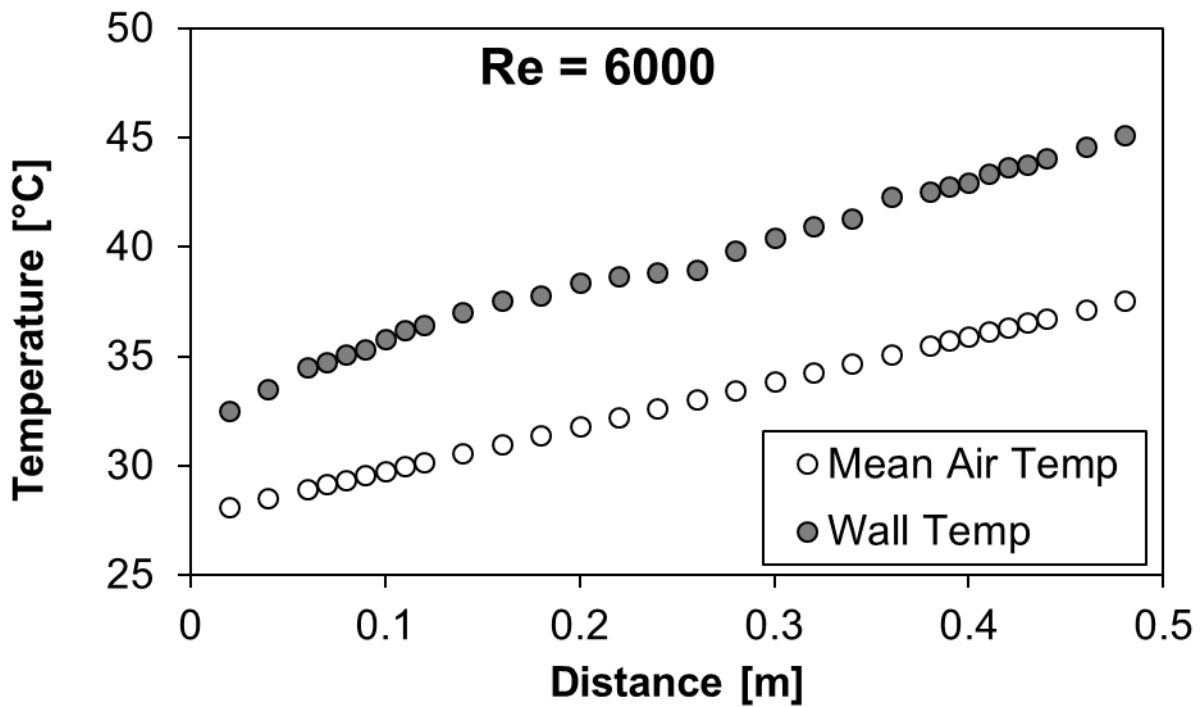


Figure E.44: Wall and mean air temperatures for mesh 5.3 under two-heated wall boundary condition at Re = 6 000

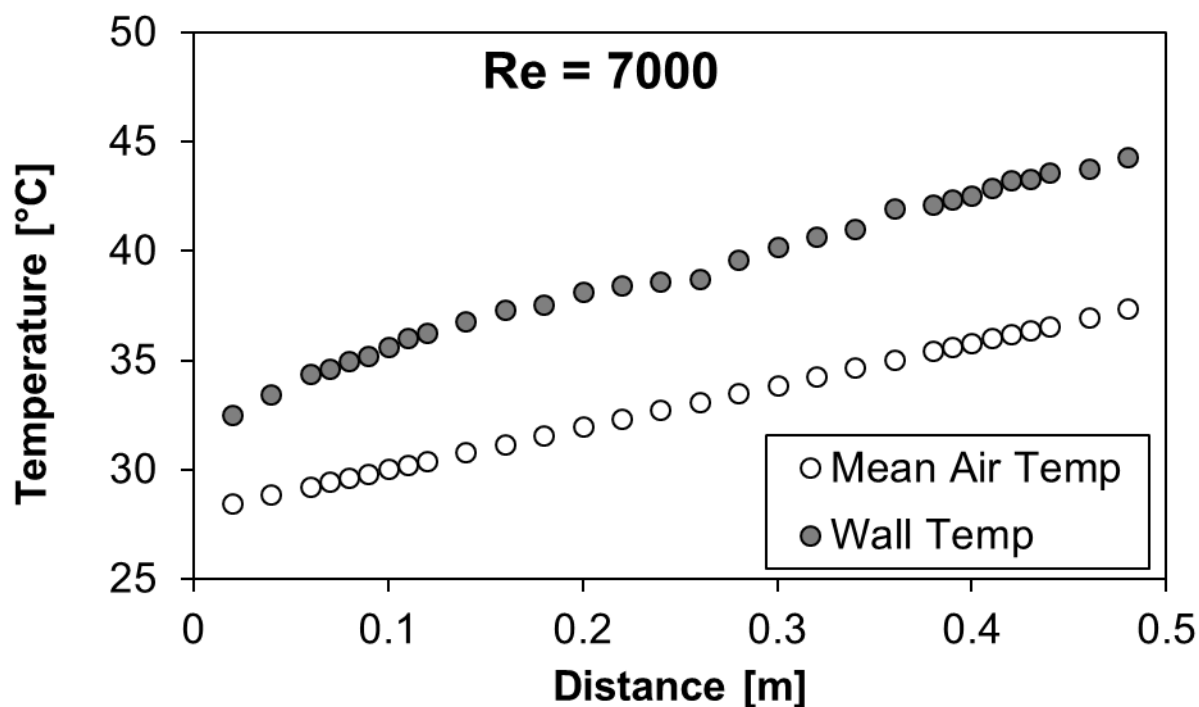


Figure E.45: Wall and mean air temperatures for mesh 5.3 under two-heated wall boundary condition at Re = 7 000

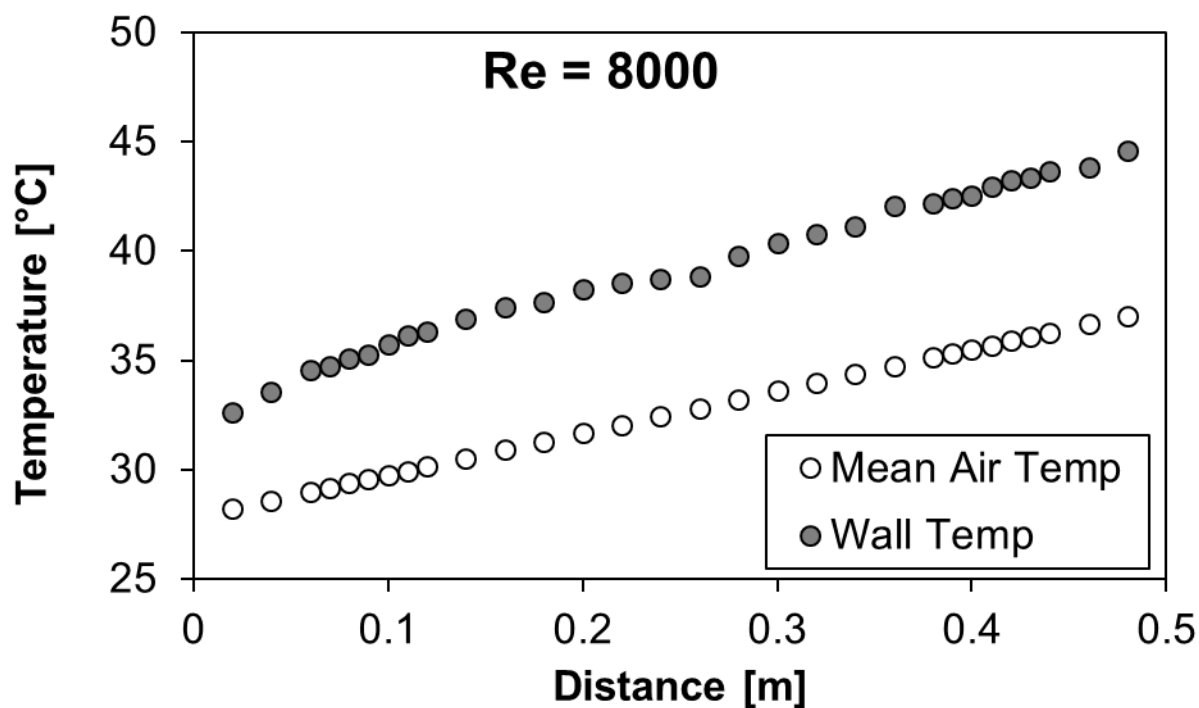


Figure E.46: Wall and mean air temperatures for mesh 5.3 under two-heated wall boundary condition at Re = 8 000

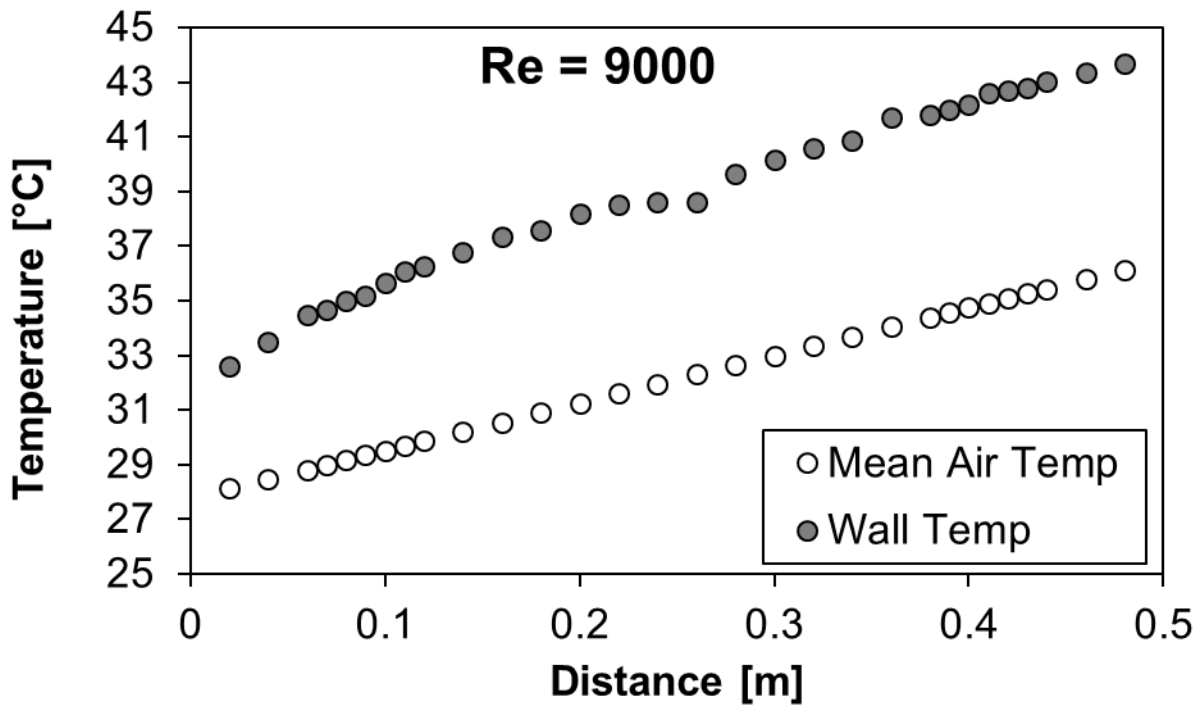


Figure E.47: Wall and mean air temperatures for mesh 5.3 under two-heated wall boundary condition at Re = 9 000

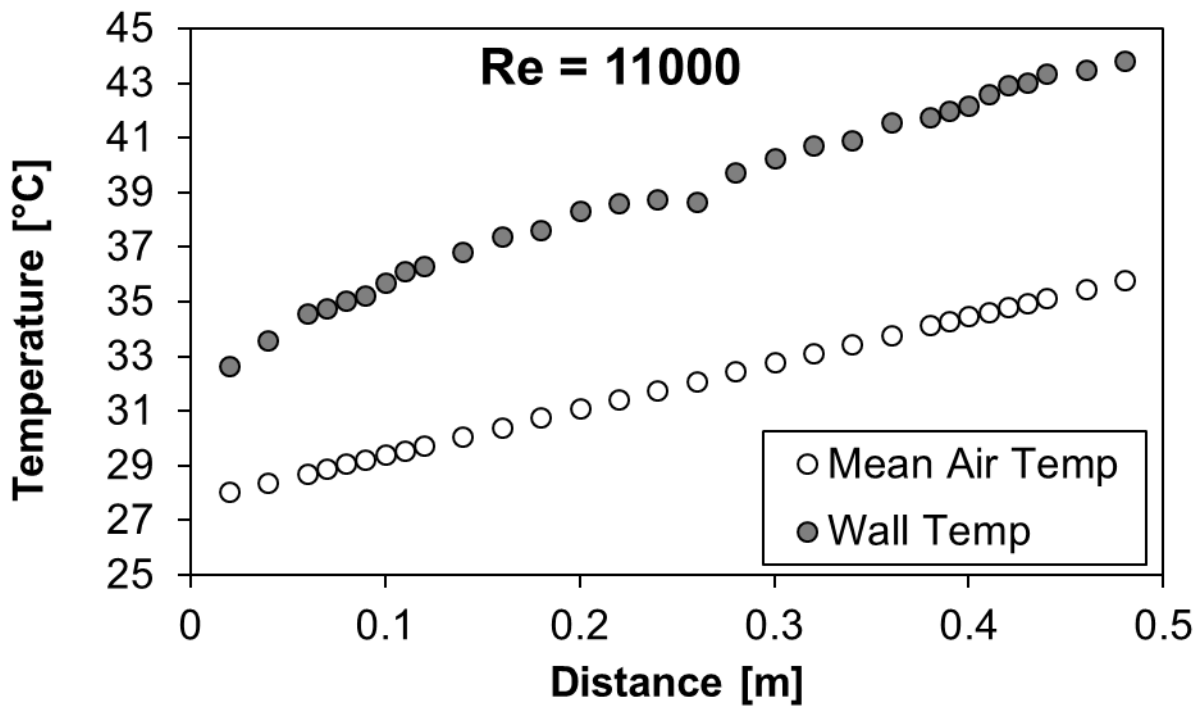


Figure E.48: Wall and mean air temperatures for mesh 5.3 under two-heated wall boundary condition at Re = 11 000

14 MM CHANNEL HEIGHT – MESH 2.1

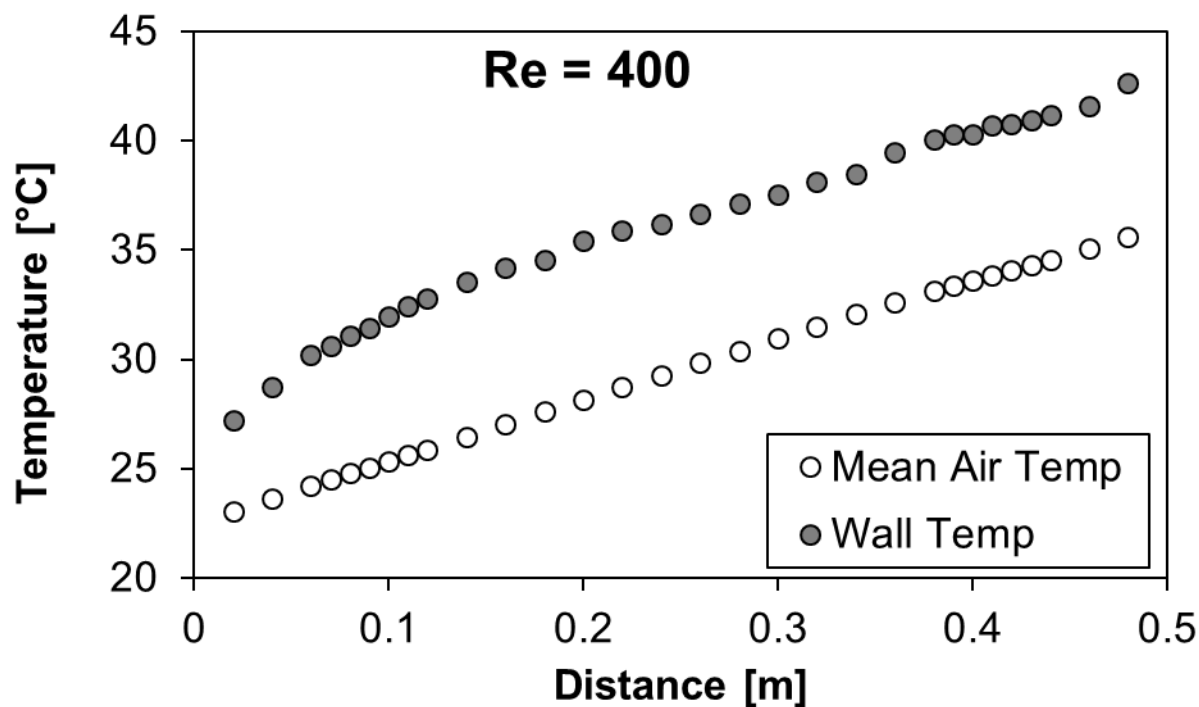


Figure E.49: Wall and mean air temperatures for mesh 2.1 under two-heated wall boundary condition at Re = 400

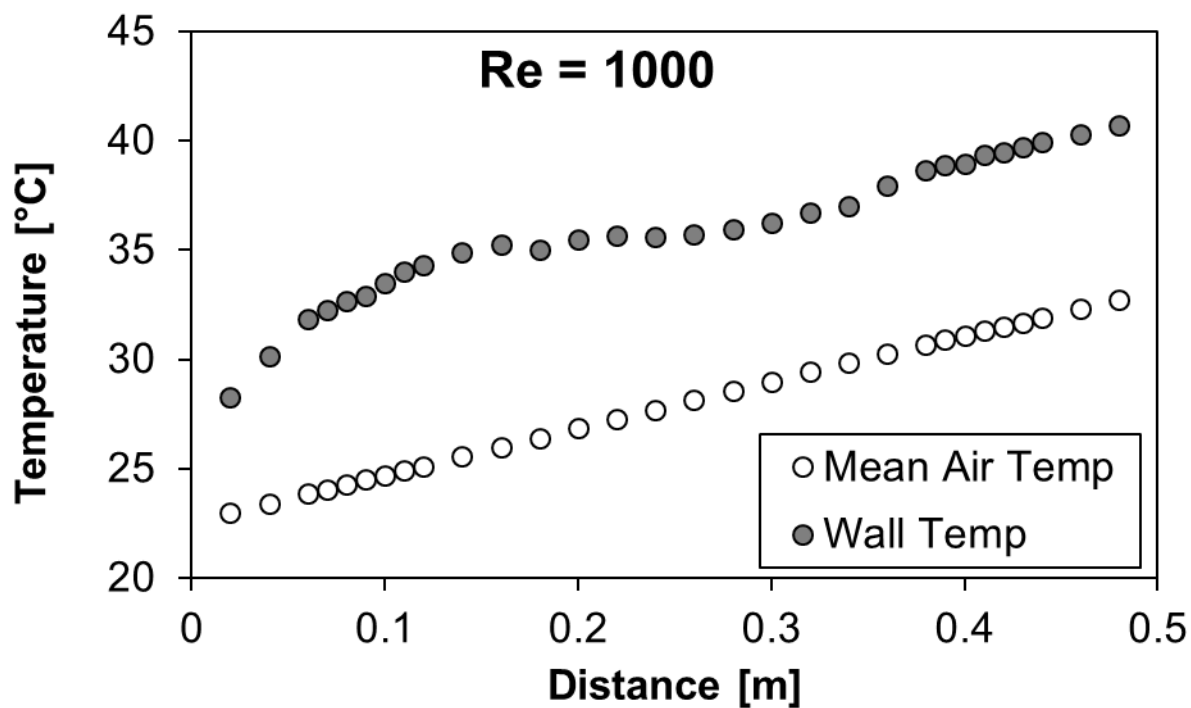


Figure E.50: Wall and mean air temperatures for mesh 2.1 under two-heated wall boundary condition at Re = 1 000

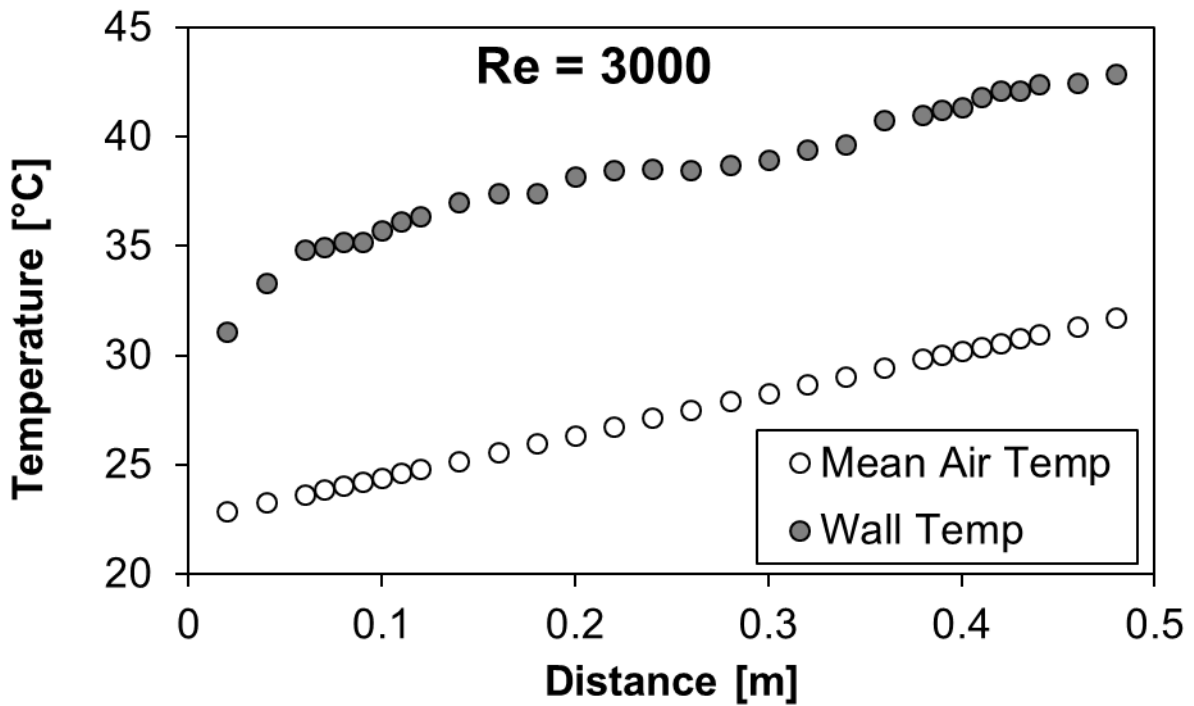


Figure E.51: Wall and mean air temperatures for mesh 2.1 under two-heated wall boundary condition at Re = 3 000

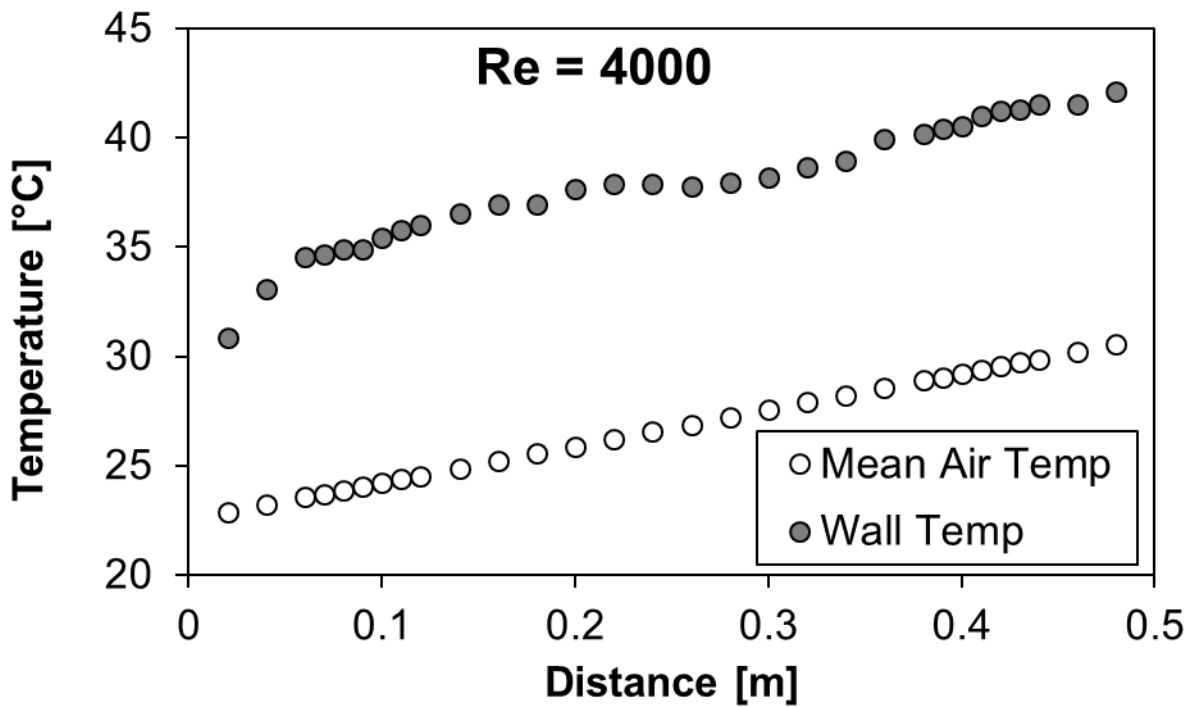


Figure E.52: Wall and mean air temperatures for mesh 2.1 under two-heated wall boundary condition at Re = 4 000

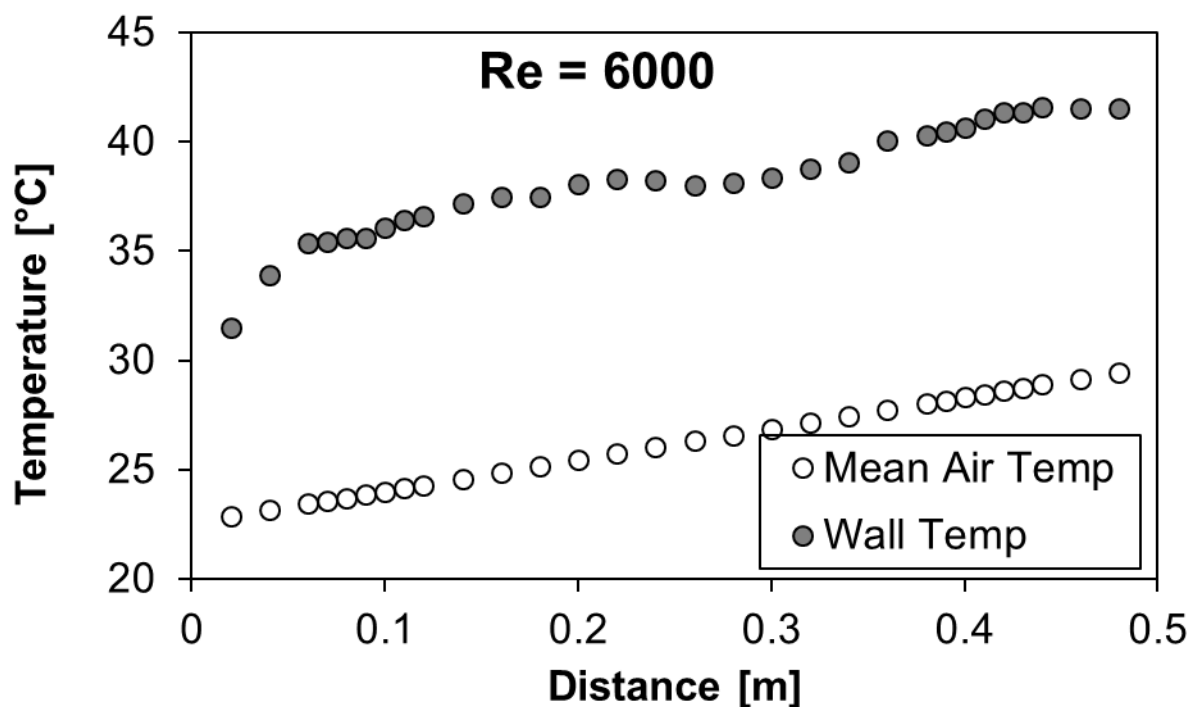


Figure E.53: Wall and mean air temperatures for mesh 2.1 under two-heated wall boundary condition at Re = 6 000

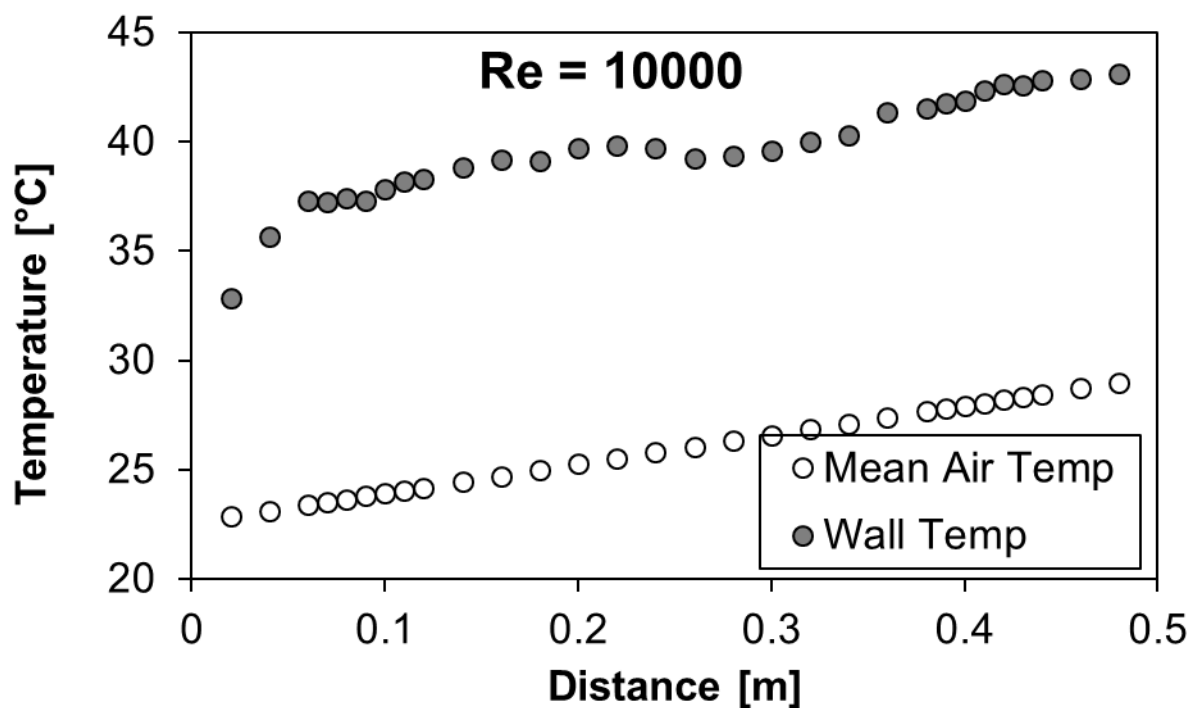


Figure E.54: Wall and mean air temperatures for mesh 2.1 under two-heated wall boundary condition at Re = 10 000

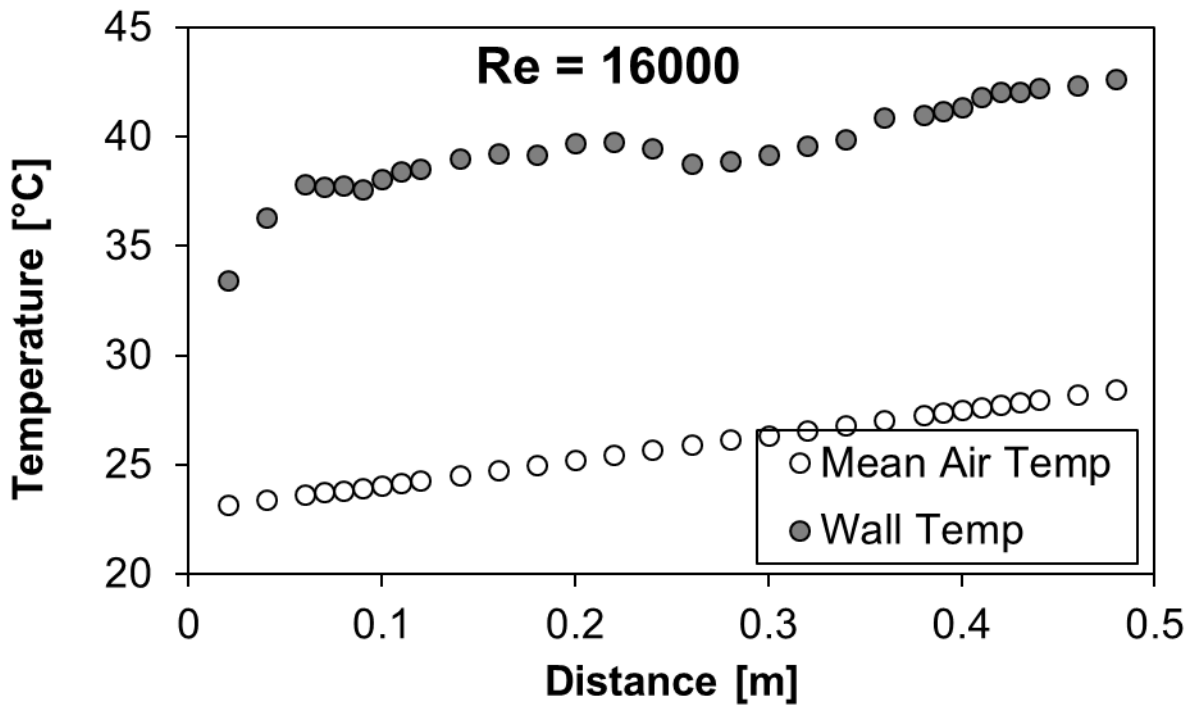


Figure E.55: Wall and mean air temperatures for mesh 2.1 under two-heated wall boundary condition at Re = 16 000

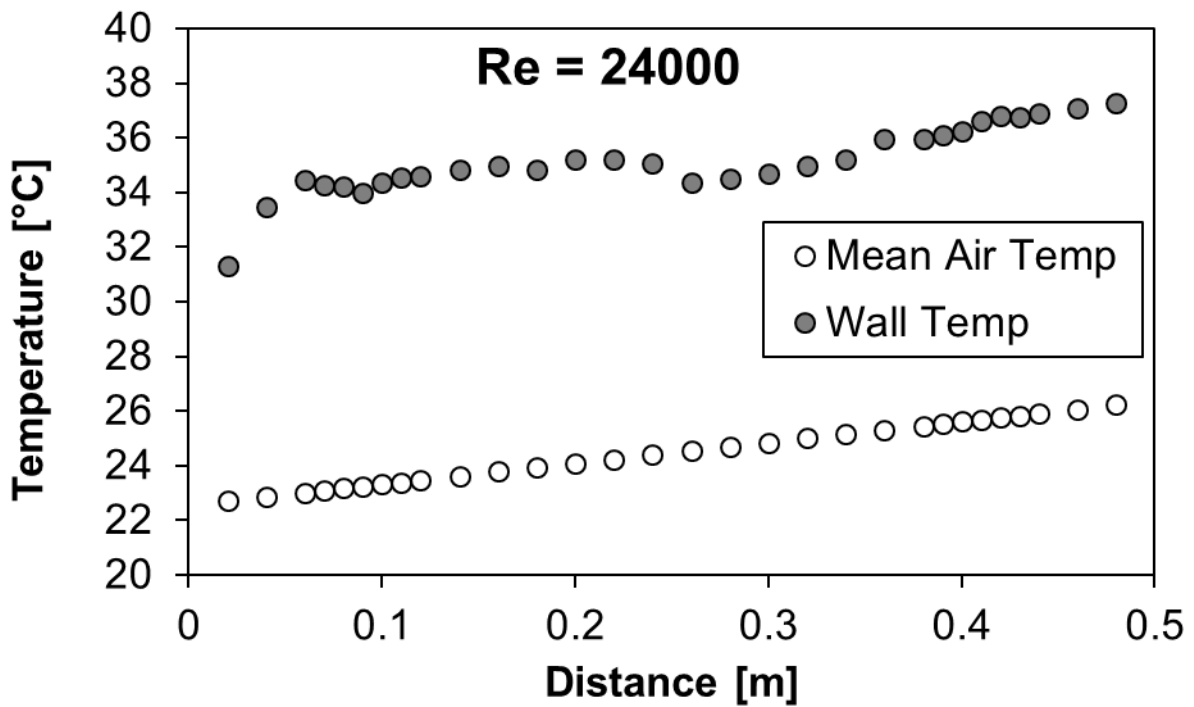


Figure E.56: Wall and mean air temperatures for mesh 2.1 under two-heated wall boundary condition at Re = 24 000

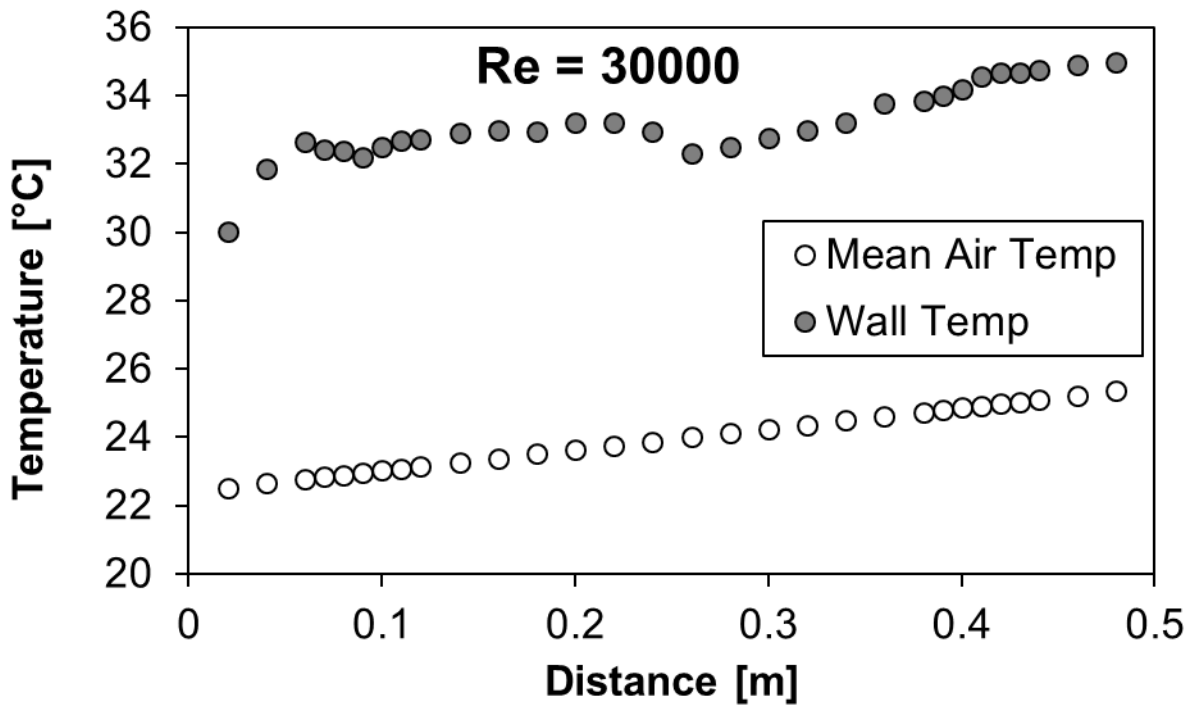


Figure E.57: Wall and mean air temperatures for mesh 2.1 under two-heated wall boundary condition at $Re = 30\ 000$

14 MM CHANNEL HEIGHT – MESH 2.3

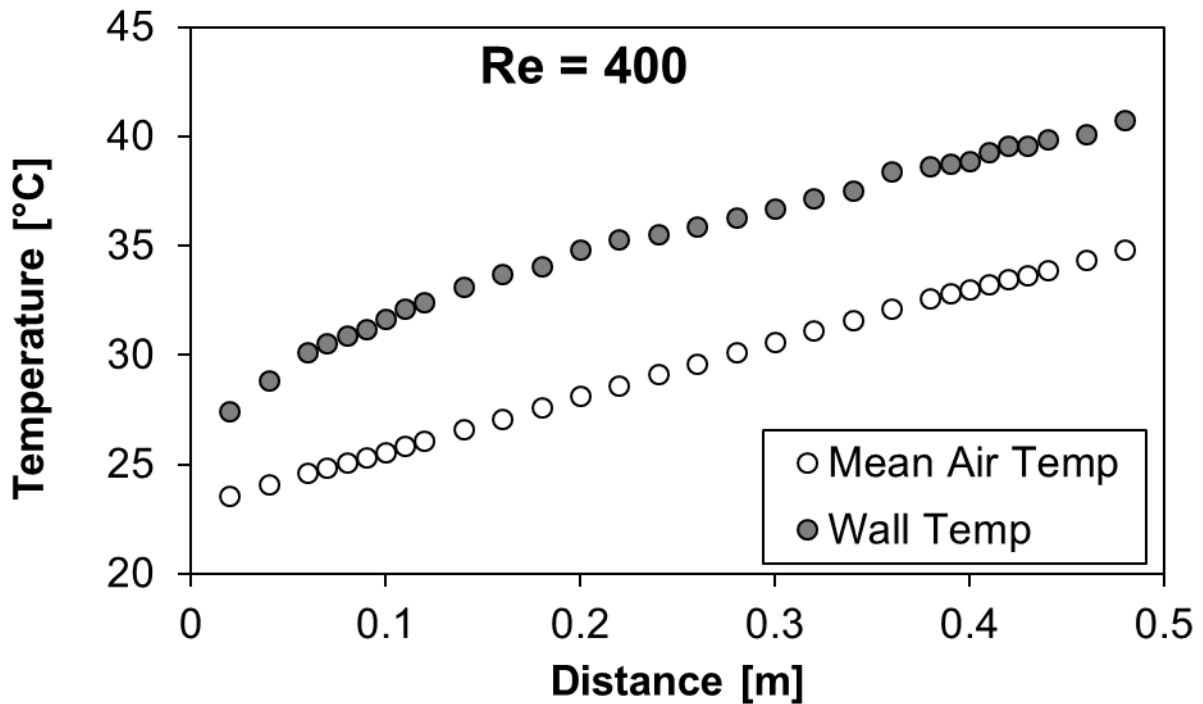


Figure E.58: Wall and mean air temperatures for mesh 2.3 under two-heated wall boundary condition at $Re = 400$

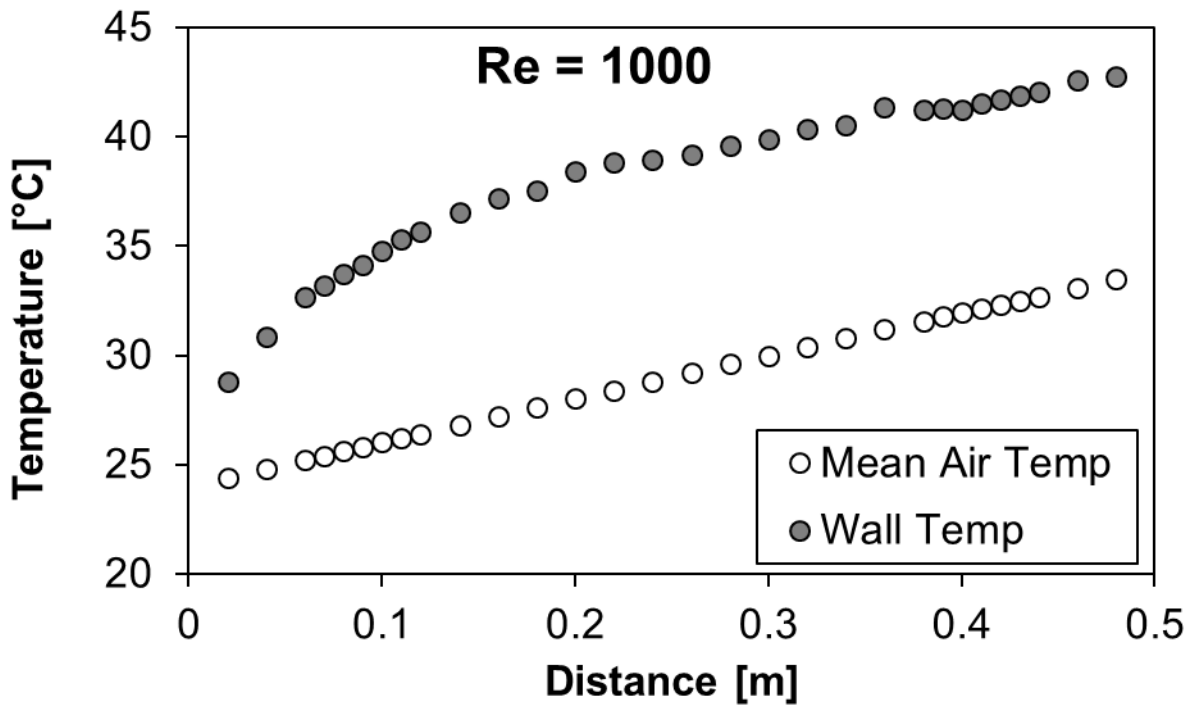


Figure E.59: Wall and mean air temperatures for mesh 2.3 under two-heated wall boundary condition at Re = 1 000

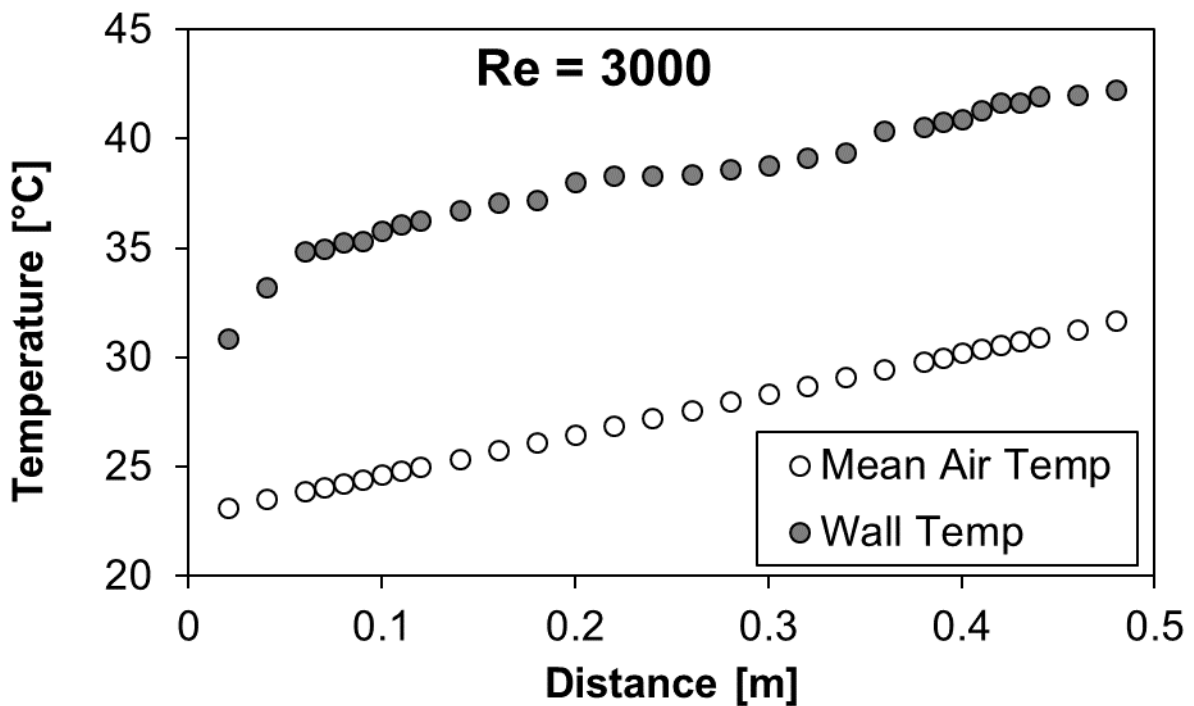


Figure E.60: Wall and mean air temperatures for mesh 2.3 under two-heated wall boundary condition at Re = 3 000

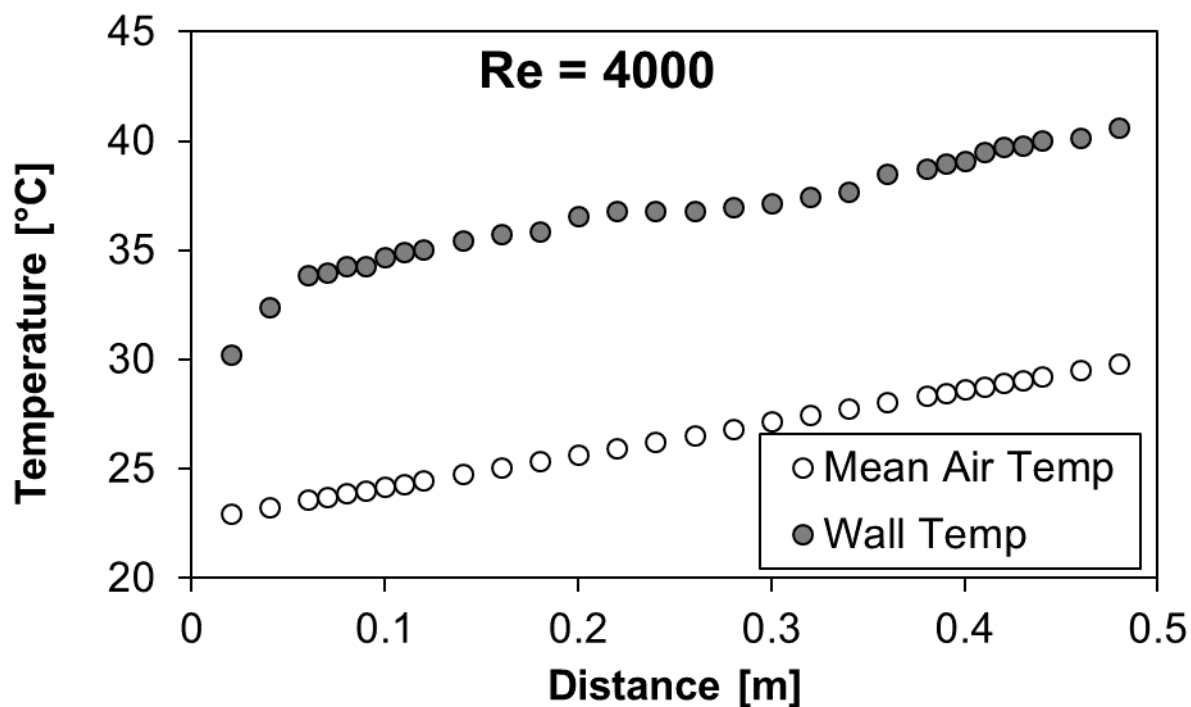


Figure E.61: Wall and mean air temperatures for mesh 2.3 under two-heated wall boundary condition at Re = 4 000

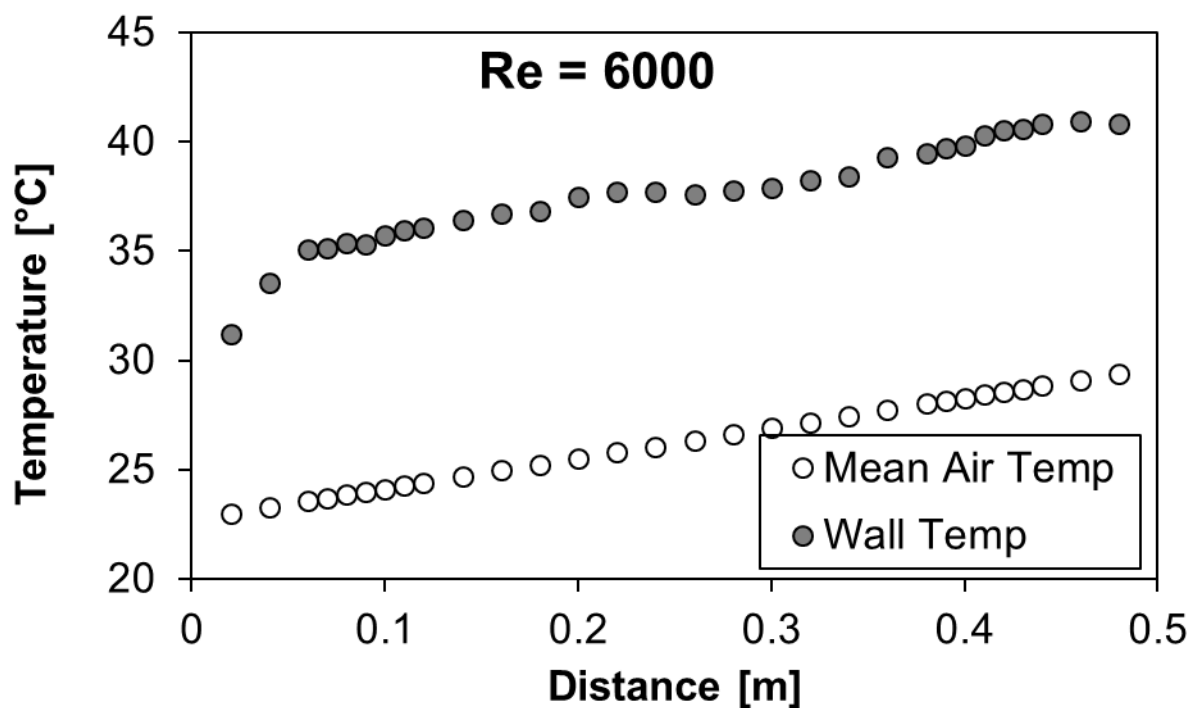


Figure E.62: Wall and mean air temperatures for mesh 2.3 under two-heated wall boundary condition at Re = 6 000

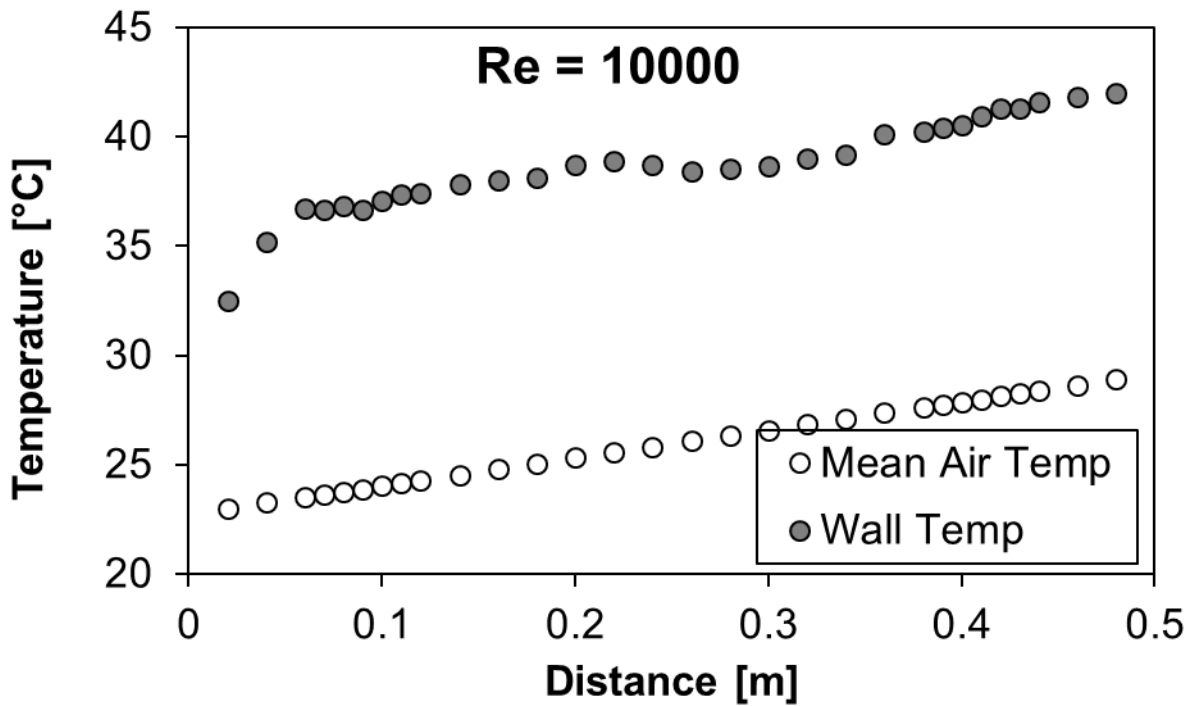


Figure E.63: Wall and mean air temperatures for mesh 2.3 under two-heated wall boundary condition at $Re = 10\ 000$

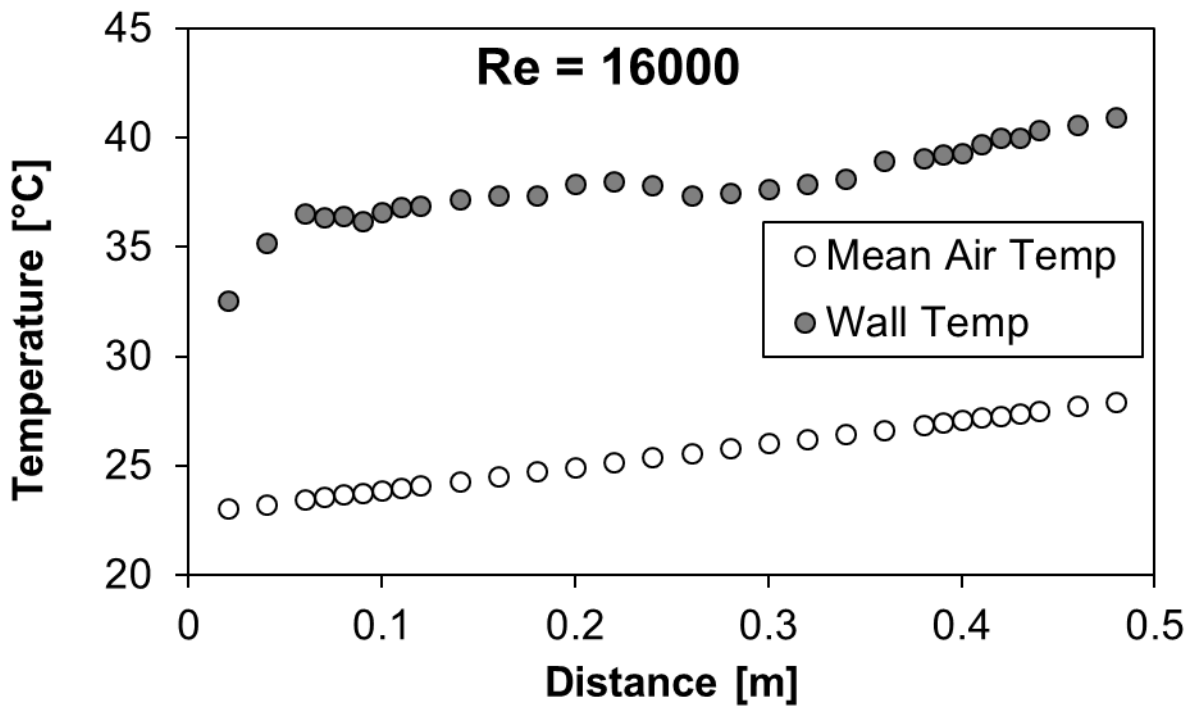


Figure E.64: Wall and mean air temperatures for mesh 2.3 under two-heated wall boundary condition at $Re = 16\ 000$

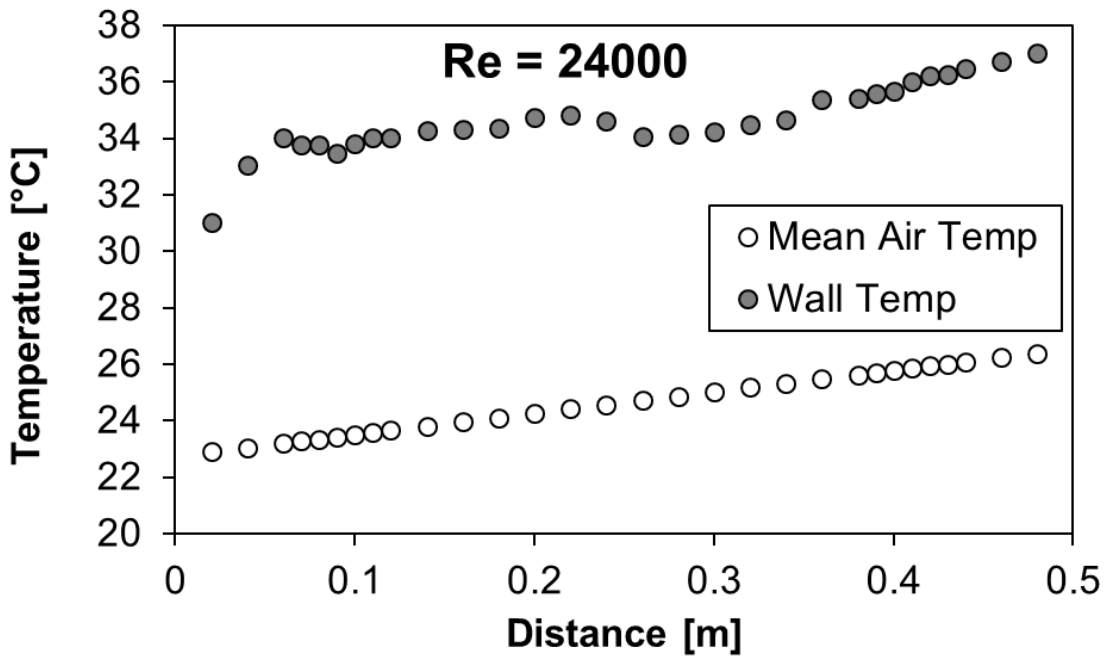


Figure E.65: Wall and mean air temperatures for mesh 2.3 under two-heated wall boundary condition at $Re = 24\ 000$

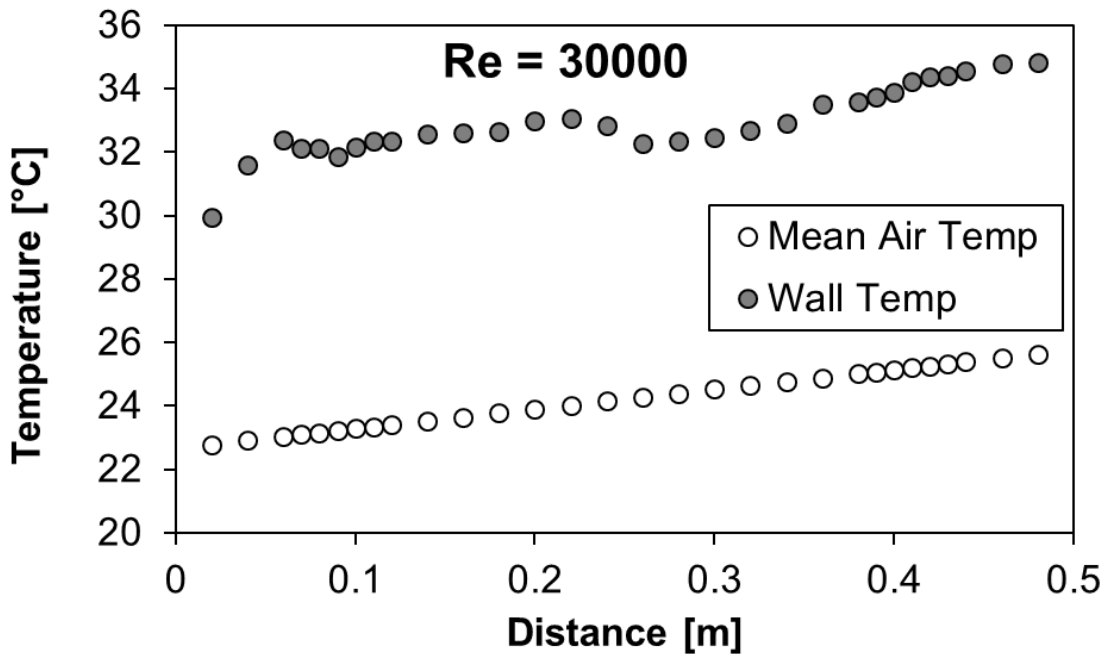


Figure E.66: Wall and mean air temperatures for mesh 2.3 under two-heated wall boundary condition at $Re = 30\ 000$

The variation in wall temperature could be due to the variation of heat flux across the channel. The heating pad was glued with epoxy glue which could have affected the heat transfer coefficient. The change in wall temperature around the centre point of the test section can also be attributed to the change in heat flux due to the joint of the two heating pads.

Appendix F: ONE WALL HEAT TRANSFER DATA

5 MM CHANNEL HEIGHT – MESH 4.1

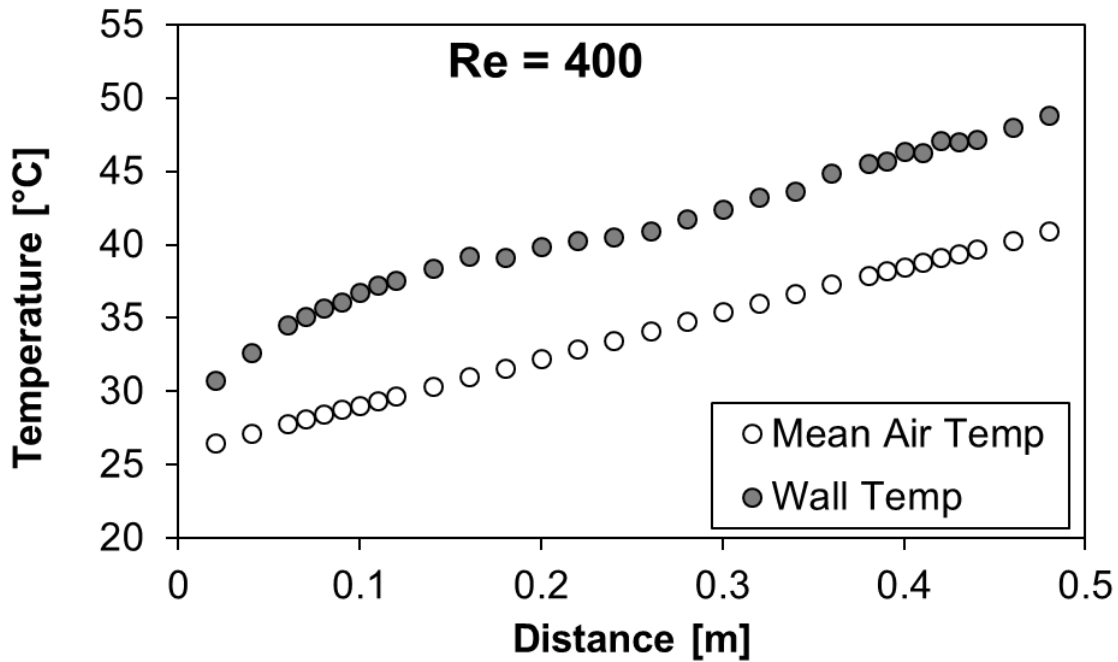


Figure F.1: Wall and mean air temperatures for mesh 4.1 under one-heated wall boundary condition at Re = 400

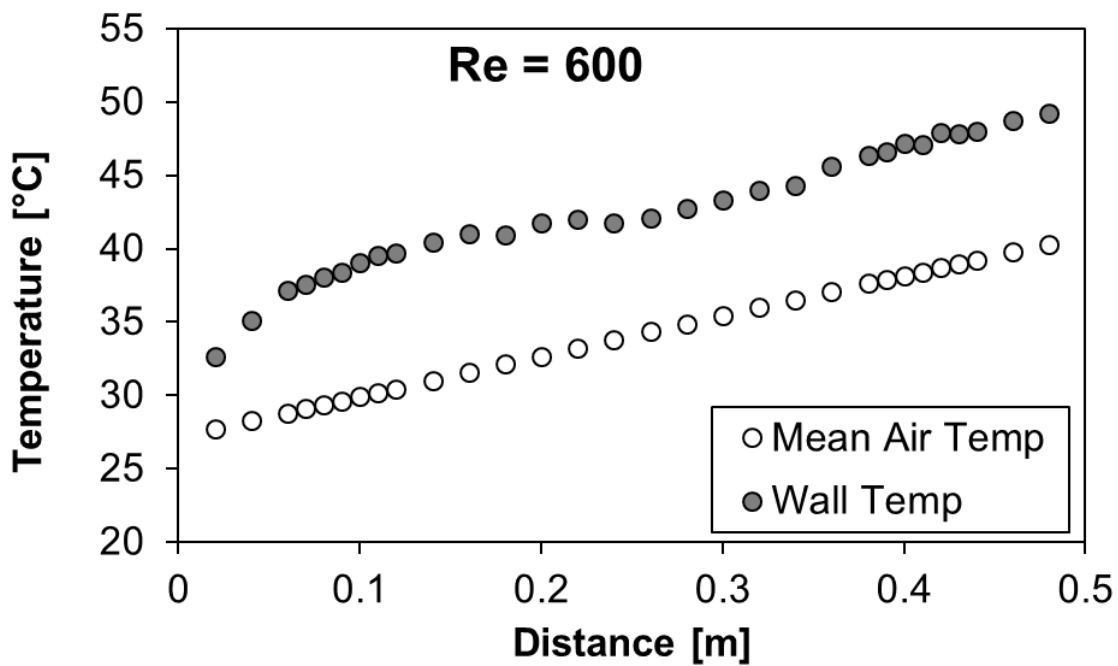


Figure F.2: Wall and mean air temperatures for mesh 4.1 under one-heated wall boundary condition at Re = 600

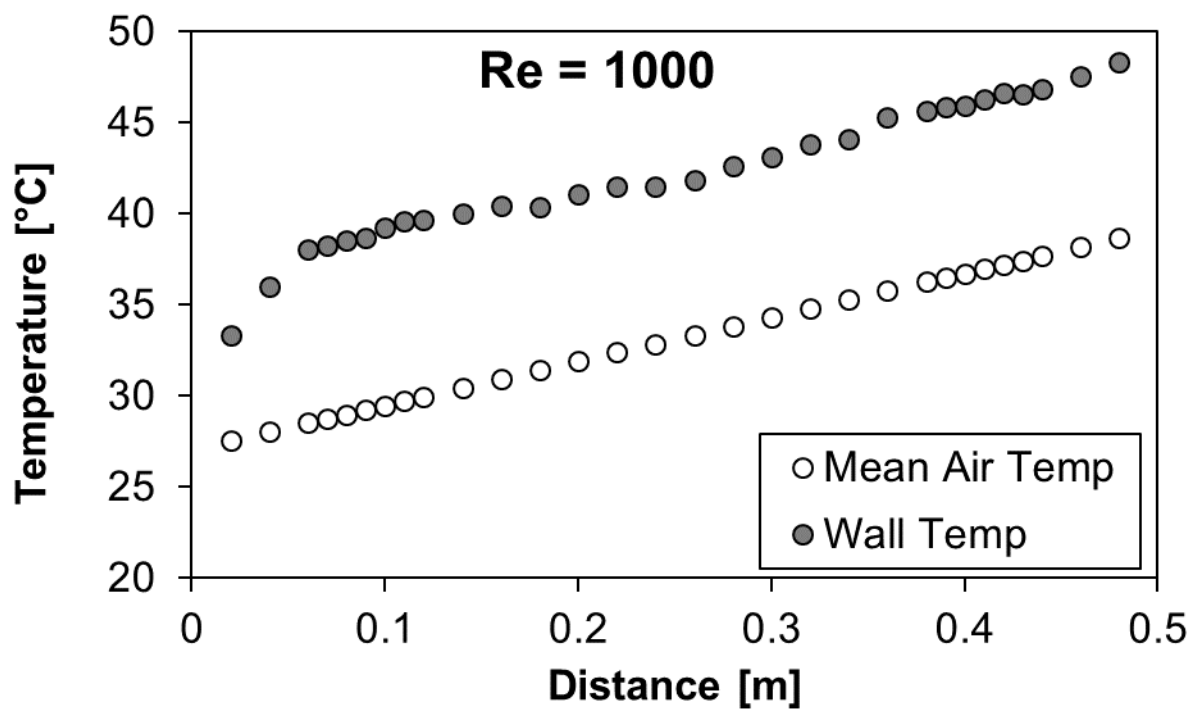


Figure F.3: Wall and mean air temperatures for mesh 4.1 under one-heated wall boundary condition at Re = 1 000

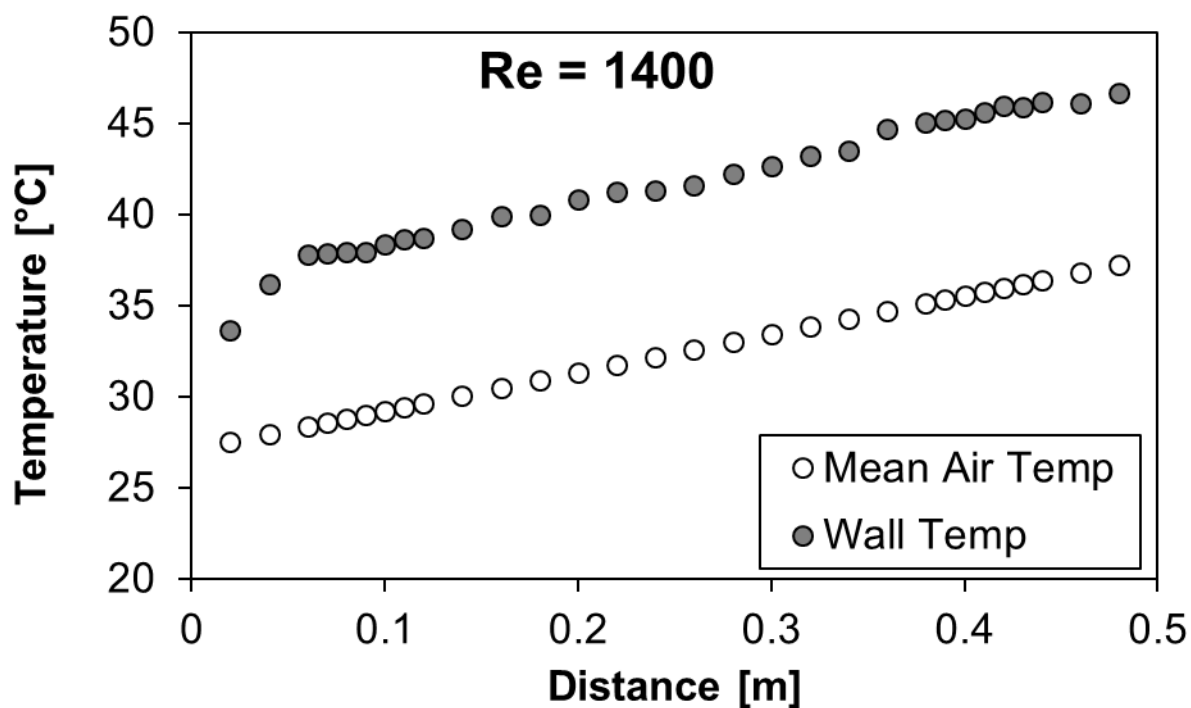


Figure F.4: Wall and mean air temperatures for mesh 4.1 under one-heated wall boundary condition at Re = 1 400

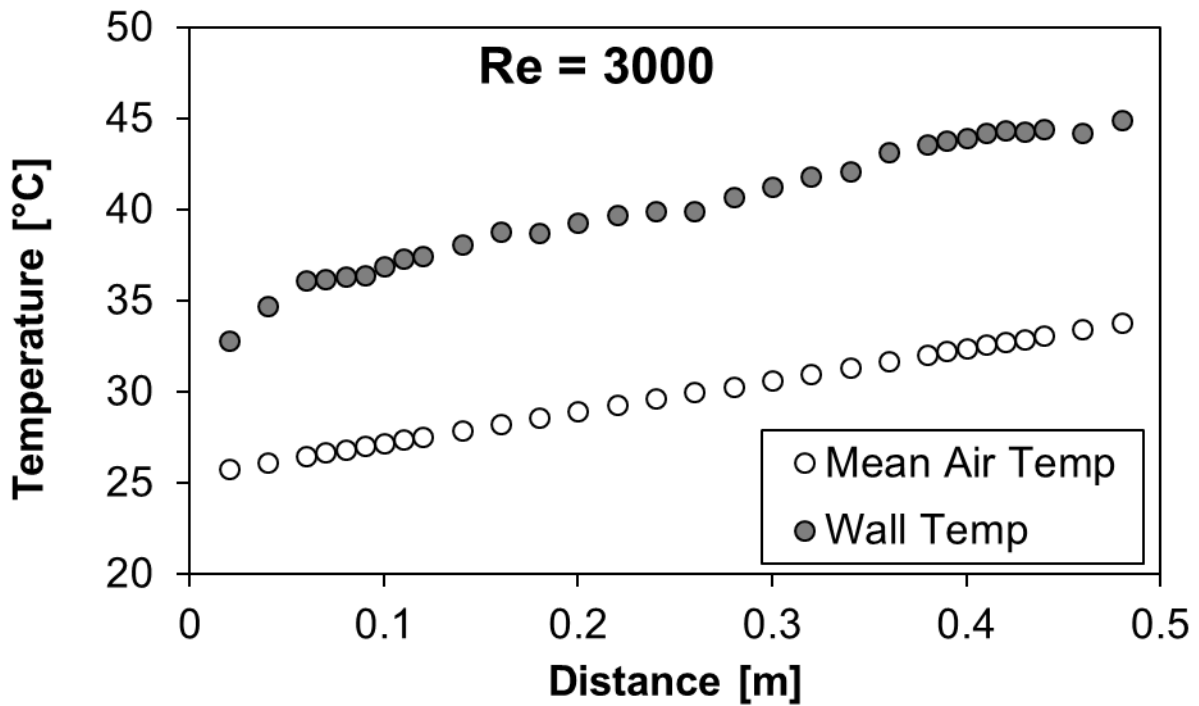


Figure F.5: Wall and mean air temperatures for mesh 4.1 under one-heated wall boundary condition at $Re = 3\ 000$

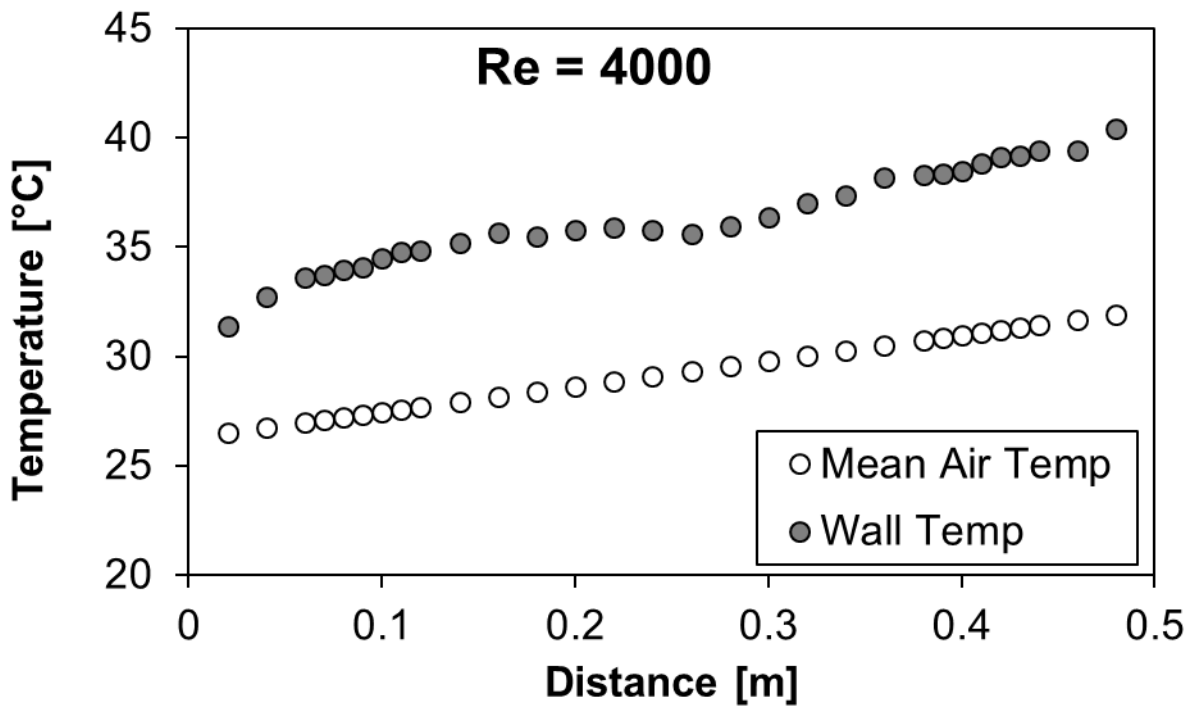


Figure F.6: Wall and mean air temperatures for mesh 4.1 under one-heated wall boundary condition at $Re = 4\ 000$

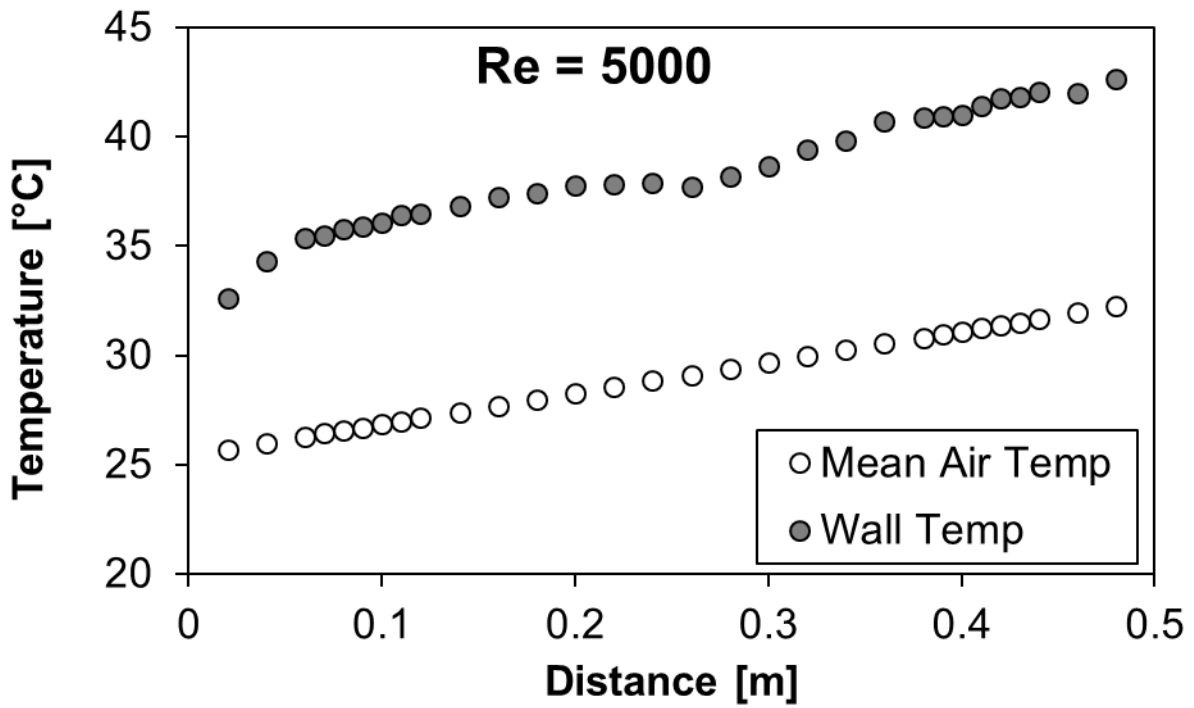


Figure F.7: Wall and mean air temperatures for mesh 4.1 under one-heated wall boundary condition at Re = 5 000

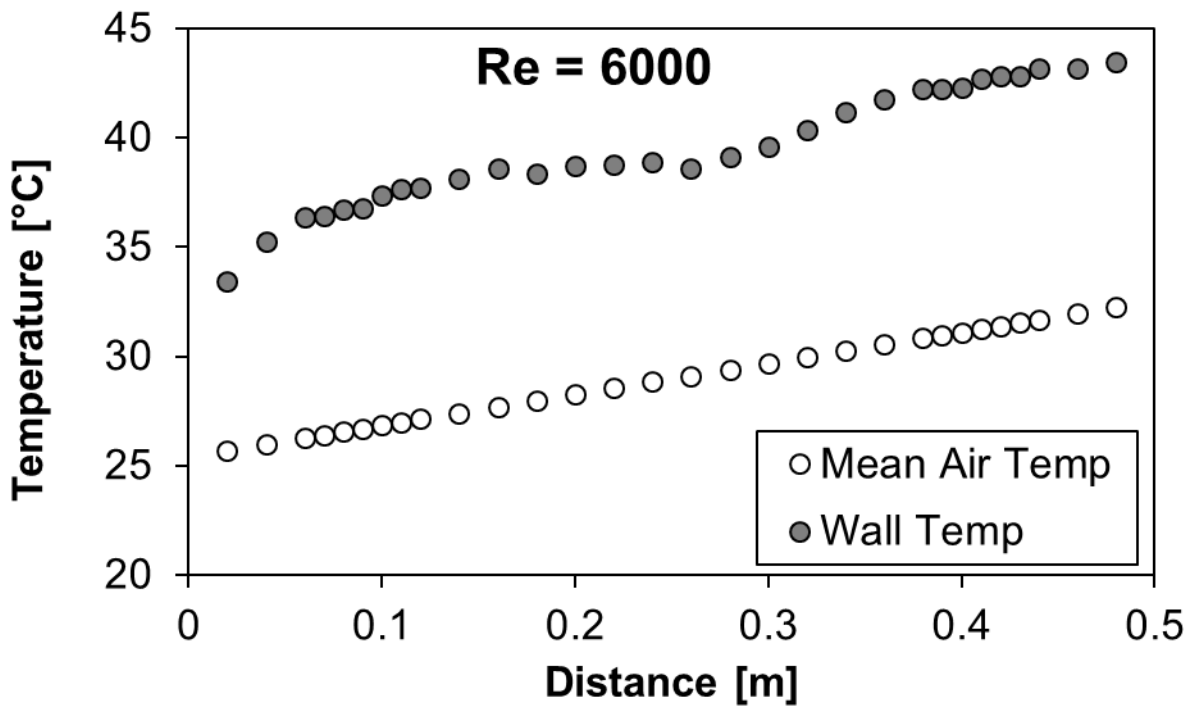


Figure F.8: Wall and mean air temperatures for mesh 4.1 under one-heated wall boundary condition at Re = 6 000

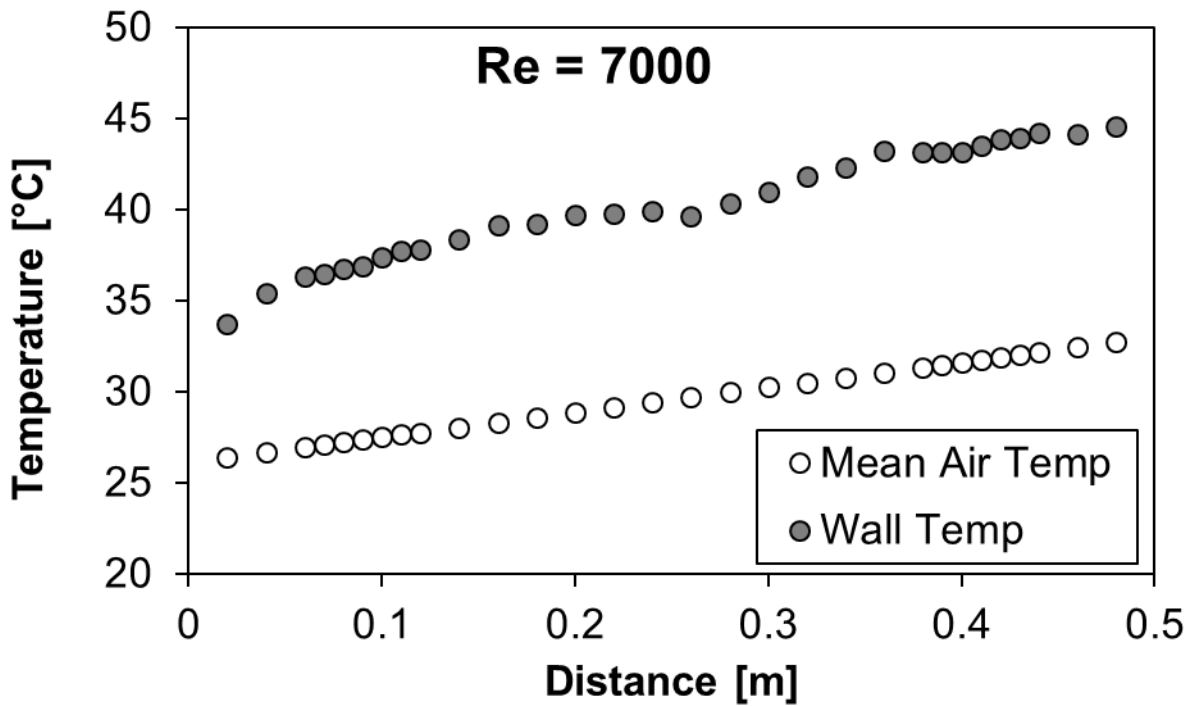


Figure F.9: Wall and mean air temperatures for mesh 4.1 under one-heated wall boundary condition at Re = 7 000

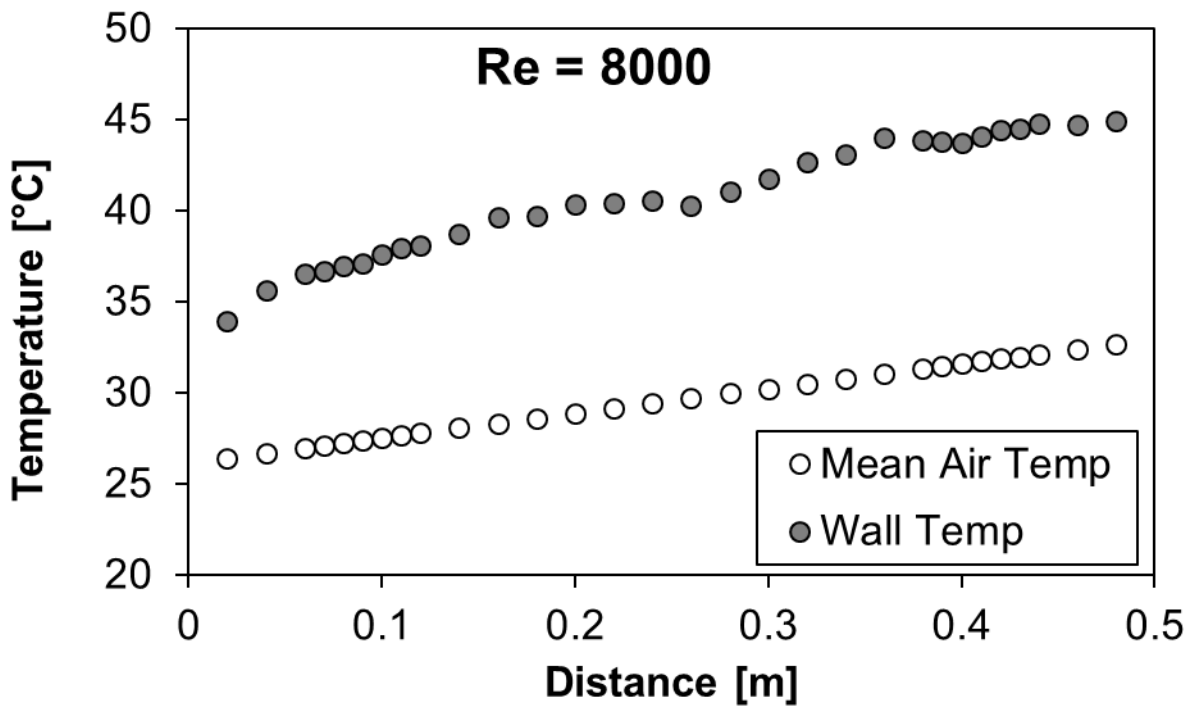


Figure F.10: Wall and mean air temperatures for mesh 4.1 under one-heated wall boundary condition at Re = 8 000

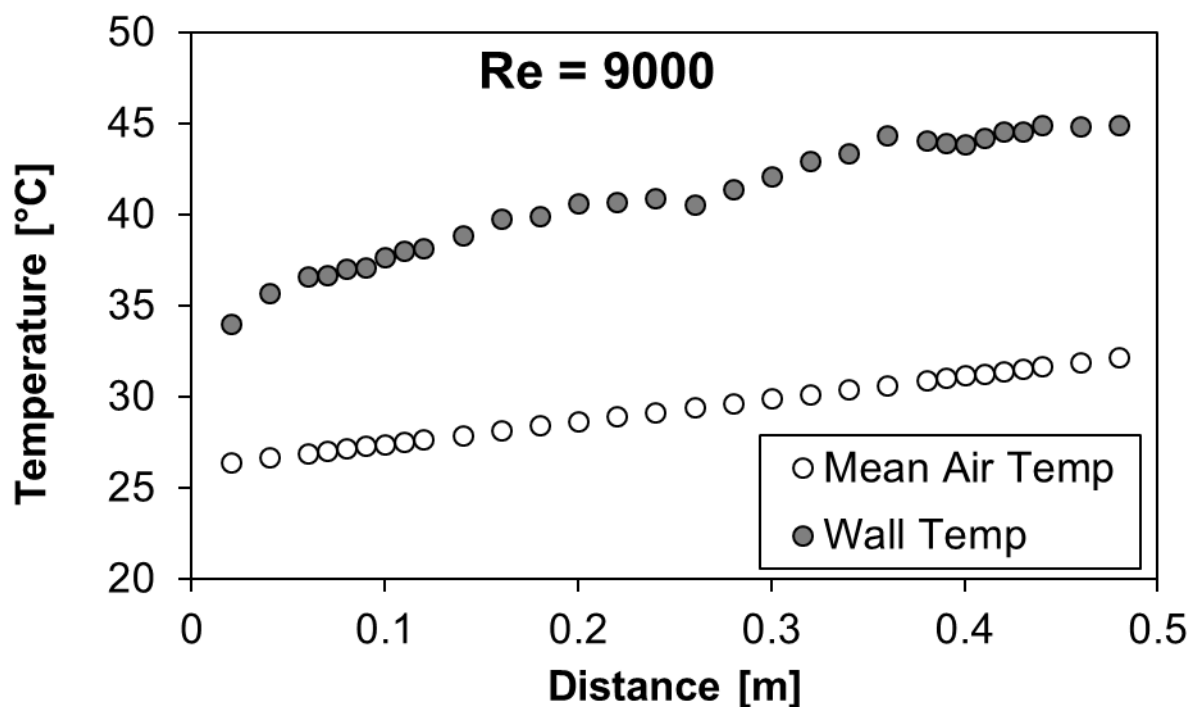


Figure F.11: Wall and mean air temperatures for mesh 4.1 under one-heated wall boundary condition at Re = 9 000

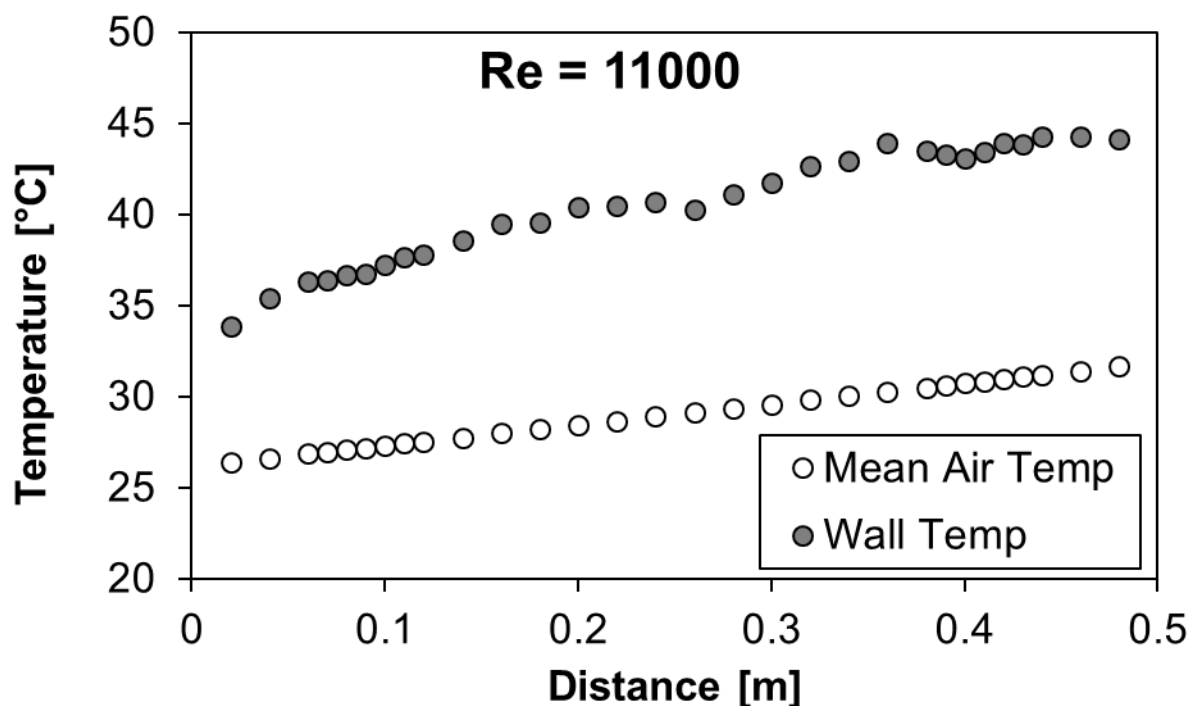


Figure F.12: Wall and mean air temperatures for mesh 4.1 under one-heated wall boundary condition at Re = 11 000

5 MM CHANNEL HEIGHT – MESH 4.3

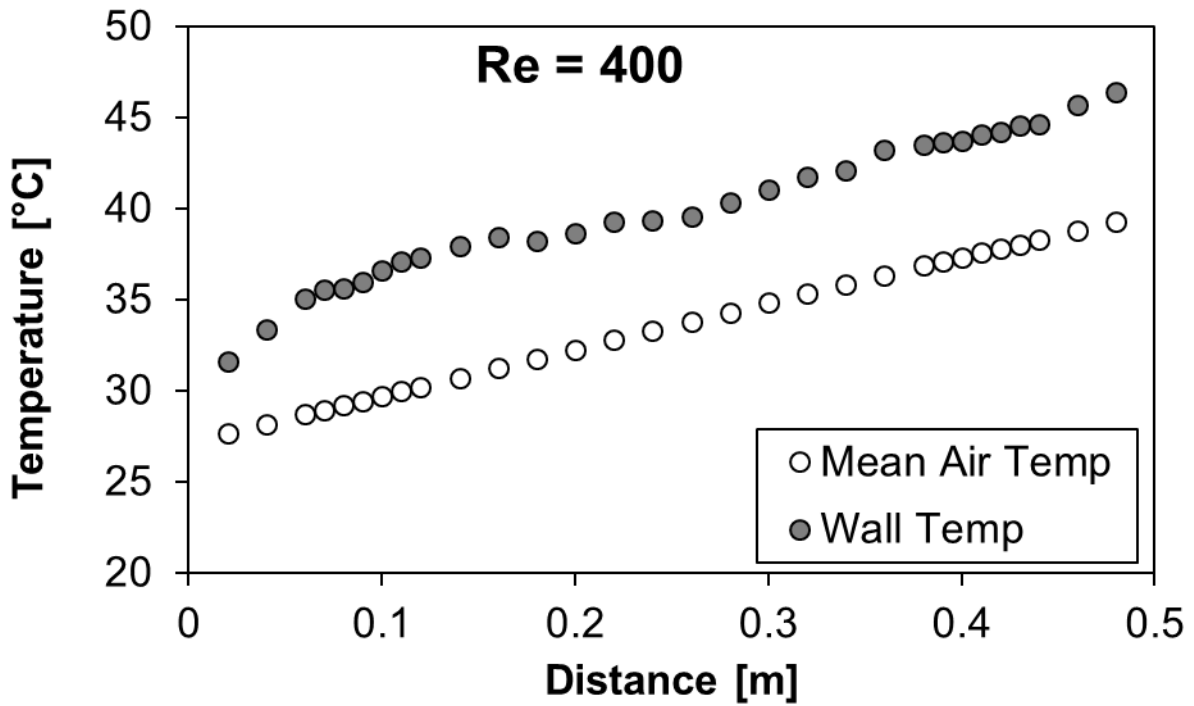


Figure F.13: Wall and mean air temperatures for mesh 4.3 under one-heated wall boundary condition at Re = 400

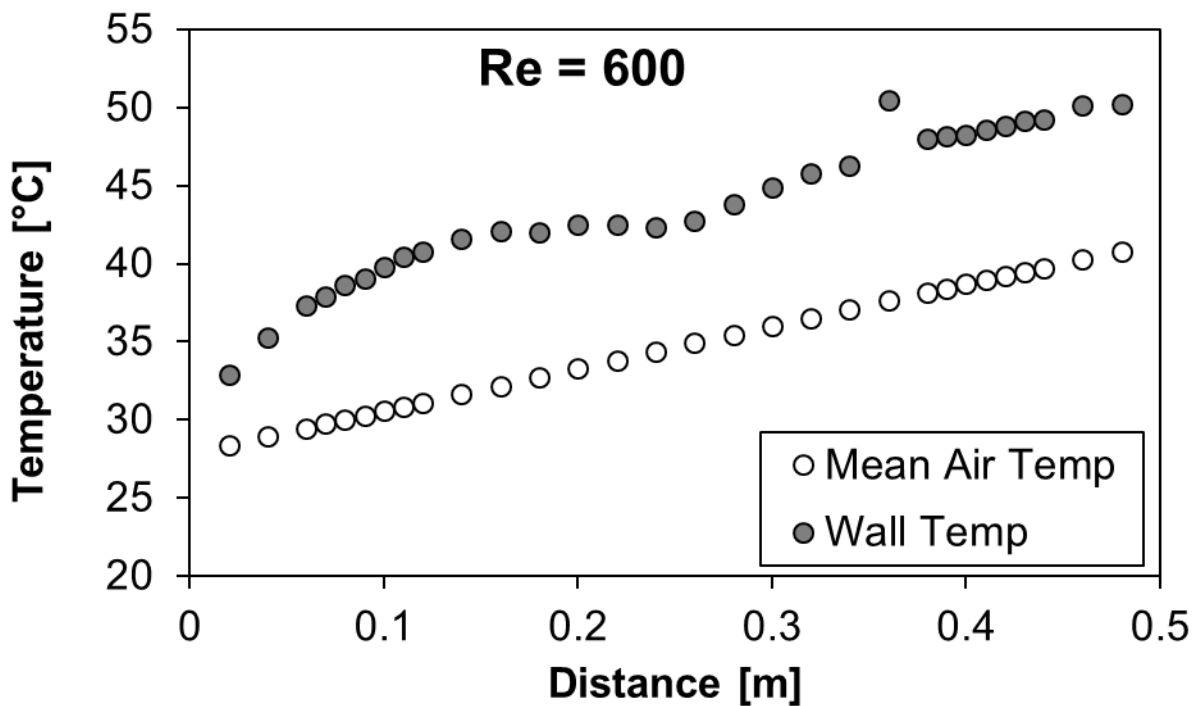


Figure F.14: Wall and mean air temperatures for mesh 4.3 under one-heated wall boundary condition at Re = 600

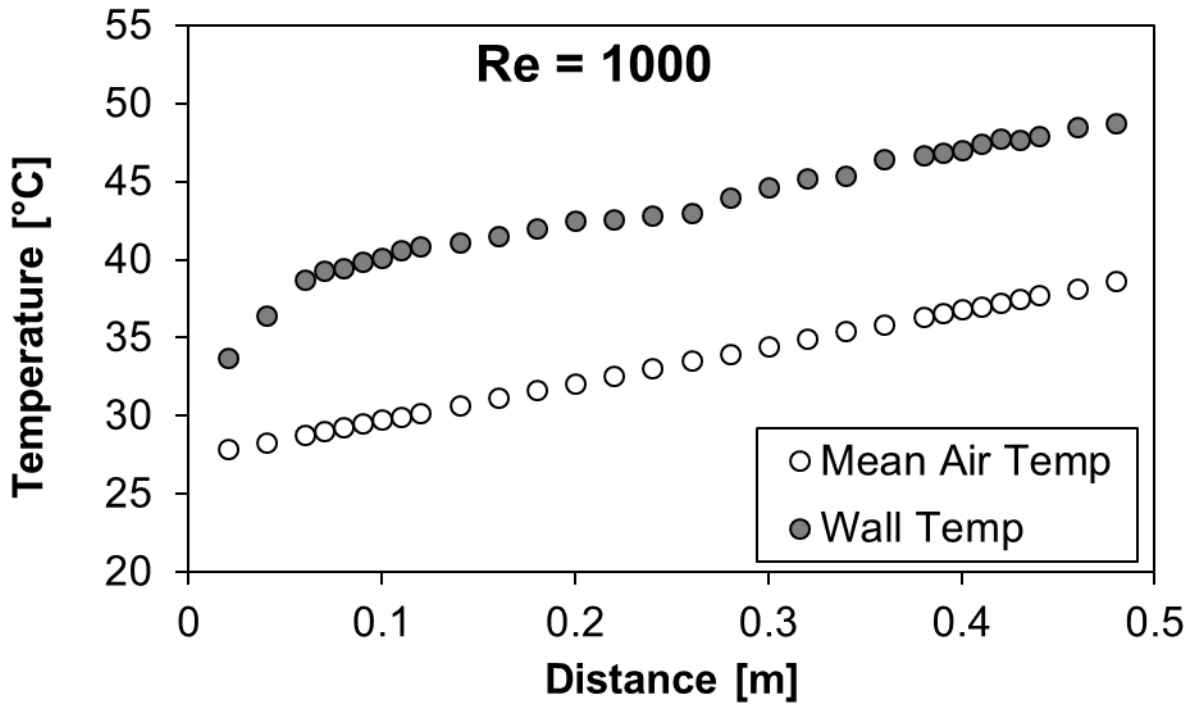


Figure F.15: Wall and mean air temperatures for mesh 4.3 under one-heated wall boundary condition at Re = 1 000

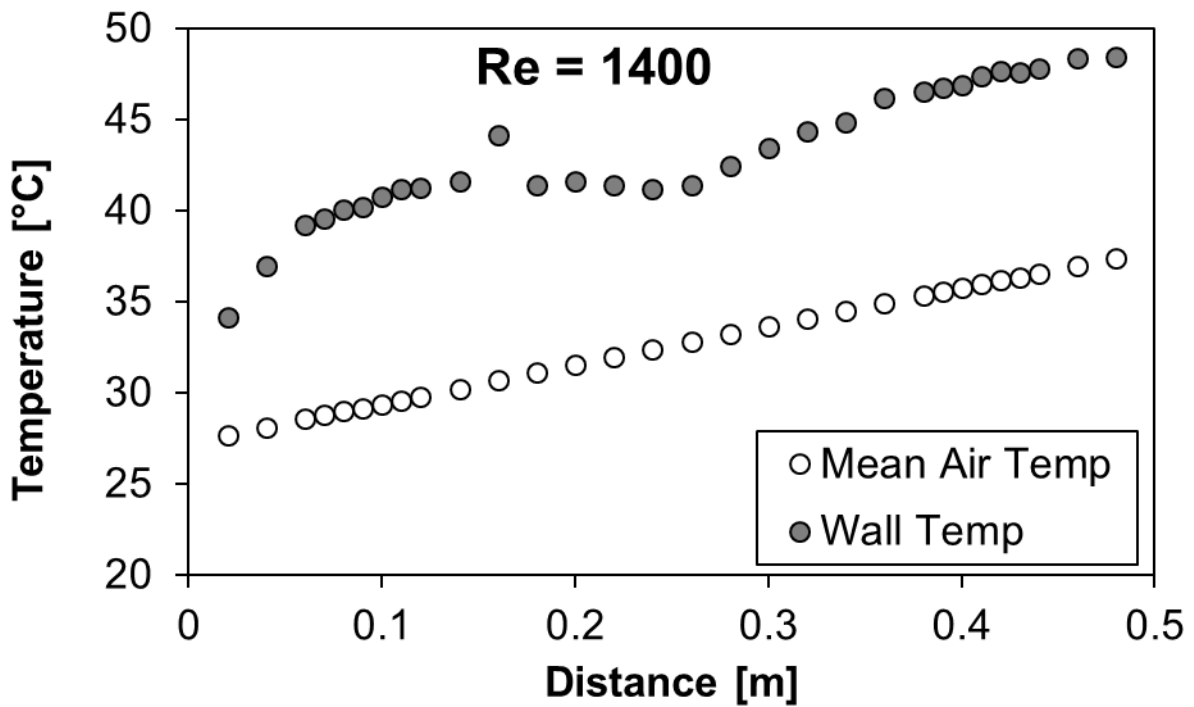


Figure F.16: Wall and mean air temperatures for mesh 4.3 under one-heated wall boundary condition at Re = 1 400

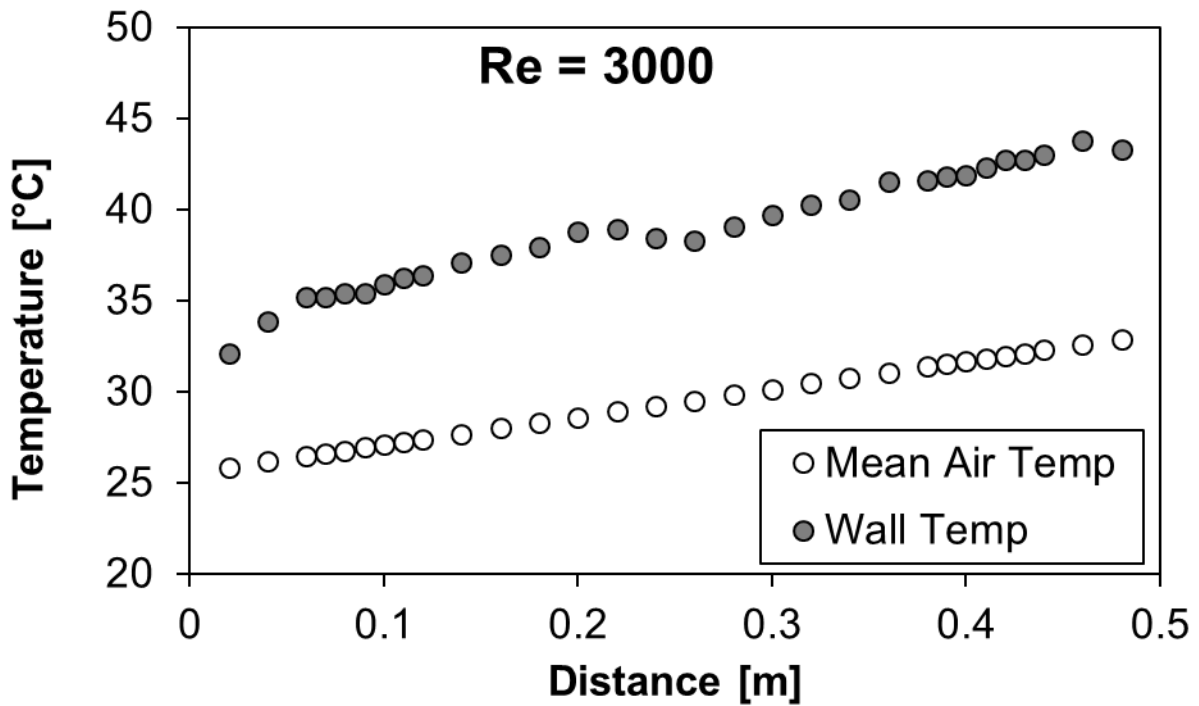


Figure F.17: Wall and mean air temperatures for mesh 4.3 under one-heated wall boundary condition at Re = 3 000

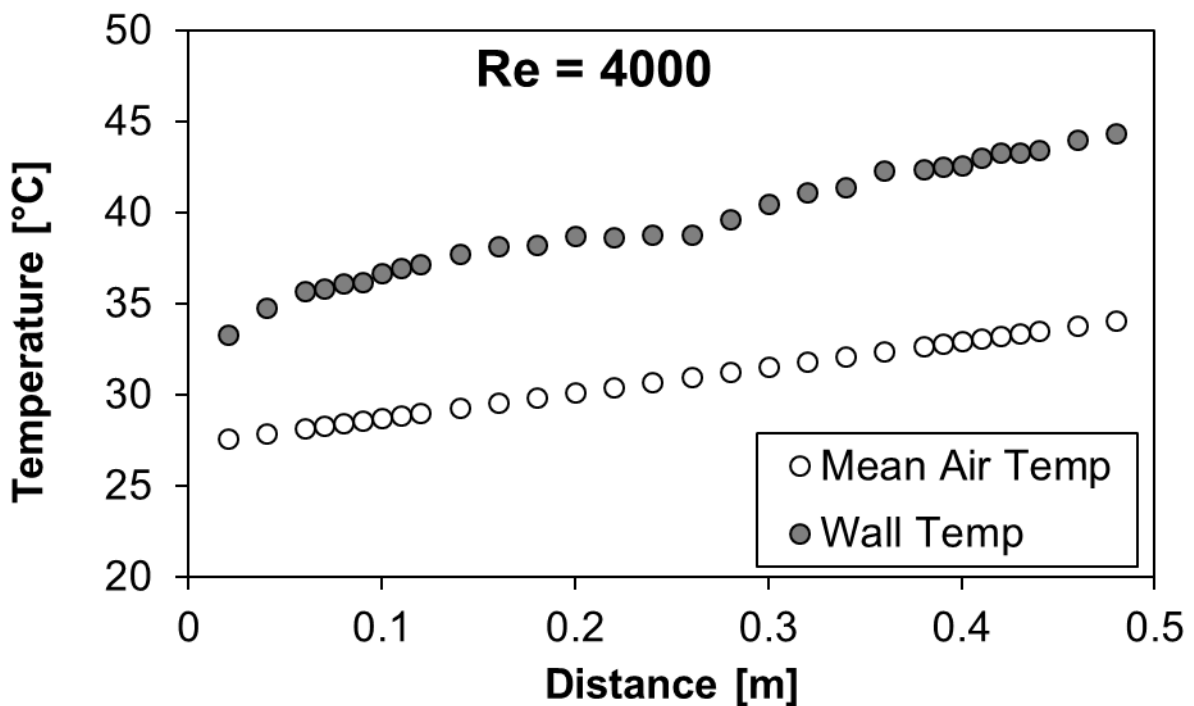


Figure F.18: Wall and mean air temperatures for mesh 4.3 under one-heated wall boundary condition at Re = 4 000

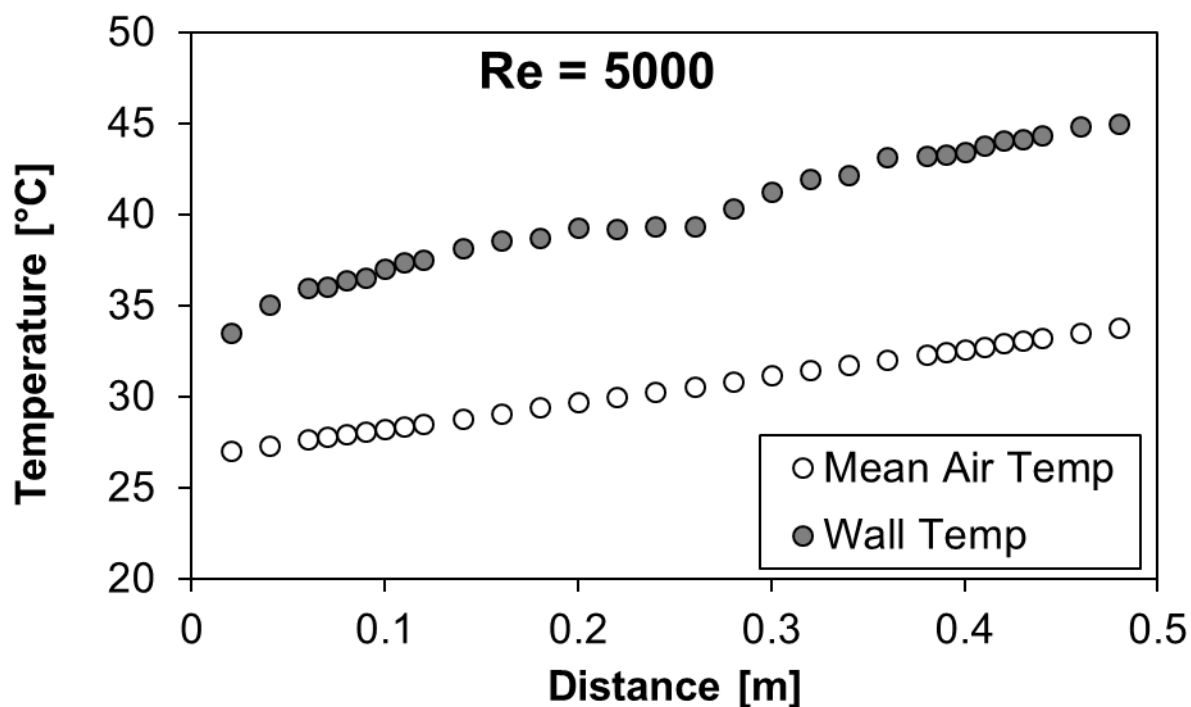


Figure F.19: Wall and mean air temperatures for mesh 4.3 under one-heated wall boundary condition at Re = 5 000

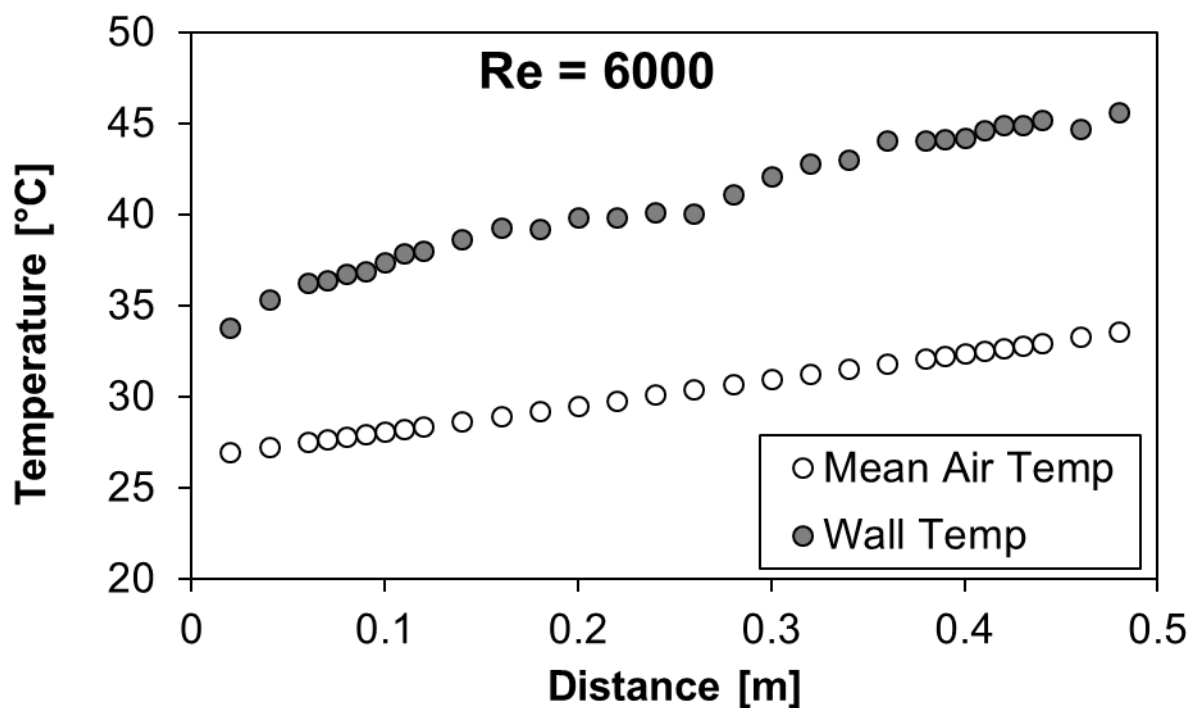


Figure F.20: Wall and mean air temperatures for mesh 4.3 under one-heated wall boundary condition at Re = 6 000

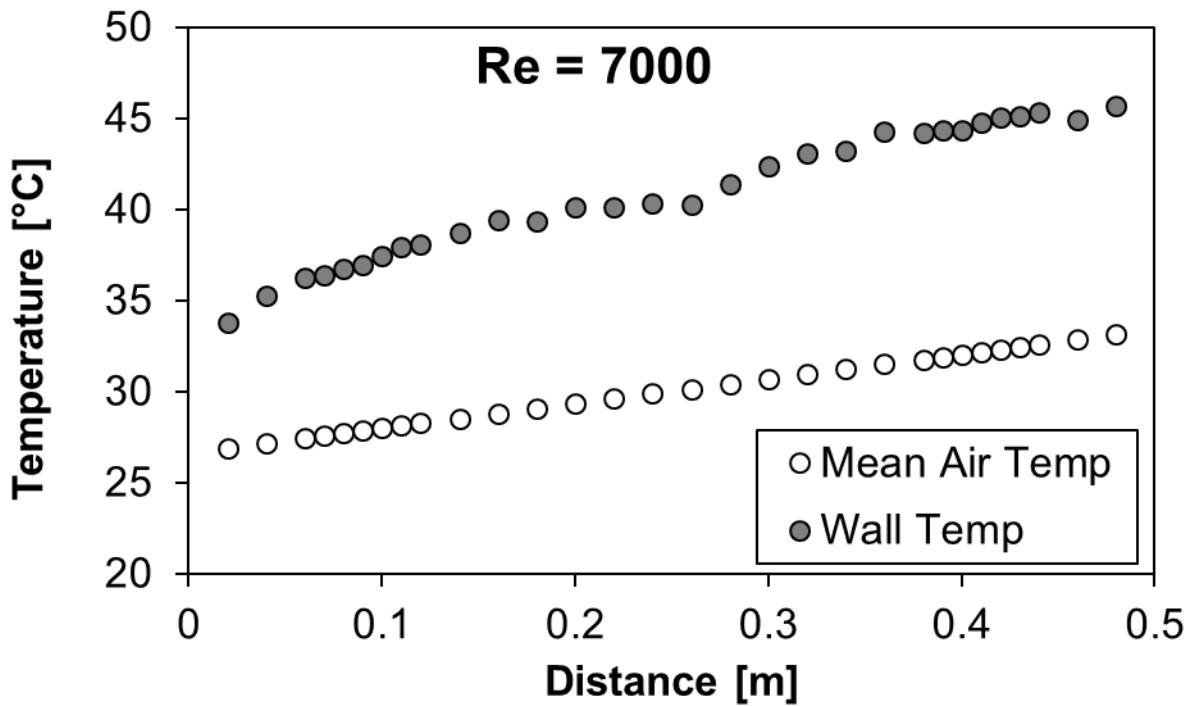


Figure F.21: Wall and mean air temperatures for mesh 4.3 under one-heated wall boundary condition at Re = 7 000

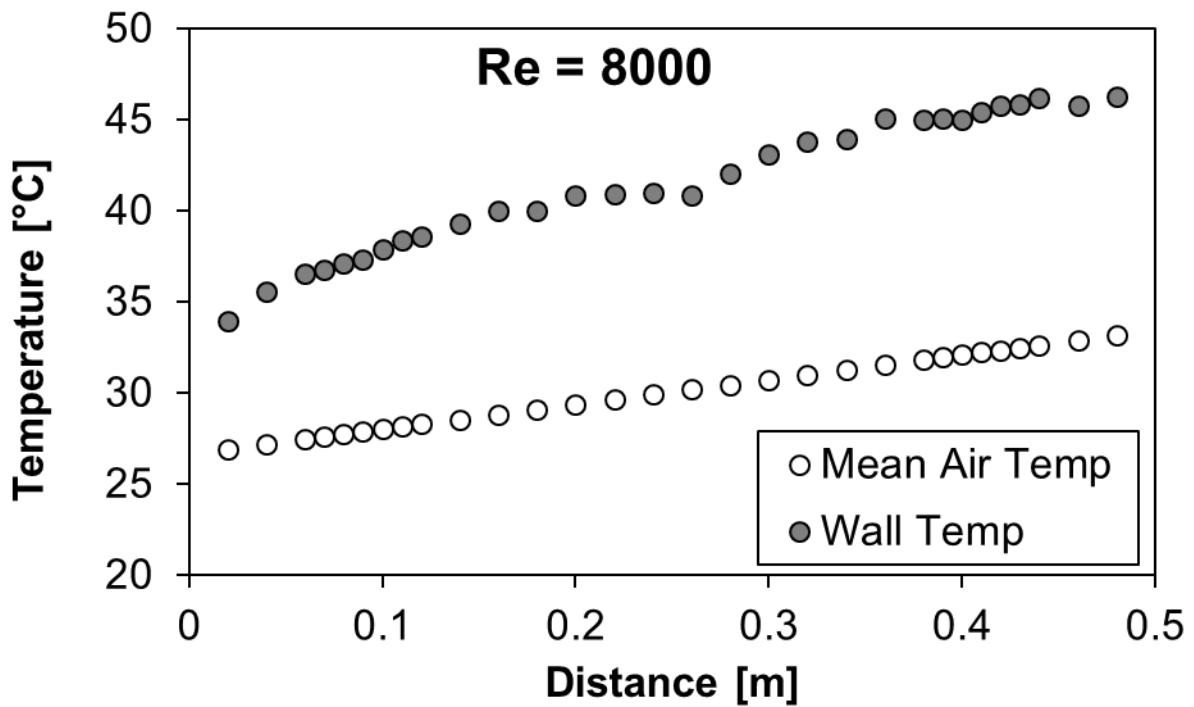


Figure F.22: Wall and mean air temperatures for mesh 4.3 under one-heated wall boundary condition at Re = 8 000

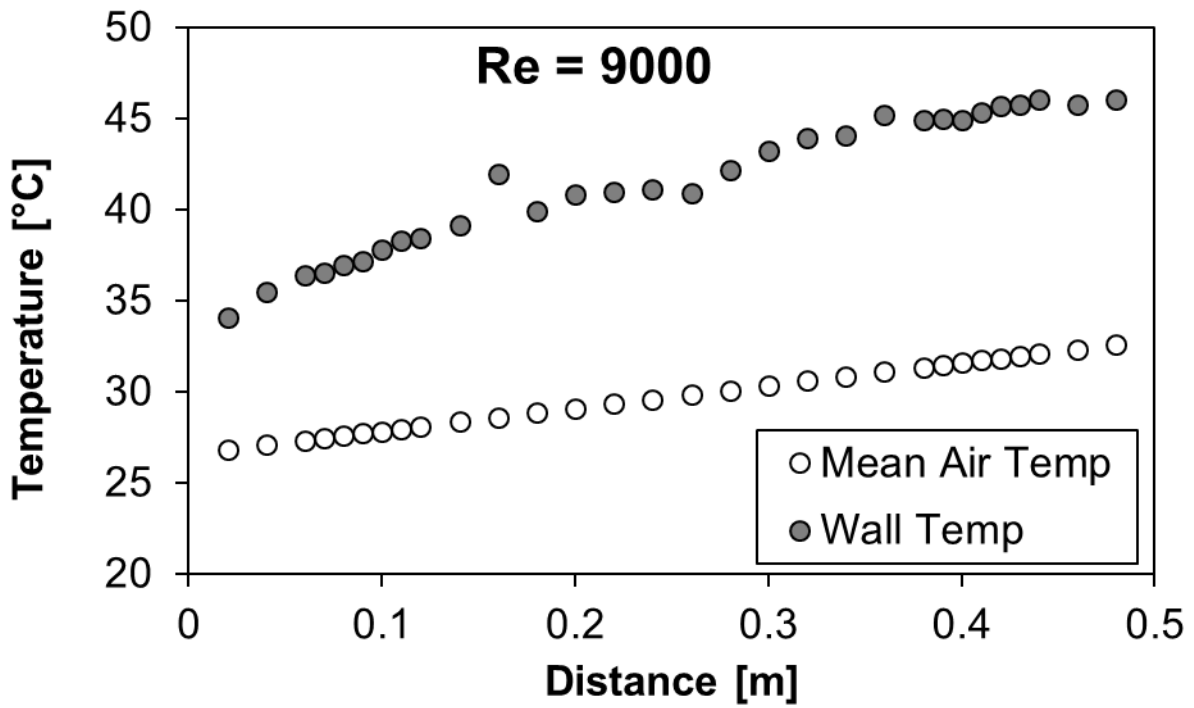


Figure F.23: Wall and mean air temperatures for mesh 4.3 under one-heated wall boundary condition at Re = 9 000

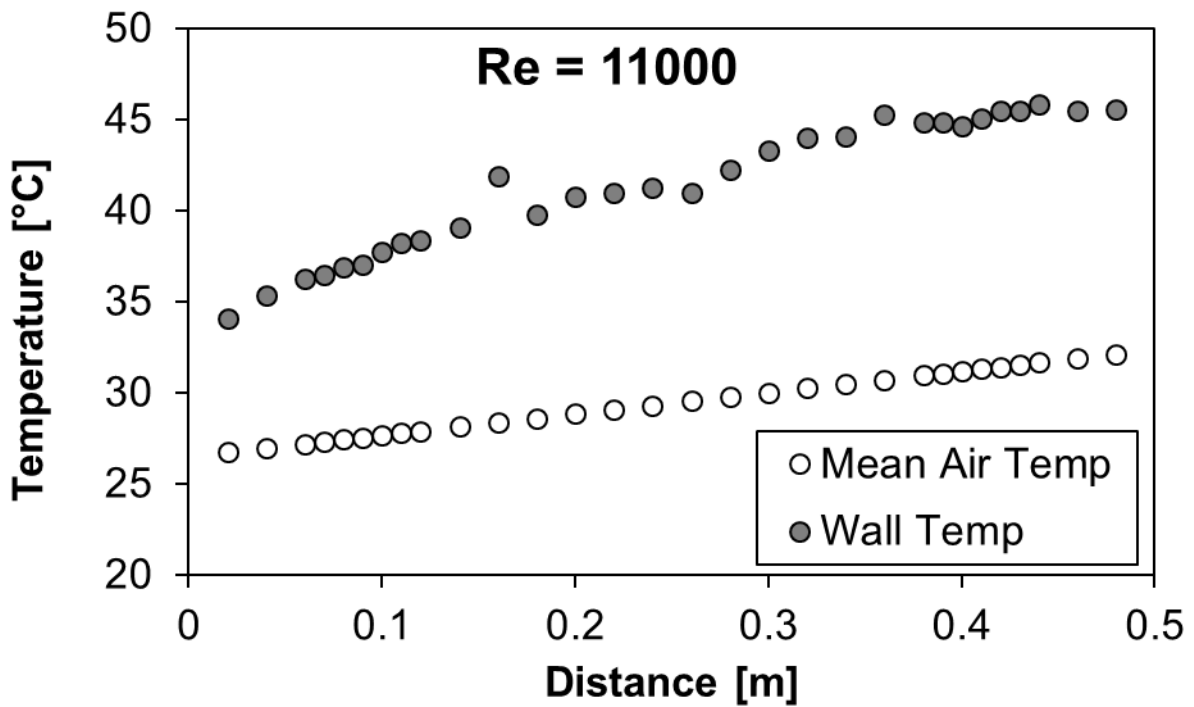


Figure F.24: Wall and mean air temperatures for mesh 4.3 under one-heated wall boundary condition at Re = 11 000

5 MM CHANNEL HEIGHT – MESH 5.1

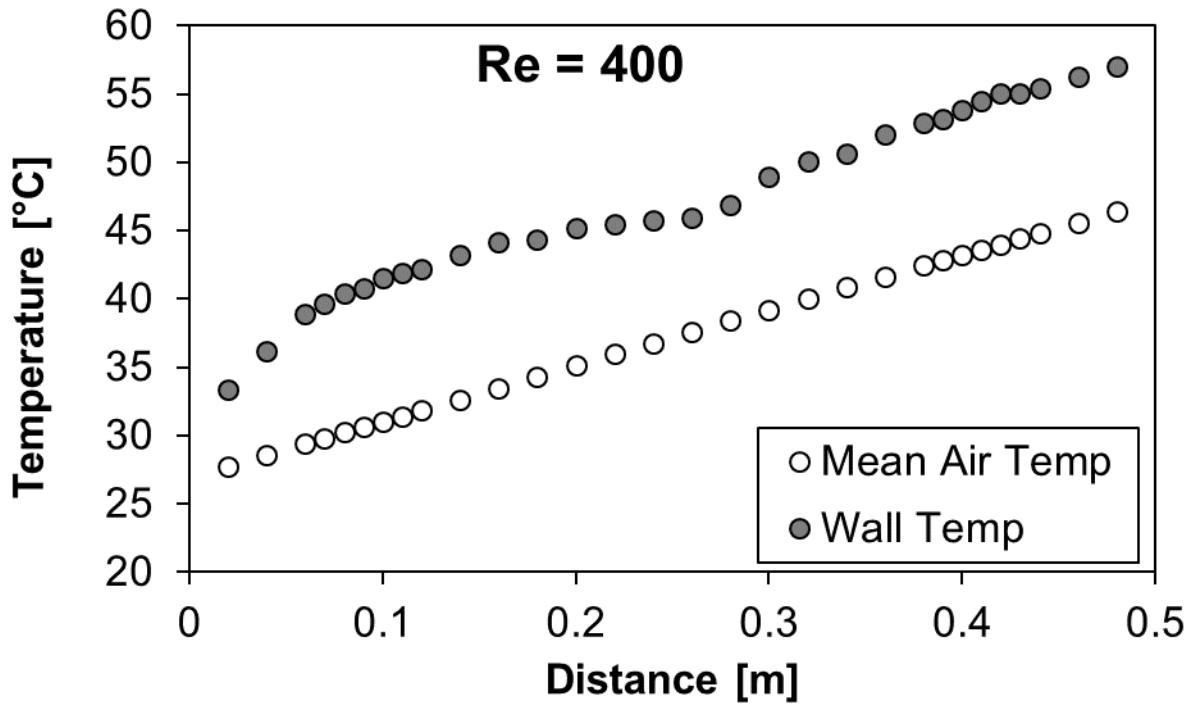


Figure F.25: Wall and mean air temperatures for mesh 5.1 under one-heated wall boundary condition at Re = 400

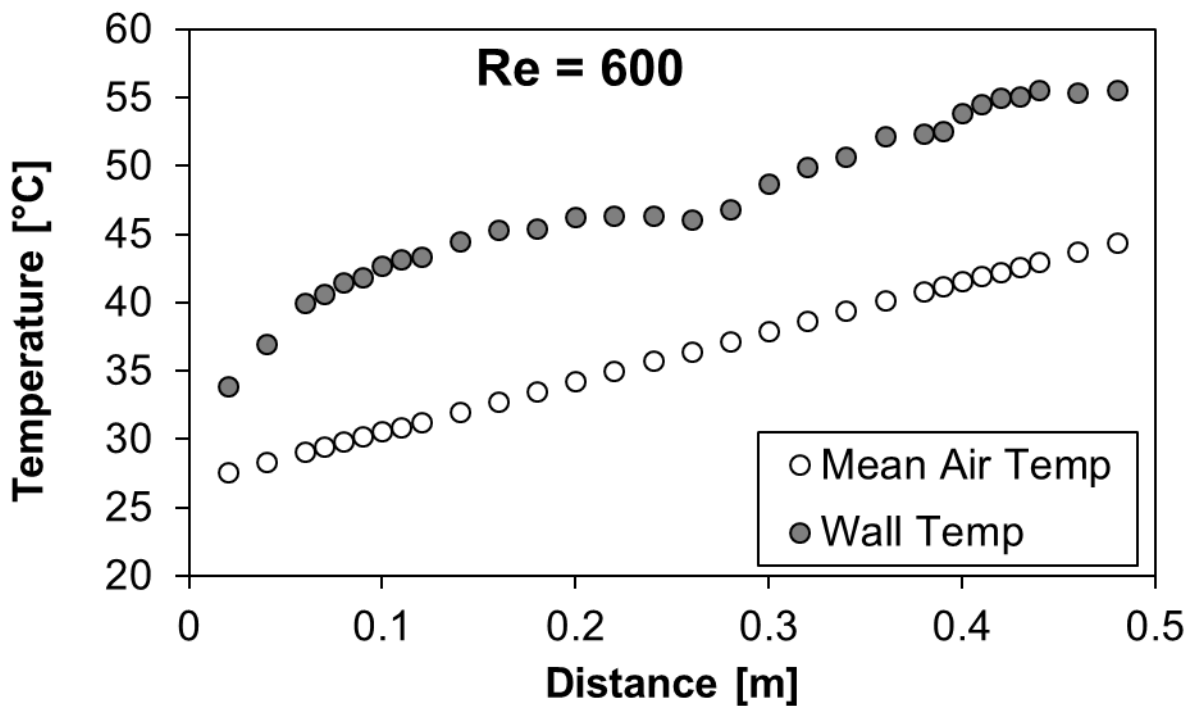


Figure F.26: Wall and mean air temperatures for mesh 5.1 under one-heated wall boundary condition at Re = 600

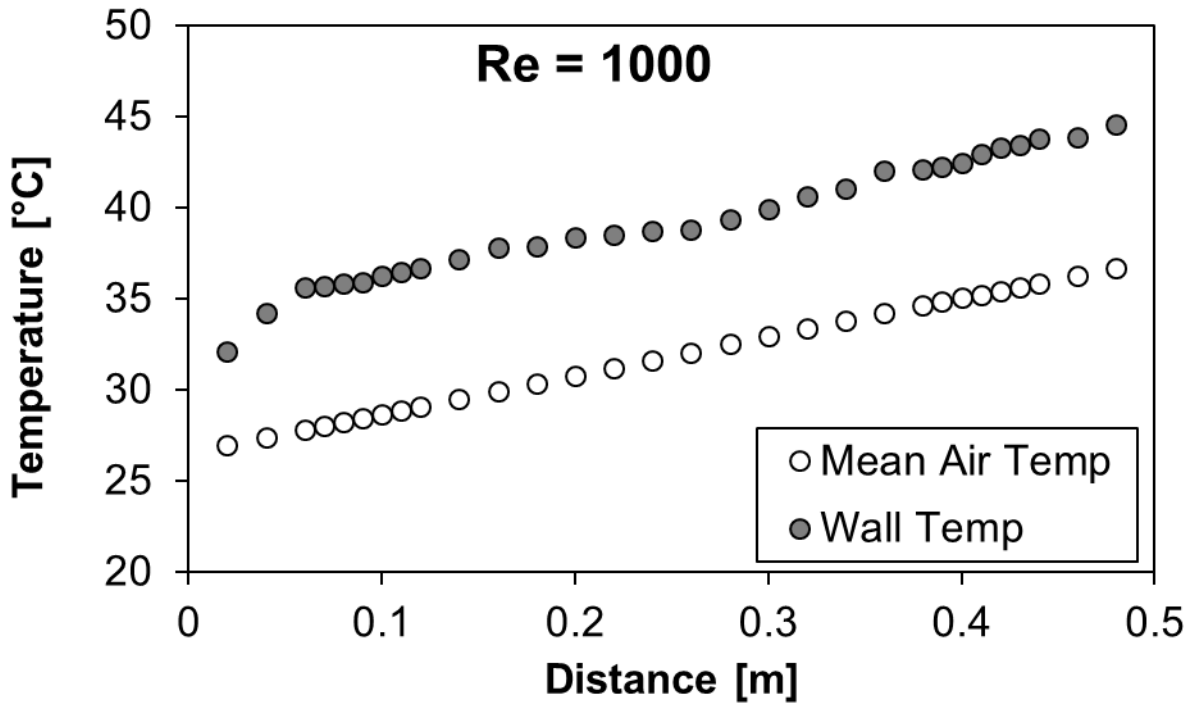


Figure F.27: Wall and mean air temperatures for mesh 5.1 under one-heated wall boundary condition at Re = 1 000

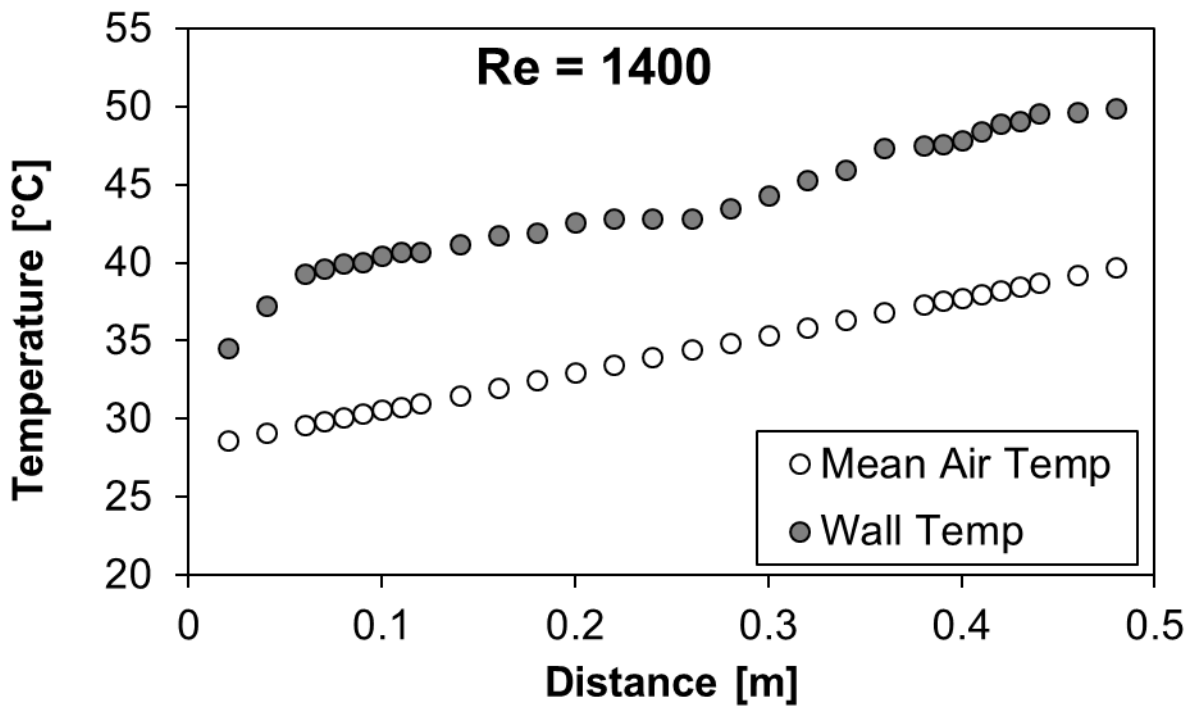


Figure F.28: Wall and mean air temperatures for mesh 5.1 under one-heated wall boundary condition at Re = 1 400

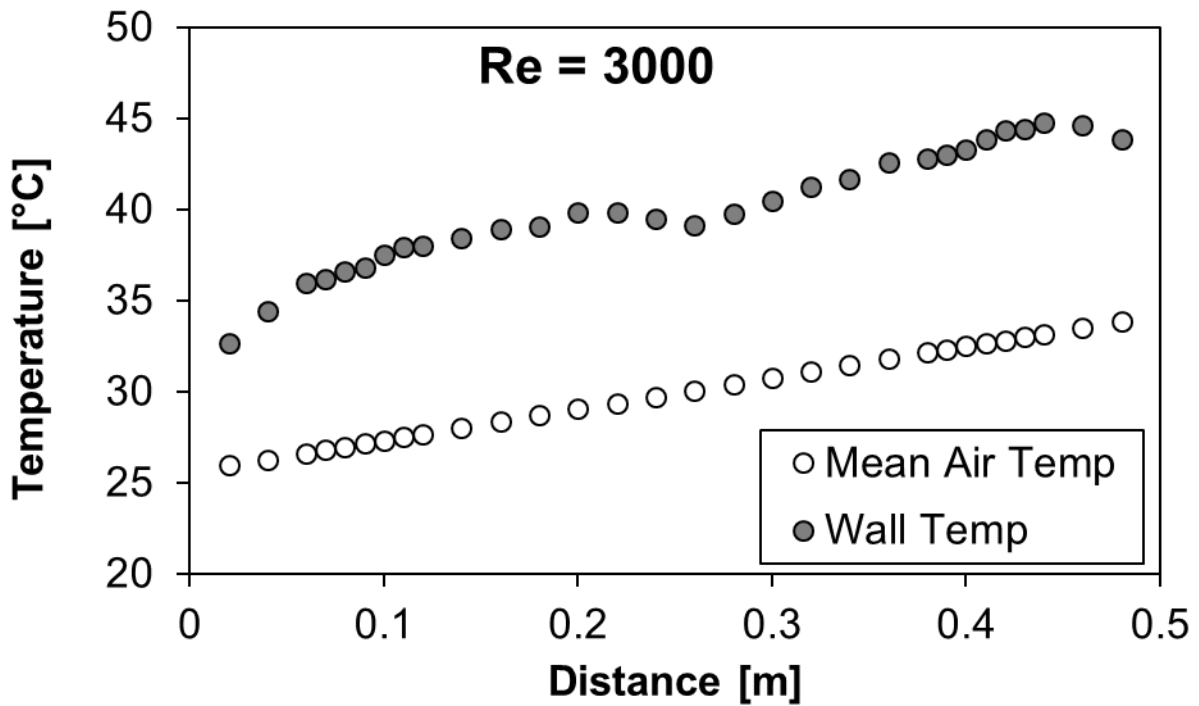


Figure F.29: Wall and mean air temperatures for mesh 5.1 under one-heated wall boundary condition at Re = 3 000

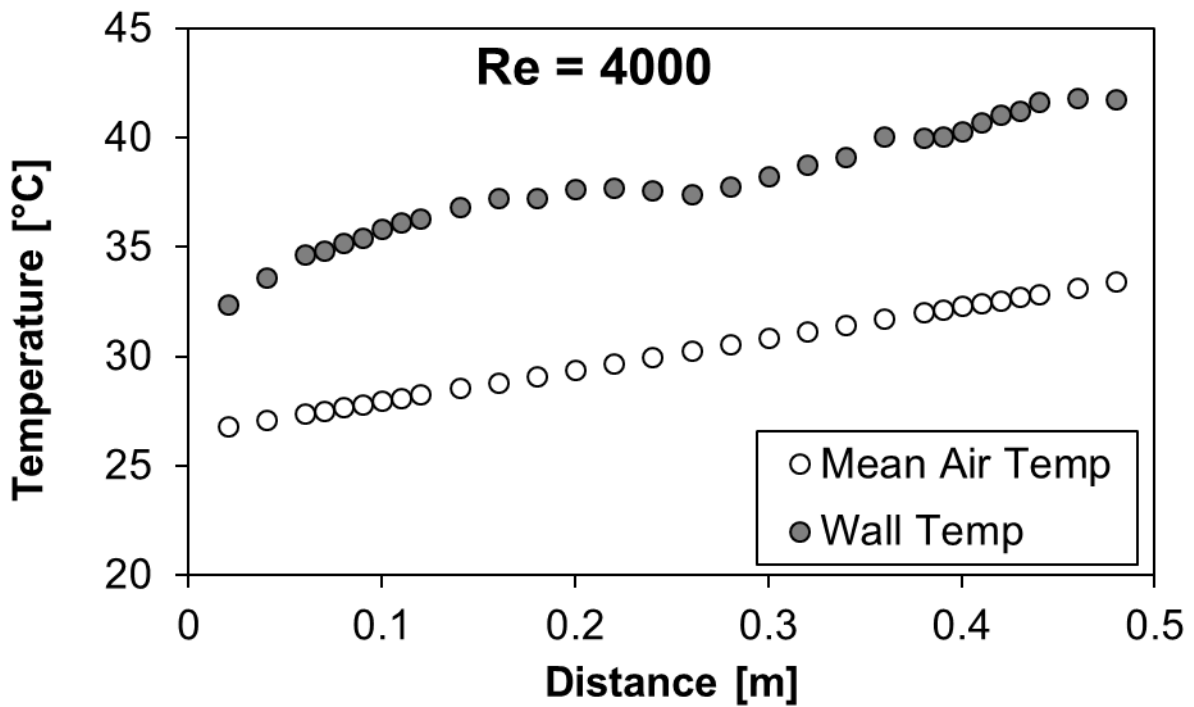


Figure F.30: Wall and mean air temperatures for mesh 5.1 under one-heated wall boundary condition at Re = 4 000

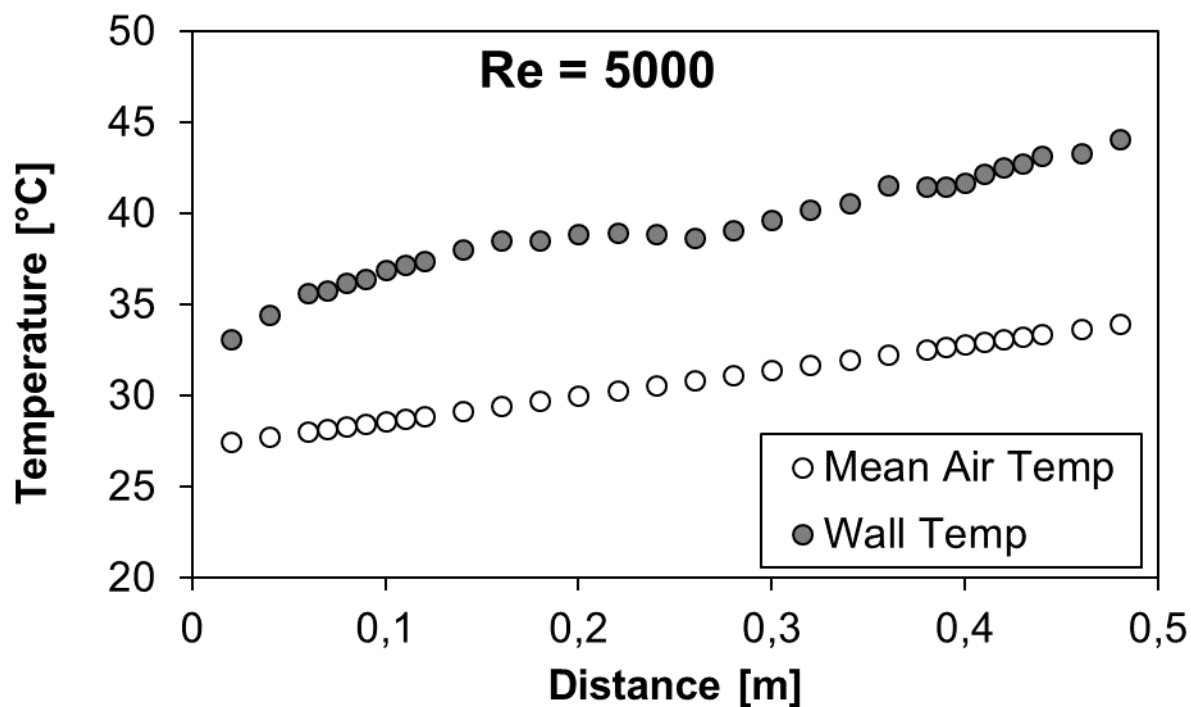


Figure F.31: Wall and mean air temperatures for mesh 5.1 under one-heated wall boundary condition at Re = 5 000

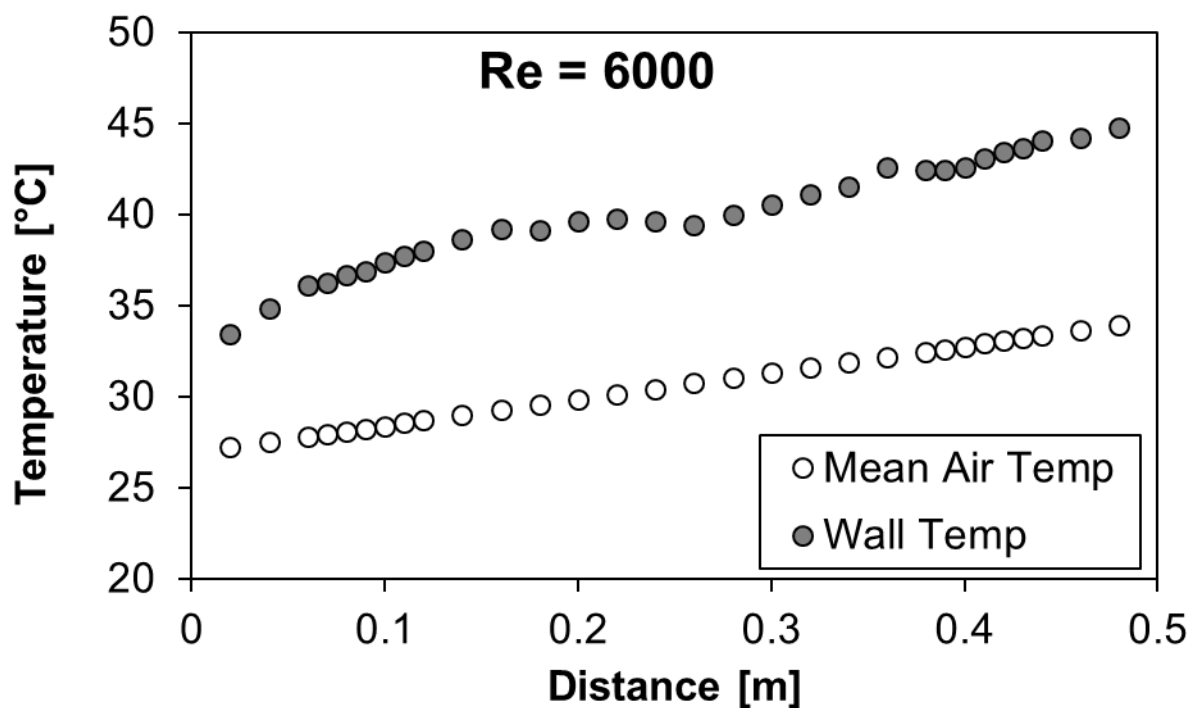


Figure F.32: Wall and mean air temperatures for mesh 5.1 under one-heated wall boundary condition at Re = 6 000

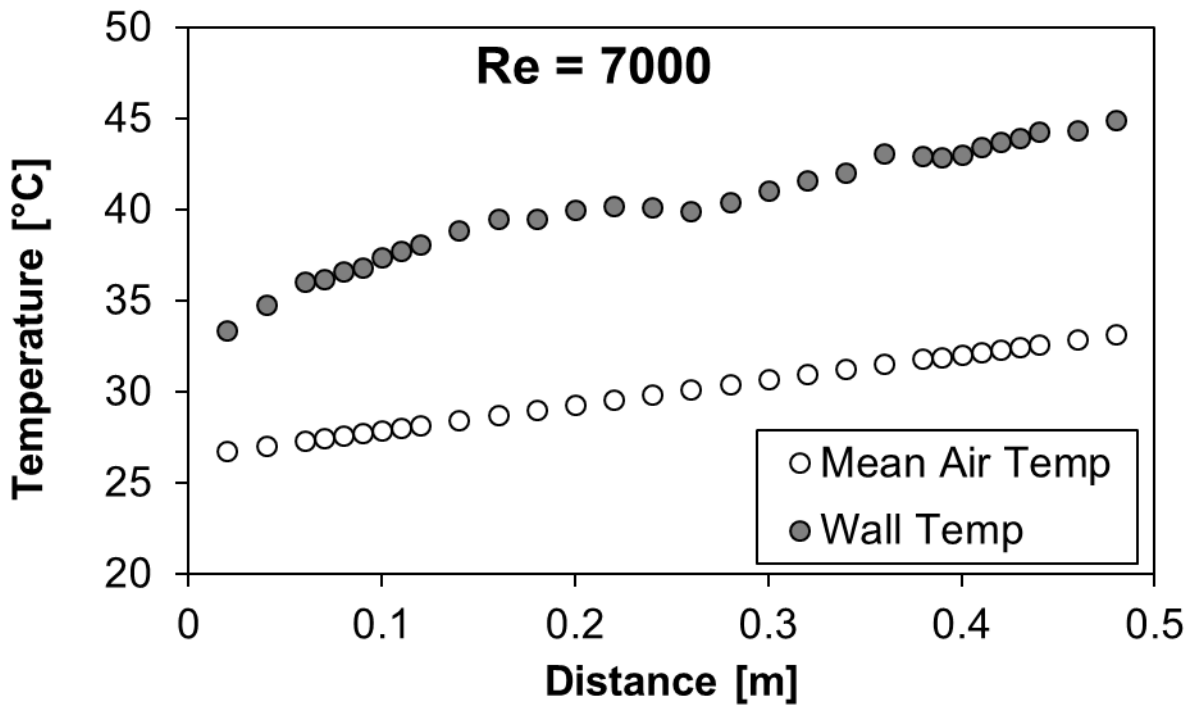


Figure F.33: Wall and mean air temperatures for mesh 5.1 under one-heated wall boundary condition at Re = 7 000

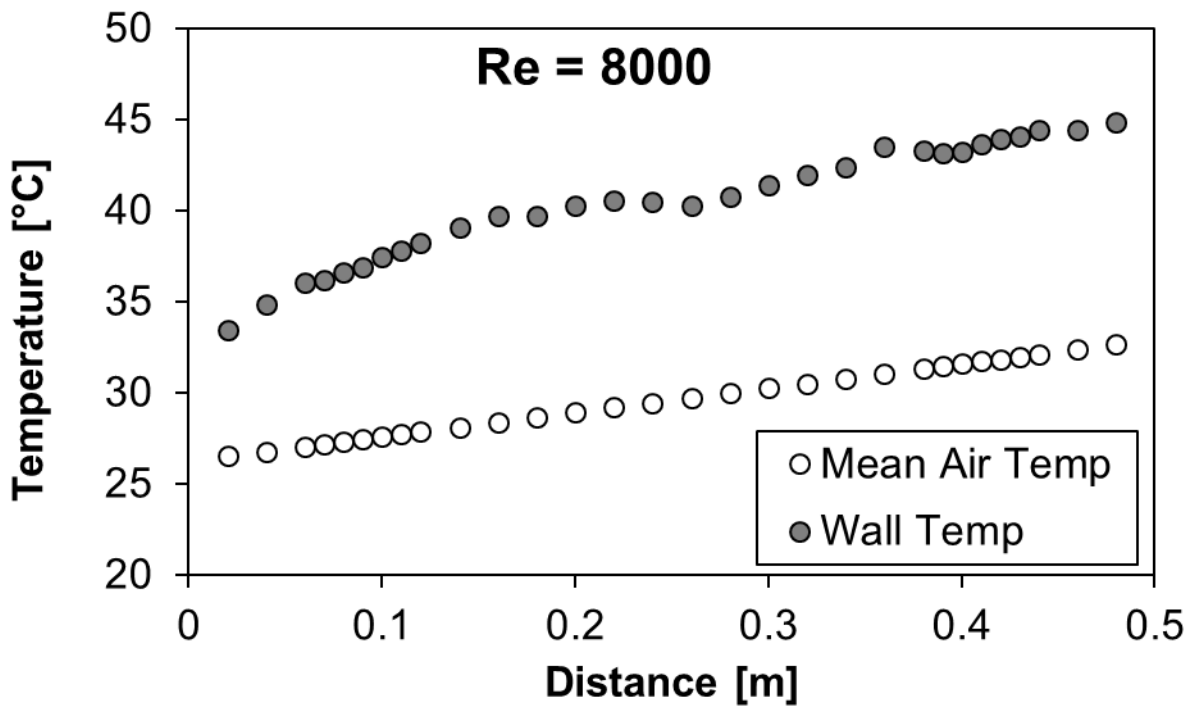


Figure F.34: Wall and mean air temperatures for mesh 5.1 under one-heated wall boundary condition at Re = 8 000

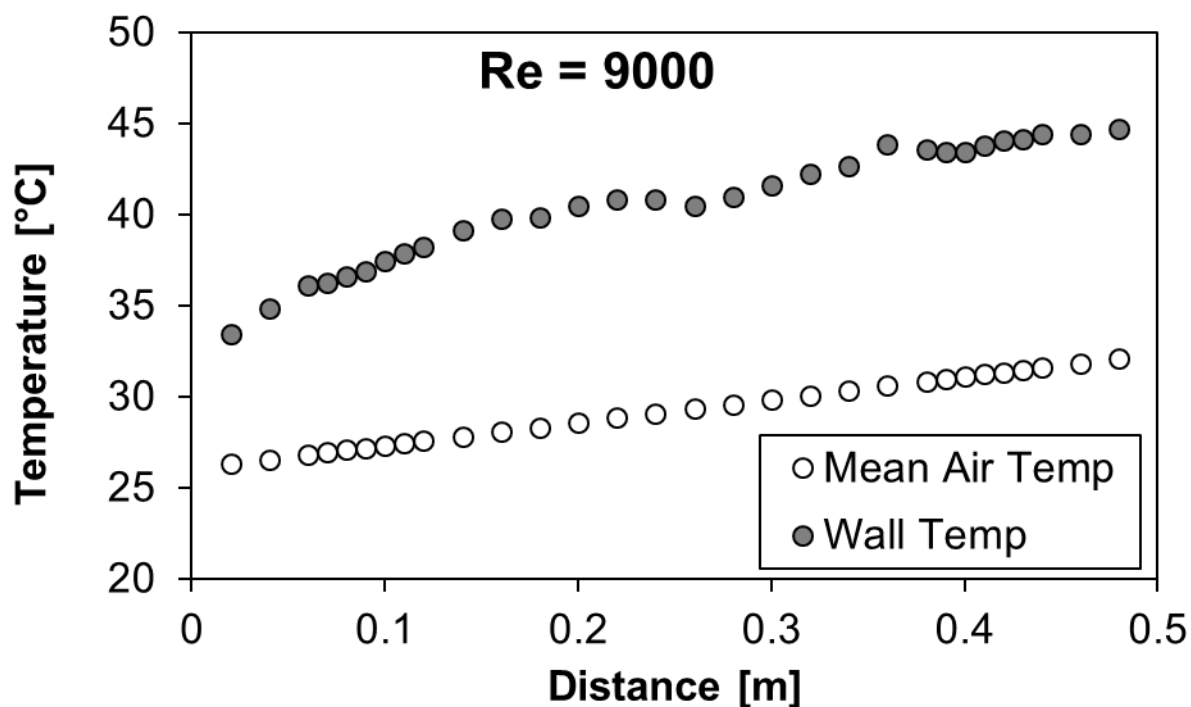


Figure F.35: Wall and mean air temperatures for mesh 5.1 under one-heated wall boundary condition at Re = 9 000

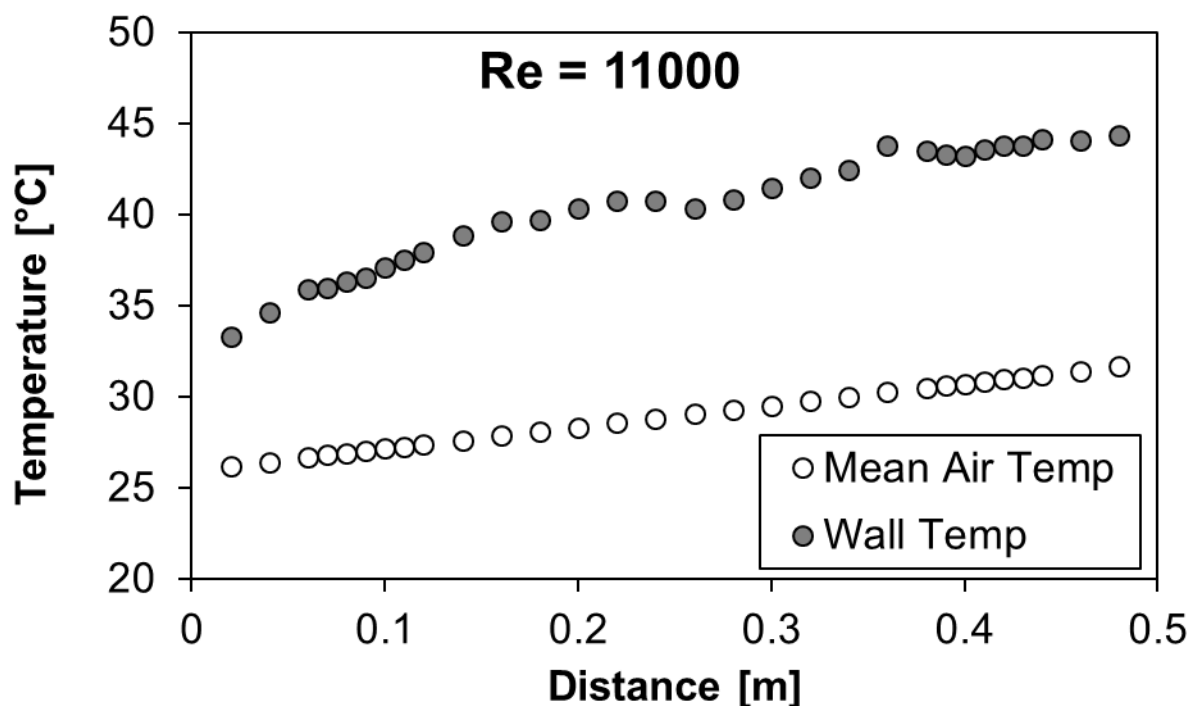


Figure F.36: Wall and mean air temperatures for mesh 5.1 under one-heated wall boundary condition at Re = 11 000

5 MM CHANNEL HEIGHT – MESH 5.3

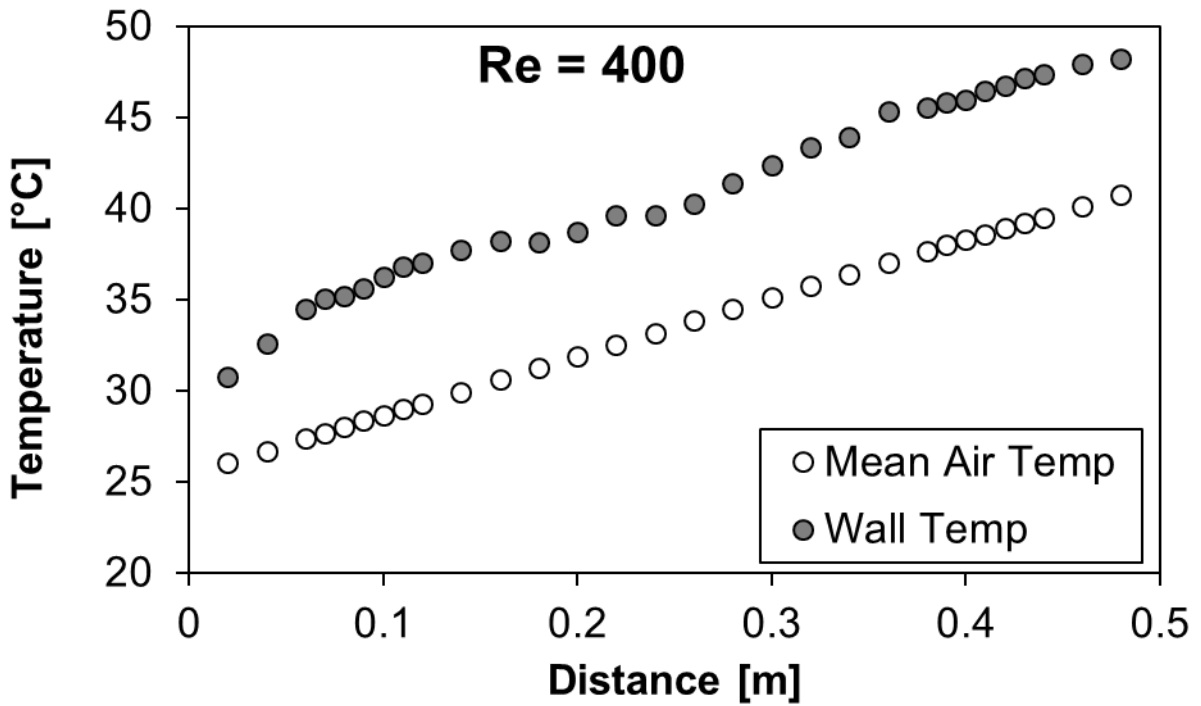


Figure F.37: Wall and mean air temperatures for mesh 5.3 under one-heated wall boundary condition at Re = 400

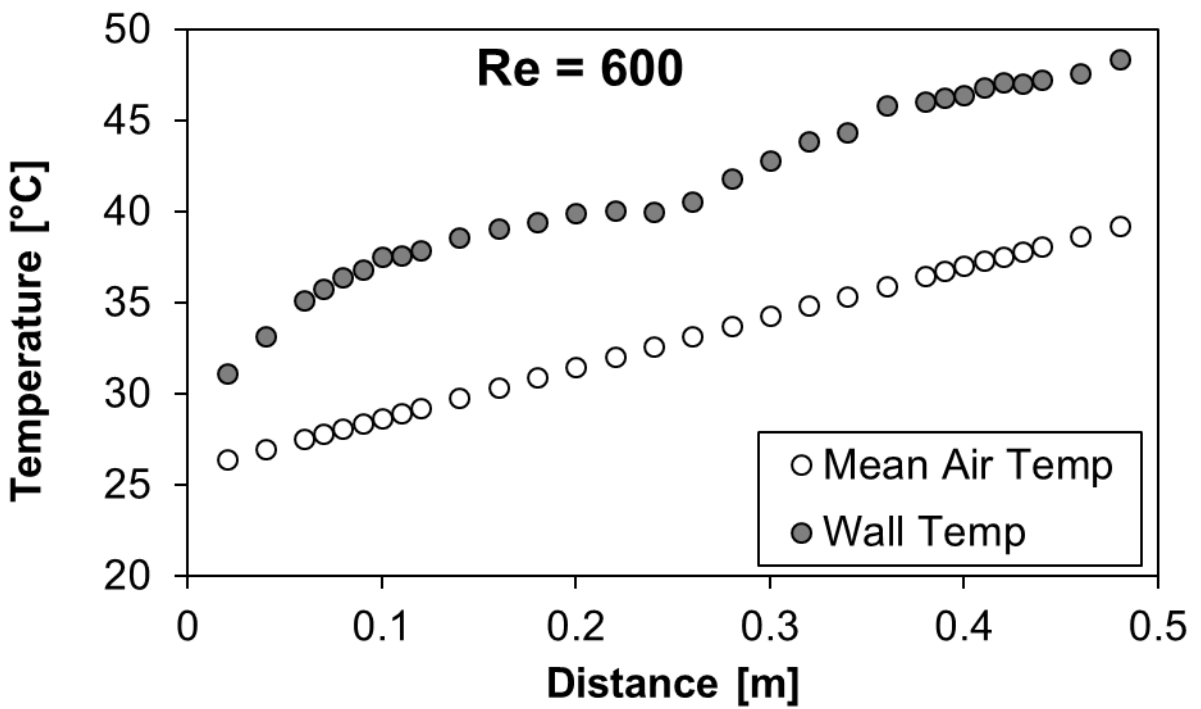


Figure F.38: Wall and mean air temperatures for mesh 5.3 under one-heated wall boundary condition at Re = 600

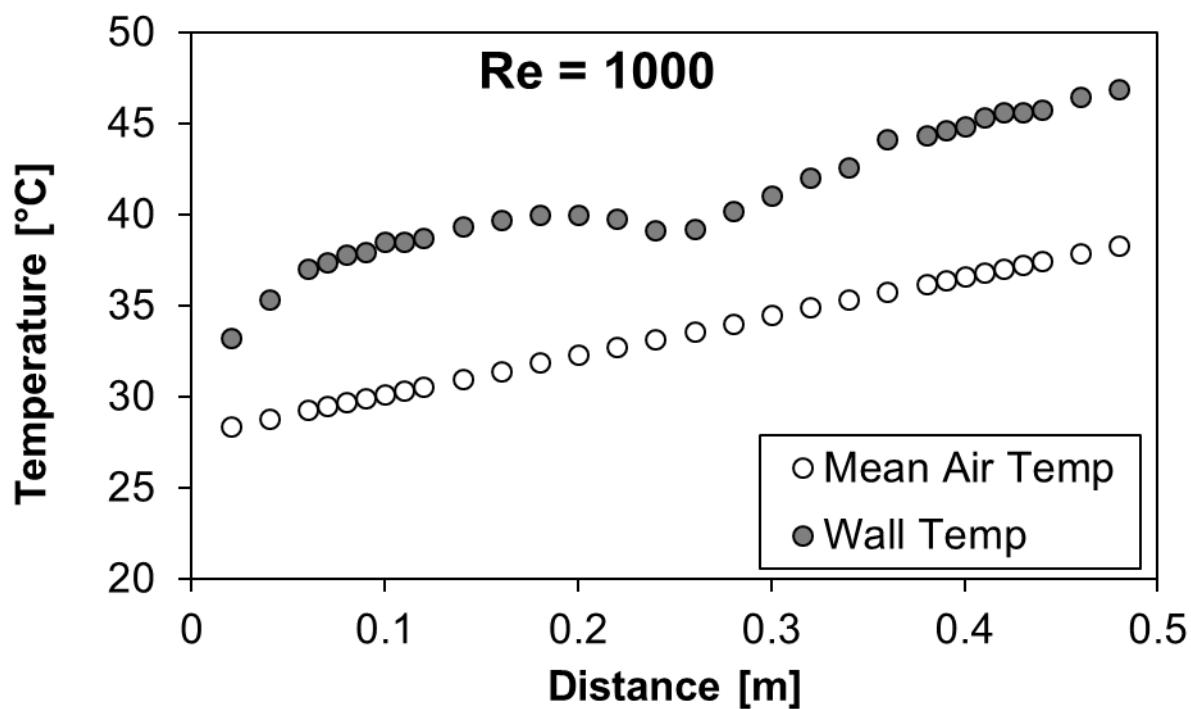


Figure F.39: Wall and mean air temperatures for mesh 5.3 under one-heated wall boundary condition at Re = 1 000

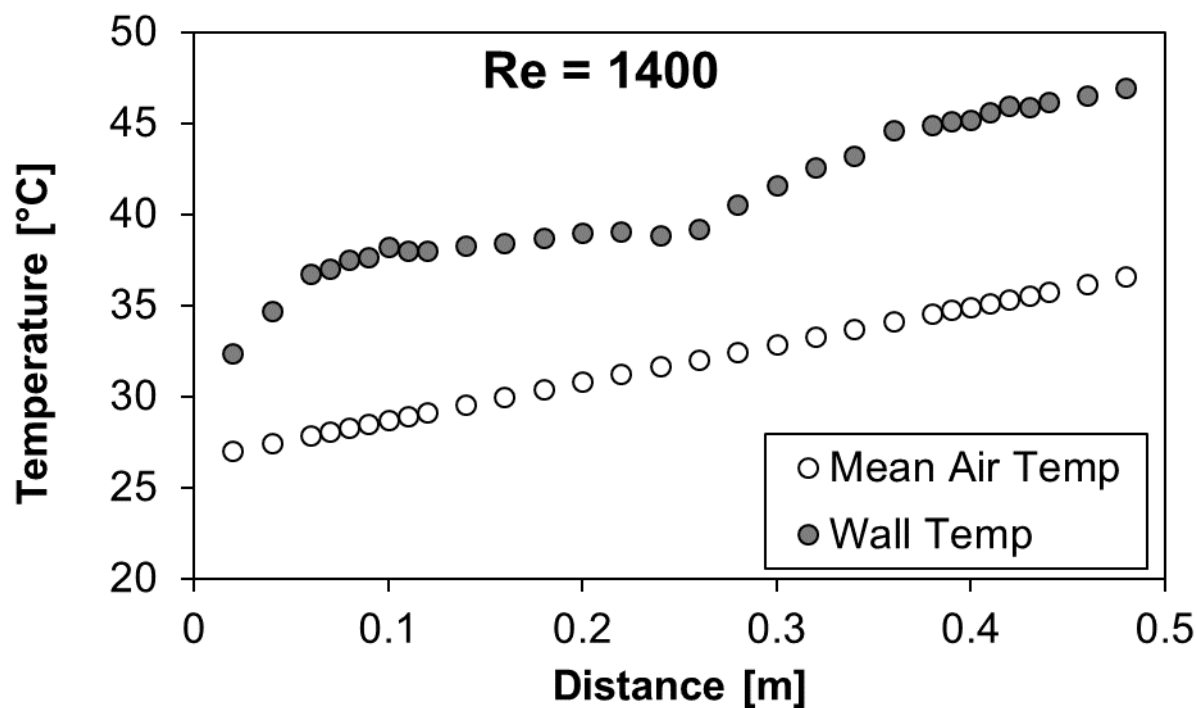


Figure F.40: Wall and mean air temperatures for mesh 5.3 under one-heated wall boundary condition at Re = 1 400

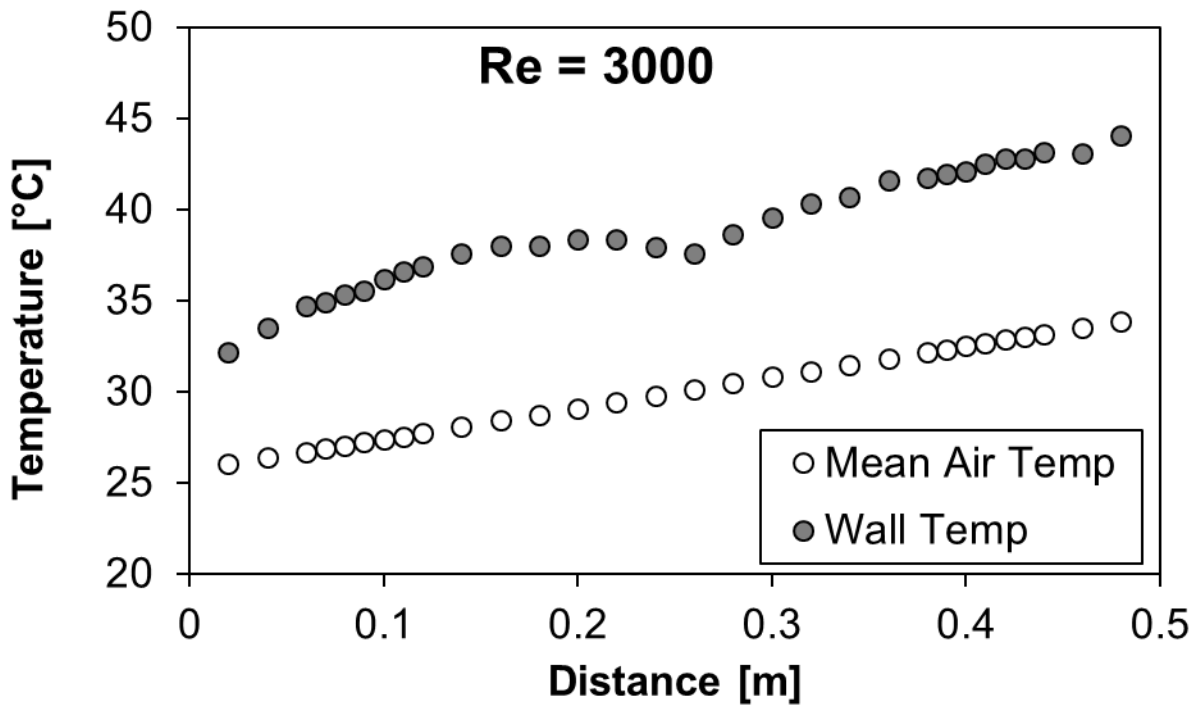


Figure F.41: Wall and mean air temperatures for mesh 5.3 under one-heated wall boundary condition at Re = 3 000

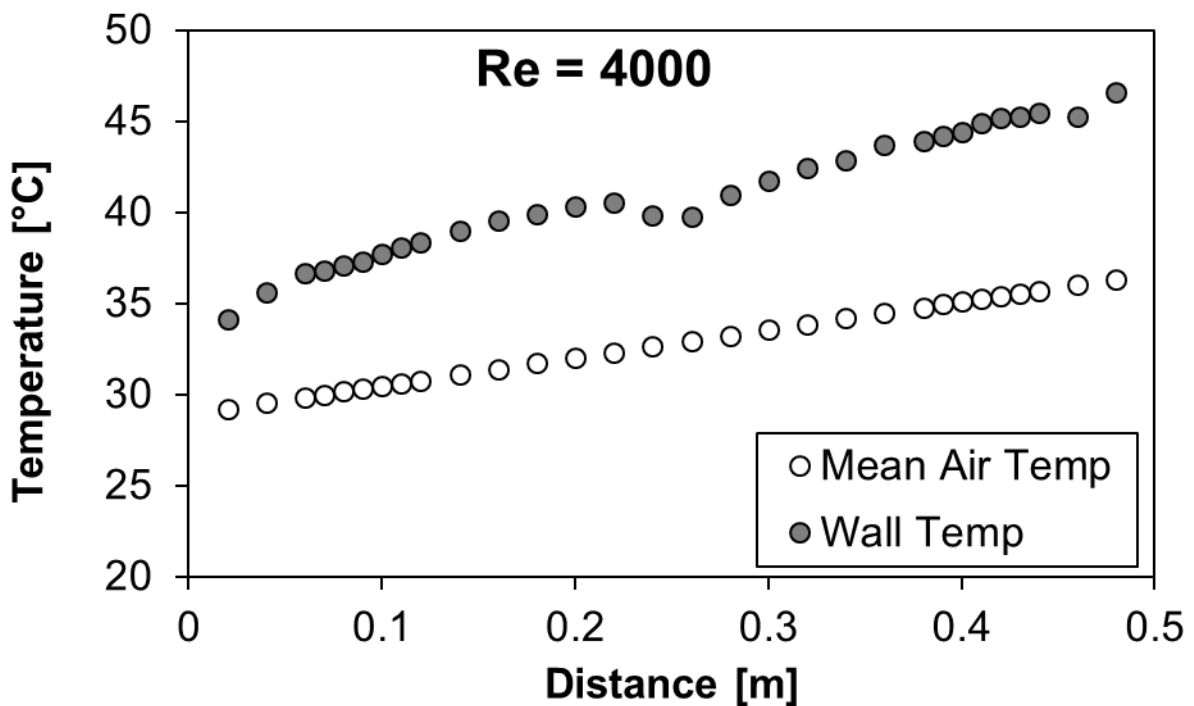


Figure F.42: Wall and mean air temperatures for mesh 5.3 under one-heated wall boundary condition at Re = 4 000

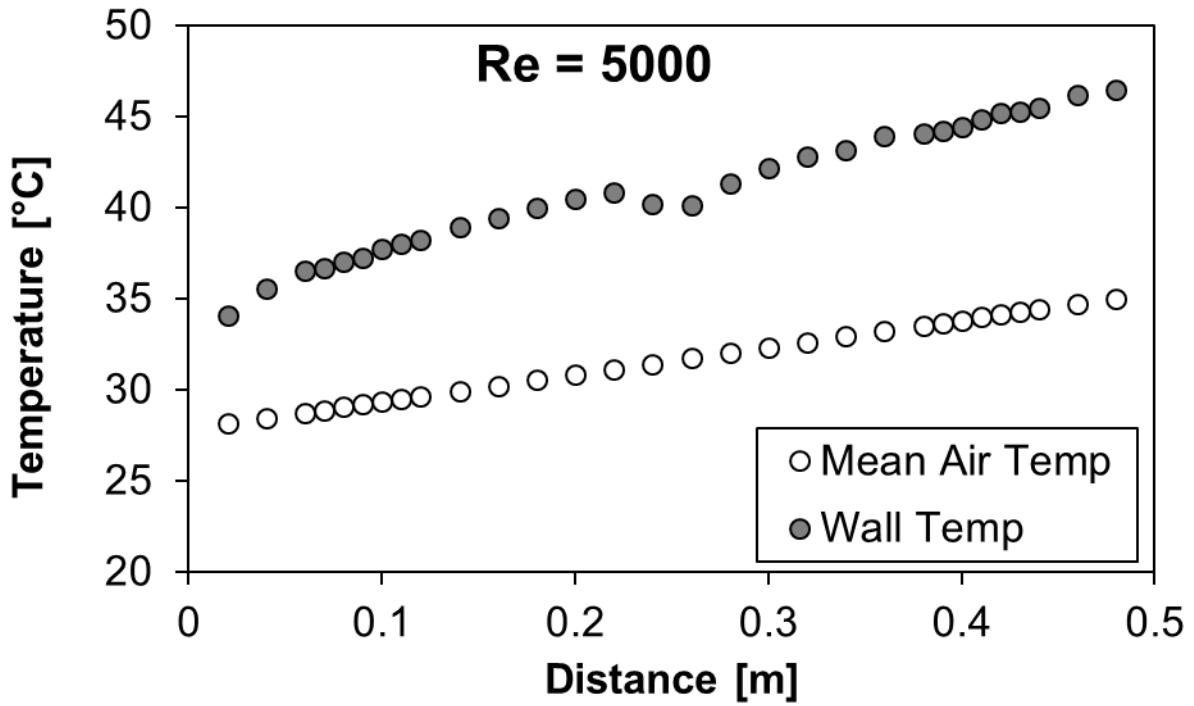


Figure F.43: Wall and mean air temperatures for mesh 5.3 under one-heated wall boundary condition at Re = 5 000

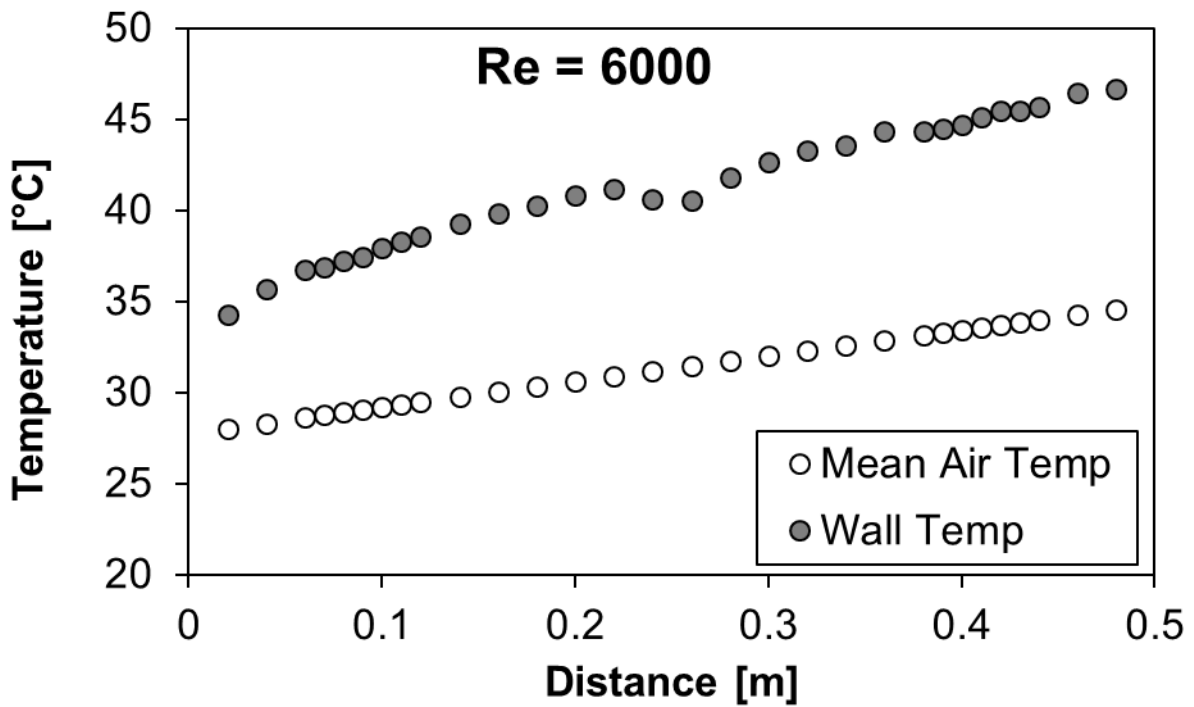


Figure F.44: Wall and mean air temperatures for mesh 5.3 under one-heated wall boundary condition at Re = 6 000

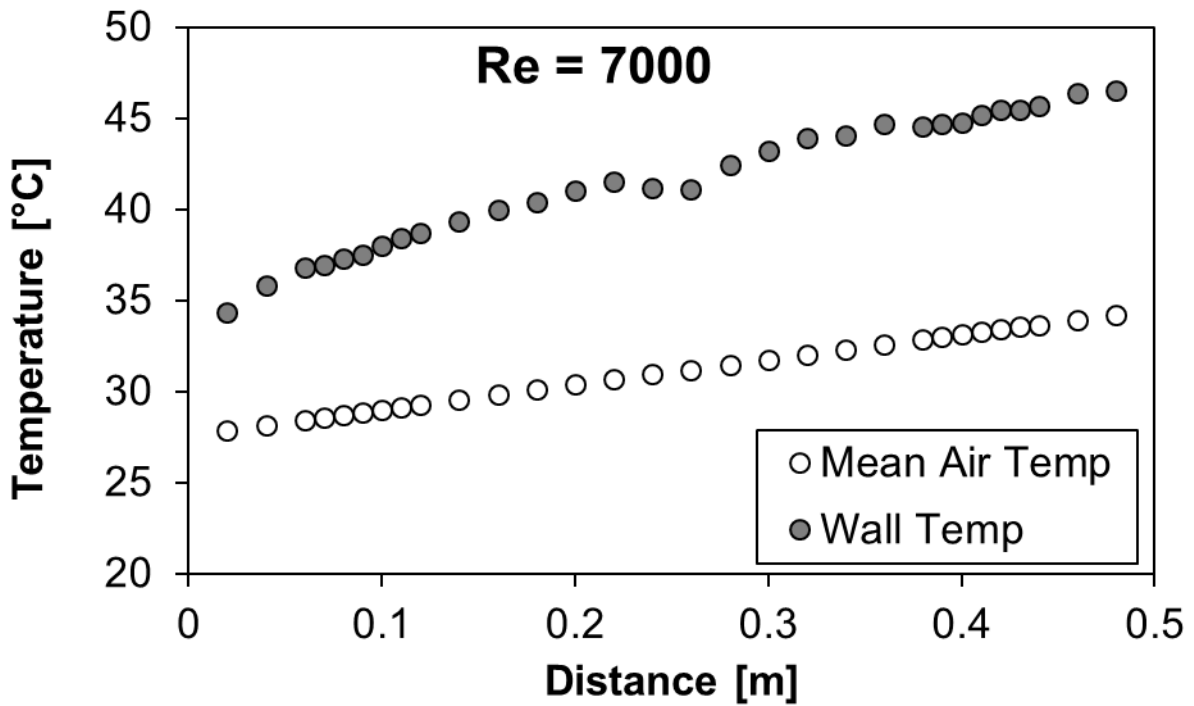


Figure F.45: Wall and mean air temperatures for mesh 5.3 under one-heated wall boundary condition at Re = 7 000

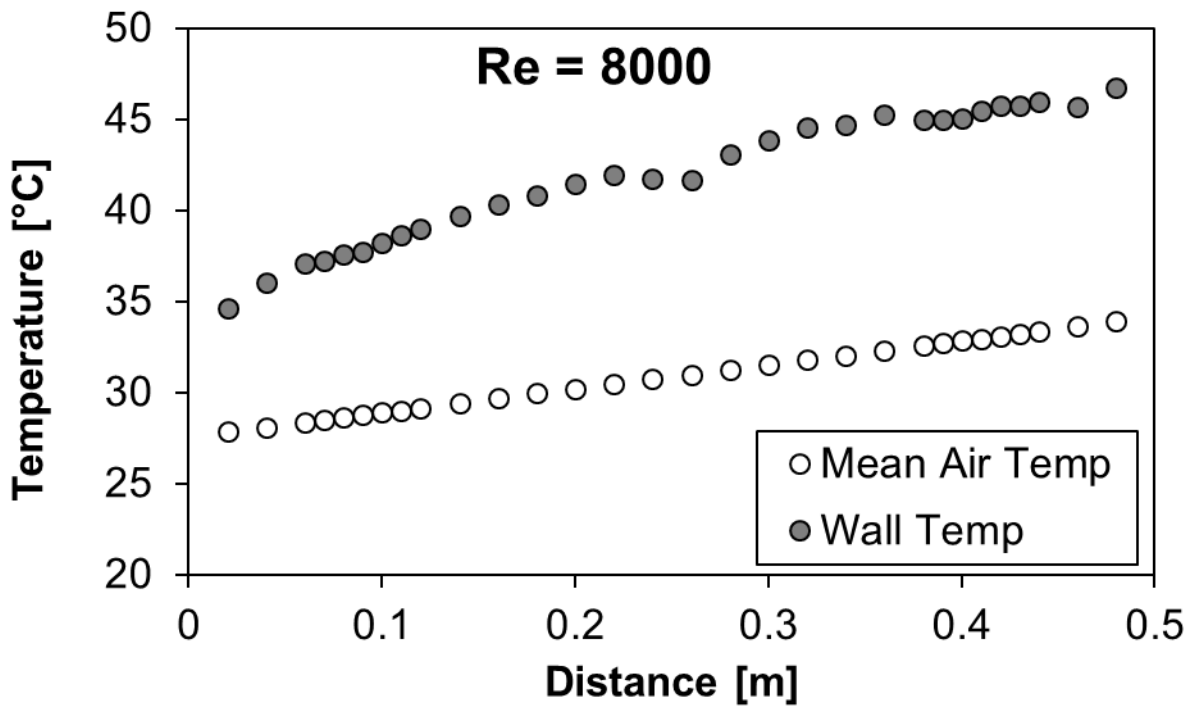


Figure F.46: Wall and mean air temperatures for mesh 5.3 under one-heated wall boundary condition at Re = 8 000

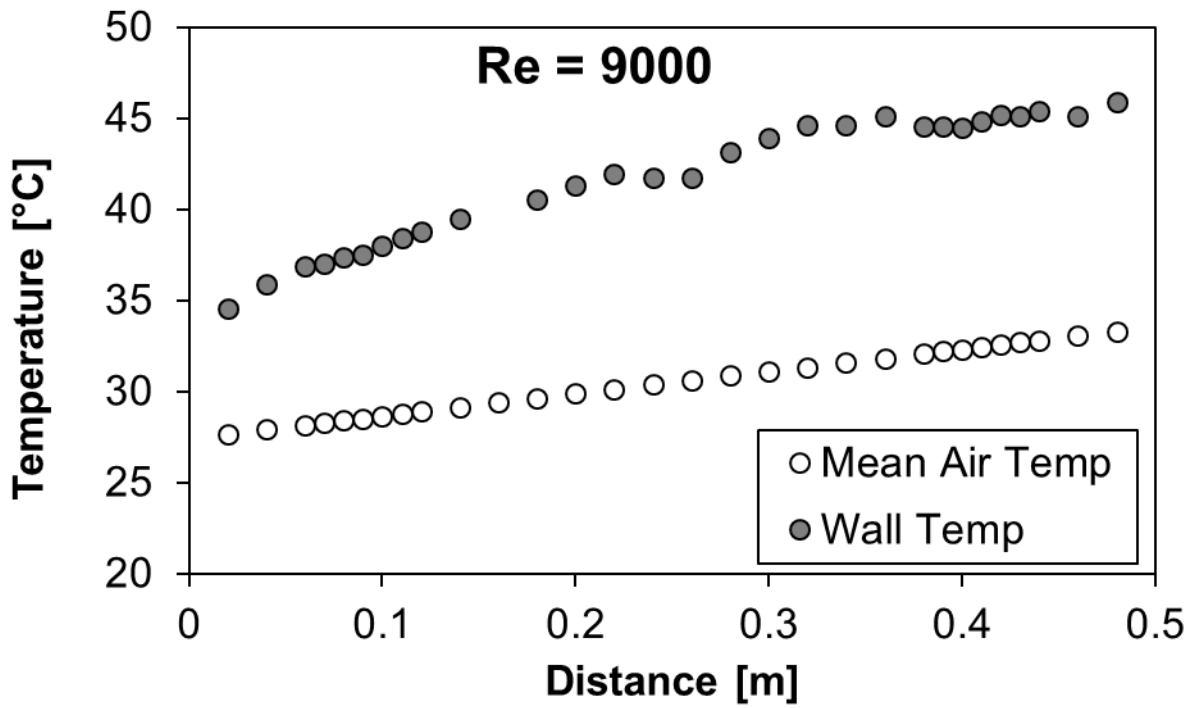


Figure F.47: Wall and mean air temperatures for mesh 5.3 under one-heated wall boundary condition at $Re = 9\ 000$

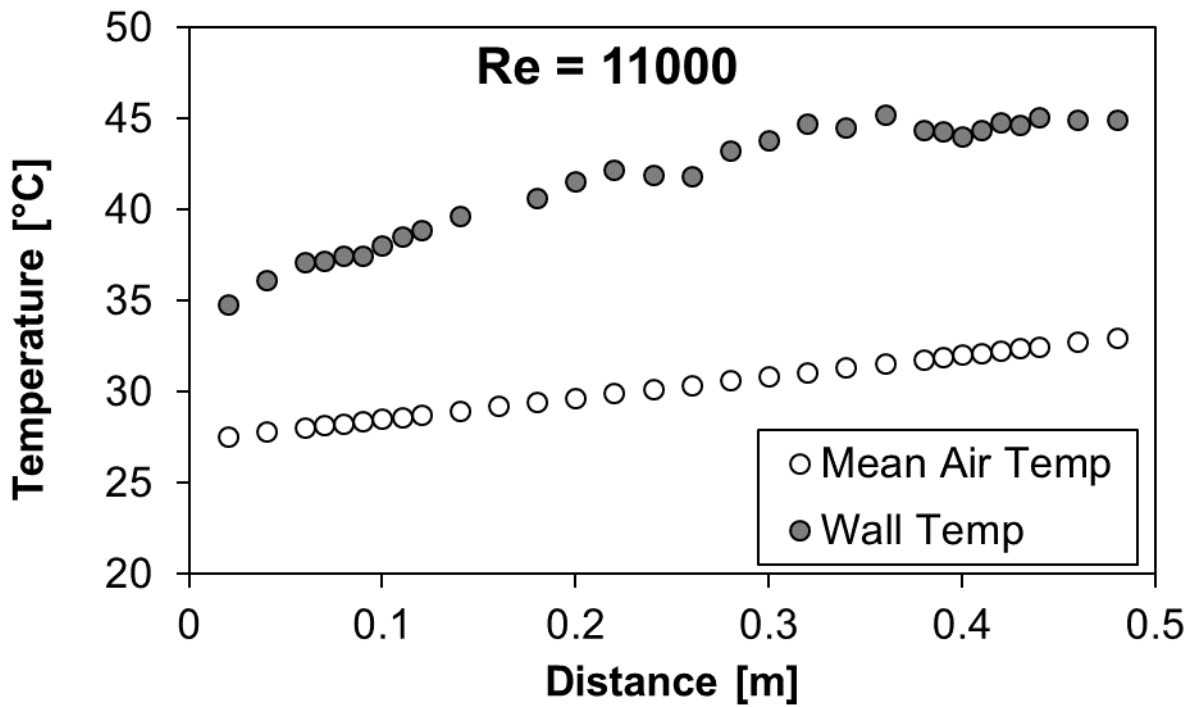


Figure F.48: Wall and mean air temperatures for mesh 5.3 under one-heated wall boundary condition at $Re = 11\ 000$

14 MM CHANNEL HEIGHT – MESH 2.1

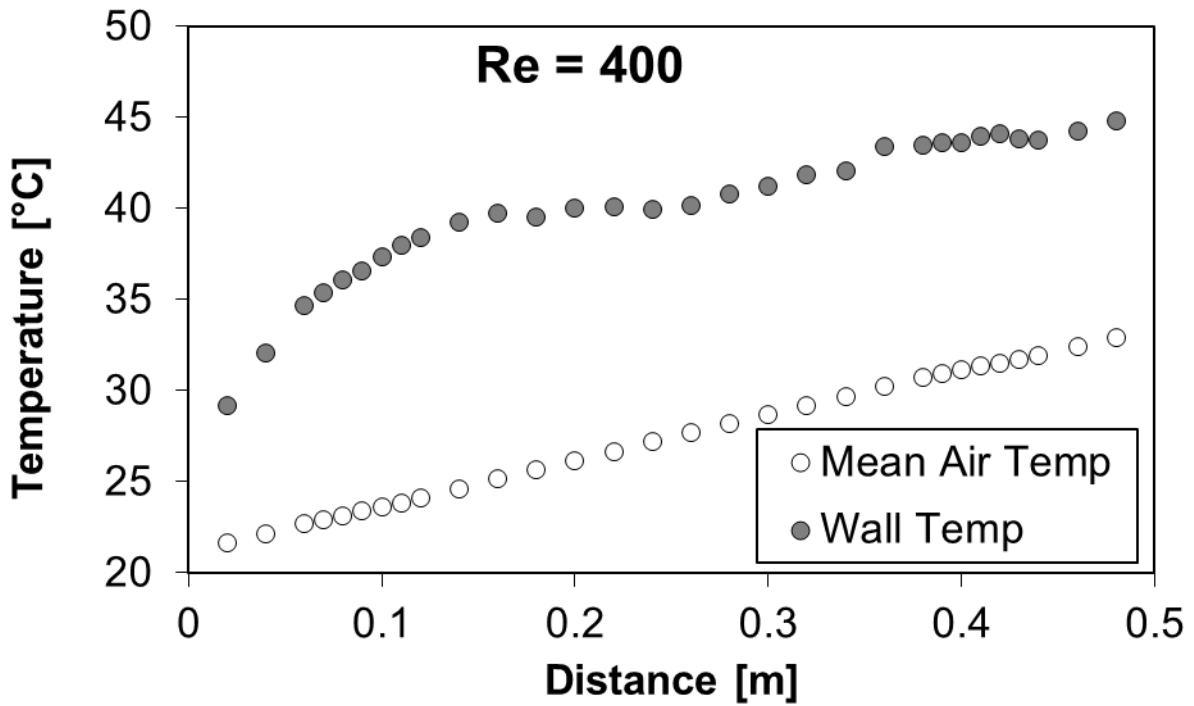


Figure F.49: Wall and mean air temperatures for mesh 2.1 under one-heated wall boundary condition at Re = 400

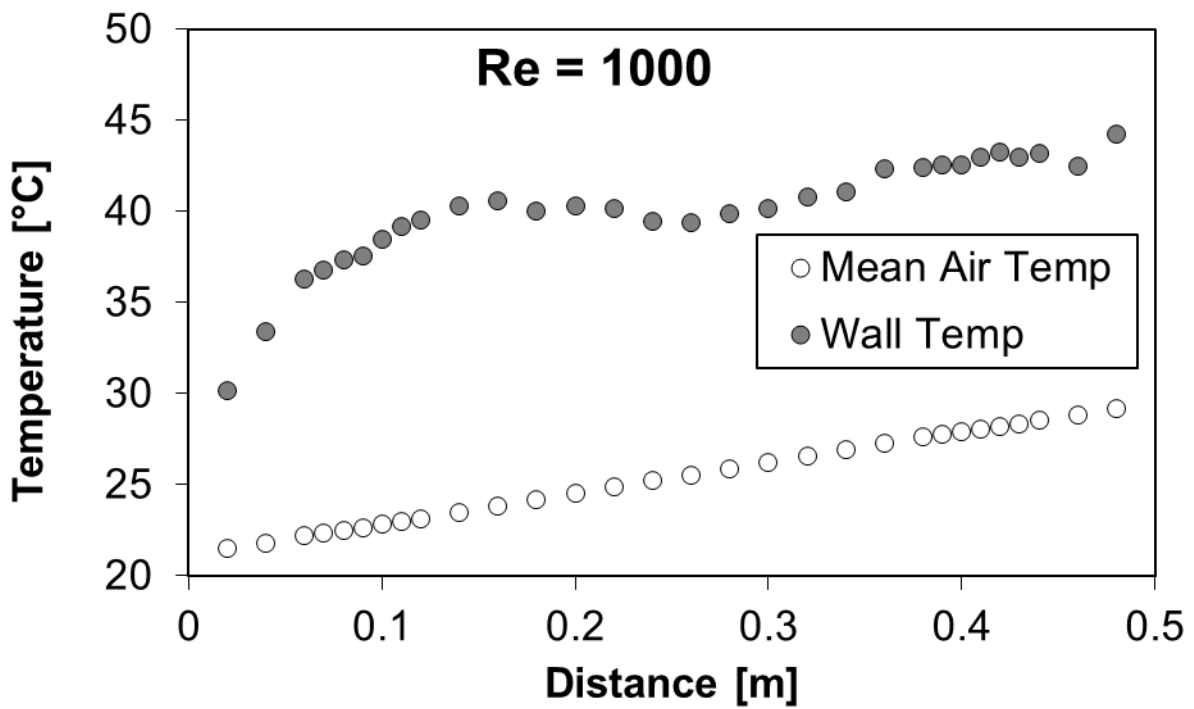


Figure F.50: Wall and mean air temperatures for mesh 2.1 under one-heated wall boundary condition at Re = 1 000

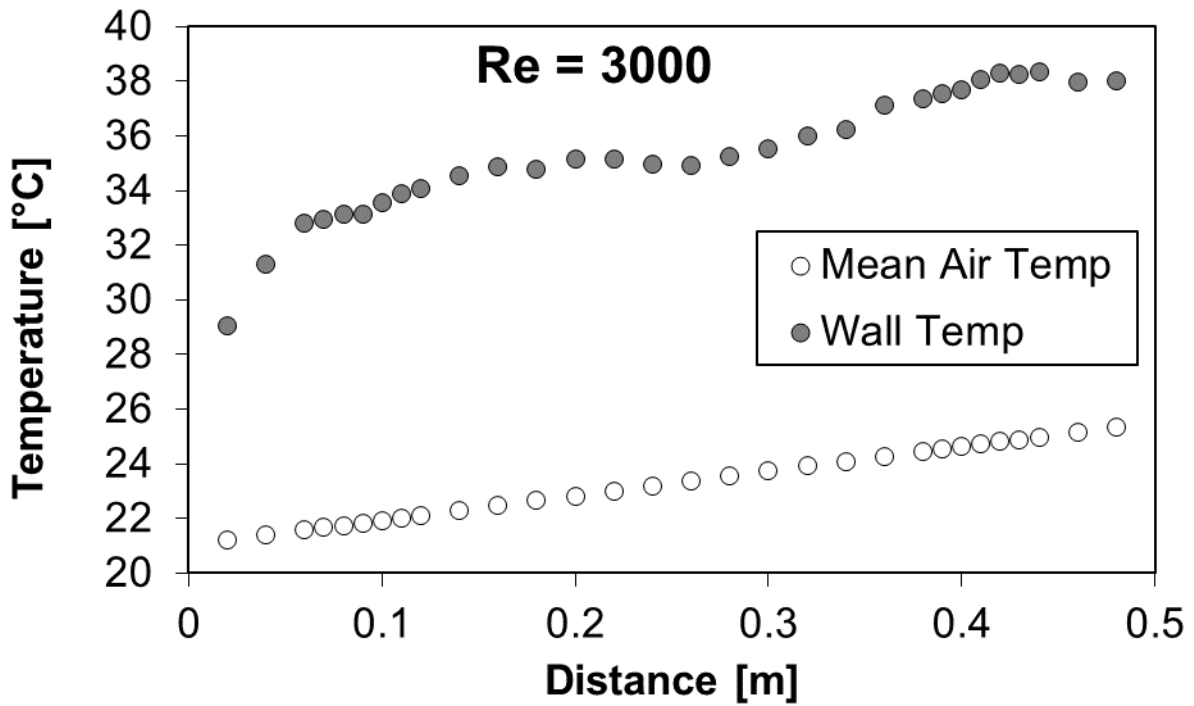


Figure F.51: Wall and mean air temperatures for mesh 2.1 under one-heated wall boundary condition at Re = 3 000

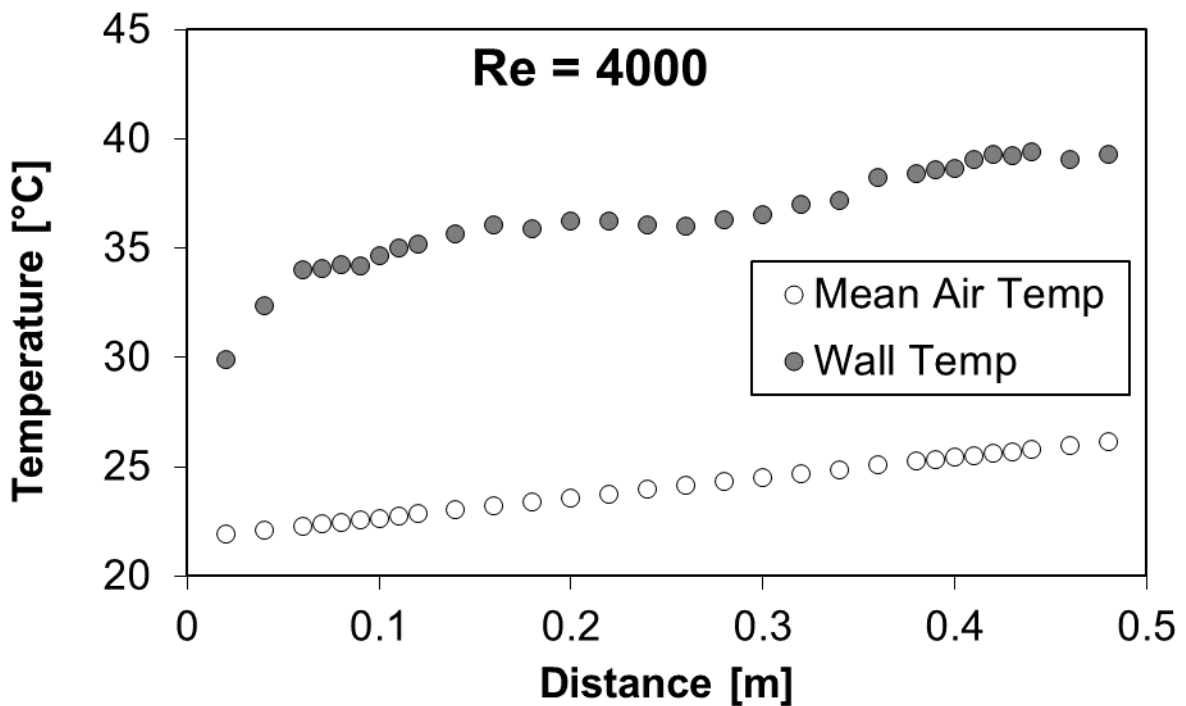


Figure F.52: Wall and mean air temperatures for mesh 2.1 under one-heated wall boundary condition at Re = 4 000

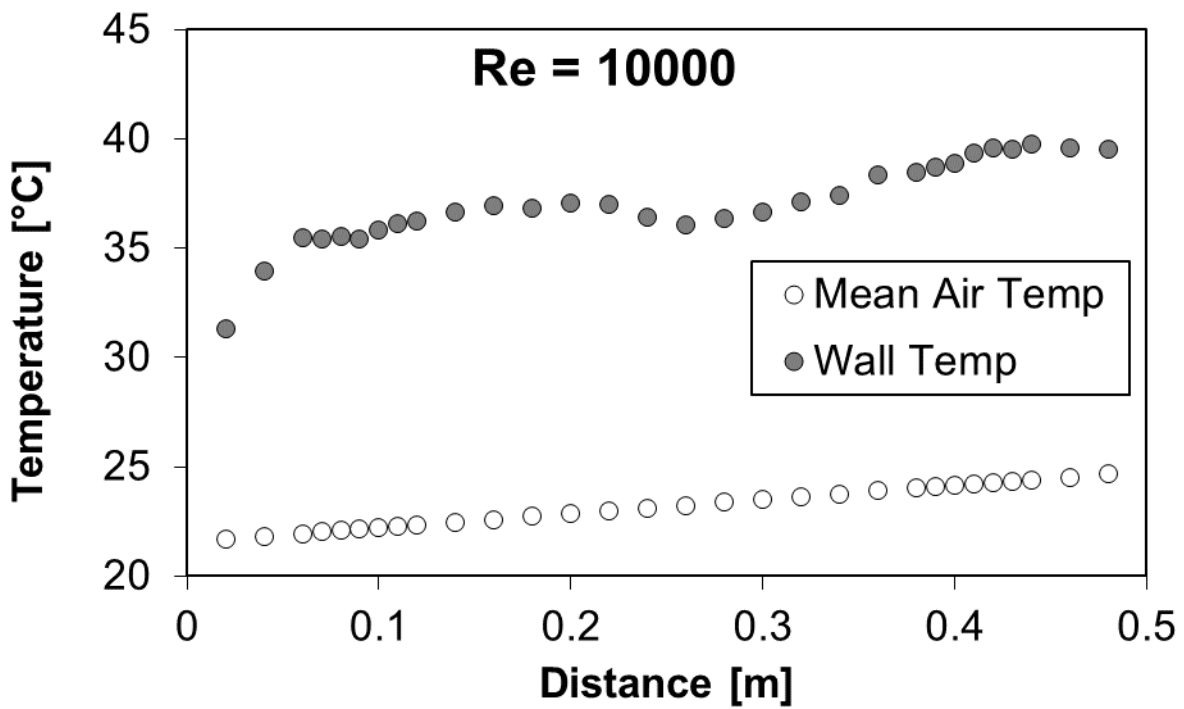


Figure F.53: Wall and mean air temperatures for mesh 2.1 under one-heated wall boundary condition at Re = 10 000

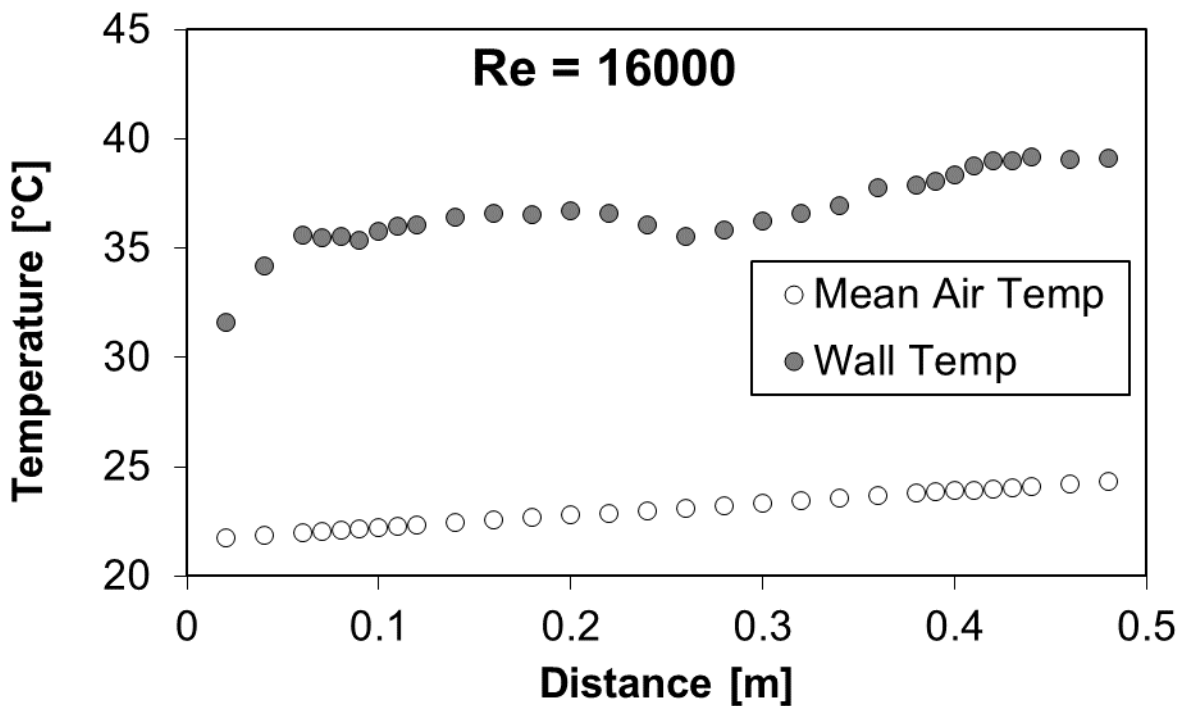


Figure F.54: Wall and mean air temperatures for mesh 2.1 under one-heated wall boundary condition at Re = 16 000

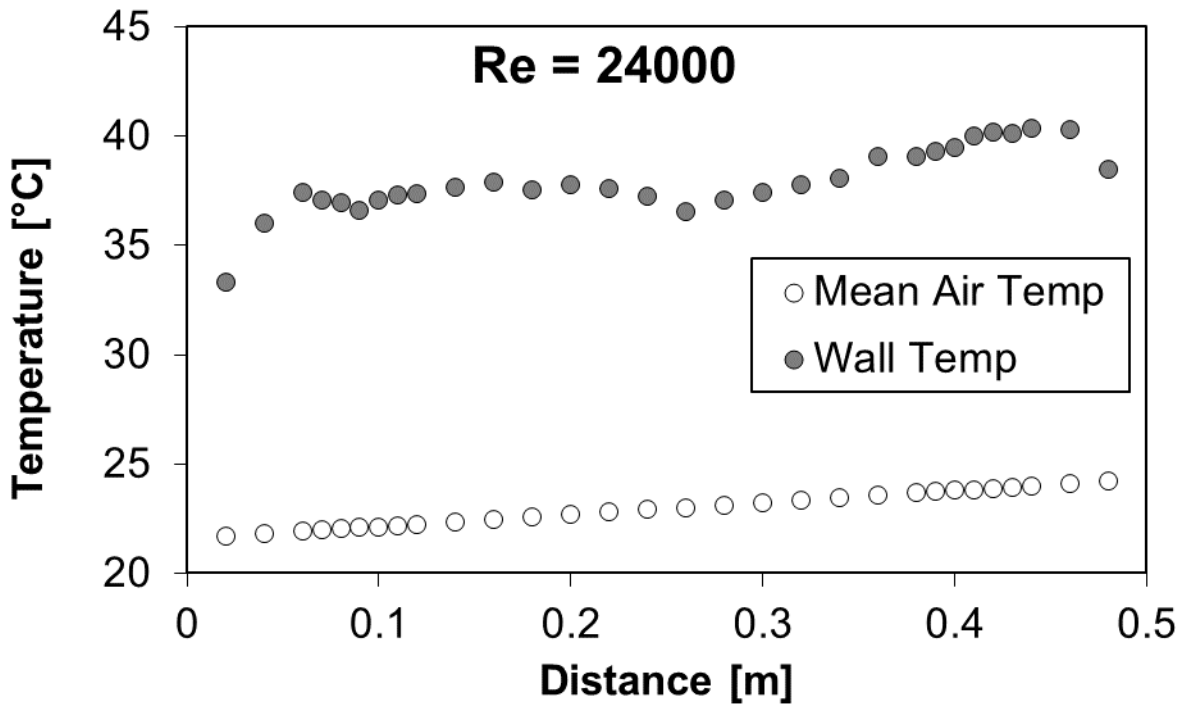


Figure F.55: Wall and mean air temperatures for mesh 2.1 under one-heated wall boundary condition at Re = 24 000

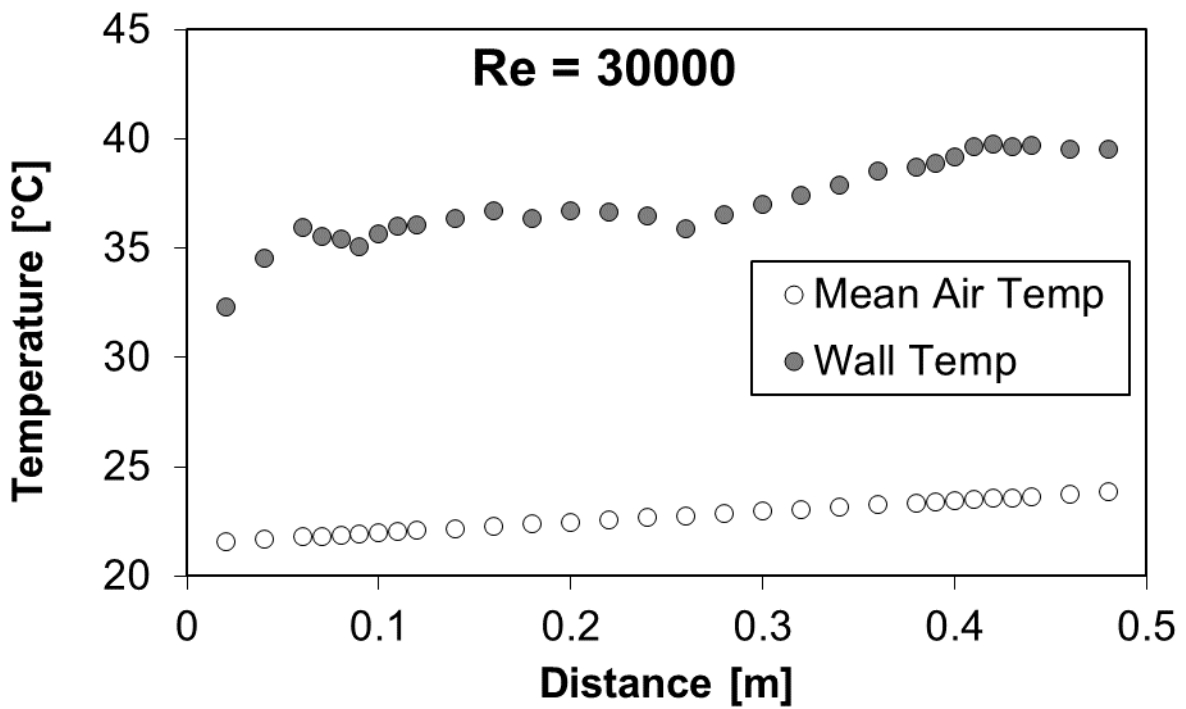


Figure F.56: Wall and mean air temperatures for mesh 2.1 under one-heated wall boundary condition at Re = 30 000

14 MM CHANNEL HEIGHT – MESH 2.3

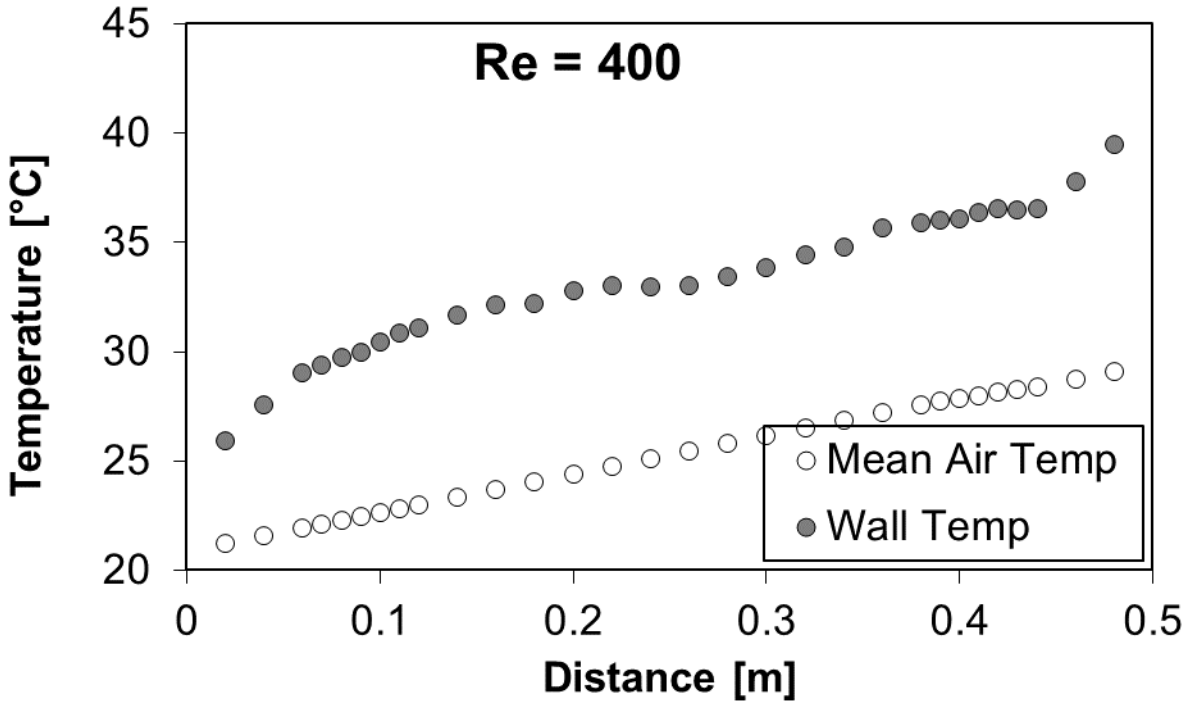


Figure F.57: Wall and mean air temperatures for mesh 2.3 under one-heated wall boundary condition at Re = 400

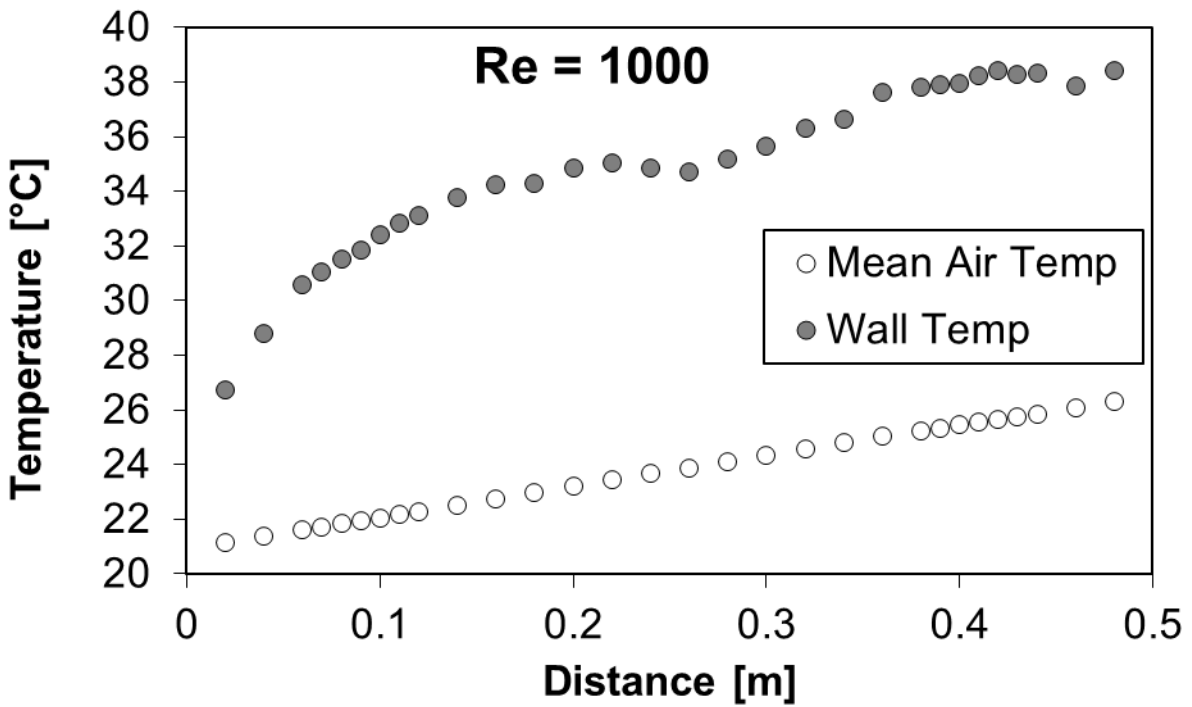


Figure F.58: Wall and mean air temperatures for mesh 2.3 under one-heated wall boundary condition at Re = 1 000

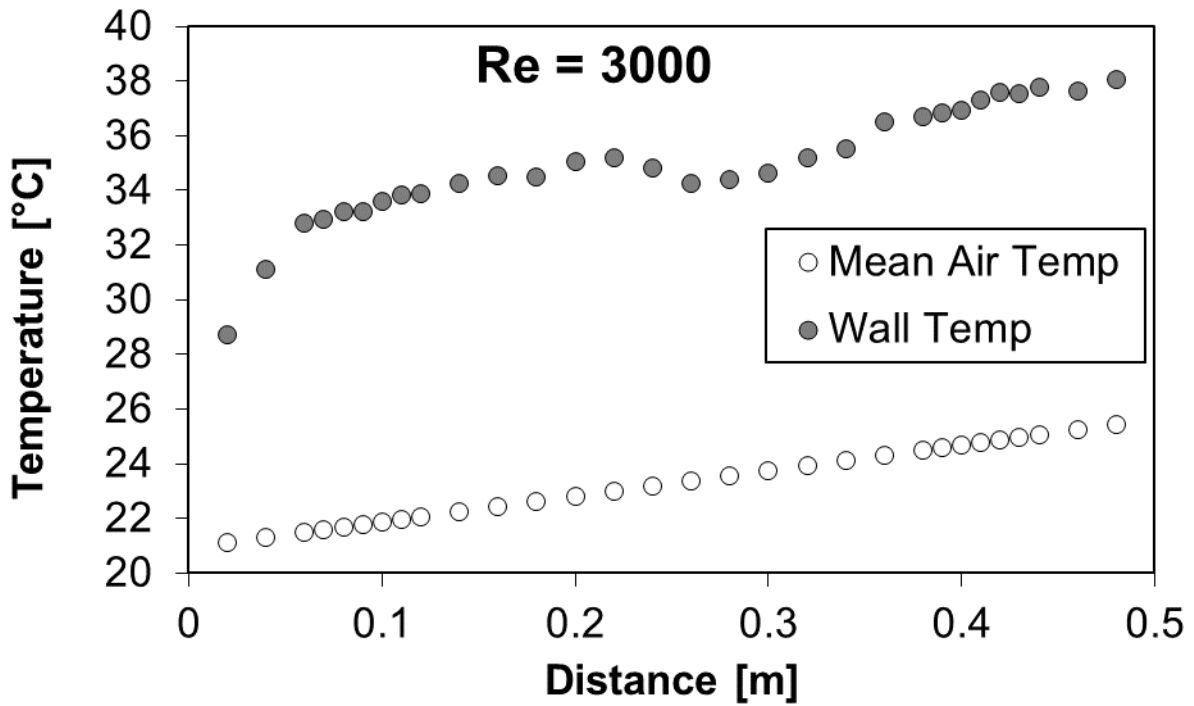


Figure F.59: Wall and mean air temperatures for mesh 2.3 under one-heated wall boundary condition at Re = 3 000

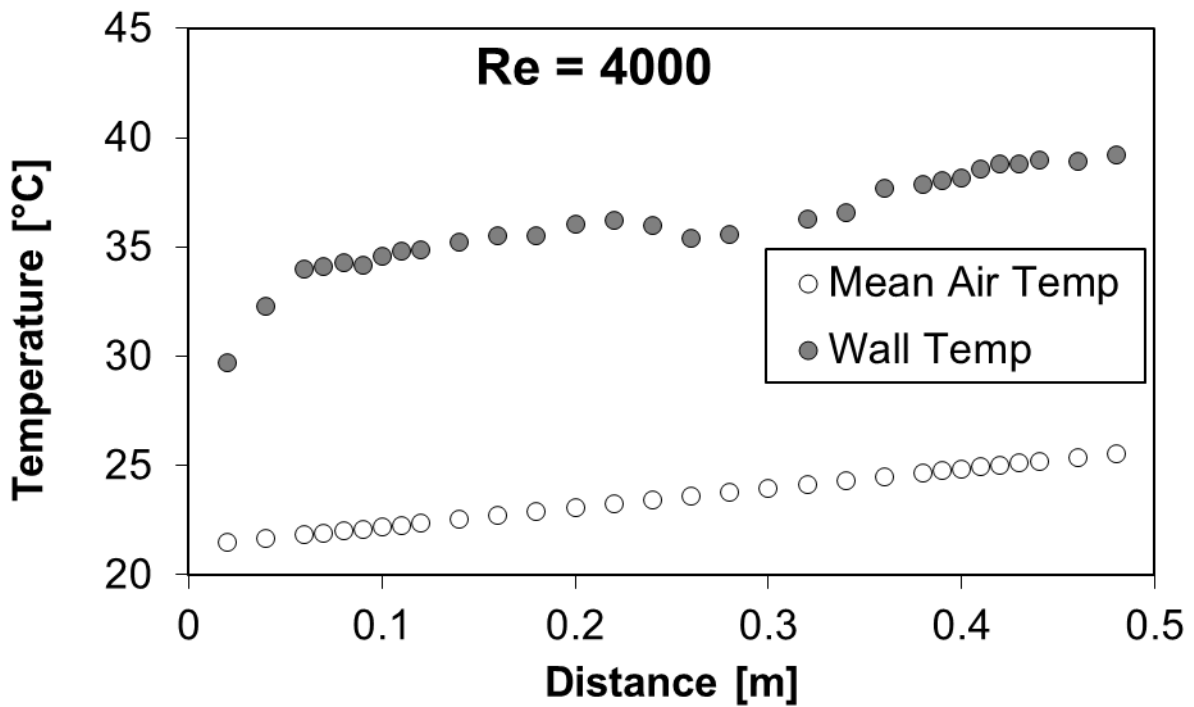


Figure F.60: Wall and mean air temperatures for mesh 2.3 under one-heated wall boundary condition at Re = 4 000

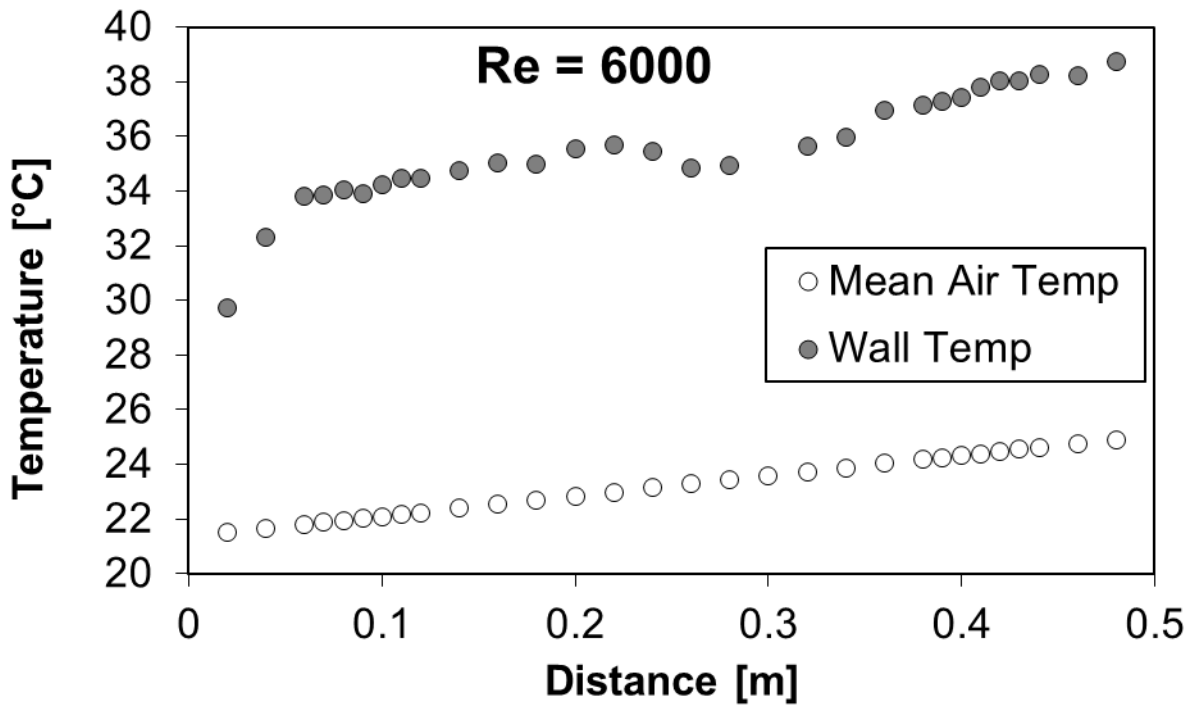


Figure F.61: Wall and mean air temperatures for mesh 2.3 under one-heated wall boundary condition at Re = 6 000

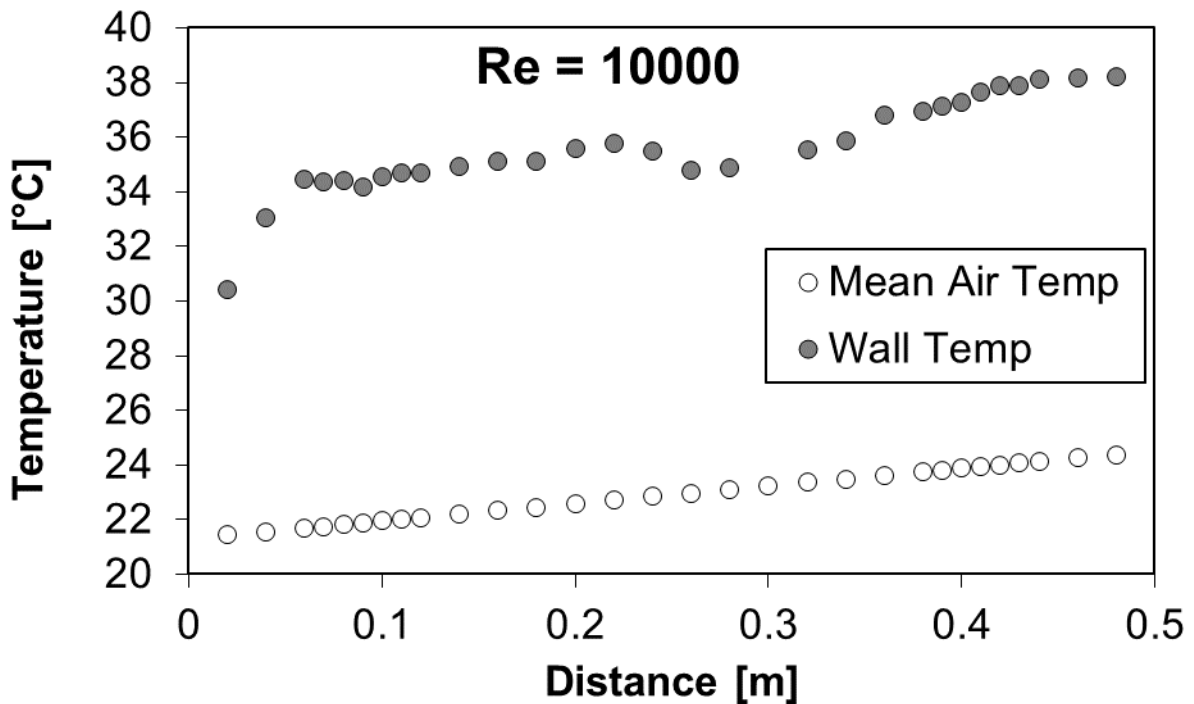


Figure F.62: Wall and mean air temperatures for mesh 2.3 under one-heated wall boundary condition at Re = 10 000

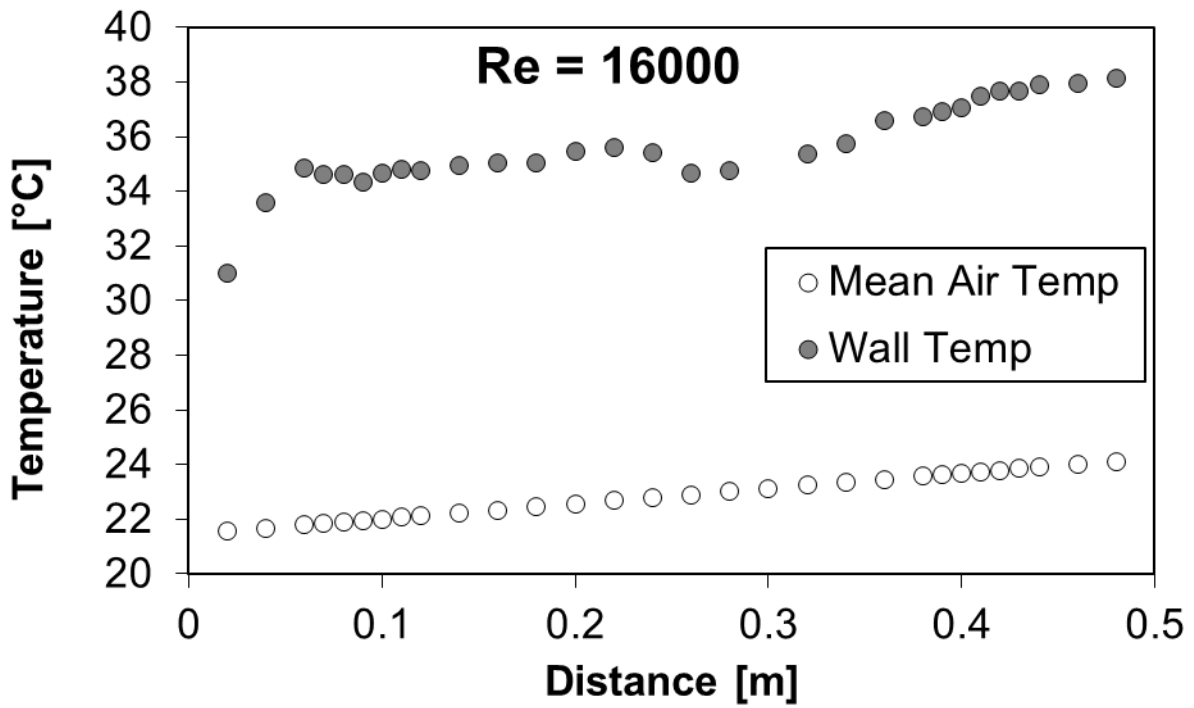


Figure F.63: Wall and mean air temperatures for mesh 2.3 under one-heated wall boundary condition at Re = 16 000

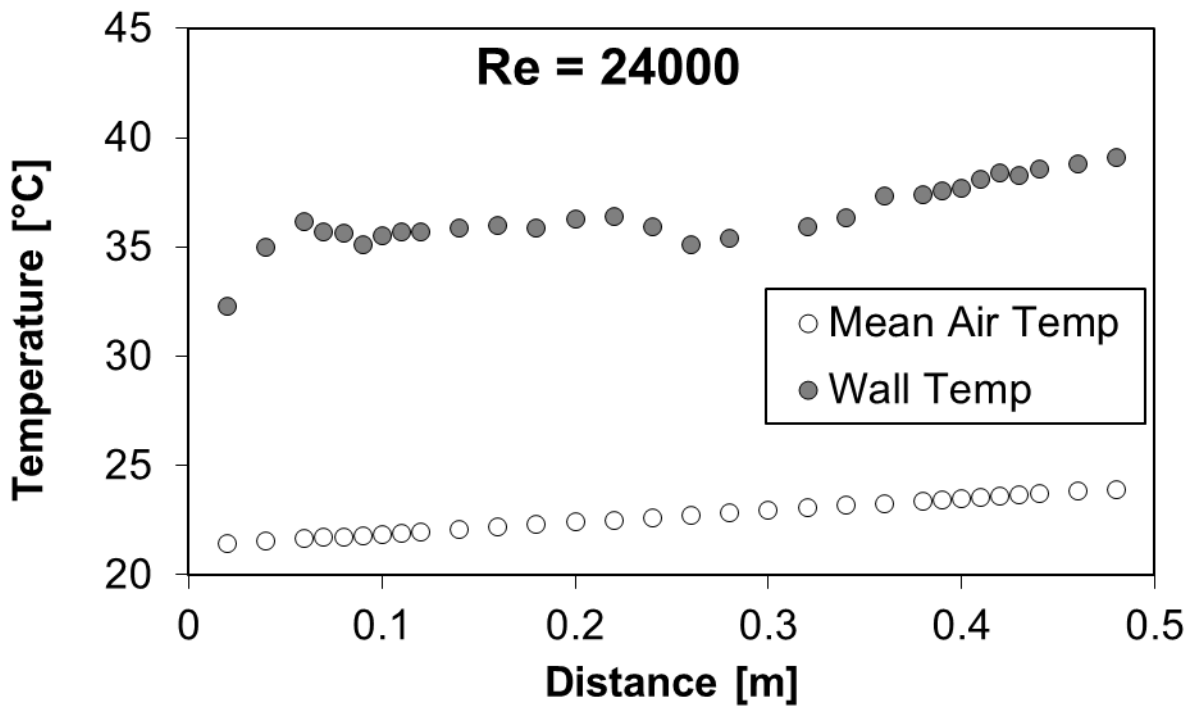


Figure F.64: Wall and mean air temperatures for mesh 2.3 under one-heated wall boundary condition at Re = 24 000

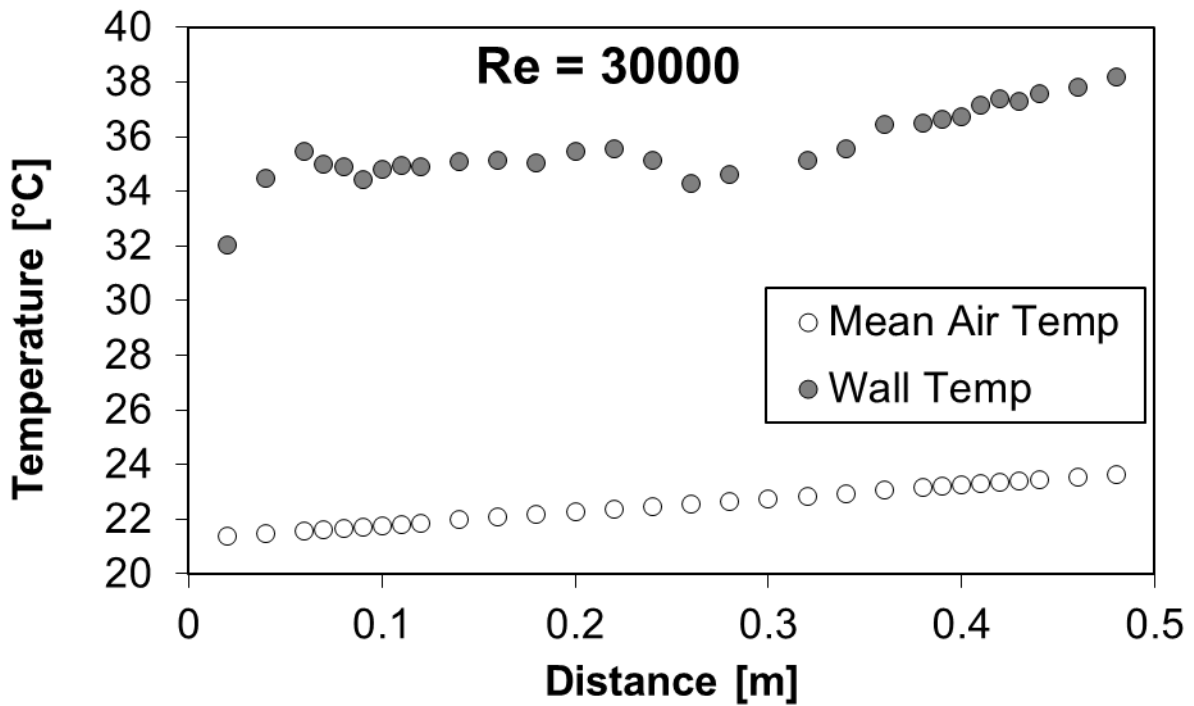


Figure F.65: Wall and mean air temperatures for mesh 2.3 under one-heated wall boundary condition at Re = 30 000

The variation in wall temperature could be due to the variation of heat flux across the channel. The heating pad was glued with epoxy glue which could have affected the heat transfer coefficient. The change in wall temperature around the centre point of the test section can also be attributed to the change in heat flux due to the joint of the two heating pads.